

E9727
8/31/95

NASA Conference Publication 10174

Third International Microgravity Combustion Workshop

*Proceedings of a workshop
hosted by NASA Lewis Research Center
Cleveland, Ohio
April 11-13, 1995*



Third International Microgravity Combustion Workshop

*Proceedings of a workshop sponsored by
NASA Headquarters
Microgravity Science and Applications Division;
organized by the Microgravity Combustion Discipline Working Group;
and hosted by NASA Lewis Research Center,
Space Experiments Division;
held at the Cleveland Airport Marriott Hotel
April 11-13, 1995*



National Aeronautics and
Space Administration

Office of Management

**Scientific and Technical
Information Program**

1995

Preface

The Third International Microgravity Combustion Workshop, hosted by NASA's Microgravity Research Program and its group of external combustion science experts known as the Combustion Discipline Working Group, was held in Cleveland, Ohio on April 11-13, 1995. The 230 attendees from more than 10 countries participated in 70 technical presentations that described the objectives, progress, and plans for research endeavors in the following topical areas in microgravity combustion science: droplet combustion, ignition and flame spread, combustion synthesis, fire safety, combustion diagnostics, diffusion flames, and premixed gases. The number of participants represents a 40% increase over the previous workshop held in 1992, despite reduced advertising.

Distinguishing this workshop from its predecessor workshops, among other things, were the following:

- International participation and research activities climbed sharply, with many experiments being conducted in the Japanese 10 second drop facility, the European Space Agency's drop tower and low-gravity aircraft, NASA's low-gravity facilities and aircraft. Also noteworthy were the first combustion experiments on Russia's *Mir* space station.
- Spaceflight combustion experimental results since the previous workshop in 1992 were described with 4 different experiments on the Shuttle, 1 on a sounding rocket, and 1 on the Russian *Mir* space station having been operated successfully.
- The magnitude of NASA's program has expanded by more than a factor of 2 in terms of the number of ground-based and spaceflight investigations.
- Especially noteworthy was that nearly all of the investigators, including those newly funded, had already obtained some low-gravity experimental data or advanced low-gravity models for comparison to or as explanation of experimental observations.

A bibliography of more than 500 publications and conference papers in microgravity combustion science was given to each participant. This bibliography and its updates are presently available on the Internet, at "http://www.lerc.nasa.gov/Other_Groups/MCEP". In addition, a written summary (NASA TM106858) and video summaries of the following were provided to participants: operations and capabilities of NASA's drop towers and low-gravity aircraft, capabilities of NASA's spaceflight combustion hardware, and highlights of NASA-sponsored combustion science experiments in microgravity environments. This information was provided to educate the scientific research community on these subjects so that they may successfully propose and develop the next generation of experiments and models in microgravity combustion science. These summaries are available by contacting me at MS 500-115; NASA Lewis Research Center; 21000 Brookpark Rd; Cleveland, OH 44135.

Howard D. Ross

Preceding Page Blank

TABLE OF CONTENTS

<u>SESSION</u>	<u>Page</u>
PREFACE	iii
<i>Keynote</i>	
Overview: NASA Microgravity Combustion Science Program Merrill K. King, NASA-Headquarters	3
Solid Surface Combustion Experiment Flame Spread in a Quiescent, Microgravity Environment: Implications of Spread Rate and Flame Structure Matthew Bundy, Jeff West, Peter C. Thomas, Subrata Bhattacharjee, San Diego State University; Lin Tang and Robert A. Altenkirch, Mississippi State University; Kurt Sacksteder, NASA-Lewis	11
Microgravity Smoldering Combustion on the USML-1 Space Shuttle Mission Dennis P. Stocker and Sandra L. Olson, NASA-Lewis; Jose L. Torero and A. Carlos Fernandez-Pello, University of California-Berkeley	19
The USML-1 Wire Insulation Flammability Glovebox Experiment Paul S. Greenberg and Kurt R. Sacksteder, NASA-Lewis; Takashi Kashiwagi, NIST	25
Candle Flames in Microgravity Daniel L. Dietrich and Howard D. Ross, NASA-Lewis; James S. T'ien, Case Western Reserve University	31
Flame Spread Across Liquids Howard D. Ross, NASA-Lewis; Fletcher J. Miller, Case Western Reserve University; David Schiller and William Sirignano, University of California-Irvine	37
<i>Droplets and Aerosols</i>	
Multicomponent Droplet Combustion and Soot Formation in Microgravity C. Thomas Avedisian, Cornell University	47
The Effects of Sooting in Droplet Combustion Kyeong-Ook Lee, Kirk Jensen, Mun Young Choi, University of Illinois-Chicago	53
Combustion of Interacting Droplet Arrays in a Microgravity Environment Daniel L. Dietrich, NASA-Lewis	59
The Effects of Detailed Chemistry and Transport on Microgravity Droplet Combustion A. J. Marchese, J. C. Lee, T. J. Held, F. L. Dryer, Princeton University	65
High Pressure Droplet Burning Experiments in Reduced Gravity Christian Chauveau and Iskender Gökalp, Centre National de la Recherche Scientifique	71

Spray Combustion at Normal and Reduced Gravity in Counterflow and Co-Flow Configurations	
Alessandro Gomez and Gung Chen, Yale University	77
Japan's Research on Droplet and Droplet Array Combustion	
Michikata Kono, University of Tokyo	83
Japan's Research on Particle Clouds and Sprays	
Jun'ichi Sato, Ishikawajima-Harima Heavy Industries	89
Combustion of Two-Component Miscible Droplets in Reduced Gravity	
Benjamin D. Shaw, Israel Aharon, James W. Gage, University of California-Davis; Andrew J. Jenkins and Thomas J. Kahoe, NASA-Lewis	95
High-Pressure Combustion of Binary Fuel Sprays	
Masato Mikami and Michikata Kono, University of Tokyo, Jun'ichi Sato, Ishikawajima-Harima Heavy Industries; Daniel L. Dietrich, NASA-Lewis; Forman A. Williams, University of California-San Diego	103
Studies of Droplet Burning and Extinction	
Forman A. Williams, University of California-San Diego	109
Combustion of a Polymer (PMMA) Sphere in Microgravity	
Jiann C. Yang and Anthony Hamins, NIST	115
<i>Metals, Combustion Synthesis, and Fire Safety</i>	
Ignition and Combustion of Bulk Metals Under Elevated, Normal and Reduced Gravity Conditions	
Angel Abbud-Madrid, Melvyn C. Branch, John W. Daily, University of Colorado	123
Internal and Surface Phenomena in Metal Combustion	
Edward L. Dreizin, AeroChem Research Laboratories; Irina E. Molodetsky and Chung K. Law, Princeton University	129
Effect of Pressure on a Burning Solid in Low-Gravity	
Jeffrey S. Goldmeer and James L. T'ien, Case Western Reserve University; David L. Urban, NASA-Lewis	135
Microgravity Combustion of Dust Clouds: Quenching Distance Measurements	
S. Goroshin, H. Kleine, J. H. S. Lee, D. Frost, McGill University	141
Thermal Degradation of Polytetrafluoroethylene in Tube Reactors	
J. Thomas McKinnon and H. M. Duan, Colorado School of Mines	147
Filtration Combustion: Smoldering and SHS	
Bernard J. Matkowsky, Northwestern University	153

Combustion and Structure Formation in SHS Processes under Microgravity Conditions (SHS Plans for Microgravity Experiments)	
A. G. Merzhanov, Institute for Structural Macrokinetics	159
Combustion Synthesis of Ceramic-Metal Composite Materials in Microgravity	
John Moore, Colorado School of Mines	165
Self-Propagating High-Temperature Synthesis of High Porosity Foam Materials in Microgravity	
Alexander S. Shteinberg and Vladimir A. Scherbakov, Institute for Structural Macrokinetics	171
Smoke Detection in Low-G Fires	
David L. Urban, DeVon W. Griffin, NASA-Lewis; Melissa Y. Gard, NASA-Marshall, Michael Hoy, NASA-Johnson	175
The Effect of Gravity on the Combustion Synthesis of Ni-Al and Ni₃Al-TiB₂ Composites from Elements	
Arvind Varma, Hu Chun Yi, Paul J. McGinn, University of Notre Dame	181
<i>Ignition and Flame Spread</i>	
Low Velocity Opposed-Flow Flame Spread in a Transport-Controlled Environment: DARTFire	
Jeff West, Pete Thomas, Ruian Chao, Subrata Bhattacharjee, San Diego State University; Lin Tang and Robert A. Altenkirch, Mississippi State University; Sandra L. Olson, NASA-Lewis	189
Fire Safety Experiments on <i>Mir</i> Orbital Station	
S. D. Egorov, A. Yu Belayev, L. P. Klimin, V. S. Voiteshonok, A. V. Ivanov, Keldysh Research Institute of Thermal Processes; A. V. Semenov, E. N. Zaitsev, E. V. Balashov, T. V. Andreeva, RKK "Energia"	195
Research on Ignition and Flame Spread of Solid Materials in Japan	
Kenichi Ito and Osamu Fujita, Hokkaido University	201
Ignition and Subsequent Transition to Flame Spread in a Microgravity Environment	
Takashi Kashiwagi, Kevin McGrattan, Howard Baum, NIST	207
Premixed Atmosphere and Convection Influences on Flame Inhibition and Combustion (PACIFIC)	
Paul D. Ronney, University of Southern California	213
Flame Spread over Solid Fuel in Low-Speed Concurrent Flow	
James S. T'ien, Ching-Biau Jiang, Richard D. Pettegrew, Case Western Reserve University; Kurt R. Sacksteder and Paul S. Greenberg, NASA-Lewis; Paul Ferkul, Analex Corporation	219

On the Effect of Pressure, Oxygen Concentration, Air Flow and Gravity on Simulated Pool Fires	
J. L. Torero, J. M. Most, P. Joulain, Université de Poitiers	227
Interactions Between Flames on Parallel Solid Surfaces	
David L. Urban, NASA-Lewis	233
Triple Flames in Microgravity Flame Spread	
Indrek S. Wichman, Michigan State University	239
<i>Combustion Diagnostics</i>	
Laser Doppler Velocimetry and Full-Field Soot Volume Fraction: Measurements in Microgravity	
Paul S. Greenberg, NASA-Lewis	247
Full Field Gas Phase Velocity Measurements in Microgravity	
DeVon W. Griffin, NASA-Lewis; William Yanis, NYMA, Inc.	253
Diagnostics in Japan's Microgravity Experiments	
Toshikazu Kadota, University of Osaka Prefecture	257
An Innovative Approach to the Development of a Portable Unit for Analytical Flame Characterization in a Microgravity Environment	
Mark A. Dubinskiy, Mohammed M. Kamal, Prabhakar Misra, Howard University	263
Development of Advanced Diagnostics for Characterization of Burning Droplets in Microgravity	
Subramanian V. Sankar, Dale H. Buermann, William D. Bachalo, Aerometrics, Inc.	269
Quantitative Measurement of Oxygen in Microgravity Combustion	
Joel A. Silver, Southwest Sciences, Inc.	279
Development and Applications of Laser-Induced Incandescence	
Randy L. Vander Wal, NYMA, Inc.; Daniel L. Dietrich, NASA-Lewis; Zhiquang Zhou and Mun Y. Choi, University of Illinois-Chicago	285
Qualitative and Quantitative Imaging in Microgravity Combustion	
Karen J. Weiland, NASA-Lewis	291
Laser Diagnostics for Microgravity Droplet Studies	
Michael Winter, United Technologies Research Center	297
An Imaging Spectrometer for Microgravity Application	
Wallace K. Wong, SSG, Inc.	303

Gaseous Diffusion Flames

Effects of Energy Release on Near Field Flow Structure of Gas Jets

Ajay K. Agrawal and Subramanyam R. Gollahalli, University of Oklahoma; DeVon Griffin, NASA-Lewis 311

Radiant Extinction of Gaseous Diffusion Flames

Arvind Atreya, Sanjay Agrawal, Tariq Shamim, Kent Pickett, University of Michigan; Kurt R. Sacksteder, NASA-Lewis; Howard R. Baum, NIST 319

Characteristics of Transitional and Turbulent Jet Diffusion Flames in Microgravity

M. Yousef Bahadori and James F. Small, Jr., Science Applications International Corporation; Uday G. Hegde, NYMA, Inc.; Liming Zhou, Analex Corporation; Dennis P. Stocker, NASA-Lewis 327

Dynamic Response of a Pulsed Burke-Schumann Diffusion Flame

Jyh-Cherng Sheu and Lea-Der Chen, University of Iowa; Dennis P. Stocker, NASA-Lewis 333

Flame-Vortex Interactions Imaged in Microgravity

James F. Driscoll, Werner J. A. Dahm, Martin Sichel, University of Michigan 339

Effects of Gravity on Sheared and Nonsheared Turbulent Nonpremixed Flames

S. Elghobashi, Y. Y. Lee, R. Zhong, University of California-Irvine 345

Laminar Soot Processes

P. B. Sunderland, K.-C. Lin, G. M. Faeth, University of Michigan 351

Unsteady Planar Diffusion Flames: Ignition, Travel, Burnout

F. Fendell and F. Wu, TRW Space & Electronics Group 357

Three-Dimensional Flow in a Microgravity Diffusion Flame

Jean Hertzberg, University of Colorado; Mark Linne, Colorado School of Mines 363

Effect of CF₃H and CF₃Br on Laminar Diffusion Flames in Normal and Microgravity

B. A. VanDerWege, Michael T. Bush, Simone Hochgreb, Massachusetts Institute of Technology; Gregory T. Linteris, NIST 369

Detailed Modeling Analysis for Soot Formation and Radiation in Microgravity Gas Jet Diffusion Flames

Jerry C. Ku and Li Tong, Wayne State University; Paul S. Greenberg, NASA-Lewis 375

Structure and Dynamics of Diffusion Flames in Microgravity

Moshe Matalon, Northwestern University 381

Premixed Gases

Modeling of Microgravity Combustion Experiments

John Buckmaster, University of Illinois 389

Coupling of Wrinkled Laminar Flames with Gravity	
Benoit Bédard, Larry W. Kostiuk, Robert K. Cheng, Lawrence Berkeley Laboratory	395
Aerodynamic, Unsteady, Kinetic, and Heat Loss Effects on the Dynamics and Structure of Weakly-Burning Flames	
Fokion N. Egolfopoulos, University of Southern California	401
Unsteady Numerical Simulations of the Stability and Dynamics of Flames	
K. Kailasanath, G. Patnaik, E. S. Oran, Naval Research Laboratory	409
On Burner-Stabilized Cylindrical Premixed Flames in Microgravity	
James A. Eng, Delin Zhu, Chung K. Law, Princeton University	415
Premixed Turbulent Flame Propagation in Microgravity	
S. Menon, J. Jagoda, R. Sujith, Georgia Institute of Technology	421
Japan's Research on Gaseous Flames	
Takashi Niioka, Tohoku University	427
Excitable Dynamics in High-Lewis Number Premixed Gas Combustion at Normal and Microgravity	
Howard Pearlman, NASA-Lewis/NRC	433
Structure of Flame Balls at Low Lewis-number (SOFBALL)	
Paul D. Ronney, University of Southern California	439
Numerical Modeling of Flame-Balls in Fuel-Air Mixtures	
Mitchell D. Smooke and Alexandre Ern, Yale University	445
<i>Germany's Five-Year Space Plan</i>	
Germany's Five-Year Space Plan	
Christian Eigenbrod, ZARM	453
<i>Session Summaries</i>	
Session Chair Report: Parallel Session I: Droplets and Aerosols	
Chung K. Law, Princeton University	461
Session Chair Report: Parallel Session I: Metals, Combustion Synthesis, and Fire Safety	
Robert A. Altenkirch, Mississippi State University	463
Session Chair Report: Parallel Session II: Ignition and Flame Spread	
Raymond Friedman, Independent	466
Session Chair Report: Parallel Session II: Combustion Diagnostics	
Jack B. Howard, Massachusetts Institute of Technology	467

Session Chair Report: Parallel Session III: Gaseous Diffusion Flames

Gerard M. Faeth, University of Michigan 469

Session Chair Report: Parallel Session III: Premixed Gases

Mitchell D. Smooke, Yale University 471

ATTENDANCE LIST 473

AUTHOR INDEX 493

Keynote

Preceding Page Blank

OVERVIEW: NASA MICROGRAVITY COMBUSTION SCIENCE PROGRAM

Merrill K. King
NASA Headquarters, Code UGS
Washington, DC 20546

INTRODUCTION

Combustion is a key element of many critical technologies used by contemporary society. For example, electric power production, home heating, surface and air transportation, space propulsion, and materials synthesis all utilize combustion as a source of energy. Yet, although combustion technology is vital to our standard of living, it poses great challenges to maintaining a habitable environment. For example, pollutants, atmospheric change and global warming, unwanted fires and explosions, and the incineration of hazardous wastes are major problem areas which would benefit from improved understanding of combustion. Thus, combustion phenomena have an unusually large impact on major problems facing us today. The main goals of combustion science are: (1) to understand, from a fundamental perspective, the interactions between fluid dynamics, scalar transport, thermodynamics, and chemical kinetics making up combustion processes, and; (2) to provide predictive and design capabilities to enable and enhance combustion energy utilization and fire safety.

RATIONALE FOR MICROGRAVITY COMBUSTION STUDIES

Effects of gravitational forces on earth impede combustion studies more than they impede most other areas of science. Combustion intrinsically involves the appearance of high-temperature gases whose low density triggers buoyant motion, vastly complicating the execution and interpretation of experiments. The effects of buoyancy are so ubiquitous that we often do not appreciate the enormous negative impact that they have had on the rational development of combustion science. Perversely, the effects of buoyancy are strongest in the highest temperature regions of flames, where most of the chemical reactions occur. This causes these reaction zones, where current understanding is most limited, to collapse into very thin sheet-like regions not resolvable by existing or anticipated instrumentation. Buoyant motion also triggers the onset of turbulence, yielding unsteady effects as an additional complication. Finally, buoyancy causes particles and drops to settle, inhibiting studies of heterogeneous flames important to furnace, incineration and power generation technologies. Thus, effects of buoyancy have seriously limited our capabilities to carry out experiments needed to develop an understanding of flame phenomena.

Microgravity offers potential for major gains in combustion science understanding in that it offers unique capability to establish the flow environment rather than having it dominated by uncontrollable (under normal gravity) buoyancy effects, and through this control extend the range of test conditions that can be studied. For example, turbulent combustion is a crucial fundamental problem of combustion science since most practical flames are turbulent. In this area, powerful approaches (laminar flamelet theories) for treating coupling between fluid motion and combustion chemistry have been developed; these are promising for providing a tractable representation of turbulent combustion. The extension of laminar flamelet theories to predict fully turbulent flames cannot presently be fully exploited, however, due to limitations in our knowledge base caused by the interferences of buoyancy in laminar flame studies. Microgravity provides an opportunity to eliminate these interferences and, thus, markedly advance our capability to address turbulent combustion phenomena. Also, through removal of unwanted buoyant convection via use of microgravity, soot and pollutant production can be better controlled, and mechanisms leading to their formation, aggregation, and oxidation studied in a planned, scientific fashion. In addition to fundamental studies, ground and shuttle-based microgravity combustion experiments have been motivated by concerns about spacecraft fire safety. Findings thus far suggest that fire signatures—heat release, smoke production, flame visibility and radiation—will be quite different in space from our Earthbound experience.

One approach to defining the utility of the microgravity combustion program is through definition of desirable benefits, key scientific barriers to achievement of such benefits, and how microgravity studies can be utilized to overcome these barriers. One goal of combustion research is reduction of combustion-generated pollutants which pollute the atmosphere and lead to global warming. Barriers to progress in this area include lack of understanding of reaction, pyrolysis, and devolatilization kinetics, of soot nucleation, growth, and oxidation processes, of flame stabilization mechanisms, and of kinetic-transport interactions; microgravity research can contribute to overcoming these barriers by providing increased spatial resolution through use of larger length scales which cannot be achieved at normal gravity without confounding buoyancy effects. Another potential benefit of combustion research is reduction of fire and explosion hazards, which result in large annual losses in lives and property. Technological barriers here include lack of understanding of flammability limit mechanisms, ignition limit mechanisms, smolder-to-fire transition, and fire growth processes; microgravity studies can contribute significantly here by elimination of the intrusion of buoyancy effects which obscure these fundamental phenomena under normal gravity conditions. With regard to questions of fire safety on space platforms, it has been conclusively shown that ignition and flamespread of materials is considerably different in microgravity and normal gravity; in addition, the nature of soot produced in the two environments differs sufficiently to cast doubt on applicability of fire detectors optimized for normal gravity operation in the microgravity environment.

Another goal is development of improved hazardous waste incineration processes, currently hindered by lack of understanding of reaction pathways leading to pollutants and toxic products; microgravity can help by providing improved spatial resolution, long controllable residence times, and elimination of settling of condensed phase species. Still another objective is development of increased efficiency of conversion of chemical energy stored in fuels to useful heat and work in practical combustion devices; progress is hampered under normal gravity conditions by lack of understanding of soot production processes, turbulence, flame interactions, droplet vaporization, near-critical behavior, and very fuel-rich or fuel-lean combustion. Microgravity is useful here in providing controllable residence times, reduction of turbulence scales to allow direct model comparison, provision of truly one-dimensional geometries (allowing meaningful comparison of tractable models with experimental data), and general simplification of experiments. Production of improved materials via combustion synthesis is an important development area today; barriers to progress include lack of understanding of heterogeneous kinetics and of processes leading to improved structural ordering and infiltration of materials in composites; a microgravity environment can help here by eliminating sedimentation (which leads to particle agglomeration) and by eliminating gravity-induced flow through pores in the developing structure.

Last, but certainly not least, microgravity combustion research can lead to fundamental knowledge of direct use to combustion science textbooks and practical handbooks by allowing direct experimental verification of theories/models in a much simplified geometry possible only in the absence of buoyancy, which destroys true one-dimensionality.

CURRENT MICROGRAVITY COMBUSTION PROGRAM

The Microgravity Combustion Research Program currently includes research in the areas of Premixed Gas Flames, Gaseous Diffusion Flames, Droplet/Spray Combustion, Surface Combustion, Smoldering, and Combustion Synthesis. 39 awards were made in 1994 to investigators responding to a 1993 Microgravity Combustion NASA Research Announcement (NRA); of these, 6 were in the Flight Definition area, while the remainder were for Ground-Based (R&A) research. In addition, 8 Flight and Flight Definition programs were carried over from previous selection. Of this total of 47 programs, 6 are in the area of premixed gas flames, 11 address gaseous diffusion flames, and 2 have aspects of both categories. 11 programs are directed at droplet or spray combustion, 11 at surface combustion, 2 at smoldering combustion, and 2 at combustion synthesis, with the remaining 2 programs falling into multiple categories. A topical breakout (somewhat arbitrary) of programs, listed by Principal Investigator, is given in Table 1. (This list includes Shuttle Glovebox Experiments spun off R&A programs and thus adds to more than 47 entries.) In addition, a number of advanced diagnostic instrumentation technologies are being developed for various experimental studies in the limited confines available for most microgravity experiments; these include: (1) Soot temperature measurements using pyrometric approaches; (2) Rainbow schlieren for measurement of temperature distributions in liquid and gas phases; (3) Planar 2D temperature and CH and OH concentration measurements via Rayleigh scattering and Laser-Induced Fluorescence; (4) Light

sheet flow visualization and/or velocimetry; (5) Laser Doppler Velocimetry; (6) Liquid surface temperature and vapor phase concentration measurements via exciplex fluorescence; (7) Determination of CH₄, CO₂, and H₂O concentrations via line absorption techniques; (8) Planar Laser-Induced Fluorescence for determination of flame front position; (9) Particle imaging velocimetry; (10) Liquid phase thermometry and fluorescence of aromatics for evaluation of droplet surface temperature and internal flow; (11) Diode laser wavelength modulation spectroscopy for quantitative molecular oxygen concentration measurements; (12) Compact laser-diode CCD array for measuring instantaneous radial variations in temperature fields within a burning droplet and in the gas-phase, with simultaneous measurement of droplet size and regression rate; and, (13) Laser-induced incandescence for measurement of soot volume fractions.

In the area of premixed gas combustion, we currently support experimental and modeling studies of the effects of gravity on flammability limits, flame stability and extinction, and flame structure and shape. In particular, we are funding studies of the effects of radiative heat losses on premixed flames in microgravity environments where such effects dominate flammability limits and near-limit flame structure. Modeling activities being supported include simplified analytical approaches aimed at elucidating mechanisms and detailed numerical analysis aimed at quantifying them. In addition, we are funding microgravity studies of low flow premixed turbulent flames which cannot be studied in normal gravity environments due to strong buoyancy-induced flows. From these studies, we hope to resolve the effects of buoyant convection on flammability limits and define mechanisms which control flammability limits and contribute to flame stability and shape. To date, several discoveries, possible only via microgravity experiments, have been made in this area; these include self-extinguishing flames, flameballs, flame cylinders, and dilution-enhanced flammability, all important as regards hazard control and basic combustion science.

Activities in the area of gaseous diffusion flames include study of the effects of diffusion-flame structure (quite different in normal gravity and microgravity) on soot formation in diffusion flames, effects of altered relationships between chemical kinetic time scales and flow time scales accompanying change from a normal gravity environment to a microgravity environment on such parameters as flammability limits and burning rates, and effects of buoyancy on the structure of gas-jet diffusion flames in laminar, transition, and turbulent flow regimes. Within this area, the first data on turbulent and transition gasjet flames in microgravity have recently been obtained, offering potential toward development of understanding of turbulent combustion phenomena, of widespread practical interest. In addition, data on soot production in microgravity flames are being obtained for use in developing soot kinetics models, with eventual potential application to development of effective strategies for control of soot formation in practical burners.

In the area of combustion of fuel droplets, particles, and sprays, we are supporting fundamental studies of microgravity combustion of single-component and multicomponent truly spherical droplets. In addition, we support studies of the combustion of ordered arrays of fuel droplets in a microgravity environment and of sprays produced by electrostatic dispersion for improved understanding of the interactions of combustion of individual droplets in sprays. Several new droplet combustion phenomena have been revealed in droptower microgravity testing. From these studies, greatly improved understanding of spray combustion processes should result, leading to major improvements in design of combustors utilizing liquid fuels.

Currently, we support several experimental and analytical studies of the spread of flames across solid and liquid fuel surfaces, both in quiescent oxidizer environments and with low velocity flows in the same direction as and opposed to the flame spread direction. This research has revealed major differences in ignition and flame spreading characteristics of liquid and solid fuels under microgravity versus normal gravity conditions. Benefits of development of better understanding of the fundamental processes controlling flamespread over solid or liquid fuels lie mainly in the area of fire safety. At this time, we are also supporting experimental and analytical studies of smoldering combustion. Development of better understanding of the fundamental mechanisms of such combustion should have significant impact on prevention of unwanted fires both on the ground and in space.

A relatively new area of combustion is the combustion synthesis of materials; one subcategory of particular interest is referred to as self-deflagrating high temperature synthesis (SHS). Gravity fields can have major impact on this process, through buoyancy-induced flow effects on heat transport processes and through gravity-driven flow of liquid-phase intermediates through a porous solid matrix prior to cooldown/freezing of the product behind the reaction front. Since the composition and particularly the crystal morphology of the final product (which strongly affects its properties) tend to be very sensitive to the temperature-time history seen during the passing of the SHS combustion wave, these gravity-dependent effects can have major effects on the product produced.

To date, our work in microgravity combustion has demonstrated major differences in structures of various types of flames from that seen in normal gravity. Besides the practical implications of these results to combustion efficiency (energy conservation), pollutant control (environmental considerations), and flammability (fire safety), these studies establish that better mechanistic understanding of individual processes making up the overall combustion process can be obtained by comparing of results gathered in microgravity and normal gravity tests, with potential for major improvements in design of combustion processes and hardware for use on earth as well as in space.

Although most work to date has been centered on ground-based studies, involving analytical modeling activities and testing in drop towers at NASA/Lewis and in aircraft flying parabolic trajectories, limited testing has been carried out on Sounding Rockets and the Shuttle. During 1994 and early 1995, the seventh and eighth flights of the Solid Surface Combustion Experiment (SSCE) were completed during the STS-63 and STS-64 missions, with samples of PMMA being burnt in various oxygen-nitrogen atmospheres under quiescent conditions. Computer image enhancement techniques are being employed to analyze the film records of these experiments, described in more detail in another paper at this meeting, with the images and recorded temperature data being compared with computer simulations of the flame spreading process to provide new insights into the flame spreading process.

The first Sounding Rocket test on the Spread Across Liquids (SAL) Program was successfully launched in November, 1994. This flight provided approximately six minutes of microgravity time (during which three burns were accomplished) for investigation of the flame spread characteristics across a deep pool of liquid fuel in a microgravity environment, with particle imaging velocimetry, rainbow schlieren, and flamespread data being obtained for comparison with model predictions.

The Microgravity Smoldering Combustion Experiment will fly for the first time as a Getaway Special Canister (GASCAN) payload on STS-69 in mid-1995. In addition, the second Sounding Rocket flight of the Spread Across Liquids program will take place in late 1995, as will the first Sounding Rocket test on the Diffusive and Radiative Transport in Fires (DARTFire) program. Major efforts are being expended on development of flight hardware for the Droplet Combustion Experiment (DCE), the Study of Flameballs at Low Lewis Numbers Experiment (SOFBALL), and the Laminar Soot Processes in Flames Experiment (LSP) all scheduled to fly on MSL-1 in early 1997. In addition, the Turbulent Gas Jet Diffusion Flame experiment (TGDF) is tentatively scheduled to go to flight in mid-1996. All of these programs are also described in other papers being presented at this meeting.

An experiment on Fiber-Supported Droplet Combustion (FSDC) is currently planned for the Shuttle Glovebox on USML-2 in September, 1995, while three other Glovebox investigations, Forced Flow Flame Spreading Test (FFFT), Comparative Soot Diagnostics (CSD), and Radiative Ignition and Transition to Flame Spread Investigation (RITSI) are scheduled for flight on USMP-3 in early 1996. Of the six new Flight Definition Programs resulting from the 1993 Microgravity Combustion NRA, four are anticipated to move forward to their Science Concept Reviews in 1995.

UPCOMING MICROGRAVITY COMBUSTION NRA

In the Microgravity Combustion Program at NASA, investigators are selected in response to a NASA Research Announcement (NRA), issued once every two years and are placed either in the Ground-based Category or in the Flight Definition Category. (At this time, it is anticipated that an NRA will be released

toward the end of May, 1995; it is suggested that potential proposers contact the author if they wish to be placed on the distribution list for this NRA.) This selection is done with the aid of peer review panels, with each proposal being reviewed in detail by at least three panel members, followed by discussion and rating of the proposal by an entire panel. From the Flight Definition category, the programs may proceed, following passing a peer-reviewed Science Concept Review (SCR) and Requirements Definition Review (RDR) and acceptance of a Science Requirements Document (SRD) generated by the Principal Investigator, into the Flight Program. In addition, there is opportunity for Ground-Based investigators to participate as "guest" investigators in Glovebox Experiments on a Space Platform based on internal NASA review of proposals submitted in response to Glovebox Opportunity Announcements. More details on these processes will be presented in handout material to be provided at the meeting. Both experimental and theoretical modeling efforts are supported in the Microgravity Combustion Program. Experimental test beds for microgravity experiments include drop-towers at NASA/Lewis, capable of providing 2.2 to 5 seconds of microgravity time, aircraft flying parabolic trajectories, providing up to twenty seconds of reduced gravity (0.001 to 0.01 g), sounding rockets which supply very low gravity for up to 6-7 minutes, and Shuttle or Space Station facilities of various types, allowing basically unlimited microgravity operating times. In addition, we have participated in cooperative studies with Japanese investigators allowing us access to a 10-second drop tower at Hokkaido, Japan.

Development of criteria for prioritizing combustion subtopics is complex. However, it appears possible to reduce considerations to two major objectives: (1) Making major breakthroughs in understanding the basic processes associated with various combustion processes to permit these processes to be 'laid bare'; and, (2) Defining technology approaches that will lead to major improvements in fuel utilization, pollution minimization, hazards abatement, and production of high-value-added materials via combustion processes. At this point, the Microgravity Combustion Discipline Working Group (DWG) has tentatively ranked three areas as being of highest priority:

- (1) Turbulent reacting flows (turbulent premixed and diffusion flames), chosen because this is considered by most to be the foremost unresolved combustion problem and because most practical flames are turbulent.
- (2) Heterogeneous combustion (both droplets/particles and surfaces), chosen since condensed fuels are heavily utilized and because of fire safety issues.
- (3) Laminar homogeneous gas flames, of importance as regards pollution and hazard control issues, as well as providing an optimum scenario for extraction of fundamental combustion kinetic information.

Future proposals are not limited to these topics; extension to combustion topics not currently included in the Microgravity Combustion program is strongly encouraged to permit us to broaden the program scope.

Beyond the question of prioritization of topic areas lies the development of evaluation criteria for individual programs; such criteria are of particular importance since prioritization in terms of topic areas is not well developed at this time. In this latter area, the following list of criteria is suggested.

1. Is microgravity of fundamental importance to the proposed study?
2. Do the issues addressed by the research have the potential to close major gaps in the understanding of fundamentals of combustion processes?
3. Does the potential exist for identification or elucidation of previously unknown phenomena or interactions between phenomena?
4. Is the project likely to have significant benefits/applications to ground-based as well as space-based operations involving combustion processes?
5. Are the results likely to be broadly useful and lead to further complementary theoretical or experimental studies?
6. Can another project in the area be justified in terms of limited resource allocation?

7. Is the project technologically feasible---are substantial new technological advances required for successful completion?
8. How will this project stimulate research and education in the combustion area?
9. How does the projected cost/benefit ratio of this project compare with those of other projects competing for the same resources?
10. What is the potential of this project in terms of stimulating technological developments which will reach beyond the project itself?
11. Are the project goals consistent with broader public policy objectives such as national economic growth or human welfare?

It appears that the most fruitful approach to achieving meaningful technology gains in processes involving combustion is to concentrate on developing better understanding of the fundamentals of the individual processes involved. With full understanding of the physics and chemistry involved in a given combustion process, including details of the unit processes and their interactions, physically accurate models which can then be used for parametric exploration of new combustion domains via computer simulation can be developed, with possible resultant definition of radically different approaches to accomplishment of various combustion goals. Accordingly, it appears that emphasis should be placed on studies of combustion fundamentals which are not currently well understood. As discussed earlier, normal-gravity conditions have prevented study of many elementary processes which are over-shadowed by processes such as buoyancy; also, gravity-induced settling of particles in two-phase combustion processes and distortion of one-dimensional spherical geometries by buoyancy effects vastly complicate comparisons of theory and experiment, making it difficult to develop mechanistic understanding of unit phenomena making up overall combustion processes. It cannot be emphasized too strongly that our program is dedicated to taking advantage of microgravity to untangle the complications resulting from the influence of normal gravity.

TABLE 1: BREAKOUT OF FUNDED PRINCIPAL INVESTIGATORS BY TOPIC

GASEOUS FLAMES

<u>Analytical</u>	<u>DNS</u>	<u>Structure</u>	<u>Vortices, Wrinkling</u>	<u>Flame Speeds, Limits</u>	<u>Sooting</u>
Kailasanth Matalon Smooke	Elghobashi	Law Menon LD Chen Dietrich/Ross (DEF,GBX) Fendell (DEF) Ronney (F)	Driscoll Cheng Agrawal J Hertzberg Bahadori (F)	Egofopoulos Hochgreb	Ku Faeth (F) Urban (GBX)

DROPLETS, SPRAYS, PARTICLES, DUSTS

<u>Single Drops</u>	<u>Arrays</u>	<u>Sprays</u>	<u>Solid Particles</u>	<u>Droplet Diagnostics</u>	<u>Other</u>
Avedisian Choi (DEF) Shaw Williams (F) Haggard (GBX)	Dietrich	Williams Gomez	Dreizen Yang	Bachalo Winter	Branch Buckmaster

SURFACE COMBUSTION, SMOLDERING, COMBUSTION SYNTHESIS

<u>Flame Spread</u>	<u>Surface Ign. Extinction</u>	<u>Smoldering</u>	<u>SHS</u>	<u>Ultrafine Powders</u>
T'ien (DEF) Silver Wichman Sacksteder (GBX)	Ronney Urban Altenkirch (3,F) Ross (F)	Kashiwagi (GBX,DEF) Matkowsky Fernandez-Pello (F)	Moore Varna	McKinnon

F = Flight Investigation DEF = Flight Definition Study GBX = Glovebox Investigation

Solid Surface Combustion Experiment Flame Spread in a Quiescent, Microgravity Environment Implications of Spread Rate and Flame Structure

Matthew Bundy, Jeff West, Peter C. Thomas, and Subrata Bhattacharjee
Department of Mechanical Engineering
San Diego State University, San Diego, CA 92182-0191

Lin Tang and Robert A. Altenkirch
Department of Mechanical Engineering and
NSF Engineering Research Center for Computational Field Simulation
Mississippi State University, Mississippi State, MS 39762

and
Kurt Sacksteder
NASA Lewis Research Center
Cleveland, OH 44135

Introduction:

A unique environment in which flame spreading, a phenomenon of fundamental, scientific interest, has importance to fire safety is that of spacecraft in which the gravitational acceleration is low compared with that of the Earth, i.e., microgravity. Experiments aboard eight Space Shuttle missions between October 1990 and February 1995 were conducted using the Solid Surface Combustion Experiment (SSCE) payload apparatus in an effort to determine the mechanisms of gas-phase flame spread over solid fuel surfaces in the absence of any buoyancy induced or externally imposed oxidizer flow. The overall SSCE effort began in December of 1984.

The SSCE apparatus consists of a sealed container, approximately 0.039 m^3 , that is filled with a specified O_2 / N_2 mixture at a prescribed pressure. Five of the experiments used a thin cellulosic fuel, ashless filter paper, 3 cm wide by 10 cm long, 0.00825 cm half-thickness, ignited in five different ambient conditions. Three of the experiments, the most recent, used thick polymethylmethacrylate (PMMA) samples 0.635 cm wide by 2 cm long, 0.32 cm half-thickness. Three experiments, STS 41, 40 and 43, were designed to evaluate the effect of ambient pressure on flame spread over the thin cellulosic fuel while flights STS 50 and 47 were at the same pressure as two of the earlier flights but at a lower oxygen concentration in order to evaluate the effect of ambient oxygen level on the flame spread process at microgravity. For the PMMA flights, two experiments, STS 54 and 63, were at the same pressure but different oxygen concentrations while STS 64 was at the same oxygen concentration as STS 63 but at a higher pressure.

Two orthogonal views of the experiments were recorded on 16 mm cine-cameras operating at 24 frames/s. In addition to filmed images of the side view of the flames and surface view of the burning samples, solid- and gas-phase temperatures were recorded using thermocouples. The experiment is battery powered and follows an automated sequence upon activation by the Shuttle Crew.

In this study we separate the SSCE data into two groups according to the fuel type: i) thin cellulose, and ii) thick PMMA. The experimental spread rates are compared with prediction from a number of models in an effort to uncover the important physics that characterize microgravity flame spread. Both steady and unsteady solutions are employed to explore the flame evolution, especially for thick fuels. Finally, the flame structure in downward spread is compared with the microgravity flame structure and modeling results to delineate the difference between the two configurations and the influence of normal gravity.

Mathematical Model:

The mathematical model employed has been reported before [1], so only a brief description is presented here. The conservation equations can be expressed in a generic format as follows:

$$\frac{\partial(\rho\phi)}{\partial t} + \frac{\partial(\rho u\phi)}{\partial x} + \frac{\partial(\rho v\phi)}{\partial y} = \frac{\partial}{\partial x} \left\{ \Gamma_\phi \frac{\partial\phi}{\partial x} \right\} + \frac{\partial}{\partial y} \left\{ \Gamma_\phi \frac{\partial\phi}{\partial y} \right\} + \dot{s}_\phi''' \quad (1)$$

where the terms are explained in Table 1. The ignition source term applies only to the shaded ignition zone of Fig. 1. The Planck mean absorption coefficient, $a_{p,GB}$, calculated from the method of Global Energy Balance [2], accounts for reabsorption of radiation despite the apparent thin optical limit of the radiation source term.

In addition to the conservation equations, the equations of state for density, viscosity and thermal conductivity in the gas phase, a pyrolysis formula based on negligible surface regression and constant solid density for the thick fuel, and variable density and first-order kinetics for the thin fuel are used to complete the formulation.

$$\rho = \frac{P_\infty M_\infty}{RT}; \quad \frac{\mu}{\mu_r} = \frac{\lambda}{\lambda_r} = \sqrt{\frac{T}{T_r}}; \quad \dot{m}_{thin}'' = B_p \rho_s \tau \exp\left(-\frac{T_{a,p}}{T_s}\right);$$

$$\dot{m}_{thick}'' = \left\{ \frac{\rho_s T_s^2 B_p \lambda_s}{T_{a,p} [3.615 \Delta h_v^o + 4.605 c_s (T_s - T_\infty)]} \right\}^{1/2} \exp\left(-\frac{T_{a,p}}{2T_s}\right) \quad (2)$$

The boundary conditions are depicted in Fig. 1. The properties used for thick and thin fuels are: $s = 1.92, 1.185$; $\Delta h_c^o = 25.9, 16.74$ MJ / kg_{fuel}; $B_c = 5.928 \times 10^9, 1.58 \times 10^{11}$ m³ / kg · s; $T_{a,c} = 10.7, 14.04$ kK; $c_g = 1.183, 1.465$ kJ / kg · K; $\lambda_r = 0.086$ W / m · K; $\mu_r = 0.675 \times 10^{-3}$ N · s / m²; $T_r = \frac{T_\infty + T_{ad}}{2} = 1958$ K; $M_\infty = 30$ kg / kmol; $c_s = 1.465, 1.256$ kJ / kg · K; $\Delta h_v^o = 0.941, 0.368$ MJ / kg_{fuel}; $\lambda_s = 0.035, 0.12$ W / m · K; $\rho_s = 1190, 518.7$ kg / m³; $\tau = 3.2, 0.083$ mm; $B_p = 2.282 \times 10^9, 7.8 \times 10^{16}$ s⁻¹; $T_{a,p} = 15.6, 30.0$ kK. The boundary conditions and typical numerical parameters are: $y_{O,\infty} = 0.53$; $P_\infty = 1$ atm; $V_g = 0$ or 1 cm/s; $y_{max} = 100$ mm; $y_{min} = 3.2$ mm; $x_{max} - x_{min} = 200$ mm; Number of grid points 37×90; the time step ranges from 0.01 s to 0.25 s. The ignition volume (ΔV_{ign}) is $1.6 \times 1.6 \times 6.3$ mm³ in each phase.

Results and Discussion:

1. Thin Fuel:

1.1 Spread Rate: The experimental flame spread rates, $V_{f,expt}$, over the thin cellulosic fuel in five different quiescent environments, at three different ambient pressures and two oxygen levels, are plotted in Fig. 2. Superposed on this figure is the prediction from the de Ris theory [3], $V_{f,deRis}$, the prediction from a non-radiative computational model similar to that of Frey and T'ien [4], $V_{f,non-rad}$, and, the prediction from a radiative model [5]. The non-radiative models over-predict V_f by almost a factor of 2 to 3. Moreover, the clear trend seen in the experiments, an increase in V_f with P_∞ , is completely missed by these models. The model with radiation produces the best agreement (within 10%) with experiment.

The near-perfect agreement between the de Ris formula and the non-radiative model needs some explanation. The spread rate is computed using a succession of models in which the major assumptions in the de Ris theory - zero hang-distance (#2), Oseen flow (#3), constant gas density (#4), no wall blowing (#5), infinite-rate chemistry (#6), constant vaporization temperature (#7), constant solid density (#8), constant gas conductivity (#9), and no radiation (#10-#13) - are removed one by one, and the resulting spread rates are plotted in Fig. 3 for two ambient pressures and two V_g 's. On the very left of the abscissa is the prediction from the de Ris formula (#1), and on the extreme right are the data (#14) from the SSCE and literature [6] with the intermediate points being the various mathematical models with increasing complexity. It is clear from this figure that many of the assumptions in the de Ris theory have a canceling affect, and that is why the non-radiative model (#9) produces the same spread rate as the de Ris formula (#1).

Results from four different radiative models (#10: surface re-radiation only; #11: gas radiation only; #12: surface and gas radiation loss; #13: surface and gas radiation with radiation feedback from gas to solid) are also shown in

Fig. 3. With the inclusion of any sort of radiative mechanism, V_f shows a significant decrease, and the observed behavior of V_f with P_∞ is qualitatively reproduced. It is also evident that the radiative effects on spread rate decrease as the ambient pressure is reduced or V_g is increased.

1.2 Flame Structure: Photographs showing the side view of the flame at two different pressures are shown in Figs. 4(a) and 4(b) (see color appendix). Temperature recorded by a thermocouple embedded in the solid and a gas-phase thermocouple 7 mm above the surface are superposed on these photos after converting time into distance assuming the flame to be steady. At higher pressure, the presence of bright soot near the leading edge makes it impossible for the photograph to capture the entire flame image. At 1.0 atm, the flame length seems to correspond to the distance between the two peaks shown by the gas-phase thermocouple. If this is also true at 1.5 atm, the flame size must increase with the ambient pressure, a conclusion predicted from the model with radiation [5].

Another feature that is immediately noticeable in Fig. 4 is the presence of a large, 10 mm long hang-distance [7], the distance between the flame leading edge and the pyrolysis front, with the latter location identified by the surface temperature reaching a plateau following the preheat region. Contrast these flame pictures with that of a downward spreading flame at 1-g shown in Fig. 5. The flame size as well as the hang-distance is much smaller at 1-

g because the diffusion length, $L_g \equiv \frac{\alpha_g}{(V_g + V_f)}$, is only about 0.158 cm ($V_g \approx 20$ cm / s) as opposed to 11.1 cm in the quiescent, microgravity environment.

The dependence of vaporization temperature on pressure and the velocity scale in Figs. 4 and 5 can be qualitatively explained from the correlation developed by Bhattacharjee et al. [8]. The presence of soot in Figs. 4(b) and 5 can be qualitatively explained by the smaller residence time, $t_{res} = \frac{L_g}{(V_g + V_f)}$, at higher P_∞ or V_g .

2. Thick Fuel:

2.1 Ignition Transient for Thick Fuel: For thick PMMA, the ignition transient is more prominent than in the case of the thin cellulosic fuel; it can be divided into the following sequence of events: i) preheating, ii) premixing, iii) ignition, iv) premixed flame propagation, and v) reverse flame propagation. The premixed flame propagation is captured by the unsteady model. The gas-phase thermocouple data, with the thermocouple fixed at $x = 10$ mm, $y = 1$ mm, shows an initial spike at around $t=5$ s (see Fig. 6) as the premixed flame approaches the thermocouple, stops at $x=6$ mm, and then retreats back to $x=3$ mm. The temperature starts rising again as the stabilized spreading flame arrives. The premixed propagation phase has been computationally found to last for a shorter duration with a decrease in E_{ign} and can be completely absent as in the case of thin fuels. The latter conclusion is supported by the lack of the initial spike in the gas-phase thermocouple traces of Fig. 4.

2.2 Unsteady Flame Spread: After the ignition transient is over, the flame, still very small in size, starts spreading in the x-direction. Computed and experimental V_f , plotted against x in Fig. 7, decrease smoothly, and extinction results at high values of x . The steady code also predicts a zero value for V_f as does the de Ris formula. In the experiments, the spread rate decreases with x ; however, self extinguishment was not observed, perhaps because of the short length of fuel over which the spread occurred.

The time of extinction for different ambient conditions in Fig. 7 can be explained if the diffusion time scale,

$t_{diff} \approx \frac{L^2}{\alpha_g}$, is obtained from a fixed imposed length. As pressure is doubled, so is t_{diff} , which may explain why the

50%, 2 atm flame lasts almost twice as long as the 50%, 1 atm flame. The time scale is almost independent of O_2 level; however, because of the higher O_2 level at $t=0$, it takes longer for the near-limit condition to be reached at higher O_2 level.

Conclusions:

Experimental results from the SSCE and computational results from steady and unsteady modeling are presented. It is established that for thin cellulosic fuel the flame spread phenomenon is fairly steady after the initial ignition transients are over. The flame size and the hang distance are much larger in microgravity than in downward flame propagation. The fundamental mechanism behind the striking differences between the 0-g and 1-g flame seems to be the enhancement of radiation heat transfer in the quiescent, microgravity environment because of the large residence time. For thick fuels, a premixed flame propagation during ignition has been captured by the unsteady model as well as the experiments. The models also indicate that the flame spreads with a decreasing spread rate and finally may extinguish even at high oxygen levels.

Acknowledgments: This work was supported by NASA through Contract NAS3-23901.

References:

1. Bullard, D.B., Tang, L., Altenkirch, R.A., and Bhattacharjee S., *Finite-Rate Chemistry in Unsteady Flame Spread Over Solid Fuels in Microgravity*, Adv. Space Research, Vol. 13, No. 7, pp.(7)171-(7)184, (1993).
2. Bhattacharjee, S., and Altenkirch, R.A., *Radiation- Controlled, Opposed-Flow Flame Spread in a Microgravity Environment*, Twenty-Third Symp. (Int.) on Comb., The Comb. Inst., Pittsburgh, pp. 1627-1633, (1990).
3. de Ris, J.N., *Spread of a Laminar Diffusion Flame*, Twelfth Symp. (Int.) on Comb., The Comb. Inst., Pittsburgh, PA, p. 241, (1969).
4. Frey, A.E., and T'ien, J.S., *A Theory of Flame Spread over a Solid Fuel Including Finite-Rate Chemical Kinetics*, Combustion and Flame, Vol. 36, pp. 263-289, (1979).
5. Bhattacharjee, S., Altenkirch, R.A., and Sacksteder, K., *The Effect of Ambient Pressure on Flame Spread Over Thin Cellulosic Fuels in a Quiescent, Microgravity Environment*, Journal of Heat Transfer, To Appear, (1995).
6. Fernandez-Pello, A.C., Ray, S.R., and Glassman, I., *Flame Spread in an Opposed Forced Flow: The Effect of Ambient Oxygen Concentration*, Eighteenth Symp. (Int.) on Comb., The Comb. Inst., Pittsburgh, PA, p. 579, (1981).
7. Bhattacharjee, S., West, J., and Dockter, S., *A Simplified Theory for de Ris Flame over Thin and Thick Fuels*, Combustion and Flame, Accepted, (1995).
8. Bhattacharjee, S., Bhaskaran, K.K., and Altenkirch, R.A., *Effects of Pyrolysis Kinetics on Opposed Flow Flame-spread Modeling*, Combustion Science and Technology, Vol. 100, pp. 163-183, (1994).

Equation	ϕ	Γ_ϕ	\dot{s}_ϕ'''
Mass	1	0	0
x-mom.	u	μ	$-\frac{\partial P}{\partial x}$
y-mom.	v	μ	$-\frac{\partial P}{\partial y}$
Species: Fuel	y_F	λ / c_p	$-B_c \rho_s^2 y_F y_O \exp\left\{-\frac{T_{a,c}}{T}\right\}$
Species: Oxygen	y_O	λ / c_p	$s \dot{s}_F'''$
Species: Nitrogen	y_N	λ / c_p	0
Energy: Gas-Phase	T	λ / c_p	$\frac{\Delta h_c^o \dot{s}_F''' + \dot{q}_{ign}'''}{c_p} - 4a_{p,GB}(T^4 - T_\infty^4)$
Energy: Solid-Phase	T_s	λ / c_p	$\frac{\dot{q}_{ign}'''}{c_s}$

Table 1. Description of the generic terms of Eq. (1).

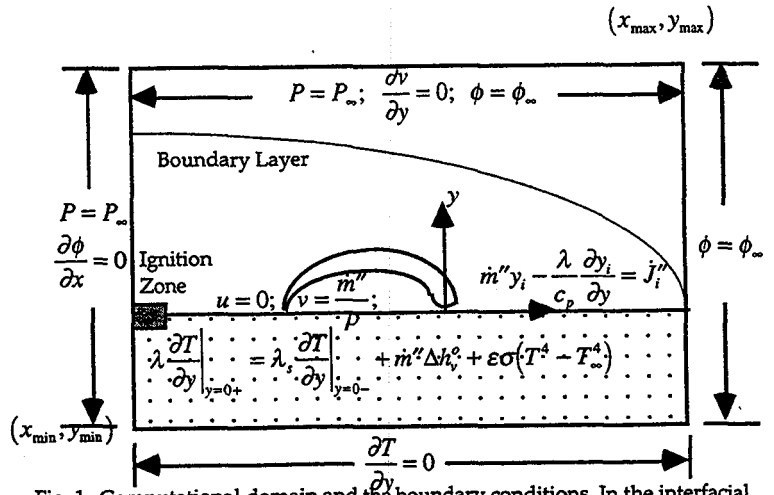


Fig. 1. Computational domain and the boundary conditions. In the interfacial species continuity equation $J_i'' = m''$ for fuel, and $J_i'' = 0$ for others.

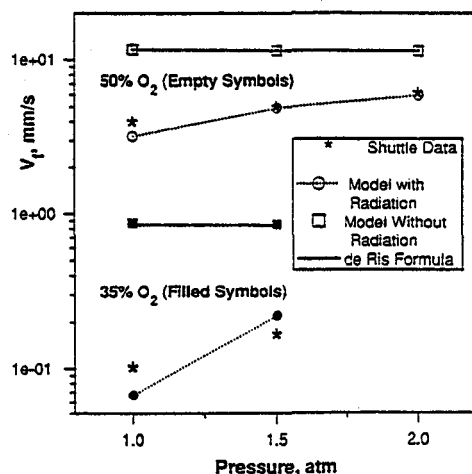


Fig. 2. V_f vs. P_∞ at two different O_2 levels. Data from Space Shuttle experiments, predictions of the de Ris formula, and models with and without radiation.

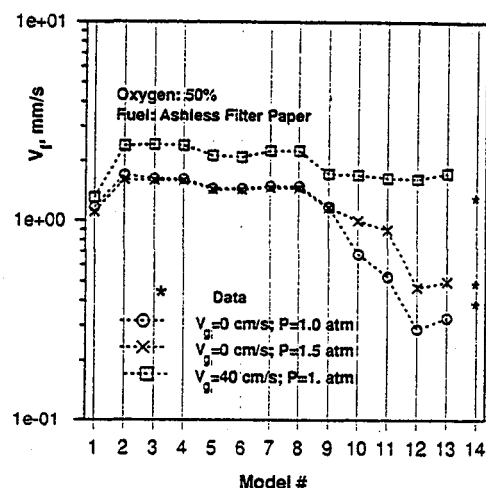


Fig. 3. Model sweep for spread rate. On the left is the de Ris model and on the right are data from the Space Shuttle experiments and literature [6] with intermediate models removing the assumptions in the de Ris theory one by one.

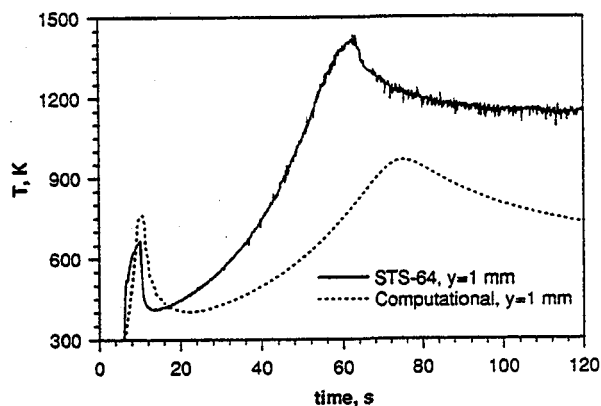


Fig. 6. Temperature recorded by a thermocouple 1 mm away from the surface in flame spread over PMMA. The initial temperature spikes in the Shuttle data (solid line) and the unsteady theory indicate the propagation of a premixed flame during the ignition transient.

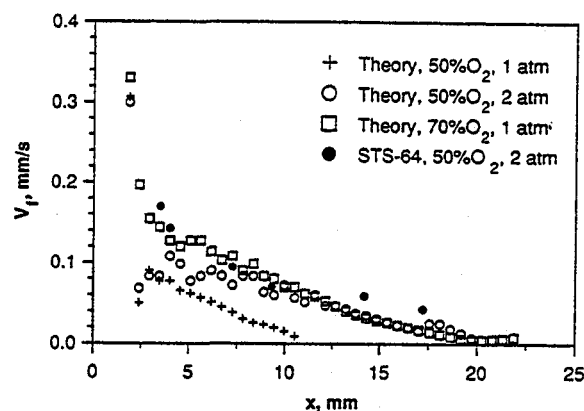
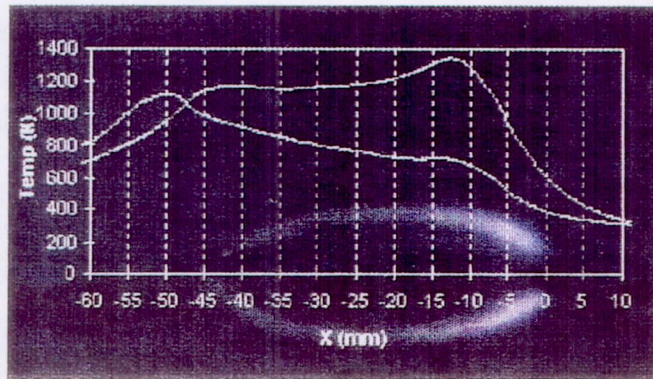
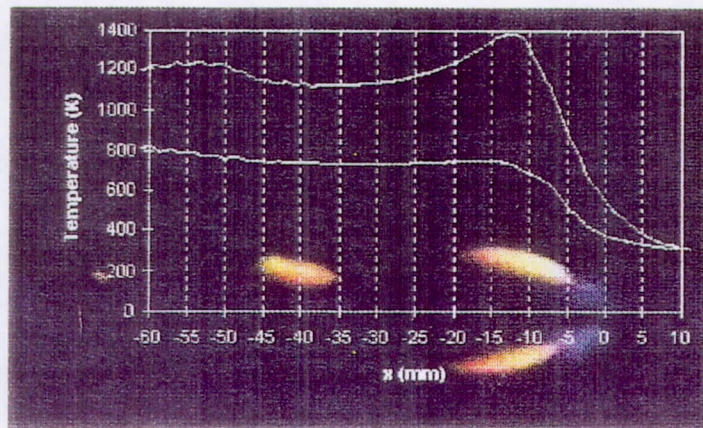


Fig. 7. Unsteady computations of V_f over PMMA for three different ambient conditions showing eventual extinguishment.



(a)



(b)

Fig. 4. Visual side view of the flame spreading over thin fuel at 50% O_2 , and, a) $P_\infty = 1.0$ atm, b) $P_\infty = 1.5$ atm. Superposed are the thermocouple traces, one embedded in the solid and the other in the gas phase, 7 mm away from the surface.

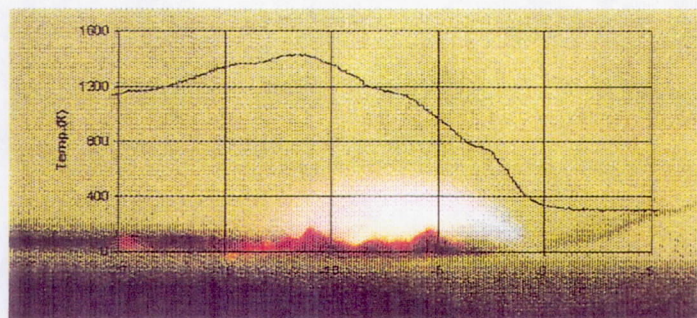


Fig. 5. Visual side view of a downward spreading flame over Ashless Filter Paper at 21% O_2 , $P_\infty = 1.0$ atm. Superposed is the surface thermocouple trace.

Solid Surface
Combustion Experiment

MICROGRAVITY SMOLDERING COMBUSTION ON THE USML-1 SPACE SHUTTLE MISSION

Dennis P. Stocker and Sandra L. Olson
NASA Lewis Research Center
Cleveland, Ohio

Jose L. Torero and A. Carlos Fernandez-Pello
Department of Mechanical Engineering
University of California at Berkeley
Berkeley, California

ABSTRACT

Preliminary results from an experimental study of the smolder characteristics of a porous combustible material (flexible polyurethane foam) in normal and microgravity are presented. The experiments, limited in fuel sample size and power available for ignition, show that the smolder process was primarily controlled by heat losses from the reaction to the surrounding environment. In microgravity, the reduced heat losses due to the absence of natural convection result in only slightly higher temperatures in the quiescent microgravity test than in normal gravity, but a dramatically larger production of combustion products in all microgravity tests. Particularly significant is the proportionately larger amount of carbon monoxide and light organic compounds produced in microgravity, despite comparable temperatures and similar char patterns. This excessive production of fuel-rich combustion products may be a generic characteristic of smoldering polyurethane in microgravity, with an associated increase in the toxic hazard of smolder in spacecraft.

INTRODUCTION

Smoldering is a non-flaming surface combustion reaction that takes place in the interior of porous combustible materials. The characteristics of the smolder reaction and its rate of propagation are determined by the balance between the transport of oxidizer to the reaction zone and the transport of energy to and from the reaction zone [1,2]. When the smolder conditions are such that the resulting smolder reaction is vigorous, its rate of propagation is directly proportional to the rate of oxygen supply. When it is weak, however, the rate of heat loss determines whether the reaction will continue to propagate or eventually extinguish [1,3,4].

Although smoldering is present in a variety of combustion processes, it is of particular interest in fire safety because of its role as a potential fire-initiation source. It can propagate slowly, undetected, for long periods of time, and suddenly undergo a transition to flaming. The products of smolder combustion themselves are toxic. Recently, with the planned establishment of a space station, there has been an increased interest in the study of smoldering in microgravity because of the potential danger of a smolder-initiated fire in remote facilities. The absence of gravity is expected to influence smoldering through its effect on the mass and heat transport within the smoldering material.

Considerable work has been conducted to date on smoldering at normal gravity [1,2], but very limited information is available on smolder in low gravity [5-7]. This is in part because of the long periods of microgravity needed to conduct smolder experiments. The present work attempts to provide further information about smoldering in a microgravity environment. To provide for extended periods of microgravity, a comprehensive smolder experiment was approved for testing on the Space Shuttle and is now under development. A preliminary set of tests were approved to specifically study the ignition and transition effects of low-gravity smolder. The Spacelab Glovebox on the United States Microgravity Laboratory mission, of the Space Shuttle Columbia, of June/July 1992 (USML-1, STS-50), was used for these preliminary tests. The use of the Glovebox limited the size of the fuel sample that could be tested and the power available for ignition, but had the advantage of much reduced costs and development time. A series of comparative tests were also conducted in normal gravity. The normal and microgravity smolder characteristics were determined from interpretation of the available temperature histories obtained at several locations within the sample, visual inspection of the smoldered foam sample, and analysis of the post-combustion gases.

EXPERIMENT

The flight hardware consisted of four experiment modules, two data displays, a control box, and four cables. Each module contained a cylindrical foam sample, with an embedded igniter, and a fan to produce a forced flow in the longitudinal direction (Fig. 1). The test variables during the experiment were the igniter geometry and the convective environment. Through the use of an axial igniter and a plate igniter, both radial and axial smolder were investigated. For each igniter geometry, a test was conducted in a quiescent environment and with a low-velocity air flow for a total of four test conditions. Each experiment module was a sealed polycarbonate box, nominally 0.15 m x 0.15 m x 0.20 m, filled with dry air at one atmosphere pressure. The fuel consisted of a 50 mm diameter, 80 mm long cylinder of open-cell, unretarded, white flexible polyurethane foam, with a 26.5 Kg/m³ density and 0.975 void fraction, which weighed 4 grams. The fuel sample was positioned axisymmetrically in a polycarbonate tube, 76 mm in diameter, that had a fan at one end to provide a convective air flow past the sample with a velocity of the order of 100 mm/sec. For the quiescent tests, large sections of the tube were removed to provide free exchange of air throughout the module. The plate and axial igniters were resistively-heated elements, consisting of nickel-chromium wire sheathed in ceramic.

The foam sample was instrumented with six sheathed, cold-junction compensated, chromel-alumel thermocouples, 0.5 mm in sheath diameter, to measure the smolder reaction temperature and its propagation throughout the sample. A seventh thermocouple was used to measure the local gas-phase temperature outside the foam. The output of the thermocouples and the igniter current was recorded with a video camera through the use of two data displays (with four readings each). A second video camera viewed the side of the smoldering sample.

RESULTS

Temperature Histories: A representative example of the temperature histories obtained in these experiments is shown in Fig. 2. It presents the temperature histories provided by thermocouples 1 to 4 in the microgravity and normal-gravity experiments for test 2 (axial igniter/fan on). The temperature histories for the other thermocouples will not be presented here. They were positioned near the surface of the foam to detect flaming, which did not occur in any of the tests. Given the relative mass of the thermocouples as compared to that of the foam, it is possible that the measured temperatures were significantly affected by conductive losses. Normal-gravity tests also suggest that the temperatures may have been depressed due to the thermocouple's compression of the foam, which may have locally inhibited smolder.

From a comparison of the microgravity and normal-gravity temperature profiles, it appears that gravity had a limited effect on the temperature histories. In most cases, the peak temperatures were greater in microgravity than normal gravity for all four thermocouples, with the difference increasing with distance from the igniter. The temperature difference is presumably due to buoyant cooling in normal gravity, which would be most strongly felt

near the surface of the foam. These temperature histories can be used to roughly calculate smolder propagation velocities using the method previously developed for ground-based experiments [4]. Using that technique, it is found that for all tests, the smolder was not steady but decayed from approximately 0.08 mm/s to 0.02 mm/s, and finally extinguished. The smolder propagation velocities obtained for the normal-gravity tests experiments are also similar. The calculated smolder velocities are of the same order of magnitude as those measured in larger experiments of opposed-flow smolder at low flow velocities (0.5 mm/sec) and natural convection smolder [8]. They correspond to the "weak" smolder cases tested. The maximum smolder velocities measured in those experiments were obtained for flow velocities of 3 mm/sec and were of the order of 0.15 mm/sec.

Char Patterns: During the testing, the smoldering foam was observed to expand and smoke, much of which later condensed as a yellow residue on the module interior. Upon removal after testing, the samples were cut open to reveal the extent of the smolder propagation. The char pattern from normal-gravity tests were found to be similar to the pattern from the microgravity test. The visible extent of propagation was similar in both tests, but there were two notable differences. First, large voids, on the order of 1 cm long, were created in the normal-gravity char region, whereas there were none apparent in the microgravity char. The voids were found in other, but not all, of the normal-gravity tests and none of the microgravity tests. It is speculated that the voids result from gravitational forces on the weakened polymeric structure, but it is not clear what controls their occurrence. A close comparison of the char structure of the microgravity and normal-gravity tests also shows significant differences. The normal-gravity voids had a crust of melted material which appeared to clog the foam pores. Microscopic observation of the normal-gravity char showed that discolored filaments in some cases had melted into spheres. Furthermore, strong signs of fuel pyrolysis could also be observed at the edges of the char region. These observations are typical of a low temperature smolder process [3,4]. In contrast, the char in the microgravity samples was more typical of high temperature smolder with a fibrous, relatively dense structure, despite the similar temperature profiles.

Gas Analyses: The results of the analyses of the post-combustion gases are presented in Table I, for the microgravity and normal-gravity tests. Only the major components have been included in the table. The results are based on analyses, performed at the Toxicology Laboratory at NASA Johnson, with both Gas Chromatography (GC) and Gas Chromatography/Mass Spectrometry (GC/MS). Oxygen depletion and the production of carbon dioxide, carbon monoxide, and hydrocarbon species are good indicators of the combustion reaction characteristics. However, in interpreting the data, it should be kept in mind that smoldering is a low-temperature surface reaction that is generally oxygen limited. It is seen that the microgravity smolder tests produced significant amounts of carbon monoxide and carbon dioxide, as well as a number of light organic compounds. These species are characteristic of pyrolysis and oxygen-limited combustion. It is believed that the chlorinated compounds are contaminants resulting from the methylene chloride that was used to solvent bond the joints in the polycarbonate modules. The normal-gravity tests produced these species in substantially smaller amounts than the microgravity tests. This is somewhat surprising, since the extent of smolder propagation as apparent in the char patterns was not strongly effected by gravity for any of the tests. Yet in all cases, the amount of carbon monoxide was much greater (89 to 3900 ppm) than that produced in normal gravity (<3 to 6 ppm). In most cases, the microgravity tests produced twice as much carbon dioxide as the normal-gravity tests. Methane and propene are evident in the microgravity cases, whereas they are hardly detected in the normal gravity samples. Other products (e.g., 2-propanol) are detected in the microgravity samples and are undetected, or weakly detected, in the normal-gravity samples.

Heat Losses: The present results indicate that heat losses were an important factor in the smolder propagation for the present experimental conditions in microgravity as well as normal gravity. This is somewhat unexpected and specific to the smolder (not flaming) combustion process. Since air has such a low thermal conductivity and mass diffusivity, one would expect that with the absence of natural convection in microgravity, the heat losses to the environment would be small and that the deterrent to the progress of the reaction would be a small supply of oxidizer to the reaction zone. However, these concepts are somewhat modified by the fact that the smolder process is very slow, and consequently, the characteristic time for smolder propagation can be significantly smaller than

that for diffusion of heat and mass. With a thermal diffusivity for air of $5 \times 10^{-5} \text{ m}^2/\text{s}$ and a characteristic length of 25 mm (based on the foam radius), the characteristic times for heat and mass diffusion are of the order of 12.5 seconds (Lewis number assumed unity), which is relatively small compared with the characteristic time of smolder propagation, which with a smolder velocity of 0.05 mm/s and a characteristic sample length of 25 mm is of the order of 500 seconds. Thus, from the point of view of transport of mass and heat, the smolder reaction is basically stationary and there is ample time for the heat and mass to diffuse to and from the reaction zone. If the sample size is small, as it is in this case, the percentage of the heat generated by the smolder reaction that is transferred by conduction to the surroundings becomes increasingly significant as the smolder propagates away from the igniter and the contribution of the external heat source (igniter) is diminished. When the percentage of heat generated by smolder becomes insufficient to overcome the heat losses due to conduction, the smolder reaction weakens and extinguishes.

CONCLUSIONS

The present experiments, although limited in fuel sample size and igniter power, provided valuable information about the smolder characteristics of a porous polymeric fuel in microgravity. The following conclusions can be drawn from these preliminary tests.

- (1) Temperatures in microgravity were in general similar to those measured in normal gravity, with only a slight increase in microgravity temperatures noted in the quiescent test, where convective losses are effectively eliminated.
- (2) Char patterns were also similar between normal and microgravity samples, with the effect of gravitational orientation having a minor effect on the char patterns.
- (3) Under the present conditions of fuel size and external heating, the smolder process was in a "weak" regime because the heat losses from the reaction zone were significant in comparison to the heat generated by the reaction. Under these conditions, smolder was primarily limited by heat losses from the reaction to the surrounding environment.
- (4) Despite similar temperatures and visible extent of smolder, significant production of light combustion gases was found to have occurred in microgravity. Of particular note, the microgravity levels of carbon monoxide were orders of magnitude higher than that observed in the normal-gravity tests. This may be a specific result of smoldering in a microgravity environment, which would imply that microgravity smolder products may be more toxic than smolder products produced on Earth.

ACKNOWLEDGEMENTS

The authors would like to acknowledge the contributions of the many NASA personnel that made this space experiment possible. In particular, we would like to thank the Toxicology Branch of NASA Johnson, who conducted the gas analyses. We would like to thank the USML-1 crew for their design suggestions and for their hard work during experiment training and simulations. Special thanks go to Col. Carl J. Meade and Dr. Lawrence J. DeLucas for their interest and dedication while conducting the experiments during the USML-1 mission.

REFERENCES

1. Ohlemiller, T.J., *Prog. Energy Combust. Sci.*, **11**, (1986), 277.
2. Drysdale, D., 1987, *An Introduction to Fire Dynamics*, John Wiley, (1987), 265.

3. Dosanjh, S.S., Peterson, J., Fernandez-Pello, A.C., and Pagni, P.J., *Acta Astronautica*, 13, No. 11/22, (1987), 689.
4. Torero, J.L., Kitano, M. and Fernandez-Pello, A.C., *Combust. Sci. Tech.*, 91, 1-3, (1993), 95.
5. Cantwell, E., and Fernandez-Pello, A.C., 28th Aerospace Science Meeting, paper # AIAA-90-0648, (1990a).
6. Cantwell, E. and Fernandez-Pello, A.C., "Smoldering Combustion Under Low Gravity Conditions" 1990 Fall Meeting, WSS/CI, San Diego, CA, (1990b).
7. Torero, J.L., Fernandez-Pello, A.C., and Urban D., *AIAA Journal*, 32, 5, (1994) 991. Also paper # AIAA-93-0829, 31st Aerospace Science Meeting, Reno, NV, (1993).
8. Torero, J.L., Fernandez-Pello, A.C., and Kitano, M, *Fire Safety Science*, Proc.Fourth Int. Symp., (1994), 409.

TABLE I: ANALYSIS OF THE POST-COMBUSTION GAS SAMPLES

Compound	Microgravity				Normal-Gravity			
	1.0	2.0	3.0	4.0	1.1	2.1	3.1	4.1
Oxygen	21%	19%	21%	20%	20%	20%	20%	20%
Nitrogen	78%	79%	78%	78%	79%	79%	79%	79%
Hydrogen	ND	40	ND	ND	ND	ND	ND	ND
Methane	17	570	96	180	ND	ND	ND	ND
Carbon Monoxide	89	3900	150	610	4.0	Trace	Trace	5.5
Carbon Dioxide	2300	7400	7600	10700	2100	3000	3300	3800
Propene	15.2	107	12.1	43.8	---	---	---	---
Acetaldehyde	6.33	117	36.4	85.1	120	66	66	150
Propanone	25.8	47.7	4.89	40.9	41	18	13	26
Propanal	ND	7.91	ND	ND	13	4.4	ND	9.1
2-Propanol	6.08	19.0	0.18	13.2	3.7	1.0	0.83	3.7
Dichloromethane	63.5	70.7	70.3	49.7	46	26	44	46
ND: Not detected; limit is 3 ppm for carbon monoxide, and 5 ppm for hydrogen and methane. Trace: Amount detected is sufficient for compound identification only. --- : Not reported in analysis.								

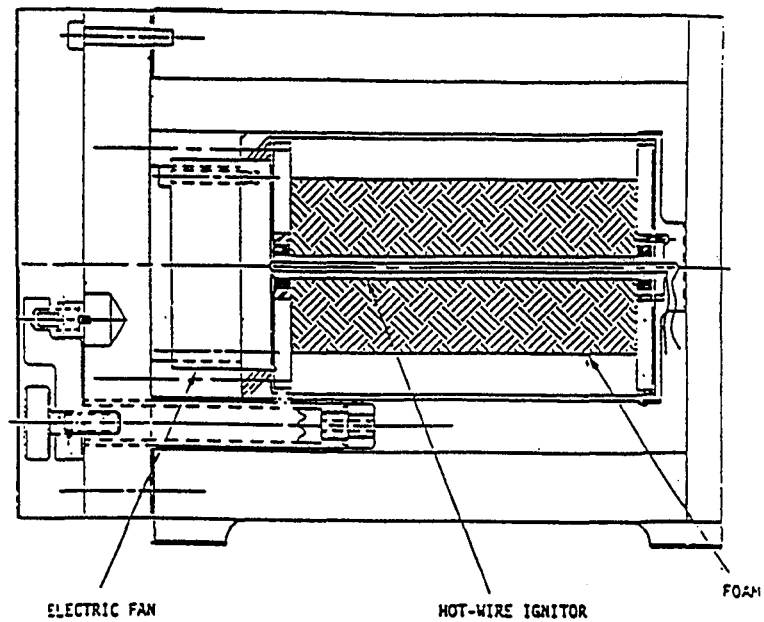


Figure 1. Schematic of experimental module, axial ignitor.

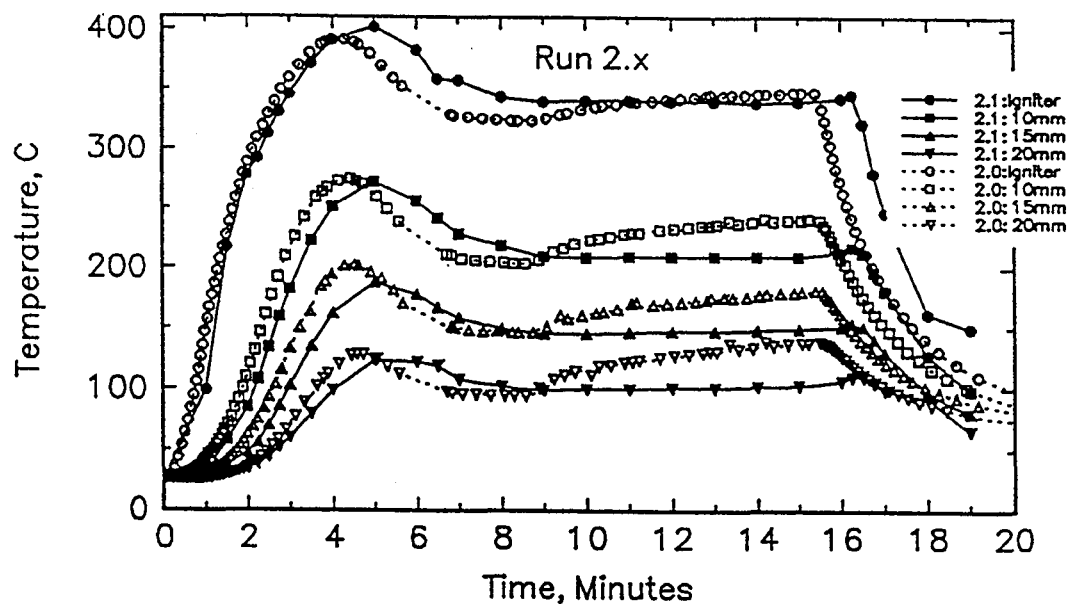


Figure 2. Temperature data from runs 2.0 and 2.1 (axial ignitor, fan on); thermocouples 1 to 4.

The USML-1 Wire Insulation Flammability Glovebox Experiment

Paul S. Greenberg/NASA Lewis Research Center
Kurt R. Sacksteder/NASA Lewis Research Center
Takashi Kashiwagi/National Institute of Standards and Technology

Introduction

Flame spreading tests have been conducted using thin fuels in microgravity where buoyant convection is suppressed. In spacecraft experiments^[1] flames were ignited in quiescent atmospheres with an elevated oxygen content, demonstrating that diffusional mechanisms can be sufficient alone to sustain flame spreading. In ground-based facilities (ie. drop towers and parabolic aircraft) low-speed convection sustains flames at much lower concentrations of atmospheric oxygen^[2,3,4,5] than in quiescent microgravity. Ground-based experiments are limited to very thin fuels (eg. tissue paper); practical fuels, which are thicker, require more test time than is available.

The Glovebox Facility provided for the USML-1 mission provided an opportunity to obtain flame spreading data for thicker fuel. Herein we report the results from the Wire Insulation Flammability (WIF) Experiment performed in the Glovebox Facility. This experiment explored the heating, ignition and burning of 0.65mm thick polyethylene wire insulation in low-speed flows in a reduced gravity environment. Four tests were conducted, two each in concurrent flow (WIF A and C) and opposed flow (WIF B and D), providing the first demonstration of flame spreading in controlled forced convection conducted in space.

Experiments

The Wire Insulation Flammability Experiment (WIF) was designed to observe: Joule heating of electrical wire in quiescent and low-speed forced-flows, and the ignition and spreading of a flame over the insulation of overheated electrical wire in very-low-speed flows. Four nearly-identical WIF test modules, designated WIF-A,B,C, and D were flown. Each module consisted of a miniature wind tunnel with flow provided by the glovebox air circulation system. A small spring-loaded anemometer indicated airflow velocity. A metal screen covering the exit port cooled combustion products and contained particulates released during combustion.

In each module a single polyethylene-insulated nichrome wire sample, 1.5 mm diameter, 110 mm long, was mounted parallel to the airflow direction. All tests were performed using Spacelab cabin air at approximately 21% oxygen at 1 atm. pressure. The polyethylene insulation was approximately 0.65 mm thick. Samples were ignited using Joule heated Kanthol wire wound around the sample end: near the flow-duct exit for opposed-flow burning or the entrance for concurrent flow. Each sample was instrumented with six type K thermocouples to measure wire, wire insulation and gas phase temperatures. Two windows were incorporated into the tunnel for photographic access. One window provided simultaneous video imaging of the sample and the thermocouple displays, the second window was used for 35 mm still photographs. Two 10 cc vacuum bottles with solenoid valves accompanied each test module to collect samples of off-gassing and combustion products. Two transmission electron microscope grids were attached to each exit screen to collect emitted particles.

The nominal test procedures consisted of heating the wire and insulation samples first in quiescent then in flowing air; thereafter the samples were ignited with the insulation at a temperature of approximately 373K. Video recordings were made of the entire sequence, motor-driven 35 mm still photographs were exposed during the flame spreading portion. Complementary flame spreading tests of duplicate but unheated WIF fuel samples were performed in normal gravity in ambient air. The fuel samples were oriented to burn either vertically upward, vertically downward, or horizontally.

Test Results and Discussion

Sample Preheating

Measurements of the sample preheating temperatures were obtained for each WIF module, each configured for different heating rates, in both quiescent and flowing conditions. The results, described in reference 6, show a similarity between quiescent microgravity heating in air and normal-gravity heating in a vacuum.

Ignition and Flame Spreading

Ignition of the insulation material was achieved in all four tests. The flames were quite bright and produced surprising amounts of soot. Soot and particles of condensed unburnt fuel vapor collected on the module exit screens. As the flames spread the fuel melted before vaporizing, and the molten fuel flowed into a quasi-spherical bulb moving with the flame.

Concurrent Flow Flame Spreading

WIF-A. The flame was quite bright, saturated the video imaging device, and appeared to pulsate. Analysis of the anemometer behavior indicates the pulsations could not be attributed to the forced flow but were intrinsic to the flame and attributed to bursting fuel vapor bubbles. Figure 1 is a monochrome reproduction of a 35mm color still photograph representing the concurrent flow flames. The flame was blue where the flow first met the flame, and became yellow further downstream. The tip of the flame was open, changing from yellow to a dark red, and soot visibly escaped from the flame, often in large thread-like structures.

As the flame propagated, the molten fuel accumulated, forming a growing, quasi-spherical bead 2-3 times the initial diameter of the insulation and not always symmetric with respect to the wire. Near the end of the test the gas-phase thermocouple, 1.5 mm from the virgin fuel surface, was occluded by the molten fuel. The surface of the fuel near the flame in WIF-A, as seen in the still photographs, was discolored and opaque, perhaps due to oxidative degradation of the polyethylene (this discoloration does not occur in normal gravity heating tests conducted in a nitrogen environment^[7].) In a few of the still photographs, the opaque fuel surface appears to have been fractured or chipped, with an irregularly shaped gap in an otherwise uniformly brown surface. We speculate that a part of a rigid surface layer may have been ejected by a bursting vapor bubble.

WIF-C. In the third test, WIF-C, ignition was attempted without flow. A toroidal cloud of vapor or condensed pyrolysis products formed around the igniter and was rendered visible by the scattering of light emitted by the hot igniter. The cloud ignited suddenly, and hot gas expansion was felt quickly by the anemometer 75 mm downstream. The flame burned weakly in quiescent air until 17 seconds after ignition when the flow was initiated. The flame immediately brightened, but ultimately failed to propagate. The downstream fuel ignited then extinguished under the combined effect, we speculate, of oxygen depletion by the upstream flame and retarded fuel vaporization suppressed by the layer of degraded polyethylene and soot on the fuel surface.

Opposed Flow Flame Spreading

WIF-B. The flames in all the WIF tests were quite bright. The more sensitive monochrome camera was selected before the flight to capture the expected dim flames, but could not accommodate both the bright flames and the dimmer temperature displays. In the second test, WIF-B, the crew member took the initiative, in real time, to adjust the video camera exposure to de-saturate the flame image. In so doing, the temperature displays were brought below the detection threshold of the video camera, but some imaging of the flame structure was recovered.

As in the concurrent flow test, the molten fuel accumulated into a bead under the flame, growing as the flame spread into the flow until reaching the steady size shown in fig. 2 in about 15-18 seconds. A dark surface layer, about 1-2 mm in length, appears near the flame stabilization point, again suggesting oxidative degradation. The still photographs show vapor bubbles in the molten fuel. Fluctuations in the flame and observed ejection of

small burning particles suggest the bursting of these bubbles. As the flame reached the end of the fuel sample, the flame shape altered, diverging downstream and more completely enveloping the molten fuel bead. As the stationary ball of fuel burned, more frequent flame perturbations occurred, suggesting higher vaporization rates. The fuel burned until it was completely consumed.

WIF-D. For the fourth test the monochrome video camera was replaced with a color camera. Real-time exposure adjustments provided balance between the flame and temperature display images. Acting on a suggestion of J.S. T'ien, the air flow was switched off after the flame reached the end of the sample. The flame quenched rapidly, leaving a nearly spherical fuel bead, 4-5 mm in diameter. This result provides a dramatic demonstration of the effect of low-speed flow on the flammability of materials in microgravity.

Normal-Gravity Flame Spreading

The normal-gravity experiments were characterized by significant dripping of the molten fuel away from the spreading flame. The mass of dripped fuel was as much as 1/2 of the total initial fuel mass. Flames in the normal gravity tests all had closed tips in contrast to the open downstream flame tips observed in all the WIF tests.

Flame Spread Rates and Lengths

The 35 mm photographic sequences provided better reproductions of the flame structure, particularly the blue leading edge of the flame (not visible in the video record). Thus while lacking the time resolution of the video record, the still photographs were used to obtain the flame spread rates of tests WIF-A,B, and D. Similar measurements were made from images of the normal gravity flames. The spread rate results are summarized in Table 1, where the normal gravity reflect average values from several tests.

Flame Spreading Direction	Flame Spread Rate	Fuel Burnout-Front Speed	Flame Length
Concurrent (WIF-A)	0.16 cm/sec	0.12 cm/sec	1.8-2.6 cm
Opposed (WIF-B)	0.070 cm/sec	-	1.8 cm
Opposed (WIF-D)	0.066 cm/sec	-	1.9 cm
Upward (1g)	-	0.13 cm/sec	-
Downward (1g)	0.24 cm/sec	0.18 cm/sec	
Horizontal (1g)	0.14 cm/sec	0.13 cm/sec	-

Table 1. Flame Spread Rates and Flame Lengths

Concurrent Flow. In concurrent flow, WIF-A, the visible downstream tip of the flame spread at an apparently steady 0.16 cm/sec; while the base of the flame (where the flame is stabilized and the fuel burnout occurs) spread at 0.12 cm/sec. The length of the flame grew slowly throughout the test at about 0.04 cm/sec. Thus even in the extended test time provided by the glovebox, concurrent flow flames clearly did not reach an equilibrium length. Though the possibility of steady propagation has been predicted for non-melting thin fuel^[5], the WIF experiment did not provide a steady result.

The spreading of the flame tips in the normal-gravity upward burning tests were too rapid to measure with the 35mm still camera, ie. the flame length exceeded the length of the fuel sample within about three seconds. Propagation speeds of the fuel burnout front in the upward-burning test and the WIF-A concurrent-flow test were similar (0.13 and 0.12 cm/sec, respectively). Fuel consumption via melting and vaporization in the case of the

WIF-A experiment is quite different than the dripping observed in the upward burning experiment, however, so the similar burnout rates therefore appear to be coincidental.

Opposed Flow. The measured steady spread rates for the WIF-B and WIF-D, opposed-flow cases differ by only 6%, having values of 0.070 and 0.066 cm/sec respectively. The fuel in WIF-B was heated to 353K at ignition compared to 343K for WIF-D. Higher bulk-fuel temperatures have been correlated with increased flame spread rates in normal gravity.^[8]

The normal-gravity downward burning flame spread rate of 0.24 cm/sec is much higher than the microgravity forced flow result. The open shape of the downstream flame tips in microgravity suggests under-ventilation. However, the overall equivalence ratio in the microgravity tests were very fuel-lean at about 1/45, and the bright leading edge of the flames suggest oxygen deprivation cannot account for the spread rate difference. In the several normal gravity tests, spread rates varied inversely with the measured fuel mass lost to dripping. Molten fuel in downward burning might enhance forward heat transfer (and the spread rate) if it flows ahead of the flame but does not drip completely from the fuel sample. Thermocapillary effects re-distribute molten fuel differently in microgravity, but more measurements would be needed to be quantitative. It is reasonable to infer that radiative losses, as in other microgravity tests,^[1,5] contribute to lower microgravity spread rates; additional tests with varied flow velocities would help to clarify this issue.

Flame Temperatures

Temperature histories were obtained from the video record, and the data for the WIF-A and WIF-D experiments (Fig. 3). In WIF-A (concurrent flow) the first profile shows two gas-phase temperature peaks, representing first the flame tip and then the flame leading edge. The second profile shows the effect of the thermocouple being occluded by the molten fuel. The highest uncorrected temperature measured in the concurrent flow flame was 1333K. In normal gravity upward burning, the peak temperature of 1287K occurred near the flame bottom.

In WIF-D (opposed flow) the gas-phase temperature shows two peaks, represents first the flame leading edge then another peak near the trailing edge. The peak temperature in opposed flow was about 1273K. The temperature of the insulation rises rapidly to the pyrolysis temperature as the flame approaches, remains flat as the fuel vaporizes, then at burnout increases briefly to a high gas-phase temperature. Peak flame temperatures in normal gravity downward burning were found downstream, away from the leading edge and peaked at 1402K.

Soot and Particulate Production

Soot escaped from each WIF flame, most prolifically in the opposed-flow tests. Soot left the flame in strand-like structures approximately 10cm long and accumulated on the exit screens. In normal-gravity tests some soot also escapes and can be collected from the plume above the flames.

Transmission electron microscopic (TEM) analysis of the primary soot particles revealed mean diameters of 31 nanometers in the opposed-flow tests and 27 nanometers in concurrent flow, less than one standard deviation difference. Soot primaries collected in normal gravity showed mean diameters of 13 nanometers. The TEM analysis also showed transparent particles, 100-200 nm in diameter, on the exit screen of module WIF-C, perhaps condensed vapor from the quiescent ignition described above.

Many small bubbles were visible within the molten region, particularly in the opposed flow cases. Since the boiling temperatures of some polyethylene degradation products (products range from C_1 to C_{100} or higher)^[7] are much less than the degradation temperature of polyethylene, when the degradation products are formed inside the sample they are immediately superheated and form bubbles. These bubbles grow by accumulation of degradation products through diffusion in the molten polyethylene. When they become sufficiently large and close to the surface, the pressure in the bubbles is sufficient to cause a sudden rupture, ejecting fragments of the molten polyethylene into the gas phase. The ejection of small burning polymer fragments were often observed during the flame spread process.

Conclusions

The WIF experiment results provide some introductory data for electrical wire insulation overheating and burning in a low-speed convecting environment, including flame size, structure, spread rates and temperatures. Some quantitative results were obtained: opposed flow flames were cooler, propagated slower and produced more soot than concurrent flow flames. These data are not sufficient to carry out extensive comparisons with normal gravity results mainly because of the limited number of tests, but provide quantitative information useful to the formulation of theoretical modeling and focussed additional tests.

Additionally, the WIF results provide stimulating demonstrations of some unique microgravity phenomenon. The behavior of the molten fuel, including the bead formation and bubble-bursting phenomena, the prodigious production and size of the soot agglomerates, the transient quenching in an abruptly-created quiescent environment, and the accumulation and ignition of vapor from overheated fuel are all phenomena seen first in these tests. Each of these phenomena have important implications in spacecraft fire scenarios: the quiescent quenching demonstration has been used to convince the STS program to adopt ventilation flow cutoff as a fire fighting procedure.

References

- 1.) Bhattacharjee, S., Altenkirch, R.A., and Sacksteder, K.R., "Implications of Spread Rate and Temperature Measurements in Flame Spread Over a Thin Fuel in a Quiescent, Microgravity, Space-Based Environment," *Combust. Sci. Tech.*, 91, pp.225-242, (1993).
- 2.) Olson, S.L., Ferkul, P.V., and T'ien J.S., "Near-Limit Flame Spread Over a Thin Solid Fuel in Microgravity," *Twenty-Second Symposium (International) on Combustion*, the Combustion Institute, pp. 1213-1222, (1988).
- 3.) Olson, S.L., "Mechanisms of Microgravity Flame Spread Over a Thin Solid Fuel: Oxygen and Opposed Flow Effects," *Combust. Sci. and Tech.*, 76, pp. 233-249, (1991).
- 4.) Sacksteder, K.R., and T'ien, J.S., "Buoyant Downward Diffusion Flame Spread and Extinction in Partial-Gravity Accelerations," presented at the *Twenty-Fifth Symposium (International) on Combustion*, The Combustion Institute, in press (1995).
- 5.) Grayson, G.D., Sacksteder, K.R., Ferkul, P.V., and T'ien, J.S., "Flame Spreading Over a Thin Solid in Low Speed Concurrent Flow: Drop Tower Experimental Results and Comparison with Theory," *Microgravity Sci. Technol.*, Vol.7, no.2, (1994).
- 6.) Greenberg, P.S., Sacksteder, K.R., Kashawagi, T., "Wire Insulation Flammability Experiment: USML-1 One Year Post Mission Summary," *Proceedings of the Joint Launch Plus One Year Science Review of USML-1 and USMP-1 with the Microgravity Measurement Group*, NASA CP 3272, Vol.2, (1994).
- 7.) Madorski, S.L., *Thermal Degradation of Organic Polymers*, John Wiley and Sons, Chapter 4, 1964.
- 8.) Borgeson, R.A., and T'ien, J.S., "Modelling the Fuel Temperature Effect on Flame Spread Limits in Opposed Flow," *Combust. Sci. and Tech.*, 32, pp. 125-136, (1983).

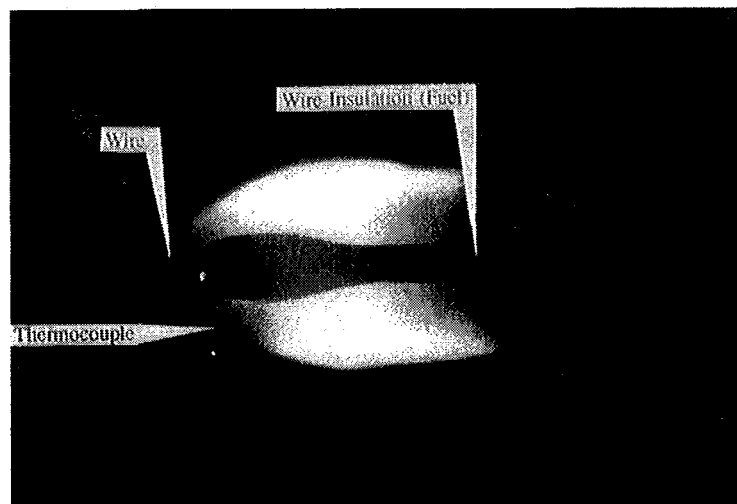


Figure 1. WIF A, Concurrent-Flow Flame

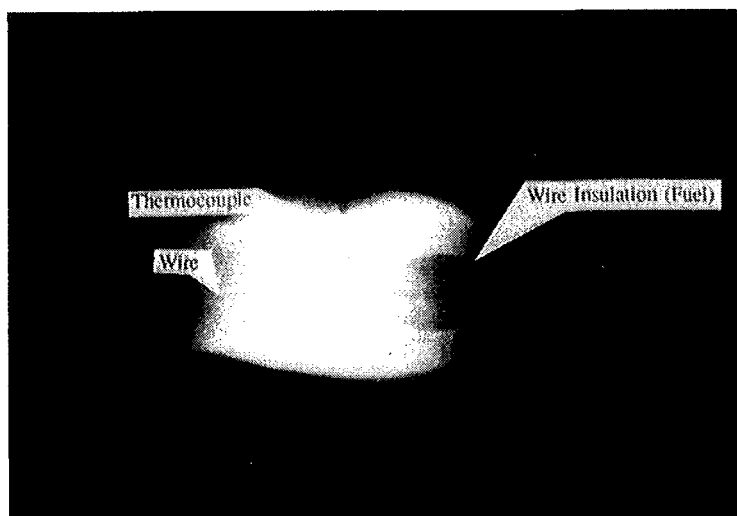


Figure 2. WIF B, Opposed-Flow Flame

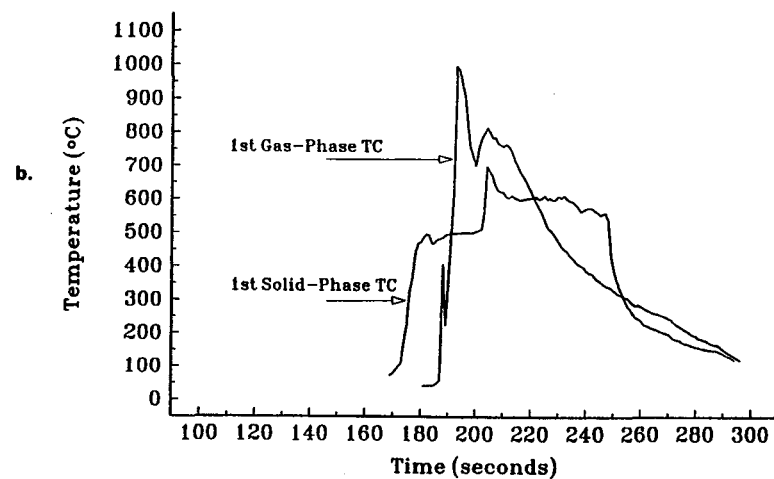
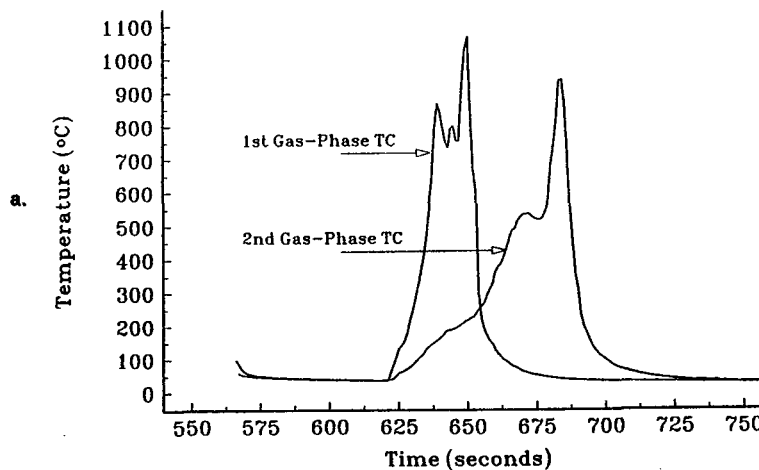


Figure 3. Temperature Measurements: a) Concurrent Flow and, b) Opposed Flow

CANDLE FLAMES IN MICROGRAVITY

D. L. Dietrich and H. D. Ross
NASA Lewis Research Center, Cleveland, Ohio

J. S. T'ien
Case Western Reserve University, Cleveland, Ohio

Introduction

The candle flame is one of the oldest functional combustion systems, used primarily as a source of light. As a result, various practical aspects of candle burning have been understood for centuries (for a history of candle making and candles, see [1]). From a fundamental perspective, however, the candle flame is a complex combustion system. The fuel is a mixture of long chain hydrocarbon molecules whose oxidation chemistry is extremely complex. The flame interacts with a porous wick, the dynamics of which are complicated. Despite this, however, educators at all levels frequently use the candle as an introductory or example combustion problem. In addition, the candle flame occasionally serves as a model convective-diffusive flame in normal gravity theory and experiments. For example, candles were used to study flame flicker [2], spontaneous, near-extinction flame oscillations [3], electric field effects [4], enhanced gravitational effects [5], and magnetic field effects [6].

The candle flame in both normal and microgravity is non-propagating. In microgravity, however, the candle flame is also *non-convective* where (excepting Stefan flow) pure diffusion is the only transport mode. It also shares many characteristics with another classical problem, that of isolated droplet combustion. Given their qualitatively similar flame shapes and the required heat feedback to condensed-phase fuels, the gas-phase flow and temperature fields should be relatively similar for a droplet and a candle in reduced gravity (discussed later). Unless the droplet diameter is maintained somehow through non-intrusive replenishment of fuel, the quasi-steady burning characteristics of a droplet can be maintained for only a few seconds. In contrast, the candle flame in microgravity may achieve a nearly steady state over a much longer time and is therefore ideal for examining a number of combustion-related phenomena.

In this paper, we examine candle flame behavior in both short-duration and long-duration, quiescent, microgravity environments. Interest in this type of flame, especially "candle flames in weightlessness", is demonstrated by very frequent public inquiries. The question is usually posed as "will a candle flame burn in zero gravity," or, "will a candle burn indefinitely (or steadily) in zero gravity in a large volume of quiescent air." Intuitive speculation suggests to some that, in the absence of buoyancy, the accumulation of products in the vicinity of the flame will cause flame extinction [4]. The classical theory for droplet combustion with its spherically-shaped diffusion flame, however, shows that steady combustion is possible in the absence of buoyancy if the chemical kinetics are fast enough. Previous experimental studies of candle flames in reduced and microgravity environments [4,7] showed the flame could survive for at least 5 seconds, but did not reach a steady state in the available test time.

Experimental Apparatus

Candle flame experiments have utilized nearly all of the microgravity facilities available, i.e. the 2.2 and 5.2 sec drop towers and NASA Learjet at NASA Lewis, the 10 sec drop tower (JAMIC) in Hokkaido, Japan, and the Space Shuttle (Columbia) during the USML-1 mission in June, 1992.

In the drop towers' experimentation, large, sealed combustion chambers (to establish the desired

environmental conditions) enclosed the candle. Instrumentation was usually flame visualization by movie or video cameras. In the NASA Learjet, testing was in an unsealed chamber open to cabin pressure (estimated at about 0.8 atm). This provided an environment in which the effective gravity was reduced to 0.01 to 0.04 times that of normal gravity (g_0), with substantial variation in direction and magnitude. This is quite different from the reduction of 10^{-4} to $10^{-5} g_0$ without much variation provided by the drop towers or shuttle, respectively.

The principal difference between the shuttle test hardware and the basic drop tower hardware was (for safety purposes) the required use of a cubic perforated candlebox (11.5 cm on a side) for the shuttle tests. The box permitted fresh oxidizer to reach the candle but prevented a glove or other material from being accidentally ignited. The candlebox then fit inside a 25 liter sealed chamber called the glovebox working volume. The data was primarily black and white video obtained from orthogonally located video cameras. Color photographs of the flame were from a 35 mm SLR camera used in a few tests. Post-mission analysis of the video footage yielded the data presented below. In addition, data was also available from a 3-axis accelerometer sampling at 125 Hz mounted to the underside of the floor of the glovebox working volume. The Spacelab pressure and oxygen mole fraction were 1 atm and 0.217 at the time of each experiment.

The candles for all of the testing reported here were 5 mm in diameter, 2 cm long with a 1-2 mm diameter cotton braided wick. The composition of the candle was 80 percent of an n-paraffin wax (typically C_{19} - C_{35} hydrocarbon) with 20 percent stearic acid ($C_{18}H_{36}O_2$) to impart toughness. Ignition in all cases was by an electrically heated aluminum alloy hot-wire (approximately 3 amperes current) that was removed after ignition. In the drop tower tests the igniter was on for a preset time and then withdrawn, and for the shuttle experiments, the crew manually removed the igniter after ignition.

Initial and Quasi-Steady Flame Behavior

The results described in this section are from about 10 single-candle shuttle experiments. Immediately after ignition, the candle flame was spherical and bright yellow. After 8-10 seconds, the yellow, presumably from soot, disappeared, and the flame became blue and nearly hemispherical (Figure 1d, Figures 1a-c show for reference a normal gravity, drop tower and lear jet candle flame, respectively) with a diameter of approximately 1.5 cm. These behaviors are consistent with the earlier, short-duration studies in aircraft [4], the NASA Lewis Research Center 5.2 second drop tower [7] and the JAMIC 10-second drop tower (unpublished).

The visible flame in microgravity is different from that in normal gravity in a number of aspects: shape, size, color and flame structure. The microgravity candle flame has a large flame standoff distance from the wick, typically on the order of 7 mm (Figure 1d) as compared to 1-2 mm for normal gravity candle flames (at the base region). This large flame standoff distance implies a weaker heat feedback from the flame and a smaller wax mass burning rate. The nearly spherical nature of the microgravity flame implies that all of the flame provides heat feedback to the wick. This is unlike normal gravity where only a portion of the vaporized fuel reacts in the vicinity of the wick; the rest of the fuel vapor is swept downstream by buoyant convection and reacts in the plume region.

The different flame shapes and quench (thermal) distances imply that the flame structure of these of the normal and microgravity flames is different, as illustrated in Figure 2. In normal gravity, the gas-phase structure of the candle flame resembles that of a downward propagating diffusion flame over a thin solid [8,9]; models of the later system show that the highest fuel vapor reaction (consumption) rate (will be called reactivity for the rest of the text) is close to the bottom of the flame near the wick. This region stabilizes the flame and provides the heat feedback for fuel vaporization (Figure 2a). Note that the highest reactivity requires not only high temperature, but also high fuel and oxygen concentrations. Although the temperature is high in the upper part of the flame (downstream), the fuel supply rate is small and thus the reactivity decreases.

The structure of the microgravity candle flame is different (Figure 2b). Its nearly spherical shape resembles the droplet flame in microgravity. The visible candle flame, however, disappears at the bottom or base because of heat loss to the wax. Because of this quenching, the reactivity does not have the same spherical symmetry as a droplet flame. Contrary to normal gravity, the highest reactivity in

microgravity exists at the top of the wick and diminishes in strength toward the bottom because of the quenching by the wax. Experimentally measured luminous intensities (from the video tape) of the flames show that the top of the flame was always brighter than the sides, indicating that the reactivity was higher at the top of the flame.

Analysis of the video footage from the shuttle experiment yielded the flame radius and height (see Figure 2b) as a function of time. Only some flames reached steady-state with respect to both radius and height. For some the flame radius and height increased with time and for others decreased with time. This is probably due to variations in wick/liquid initial conditions resulting from the manual ignition process. The size of the flame is determined by not only the gas phase but by the size of the evaporating surface of the wick, and the magnitude of the heat loss to the solid/liquid wax. The last two parameters are determined to a large extent by the initial condition of the wick/liquid which varied from test to test. Normalizing H by R , however, provides more a measure of the flame shape than the absolute flame size. Figure 3 shows H/R as a function of time for a typical test. For nearly all flames this ratio was 1.8 early in the flame lifetime and gradually decreased to 1.3 at extinction.

The decrease in H/R throughout the flame lifetime occurs primarily from changes in H . Because the glovebox is a relatively small, sealed volume, the candle burns in an ambient of continuously decreasing oxygen content. As a result the local reactivity decreases everywhere in the flame as a function of time. The flame then retreats (H decreases) as the local reactivity falls below a critical value required for a luminous flame [10]. The reactivity at the base of the flame will decrease below this critical value first since the reactivity is always the lowest there.

A common question is why the microgravity candle flame color is blue while normal gravity candle flames in the same atmosphere are sooty (yellow). There are three possibilities for this. The first is that the flame temperature is low enough (everywhere) such that soot cannot form [16]. The second is that soot exists but is cool and not luminous. The third is that the flame is partially premixed because oxygen can diffuse through the quenched base. The second possibility is unlikely since soot forms only at temperatures in excess of 1300 K at which yellow would be visible. Although the oxygen leakage can contribute to reduced soot formation in our candle experiment, it alone is probably not enough to eliminate soot. Near the top of the flame, the mixture should be non-premixed even with oxygen leakage.

The suppression of soot formation in the microgravity candle flames is most likely the result of the reduced flame temperature. The measured maximum flame temperature in a visually similar reduced pressure candle flame is around 1530 K [3]. This temperature is close to the soot formation threshold given by Glassman [11]. Other microgravity diffusion flames which have configurations not favoring oxygen leakage also are completely blue [12]. These near-limit flames, according to theory [10], should also have low flame temperatures. The reduced flame temperature results from the fact that the heat loss relative to the heat generation rate is larger in microgravity even though the heat loss in microgravity is smaller. Radiative heat loss which is considered negligibly small in normal gravity can also be significant in the microgravity candle flame, and can ultimately lead to quenched extinction. These radiative losses can be either from the surface [10], from gas-phase species such as CO_2 and H_2O [17] or from a combination of both [8,9].

Extinction

Extinction occurred between 40 and 60 seconds for all flames except one which had a lifetime of 105 seconds. This long-lived flame started and stayed smaller than normal (approximately 0.6 cm diameter) for most of its lifetime because it stabilized on only a portion of the wick. The cause of extinction for the shuttle experiments was oxygen depletion due to the finite glovebox/candlebox volume. This is different than a local accumulation of products around a diffusion flame that occur in any, even an infinite, ambient. In answer to the common question posed earlier, we assert that a steady-state candle flame would exist in an infinite ambient of air, i.e. the kinetics and diffusion rates are sufficiently fast and heat losses sufficiently small for the candle flame to be maintained until the wax is consumed.

A candle burning in a small sealed volume, such as the glovebox, will never reach a true steady state.

The flame characteristics will continue to change as the ambient oxygen is depleted. At best, then our flames would be quasi-steady. The candle burning in a sealed volume will be quasi-steady if the flame characteristics remain steady over a time scale on the order of a characteristic gas-phase transport time and further that this time is small compared to the time scale over which oxygen is depleted.

The question then comes to a comparison of these two time scales and the observed flame behavior. Over the flame lifetime, the flame shape as measured by H/R changes from 1.8 early in the flame lifetime to close to 1.3 at extinction. During this time the flame luminosity, as measured from the video tape, also decreases throughout the flame lifetime. The results show, however, that over a time period on the order of more than 5 seconds, the flame behavior as measured by the size (R and H), shape (H/R) and intensity (grayscale value from the video tape) does not change significantly.

The characteristic time scale over which oxygen is depleted in the glovebox is large (more than 1 minute). The glovebox contains about 0.25 gmol of oxygen and the estimated consumption rate is on the order of 10^{-5} gmol of oxygen per second. The candle, however, does not burn in the open glovebox. Oxygen transport to the flame is impeded by the safety-mandated candle box. While the candlebox causes extinction earlier than if the candle burned in the glovebox, the depletion timescale is over 30 seconds. Over a time period on the order of 5 seconds, the flame sees a near constant ambient even with the candle box, based on the consumption rate above.

The last time to estimate is the characteristic gas-phase transport time. A simple estimate of this time is $\tau_g = [(C \delta^2) / D]$, where δ is the *measured* flame standoff distance from the wick, D is the diffusion coefficient and the coefficient C is a geometric factor (approximately 1, 2 and 3 for planar, cylindrical and spherical geometries, respectively [13]). Using a D evaluated at a mean temp of 800 K, C=3 and $\delta = 6$ mm, τ_g will be on the order of 1 sec for the microgravity candle. Comparing this time to the oxygen depletion time shows that the candle flames in the Shuttle experiments were certainly quasi-steady.

This gas-phase transport time is valid where the region of interest is in the immediate vicinity of the flame. This area reaches steady-state relatively quickly because of the balance between the convective and diffusive transport. Outside the flame, however, where the convective transport is small, the characteristic gas-phase transport time is much longer. The estimate of this time is more difficult, because of the selection of an appropriate length scale. Using a somewhat arbitrary length scale of ten times the flame radius, we find the radial combustion product profile will reach approximately 90% of its steady state value in a time on the order of 8 seconds. This estimate is based on the theoretical solution [14] of the spherically symmetric transient-diffusion equation with a source at the flame radius.

Based on the latter estimate of the gas-phase diffusion time, the assertion of a quasi-steady gas-phase is not as clear. This latter time is in all likelihood, however, an overestimate. Theoretical treatments of droplet burning show that the assumption of a quasi-steady gas-phase yields accurate results [15,16] as long as the flame lies in a radius $r_f < r_D (\rho_l / \rho_g)^{1/2}$. If we use the wick diameter as the droplet size, this condition is met for the candle flame. This condition, however, is more appropriate for the transient droplet problem.

Near-extinction flame oscillations

Each candle flame on the space shuttle oscillated (spontaneously) in the final 5 seconds. The flame symmetrically traced back and forth along the candle axis in each cycle. The oscillation had a frequency of about 1 Hz with an amplitude that started small and grew until extinction (Figure 3). This type of oscillation is fundamentally different than the well-known flame flicker, owed to hydrodynamic instability [2], as will be explained below.

As the ambient oxygen concentration decreases, the flame oscillations initiate when the flame base extinguishes, i.e. it visibly begins to retreat. The liquefied wax and wick are still hot, so fuel vaporizes, and the fuel vapor and oxygen diffuse toward each other in the base region. Eventually a combustible mixture exists and a flashback of the flame base occurs. This further depletes the ambient oxygen concentration, so that more of the base or weakest part of the flame (compared to the previous cycle)

extinguishes, and the cycle repeats. The oscillations continue, increasing in amplitude as the ambient oxygen is continuously depleted, until the ambient oxygen concentration becomes too low to sustain any part of the flame.

Chan and T'ien [3] observed this type of oscillation at 6-9 Hz in normal gravity, low pressure (0.14 atm) candle flames that were visually similar to the shuttle candle flames. Scaling analysis of the experimental conditions of Chan and T'ien show that a buoyant flow existed even at reduced pressure. Analysis of the acceleration data shows that oscillations for the shuttle tests occurred at acceleration levels of 10^{-5} to $10^{-6} g_0$ where buoyant convection is much smaller than diffusive transport rates. Therefore buoyant convective flow is not required for the oscillation.

The different frequencies are due to the different diffusive transport time scales in the two environments. The time for fuel vapor transport from the wick to the flame surface provides a comparative measure of these characteristic times. τ_g for the microgravity candle flame was shown above to be approximately 1 second. Using the same equation with the experimentally measured δ , and an appropriate D yields a reduced pressure τ_g of 0.12 sec. The magnitude and the ratio (about 9) of the characteristic times in the two environments are in the range of the experimentally measured frequencies. Since the flame radii for the two cases are sufficiently close, the difference in transport times comes mainly from the pressure dependence of the diffusion coefficient. The identification of time scales, however, does not necessarily explain why oscillations have to occur; this requires a proper phase relationship between the involved processes.

Future Plans

The work on candle flames is continuing with three distinct phases. The most significant part is the development of a comprehensive model of the candle flame. An initial model that is comprehensive in the gas-phase is being developed. Next, the model will be coupled with a model of the wick/liquid phase. Another glovebox experiment is currently planned for operation in the MIR space station. The experiment is an enhanced version of the USML-1 experiment with a larger candle box with more free area. In addition to videography of the flames, thermocouple measurements, point measurement of the far-field oxygen concentration and radiometric measurements of the flame are planned. Ground-based work in the drop towers and normal gravity is also continuing.

References

1. Sherman, D.R. *The Complete Anachronist*, #68, Society for Creative Anachronism, Inc., Milpitas, California (1993).
2. Buckmaster, J. and Peters, N. *Twenty-First Symposium (International) on Combustion* / The Combustion Institute, 1829-1836 (1986).
3. Chan, W.Y. and T'ien, J.S. *Combust. Sci. Tech.* 18: 139-143 (1978).
4. Carleton, F. and Weinberg, F. *Nature* 330: 635-636 (1989).
5. Villiermaux, E. and Durox, D. *Combust. Sci. Tech.* 84: 279-294 (1992).
6. Lawton, J., and Weinberg, F.J. *Electrical Aspects of Combustion*, Clarendon, Oxford (1969).
7. Ross, H., Sotos, R. and T'ien, J.S. *Combust. Sci. Tech.* 75: 155-160 (1991).
8. West, J., Bhattacharjee, S., and Altenkirch, R.A., *Combust. Sci. Tech.* 83: 233-244 (1992).
9. Chen, C.H. and Cheng, M.C. *Combust. Sci. Tech.*, 97: 63-83 (1994).
10. Ferkul, P.V. and T'ien, J.S. *Combust. Sci. Tech.*, 99, No. 4-6: 345-370 (1994).
11. Glassman, I. *Twenty-Second Symposium (International) on Combustion* / The Combustion Institute, Pittsburgh, Pennsylvania, 295-311 (1988).
12. Grayson, G.D., Sacksteder, K.R., Ferkul, P.V., and T'ien, J.S. *Microgravity Sci. Tech.*, VII/2: 182-195 (1994).
13. Kanury, A.M. *Introduction to Combustion Phenomena*, Gordon and Breach Science Publishers, New York, New York, (1982).
14. Carslaw, H.S. and Jaeger, J.C. *Conduction of Heat in Solids*, Clarendon, Oxford (1959).
15. Crespo, A. and Linan, A. *Comb. Sci. Tech.*, 11: 9-18 (1975).
16. Law, C.K., Chung, S.H. and Srinivasan, N. *Comb. Flame* 38: 173-198 (1980).
17. Chao, B.H., Law, C.K. and Tien, J.S. *Twenty-Third Symposium (International) on Combustion* / The Combustion Institute, 523-531 (1990).

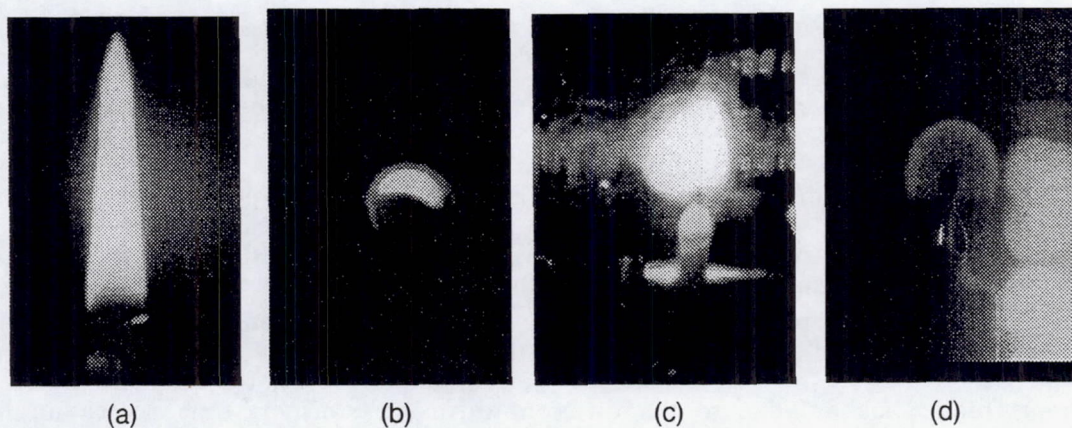


Figure 1. Pictures of candle flames in a. normal gravity, b. 5.2 second drop tower, c. Lear jet, and d. Space Shuttle.

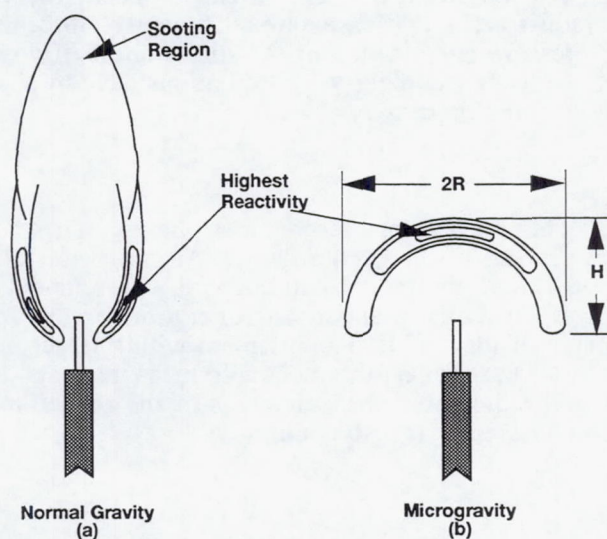


Figure 2. Schematic representation of the difference of the reactivity contour between a (a) normal gravity candle flame and (b) microgravity candle flame.

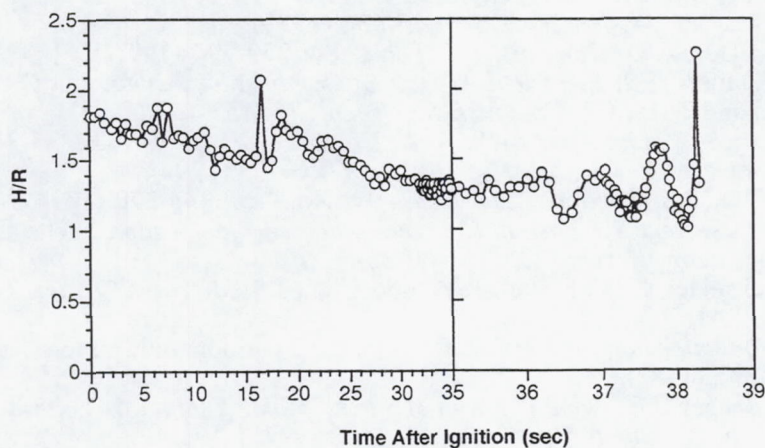


Figure 3. Flame shape, shown as H/R , as a function of time for a typical Space Shuttle test.

FLAME SPREAD ACROSS LIQUIDS

Howard D. Ross (NASA Lewis Research Center), Fletcher Miller (Case Western Reserve University)
David Schiller and William Sirignano (University of California, Irvine)

Introduction

Recent reviews [1,2] of our understanding of flame spread across liquids show that there are many unresolved issues regarding the phenomenology and causal mechanisms affecting ignition susceptibility, flame spread characteristics, and flame spread rates. One area of discrepancy is the effect of buoyancy in both the uniform and pulsating spread regimes. The approach we have taken to resolving the importance of buoyancy for these flames is: (a) normal gravity (1g) and microgravity (μg) experiments, and (b) numerical modeling at different gravitational levels. Of special interest to this work, as discussed at the previous workshop, is the determination of whether, and under what conditions, pulsating spread occurs in μg . Microgravity offers a unique ability to modify and control the gas-phase flow pattern by utilizing a forced air flow over the pool surface.

Normal Gravity Experiments Since Last Workshop

The subsurface temperature field was examined using rainbow schlieren deflectometry (RSD) [3], and subsurface velocity field measurements were taken using particle image velocimetry (PIV) [4] for 1g, near-flash, uniform flame spread across 1-propanol between 18 and 23 °C. Prior to ignition both the RSD and the PIV system revealed that a seemingly quiescent pool was in fact in cellular motion with velocities on the order of 2 mm/s (small compared to the flame spread rate, U_{fl}). Due to evaporative cooling, the liquid surface temperature, T_{lg} , dropped 1 °C or more compared to the bulk liquid; this change can affect U_{fl} .

One goal of this 1g work was to determine the controlling mechanism of uniform flame spread. Assuming that the 2 cm wide tray was wide enough to represent asymptotic behavior for our test conditions (uniform spread experiments in wider trays are clearly needed), the PIV revealed the onset of liquid-phase convection more than 1 cm ahead of the spreading flame; however, the flame overtook this moving surface. In flame-fixed coordinates, therefore, there was no convection away from the flame. This behavior suggests that preheating is via a mixed mode, with convection contributing along with other mechanisms, the most likely candidate being gas-phase conduction. Despite its sensitivity, the RSD system did not show any subsurface heating ahead of the flame, indicating the preheating is confined to a very thin (sub mm) surface layer. A computer program, described in [5] as well as below, was used to model the flame spread process and agreed well with the RSD observations. Both the model and the RSD results, however, are in contrast to the holographic interferometric results in [6] for reasons described in [4].

Microgravity Experiments Since Last Workshop

The experiment was flown on a Terrier-Black Brant sounding rocket; this was the first μg combustion experiment to be performed in a sounding rocket. The two major hardware components were the Experiment Package (EP) and the Avionics Package (AP). The EP housed the fuel tray test section, fuel delivery system, Data Acquisition System, and all video diagnostic systems. The AP housed the control computer, video tape recorders, power supplies and experiment control circuitry. The 30 cm long x 2 cm wide x 2.5 cm deep fuel tray was located inside a 10 cm x 10 cm cross-sectional area flow duct which provided a low-speed forced air flow over the fuel tray. Hot-wire igniters were located 1 cm from each end of the tray. Thermocouples were at several locations in the fuel and surrounding gas. The sides of the fuel tray were constructed of schlieren quality windows to allow viewing of the fuel from the side. The top and sides of the flow duct were also fitted with windows to allow recording of the propagating flame by eight camera systems. Two top cameras and two side cameras each recorded half of the flame spread. These images were video-mixed to generate two video signals, each with a top and side view. Two side-viewing PIV systems, with a wide Field Of View (FOV) — 2.5 cm x 10 cm — and a narrow FOV — 2 cm x 2.6 cm — respectively, recorded liquid-fuel flow patterns as the flame crossed the midsection of the tray. An infrared camera (8-12 μm spectral range) with

a 2.5 cm x 7 cm FOV through a salt window recorded the liquid surface temperature field ahead of the flame crossing this same region. Finally, an RSD system with a 10 cm circular FOV centered at the axial midpoint of the tray recorded liquid-phase temperature gradients.

The experiment payload was a sealed pressure vessel filled with dry air so the experiment could be conducted at 1 atm (actual pressure at ignition was 15.1 psia due to heating during ascent). The temperature of the air and fuel was 20.5 °C at the time of ignition. The experiment operated autonomously, except for selected data downlink and uplink capabilities so the operation of the experiment could be observed in real-time and the igniters and the air flow could be controlled. The sounding rocket flight provided just over 6 minutes of μg time to perform the experiment. Seventy-five seconds after launch, the rocket was in μg and the experiment payload was energized. The 1-butanol fuel circulated internally for 60 s before filling the tray to ensure the PIV particles were well distributed in the fuel. The fuel tray was then filled completely by turning a valve which routes the fuel to the tray. Filling the tray in μg required 75 s; only a very few small bubbles located near the bottom of the fuel tray were observed and they did not apparently affect subsequent observations. This was an important engineering accomplishment regarding fuel management in μg . The experiment depended on surface tension and a sharp "pinning" edge at the inside top of the tray edges to maintain the fuel in the tray in μg . After filling the tray, a 10 cm/s bulk opposed air velocity (U_{opp}) was started. This value of U_{opp} was selected to be less than that normally found in 1g experiments of this scale, but much greater than diffusional velocities associated with quiescent, μg experiments. A 29 s waiting period then began, which allowed any pool surface deformations to damp out and any internal fluid motion from the filling process to cease (confirmed by PIV and RSD data). The primary igniter was then energized. Via an up-link manual command, the igniter was shut off once a flame appeared. At the end of the test, all experiment systems were de-energized and a valve was opened to the vacuum of space to evacuate the payload for safe handling upon retrieval. The evacuated payload returned to Earth via parachute and was recovered without damage one hour after flight.

Figure 1 shows a comparison between 1g and μg flame shapes (tick marks at the bottom of all figures indicate a cm scale). Note the absence of soot and a buoyant plume in the μg flame. In general the intensity of the μg flame was much less than the 1g flame; until it reached the tray midpoint, the μg flame front monotonically decreased in intensity as it propagated. The flame stood off the surface more in μg than in 1g. The top camera view showed that the 1g flame front was much less curved than the μg flame front, due most likely to the slower rate of propagation (discussed next) and increased sidewall heat and momentum losses in μg .

Figure 2 shows the flame position versus time for both 1g and μg . Ignition and spread are completed in 6–7 s in 1g. As expected, the 1g flame exhibits rapid, pulsating spread alternating in 1–2 s intervals between the slow and fast propagation phases of the pulsating cycle; the "crawling" velocity was 1–2 cm/s and the "jump" velocity was 8 cm/s. Ignition and spread took more than twice as long in μg . The character of the spread was also distinctly different than in 1g. In the first half of the tray, the flame moved slowly, without pulsation, and reached a near-steady spread velocity of about 1.5 cm/s; this value is an order of magnitude less than that which occurs in the 1g uniform spread regime, and is more similar to the crawling velocity described above. Just before the halfway position, the flame jumped forward at about 6 cm/s. It then paused at about the 20 cm position, which coincides with a thermocouple rake. After this, it rapidly and erratically spread. Hypotheses (not yet verified) as to why the flame spread behavior changed include: air flow irregularities, thermocouple rake interferences, mass flow reductions in the air stream due to heat release from the flame or pressure buildup, and ignition transients.

Figure 3 shows comparative 10 cm FOV RSD images centered at the midpoint of the fuel tray. The 1g image shows a series of vortices, close to the pool surface, which formed during 2–3 pulsation cycles when the flame slowly propagated. The μg image shows only 1 very large vortex, associated with the near-steady spread, which extends much deeper into the fuel depth and shows a much longer preheat distance. This clearly indicates that, consistent with numerical predictions [7], buoyancy stratifies the warmer liquid near the surface in 1g, which affects the liquid surface temperature profile that governs the thermocapillary-driven liquid surface velocity. Without appreciable buoyancy, the warm liquid is carried into the fuel depth by the thermocapillary-driven motion of the liquid fuel. The transfer of this energy deeper into the bulk fluid means less is available for surface preheating and evaporation, which is one reason the flame spread is slower. The steepness of the thermal gradients is such that in both 1g and μg the RSD image is driven off-scale near the

fuel surface.

A review of the PIV video indicates slow particle motion begins shortly after the igniter is energized in both 1g and μ g. The flow accelerates sharply as the flame and its accompanying vortex approach. Figure 4 shows comparative PIV images for a time when the flame is near the center of the field of view. A time-lapse reconstruction of about 0.23 s is shown to clarify the flow patterns and average velocities. The center of the vortex under the flame is 7.2 mm deep in μ g, compared to 3.8 mm in 1g. A comparison of the RSD and PIV images, as we noted in [4], shows how misleading refractive index measurement methods can be when used to infer flow pattern; for example the RSD shows nothing below the vortex, but the PIV clearly indicates motion near the bottom of the pool. We are presently in the process of measuring the detailed velocity field from the PIV.

Figure 5 shows comparative infrared images of the fuel surface temperature. Measurements of the absorption spectra as a function of liquid depth showed that 1-propanol and 1-butanol both are strong absorbers in the 8–12 μ m range, thus the images are believed to represent surface or very near-surface temperatures. The camera was set for a 20–70 °C range, so when the flame entered the IR camera's field of view, it saturated the IR image; reconstruction of the visible flame position was possible, however, via the time-synchronization of all the video images. The 1g flame shows a unique structure we have called twinning. As the 1g flame began the crawling portion of the pulsating cycle, the preheat region extended, as expected, a greater distance ahead of the flame. It then developed very symmetric vortices which rolled up toward the side walls while a central portion of preheated liquid continued to proceed upstream of the flame. At a later time, the flame jumped forward and obscured the twin vortices. The cycle then repeated itself with the reformation of the twin vortices. The liquid preceding the μ g flames showed an entirely different heating pattern; recall, in this case, the flame was spreading steadily and much more slowly. As also seen by the RSD, the IR revealed the preheat distance ahead of the flame was much greater in μ g than in 1g. While the flame itself showed side-to-side symmetry, no twin structures were observed in the IR image. Instead, asymmetric vortical motion was clearly apparent in μ g. To summarize, the IR images show several novel findings. First, the IR view implied significant sideflow in both 1g and μ g. This has not been revealed by line-of-sight, refractive index methods to date or by the shape of the visible flame front. Furthermore, these 3D spanwise effects cannot be predicted by current 2D numerical models. Secondly, symmetrical processes were found in 1g but not in μ g. Third, a much longer preheat region exists in μ g. Finally, Fig. 5 shows that a surface temperature valley exists ahead of portions of the flame leading edge, caused by fingers of hot liquid that curl sideways trapping cooler liquid between them and the flame front. This result is consistent with the observation reported in [8] and heretofore unverified or unexplained.

Numerical Modeling

Figure 6 shows the geometry and select boundary condition and grid construction information for the numerical model used to simulate the sounding rocket experiment. The gravity level is assumed to be zero in the simulations reported herein. Using a gravity of 10^{-4} g yields essentially identical results. The igniter (size = 0.4 x 0.09 mm) is modeled as a hot pocket of gas with a temperature that increases linearly from $T_o = 21$ °C to 1700 K in 0.2 s. The igniter temperature remains constant until the flame reaches the location $x_{fl} = 3$ cm, after which time the temperature of the igniter is no longer held fixed (i.e., the hot pocket of gas is treated the same as any other point in the interior of the domain). The initial condition for the streamwise velocity, $u(x, y)$, is equal to the inlet boundary condition at $x = 32$ cm. A linear inlet velocity profile is used for $0 < y < 0.5$ mm to avoid unrealistically high initial shear stresses at the liquid surface. For $y \geq 0.5$ mm, the inlet velocity is uniform and equal to 10 cm/s. The other boundary conditions at the inlet of the gas phase are $h_1 = h_{1,o}$, $v = 0$, $Y_F = Y_P = 0$, and $\chi_{O_2} = 0.21$. The boundary conditions at the outlet of the gas phase ($x = 0$) are given in Figure 6. A convective boundary condition for u yields slightly better convergence and satisfaction of global continuity as compared to a zero normal gradient condition, $\partial u / \partial x = 0$. The initial condition for the fuel vapor concentration in the gas phase is assumed to be $\chi_{F,o} = P_{sat}(T_o) \exp[-y/(1 \text{ mm})]$. Prior to activating the igniter, the fuel is allowed to vaporize and convect/diffuse through the gas phase in the presence of the forced opposed flow without external heating for 6 s. This results in a steady fuel vapor concentration profile at the time of ignition.

The boundary conditions at the gas/liquid interface include balance of the stresses, continuity of the tangential velocity, no dissolving of air into the liquid (Stefan flow assumption), neglect of recession of the

liquid surface, balance of the normal heat flux, and continuity of the temperature. A nonuniform grid is used in the x and y directions in both phases. Since the thickness of the reaction zone in the flame leading edge region is two orders of magnitude smaller than the length of the computational domain, a partially adaptive gridding scheme is used in the x -direction to provide fine resolution of the steep gradients in the reaction zone throughout the simulation. As shown in Figure 6, a uniform mesh of $\Delta x_f = 0.4$ mm is used in a 4 mm region around the flame. Behind and ahead of this region, the mesh size increases with geometric progression factors. A 132×102 gas-phase mesh, 132×52 liquid-phase mesh, and 1 ms time step were used for the calculations. Each simulation exhibited excellent convergence and satisfaction of global continuity. Other details of the numerical model and the governing equations are the same as for the open pool configuration without forced flow described in [5].

Figure 2 summarizes the numerical results for $U_{opp} = 10$ cm/s and different values of the input parameters A (nondimensional pre-exponential constant) and E_a (nondimensional activation energy). These parameters are nondimensionalized using reference values of $E_{a,*} = 30$ kcal/gmole and $A_* = 4.69 \times 10^{11}$ m³/(kmol·s) (taken from [9] and previous calculation for propanol [5]). As shown in Figure 2, the numerical results are sensitive to the choice of activation energy, E_a , and (to a lesser extent) pre-exponential constant, A , for the first-order, finite chemical reaction rate expression. For unity values of A and E_a , the flame remained at the igniter location, $x = 1$ cm, when the simulation was halted 15 s after the igniter was activated. The flame extinguishes quickly if the igniter is subsequently de-activated.

In all the cases except for $A = 1$ and $E_a = 0.8$ (which yielded uniform flame spread with very little ignition transient), after the igniter is activated the flame initially spreads very slowly (with speed 0.5–2 cm/s) and a relatively large region of liquid flow forms ahead of the flame. The overall length of this flow ahead of the flame, δ_{flow} , is due to the ignition transient and is appreciably larger than that which is formed during the subsequent flame spread. After this initial period during which the flame spreads slowly, the flame accelerates across a distance of order δ_{flow} at approximately 20 cm/s. The ensuing flame spread consists of a series of slow-moving and rapid-moving movements across the liquid surface. In some cases, the flame moves backward before accelerating forward. The pulsation frequency increases with increasing A or decreasing E_a . A comparison of runs with $E_a = 1$ and $A = 3, 5$ and 8 indicate that the mean flame spread rate, \bar{U}_f , after the ignition transient does not vary strongly with A . The dependence appears to be much weaker than $\bar{U}_f \propto \sqrt{A}$, which one would expect if most of the flame advancement was of a premixed nature.

Simulations were performed for a range of U_{opp} from 1 cm/s to 30 cm/s for $A = 5$ and $E_a = 1$. For $U_{opp} \geq 10$ cm/s, as U_{opp} increases, the flame begins to propagate sooner (i.e., the ignition transient decreases), the pulsation frequency increases, and the mean flame speed increases slightly. Consistent with results of μ g experiments conducted in the NASA-LeRC Zero Gravity Facility, the flame extinguishes in a nearly quiescent environment ($U_{opp} = 1$ cm/s). For $U_{opp} = 10$ cm/s, flame pulsations occur more frequently and regularly for a 5 mm pool depth compared to a 25 mm depth. This suggests that one can reduce the ignition transient and increase the number of pulsations in μ g experiments by using a shallower pool.

The conditions which yield pulsating flame spread in normal gravity without forced opposed flow appear to be the same as those which cause pulsating flame spread at zero gravity or microgravity with forced opposed flow. The flame spread mechanism was described in detail in [5] and is briefly summarized here. Figure 7 shows details of the zero gravity flow field, contours of Y_F , Y_{O_2} and fuel consumption rate, and liquid surface temperature and velocity data near the flame leading edge at the beginning of a pulsation cycle for $A = 5$, $E_a = 1$. This figure shows that the liquid surface is heated up to 2 cm ahead of the flame leading edge. The liquid surface velocity in this region is due to thermocapillary convection. Pulsating flame spread is caused by a gas-phase recirculation cell which entrains fuel vapor just ahead of the flame leading edge. This recirculation cell forms due to the combination of thermocapillary-driven concurrent flow of the liquid surface and opposed gas-phase flow (due to the forced inlet flow in this case, or due to buoyancy in 1g). While the recirculation cell entrains fuel vapor, the maximum fuel consumption rate is relatively small and the flame propagates slowly at a speed of 1–2 cm/s. When the fuel vapor concentration ahead of the flame approaches a lean flammability limit, the maximum reaction rate increases significantly, causing the flame to accelerate up to a speed of the same order as the lean-limit, premixed laminar flame speed. Simultaneously, the increased rate of hot gas expansion destroys the recirculation cell structure ahead of the flame by forcing the flow to diverge away from the flame leading edge rather than be drawn toward the liquid surface by shear induced from the liquid motion. After the flame accelerates through the premixed region that was formed in

the recirculation cell, the maximum reaction rate and the rate of hot gas expansion decrease, thus allowing the forced flow to create opposed flow just ahead of the flame leading edge. The reduction in the hot gas expansion also allows the gas-phase shear from the liquid surface motion to pull the gas just ahead of the flame toward the liquid surface and thus re-form the recirculation cell.

Future Work

Two additional sounding rocket experiments are presently scheduled to take place within the next year. The gas-phase thermocouple and some of the subsurface thermocouple rake which apparently restrained flame propagation in μg will be removed or re-positioned to produce less obstruction. Test conditions for the flights are being established, and will likely be at different opposed flow velocities, spanning values closer to those found naturally in 1g buoyant situations and then to those closer to near-quiescent conditions. Supporting ground-based tests in drop tower facilities will be utilized to establish that a flame will be sustained in these conditions at least for the first few seconds of μg (the sounding rocket experiments are needed to verify their persistence). Tests in 1g with various tray widths may commence. Additional μg tests (in a sounding rocket) with a concurrent air flow will be sought to complete the originally proposed test matrix. Modeling will continue for the 1g open pool and forced flow cases in which numerical convergence is challenging due to buoyancy-induced vorticity which must be convected past an artificially imposed outflow boundary. In addition, we will continue numerical calculations to predict μg flame spread behavior in both the opposed flow and concurrent flow cases.

Acknowledgments: The computational research was supported in part by the San Diego Supercomputer Center and NASA Center for Computational Sciences through allocations of computer time. The Lewis and Case Western researchers wish to acknowledge the build-up and test support provided by the Spread Across Liquids (SAL) engineering team at Lewis, and the rocket launch expertise provided by Wallops Island Flight Facility and White Sands Missile Range personnel.

References

1. Ross, H. D., "Ignition of and Flame Spread Over Laboratory-Scale Pools of Pure Liquid Fuels," *Prog. Energy Combust. Sci.*, Vol. 20, 1994, pp. 17-63.
2. Sirignano, W. A. and Schiller, D. N., "Mechanisms of Flame Spread Across Condensed-Phase Fuels," to appear in *Comb. Sci. Tech.* Book Series honoring Professor Irvin Glassman, 1995.
3. Miller, F. J., Ross, H. D., and Schiller, D. N., "Temperature Field During Flame Spread over Alcohol Pools: Measurements and Modelling," presented at the Eastern States Section, Combustion Institute, Clearwater, FL, 1994.
4. Miller, F. J. and Ross, H. D., "Liquid-Phase Velocity and Temperature Fields During Uniform Flame Spread over 1-Propanol," accepted for Eighth Int'l Symp. on Transport Processes, San Francisco, CA, July, 1995.
5. Schiller, D. N., Ross, H. D., and Sirignano, W. A., "Computational Predictions of Flame Spread over Alcohol Pools," AIAA-93-0825, 31st AIAA Aero. Sci. Mtg., Reno, Nevada, 1993; submitted to *Comb. Sci. Tech.* as "Computational Analysis of Flame Spread over Alcohol Pools."
6. Ito, A., Masuda, D., and Saito, K., "A Study of Flame Spread Over Alcohols Using Holographic Interferometry," *Combustion and Flame*, Vol. 83, 1991, pp. 375-389.
7. Schiller, D. N. and Sirignano, W. A., "Buoyant-Thermocapillary Flow With Nonuniform Supra-Heating: I. Liquid-Phase Behavior," *Journal of Thermophysics and Heat Transfer*, Vol. 6, No. 1, Jan. 1992, pp. 105-112.
8. Glassman, I. and Dryer, F., "Flame Spread Across Liquid Fuels," *Fire Safety J.*, Vol. 3, 1980/1981, pp. 123-138.
9. Westbrook, C. K. and Dryer, F. L., "Simplified Reaction Mechanisms for the Oxidation of Hydrocarbon Fuels in Flames," *Comb. Sci. Tech.*, Vol. 27, 1981, pp. 31-43.

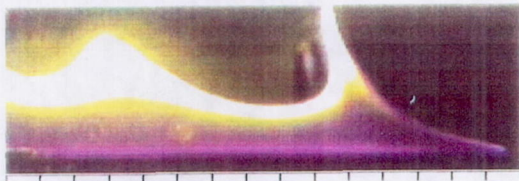


Fig. 1a Side view of flame in 1-g.



Fig. 1b Side view of flame in 0-g



Fig. 4a Particle Tracks for 1-g spread

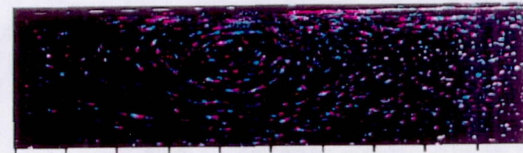


Fig. 4b Particle Tracks for 0-g spread

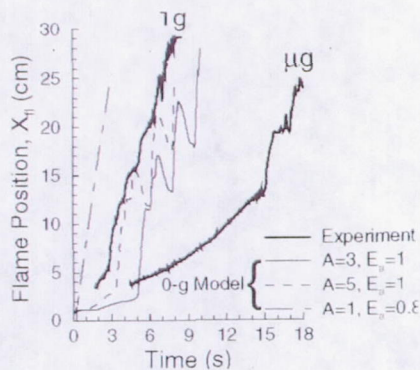


Fig. 2 Flame position vs. time

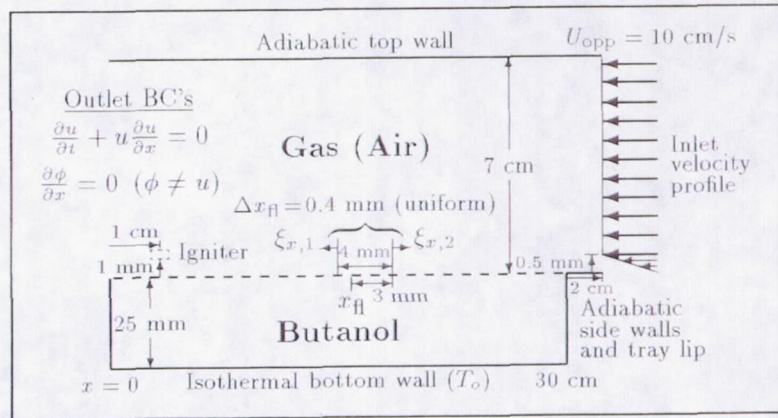


Fig. 6. Schematic of computational domain and boundary conditions for model



a) 1-g prior to jump b) 1-g after jump (0.5 s later)

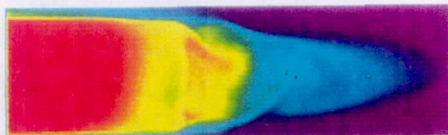


Fig. 5. Pool surface temperature. c) 0-g

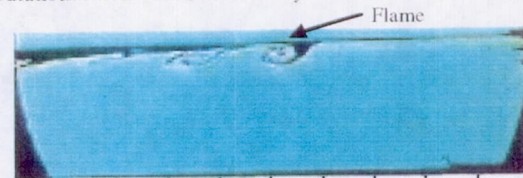


Fig. 3a Schlieren view of liquid in 1-g.



Fig. 3b Schlieren view of liquid in 0-g

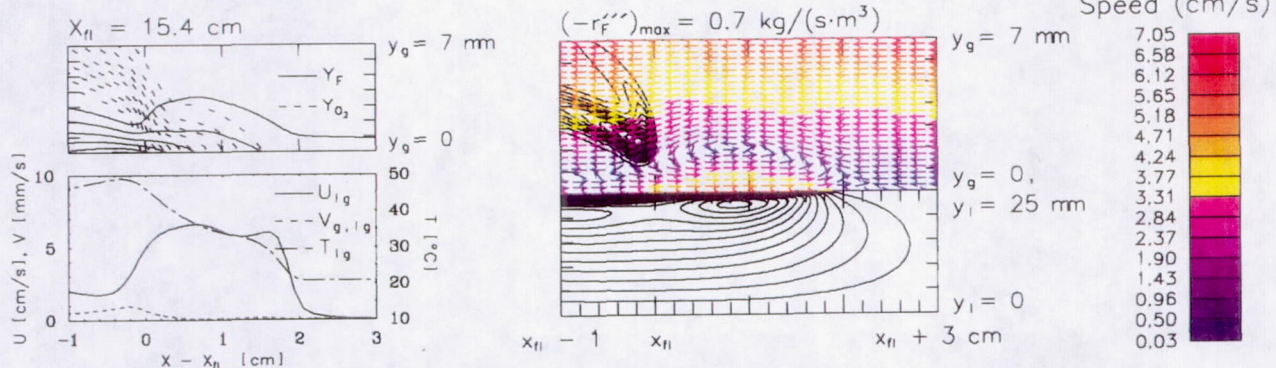


Fig. 7 Predicted velocity, fuel concentration, temperature, and flow field contours ($A = 5$, $E_a = 1$, $t = 5.0$ s)

Droplets and Aerosols

Preceding Page Blank

MULTICOMPONENT DROPLET COMBUSTION AND SOOT FORMATION IN MICROGRAVITY

C. Thomas Avedisian
Cornell University
Ithaca, New York

Introduction

Most practical fuels which are burned in combustion-powered devices, stationary power plants, and incinerators are multicomponent in nature. The differing properties of fuels effects the combustion behavior of the blend. Blending can be useful to achieve desired ends, such as increasing burning rates and reducing extinction diameter and soot formation. Of these, particulate emissions is one of the most important concerns because of its impact on the environment. It is also the least understood and most complicated aspect of droplet combustion. Because of this fact, a well characterized flow field and simplified flame shape can improve the understanding of soot formation during droplet combustion. The simplest flame shape to analyze for a droplet, while still maintaining the integrity of the droplet geometry with its inherent unsteadiness, is spherical with its associated one-dimensional flow field.

This project will concern soot formation in microgravity droplet flames and some parameters that effect it. Because it has not yet begun, this paper will briefly review some related results on this subject.

Experiment

For combustion in an ambience of air (the most practical environment), the pressure must be reasonably high (usually atmospheric or higher) for soot formation to be a factor. Low pressure tends to suppress sooting for an ambience of air. With increasing pressure, buoyancy becomes a factor so a microgravity environment can compensate. In past work, low gravity was realized by conducting experiments on board a drop tower, and both free and fiber-supported droplets were studied. Free droplets were formed and deployed by a piezoelectric droplet generator [1]. For fiber supported droplets, the ratio of the fiber to the droplet diameter at ignition is kept small to minimize the influence of the fiber, which can effect soot patterns as shown in fig. 1 [2]. Burning rates for fiber-supported droplets need to match (within experimental error) the burning rates of unsupported droplets of similar size to avoid a fiber influence on burning. Then, results from fiber supported droplets can be useful for single component fuels.

Typical data are the evolution of the droplet diameter. If the luminous zone is especially pronounced in photographs, the flame 'diameter' can also be measured but few data exist for the flame or luminous zone boundary that spans a significant portion of the burning history. The flame is ideally identified by a peak in a radical species like OH or temperature distribution, but the diagnostics necessary to measure OH distribution around burning droplets have not yet been utilized in microgravity droplet combustion experimentation. In practice, the flame and soot shell diameters are identified from photographs. This type of recording medium will continue to be indispensable for data extraction. Simultaneous measurement of the droplet diameter, D , the mean soot shell diameter, D_s , and the 'flame' diameter, D_f , however, is difficult or impossible if soot image intensity dominates.

Data reduction from the motion picture negatives is via commercial data acquisition software. Sooting is inferred from examination of digitized photographs by scanning the pixels. This method is obviously qualitative but necessary because of the difficulty of employing more quantitative soot diagnostic methods in a drop tower environment.

Mixtures and Emulsions

Many models have been formulated for spherically symmetric burning of multicomponent fuels, including emulsions, but few relevant data have been published. Combustion of a mixture droplet, especially, can be effected by the experimental method. For fuel blends, fiber supported droplets can effect the species distribution within the droplet, promote heterogeneous nucleation on the fiber surface, and (for an emulsion) cause coalescence of the dispersed phase. Unsupported droplets avoid these effects but it is more difficult to capture their complete combustion history on film because of the necessity of keeping the droplet stationary. Unsupported droplets of methanol/dodecanol, heptane/hexadecane, and methanol/toluene have been examined in microgravity [3-6]. Some of the observations showed multistage combustion and microexplosions, and an influence of composition on soot formation.

Concerning emulsions, two studies are known for microgravity droplet flames [7,8]. Emulsions of water and oil, and hydrazine and oil, were examined [8] using the suspended droplet technique in which disruptions akin to microexplosions were noted. For the present project, emulsions using free droplets will be studied. The continuous phase will be heptane and the dispersed phase will be water. Water is selected as the dispersed phase because of its expected influence on soot formation through the flame temperature. Heptane as the continuous fuel phase permits referencing the results with microgravity heptane droplet flames. The similar volatility of heptane and water should not lead to microexplosions. The presence of a low volatility surfactant that is usually needed to stabilize an emulsion, however, will be assessed in the experiments.

Evolution of the Flame and Soot Shell 'Diameter'

The appearance of a ring of soot or 'shell' is unique to spherical droplet flames for sooting fuels. In a convective environment, soot entrapment will also occur but the soot pattern shape will roughly follow that of the flame which is stretched out in a tear-drop shape. First observed by Okajima and Kumagai [9], spherical soot patterns formed between droplet and flame have been more prominent in recent studies. The shell of soot will form where the forces acting on the aggregates balance. Thermophoretic forces on aggregates are directed toward the flame. The force due to Stefan drag is directed away from the droplet. The 'shape' of the shell is dictated by the velocity distribution around the droplet which is spherical for a purely radial flow field.

The time dependence of D_s (the shell "diameter" really has a finite thickness) reflects the temporal variation of D_f during burning. An example is illustrated in fig. 2a, where the evolution of D_s/D is shown for n-heptane [1] and compared with measurements of the outer luminous zone, D_f/D , which is here taken to be the flame diameter. Similar results for a 1-chloro-octane (CHC) flame are also shown in fig. 2b. That both D_s/D and D_f/D track together, with $D_s/D < D_f/D$ as shown in fig. 2, is consistent with the fact that soot precursors form on the fuel rich side of the flame. Based on the time dependence of D_f/D shown in fig. 2, 'quasi-steady' droplet combustion which requires D_f/D to be constant [10] is not realized in the experiments.

Effect of Droplet Diameter on Soot Formation and Burning Rate

The evidence for this effect is qualitative because it is based on subjective judgements from comparing intensities of photographs for droplets of different size. Generally, smaller droplets show less intense soot images than large droplets. Fig. 3 shows four different fiber-supported heptane droplets under similar backlighting conditions [1]. The fiber diameter was 30 μ m for the two smallest droplets and 50 μ m for the two largest droplets. The initial (equivalent) diameters range from .44mm to 1.01mm and the value of t/D_0^2 is approximately the same to facilitate comparisons. Differences in soot image intensity are evident.

The mass of soot formed during droplet combustion should increase as the initial droplet diameter increases because of the larger mass of fuel vaporized. Less clear is whether or not the 'proportional' amount of soot formed, that is the amount of soot formed per unit mass of fuel vaporized, is effected by droplet size. No measurements of this quantity have been made for spherical droplet flames. However, for droplets burning in a convective environment, the amount of

soot formed per unit mass of fuel burned appears to increase as the droplet diameter increases and to scale as D^n [11] where $3 < n < 4$.

Concerning the burning rate, some evidence exists to show that the droplet burning rate is influenced by D_0 [1]. Fig. 4 shows how K ($\equiv -d(D^2)/dt$) varies with D_0 for heptane (for two-spark ignition) for $.4\text{mm} < D_0 < 1.1\text{mm}$. K increases as D_0 decreases, which is not consistent with the classical theory of droplet combustion [10] which, though, neglects soot formation.

Soot formation can cause K to change continuously during burning. Aggregates formed in the early of burning where the droplet diameter is largest will become trapped between the droplet and flame. In the later period where the droplet diameter is considerably reduced from the initial value, proportionally less soot should be produced. However, entrapped aggregates from the earlier period of burning can still remain near the droplet late in the burning history. Also, the heat generated at the flame (relative to the droplet size) should increase proportionally as diameter is reduced because proportionally fewer fuel molecules are converted to soot if smaller droplets soot proportionally less than larger ones. As a result, K could progressively increase as burning proceeds. The evidence for this effect is circumstantial as shown in fig. 5 for CHC [1], but it does suggest a more constant K for smaller, less sooting, droplets than larger ones. Variations in K during burning can be difficult to identify because it requires obtaining second derivatives which can greatly magnify data uncertainty. The early period of burning (the first 10% of it or so), and the end of burning where the droplet diameter can be too small, can be difficult to resolve using conventional photographic means. There will continue to be a need for increased precision of droplet diameter measurements.

The residence time of fuel molecules on the fuel-rich side of a flame can be used to explain qualitatively trends shown in fig. 3. The longer fuel molecules reside on the fuel rich side of the flame the greater will be the probability of their ultimate conversion to soot aggregates. Two characteristic times are the transport time of fuel molecules between the droplet and flame (D_0^2/α) and a pyrolysis reaction time. The ratio of these two times, τ , is $\tau \equiv AD_0^2 \exp[-E/(RT)]/\alpha$ [12] where E is an activation energy associated with a first order pyrolysis reaction, A (s^{-1}) is the corresponding pre-exponential factor for an Arrhenius rate constant, and α is a mean gas diffusivity. The propensity for soot formation increases as conditions are adjusted to increase τ , and vice versa for decreasing values of τ . Trends based on this proportionality are consistent with experimental observations. For example, decreasing D_0 lowers τ which should lower the propensity to soot. This is consistent with experimental results [1,11].

Modelling

Soot formation processes have not yet been included in a model for droplet combustion. Such things as complex chemistry, the steps and associated rates for forming soot aggregates, soot aggregate entrapment, and the effect of converting fuel molecules to soot on the heat release at the flame would have to be included in a detailed model. Some of the building blocks for detailed modelling have been developed in past research, for example the influence of flame radiation [13,14], complex chemistry for several fuels [15-17], the forces acting on soot aggregates [17,18], and models for soot production rates in flames [19-21].

If soot formation is not accounted for, the resulting analysis will be of limited applicability, for example to a small droplet or low pressure limit where soot formation is minimal. Such a limit was assumed for a spherically symmetric flame for quasi-steady conditions and neglecting flame radiation [17]. Complex chemistry for heptane [22] was, however, included in the model. The temperature and velocity distributions calculated from this model were used to predict the net force ζ on particles (due to thermophoresis and the Stefan drag force) for a fictitious situation in which the soot particles do not influence the transport processes. Fig. 6 [17] shows two equilibrium positions for particle entrapment for a given particle radius, r_p , but only one of them is stable: the one closest to the droplet. Concerning a soot precursor species, fig. 7 [17] shows that the calculated mass of

acetylene formed per mass of fuel vaporized decreases as the initial droplet diameter decreases.

Summary and Future Work

Past research has shown that composition and droplet size can influence the droplet burning rate and soot formation for near spherically symmetric burning. Future work will extend the range of droplet diameters to smaller droplets than has been examined in a near convection-free environment, compare the results to a nonsooting fuel for referencing, and extend the analysis for sooting fuels. The experiments will also include study of emulsions using free droplets to examine the effect of water. Metal-based additives may also be examined because of their known role of influencing soot formation in some cases by the effect of the ions produced.

references

1. Jackson, G.S. and Avedisian, C.T. *Proc. R. Soc. Lond.*, **A446**, 1994, 255-276
2. Wellin, J.D., Jackson, G.S. and Avedisian, C.T. paper no. 88, Fall Eastern States Section Meeting of the Combustion Institute, Princeton, N.J. October 25-27, 1993.
3. Yang, J.C., Jackson, G.S. and Avedisian, C.T. *23rd Symp. (Int.) Comb.*, Pittsburgh, Pa.: The Combustion Institute, 1990, pp. 1619-1625.
4. Mikami, M., Kono, M., Sato, J., Dietrich, D.L. Williams, F.A. *Com. Sci. Tech.* **90**, 1993, 110-123.
5. Yang, J.C. and Avedisian, C.T. *22nd Symp. (Int.) on Combust.*, Combustion Institute, 1989, pp. 2037-2044
6. Jackson, G.S., Avedisian, C.T., and Yang, J.C. *Proc. R. Soc. Lond.*, **A435**, 1991, 359-369.
7. Okajima, S., Kanno, H., and Kumagai, S. *Acta Astronaut.* **12**, 1985, 555-563.
8. Kimura, M., Ihara, H. Okajima, S., and Iwama, A. *Comb. Sci. Tech.*, **44**, 1986, 289-306.
9. Okajima, S. and Kumagai, S. *15th Symp. (Int.) Comb.*, Pittsburgh, Pa.: The Combustion Institute, 1975, pp. 401-407.
10. Glassman, I. *Combustion*, 2nd ed., Orlando, Fla.: Harcourt, Brace, Jovanovich, 1987.
11. Gupta, S.B., Ni, T. and Santoro, R.J. paper no. 50, Fall Eastern States Section Meeting of the Combustion Institute, Clearwater Beach, Fl., December 5-7, 1994.
12. Avedisian, C.T. *Comb. Sci. Tech. Book Series*, vol. 2, in press.
13. Lage, P.L.C. and Rangle, R.H. *J. Thermophys. Heat Transf.* **7**, 1993, 101-109.
14. Saitoh, T., Yamazaki, K. and Viskanta, R. *J. Thermophys. Heat Transf.* **7**, 1993, 94-100.
15. Cho, S.Y., Choi, M.Y., and Dryer, F.L. *23rd Symp. (Int.) Comb.*, Pittsburgh, Pa.: The Combustion Institute, 1990, pp. 1611-1617.
16. Cho, S.Y., Yetter, R.A., and Dryer, F.L. *J. Comp. Phys.*, **102**, 1992, 160-179.
17. Jackson, G.S. and Avedisian, C.T. *AIAA* paper no 95-0286, 1995.
18. Jackson, G.S., Avedisian, C.T., and Yang, J.C. *Int. J. Heat Mass Trans.*, **35** (8), 1992, 2017-2033.
19. Kesten, A.S., Sangiovanni, J.J. and Goldberg, P. *J. Eng. for Power*, **102**, 1980, 613-618.
20. Kennedy, I.M., Kollman, W. and Chen, J.Y. *Comb. Flame.* **81**, 1990, 73-85.
21. Frenklach, M. and Wang, H. *1990 23rd Symp. (Int.) Comb.*, Pittsburgh, Pa.: The Combustion Institute, 1990, pp. 1559-1566.
22. Warnatz, J. *20th Symp. (Int.) Comb.*, Pittsburgh, Pa.: The Combustion Institute, 1984, pp. 845-856.

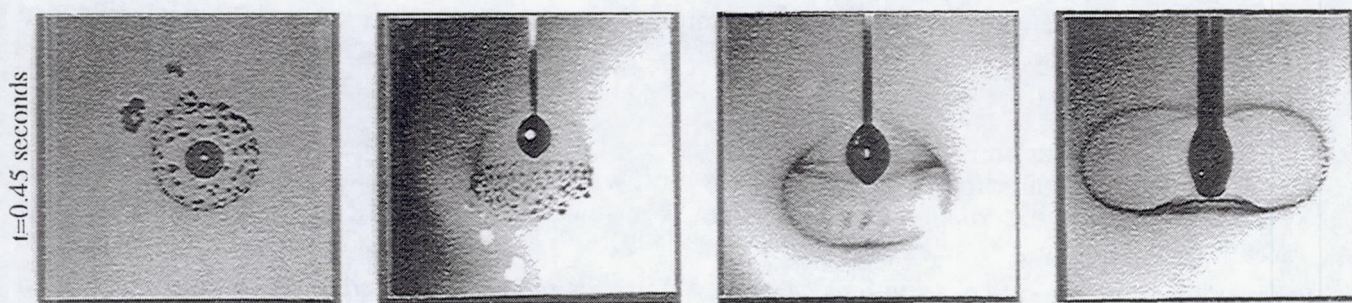


Figure 1: Effect of support fiber diameter on soot patterns and droplet shape .45s after ignition. a) free droplet; b) .057 μ m fiber, $D_0=700\mu$ m; c) 110 μ m fiber, $D_0=770\mu$ m; d) 330 μ m fiber, $D_0=610\mu$ m

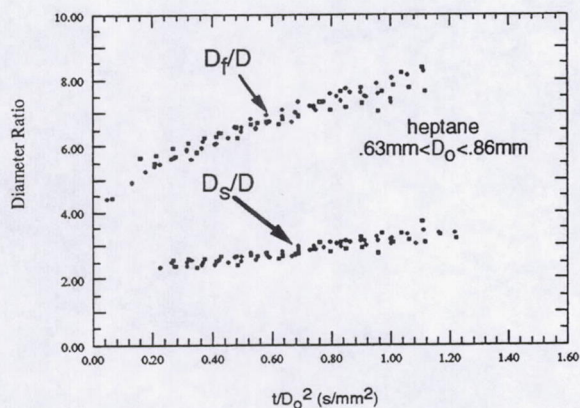
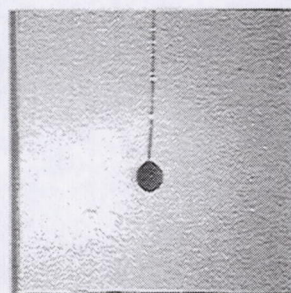
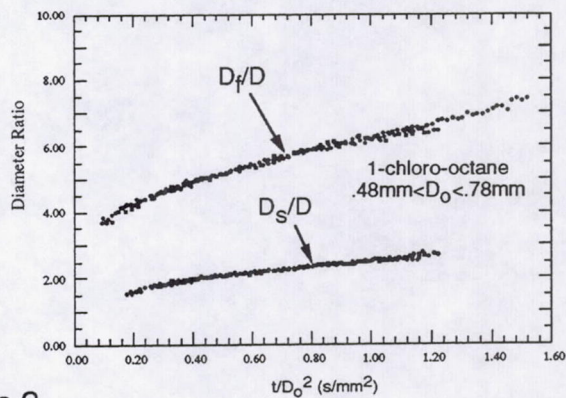
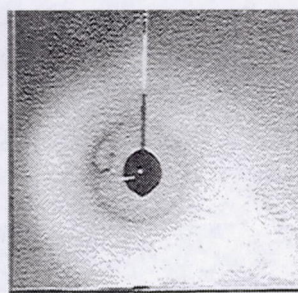


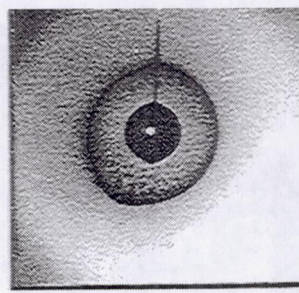
Figure 2



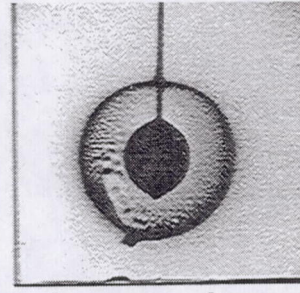
$t/d_0^2 = 0.39 \text{ s/mm}^2$ (0.075 s)
 $D_0 = .44\text{mm}$



$t/d_0^2 = 0.40 \text{ s/mm}^2$ (0.15 s)
 $D_0 = .61\text{mm}$



$t/d_0^2 = 0.38 \text{ s/mm}^2$ (0.28 s)
 $D_0 = .86\text{mm}$



$t/d_0^2 = 0.38 \text{ s/mm}^2$ (0.39 s)
 $D_0 = 1.01\text{mm}$

Figure 3: Effect of D_0 on soot image intensity for suspended heptane droplets.

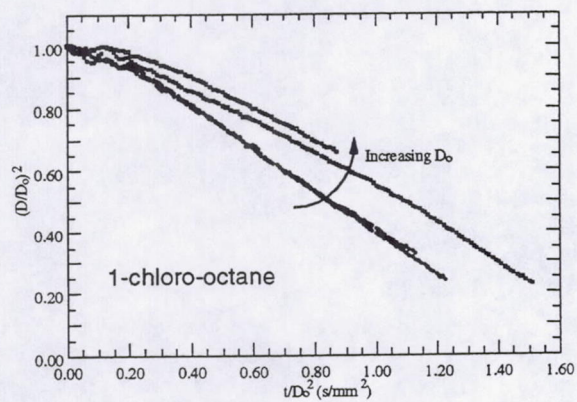


Figure 4

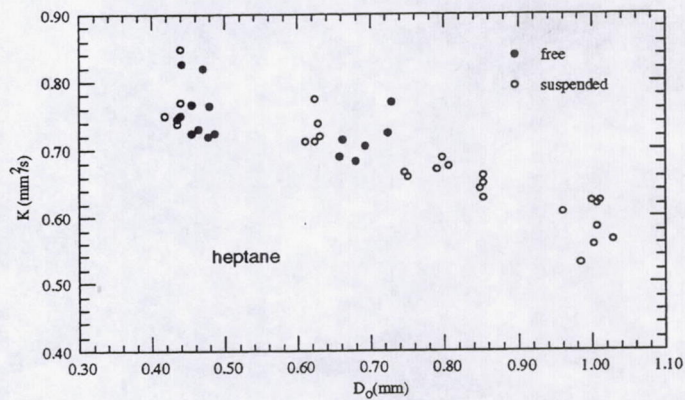


Figure 5

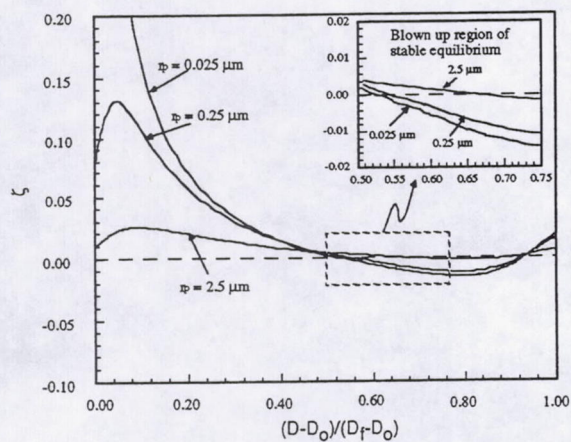


Figure 6

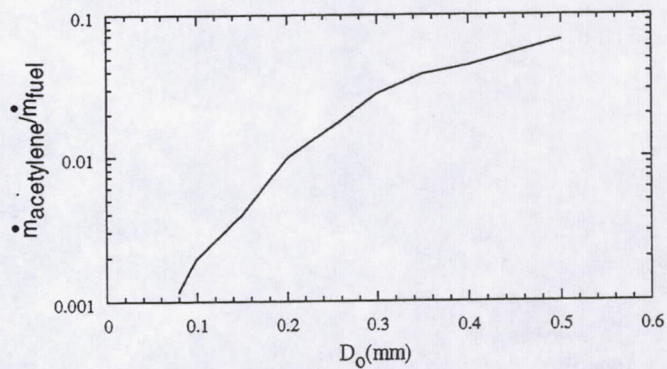


Figure 7

THE EFFECTS OF SOOTING IN DROPLET COMBUSTION

Kyeong-Ook Lee, Kirk Jensen and Mun Young Choi
Department of Mechanical Engineering
University of Illinois at Chicago
Chicago, IL 60607

1.0 INTRODUCTION

The study of the burning of a single droplet is an ideal problem from which to gain fundamental understanding of diffusion flame characteristics. Droplet combustion is a complex physico-chemical process that involves a chemically-reacting two-phase flow with phase changes and yet simple experiments and analysis can be used to attain important insights into the burning rate, flame dynamics, kinetic extinction and disruption processes. It is a subject that has been actively studied for the past 40 years with most of the fundamental experiments being performed under reduced-gravity conditions for direct comparisons with theoretical/computational analyses that invoke spherical symmetry assumptions.

In the earlier studies, the effects of sooting on the overall burning characteristics were not considered [Kumagai and Okajima, 1957; Kumagai, Sakai and Okajima, 1971]. However, recent microgravity investigations performed at the NASA-LeRC droptowers (**Droplet Combustion Experiment of Professor F.A. Williams and Professor F.L. Dryer**) and others indicate that effects of soot and sootcloud formation may be significant during the lifetime of the droplet and therefore must be included in the analysis [Knight and Williams, 1980; Shaw et al., 1988; Choi et al., 1990; Jackson et al., 1991; Avedisian, 1994].

1.1 Droplet Burning Rate

Sooting mechanisms can have profound effects on the overall droplet burning rate. In an earlier study on microgravity n-heptane droplet combustion experiments, vaporization rates that were as much as 30% to 40% lower than the classically-accepted results were reported [Choi et al., 1990]. The main conclusion drawn from that investigation was that the effects of formation and accumulation of the sootshell and its asymmetric configuration caused by small degrees of relative droplet/gas convection were responsible for the observed discrepancies. There are several mechanisms through which soot/sootshell formation can affect the burning rate. Soot formation is an endothermic process and will act as a heat sink for the energy that would otherwise be used to vaporize the fuel. Although, exact figures for the conversion to soot is not presently known for microgravity droplet combustion, results from normal gravity pyrolysis experiments suggest relatively large conversion rates ~ 30% [Vranos and Liscinsky, 1984]. Furthermore, heat loss at the flame due to soot radiation can reduce the effective transfer number by decreasing the amount of energy available to vaporize the fuel. Related to these phenomena is the accumulation of the formed soot in the region bounded by the droplet and the flame. This represents unrealized chemical energy resulting in the reduction of the heat of combustion available from the vaporized fuel.

1.2 Extinction

Analysis of the extinction mechanism during droplet combustion is important for extracting overall chemical kinetic rates for large hydrocarbons for which detailed information does not exist [Chung and Law, 1986; Williams and Dryer, 1994]. Extinction occurs when the flow time of the reactants becomes smaller than the time needed for the reactants to be consumed (when the Dahmkohler number is reduced below a critical value). The critical Dahmkohler number is given by where d_{ext} is the extinction diameter, D_g is the diffusivity and t_c is the characteristic chemical reaction time.

$$Da_{cr} = \frac{d_{ext}^2 D_g}{t_c} \quad (1)$$

However, extinction can occur prematurely if radiative losses from the flame decreases the flame temperature and therefore affect the chemical reaction time. Chao and coworkers [Chao et al., 1990] suggest that radiative losses from the flame can promote the onset of kinetic extinction. For droplet flames that produce soot, it is likely that soot radiation will dominate and therefore affect the kinetic extinction process [Grosshandler, 1992]. Thus far, only a limited number of extinction measurements have been reported for n-heptane droplets burning in air [Yang and Avedisian, 1988; Hara and Kumagai, 1990]. However, the extinction diameter is usually very small and not always reproducible under mildly sooting conditions. Without accurate determination of the soot concentration near the flame, it is not known to what degree soot formation may eventually affect droplet extinction.

1.3 Disruptive Burning

In a previous work by Knight and Williams [1980], disruption was observed during the combustion of alkane droplets in a microgravity environment. Disruption is a process by which the original droplet is violently shattered and burns as smaller satellite droplets. In subsequent experiments in the NASA-Lewis droptower [Shaw et al., 1988], it was found that the likelihood of observing the disruption behavior was higher for fuels (and/or conditions such as higher oxygen concentrations) that produced high soot loading.

Shaw and Williams [1990] presented results that suggest that the absorption of heavy soot precursors on the droplet surface can create conditions in which an outer layer (of soot precursors) can reach temperatures exceeding the superheat temperature of the original fuel. Another possible mechanism suggests that the soot particles can come in contact with the droplet and cause rapid heating. Although a definitive explanation does not exist, it is clear that the sooting mechanism is very important in the disruptive burning process.

1.4 Thermophoresis

For droplet combustion, soot particles form in the fuel-rich region of the diffusion flame through pyrolysis reactions. These reactions are high-activation energy processes and thus maximum soot production will likely occur near the flame [Shaw et al. 1988]. Once soot is formed in the fuel-rich region, they are acted upon by viscous drag (caused by Stefan flow) and Thermophoresis. Thermophoresis is a mechanism through which particle transport is caused by a temperature gradient in the surrounding gas-phase [Friedlander, 1977]. Waldmann and Schmitt [1966] analyzed the viscous drag and thermophoretic force acting on a small spherical particle by calculating the momentum transferred per unit time to the particle by the impinging and rebounding gas molecules. At equilibrium [ΣF is equal to 0], these two forces are balanced. The resulting equation can then be solved for the flux, ρV_t .

$$\rho V_t = \frac{-3\mu dT/dr}{4(1+\pi\alpha/8)T} = g(r) \quad (2)$$

The term, ρV_t , is defined as the thermophoretic flux. The thermophoretic flux is the convective flux necessary for the above-mentioned force equilibrium on the particle to be maintained.

Opposing the thermophoretic forces is the viscous drag caused by the Stefan flux, where (dm/dt) is the droplet mass gasification rate.

$$\rho V_r = \frac{dm/dt}{4\pi r^2} \quad (3)$$

Eqn. 3 is valid under conditions of negligible surface regression rate compared to the gas velocity at the surface which is satisfied when the ratio of the liquid to gas densities is large. The sootshell will form at the radial position where the viscous drag and thermophoretic forces are in balance.

The above formulation is valid for soot particles that are much smaller than the mean free path. Jackson and coworkers [1991] implemented the thermophoretic model of Talbot and coworkers [1980]. In this model, the sootshell location can be calculated by assuming the soot particle dimension. Therefore, the measurement of the characteristic dimensions of the soot particles (including the radius of gyration and primary particle size using thermophoretic sampling and TEM) will be important in comparing the experimental and theoretical sootshell locations.

1.5 Droplet Flame Dynamics

The flame diameter is also affected by the soot formation through reductions in the specific volume [Choi et al., 1993]. After the initial period of fuel vapor accumulation (during which fuel vapor fills the increasing volume between the droplet surface and the flame front), quasi-steady conditions should exist under which the gasified mass will equal the mass consumed at the flame front. However, under sooting conditions, portions of the gasified fuel are converted to soot (which possess negligible specific volume when compared to that of the gaseous species). Therefore, soot accumulates in the sootshell and never reaches the flame front.

2.0 The Need for Accurate Measurement of Soot Volume Fraction and Temperature

Since the pioneering microgravity droplet combustion experiments of Kumagai and coworkers back in 1957, there have been numerous theoretical, computational and experimental studies analyzing the burning characteristics of isolated droplets. In all subsequent microgravity droplet combustion studies, the degree of sooting was estimated by visual observations of the sootshell. This practice could not provide detailed information regarding the transient distribution of the soot and temperature in the region bounded by the flame and the droplet. For all of the important parameters of interest in droplet combustion including the variations in the

burning rate, promotion of extinction, reduction in flame size, onset of disruptive burning and soot dynamics, it is clear that accurate measurements of the degree of sooting and the temperature field within the region bounded by the droplet and the flame is needed to further advance our understanding.

In the present study, the sooting behavior will be studied using light extinction measurements and Abel deconvolution to determine the radial distribution of soot volume fraction; two-wavelength optical pyrometry to determine the soot temperature within the region between the flame and the droplet; and thermophoretic sampling/transmission electron microscopy to determine the soot morphology (radius of gyration and primary particle size). In addition, computational modeling [using the Chemically-Reacting-Flow-Model of Princeton] of the soot particle dynamics involving the balance between thermophoresis and Stefan drag will be compared with the experimental measurements. The modeling efforts will be advanced interactively with the experimental measurements of the soot volume fractions and the soot particle dimensions.

These experiments will be performed for a wide range of conditions to vary the sooting propensity of the droplet using various fuels (including decane, heptane, toluene/methanol mixtures, benzene/methanol mixtures and ethanol etc.), pressure (0.1 to 1.0 atm), oxygen indices (0.15 to 0.50), initial droplet diameters (1.0 to 5.0 mm) and inerts (N_2 , He, CO_2 , etc.) as parameters.

3.0 EXPERIMENTAL APPROACH

3.1 Soot Volume Fraction Measurements

Kadota and Hiroyasu [1984] first measured soot concentration in droplet flames using optical techniques. In their study, light extinction measurements were performed at a fixed location below the droplet and the radial variation was deduced by assuming that the regressing flame maintained constant spherical structure. This procedure may produce realistic information since the flame geometry is nearly spherical in the region below the droplet. However, the same approach will produce unrealistic results in the region above the flame where it displays both axial and radial variations.

In the present experiment, the soot volume fraction will be measured using a full-field light extinction technique that was developed at NASA-Lewis Research Center by Greenberg, Griffin and Ku [Griffin and Greenberg, 1992; Greenberg and Ku, 1995] for eventual use in measuring the soot volume fraction for microgravity droplet combustion. Feasibility of this technique was investigated by performing soot volume fraction measurements for suspended droplets burning under normal-gravity conditions.

Fig. 1 displays the schematic of the experimental apparatus similar to the system of Greenberg and Ku [1995]. Light from the HeNe laser is first passed through a variable neutral density filter and expanded through a spatial filter/collimator to produce a 50mm diameter beam. The beam is directed through opposing optical ports (each fitted with 51mm diameter quartz windows) of the stainless steel droplet combustion chamber. The transmitted beam is imaged using a high-resolution CCD camera (with attached interference and neutral density filters). The entire burning history is recorded onto a S-VHS recorder and subsequently the image is digitized frame-by-frame using a high-resolution (512x480 pixels) data acquisition board. Measurements indicate that the laser/detection system is very stable with temporal fluctuations of the light intensity less than 0.5% of the total magnitude of the intensity.

For the normal-gravity droplet combustion experiment, a single droplet of 2mm diameter is deposited on a bead that is formed at the end of the suspending quartz fiber (diameter is approximately 150 micrometers) using a hypodermic needle. The orientation of the fiber as shown in inset A in fig. 1 was designed to minimize interactions with the burning by reducing its contact with the flame (For the proposed microgravity experiment, droplets will be suspended by using cross-hairs of 50 micron silica carbide fibers). The droplets are ignited using an induction coil discharge igniter.

For each horizontal plane, the line of sight projection data, $P_f(x)$, is given by:

$$P_f(x) = \int_{-\infty}^{\infty} f_v \sqrt{x^2 + y^2} dy \quad (4)$$

The Abel transform allows the calculation of the field distribution $f_v(r)$ corresponding to the projection data with the underlying assumption that it is radially symmetric [Santoro et al., 1983; Dasch, 1992; Sunderland et al., 1995]. The soot volume fraction distribution (based on extinction) is found from the measured transmission of each projection:

$$\tau_\lambda(x) = \frac{I_\lambda(x)}{I_{\lambda_0}} = \exp\left[-\frac{K_e}{\lambda} \int_{-\infty}^{\infty} f_v \sqrt{x^2 + y^2} dy\right] \quad (5)$$

where K_e is the dimensionless extinction constant of soot. In this study, K_e value of 8.8 which was measured for soot in the post-flame region of a rich acetylene flame was used [Choi et al., 1995]. Equation 5 can be rearranged into the form of the projection value as:

$$P_{f_v}(x) = -\frac{\lambda}{K_s} \ln\left(\frac{I_\lambda}{I_{\lambda_0}}\right) = \int_{-\infty}^{\infty} f_v \sqrt{x^2 + y^2} dy \quad (6)$$

For a typical experiment, nearly 200 images are produced, therefore, full-field determination of the soot volume fraction measurements requires the analysis of more than 30,000 projection data files. To increase the efficiency, a full-field algorithm was written to analyze the entire experiment [Greenberg and Ku, 1995 have also written a similar algorithm].

In the present study, the soot volume fraction is measured as a function of radial position for hydrocarbon mixture flames at various heights above the droplet. Figure 2 displays the resulting G/G_0 (where G corresponds to graylevel) profiles for $t = 2$ sec after ignition. The entire image is filtered using a 3x3 low-pass filter and the individual vertical position data is 5-pt averaged. The horizontal axis corresponds to the column position and the vertical axis corresponds to row positions. The maximum attenuation is approximately equal to 0.4. From this profile, the soot volume fraction is determined using the full-field Abel-deconvolution algorithm [See fig. 3]. A curve-fitting algorithm is used to define the center of the sooting region for each vertical position and the soot volume fraction on either side of the center is averaged to obtain the final output. The soot volume fraction increases from as a function of height and radial position from the center. The soot volume fraction is maximum near the flame at all vertical locations which is consistent with the structure of diffusion flames.

3.2 Soot Temperature Measurement Technique

The temperature of the soot particles within the region between the droplet surface and the flame front will be measured using a two-wavelength pyrometry and Abel deconvolution [Faeth, 1994]. The emission from the flame will be simultaneously directed to two separate CCD cameras (with a narrow bandpass filters at 800 nm and 900 nm) using a beamsplitter. Due to the small size of soot particles, the discrepancy with the local gas temperatures is expected to be small [Köylü and Faeth, 1993]. The emission intensity at each central wavelength measured for a vertical plane corresponds to the projection value of the integrated emission.

$$P_{I_\lambda}(x) = \int_{-\infty}^{\infty} K_\lambda I_{b\lambda} dy \quad (7)$$

$$K_\lambda = \frac{36\pi nk}{(n^2 - k^2 + 2)^2 + 4n^2 k^2} \frac{f_v}{\lambda} \quad (8)$$

where $I_{b\lambda}$ is Planck's function. The projections values for 800 nm and 900 nm can be deconvoluted separately using the Abel technique to determine the corresponding product of $(K_\lambda I_{b\lambda})$ as a function of radial position. The ratio of the emission at 800 nm and 900 nm can then be used to determine the temperature using the two-wavelength pyrometry formula [Sivathanu and Faeth, 1990].

3.3 Soot Morphology Measurement Technique

The morphology of soot aggregates will be determined by performing thermophoretic sampling experiments [Megaridis and Dobbins, 1988]. Thin ribbons of copper mesh grids will be rapidly inserted into the flame to obtain instantaneous distribution of soot morphology. Temporal variation of the soot will be determined by inserting different ribbons at pre-determined times. Subsequent analyses will involve obtaining transmission electron micrographs and analyzing the radius of gyration using a non-subjective digital image processing technique that was developed as part of this project [Choi and Zhou, 1995].

4.0 PROGRESS TO DATE

- A droplet combustion chamber which utilizes several features of the DCE droptower hardware is being fabricated at NASA-LeRC to take advantage of the design solutions. The UIC team will incorporate all of the optical diagnostic equipment to the experimental package. It is anticipated that an operational soot volume fraction/temperature rig to be used in the DC-9 and in the 2.2 sec droptower will be ready by mid-summer of 1995.
- A full-field normal-gravity droplet combustion apparatus to perform soot volume fraction measurements was implemented at UIC. Performed experiments using various hydrocarbon mixture droplets. (results will be presented at the Central States Sectional Meeting of the Combustion Institute, 1995).
- Developed an interactive Abel-deconvolution algorithm to determine soot volume fraction for full-field light extinction data. This program manipulates the full-field digitized image data and produces the I/o information at every single pixel location. The information is then used to determine the soot volume fraction information for each horizontal plane.

Similar program was also written for two-wavelength pyrometry.

- d) Developed a digital image processing program to determine the radius of gyration from transmission electron micrographs. The students are fully trained in TEM and Selected Area Electron Diffraction Techniques.
- e) Submitted a proposal (with P. Ferkul and D. Schultz of NASA-LeRC) to perform soot volume fraction measurements for droplets using the Glovebox facility.
- f) The PI was at Lewis during the summer of 1994 working with Dr. Randy Vander Wal using laser-Induced Incandescence for performing soot volume fraction measurements in droplet combustion. (results were presented by RVW at the Eastern States Sectional Meeting of the Combustion Institute, 1994).

5.0 FUTURE WORK

- a) Perform soot volume fraction/temperature measurements under normal-gravity for test conditions outlined in section 2.
- b) Incorporate optical diagnostic apparatus on the droplet combustion apparatus (that is being built at NASA-LeRC) for use in 2.2 sec droptower and aboard the DC-9. Reduced-gravity droplet combustion experiments for soot volume fraction and temperature measurements are scheduled for mid-summer, 1995.
- c) Collaborate with Princeton researchers in incorporating revised thermophoretic models to calculate sootshell location.
- d) Determine soot extinction constants for various fuels to be used in soot volume fraction experiments.

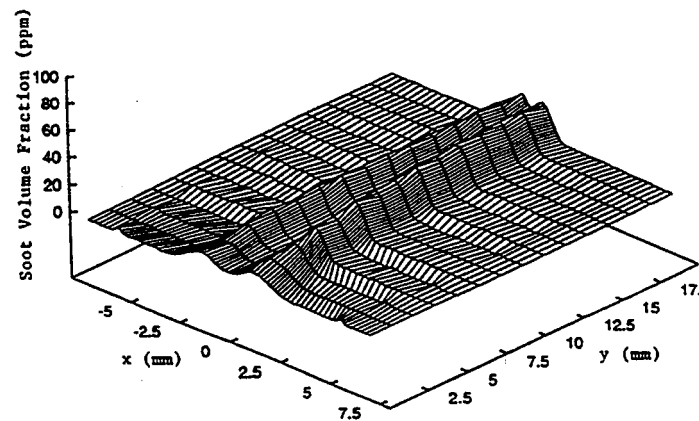
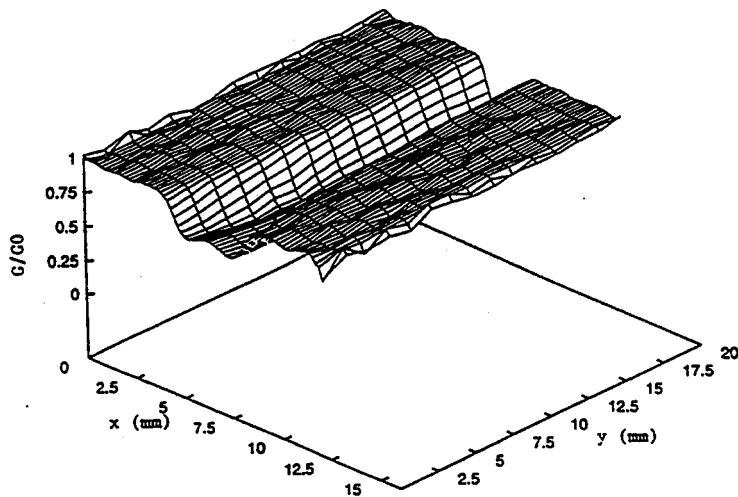
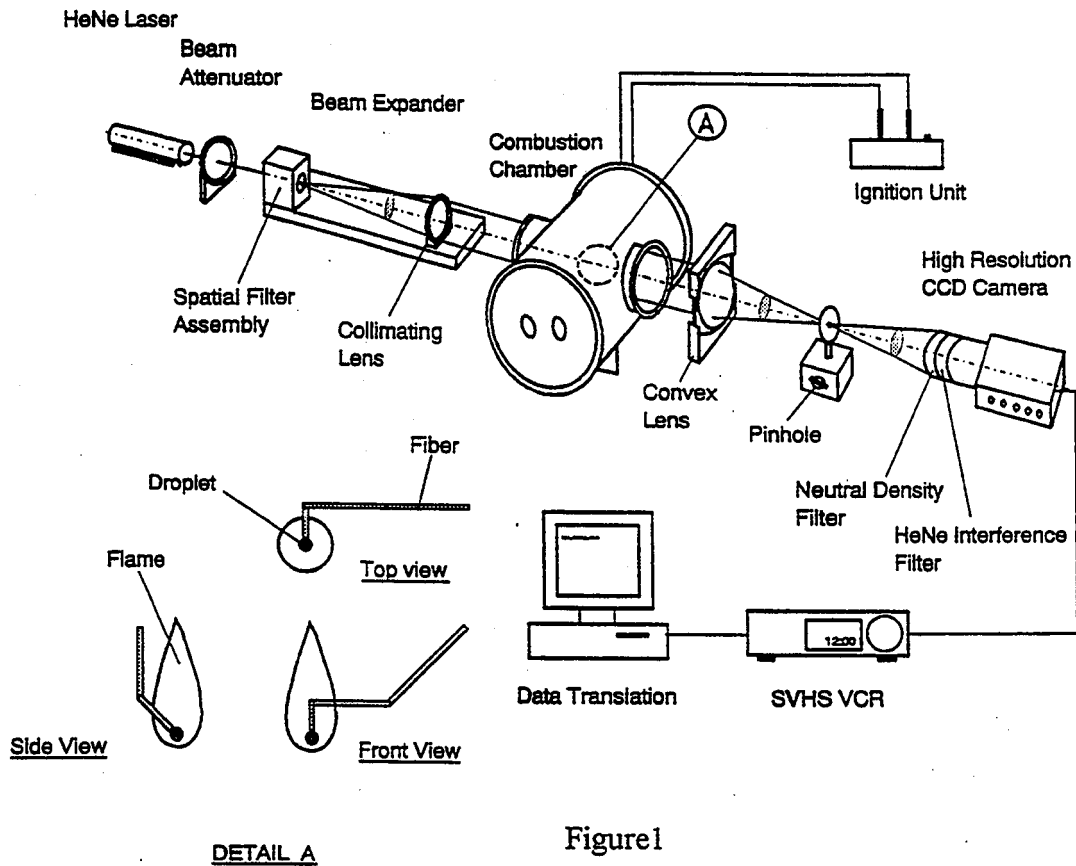
6.0 ACKNOWLEDGEMENTS

The authors gratefully acknowledge helpful advice regarding the implementation of a full-field light extinction technique provided by Mr. P. Greenberg, Dr. D. Griffin, Mr. B. Whiteside and Dr. D. Urban of NASA-LeRC. We would also like to thank Professor F.L. Dryer of Princeton, Professor F.A. Williams of UCSD, Dr. R. Vander Wal, Dr. P. Ferkul, Mr. D. Schultz and Dr. M. Vedha-Nayagam of NASA-LeRC and Drs. A. Hamins, T. Kashiwagi and C. Shaddix of NIST for helpful discussions regarding the work. This work was supported by NASA-LeRC through grant #NAG3-1631. Kirk Jensen would like to acknowledge support from the AMOCO Foundation Fellowship.

7.0 REFERENCES

1. Kumagai, S. and Isoda, H., Sixth Symposium (Int'l) on Combustion, p. 139. (1957).
2. Kumagai, S., Sakai, T. and Okajima, S., Thirteenth Symposium (Int'l) on Combustion, p. 779 (1971).
3. Knight, B. and Williams, F.A., Combustion and Flame, 38:111 (1980).
4. Shaw, B.D., Dryer, F.L., Williams, F.A. and Haggard, J.B., Jr., Acta Astronautica, 17:1195 (1988).
5. Choi, M.Y., Dryer, F.L., and Haggard, J.B., Twenty-Third Symposium (Int'l) on Combustion, The Combustion Institute, Pittsburgh, PA., p.1597 (1990).
6. Jackson, G.S., Avedisian, C.T. and Yang, J.C., Proc. R. Soc. Lond A, 435:359 (1991).
7. Avedisian, C.T., "Droplet Combustion and Soot Formation in Microgravity", Eastern States Section of the Combustion Institute, Clearwater Beach, FL (1994).
8. Vranos, A. and Liscinsky, D.S., Combustion Sci. Tech., 38:145 (1984).
9. Chung, S.H. and Law, C.K., Combustion and Flame, 64:237 (1986).
10. Williams, F.A. and Dryer, F.L., Science Requirements Document for Droplet Combustion Experiment, 1994.
11. Chao, B.H., Law, C.K. and T'ien, J.S., Twenty-Third Symposium (Int'l) on Combustion, The Combustion Institute, Pittsburgh, PA., p.523 (1990).
12. Grosshandler, W.L., RADCAL: A Narrow Band Model for Radiation Calculation in a Combustion Environment, NIST Technical Note 1402 (1992).
13. Yang, J.C. and Avedisian, C.T., Twenty-Second Symposium (Int'l) on Combustion, The Combustion Institute, p. 2037 (1988).
14. Hara, H. and Kumagai, S., Twenty-Third Symposium (Int'l) on Combustion, The Combustion Institute, p. 1605 (1990).
15. Shaw, B.D. and Williams, F.A., Int. J. of Heat and Mass Transfer, 33:301 (1990).
16. Friedlander, S.K., Smoke, Dust and Haze, Wiley and Sons, N.Y., (1977).
17. Waldmann, L. and Schmitt, K.H., Thermophoresis and Diffusiophoresis of Aerosols, Chap VI in Aerosol Science (C.N. Davies, ed.), Academic, N.Y., (1966).
18. Talbot, L. and Cheng, R.K., Schefer, R.W. and Willis, D.R., J. Fluid Mech. 101:737 (1980).
19. Choi, M.Y., Dryer, F.L., Green, G.J. and Sangiovanni, J.J., AIAA Paper 93-0823 (1993).
20. Kadota, T. and Hiroyasu, H., Comb. Flame, 55:195 (1984).
21. Griffin, D.W. and Greenberg, P.S., "Selected Microgravity Combustion Diagnostics Techniques", 2nd Int'l Microgravity Combustion Workshop Proceedings, Sept. 1992.
22. Greenberg, P.S. and Ku, J.C., "Soot Volume Fraction Imaging", Applied Optics, submitted, 1995.
23. Santoro, R.J., Semerjian, H.G., and Dobbins, R.A., Combust. Flame 51:203 (1983).

24. Dasch, C.J., Applied Optics, 31:146 (1992).
25. Sunderland, P.B., Koylu, U.O. and Faeth, G.M., Combust and flame, 110:310 (1995).
26. Zhou, Z. and Choi, M.Y., "Measurement of Dimensionless Extinction Constant of Soot Generated Using Various Fuels", To be presented at the Central/Western/Mexican Sections of the Combustion Institute, San Antonio, TX, April, 1995.
27. Faeth, G.M., Science Requirements Document for Laminar Soot Processes Experiment, 1994.
28. Köylü, Ü.Ö. and Faeth, G.M., J. Heat Transfer, 115:409 (1993).
29. Sivathanu, Y.R. and Faeth, G.M., Combustion and Flame, 81:150 (1990).
30. Megaridis, C.M. and Dobbins, R.A., Twenty-Second Symposium (Int'l) on Combustion, p. 353, 1988.
31. Choi, M.Y. and Zhou, Z., Digital Image Processing Algorithm for the Measurement of Soot Radius of Gyration, in progress, 1995.



COMBUSTION OF INTERACTING DROPLET ARRAYS IN A MICROGRAVITY ENVIRONMENT

Daniel L. Dietrich
NASA Lewis Research Center, Cleveland, Ohio 44135

Introduction

This research program involves the study of one and two dimensional arrays of droplets in a buoyant-free environment. The purpose of the work is to extend the database and theories that exist for single droplets into the regime where droplet interactions are important. The eventual goal being to use the results of this work as inputs to models on spray combustion where droplets seldom burn individually; instead the combustion history of a droplet is strongly influenced by the presence of the neighboring droplets.

Throughout the course of the work, a number of related aspects of isolated droplet combustion have also been investigated. This paper will review our progress in microgravity droplet array combustion, advanced diagnostics (specifically LII) applied to isolated droplet combustion, and radiative extinction large droplet flames. A small-scale droplet combustion experiment being developed for the Space Shuttle will also be described.

Droplet Array Combustion (with Kunihiro Kitano and Senji Honma, Hokkaido National Industrial Research Institute, Sapporo, JAPAN)

Recently, Annamali and Ryan [1] have summarized the current status of droplet array, cloud and spray combustion. A number of simplified theories [2-8], and detailed numerical studies [9,10] of droplet vaporization/combustion where multiple droplet effects are present are now available. These theories all neglect the effect of buoyancy. Experimentally, most studies to date suffer the effects of buoyancy is; it becomes the dominant transport mechanism in the problem. Only the works of Law and co-workers [11,12] and more recently by Mikami *et al.* [13] were performed in an environment where buoyancy effects were small. Law and co-workers were limited to high oxygen index, low pressure ambient environments since their studies were conducted in normal gravity.

Studies are now being conducted in normal and microgravity involving interacting droplet arrays in sealed chambers, where the ambient can be controlled. Droplets are typically suspended on 125 μm optical fibers with small ($\sim 250 \mu\text{m}$) beads on the end. A coiled hot-wire ignites the droplet, and then is removed immediately. Backlit images provide droplet diameter-time history and an orthogonal view provides flame-diameter time history. Recently Mikami *et al.* [13] showed that droplet arrays burning in microgravity do not burn in accordance with the d-squared law. The burning rates discussed below nonetheless are obtained by a linear least squares fit of the data.

Figure 1 shows results from a three-droplet array burning in air in microgravity. The fuel was n-heptane with initial droplet sizes of approximately 1.4 mm. Figure 1a (left) shows the burning history of each droplet in the array for $L/D = 7.1$, and Figure 1b (right) shows the burning history

of the center droplet of the array for different L/D's. Figure 1a shows that the center droplet in the array had the slowest burning rate of the three droplets. Figure 1b shows that a single n-heptane droplet has the largest burning rate. The burning rate then continuously decreases as the inter-droplet separation distance decreases.

In normal gravity tests, a horizontal two-droplet array of n-decane burning in air at 1 atm shows just the opposite behavior. The burning rate increases due to droplet interactions. For instance, the burning rate of a single n-decane droplet is $1.0 \text{ mm}^2/\text{s}$, but for a two droplet array with an initial, normalized (L/D) inter-separation distance of 4 the burning rate increases slightly to $1.1 \text{ mm}^2/\text{s}$.

In normal gravity, oxygen transport is enhanced by buoyant convection. In this case, the neighboring droplets reduce the heat loss during burning, and the burning rate increases. In microgravity, the buoyant heat loss is greatly reduced but so is the oxygen transport rate to the flame. In this case, the droplets actually compete with each other for oxygen. The burning rate, thus decreases. The center droplet, which is surrounded by other droplets receives the least amount of oxygen even though this droplet has the minimum heat loss. The burning rate of the center droplet is thus smaller than the other two. Symmetry dictates that the left and right droplets should have the identical burning rates, as is verified by the experimental data.

Isolated Droplet Combustion (with R. Vander Wal, NYMA, Inc.)

Traditionally, the diagnostics used on droplet combustion studies (especially in microgravity) have been limited to orthogonal views of the flame and droplet. While backlighting provides simple and accurate measurements of the droplet size (assuming proper adjustment of the light source and imaging system), simple pictures of the flame do not always provide accurate information. There are ambiguities regarding exactly what is being visualized, including the fact that a two-dimensional image of a three dimensional object is formed. Also, with the increasing use of video cameras, experimental results show that the observed size of the flame can vary as a function of camera gain, with large errors if saturation occurs. Since there is a range of colors and intensities in a droplet flame, it is difficult to select a single gain which is appropriate for the entire flame.

Studies in normal gravity have been conducted to try to gain an understanding of how the visible flame compares with different types of measurements. The most significant comparison has been with Laser-Induced Incandescence (LII) which measures the absolute and relative soot volume fraction during droplet combustion. Simultaneous LII and natural flame, simultaneous LII and OH chemiluminescence, and simultaneous droplet size history, natural flame and radiometric measurements of the flame studies have all been conducted. Although not simultaneously, backlit droplet size histories, which are quite reproducible, have been obtained for all of the fuels in the identical configurations to those above. An example of some of the data collected is given below.

These studies were conducted in a sealed chamber in air at 1 atm. The droplets were suspended by fibers with diameters of 125, 230 and 500 μm with beads on the end with diameters of 250, 400, and 1000 μm respectively. The initial droplet sizes for the three fibers were 1.2, 1.5 and 3 mm, respectively. The ignition system for the smaller droplets was a length of 250 μm Kanthal (Aluminum alloy) wire heated with a current of approximately 3 amps, that was removed immediately after ignition. The ignition system for the tests using the largest fiber and bead was a spark. The droplet dispense, deployment, and ignition systems were controlled by a portable computer which also provided a trigger pulse for the data acquisition system (LII). The fuels used in the tests were selected to show a wide range of sooting tendencies, heptane, decane (commonly used fuels), chloroheptane and chlorodecane.

A description and characterization of the two-dimensional LII system are described elsewhere [14,15, also presented at this workshop]. Both natural flame images and OH chemiluminescence images were taken with a second gated, intensified camera synchronized with the LII camera. For the largest droplet studies, the intensified array camera was used to capture backlit views of the droplet, but for all others, either black and white or color CCD cameras connected to a long working-distance microscope were used.

Figure 2 shows representative burning histories for each of the fuels, along with the least squares fit burning rate constants. Also shown are the relative average soot volume fractions for the produced for the two fuels [completely described in 15,16]. All of the tests were conducted in normal gravity with a 1 atm, air ambient. As the droplet hangs on the fiber, it is not spherical, but elongated. The equivalent droplet diameter plotted in Fig 2 was computed by three different methods, two from the volume and surface area equivalent diameter of an ellipsoid, and another from the projected area of the droplet. All methods produced equivalent droplet diameters and burning rate constants that were within a few percent of each other. Figure 3 shows both natural flame and LII images of n-decane and 1-chlorodecane.

Figure 2 shows that the burning rate constants for the heptane and decane are nearly identical, as expected. The burning rate constants for the chloroheptane and chlorodecane are also nearly equal to each other and to the value obtained for heptane and decane (within 12 percent). As seen in the table of Figure 2, the relative soot production from the fuels, however, is dramatically different.

The LII results show that, relative to heptane, decane has soot volume fractions twice that of heptane. The visible structure of the two flames, however, is nearly identical. Both are blue at the base or bottom and yellow near the top. The flame sizes (relative to the droplet) are also similar for the two fuels. The chlorinated fuels produce average soot volume fractions more than an order of magnitude larger than that of heptane. The structure of the flames is very different also. Both chlorinated fuels are open-tipped at the top, with significant soot escape. No soot was present at the bottom of the flame for the chlorinated fuels and the flame was blue there.

The fact that the burning rates were identical but the soot production varied so much can be explained as follows. The vaporization of the droplet is controlled by the heat feedback to the droplet. In normal gravity, the soot production occurs downstream of the droplet and the heat produced here does not significantly the vaporization rate of the fuel. Instead, the vaporization is controlled by the flame close to the bottom of the droplet.

Radiation Losses in Large Droplet Burning (with P. Struk, GSRP, and J.S. T'ien, CWRU)

Radiative losses in droplet burning are usually neglected in theoretical and numerical treatments of droplet burning. The limitingly small droplet diameter below which a spherical flame cannot exist is well documented and is a topic of a space flight microgravity investigation (DCE). A recent theoretical treatment by Chao et al. [17] shows that for a droplet burning with spherical symmetry, there will be a *large* droplet size above which a flame will not exist. The mechanism for the existence of this limit is radiative extinction.

Some preliminary experimental evidence was obtained in the JAMIC facility for the burning of a large (3-4 mm) decane droplet. Immediately after ignition the flame was as expected, bright yellow, sooty and spherical (except for a small non-uniformity due to a small convective flow). As the burning progressed, the luminosity of the flame decreased, and by the end of the drop, the droplet had not yet burned to completion, and the flame was nearly invisible to the CCD camera. While the flame was barely visible by the end of the test, it also did not extinguish. In a subsequent test, a smaller (1-2 mm initial diameter) n-decane droplet burned to completion as expected, with a bright yellow, sooty, spherically symmetric flame.

Further testing and analysis is required before any conclusions can be drawn from this preliminary data. This could be an indication, however, of increased radiative heat transfer cooling the flame such that less soot is produced. On the other hand, since these were the first tests in a new experimental apparatus, there could have been some experimental problem that caused this unusual result.

The radiative extinction phenomena for droplets is most easily observed in reduced gravity, where a droplet can burn with spherical symmetry and convective losses are minimized. To further study this problem, steady-state droplet combustion is simulated using a porous sphere which is continually fed with liquid. The liquid flowrate is controlled by a computer operated syringe pump that allows precise control of the flowrate. Initial work in normal gravity has been conducted at reduced pressure ambients. The chamber was the same one described in the previous section. The flowrate of the fuel was adjusted until a steady wetted surface was observed on the porous sphere. Because the chamber was sealed, the burning rate decreased slightly throughout the flame lifetime as a result of the continuously decreasing ambient oxygen concentration. An equivalent burning rate constant was computed as $k = [4Q/(\pi D)]$ where Q is the volumetric flowrate and D is the sphere diameter. The burning rate constant calculated this way is considered valid only when a steady wetted surface is observed.

For n-decane fuel, and a 4 mm diameter bronze sphere, steady burning was achieved at 1/3 atm. The equivalent burning rate constant was approximately 1.2 mm²/s. This is higher than the 0.9 mm²/s observed for 1.3 mm initial diameter fiber-supported droplets burned in the same facility. The difference is probably due to increased buoyancy effects at the larger droplet sizes with the porous sphere. Visibly, except for the scale factor, the flames from the fiber supported droplets and the porous sphere looked nearly identical; the only difference being that the flame was quenched at the base in the vicinity of the fuel supply tube in the case of the porous sphere.

The droplet diameter can be changed by varying the size of the porous sphere. In reduced gravity, small changes in droplet diameter may be obtained by changing the thickness of liquid film on the surface of the sphere. An experimental apparatus is currently being built which will be flown in the NASA LeRC DC-9 in the near future.

Glovebox Experiment (with F.A. Williams, UCSD; F.L. Dryer, Princeton; B.D. Shaw, UCD; M. Vedha-Nayagam, Analex; J.B. Haggard, NASA LeRC)

Currently manifested on STS-73, the Second United States Microgravity Laboratory (USML-2), is a small-scale droplet combustion experiment called the Fiber-Supported Droplet Combustion (FSDC) experiment. The FSDC is a multi-user facility that supports a wide range of experiments. Single droplets and droplet arrays will be suspended and burned on 80 and/or 150 μ m Si-C fibers. The droplets are ignited by a coiled hot-wire that withdraws immediately after ignition. The unit is also capable of imparting a uniform, sub-buoyant forced flow (0 - 20 cm/s) on the droplet. The data is derived from a backlit microscope image of the droplet, and an orthogonal view (by either a black and white or color CCD camera) of the flame. Simultaneous 3-axis acceleration measurements will also be made.

This experiment, like all glovebox efforts, is very crew-intensive. The crew sets up the microscope and flame view cameras. The crew also manually dispenses a droplet from a modified syringe(s) onto the fiber and controls the ignition process. The current test matrix will include the combustion of droplets with 3 to 5 mm initial diameter, although smaller droplets can also be burned. Two pure fuels, heptane and methanol (in support of the Droplet Combustion Experiment) will be burned; heptane will also be studied with a forced flow. Fuel mixtures of methanol/dodecanol, methanol/water and heptane/hexadecane will be studied. Finally, several tests of a three-droplet array of pure methanol will be studied.

Future Work

The porous sphere droplet experiment requires a long-duration reduced gravity environment to observe radiative extinction. The small (2.2 second) drop tower is not suitable for this experiment. The apparatus is currently being modified for use on the DC-9 to see if the aircraft g-levels and duration are sufficient. An existing experiment package will be modified to include a syringe pump and a porous sphere with the ignition system. The majority of the data will be a view showing the state of the porous sphere and an orthogonal view of the flame. The existing color schlieren system will be used in some tests also.

The FSDC investigation will fly aboard the Space Shuttle Columbia in late September 1995. Since the major data is video, experimental results, with the exception of the acceleration data, will be available immediately. The planned test matrix includes 30 test points, although extra fuel is available if extra crew time becomes available.

References

1. Annamalai, K. and W. Ryan. "Interactive Processes in Gasification and Combustion. Part I: Liquid Drop Arrays and Clouds," *Progress in Energy and Combustion Science* 18, 1992, 221.
2. Brzustowski, T.A., E.M. Twardus, S. Wojcicki and A. Sobiesiak. "Interaction of Two Burning Fuel Droplets of Arbitrary Size," *AIAA Journal* 17, No. 11, 1979, 1234.
3. Labowsky, M. "A Formalism for Calculating the Evaporation Rates of Rapidly Evaporating Interacting Particles", *Combustion Science and Technology* 18, 1978, 145.
4. Labowsky, M. "Calculation of the Burning Rates of Interacting Fuel Droplets," *Combustion Science and Technology* 22, 1980, 217.
5. Marberry, M., A.K. Ray and K. Leung. "Effect of Multiple Particle Interactions on Burning Droplets," *Combustion and Flame* 57, 1984, 237.
6. Samson, R., D. Bedeaux and J.M. Deutch. "A Simple Model of Fuel Spray Burning II. Linear Droplet Streams," *Combustion and Flame* 31, 1978, 223.
7. Umemura, A., S. Ogawa and O. Nobunori. "Analysis of the Interaction Between Two Burning Droplets", *Combustion and Flame* 41, 1981, 45.
8. Umemura, A. "Interactive Droplet Vaporization and Combustion: Approach from Asymptotics," *Progress in Energy and Combustion Science* 20, 1994, 325.
9. Raju, M.S. and W.A. Sirignano. "Unsteady Navier-Stokes Solution for Two Interacting, Vaporizing Droplets", AIAA-87-0300, AIAA 25th Aerospace Sciences Meeting, Reno, Nevada, 1987.
10. Tal, Reuven and W.A. Sirignano. "Cylindrical Cell Model for the Hydrodynamics of Particle Assemblages at Intermediate Reynolds Numbers", *American Institute of Chemical Engineers Journal* 28, No. 2, 1982, 233.
11. Miyasaka, K. and C.K. Law. "Combustion of Strongly Interacting Linear Droplet Arrays", *Eighteenth Symposium (International) on Combustion* / The Combustion Institute, 1981, 283.
12. Xiong, T.Y., C.K. Law, C.K. and K. Miyasaka. "Interactive Vaporization and Combustion of Binary Droplet Systems", *Twentieth Symposium (International) on Combustion* / The Combustion Institute, 1984, 1781.
13. Mikami, M., Kato, H., Sato, J. and Kono, M. "Interactive Combustion of Two Droplets in Microgravity," to appear in the proceedings of the 25th Symposium (International) on Combustion / The Combustion Institute, 1994.
14. Vander Wal, R.L. and Weiland, K.J. "Laser-Induced Incandescence: Development and Characterization Towards a Measurement of Soot Volume Fraction," *Journal of Applied Physics B* (to appear).
15. Vander Wal, R.L. and Dietrich, D.L. "Laser-Induced Incandescence Applied to Droplet Combustion," *Applied Optics* 34, 6, 1995, 1103.
16. Vander Wal, R.L. and Dietrich, D.L. "Relative Soot Volume Fractions in Droplet Combustion via Laser-Induced Incandescence," Presented at the Fall Meeting of the Eastern States Section of the Combustion Institute, 1994.
17. Chao, B.H., Law, C.K. and T'ien, J.S. "Structure and Extinction of Diffusion Flames with Flame Radiation," *Twenty-Third Symposium (International) on Combustion* / The Combustion Institute 1990, 523.

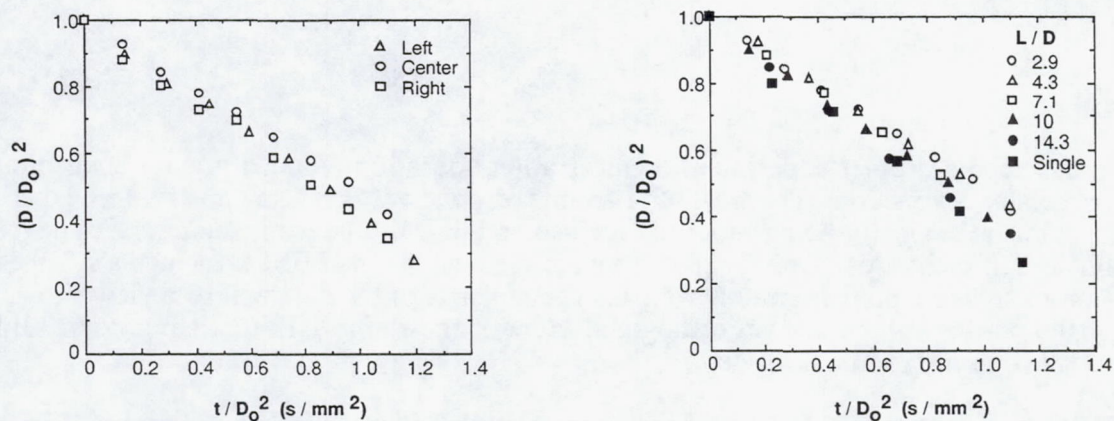


Figure 1. Droplet size histories for a three droplet array of identically sized 1.4 mm initial diameter droplets of n-heptane droplets burning in air.

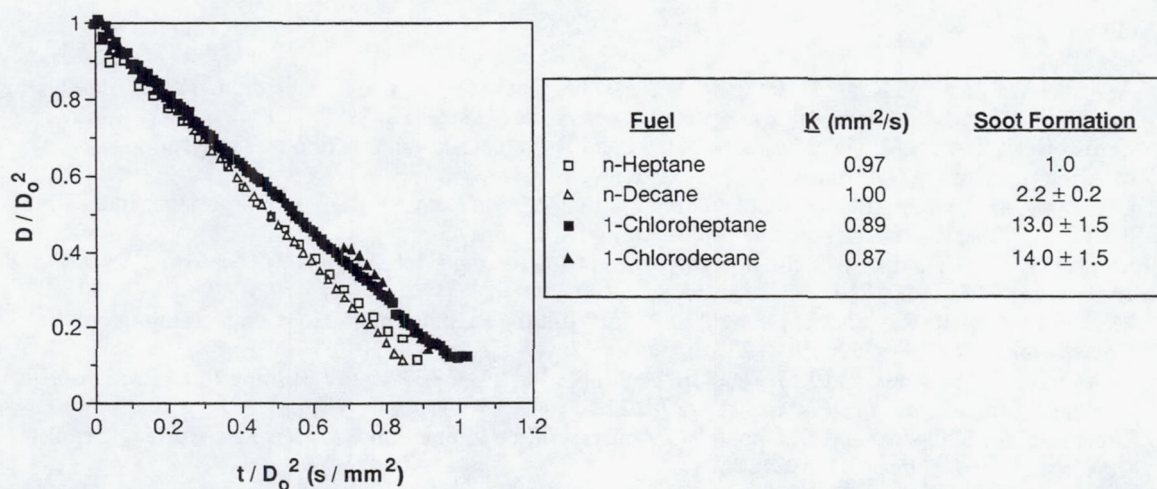


Figure 2. Burning rate constants and relative ammounts of soot formation for four different fuels. The soot formation numbers are relative to heptane.

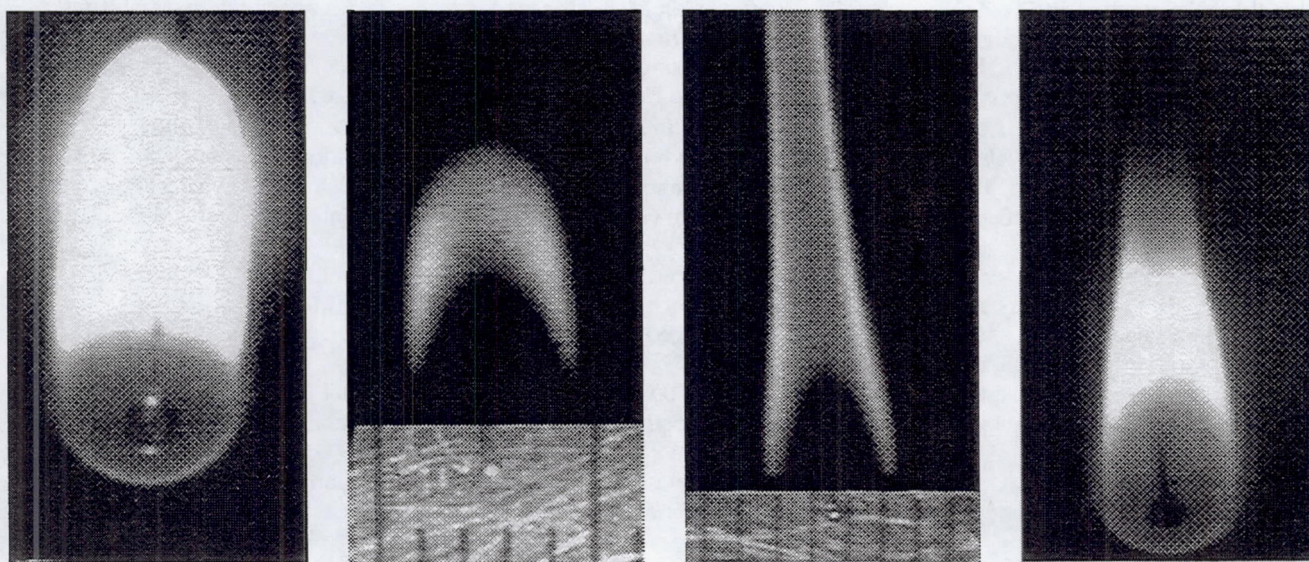


Figure 3. Natural flame (a,c) and LII (b,d) pictures of n-decane (a,b) and chlorodecane (c,d).

The Effects of Detailed Chemistry and Transport on Microgravity Droplet Combustion

A. J. MARCHESE, J. C. LEE, T. J. HELD, and F. L. DRYER

*Department of Mechanical and Aerospace Engineering
Princeton University, Princeton, NJ 08544-5263*

Abstract - A brief overview of recent advances in the theoretical study of microgravity droplet combustion is presented. Much of this work has centered on the development and utilization of spherically-symmetric transient numerical models which consider detailed gas phase chemistry and transport as well as energy and/or species transport within a regressing condensed phase. Numerical results for microgravity combustion and vaporization of methanol, methanol/water, heptane, and heptane/hexadecane droplets are summarized along with refinements in chemical kinetics and the development of a new two-dimensional axis-symmetric model.

1. INTRODUCTION

In recent years, a joint program with F. A. Williams at the University of California San Diego has been in progress to study microgravity droplet combustion. This program includes microgravity droplet experiments and theoretical studies using asymptotic and numerical methods. At UCSD asymptotic methods have been used to investigate the flame structure and extinction of n-heptane [1,2] and methanol droplets [3]. Meanwhile, theoretical efforts in this laboratory have centered on the development of transient numerical models. These models consider detailed gas phase chemistry and transport, condensed phase transport, condensed phase surface regression, and, where applicable, condensed phase surface chemistry. Much of the work has utilized a transient, spherically symmetric, moving finite element approach originally developed by Cho, *et al.* [4,5]. This modeling approach has been used to successfully simulate the microgravity combustion and/or vaporization of methanol droplets [6], methanol/water droplets [7,8], n-heptane droplets [9], n-heptane/n-hexadecane droplets [10], and carbon particles [11,12]. These studies have led to new and exciting discoveries in fields which are generally considered mature.

The results which will be briefly summarized in this paper repeatedly underscore the effects of detailed coupling between gas phase chemistry, gas phase transport, liquid phase transport, and phase equilibrium. For instance, the methanol and methanol/water results show that the droplet extinction diameter depends not only on the gas phase chemical and transport rates but on the rate of liquid mass transport as well. Moreover, even during "quasi-steady" combustion when the observed burning rate is essentially constant, a closer examination of the gas phase chemical heat release reveals a continuously varying flame structure. This result suggests a shift in the gas phase kinetic routes as the diffusional residence time decreases with decreasing droplet diameter. Finally, new regimes of droplet combustion and carbon particle oxidation have been predicted wherein traditional quasi-steady assumptions are no longer valid.

These discoveries have prompted continued numerical and experimental research efforts. A spectral element approach is being utilized to develop a 2-D axis-symmetric model which will be initially applied to the study of microgravity droplet combustion in the presence of forced convection [13]. Also, a new n-alkane reaction mechanism has been developed which contains significantly more detail than the semi-empirical mechanisms used in the n-alkane studies mentioned above [14]. Finally, continued ground-based 2.2 second drop tower and 5 second Zero Gravity Facility experiments are being conducted in conjunction with the numerical modeling described in this paper [15]. Ultimately, this research effort is focused on development and analysis of the space-based DCE and FSDC experiments which are scheduled to fly aboard upcoming shuttle flights. The DCE and FSDC will be used to study the microgravity combustion of isolated, pure n-heptane droplets and fiber supported, bi-component droplets of several fuels including methanol/water and heptane/hexadecane.

2. THE EFFECT OF TRANSIENT VAPORIZATION ON THE IGNITION OF DROPLETS

In order to minimize the disturbance by an ignition source on a droplet deployed in microgravity, a substantial effort has been made in the past to understand the interactions between the ignition source (a spark, for instance) and the droplet [16]. However, little was understood about the instantaneous evolution of the gas phase surrounding a droplet after deployment into the microgravity environment. Accordingly, in 1993 a numerical study was performed by Marchese and Dryer [17] to determine whether it was possible to achieve pure gas phase ignition in the region surrounding a droplet, or if it was always necessary to supply additional energy to the droplet surface to raise the droplet surface temperature thereby increasing the mass fraction of fuel in the gas phase.

The fact that methanol and n-heptane have flash temperatures of 11.5 °C and -4 °C respectively would suggest the possibility of achieving pure gas phase igni-

tion in the region surrounding such droplets deployed in air at 25 °C. However, experiments have shown that, under the same experimental conditions, methanol droplets are much more difficult to ignite than n-heptane droplets [15]. The modeling results have indicated that, although, methanol has a flash temperature of 11.5 °C, it would be extremely difficult to achieve pure gas phase ignition of a methanol droplet in the 1 mm size range deployed in air. As the definition of the flash temperature would suggest, initially a 25 °C droplet is surrounded by a thin layer of fuel/air mixture which is within the flammability limits of methanol/air. The modeling results show that for short time periods after deployment the mere divergence of the flow field results in a finite gas phase location wherein the gas mixture falls below its lean flammability limit. Due to the stoichiometry of the methanol/air system, this location is at most one radius from the droplet surface. Moreover, as the droplet vaporizes, the high latent heat of vaporization of methanol causes the surface temperature to rapidly drop. The gas phase location of the lean flammability limit thus moves closer to the droplet surface. After only several seconds, the droplet surface temperature falls below the flash temperature at which time the entire gas phase surrounding the droplet is outside the lean flammability limit.

Figure 1 shows the gas phase location of the lean flammability limit for 25 °C droplets of methanol and n-heptane instantaneously immersed in atmospheric pressure air at 25 °C. These results suggest that only a precisely timed and located ignition source would be able to achieve pure gas phase ignition for the methanol/air system. An ignition source located outside the locus of flammable mixture would require an ignition energy much greater than the minimum gas phase ignition energy as additional energy would have to be supplied to raise the droplet surface temperature.

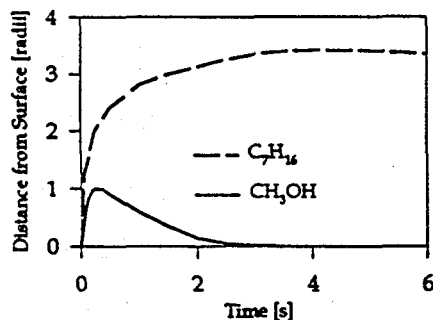


Figure 1. Gas phase location of lean flammability limit in radii from the droplet surface for 1 mm droplets dispensed in air.

The results for n-heptane show precisely why it is less difficult to ignite n-heptane droplets than methanol droplets. Firstly, the stoichiometry of the n-heptane/air system results in a lean limit locus which is much farther from the droplet surface than the methanol/air system. Furthermore, while the vaporization of an n-heptane droplet does cause its surface temperature to drop, it

does so to a much lower extent since the latent heat of vaporization of n-heptane is roughly 1/4 that of methanol. These results suggest that, since the gas phase surrounding an n-heptane droplet remains flammable at distances of 3 radii from the droplet surface, pure gas phase ignition should exist for the n-heptane/air system. Thus, the overall energy necessary to ignite an n-heptane droplet should be close to the minimum gas phase ignition energy of n-heptane.

3. COMBUSTION OF METHANOL AND METHANOL/WATER DROPLETS

The time-dependent, spherically symmetric combustion of bi-component liquid droplets of methanol and water has been simulated by Marchese and Dryer [7,8] using the finite element chemically reacting flow model mentioned above. The computations utilize the detailed multi-component molecular transport approach of Coffee and Hiernel [18] and the comprehensive methanol oxidation mechanism of Held, *et al.* [19] (89 forward chemical reactions and 21 species) to solve the gas phase energy and species equations. In addition, a semi-empirically-formulated binary vapor-liquid equilibrium relation is used to describe the phase change at the droplet surface. The conservation equations of energy and species are also solved within the droplet interior.

The numerical results for initially pure methanol droplets reproduce experimental observations wherein flame-generated water dissolves into the droplet during combustion. The results indicate that the extent of water absorption and its effect on both the quasi-steady burning rate and flame extinction phenomena are strongly dependent on the liquid mass Peclet number (defined as the ratio of the regression rate of the droplet surface to the effective mass transport rate of water within the liquid droplet).

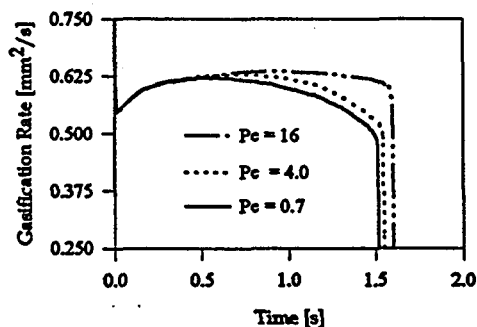


Figure 2. Instantaneous burning rate for 1000 micron initial diameter pure methanol droplets in air at 1 atm.

Figure 2 shows the instantaneous burning rate obtained from calculations in which the effective liquid phase mass diffusivity is parametrically varied resulting in various average liquid mass Peclet numbers. This figure shows that increased liquid mass transport results in increased deviation from d^2 -law behavior (i.e. gasification rate is not constant). Furthermore, as shown in

Fig. 3, increased mass transport promotes droplet extinction.

Fig. 3 suggests two extinction diameter limits. For $Pe_{l,m} \gg 1$, the extinction diameter approaches that value which would be observed if water were insoluble in methanol. For $Pe_{l,m} \ll 1$, the extinction diameter approaches that value which would be observed if the mass transport rate of water into the droplet were infinitely fast with respect to the surface regression rate.

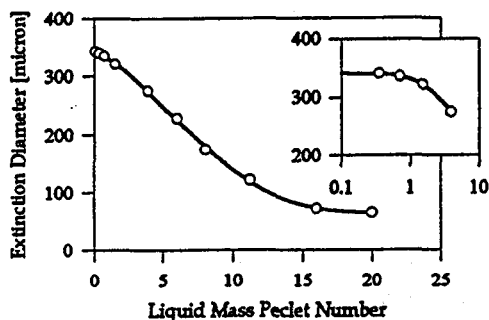


Figure 3. Variation in extinction diameter with liquid mass Peclet number for 1000 micron methanol droplets in 1 atm air.

From experimentally measured and correlated transport data the average liquid mass Peclet number for the combustion of methanol/water mixtures in air can be shown to be > 20 . Therefore, Fig. 3 suggests that if the interior of the liquid droplet were truly spherically symmetric and circulation-free, the effect of water dissolution on quasi-steady combustion and flame extinction would be minimal. However, considerable water uptake during methanol droplet combustion has been measured independently by Choi, *et al.* [20], and Lee, *et al.* [21]. Numerical modeling which simulates the conditions of the above experiments suggest that the liquid mass Peclet number present in these experiments was approximately 10. This decreased Peclet number suggests the presence of circulation within the liquid droplet which may be attributed to several sources, including the deployment technique and/or thermocapillary effects. Indeed, in a similar experimental configuration, Winter, *et al.*, [22] detected the presence of internal droplet circulation using laser induced fluorescence.

Methanol/water mixtures of 0-50% initial water content have also been modeled. These results show that for low liquid mass Peclet number, the water content at extinction is insensitive to the initial water content. Conversely, for high liquid mass Peclet number, the water content at extinction varied directly with the initial water content. Consequently, the extinction diameter is a weaker function of initial water content in the former situation than in the latter.

The low Peclet number results agree with suspended droplet results of Choi [23] which showed that a final water content of 80-85% was relatively insensitive to the initial water content. This result is not surprising since natural convection present in these experiments would not only have resulted in substantial internal droplet

circulation, but may also have increased the rate at which flame-generated water arrived at the droplet surface.

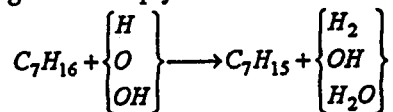
The numerical results suggest a series of drop tower droplet combustion experiments using methanol/water mixtures. The outcome of these experiments, which are presently underway [15], will indicate the magnitude of the liquid mass transport rate present in these and the future DCE space-experiments which will utilize similar deployment techniques.

4. COMBUSTION OF HEPTANE AND HEPTANE/HEXADECANE DROPLETS

The results of the previous section provide valuable insight into much of the phenomena governing multi-component liquid droplet combustion although only one of the liquid components is a fuel. Moreover, the results suggest that, while the liquid phase effects of diffusional resistance and volatility differential might be studied analytically with infinitely fast, or simplified gas phase chemistry, a full understanding of ignition, quasi-steady burning, and extinction requires accurate gas phase chemical kinetics.

In a subsequent study by Marchese and Dryer [10], binary mixtures of n-heptane (C_7H_{16}) and n-hexadecane ($C_{16}H_{34}$) have been modeled to extend the previous numerical results to systems in which both liquid components are fuels. These fuels were chosen due to the existence of experimental data [24,25], an available semi-empirical chemical kinetic mechanism for n-heptane [26], and the substantial volatility differential between the two components.

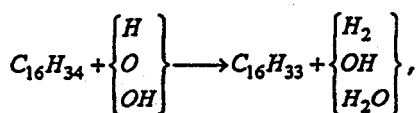
The gas phase chemical kinetics are modeled using the semi-empirical approach of Warnatz [26]. This approach had been utilized to generate a 32-species, 96-step n-heptane mechanism which accurately predicted laminar pre-mixed flame propagation. More recently, this mechanism has formed the basis for numerical studies on steady counter flow diffusion flames [27] and steady spherically symmetric diffusion flames [28]. The Warnatz model for n-heptane oxidation assumes that the predominant route of n-heptane consumption is abstraction of a hydrogen atom by O, OH, and H, thereby forming a generic n-heptyl radical:



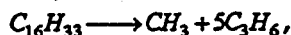
The principal empiricism in the Warnatz model is the description of the n-heptyl radical decomposition into the unlikely products of methyl radicals and propene in fixed ratio,



rather than the expected mixture of β -scission products, C_2H_4 , C_2H_5 , C_3H_6 , C_4H_8 , CH_3 , and C_5H_{10} . A similar approach is also applied to model the gas phase n-hexadecane chemistry. Hydrogen abstraction from n-hexadecane,



followed by the decomposition of n-hexadecyl into fixed proportions of methyl radicals and propene,



have been added to the original 96-step mechanism.

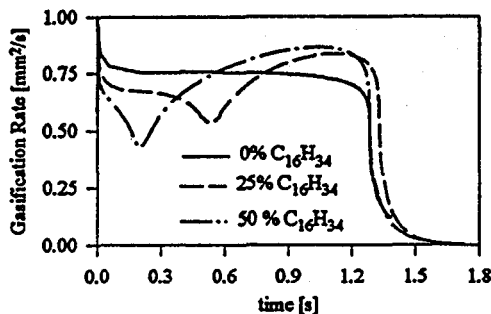


Figure 4. Instantaneous gasification rate, for 1000 micron initial diameter heptane/hexadecane droplets in 23% O₂/77% N₂ at 0.164 atm ($Pe_1=10$).

Figure 4 is a plot of the instantaneous gasification rate for 1 mm heptane/hexadecane droplets in an oxidizing environment of 23% O₂/77% N₂ at 0.164 atm. As Fig. 4 suggests, the pure n-heptane droplet closely exhibits classical d^2 -law droplet combustion behavior as the gasification rate is constant over the majority of the droplet lifetime. For mixtures of n-heptane/n-hexadecane, the gasification rate varies continuously during the droplet lifetime. The gasification rates of the 25% and 50% hexadecane droplets reflect three distinct periods of quasi-steady combustion. The first period constitutes the preferential gasification of heptane, which is the more volatile component. The second period begins when the heptane is depleted from the droplet surface. Once this occurs, the droplet heats up toward the boiling point of hexadecane resulting in a decrease in gasification rate. During the final period, the gasification rate increases as the liquid phase species gasify at fixed ratio due to the high liquid mass Peclet number.

As in the methanol/water studies, the results are found to vary depending on the value of the liquid mass Peclet number. Figure 5 shows results of computations performed to determine the effect of increased liquid mass transport. In these computations an effective liquid mass diffusivity is parametrically varied over an order of magnitude such that the average liquid mass Peclet number varied from 1 to 10. This figure suggests that the net observable effect of increased liquid mass transport is to delay the onset of the secondary droplet heating period. Once again, these results suggest that isolated droplet experiments using these fuels might be utilized to determine the effective Peclet number present in the experiments. Finally, the numerical model predicts droplet extinction diameters of 187, 225, and 312 microns for average liquid mass Peclet numbers of 10, 5, and 1, re-

spectively. This effect underscores the intimate coupling between the liquid and gas phase processes.

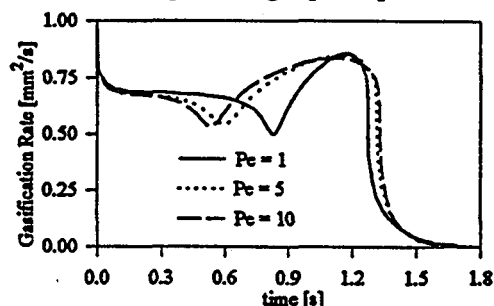


Figure 5. Instantaneous gasification rate, for 1000 micron initial diameter 25% hexadecane droplets in 23% O₂/77% N₂ at 0.164 atm ($1 \leq Pe \leq 10$).

5. A NEW REACTION MECHANISM FOR N-ALKANE DROPLET COMBUSTION MODELING

In the studies summarized in Section 3, the gas-phase chemistry is modeled using the comprehensive (89 step, 21 species) gas-phase chemical kinetic mechanism of Held and Dryer [19]. The results show the effects of complex chemistry which would not have been observed if the gas phase were modeled using single-step activation energy asymptotics. For instance, the results suggest that, rather than merely increasing leakage through a thin reaction zone, the reduction in diffusional residence time with droplet diameter results in a gas-phase flame structure that continuously evolved throughout the droplet lifetime. Figure 6 shows the local gas-phase chemical energy release surrounding a 1500-micron droplet deployed in a microgravity environment of 50% He/50% O₂, at 0.5 atmospheres at three times during the droplet lifetime. The continuous variation in flame structure, as indicated by the changing energy release pattern, suggests a shift in the gas phase kinetic routes with diffusional residence time. This result is consistent with recent microgravity n-heptane droplet studies of Jackson

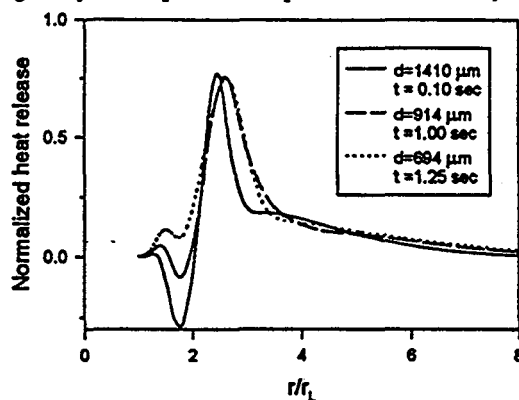
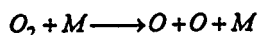


Figure 6. Gas-phase heat release profile surrounding a 1500 micron methanol droplet at 0.25, 0.50, and 1.00 seconds after ignition. (50% O₂/50% He, $P=0.50$ atm)

and Avedisian [29] which showed that sooting propensity decreased significantly with droplet size. It was sug-

gested that the decreasing diffusional residence time with decreasing initial droplet diameter results in less time for production of soot precursors on the fuel side of the diffusion flame. Such arguments are complicated, however, by an additional time scale associated with thermophoretic soot collection.

The n-heptane oxidation mechanism of Warnatz which has been used in the studies presented above in Section 4 lacks sufficient detail to capture some of the interesting transient phenomena observed in the methanol/water studies. In addition to possible flame structure variations, the model is not well-equipped to handle droplet ignition. As mentioned previously, the Warnatz mechanism postulates only one consumption route for the fuel—abstraction by H, O or OH, followed by thermal decomposition of the resulting heptyl radical (C_7H_{15}) to propene and the methyl radical (CH_3). Since, initially, only fuel, oxygen, and inert exist in the gas phase, the only initial source of radicals in this mechanism is via oxygen dissociation. Indeed, droplet ignition is not obtained for any initial conditions when the reaction:



is suppressed.

Four difficulties are perceived with regard to the use of the Warnatz mechanism in diffusion-flame modeling in general, and specifically in time-dependent droplet calculations. First, as mentioned above, the absence of a thermal decomposition route for the n-heptane presents difficulties in the study of ignition phenomena. Second, the treatment of the n-heptyl radical as a single species, rather than a mixture of isomers, results in a non-realistic distribution of olefinic intermediate species. The mechanism overemphasizes the importance of propene reactions, rather than those of the expected mixture of Beta-scission products which are, in fact, observed in n-heptane/air diffusion flame structures [30] and flow reactors [31]. Third, the C_1 – C_3 submechanism is in need of updating with current reaction paths and rate constants. The propene submechanism, in particular, lacks any abstraction routes, which are likely to be an important reaction path under combustion conditions. Finally, the kinetics are insufficient for eventual grafting of additional reactions to describe sooting effects.

A recent experimental and modeling effort by Held, *et al.* [14] has been directed toward providing a more detailed treatment of the decomposition of both the parent fuel, n-heptane, and the four isomeric heptyl radicals, while still retaining a relatively simplified view of the overall kinetics. Because each species added to a mechanism adds another differential equation to be solved in the kinetic system, while a new reaction only adds another term to an existing equation, a model may be extended by additional reactions without significant computational penalty. A major goal of the model development is the increase in site-specific detail, while maintaining a relatively small number of species. Also, the C_1 – C_3 mechanism has been updated to a detailed kinetic mechanism developed in previous and ongoing work [19,32]. The final reaction mechanism consists of 241 re-

actions among 37 species, an increase of 145 reactions, but only 5 species.

To support the development of this mechanism, a series of n-heptane oxidation and pyrolysis experiments have been performed using a variable pressure flow reactor. The calculated and measured species profiles for a rich oxidation case shown in Fig. 7. The agreement is excellent, both in terms of overall reaction rate and intermediate distribution. Similar calculations using the full Warnatz mechanism yield characteristic reaction times on the order of 300 sec, compared to the 0.5 second time scale of the experiments.

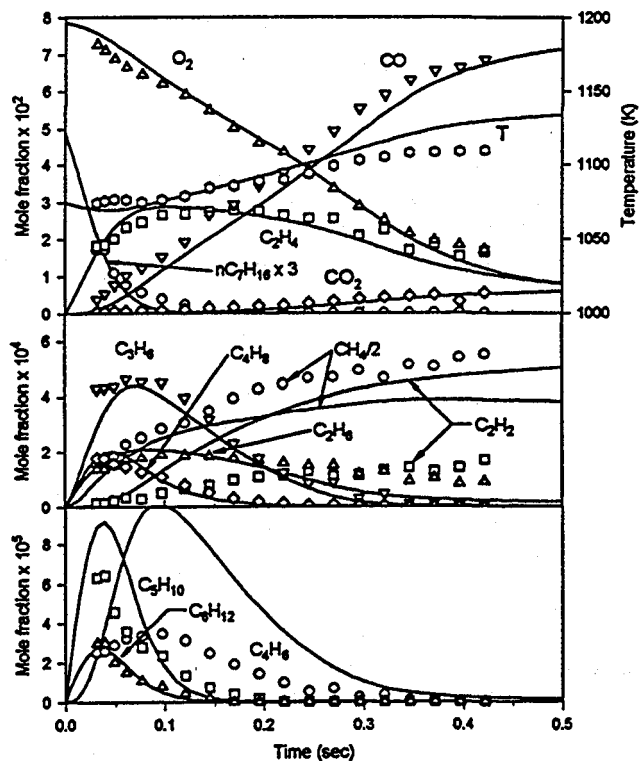


Figure 7. Measured (symbols) and calculated (lines) species and temperature profiles for n-heptane oxidation.

6. TWO-DIMENSIONAL MODEL DEVELOPMENT

The success of the spherically symmetric modeling has prompted the development of a transient, axis-symmetric, 2-D droplet combustion model [13]. The model has been developed mathematically by applying an asymptotic expansion on the square of the mach number, thereby suppressing all acoustic waves. In this formulation, the thermochemical system (species and energy equations) and hydrodynamic system (momentum and mass conservation equations) are decoupled in time. The governing equations are spatially discretized using the spectral element method. Time integration is performed using a fifth-order, fully implicit backward difference method with a general, sparse Jacobian algorithm. To date, the diffusion problem has been tested using a dif-

fusion operator based on the mixture fraction formulation of Kee, *et al.* [33]. The thermochemistry solver is currently being coupled with the momentum solver to analyze the 2-D, axis-symmetric convection situation.

7. CONCLUSIONS

Recent studies using sophisticated transient numerical models which consider detailed chemistry and transport have led to new and exciting discoveries in the field of droplet combustion. Refinement of chemical kinetic, equilibrium, and transport sub-models continues along with the development of a new 2-D axis-symmetric droplet combustion model.

Acknowledgments - The authors gratefully acknowledge NASA Lewis for supply of experimental facilities and scientific collaborations through Grant No. NAG3-1231. The authors further wish to acknowledge thought-provoking discussions with Dr. M. Vedha-Nayagam and Professor Forman A. Williams whose asymptotic droplet combustion studies continue to add much in physical insight to these areas. Experimental flow reactor studies and the contributions of Dr. Tim Held were supported by the U.S. Department of Energy, Office of Transportation Technologies through Grant No. DE-F604-90-AL65460.

REFERENCES

- [1] Card, J. M., and Williams, F. A., *Comb. Sci. and Tech.*, 84:91 (1992).
- [2] Card, J. M., and Williams, F. A., *Combustion and Flame*, 93:375 (1993).
- [3] Zhang, B. L., Card, J. M., and Williams, F. A., *Combustion and Flame*, to be submitted, (1995).
- [4] Cho, S. Y., Yetter, R. A., and Dryer, F. L., *Journal of Computational Physics*, 102:160 (1992).
- [5] Cho, S. Y., Yetter, R. A., and Dryer, F. L., *Mathl. Comput. Modelling*, 14:790 (1990).
- [6] Cho, S. Y., Choi, M. Y., and Dryer, F. L., *Twenty-third Symposium (International) on Combustion*, The Combustion Institute, Pittsburgh, 1990, p.1611.
- [7] Marchese, A. J., and Dryer, F. L., *Eastern States Sectional Meeting of the Combustion Institute*, Clearwater, FL, December, 1994.
- [8] Marchese, A. J., and Dryer, F. L., *Combustion and Flame*, Submitted.
- [9] Marchese, A. J., Choi, M. Y., and Dryer, F. L., MAE Report No 1999, August 1994.
- [10] Marchese, A. J., and Dryer, F. L., *Central States/Western States/Mexican National Sectional Meeting of the Combustion Institute*, San Antonio, TX, 1995.
- [11] Lee, J. C., Yetter, R. A., and Dryer, F. L., *Combustion and Flame*, In press.
- [12] Lee, J. C., Yetter, R. A., and Dryer, F. L., *Combustion and Flame*, Submitted.
- [13] Lee, J. C., Work in progress, 1995.
- [14] Held, T. J., Marchese, A. J., and Dryer, F. L., *Central States/Western States/Mexican National Sectional Meeting of the Combustion Institute*, San Antonio, TX, 1995.
- [15] Marchese, A. J., Vedha-Nayagam, M., and Dryer, F. L., Work in progress, 1995.
- [16] Shaw, B. D., Dryer, F. L., Williams, F. A., and Gat, N., *Combustion and Flame*, 74:233 (1988).
- [17] Marchese, A. J., and Dryer, F. L., *Eastern States Sectional Meeting of the Combustion Institute*, Princeton, NJ, October, 1993.
- [18] Coffee, T. P., and Heimerl, J. M., *Combustion and Flame*, 43:273 (1981).
- [19] Held, T. J., Ph. D. Thesis, Dept. of M.A.E., Princeton Univ., Princeton, NJ (1993).
- [20] Choi, M. Y., Cho, S. Y., Stein, Y. S., and Dryer, F. L., *Fall Eastern States Meeting of the Combustion Institute*, Orlando, FL, (1992).
- [21] Lee, A. and Law, C. K., *Combust. Sci. and Tech.*, 86:253 (1992).
- [22] Winter, M., and Melton, L. A., *Applied Optics*, 29(31):4574 (1990).
- [23] Choi, M. Y., Ph. D. Thesis, Dept. of M.A.E., Princeton Univ., Princeton, NJ (1992).
- [24] Yang, J. C., and Avedesian, C. T., *Twenty-Second Symposium (International) on Combustion*, The Combustion Institute, Pittsburgh, 1988, p. 2037.
- [25] Niioka, T., and Sato, J., *Twenty-First Symposium (International) on Combustion*, The Combustion Institute, Pittsburgh, 1986, p. 625.
- [26] Warnatz, J., *Twentieth Symposium (International) on Combustion*, The Combustion Institute, Pittsburgh, 1984, p. 845.
- [27] Bui-Pham, M. and Sheshadri, K., *Comb. Sci. and Tech.*, 79:293 (1991).
- [28] Jackson, G. S., and Avedesian, C. T., *Fall Eastern States Meeting of the Combustion Institute*, Princeton, NJ, 1993.
- [29] Jackson, G. S., and Avedesian, C. T., 31st Aerospace Sciences Meeting and Exhibit, Reno, NV (AIAA-93-0130) 1993.
- [30] Kent, J. H. and Williams, F. A., *Fifteenth Symposium (International) on Combustion*, The Combustion Institute, Pittsburgh, 1974, p. 315.
- [31] Kennedy, S., Brezinsky, K. and Dryer, F., 1985, *Eastern States Sectional Meeting of the Combustion Institute*, Philadelphia, PA, 1985.
- [32] Held, T. J., Dryer, F. L., Brezinsky, K., Pitz, W. J., and Westbrook, C. K., *Eastern States Sectional Meeting of the Combustion Institute*, 1988.
- [33] Kee, R. J., Warnatz, J., and Miller, J. A., *Sandia Report*, SAND83-8209, (1983).

HIGH PRESSURE DROPLET BURNING EXPERIMENTS IN REDUCED GRAVITY

Christian Chauveau and Iskender Gökalp

Laboratoire de Combustion et Systèmes Réactifs
Centre National de la Recherche Scientifique
45071 Orléans cedex 2, France

Introduction

Depending on the surrounding flow and thermodynamic conditions, a single droplet may experience several gasification regimes, ranging from the envelope flame regime to pure vaporization (ref. 1). The characteristic times of droplet gasification are largely influenced by the surrounding pressure and temperature. Gasification of liquid droplets under high pressure conditions is indeed one of the main phenomena characterizing liquid fueled energy systems. It is also conjectured that droplets initially injected in the high pressure combustion chamber under subcritical temperatures may heat up and attain the supercritical thermodynamic state before their total gasification. Many theoretical and computational studies have addressed sub- and supercritical droplet vaporization phenomena under spherical symmetry (refs. 2-11) or axisymmetric conditions (refs. 12-14), by solving the conservation equations associated with the problem. Most of the contributions take into account the transient effects, the thermodynamic non-idealities and the ambient gas solubility in the liquid phase due to high pressures. Some new approaches based on molecular dynamics are also emerging (ref. 15).

A parametric investigation of single droplet gasification regimes is therefore helpful in providing the necessary physical ideas for sub-grid models used in spray combustion numerical prediction codes. A research program has been initiated at the LCSR to explore the vaporization regimes of single and interacting hydrocarbon (ref. 1) and liquid oxygen droplets (ref. 16) under high pressure conditions. The research program also includes the investigation of single and interacting droplets vaporizing in laminar or turbulent, isothermal or heated flows (ref. 17). In parallel to pure liquid droplet studies, bicomponent hydrocarbon droplets are also investigated (ref. 18). Droplet interaction effects are explored for the configuration of three droplets in tandem vaporizing in a laminar heated flow (ref. 19). Reduced gravity studies are conducted to reproduce spherical symmetry conditions essentially for burning droplet studies (refs. 1 and 20).

This paper summarizes the status of the LCSR program on the high pressure burning of single fuel droplets; recent results obtained under normal and reduced gravity conditions with suspended droplets are presented. In the work described here, parabolic flights of the CNES Caravelle is used to create a reduced gravity environment of the order of $10^{-2} g_0$. For all the droplet burning experiments reported here, the suspended droplet initial diameters are scattered around 1.5 mm ; and the ambient air temperature is 300 K. The ambient pressure is varied between 0.1 MPa and 12 MPa. Four fuels are investigated : methanol ($P_c = 7.9$ MPa), n-heptane ($P_c = 2.74$ MPa), n-hexane ($P_c = 3.01$ MPa) and n-octane ($P_c = 2.48$ MPa).

Description of the experimental techniques

High pressure droplet gasification facility

Droplet gasification experiments under stagnant and variable pressure conditions are performed in a specially designed facility : High Pressure Droplet Gasification Facility (HP-DGF). The HP-DGF is designed to investigate the gasification regimes of suspended or free-floating droplets under variable pressure conditions, up to 12 MPa. Low pressure droplet burning experiments can also be performed. This facility can be used during the parabolic flights of an aircraft. This apparatus has been fully described previously (ref.1). For high pressure droplet burning experiments, an improved version of the injection system and a heated coil for ignition are used. The coil is located about 15 droplet diameter below the suspending fiber and is used to heat the air in the vicinity of the droplet. The coil heating current is shut down when droplet autoignition is attained. The sequence of injection and ignition operations is computer controlled. The results presented in this paper are obtained with droplets suspended on a quartz fiber of 0.2 mm with an enlarged extremity of 0.4 mm diameter.

Diagnostics

The principle diagnostic systems we are using are based on the visualization of the droplet burning phenomena. Suspended droplets are backlighted; this provides the necessary contrast for direct threshold definition. The recording equipment is based on the high speed video camera, Kodak-Ektapro 1000, which can record up to 1000 full frames per second, and allows detailed analysis of droplet burning. The Ektapro 1000 Motion Analyzer's live, real-time viewing makes possible to follow the investigated phenomena frame per frame. A second camera has been added to the Kodak-Ektapro 1000 system, to be able to observe simultaneously the droplet and the flame with respective appropriate magnification rates. The digitized images from the Ektapro system are transferred to a microcomputer where the image analyses are performed. For the details of the image analysis, refs. 1 and 16 can be consulted.

Results and discussion

Burning droplet experiments have been conducted both under normal gravity conditions and under reduced gravity conditions. An example of the residual gravity level recorded during a parabolic flight experiment is given on Fig. 2. The figure shows the time variation of the gravity level synchronized with the camera acquisition, during the 20 seconds of the microgravity period. On this sequence, the average gravity level corresponding to the actual droplet burning time (0.69 s for a n-octane droplet burning at 8 MPa) is $2 \cdot 10^{-2} g_0$.

Figure 3 presents the time histories of the normalized squared droplet diameter versus normalized time for methanol droplets burning under normal gravity. For the pressure range explored ($Pr = 0.9$), the droplet projected surface area regresses quasi-linearly with time, which authorizes the determination of an average burning rate K . A similar behaviour is also observed for the experiments conducted under reduced gravity. The average burning rates determined under normal and reduced gravity are compared in Fig. 4 for a pressure range extending up to $Pr = 1.15$. As expected, the reduced gravity K values are lower than the normal gravity values; both increase continuously with pressure. The strong increase of K with pressure above $Pr = 0.8$ under normal gravity remains unexplained. The results obtained with n-heptane droplets are shown on Fig. 5. As the critical pressure of n-heptane is lower, Pr values larger than 4 is obtained in the experiments in microgravity. The lowering of the pressure effect above the

critical pressure is clearly observed. The results obtained in microgravity with the four fuels tested are shown on Fig. 6. On this figure, the burning rate at a given pressure is normalized by its value at the critical pressure. The scattering of the experimental values become significant for high pressures, while a single behaviour characterizes the subcritical domain. An interesting feature of these results is that we did not observe a maximum burning rate around the critical pressure, as was observed by Sato in ref. 21. Figure 7 shows the corresponding burning times for a droplet of 1 mm initial diameter versus the reduced pressure. The subcritical domain is characterized by a strong decrease of the burning time, which seems to be stabilized during the whole supercritical domain. In ref. 21, a minimum of the burning time near the critical pressure was clearly observed.

The main differences between the two experiments are related to the reduced gravity levels; the experiments of ref. 21 were conducted by using drop towers, where the residual gravity level is much less. The increase of the burning time observed in ref. 21 in the supercritical domain can be explained by the onset of a diffusion controlled regime after the vanishing of the gas-liquid interface. In the present experiments, the residual gravity induced natural convection is enhanced with increasing pressure; also in the supercritical domain, the reduction of the surface tension makes the dense gas phase much more sensible to convection effects. All together these two effects may therefore explain the present experimental observations. In order to quantify these predictions, an attempt to introduce a Grashof number correction is presently under development (ref. 22).

Summary and future work

In the work described here, emphasis is put on recent results obtained in high pressure droplet burning experiments conducted both under normal gravity and during the parabolic flights of the CNES Caravelle which creates a reduced gravity environment of the order of $10^{-2} g_0$. The combination of high pressure droplet burning experiments with reduced gravity is crucial in order to reduce the pressure enhanced natural convection effects and also to extend the applicability of the fibre suspended droplet technique when the surface tension decreases due to the closeness of thermodynamic critical conditions. The experimental results presented in this paper show a decrease of the droplet burning time with pressure in the subcritical domain. The minimum burning time observed by other investigators around the critical pressure was not found in this study for the four fuels investigated. This may be attributed to the pressure enhanced natural convection effects due to the residual gravity during parabolic flight experiments.

The investigation of high pressure effects will continue to be the main focus of the future LCSR work on droplet gasification regimes. The supercritical regime will be approached in the pure vaporization experiments with the help of a new version of the HP-DGF which is under construction; it will allow to increase the temperature as well as the pressure of the ambient medium. This apparatus will be used to investigate the vaporization and burning of mono and multicomponent fuel droplets in high pressure and high temperature conditions and also to compare normal gravity and reduced gravity experiments to infer natural convection effects. An electrodynamic balance is developed and will be added to the apparatus. It will allow to conduct supercritical vaporization experiments under normal gravity conditions. Parabolic flights will be continued to be used for suspended droplet experiments. A new high pressure droplet burning module will be developed to be used during sounding rocket experiments with ESA.

Acknowledgments

This work is supported by the CNRS/CNES joint research program on "Transport phenomena in reduced gravity" and by the European Space Agency Microgravity Program. The continuous support of CNES (program monitor Dr. B. Zappoli) and of ESA (program monitor Dr. H.U. Walter) is greatly appreciated.

References

1. Chauveau, C, Chesneau, X, and Gökalp, I., **AIAA Paper No. 93-0824**, 1993
2. Spalding, D.B., **ARS J.** 29, 828-835, 1959
3. Wieber, P.R., **AIAA J.** 1, 2764-2770, 1963
4. Manrique, J.A. and Borman, G.L. **Int. J. Heat and Mass Transfer** 12, 1081-1095, 1969
5. Rosner, D.E. and Chang, W.S., **Combust. Sci. Technol.** 7, 145-158, 1973
6. Kadota, T., and Hiroyasu, H., **Bull. JSME** 19, 1515-1521, 1976
7. Litchford, R.J., and Jeng, S.M., **AIAA Paper No. 90-2191**, 1990
8. Hsieh, K.C., Shuen, J.S., and Yang, V., **Combust. Sci. Technol.** 76, 111-132, 1991
9. Curtis, E.W., and Farrell, P.V., **Combust. Flame** 90, 85-102, 1992
9. Delplanque, J.P., and Sirignano, W.A., **Int. J. Heat Mass Transfer** 36, 303-314, 1993
10. Yang, V., and Lin, N.N. "Vaporization of liquid oxygen droplets in supercritical hydrogen environments", submitted to **Combust. Sci. Technol.**, 1993
11. Jia H., and Gogos, G., **Int. J. Heat Mass Transfer** 36, 4419-4431, 1993
12. Delplanque, J.P., and Sirignano, W.A. **Atomization and Sprays**, vol. 4, pp. 325-349, 1994
13. Sirignano, W.A., Delplanque, J.P., Chiang, J.H., and Bahtia, R., "Liquid propellant droplet vaporization : a driving mechanism for rocket combustion instability", paper presented at the **First International Symposium on Liquid Rocket Combustion Instability**, The Pennsylvania State University, January 18-20, 1993
14. Hsia, C.C., and Yang, V., "Lox droplet vaporization in a supercritical forced convective environment", paper presented at the **Fifth Annual Symposium of the Propulsion Engineering Research Center**, The Pennsylvania State University, University Park, PA, September 8-9, 1993
15. Long, L.N., Micci, M.M., and Wong, B.C., "supercritical droplet evaporation modelled using molecular dynamics on parallel processors", paper submitted for presentation at the **30th Joint Propulsion Conference**, Indianapolis, IN, June 27-29, 1994
16. Chesneau, X., Chauveau C., and Gökalp, I., **AIAA Paper No. 94-0688**, 1994
17. I. Gökalp, C. Chauveau, O. Simon and X. Chesneau, **Combust. Flame** 89, 286-298, 1992. see also Birouk, M., Chauveau, C., Sarh, B., Quilgars, A., and Gökalp, I., Turbulence effects on the vaporization of monocomponent single droplets. **Proceedings of the 11th European Conference of ILASS-Europe on Atomization and sprays**, Nürnberg, March 21-23, 1995, pp. 457-466.
18. Gökalp, I., Chauveau, C., Berrekam, H., and Ramos-Arroyo, N.A., **Atomization and Sprays**, vol. 4, pp. 661-676, 1994
19. Ramos-Arroyo, N.A., Chauveau, C., and Gökalp, I., "An experimental study of three interacting vaporizing fuel droplets in a forced convective laminar flow", presented at the **Sixth ICLASS**, Rouen, July 18-22, 1994, also submitted to **Atomization and Sprays**
20. Chauveau, C., Chesneau, X., and Gökalp, I., High pressure vaporization and burning of methanol droplets in reduced gravity. **Adv. Space Res.** Vol. 16, No. 7, pp. (7)157-(7)160, 1995
21. Sato, J., Studies on droplet evaporation and combustion in high pressures, **AIAA paper 93-0813**, 1993
22. Chesneau, X, **PhD Thesis**, University of Orléans, 1994

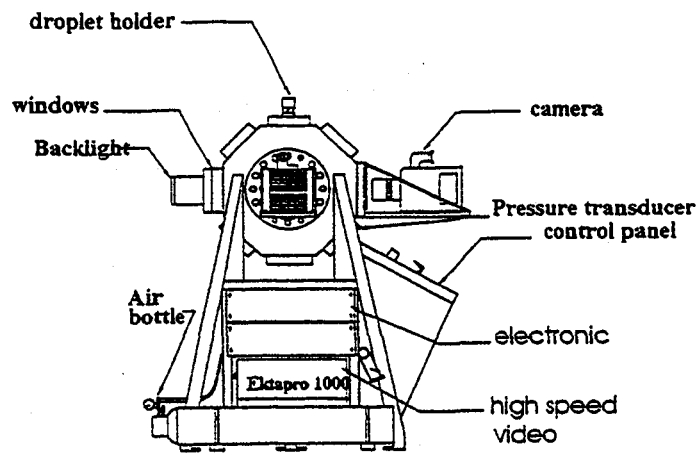


Figure 1 : Droplet Burning Facility (DBF-HP)

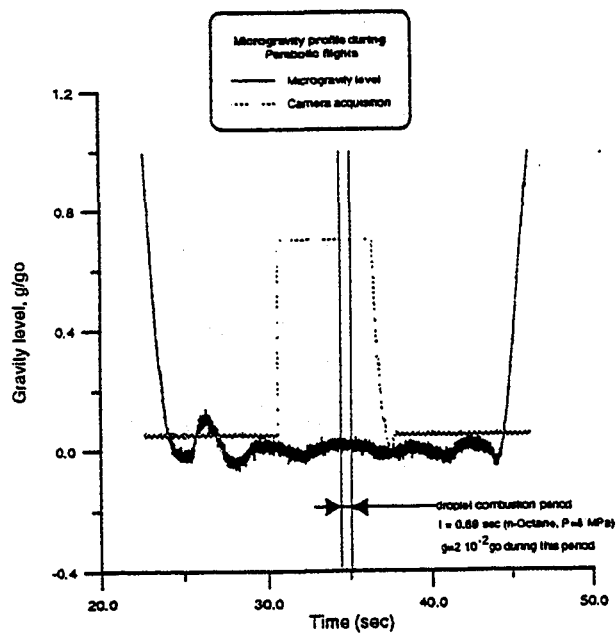


Figure 2 : Microgravity level versus time

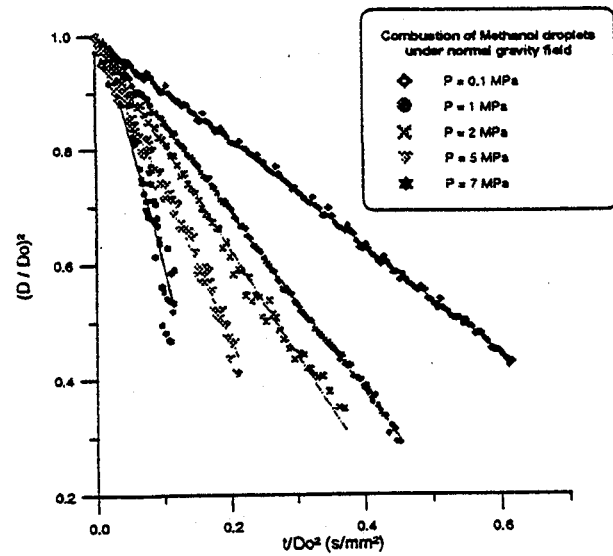


Figure 3 : Evolution of the normalized squared droplet diameter versus normalized time

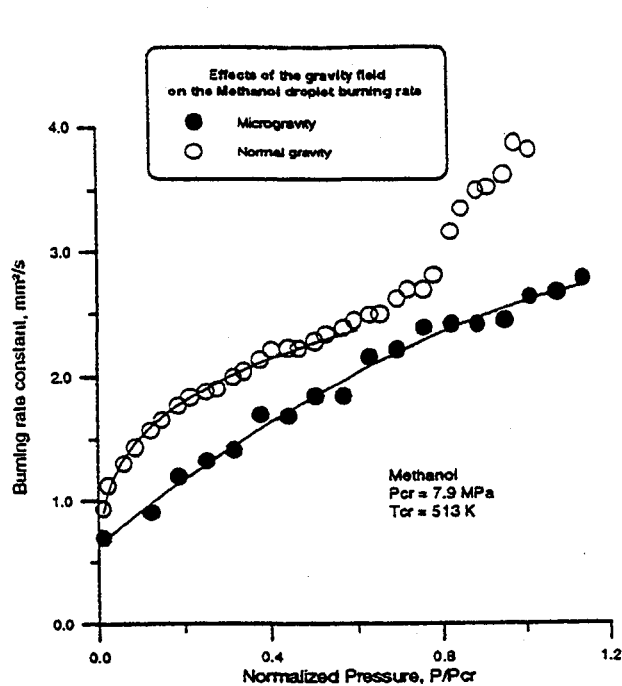


Figure 4 : Evolution of the burning rate constant versus normalized pressure.

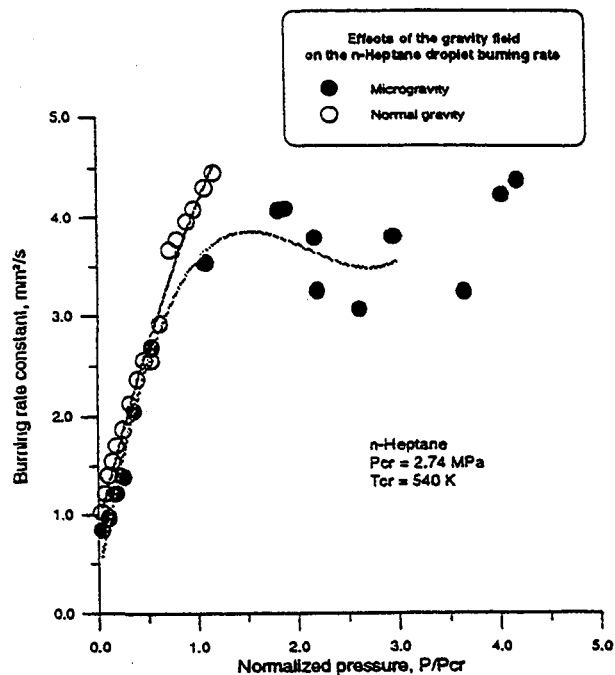


Figure 5 : Evolution of the burning rate constant versus normalized pressure.

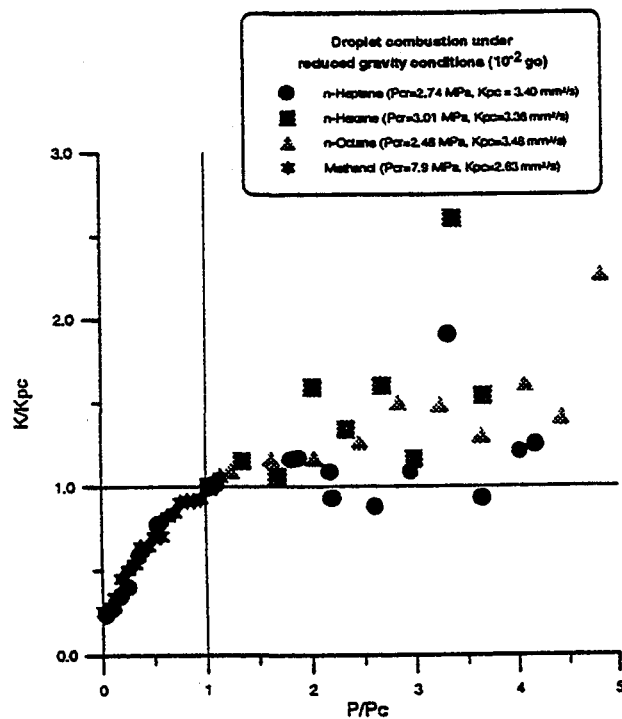


Figure 6 : Evolution of the normalized burning rate constant versus normalized pressure

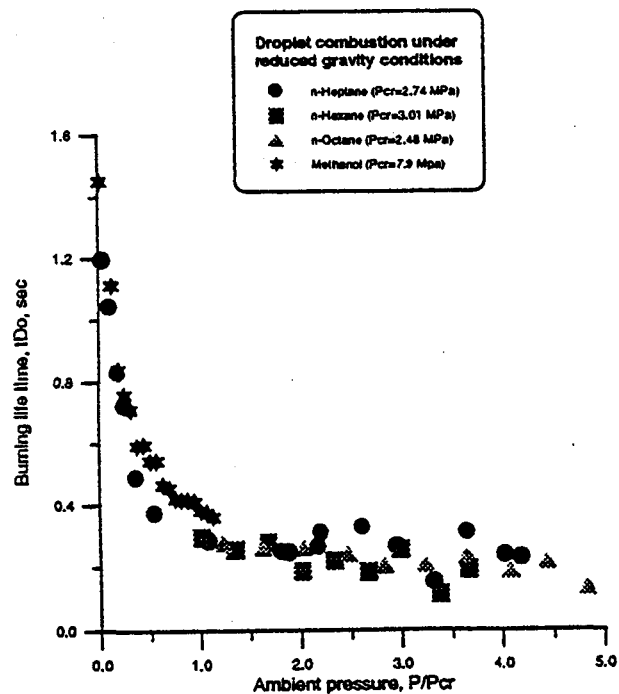


Figure 7 : Evolution of the normalized burning life time versus normalized pressure

SPRAY COMBUSTION AT NORMAL AND REDUCED GRAVITY IN COUNTERFLOW AND CO-FLOW CONFIGURATIONS

Alessandro Gomez and Gung Chen
Department of Mechanical Engineering
Yale University, P.O. Box 208286, New Haven, CT 06520-8286

Introduction

Liquid fuel dispersion in practical systems is typically achieved by spraying the fuel into a polydisperse distribution of droplets evaporating and burning in a turbulent gaseous environment. In view of the nearly insurmountable difficulties of this two-phase flow, a systematic study of spray evaporation and burning in configurations of gradually increasing levels of complexity, starting from laminar sprays to fully turbulent ones, would be useful. A few years ago we proposed to use an electrostatic spray of charged droplets for this type of combustion experiments under well-defined conditions. In the simplest configuration, a liquid is fed into a small metal tube maintained at several kilovolts relative to a ground electrode few centimeters away. Under the action of the electric field, the liquid meniscus at the outlet of the capillary takes a conical shape, with a thin jet emerging from the cone tip (cone-jet mode). This jet breaks up farther downstream into a spray of charged droplets — the so-called ElectroSpray (ES). Several advantages distinguish the electro-spray from alternative atomization techniques: i) it can produce quasi-monodisperse droplets over a phenomenal size range; ii) the atomization, that is strictly electrostatic, is decoupled from gas flow processes, which provides some flexibility in the selection and control of the experimental conditions; iii) the Coulombic repulsion of homopolarly charged droplets induces spray self-dispersion and prevents droplet coalescence; iv) the ES provides the opportunity of studying regimes of slip between droplets and host gas without compromising the control of the spray properties; v) the compactness and potential controllability of this spray generation system makes it appealing for studies in reduced-gravity environments aimed at isolating the spray behavior from natural convection complications. With these premises, in March 1991 we initiated a series of experiments under NASA sponsorship (NAG3-1259 and 1688) in which the ES was used as a research tool to examine spray combustion in counter-flow and co-flow spray diffusion flames, as summarized below. The ultimate objective of this investigation is to examine the formation and burning of sprays of liquid fuels, at both normal and reduced gravity, first in laminar regimes and then in turbulent ones.

Summary of the Research Activity from 9-1-92 to 3-15-95

The investigation focused initially on cold flow experiments aimed at examining the fundamental mechanism of electro-spray atomization and dispersion, as well as at identifying and characterizing the domain of operating variables under which monodisperse droplets were generated. Once we could synthesize sprays of desired properties, as documented in refs. 1-5, we focused on the combustion of such electro-sprays in laminar counterflow and co-flow spray burners at both normal and reduced gravity. The primary diagnostic tool at normal gravity was a commercial Phase Doppler Anemometer (PDA) used to measure distributions of droplet size and either axial or radial velocity component. Heptane, doped with 0.3% (by weight) of an antistatic additive to increase its electric conductivity, was used in all the experiments.

Laminar Counterflow Diffusion Flames—Normal Gravity

Spray combustion was first examined in a counterflow configuration comprising two opposed jets, with oxygen fed from one side and an heptane electro-spray in a co-flow of nitrogen fed from the other side. Initially we studied the combined effects of changes in droplet size, velocity and strain rate, as discussed in ref. 6 and at the last Microgravity Workshop (ref. 7). More recently, we examined the individual effect of each variable in similar flames in which CO_2 , for reasons to be discussed below, was used as diluent (ref. 8). Initial droplet size and velocity were found to affect significantly the flame appearance, its thermal structure and pollutant formation, whereas the strain rate and its effect on the inertia behavior of the droplets plays a role less important than the other two controlling variables. When droplets evaporate completely before reaching the flame, a blue spray flame is stabilized that in many respects is like an ordinary gaseous flame in which the droplets simply act as a source of vapor that is convected and diffuses towards the flame. Alternatively, if insufficient time is available for the droplets to evaporate in their journey towards the flame, they penetrate it and continue to burn on the oxidizer side, leading to a complex and thick flame zone, that is also characterized by soot formation. In the latter case, there is also some evidence of individual droplet burning. Droplet/flame interaction can be usefully interpreted in terms of a Damkhöler number of evaporation, that is the ratio of a droplet residence time and the droplet evaporation time. Namely

$$Da_{ev} = \frac{t_r}{t_{ev}} = \frac{z\bar{K}}{\bar{V}_D D^2}$$

where D is the droplet diameter, \bar{K} is an average evaporation coefficient; z_f is the location of the blue flame formed by the fuel vapor and the oxidizer, and \bar{V}_D is the average droplet velocity. When $Da_{ev} \geq 1$, droplet evaporation is completed on the fuel side of the vapor flame. Whereas, when $Da_{ev} < 1$, the complex flame structure ensues, with droplets overshooting the vapor diffusion flame. Such conditions are achievable with large droplets, large initial velocities or relatively unvolatile liquids.

An interesting byproduct of the combustion of electrostatic sprays is the occurrence of a secondary atomization when, in the course of the droplet evaporation, the electric charge density on the droplet surface increases until the so-called Rayleigh limit is reached. At this point, the repulsion of electric charges overcomes the surface tension cohesive force, ultimately leading to a disintegration into finer fragments. We completed an investigation on this phenomenon (ref. 9), that had been previously demonstrated in non-reactive environments (ref. 2). Charge-induced secondary atomization may be inhibited if direct droplet-flame interaction occurs, in which case the concentration of flame chemi-ions or electrons is sufficient for them to neutralize the charge on the droplets and thus prevent disruption. This result can be rationalized in terms of a non-dimensional number involving the Debye length, that is a characteristic length over which charge separation is induced locally by the thermal motion of charge carriers of disparate molecular mass in an electrically neutral flame. This length is on the order of a few microns in a typical flame. Only if the droplets are within such a short distance from the flame, as is the case when they actually penetrate it, neutralization does occur. Since the bulk of a "well-behaved" spray should burn with the dispersed phase all on the fuel side, i.e. without droplets overshooting the flame, charge-induced secondary atomization will occur, provided, of course, that the droplets have been charged at the injection. This approach could be practically implemented in electrostatically-assisted atomizers. We estimated that total mass loss due to multiple disruptions is approximately 7% of the droplet mass at the time of the first disruption. Since, in consideration of their size, the offspring vaporize instantaneously on the time scale of the parent droplet life, the mass loss upon disruption is "immediately" available as vapor. Thus, the disruption process would enhance the evaporation rate of a non-negligible fraction of the liquid supply and also aid in the overall stabilization of the spray flame.

Laminar Counterflow Diffusion Flames—Experiments in the 2.2s Drop Tower at NASA Lewis

We retrofitted the counter-flow spray diffusion flame burner for experiments in the 2.2 s drop-tower at NASA-Lewis that took place in April, 1993. These tests demonstrated that the electrospray is a compact spray injector system that is well-suited for the confinements of typical low gravity environments. We recorded on videotape microgravity-induced changes in the appearance of the same spray flames that had been examined at normal gravity. What used to be flat flames at normal gravity appeared now as capped, mushroom-shaped ones. The microgravity tests clearly showed that the flame flatness was apparently a buoyancy artifact and that "edge" effects were actually affecting the entire flame. Notice that the two-dimensionality of the flame would be a major drawback, especially from a computational vantage point. The observed effect was tentatively attributed to the velocity profiles at the burner mouth. On the fuel side, in fact, the need to minimize the interception of the droplets on their way to the flame imposed the use of a screen made of very thin wire that evidently did not adequately uniformize the axial velocity profile, in which case a transitional regime between a plug flow and a fully-developed Hagen-Poiseuille profile would be established. Stoichiometric requirements and constraints on the electrospray flow rates prevented us from modifying the velocity profile by changes in feed rates. Thus, we replaced N_2 with CO_2 , thereby increasing the Reynolds number at constant strain rate through a change in the kinematic viscosity of the inert and stretching the Reynolds-dependent entry length. In this way, the flatness of the stagnation surface was considerably improved. Consequently, in the latest set of experiments, such as those discussed in the previous section, CO_2 was used as inert. This first, useful experience is indicative of at least the indirect, and often unexpected, benefits of operating in the unusual microgravity environment. Further studies in microgravity on counterflow flames have been deferred until a new burner that would operate at larger liquid flow rates using an ultrasonic nebulizer is fully tested. The design of a different liquid dispersion system stems from the need to maintain close analogy between experiments and modeling capability. The numerical modeling, currently in progress, requires, in fact, small slip between droplets and gas to preserve self-similarity and one-dimensionality.

Laminar Coflow Diffusion Flames—Normal Gravity

In the experiments on counterflow flames, we saw little or no evidence of individual droplet burning. It is not clear if this observation is indicative of droplet-droplet interactions, that results in droplets evaporating in a cloud at the periphery of which burning occurs, a situation that is typical of practical sprays (ref. 10,11). It could be also an artifact of the particular combination of feed streams, with inert coflow on the fuel side. We decided to examine another configuration, a co-flow axis-symmetric diffusion flame, with the intent to operate at droplet concentrations larger than in the counterflow flames. Analytical models for a Burke-Schumann diffusion flame with fuel spray injection was recently formulated in a configuration that is similar to the one used here (ref. 12). Experimentally, no studies on strictly laminar spray diffusion flames were reported, probably because buoyancy-induced instabilities prevent the establishment of a stable laminar flame at normal gravity, at least under conditions in which there is small slip between the phases (ref. 13). We show below that using the electrospray stable laminar flames can be stabilized in well-controlled combustion environments.

A schematic of the burner is shown in Fig. 1. The typical system to produce a monodisperse electrostatic spray is seen to comprise the metal capillary, through which the liquid fuel is fed, charged at high potential and the porous plate at the top of the burner, that acted as ground electrode. This plate had a 1.9 mm central opening and was positioned at a distance of

0.9 mm downstream of the tip of the capillary where the ES was anchored. Once the cone-jet mode was established, the jet broke up near the plate opening by varicose wave instabilities into a stream of charged droplets. The droplets passed through the opening in the porous plate because their large inertia by far exceeded any electrostatic attraction with the plate. About one millimeter above the plate the stream opened up into a conical fan and ultimately dispersed downstream because of the droplet mutual repulsion. The spray fed a self-sustained, stable, continuous, axis-symmetric, candle-like flame. In the present experiments a co-flow of air at 2.5 l/min was supplied through the burner housing with a uniform velocity of about 5 cm/s. This shroud flow improved the flame stability and ensured overventilated conditions. A small teflon tube, with an inner diameter measuring 4 mm, was mounted coaxially with the capillary, to maintain fuel and oxidizer separated all the way to the burner mouth, and, also, to insulate electrically the capillary from the burner housing. The metal capillary and the teflon tube were kept coaxial by a perforated teflon plate. Gas-phase temperature was determined by an uncoated Pt-6%Rh/Pt-30%Rh thermocouple, whose bead diameter measured 75 μm .

The typical flame had in all respects an appearance very similar to that of a classic candle flame, except that a point source of droplets replaced the candle wick as a source of fuel vapor. Five regions could be readily identified by visual inspection: a) a sharp, bright, blue flame ring, at the very base of the combustion region and perpendicular to the flame axis, that acted as stabilization region of the combustion process; b) a relatively "dark" inner region, that coincided with the bulk of the droplet vaporization region, in the lower part of the flame, right above the flame ring; c) a bright yellow outer "shell" whose luminosity was due to black-body radiation from the soot at high temperature; d) a diffuse, deep blue region in the lower part of the flame, which appeared to envelope the combustion region as the outermost luminous surface; and e) an orange region, at the very top of the flame, that was presumably the soot oxidation region and appeared to be at a lower temperature as compared to the sooty region upstream. Table 1 gives values of relevant parameters for six flames, each numbered in the first column in the table. The key operating variables in each flame are given in the second and third columns in the table. They are the liquid fuel flow rate, \dot{Q} , and the voltage differential, HV, applied between needle and ground electrode. Changes in these parameters affect the initial size, D_0 , and velocity, V_0 , of the droplet, that are listed in the fourth and fifth columns, respectively. As a result of variations in the liquid flow rate and applied voltage, the initial droplet size was varied by a factor of two and the initial velocity by about 20%. The height of the ring flame, H_a , of the dark region, H_v , and of the luminous flame, H_t , all measured from the burner plate, are reported in the last three columns of the table.

Figure 2 shows the mean droplet size and velocity measured along the flame centerline for flames, #3, 4 and 5 by the PDA and plotted versus the axial distance from the porous plate. The droplets are "injected" in the combustion region with mean diameters ranging from 52 μm to 58 μm and an initial velocity ranging from 4.33 m/s to 5.0 m/s. In all flames the average droplet size slightly increased in the first few millimeters above the plate, because of the transient heat-up of the droplets and associated decrease in liquid density. Farther downstream the droplet diameters decreased because of evaporation. The Relative Standard Deviation (RSD), that is the ratio of droplet standard deviation to mean diameter, was 0.07 at the first measurement locations, that is the droplets were virtually monodisperse locally. They maintained a very narrow distribution up to $z=12$ mm. At $z=16$ mm the RSD was 0.25. Beyond that point, the size distribution continued to broaden until no droplet signal was detected. At these locations, approximately corresponding to the height of the "dark" zone of each flame (see H_v column in Table 1), evaporation was completed. The data in Fig. 2 show that in their journey along the flame axis the droplets continued to decelerate under the action of the drag force and of the small electric field due to the Coulombic repulsion from the other droplets, the velocity decreasing linearly with axial distance for all flames.

Velocity measurements enable us to convert the spatial abscissa in Fig. 2 into a temporal one and to re-plot the results in Fig. 3 as the square of the diameter versus time, the latter computed from the first measurement location. The goal is to examine whether there are regions of quasi-steady evaporation at least through part of the droplet history. The data show that after an initial transient, the droplets follow the D-square law through a significant portion of their lifetimes in all flames, under conditions in which their size distributions are either monodisperse, or sufficiently narrow to justify the use of mean diameters. The continuous lines in the figure are linear least square fits yielding average evaporation coefficients (mm^2/s) of 0.53, 0.57 and 0.60 for Flames #3, 4 and 5, respectively. Remarkably, height measurements and the knowledge of liquid flow rate can *directly* provide average evaporation coefficients of droplets in these spray flames in good agreement with these measurements, as shown in ref. 14. Computation of the evaporation coefficients with the assumption of quasisteady evaporation of an isolated droplet in a convective environment and using the thermocouple measurements on the flame centerline yielded values ranging from 0.72 to 0.80 for Flame #3, from 0.74 to 0.81 for Flame #4 and from 0.78 to 0.84 for Flame #5, all in units of mm^2/s . Several factors and uncertainties may have contributed to the discrepancy between the two sets of data, as discussed in Ref. 15. However, the evidence of the applicability of the D-square law in these flames is convincing.

Little or no evidence of individual droplet burning was found in the present experiments. Figure 4 shows the radial scans of temperature at four axial locations under conditions close to those of flame #4. The two lower scans show a pattern with the peak temperature region, that is indicative of the flame location, forming a torus centered on the flame axis, as is typical also of gaseous flames (ref. 16). Farther up into the flame, the trends are the same, albeit the measurements are incomplete because of soot deposition on the thermocouple bead. Eventually, as the flame closed in on the centerline, the location of the temperature peak reached the axis, and the profile would show a monotonically decreasing temperature as a function of radial coordinate. Under individual droplet burning we would expect a much more uniform temperature profile, especially in

the radial direction, in contrast with the data in Fig. 4. Also, since the droplets followed diverging trajectories, we should have been able to discern flame streaks under these conditions. No observations of this sort were made. We conclude that no evidence of individual droplet burning was offered by the present experiments. Rather, conditions were more akin to what is often labeled sheath combustion, with a continuous flame enveloping the entire droplet region and a relatively cooler core in which droplets are evaporating but not burning. Some oxygen was inevitably entrained on the spray axis, since the flames were stabilized approximately three millimeters above the burner plate (see Fig. 6 and the Ha column in Table 1). Yet, stoichiometric conditions in the flame core must have been sufficiently rich to prevent individual droplet burning. In conclusion, even in these relatively dilute sprays, droplet-droplet interactions do prevent individual droplet burning but they do not seem to be sufficient to cause a departure from the D-square law in the flame core.

Since the discussion of group combustion is often cast in terms of the ratio of interdroplet spacing to droplet diameter, l/D , we plotted in Fig. 5 this ratio as a function of radial coordinate at selected axial locations of flame #4, as computed from the inverse cubic root of the measured droplet number density and the size. The vertical bars on each curve of l/D indicate where the peak temperature is at each axial displacement. Also plotted in Fig. 4 is the droplet diameter variation along the radial direction at $z=11.99$ mm, with the length of the vertical bars being equal to two standard deviations of the diameter at every location. In view of the narrowness of the droplet distributions l/D is a meaningful quantity in the present experiments. This ratio typically increases along the radial direction, which is a consequence of both the expanding nature of the spray, caused by the droplet coulombic repulsion, and the stronger evaporation at locations closer to the flame, which lead to a monotonic decrease of the number density as function of distance from the spray center. Values of l/D range from 20 on the centerline to about 160 at the outermost location within the spray core enveloped by the flame. Most of the measured values, especially those in the upper portion of the evaporation region, are significantly larger than the typical value of 10-25, that experiments on droplet streams and theoretical models of multiple droplet combustion reported as upper limit for the droplets to start experiencing significant interactions (e.g., ref. 17). This discrepancy is perhaps suggestive of the inadequacy of systems of a small number of droplets, or of a single droplet stream or of even two-dimensional droplet streams to represent properly three-dimensional group combustion that should be relevant to practical spray diffusion combustion system.

The gaseous velocity field on the axis of Flame #4 was also measured using Al_2O_3 particles as tracers for LDV. During the data acquisition, both the droplet velocity and the particle velocity were simultaneously recorded. A typical velocity histogram showed two very distinguishable peaks, one corresponding to the droplet velocity and the other contingent on the presence of the tracers. The average velocity of the particles were then sorted out and the results are plotted in Fig. 6 together with the velocity of droplets as functions of the distance from the burner. Notice that since the sedimentation velocity of micron-size particles is negligible compared with the gas velocity, that was on the order of 1 m/s, the velocity of the particle measured here represents realistically the gas velocity. The gas velocity on the axis of the flame had a complex behavior. It first increase as a result of the transfer of momentum from the droplets that had been injected at velocities two orders of magnitudes larger than the shroud flow. It reached a relative peak in the neighborhood of the anchoring flame, at which point it went through an oscillating behavior, that can be attributed to the expansion from the heat release due to the presence of the ring flame. Farther downstream, after reaching a maximum, it monotonically decreased towards an asymptote at about 1.5 m/s. This behavior differs dramatically from that of gaseous laminar diffusion flames, that are known to be buoyancy controlled (ref. 18). In the latter cases, the velocity on the centerline was shown to be proportional to the square root of the axial displacement. We conclude that the velocity field in this spray flame is in the lower part of the flame momentum-controlled rather than buoyancy-controlled, which may explain why a steady flame could be stabilized in the present situation, unlike the experiments in (ref. 13). Farther downstream, near the flame tip, the low frequency flickering suggests that buoyancy effects becomes significant by inducing local instabilities.

Laminar Coflow Diffusion Flames—Experiments in the 2.2s Drop Tower at NASA Lewis

In the past few weeks we retrofitted the co-flow laminar spray burner to a drop module and observed the spray flame at different flow rates in the 2.2 s tower at NASA Lewis. Two interesting observations were made in these experiments: first, the flame geometry changes dramatically under microgravity conditions, the flame becoming longer, wider and much brighter. This result is in agreement with what was observed in gaseous diffusion flames (ref. 19). It is perhaps surprising the extent of the changes, particularly so in view of the gas-phase velocity measurements on the flame centerline (Fig. 4) that indicated a momentum-controlled flame, at least in the lower part. Second, some of the tallest flames, corresponding to the largest flow rates (#4, 5 and 6), developed instabilities with low frequency (<6 Hz) aperiodic pulsations and relatively large amplitudes. Notice that this behavior is in sharp contrast with that of gaseous diffusion flames. Numerical studies (ref. 20) have shown that the low frequency flickering that is typical of gaseous laminar flames is caused by buoyancy-induced instabilities, which should disappear under microgravity, as confirmed in experiments in ref. 20. On the contrary, for spray flames we found that the instabilities are amplified under certain conditions and affect the entire flame. Future experiments will require longer microgravity times to investigate this phenomenon fully. The numerical modelling of this two-dimensional problem, that is currently under way, will also help understanding this phenomenon. Further details on both the fundamentals of the electrospray and its application to combustion are given in the two Ph. D. dissertations that have resulted from this research (refs. 21 and 22).

Current/Future Plans

Current/future plans include the following tasks: 1) Additional microgravity experiments on the co-flow electrospray diffusion flames have to be performed to allow for longer observation times; 2) We designed, constructed and tested a counterflow spray diffusion flame burner using an ultrasonic nebulizer as spray generator. This system will allow us to operate at larger droplet concentrations and under conditions of small slip between droplets and gas, as dictated by numerical modeling constraints. Once comparisons between experiments and modeling can be performed, we plan to retrofit this apparatus to the Drop Tower and perform experiments in microgravity; 3) We designed and constructed a turbulent spray sytem using an ultrasonic nebulizer, with the intent of systematically studying the effect of turbulent intensity and scale on flame structure. In addition to the capability of measuring droplet size and velocity, we are developing a temperature measurement technique using Raman thermometry; 4) Computational modelling of laminar spray diffusion flames is being pursued under the supervision of Prof. Smooke. Specifically, the droplet phase has been incorporated in existing codes for gaseous flames with detailed tranport and kinetics using a sectional approach. Preliminary results indicate successful convergence for methanol flames and difficulties with the kinetic model for heptane combustion. We plan to revise the heptane kinetic mechanism in the near future. We will also tailor the numerical computation to the experiments in task 2. Finally, we will model two-dimensional co-flow axisymmetric spray diffusion flames to be compared with the experimental counterpart.

References

- Gomez, A. and Tang, K., "Atomization and Dispersion of Quasi-monodisperse Electrostatic Sprays of Heptane," Proceedings Of the Fifth International Conference on Liquid Atomization and Spray Systems, ICLASS-91, H. G. Semerjian, Ed., NIST Special Publication 813, Gaithersburg, MD, (1991).
- Gomez, A. and Tang, K., "Characterization of a High Charge Density Electrospray of Methanol", *ibid*.
- Gomez, A. and Tang, K., *Phys. Fluids A* 6, p. 404 (1994).
- Tang, K. and Gomez, A. *Phys. Fluids A* 6, p. 2317 (1994).
- Gomez, A. "The Electrospray: Fundamentals and Applications," *Experimental Heat Transfer, Fluid Mechanics and Thermodynamics*, Kelleher, M. D. et al., Eds., Vol. 1, p. 270, Elsevier (1993).
- Chen, G. Gomez, A., *Proc. 24th Int. Symposium on Combustion*, The Combustion Institute, p. 1531 (1992).
- Gomez, A., "The Electrospray: Fundamentals and Combustion Applications," *Proceedings of the Second International Microgravity Combustion Workshop*, Cleveland (1992).
- Chen, G. and Gomez, A. "The Individual Effect of Droplet Size and Velocity on the Structure of Counterflow Spray Diffusion Flames," *Eastern States Section of the Combustion Institute, Fall Technical Meeting*. (1993)
- Gomez, A. and Chen, G., *Combust. Sci. & Tech.*, 96, p. 47 (1994).
- Chigier, N. A., *Combust. and Flame*, 51, p. 127 (1983).
- Chigier, N.A. and Mc Creath, C.G., *Acta Astronautica*, 1,p. 687 (1974).
- Greenberg, J.B., *Combust. Sci. and Tech.*, 75, p.11 (1991).
- Levy, Y. and Bulzan, D. "On the Combustion of a Laminar Spray," NASA TM106210, (1993).
- Gomez, A. and Chen, G. "Experimental Investigation on Self-sustained Co-flow Laminar Diffusion Flames of Monodisperse Sprays," *Proceedings of the Sixth International Conference on Liquid Atomization and Spray Systems, ICLASS-94*, (A. J. Yule and C. Dumouchel, eds.) p. 718 , Begell House, (1994).
- Gomez, A. and Chen, G. "Monodisperse Electrosprays: Combustion, Scale-up and Implications for Pollutant Formation", to appear in a volume in the *Combustion Science and Technology Book Series* (1995).
- Santoro, R.J., Yeh, T.T., and Semerjian, H.G. , *Comb. Sci. & Tech.*, 53, p.89 (1983) .
- Sangiovanni, J.J. and M. Labowsky, *Combust. and Flame*, 47, p. 15 (1982).
- Gomez, A. and Glassman, I. *Proc. 21st Int. Symposium on Combustion*, The Combustion Institute, p.1087 (1987).
- Ellzey, J.L., K.J. Laskey, and E.S. Oran, *Comb. and Flame*, 84, p. 249 (1991).
- Bahadori, M.Y. et al. "Effects of Buoyancy on Laminar, Transitional and Turbulent Diffusion Flames," *Proceedings of the Second International Microgravity Combustion Workshop*, Cleveland (1992).
- Tang, K. "The Electrospray: Fundamentals and Applications to Targeted Drug Delivery," Ph. D. Thesis, Yale University, 1994.
- Chen, G. "An Experimental Investigation on Laminar Diffusion Flames of Monodisperse Fuel Sprays, Ph. D. Thesis, Yale University, 1995.

Table 1: Experimental Conditions for the Coflow Diffusion Flames

Flame #	\dot{Q} (ml/hr)	HV (V)	D_0 (μ m)	V_0 (m/s)	H_a (mm)	H_v (mm)	H_t (mm)
1	4.1	1333	34	5.39	3.1	14.1	18.6
2	6.3	1333	46	4.63	3.4	19.7	26.2
3	7.2	1333	52	4.33	2.9	22.6	32.3
4	8.4	1492	52	5.03	3.45	22.6	34.5
5	9.9	1488	58	4.69	3.5	24.6	40.4
6	11.8	1488	67	4.35	3.7	25.8	48.9

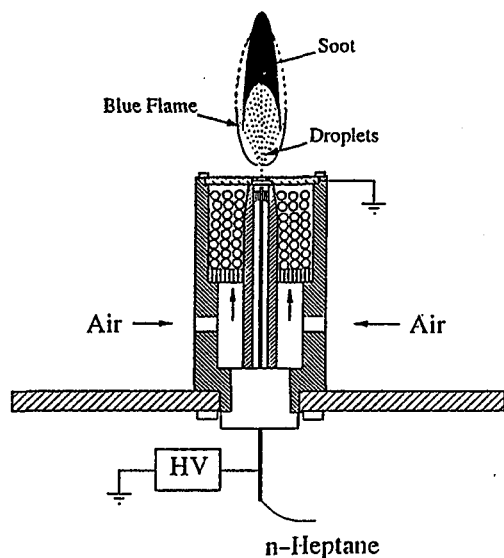


Figure 1.—Schematic of the laminar co-flow spray burner

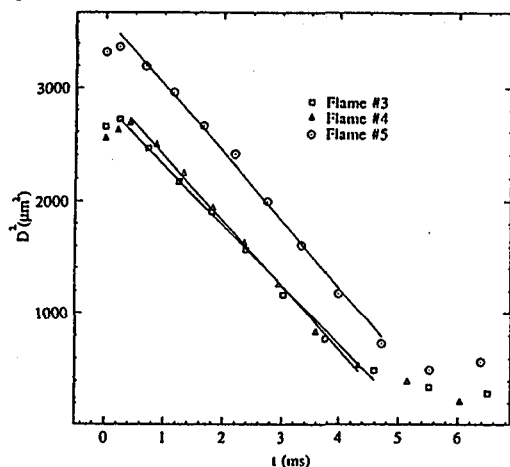


Figure 3.—Square of the average droplet diameter along center line of Flames #3, 4 and 5 vs time. Symbols as in Fig. 2.

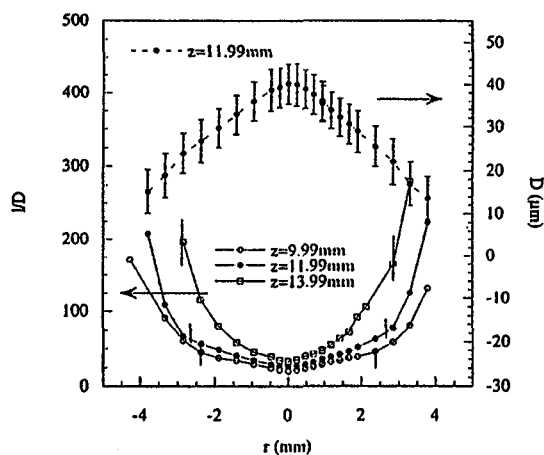


Figure 5.—Radial scan of the ratio of interdroplet spacing over droplet average diameter (left ordinate) and average droplet diameter (right ordinate) at selected axial locations.

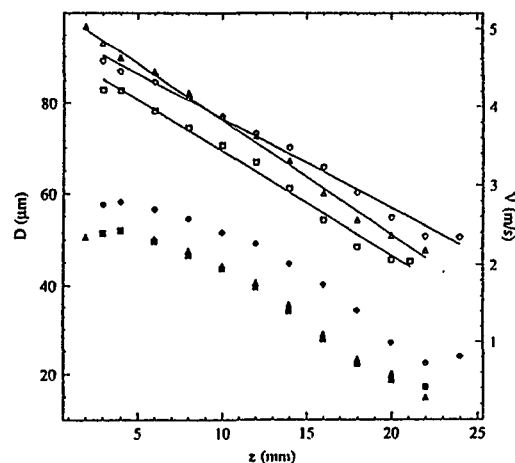


Figure 2.—Average droplet diameter (D_{10}) (full symbols) and velocity (open symbols) along the centerline of Flame #3 (squares), #4 (triangles) and #5 (circles).

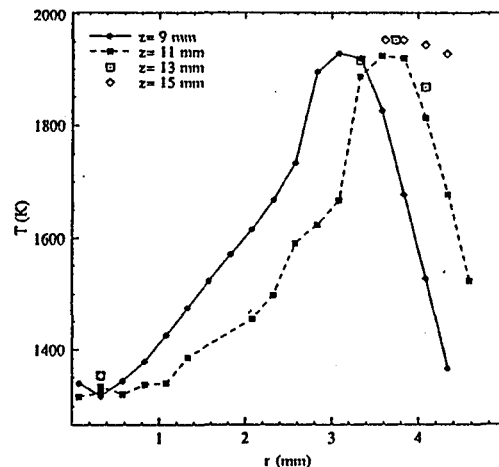


Figure 4.—Temperature vs radial coordinate at selected axial locations.

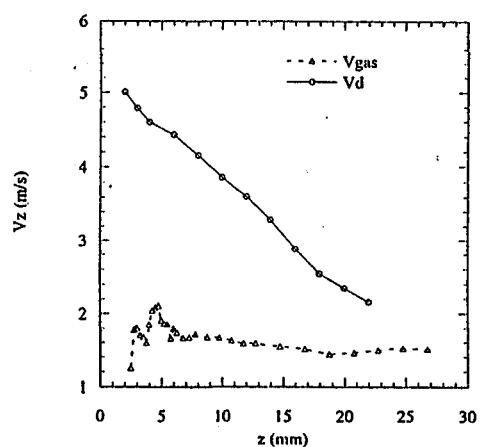


Figure 6.—Average droplet velocity and average gas velocity along the burner axis versus distance from the burner.

JAPAN'S RESEARCH ON DROPLET AND DROPLET ARRAY COMBUSTION

Michikata KONO

Department of Aeronautics and Astronautics, University of Tokyo
Bunkyo-ku, Tokyo, Japan

Introduction

In Japan, the ignition and combustion of the droplet and droplet array have been investigated by using microgravity condition. This is the short introduction of those studies; interactive combustion of two droplets (ref. 1), ignition experiment on droplet array (ref. 2), and microexplosion behavior of an emulsified fuel droplet (ref. 3).

Interactive Combustion of Two Droplets

In spray combustion, droplets burn interactively and the combustion mechanism is different from that of the single droplet due to interaction between the droplets. Droplet array combustion has been studied experimentally and theoretically to understand the interaction from a microscopic viewpoint. It is important to use the basic and the simplest configuration, that is two droplets, in order to improve understanding of multiple droplet combustion mechanisms. In the present study, experiments in microgravity have been performed on the burning of two suspended droplets for a wide range of the initial separation distance.

Two droplets (n-heptane) of the equal size were dispensed in air at atmospheric pressure and initially 295 ± 1 K at the same time. Then they were ignited by two hot wires at the same time. Microgravity conditions were attained by dropping the apparatus with a drag shield in the drop tower at University of Tokyo, which provides about 1.4 s microgravity conditions. Experiments in normal gravity were also performed. Two orthogonal views of the combustion process were taken by two CCD cameras. The suspending fiber diameter was 0.125 mm. The initial droplet diameter (d_0) was 0.81 ± 0.03 mm. The droplet was nearly elliptical in shape due to the existence of the fiber inside, and thus, an equivalent spherical droplet diameter was used as the droplet diameter.

The flame shapes are classified roughly into two modes; individual flames surrounding each droplet (Mode 1) and one merged flame surrounding two droplets (Mode 2). The flame

shapes in microgravity are qualitatively in good agreement with the theoretical predictions by quasi-steady analysis. Within a certain range of the initial separation distance (l/d_0), the transition occurs from Mode 1 to Mode 2 firstly, and then the contrary transition occurs from Mode 2 to Mode 1.

The dependence of the burning lifetime (t_{b0}) on the initial separation distance (l/d_0) is shown in Fig. 1. Here, t_{b0} is the burning lifetime of the droplet with $d_0=1$ mm, to which all the burning times (t_b) were corrected by assuming t_b is proportional to d_0^2 . l and d_0 are the distance between the droplet centers and the initial droplet diameter, respectively. The infinite l/d_0 denotes the single droplet combustion. In normal gravity, t_{b0} has a minimum at a certain l/d_0 . As l/d_0 decreases, natural convection around each droplet is enhanced. This increases oxygen supply to the flame. Further decrease in l/d_0 causes oxygen starvation between two flames.

As seen in Fig. 1, t_{b0} in microgravity decreases slightly with decreasing l/d_0 until it reaches the minimum around $l/d_0=10$ and then increases sharply. The prediction by the quasi-steady theory shows that the instantaneous burning rate decreases monotonically with decreasing instantaneous separation distance (l/d) and therefore, t_{b0} increases monotonically with decreasing the initial separation distance (l/d_0). Contrary to the prediction, t_{b0} has a minimum for a certain l/d_0 and is larger than the theoretical value for any l/d_0 . The difference between the experimental results and the theoretical prediction is mainly caused by the difference of the droplet heating, which is neglected in the theory.

The rate of the decrease in the squared droplet diameter ($d(t)^2$) is defined as the instantaneous burning rate ($K(t)$). $K(t)$ for different l/d_0 are plotted every 0.05 t/t_b versus instantaneous separation distance ($l/d(t)$) in Fig. 2. According to the quasi-steady theory, $K(t)$ is only a function of $l/d(t)$. Experimental results show that $K(t)$ is a function of $l/d(t)$ and l/d_0 . $K(t)$ for different l/d_0 increase and approach an asymptote with increasing $l/d(t)$. The deviation of $K(t)$ from the asymptote is due to the slow evaporation during heating period.

In order to investigate unsteady interaction effects, the instantaneous burning rate of two droplets was compared with that of the single droplet for the same normalized diameter (d/d_0). We introduce an instantaneous burning rate correction parameter (ϵ) which is expressed as,

$$\epsilon(d/d_0) = K(d/d_0)/K_s(d/d_0) - 1.$$

When $\epsilon(d/d_0)$ is positive, $K(d/d_0)$ is larger than $K_s(d/d_0)$ for the same d/d_0 . We call this "positive interaction". When $\epsilon(d/d_0)$ is negative, "negative interaction" occurs.

The instantaneous burning rate correction parameters ($\epsilon(d/d_0)$) were derived and are plotted versus $l/d(t)$ every 0.05 $(d/d_0)^2$ in Fig. 3. For $l/d_0 > 5.4$, the positive interaction occurs in the

earlier stage. $\Xi(d/d_0)$ decreases with increasing $l/d(t)$ (or with time), and then the positive interaction transfers to the negative one. As $l/d(t)$ increases, $\Xi(d/d_0)$ approaches an asymptote. The existence of this positive interaction causes the minimum in the burning lifetime (t_{b0}) (Fig. 1). For $l/d_0 < 5.4$, $\Xi(d/d_0)$ is negative for the entire period of combustion and to be smaller for smaller l/d_0 when $l/d(t)$ is the same. The radiative heat transferred from the other flame promotes droplet heating. On the other hand, the oxygen starvation between the flames suppresses combustion. These effects changes with l/d_0 and $l/d(t)$ (or time).

Ignition Experiment on Droplet Array

Many experimental works have been carried out on ignition of a single droplet in a high temperature ambience. The most interesting phenomena is the effect of initial droplet diameter. Another interesting point is the characteristic ignition time of a droplet consisting of blended liquid fuels with different boiling points. In ignition of an actual spray, however, there should be a strong interaction effect between droplets; experiments on droplet arrays are thus warranted to determine the fundamental aspects of spray ignition. In the present work, ignition times of droplet arrays which were quickly immersed in an electric furnace were measured by changing the diameter of the droplets and the interval between droplets.

The experimental capsule is dropped about 6 m and the test duration is about 1.1 s. The cylindrical electric furnace in the capsule with an inner diameter of 88 mm and a length of 150 mm is heated in advance. When the capsule begins to drop, the furnace is pulled by the two springs, so that the droplet array is quickly immersed in the furnace from a thin window at the bottom of the furnace. The droplet array is heated by radiation from the furnace wall and heat conduction through hot air. Ignition time is defined as the period from the entry of the droplet array into the furnace until light emission caused by ignition. In order to obtain droplets with the same diameter, an array of droplets made of porous ceramics and soaked with liquid fuel was employed. Both ends of the array of five droplets arranged horizontally were soaked with water instead of liquid fuel, because droplets there are known to ignite faster than the other three intervening droplets. As liquid fuels, n-heptane (boiling point: 371.6K) and n-hexadecane (560.0K) were mainly used.

Hexadecane has a relatively high boiling point and therefore the greatest part of ignition time is required to rise droplet temperature. If ignition time is affected mostly by heat conduction, a rough similarity should be easily available. Figure 4 is the plot of the nondimensional ignition time normalized by ignition time of a single droplet (t_{single}) versus the nondimensional span, which is the distance between droplets (S), normalized by the droplet diameter (d_0). It is shown that all data are combined into one curve. It was also found that there exists no

difference in the results under normal gravity and microgravity conditions. For a heptane droplet array, ignition time obtained shows a relatively complicated change as shown in Fig. 5. The ignition time in microgravity were about 30% shorter than those in normal gravity, because vaporized fuel gas descends and is cooled by silica fibers below droplets in normal gravity.

Microexplosion behavior of an emulsified fuel droplet under microgravity

The combustion of emulsified fuel involves vaporization of water within the combustion fields. There is the frequent occurrence of explosive vaporization of water in emulsified fuel by means of super heating above its boiling points by convective and radiative heat supply from surrounding combustion gases and flame. The explosive vaporization causes the secondary atomization which improves the mixing of fuel and air. Three process are included in the secondary atomization which are called as 'disruption', 'puffing' and 'microexplosion'.

It has been recognized that the formation and growth of the vapor bubble in the emulsion plays an important role in the microexplosion behavior. Especially, the bubble nucleation is one of key factors which has a dominant effect on the occurrence of microexplosion.

The objectives of the present study is to obtain the statistical information about the onset of microexplosion for a burning emulsion droplet. We consider that the information of this type is essential to an understanding of the mechanism of microexplosion. The falling assembly was made of steel frames and contained a combustion chamber and a 8 mm videocamera. An emulsion droplet was suspended at the tip of a quartz fiber of 0.25 mm diameter. An electrically heated wire was passed just below the droplet for ignition. The behavior of burning droplet was observed and recorded by using the 8 mm videocamera. The droplet temperature was measured by using the Pt-PtPh(13%) thermocouple of 0.05 mm in diameter. The fuel employed in the experiment was n-dodecane (boiling point; 489.5 K). The surfactant as emulsifier was polyoxyethylene nonylphenyle ether. The emulsion of oil-in-water type (O/W) composed of 79% (in volume) fuel and 20% (in volume) water was prepared with 1% surfactant. From the microphotographs of the emulsion, the microdroplets of fuel were surrounded by the water thin film of the thickness of less than 5 μm . The size of the largest microdroplet is about 15 μm . The emulsion was degassed keeping it at about 5 KPa for two hours.

Figure 6 shows the Weibull plots of distribution function of the waiting time t_{wi} which is defined as the period of time between the instant of microexplosion and the time of the first

microexplosion. The distribution is approximately plotted on the two straight line. This indicates the waiting time is correlated with the Weibull distribution expressed as the next equation.

$$f(t) = \frac{m}{\alpha} \left(\frac{t}{\alpha}\right)^{m-1} \exp\left[-\left(\frac{t}{\alpha}\right)^m\right]$$

where t is the time, m is the shape parameter and α is the scale parameter. For the microgravity, the shape parameter is about 2 in the early stage of the waiting time ($t_{wi} \leq 0.43$), and it is unity in the long waiting time region ($t_{wi} \geq 0.43$). Thus, the onset of microexplosion is classified to the wear failure type in the early stage, and it is classified to the chance failure type in the last stage of the burning.

References

1. Mikami, M., Kato, H., Sato, J. and Kono, M., 25th Int. Symp. on Comb., The Combustion Institute, 1995. (in printing)
2. Niioka, T., Kobayashi, H. and Mito, D., IUTAM Symp. on Mech. and Comb. on Droplet and Sprays. (1994) pp. 367-377.
3. Tsue, M., Yamasaki, M. and Kadota, T., IUTAM Symp. on Mech. and Comb. on Droplet and Sprays. (1994) pp. 479-488.

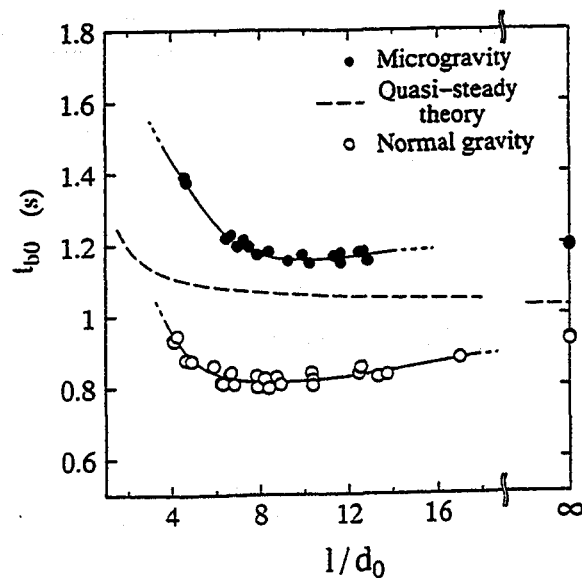


Figure 1. Dependence of the burning lifetime (t_{b0}) on the initial separation distance (l/d_0).

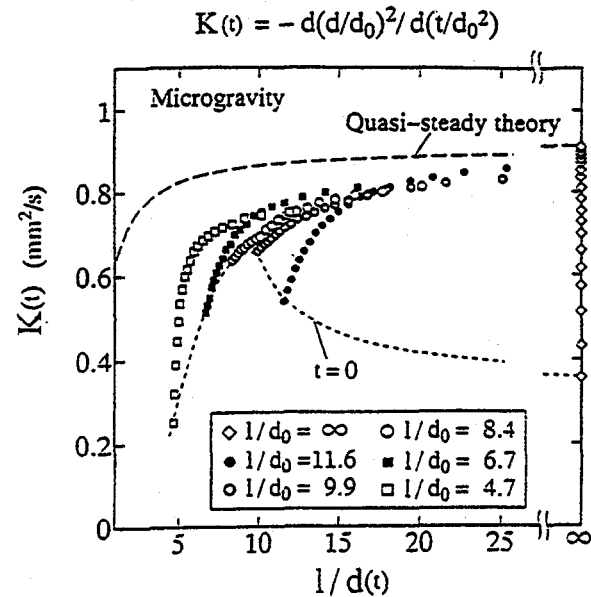


Figure 2. Dependence of the instantaneous burning rate ($K(t)$) in microgravity on the instantaneous separation distance ($l/d(t)$) for different initial separation distance (l/d_0).

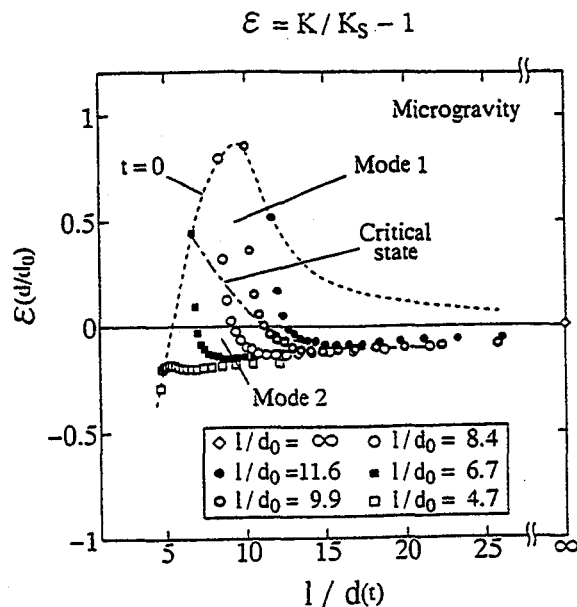


Figure 3. Dependence of the instantaneous burning rate correction parameter ($\varepsilon(d/d_0)$) on the instantaneous separation distance ($l/d(t)$) for different initial separation distance (l/d_0).

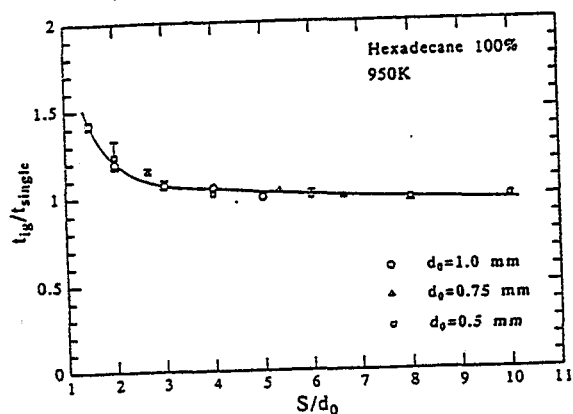


Figure 4. Nondimensionalized plot of ignition time in normal gravity.

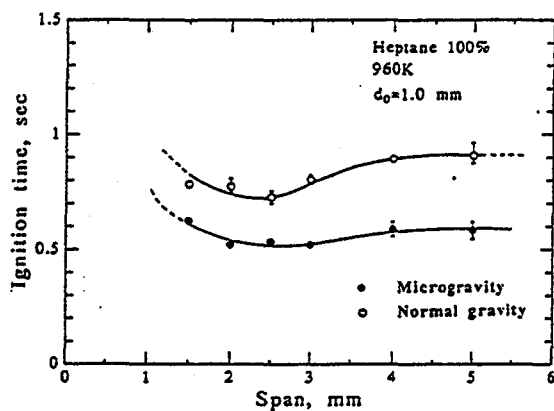


Figure 5. Comparison of ignition time in normal gravity and microgravity.

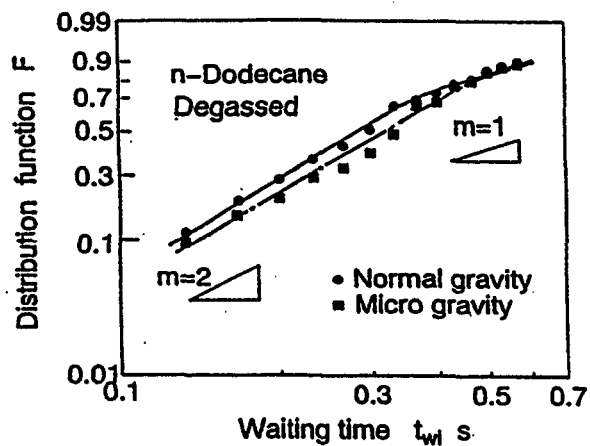


Figure 6. Weibull plots of distribution function of waiting time.

JAPAN'S RESEARCH ON PARTICLE CLOUDS AND SPRAYS

Jun'ichi Sato
Research Institute
Ishikawajima-Harima Heavy Industries Co., Ltd.
Toyosu, Koto-ku, Tokyo 135, Japan

Introduction

Most of energy used by us is generated by combustion of liquid and solid fuels. These fuels are burned in the combustors mainly as liquid sprays and pulverized solid, respectively. Knowledge of the combustion process in the combustors is needed to achieve proper designs that have stable operation, high efficiency, and low emission levels. However, current understanding on liquid and solid particle cloud combustion is far from complete.

If the combustion experiments for these fuels are performed under normal gravity field, some experimental difficulties are encountered. These are

- Particles are falling by the gravity force. It is impossible to stop the particles in the air.
- Falling speeds of particles are different each other, which depend on the particle size.
- Flame is lifted up and deformed by the buoyancy force.
- Natural convection makes the flow field to be more complex.

Since these experimental difficulties are attributable to the gravity force, the microgravity field can eliminate the above problems. It means that the flame propagation experiments in a static homogeneous liquid and solid particle clouds can be carried out under microgravity field. It will provide many informations for basic questions related to combustion processes of particle clouds and sprays.

In Japan, flame propagation processes in the combustible liquid and solid particle clouds have been studied experimentally by using the microgravity field generated by the 4.5-second dropshaft, 10-second dropshaft, and parabolic flight. They are the studies on flame propagations in a homogeneous liquid particle cloud, in a mixture of liquid particles/gas fuel/air, in a PMMA particle cloud, and in a pulverized coal particle cloud. This presentation describes recent results of these studies.

Sprays

Flame propagation in a homogeneous liquid droplet cloud:

Purpose of this study is to explore the flame propagation process in a liquid droplet cloud at elevated pressures. This study is supported by Science and Technology Agency (STA) and National Space Development Agency (NASDA). Since the no-movement liquid droplet cloud with mono-size and mono-disperse is suitable for the experiments, the droplet cloud generation system has been studied firstly. Sato and Nomura have been studying the condensation method to generate the homogeneous droplet cloud (Ref. 1). Figure 1 shows a schematic diagram of the experimental apparatus. If the pressure of the

saturated fuel vapor and air mixture is decreased adiabatically, the temperature of the mixture decreases and the liquid droplets are generated in the mixture. If this system is operated under normal gravity condition, the generated droplets fall as rain by the gravity force. The microgravity experiments were performed by the parabolic flight of a small jet airplane named MU-300 and the 4.5-dropshaft, which was constructed recently at Toki, Gifu. Figure 2 shows the photograph of the generated ethanol droplets in the ethanol vapor/nitrogen mixture. In the photograph, the black line is the thermocouple with 30 micron meter diameter. The droplets with about 10 micron meter diameter are formed homogeneously. Figure 3 shows the droplet diameter distribution. Nearly homogeneous droplet cloud is formed.

The flame propagation experiments will be started from June, 1995. The flame propagation behavior and the droplet behavior will be observed by the high-speed color video camera, interferometer, and the PIV system. In August 1996, the experiments will be performed in the longer microgravity field obtained by the sounding rocket TR-1A.

Flame propagation in a fuel droplets/gas fuel/air mixture:

Purpose of this study is to observe the flame propagation behavior in a liquid droplets/gas fuel/air mixture. This study is carried out by Hiroyasu et al. (Ref. 2) and supported by New Energy and Industrial Technology Development Organization (NEDO) under controlled by Ministry of International Trade and Industries (MITI). Figure 4 shows the experimental apparatus. The propane/air mixture is filled in the flame tube with rectangular section of 50 x 50 mm and then the kerosene is injected in it. The microgravity experiments were performed by 10-second dropshaft. The most of microgravity time was used for making the static homogeneous droplet cloud. The mixture was ignited by the electric spark. Figure 5 shows the flame propagation distance with time. The total equivalence ratio is 0.8 and the propane gas ratios in the total equivalence ratio R_g are 0.7 and 0.6. When R_g is 0.7, since the propane/air mixture is in the flammability limits, the flame propagates in the premixed gas and the droplets burns after the flame propagation. When R_g is 0.6, since the mixture is out of the flammability limits, the flame does not propagate in the premixed gas. The flame propagates from a droplet to the other one slowly. Figure 6 shows the flame propagation behavior of $R_g = 0.6$.

Solid particle clouds

Flame propagation in a PMMA particle cloud:

Purpose of this study is to explore the flame propagation mechanism in a liquid droplet cloud with lower volatility and in a solid particle cloud with high volatility. PMMA is suitable to the experiments because the round mono-size particles are easily obtained and its burning behavior is simple and well known. This research is carried out by Niioka et al. (Ref. 3) and is supported by NEDO. Figure 7 shows the experimental apparatus. The PMMA particles are fed by the fluidized bed and send to the flame tube with the

diameter of 38 mm. The microgravity experiments are performed by 10-second dropshaft. Most of the microgravity time is used to obtain the static mono-dispersed particle cloud in the flame tube. Figure 8 shows the effects of the equivalence ratio on the flame velocity. The flame velocity has a maximum at a certain value of the equivalence ratio over one. If the particle size is increased, the maximum flame velocity decreases and the equivalence ratio at which the peak appears increases. Figure 9 shows the effects of methane adding in the PMMA particle cloud. Adding one percent of methane changes the flame speed remarkably. But, more adding changes not so much.

Flame propagation in a pulverized coal particle cloud:

Purpose of this study is to obtain the flame propagation velocity in a pulverized coal particle cloud and the parameters affecting it. This study is carried out by Ito, Kitano, and Sato (Ref. 4) and supported by NEDO. Figure 10 shows the experimental apparatus. The microgravity experiments are performed by the 10-second dropshaft. The pulverized coal, which is under 200 mesh (about 70 micron meter diameter), is ejected into the burning region by the static electric force under microgravity. After about 5 second, the coal particles are homogeneously dispersed and stop. The coal particle cloud is ignited by a nichrome-wire at the center. The spherical flame propagation is observed after ignition as shown in Figure 11. The tests were performed mainly for the Taiheiyo coal, which is a kind of bituminous coal. Figure 12 shows the effects of the coal concentration on the flame speed. In this experimental range, the flame speed increases as the concentration is increased. The inert gas, nitrogen, in the air was replaced by the carbon dioxide and the argon, and then the effects of these gases were examined. The flame speed in the carbon dioxide mixture is lower than the others. The gas analysis and the particle analysis just after burning showed that the burning temperature for the carbon dioxide mixture is lower than the others. In these studies, the effects of the oxygen concentration, the ambient pressure, and the kind of coal were studied.

References

1. Nomura, H., Sugawara, N., Meguro, T., Ujiie, Y., Masuko, K., Sato, J., and Kono, M. "Generation of static droplet cloud under microgravity conditions using a rapid expansion apparatus," Proceedings of Droptower Days '94, Bremen, Germany, 1994.
2. Hiroyasu, H., Private communication, (to be appear).
3. Kobayashi, H., Ono, N., Okuyama, Y., and Niioka, T., "Flame propagation experiment of PMMA particle cloud in a microgravity environment," Twenty-fifth International Combustion Symposium, 1995.
4. Ito, K., Fujita, O., Tagashira, T., Sakamoto, A., and Sato, J., "Utilization of a 10 second microgravity environment for the measurement of coal dust flame propagation speeds," Proceedings of Droptower Days '94, Bremen, Germany, 1994.

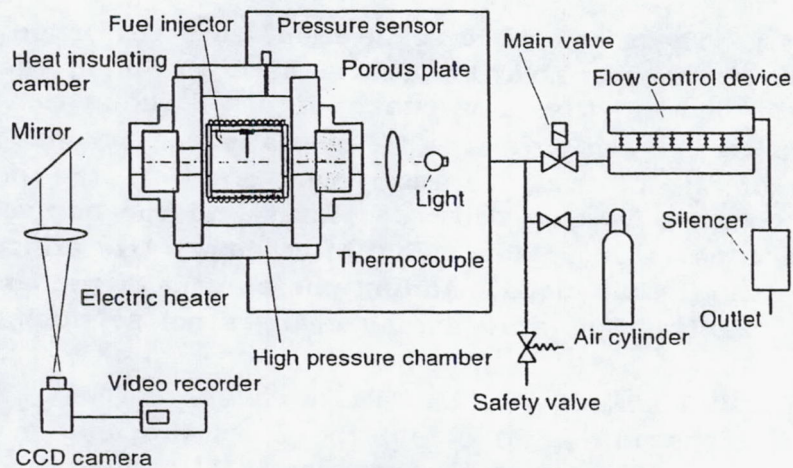


Figure 1. Experimental apparatus for Droplet cloud generation by the condensation method.

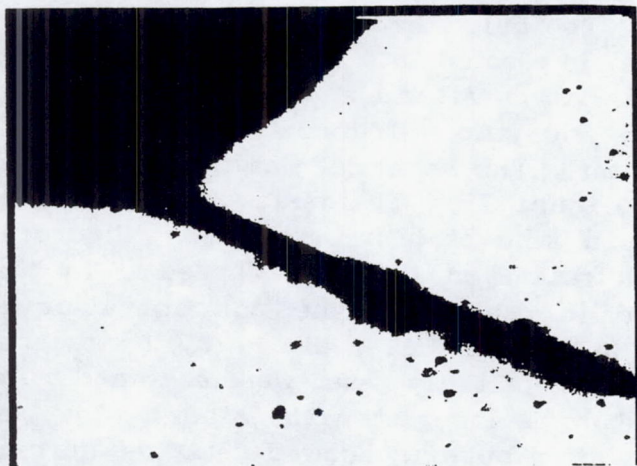


Figure 2. Ethanol droplets generated in the ethanol vapor/nitrogen mixture.

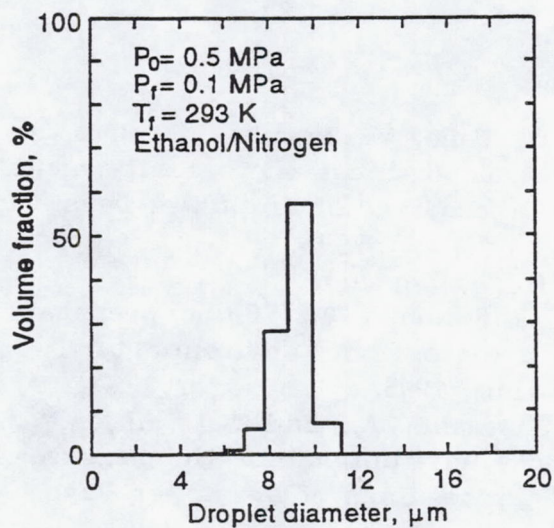


Figure 3. Distribution of the droplet diameter.

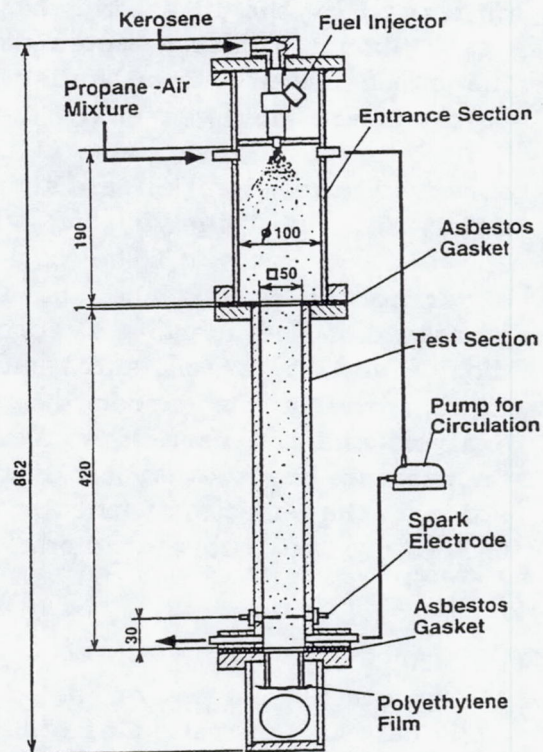


Figure 4. Experimental apparatus for flame propagation in the fuel droplets/gas fuel/air mixture.

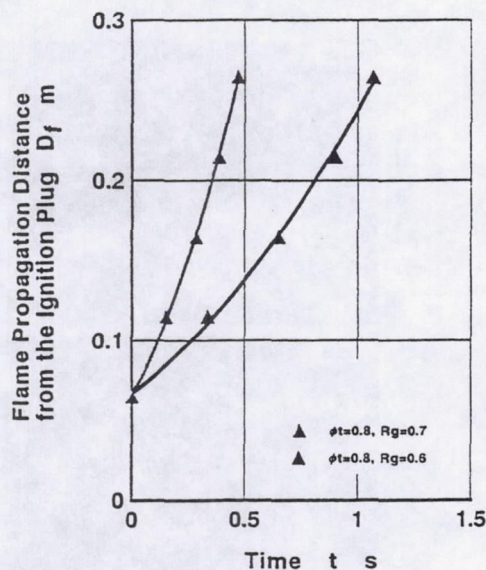


Figure 5. Flame propagation distance with time.

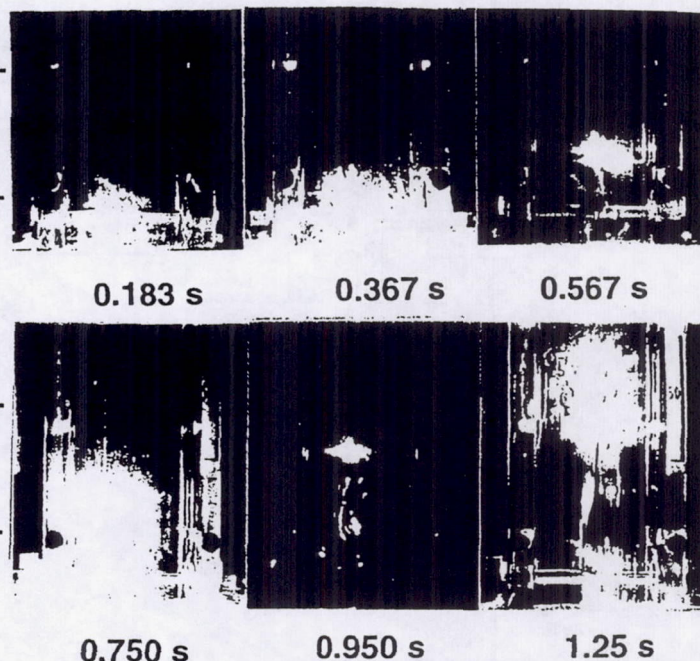


Figure 6. Flame propagation behavior in the fuel droplet/gas fuel/air mixture.

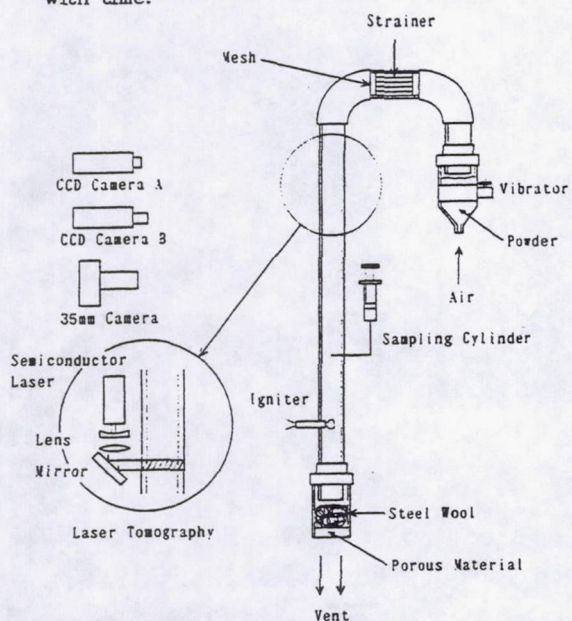


Figure 7. Experimental apparatus for flame propagation in the PMMA particle cloud.

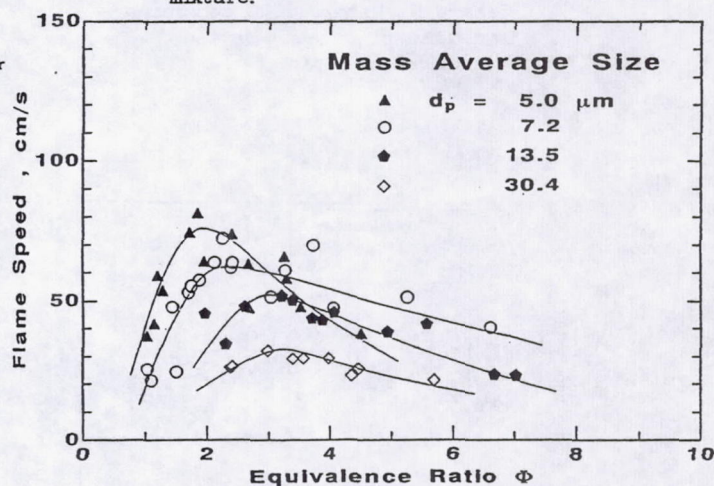


Figure 8. Effects of the equivalence ratio on the flame velocity in the PMMA particle cloud.

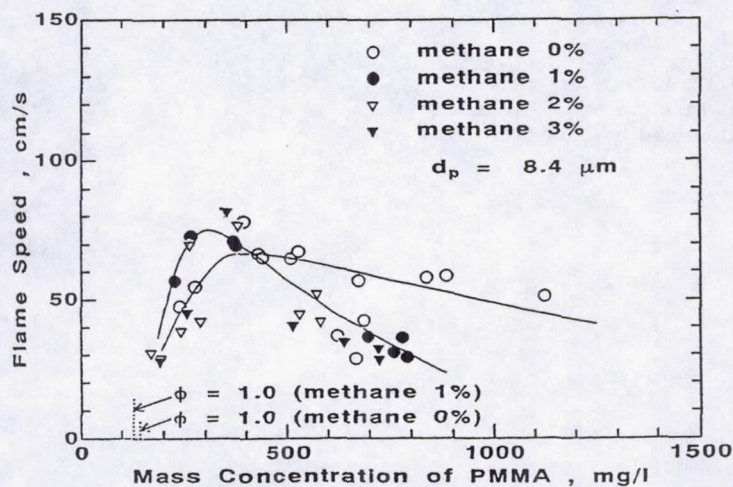


Figure 9. Effects of methane adding in the PMMA particle cloud.

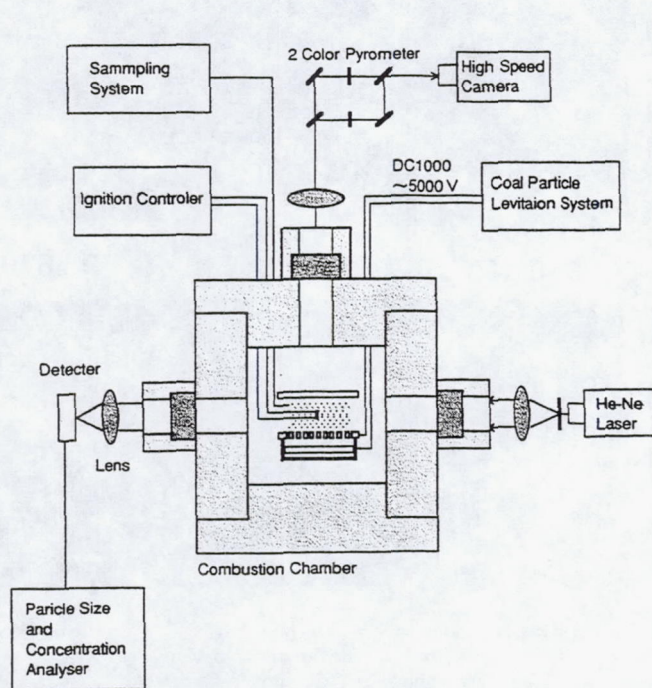


Figure 10. Experimental apparatus for flame propagation in the pulverized coal particle cloud.

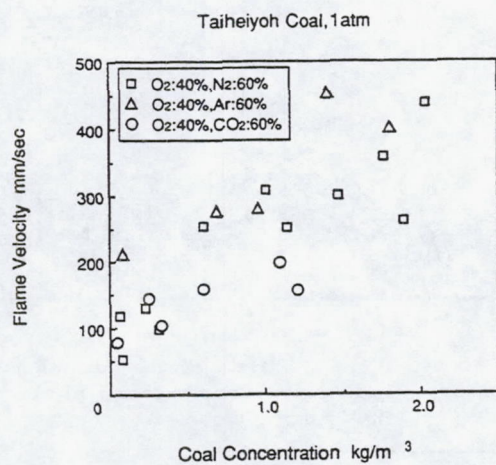


Figure 12. Effects of the coal concentration on the flame speed in the pulverized coal particle cloud.

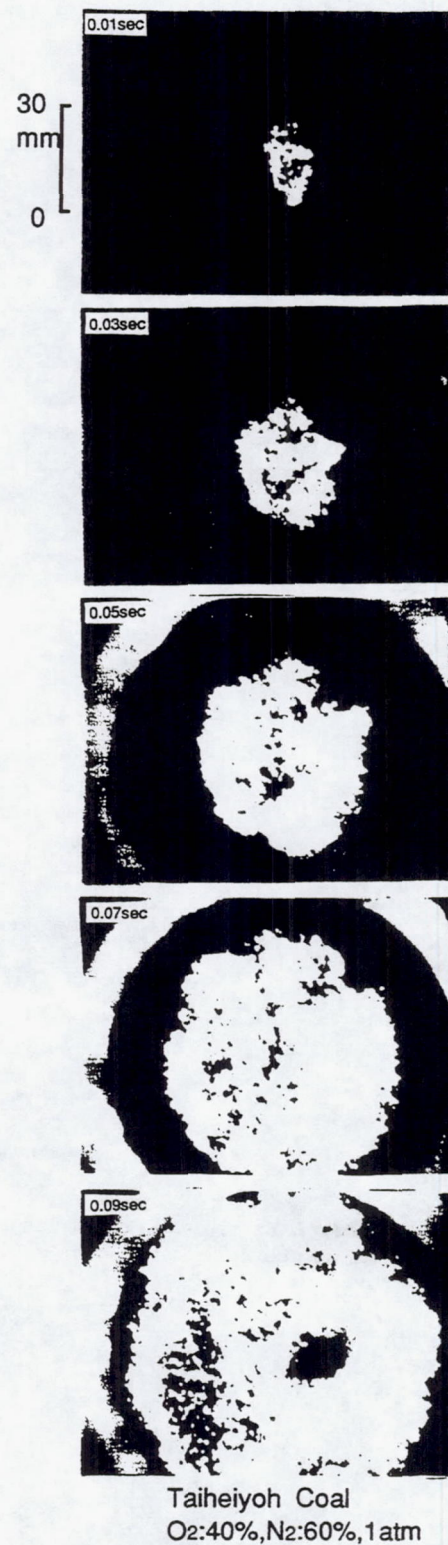


Figure 11. Flame propagation behavior in the pulverized coal particle cloud.

COMBUSTION OF TWO-COMPONENT MISCIBLE DROPLETS IN REDUCED GRAVITY

Benjamin D. Shaw, Israel Aharon and James W. Gage
University of California, Davis

and

Andrew J. Jenkins and Thomas J. Kahoe
NASA Lewis Research Center
Cleveland, OH

Research Start Date - August 31, 1991

Background

Many efforts to understand sprays have focused upon studying isolated droplets. Information gained from these studies is often not directly transferable to spray situations. However, isolated-droplet studies are useful in that they allow certain phenomena to be studied under well-controlled and simplified conditions. When theory and experiment agree for simplified situations, predictions for more complex cases (where accurate experimental data may not exist) may be made with more confidence. Though small droplets are of practical concern (e.g., < 50 μm as found in some spray systems), it is difficult to perform detailed experiments with them. This is because small droplets are difficult to deploy and ignite without significant perturbations, and they may be difficult to resolve photographically. Hence, most detailed investigations into single-droplet combustion have focused upon larger droplets which are easily observed. In this program, reduced-gravity combustion behaviors of miscible binary droplets initially about 1 mm in diameter are studied. Gravity levels significantly less than 10^{-3} g's are required to render buoyancy negligible for these size droplets.

In practice, liquid fuels are usually multicomponent. It is important to understand the vaporization mechanisms of multicomponent fuels, especially the rates that fuel components with differing properties are vaporized from the liquid phase. This is because gas-phase phenomena depend on the components that have been vaporized, while liquid-phase phenomena depend on the components remaining in the liquid. The simplest multicomponent fuels are (arguably) binary and miscible. When there is a significant volatility difference between droplet components, binary droplets may exhibit a three-stage combustion history where two periods of nearly d^2 -law combustion (where the square of the droplet diameter decreases linearly with time) are separated by an intermediate period where vaporization rates are low and flame diameters decrease significantly. These behaviors are thought to be a result of a sudden buildup of the lower-volatility component at the droplet surface^{1,2}, necessitating a sudden increase in the droplet surface temperature. During the first period of d^2 -law vaporization, most of the fuel being vaporized is the higher-volatility component, while during the second d^2 -law vaporization period, if liquid-phase species diffusivities are sufficiently small, both liquid components are vaporized at rates nearly proportional to their average liquid mass fractions³. As the droplet surface temperature increases, the droplet interior may be heated above temperatures required for bubble nucleation and growth in regions rich in high-volatility species that are present as a result of chemical stratification in the liquid¹⁻³. As a result, a bubble may grow and fragment a droplet (the droplet may experience a "disruption" or "microexplosion").

Scientific Objectives

This research focuses on the combustion of binary miscible droplets initially in the mm size range. Experiments are performed using the NASA Lewis 2.2 sec drop tower in Cleveland, Ohio, where mixtures of alkanes and/or alcohols are studied. The fuel components are selected to have significantly different volatilities. Initial oxygen mole fractions from about 0.15 - 0.5 and initial pressures from 0.3 - 2 atm are employed. Different inerts are used (He, CO₂, Ar, N₂) to change burning rates and sooting behaviors. Objectives are to observe the following:

- Transient droplet diameters (including three-staged combustion behaviors and microexplosion).
- Transient flame behaviors (sudden flame contraction, luminosity, extinction).
- Behaviors of observable soot particles.

Theoretical and computational research in support of this program has also been undertaken. This research includes:

- Analytical studies to determine the effects of small but nonzero gravitational levels on droplet gasification.
- Analytical studies of hydrodynamic stability of spherically-symmetrical droplet gasification (to address the question as to whether spherically-symmetrical droplet gasification may be destabilized from capillary, i.e., Marangoni effects).
- Computational modeling of effects of capillary stresses on droplet gasification.

Significance

The reduced gravity experiments should yield insight into the efficiency of liquid-phase species diffusion, since this diffusion may markedly influence combustion behaviors (e.g., three-staged combustion behaviors). By noting times for flame contraction to occur, calculations for effective liquid-phase species diffusivities may be made (e.g., with asymptotic or with numerical models). Finally, unique sooting behaviors may appear since gas-phase compositions may differ significantly initially (e.g., by varying diluents and oxygen concentrations) as well as during an experiment (from variations in the composition of fuel gasifying from a droplet). Differences in sooting may be observable photographically by noting behaviors of apparent flame luminosities and soot particles large enough to be observed.

The theoretical and computational efforts will aid interpretation of the reduced-gravity experiments as well as improve understanding of fundamental phenomena (e.g., capillary stresses and buoyancy effects).

Experimental Approach

The reduced-gravity experiments are performed using the NASA Lewis 2.2 sec Drop Tower. A new drop rig was built for this purpose. The electronics on the apparatus, except for some modifications, were based on the design of an existing NASA apparatus which is described elsewhere⁴. The mechanical design is new, though it is based on knowledge and experience accumulated at NASA. A ceramic fiber ($\approx 12 \mu\text{m}$) is sometimes used to stabilize droplets; concepts for the fiber were obtained from Dr. D. Dietrich⁵. In an experiment, a droplet is grown (in a pressure chamber) between two opposed hypodermic needles. The needles are retracted simultaneously in opposite directions, leaving the droplet essentially at the location where it was grown. The deployment induces oscillations in the droplet shape at a frequency higher than 370 Hz (the cine camera framing rate). These oscillations damp early in the combustion history. The droplet is ignited using two symmetrically-placed ignition sparks ($\approx 100 \text{ mJ}$ each). The spark electrodes are retracted after ignition, and droplet and flame behaviors are observed photographically using two ccd video cameras (for real-time observations) and two 16 mm cine cameras. Orthogonal views are taken; one backlit view is a close-up of the droplet while the other shows the flame (no backlight). In most experiments a ceramic fiber was used which held droplets nearly motionless and even if there was a drift along the fiber it was very small ($\approx 0.1 \text{ mm/s}$) and insignificant in terms of possible residual convection. Experiments that did not use a fiber typically had a droplet drift velocity (up to several mm/s).

A Sun workstation-based digital image processing system was developed for analysis of cine films and ccd images from drop tower experiments. Basic concepts for this system were obtained from the literature⁶. Software for the Sun-based system was developed with the assistance of Virtual Visions Software⁷.

Experimental Results

During the summer of 1992, exploratory experiments with heptane/hexadecane mixture droplets were performed at the NASA Lewis Research Center 2.2 sec drop tower. An existing droplet combustion apparatus⁴ available at NASA Lewis was used for these experiments. Experiments were attempted both with and without a ceramic support fiber ($\approx 10 \mu\text{m}$ diameter) being present. The ceramic fiber was utilized to prevent significant droplet drift after deployment. Results from these preliminary experiments have been reported elsewhere⁸.

In Fall 1994 and Winter 1995, a large number of experiments were performed at NASA Lewis with the new drop apparatus. Because of time limitations, we have not been able to analyze all of the films in time for this workshop. We are presently in the process of reviewing the experiments, though we do have some detailed results and a number of general observations regarding 35 of the 133 successful experiments (out of 203 total experiments that were performed). The high success rate is due to the fact that the support fiber was used in many of the experiments. Results and observations are listed below.

Fuel Mixtures

The experimental program covered a wide range of parameters. Two main groups of fuels were studied - alkanes and alcohols. Within the alkanes, mixtures of heptane/hexadecane ranging from pure heptane through 95, 80/20, and 60% heptane (by mass) were investigated the most. Other mixtures studied also consisted of pentane and dodecane mixed with mainly heptane at various ratios. The alcohols studied were methanol and ethanol mixed with 1-dodecanol in proportions which were much the same as for the hydrocarbons. A few exploratory experiments were also performed with mixtures of heptane/methanol, heptane/ethanol, and heptane/hexadecane/dodecanol. These tests have not yet been reviewed though one observation regarding a mixture of heptane/methanol at proportions of 80/20% shows two burning regimes with regard to sooting; in the first burning period of time the droplet is sooting and it is non-sooting the second period.

More complex mixtures involving three liquid-phase components initially in a droplet were investigated as well. The components were selected to have significantly different volatilities with the hope that two flame contractions could be observed during the combustion of a single droplet. In at least one experiment it appears that a double contraction does occur. Finally, several mixtures of heptane/hexadecane and pentane/heptane where the low volatility fuel was in excess were investigated and it was observed that flame contractions occurred. This may be due to sooting effects⁹.

Gas Mixtures

A large range of diluents (in addition to atmospheric air), consisting of N_2 , CO_2 , He and Ar were used in different mixtures and at different ratios ranging from 5 to 70% of diluent. The gas mixtures were composed mainly of O_2 and one of the diluents but some experiments were conducted with combinations of diluents. The primary reason that He was originally selected was to increase the burning rate in order to burn droplets to completion for droplets as large as possible. It turned out that He in addition strongly inhibited sooting as well as the likelihood of achieving microexplosions. Adding He also increased the brightness of the blue reaction zone. Some of these observations are discussed in the following paragraphs. CO_2 was used to observe its effect on sooting behavior; it was found that replacing N_2 with CO_2 reduced sooting.

This effect has been reported in the literature for droplets burning in normal gravity¹⁰. It was also found that replacing N_2 with Ar increased sooting, though experiments with Ar have yet to be fully analyzed. An attempt was made to determine a sooting threshold (based on visual observations) for Ar and N_2 when these species are added to a basically non-sooting mixture consisting of O_2 and He. The He or N_2 concentrations were varied systematically in order to observe changes in sooting behavior. These tests have not been yet fully analyzed but it appears that such a threshold does exist.

O_2 concentrations were varied from 15 to 50% (molar) to study the effect on burning rates and sooting. At atmospheric pressure, it was found that even with He as a diluent (which strongly inhibited sooting), raising the oxygen concentration above 35-40% produced considerable sooting. Behaviors in subatmospheric pressures were different and will be briefly discussed later.

Initial Diameter Effects

In the experiments conducted, efforts were made to provide data for droplets with different initial diameters. The largest droplets investigated were initially about 1.8 mm in diameter while the smallest ones were initially about 0.5 mm in diameter. A full analysis of the effects of initial droplet diameter on combustion histories has not yet been completed, though some initial observations can be presented. Generally, it was found that increasing the initial droplet diameter increased the amount of visible soot. In addition, the largest droplet investigated appears to have an abnormally-low burning rate (see Fig. (1)) compared to initially-smaller droplets with the same initial composition burning in the same atmospheres. Because of free-fall time limitations, the largest droplet shown in Fig. (1) could not burn to completion, so it cannot be ascertained whether the burning rate for this droplet would increase at later times in its combustion history.

Pressure Effects

Most experiments to date have been conducted at atmospheric pressure. However, some exploratory experiments were performed with pressures as low as 0.3 atm (abs) and as high as 3 atm (abs). We have not analyzed this data yet, and only general observations can be offered at this time. For example, mixtures of heptane/hexadecane which were heavily sooting at 1 atm did not visibly soot at subatmospheric pressure for the same gas composition. Vacuum also appreciably reduced burning rates and as such most of the experiments were conducted in an atmosphere consisting of O_2/He at a ratio of 50/50%; however, some experiments used air. Reducing the pressure also has the effect of making it possible to observe the blue flame zone in air for the entire burning history. Because of the brightness of soot radiation, this was not possible at 1 atm.

The tests in high pressure were performed in O_2/He environments. One definite observation that can be offered at this time is that increasing the pressure significantly increases sooting for hydrocarbon droplets (relative to 1 atm, with the same initial droplet diameters and gas-phase compositions).

Visible Soot Dynamics

Heptane/hexadecane mixture droplets burning in air were highly sooting except during the flame contraction. In O_2/He atmospheres, droplets typically were sooting only for an initial period of time after which the soot appeared to disappear, possibly because of decreased fuel residence times.

In He/O_2 environments, the blue flame zone could be observed to lie outside a yellow zone corresponding to radiant soot emissions for the entire combustion history (Fig. (2)). Interestingly, the radius of the yellow zone did not always correspond closely to the radius of the blue zone. In many of the O_2/He experiments, the yellow zone contracted slowly and typically disappeared, while the blue zone remained at about the same diameter until it also contracted, but only for a short time, after which it grew again. The contraction of the blue zone is most likely related to droplet heating effects caused by a sudden increase in the surface hexadecane mass fraction of the droplet. Data showing these behaviors are shown in Fig. (3), while data for the droplet diameter for this experiment are shown in Fig. (4). The disappearance of the yellow zone may be related to decreased fuel residence times inside the flame, since the droplet is continuously decreasing in size. This behavior needs to be explored, further, however.

Soot "shells" (i.e., high concentrations of soot that form a dark ring between the droplet and the flame that is visible in photographs, see Fig. (5)) were observed in numerous tests with heptane/hexadecane fuel mixtures, though never when O_2/He mixtures were used, even though soot was present as evidenced by the yellow colors in the flame photographs. Sometimes more than one soot shell co-existed (concentrically) for a certain period of time, as shown in Fig. (5). These soot shells would slowly merge into a single shell. Soot shells were not present when He alone was used as a diluent, though they were almost always present when N_2 or CO_2 were used as diluents above 0.4 atm (even in combination with He). When (yellow) flame contractions were observed, the soot shells also were observed to contract at the same times (Fig. (6)). The soot shell contraction in many instances ends by what appears to be absorption of soot into the liquid phase, though a soot shell may sometimes reappear (Fig. (6)); see Fig. (7) for the droplet diameter history for this experiment.

Blue Flame Zones

In air with various mixtures of heptane/hexadecane ranging from 95/5 to 60/40% (by mass) respectively one can observe the following type of behavior from the flame-view images: for approximately 0.04 - 0.06 seconds after ignition, a blue circular flame is visible after which soot starts to form inside this blue region and eventually the blue flame is no longer visible due to high light intensity soot radiation (though at 0.4 atm or lower, sooting is significantly reduced which allows observation of the blue flame zone throughout the combustion history, as noted above). In an atmosphere consisting of O_2-He 30/70% (molar) respectively with the same type of liquid fuel mixtures the blue flame sheet is visible throughout the entire test even when soot is formed inside the region between the droplet and the flame. The flame "sheet" actually has a finite visible thickness, and is at least as thick the droplet diameter (at least in O_2-He environments). A minor change in the O_2-He proportion to 35/65% causes the blue flame sheet to not be visible for most of the test even though the brightness of the luminous zone appears to be very similar. With mixtures of alcohols (methanol/1-dodecanol or ethanol/1-dodecanol) in atmospheric air the blue flame is not visible at all in the color photographs except for a short time after ignition.

Droplet Microexplosion

Microexplosions occurred quite frequently in the various tests and even though a detailed analysis of this aspect has not yet been performed the following general observations can be made: (1) in most cases where the environment was composed of O_2-He the likelihood of microexplosive events for the same liquid fuel, pressure and droplet diameter was less than when compared to air which suggests that He might inhibit this phenomenon; (2) in a large number of tests (among those that were viewed) the microexplosions did not shatter the droplets, and in most cases the droplets regained spherical shapes, though some fuel was lost during the process and the droplet diameter sometimes decreased sharply; (3) in a number of tests, there were several microexplosions after the first one, and droplets sometimes were observed to trap gas bubbles during the microexplosion event; (4) microexplosions frequently occurred after flame contractions (this behavior has also been observed in previous experiments^{11,12,13}).

Flame Contraction Analysis

The onset of flame contraction (i.e., where the flame rapidly decreases in size) is experimentally a rather abrupt event (Figs. (3), (7), (8) and (9)) that can be compared with theoretical predictions. Shown in Fig. (9) are comparisons of flame-contraction predictions of an asymptotic theory² with the experimental results that have been reduced to date. The ratio V_c/V_0 is the ratio of the droplet volume at the onset of flame contraction to the initial droplet volume. The solid lines are plots of the equation $V_c/V_0 = Y/[Y + 3\varepsilon(1 - Y)]$ where $\varepsilon = 8D/K$ is a small parameter of expansion (D is the liquid species diffusivity and K is the burning-rate constant based on droplet diameter) and Y is the initial hexadecane mass fraction. The open and closed triangles and the open circles are data points. The experimental values of V_0 used in this graph were increased by a value of 10% to approximately account for swelling which will occur when the droplets are heated after ignition. Typical ε values expected are in the range 0.01 - 0.1, and these values evidently are applicable in Fig. (9). It is noted that similar comparisons of experiment and theory have been published for heptane/hexadecane droplets that were burned in reduced-gravity at supercritical pressures though for a limited range of gas-phase compositions¹³; we will compare our results with these data shortly.

Extinction

Detailed analysis of data from two experiments showed that extinction appears to have occurred; other experiments, which have not yet been fully analyzed, show indications of extinction as well. The extinction diameter measured in one experiment was found to be about 125 μm for a droplet which was initially about 1.1 mm in diameter. This droplet was composed of heptane/hexadecane (10% hexadecane initially by mass) and burned in an O_2/He environment (70% He molar) at 1 atm. The extinction diameter measured in the other experiment was about 75 μm for a droplet which was initially about 0.91 mm in diameter. This droplet was composed of heptane/hexadecane (20% hexadecane initially by mass) and burned in an O_2/He environment (50% He molar) at 1 atm. The 12 μm fiber was used to support both droplets. It is noted that extinction has previously been observed for binary mixtures of alcohols burning in air under reduced-gravity conditions¹².

Red Flames

The side-view photos occasionally showed reddish coloring for the flames. An example of this behavior is shown in Fig. (10), which actually shows flames associated with two small droplets that were ejected during the microexplosion of a larger parent droplet. In the photo, the flame of one of the small droplets appears to be red (initially it was blue, though this is not shown. The film record shows that the other blue flame will eventually turn red as well. An explanation for this behavior is not available at present.

Analytical Approaches And Results

To aid interpretation of experimental efforts, analytical studies of the behaviors of gasifying droplets in reduced-gravity environments have been performed. These efforts focused on studying: (1) effects of small gravitational levels on droplet vaporization/combustion; and (2)

hydrodynamic stability of spherically-symmetric vaporization/combustion of two-component droplets. Each effort to date has considered evaporating droplets; combustion will be considered later.

In the gravity-level research, a mathematical model taking into account small (and constant) gravitational levels is developed for vaporization of an isolated liquid droplet suspended in a stagnant atmosphere. A goal of the analysis was to determine how small gravitational levels affect droplet gasification characteristics. Attention is focused upon determining the effects on gas-phase phenomena. The conservation equations (including viscous effects) were normalized and nondimensionalized, and a small parameter that accounts for the effects of gravity identified. This parameter is a Richardson number based on the gravitational acceleration, the droplet radius, and a characteristic gas-phase velocity at the droplet surface. Asymptotic analyses were developed in terms of this parameter, and different spatial regions were identified. Near a droplet, gravitational effects are negligible in the first approximation, and the flowfield is spherically symmetric to the leading order. Analysis shows, however, that outer zones exist where gravitational effects cannot be neglected; it is expected that a stagnation point will be present in an outer zone that is not present when gravity is totally absent. The leading-order and higher-order differential equations for each zone are derived and solved¹⁴. Sketches of predicted flowfields are shown in Figs. 11 and 12.

The stability analyses have addressed the problem of hydrodynamic stability of a two-component droplet undergoing spherically-symmetrical gasification. The problem is formulated as a linear stability analysis, with a focus of predicting when spherically-symmetric droplet gasification can be expected to be hydrodynamically unstable from surface-tension gradients acting along the surface of a droplet. The conservation equations (including viscous effects) for the gas and liquid phases were perturbed, and the perturbation equations were simplified and solved¹⁵. Droplet components were assumed to have characteristic liquid species diffusion times that are large relative to characteristic droplet surface regression times. It was initially found that for the conditions assumed (quasisteady gas phase, no initial droplet temperature gradients, diffusion-dominated gasification, appreciable initial concentrations of both components in the droplet, negligible gravity), surface tension gradients should not influence stability characteristics in the limit of vanishingly-small liquid species diffusivities. Further analyses (which have not yet been published) have shown, however, that spherically-symmetrical gasification may be hydrodynamically unstable under conditions that are representative of reduced-gravity droplet gasification experiments when liquid-phase species diffusivities are small but nonzero. A neutral stability criterion has subsequently been derived for droplet evaporation. Analysis of this result is underway.

Computational Approach And Results

Detailed computational modeling (in collaboration with H. A. Dwyer) has focused upon predicting the effects of capillary flows (from droplet surface temperature and/or composition gradients) on droplet vaporization. Briefly, the governing equations are cast in a finite-volume form, and solved numerically for transient liquid- and gas-phase variables. Variable properties in both the liquid and gas phases are allowed. Calculations are performed using the Sun workstation also used for image processing. Modeling of single-component droplet vaporization in a hot environment has clearly shown that surface-tension gradients dramatically influence droplet vaporization and internal circulation behaviors under conditions that are representative of slowly-drifting droplets in reduced-gravity experiments as well as rapidly-translating droplets in practical high-pressure sprays^{16,17,18}.

Future Plans

The UC Davis drop rig will be modified so that pressures substantially below 1 atm may be investigated; we presently have problems forming droplets at low pressures, leading to a low experiment success rate. Once this modification is completed, experiments will be performed with binary mixtures of alkanes and/or alcohols in various gas mixtures. By comparing the data obtained with the previously-obtained higher-pressure data, we hope to obtain information on the effects of sooting on droplet combustion phenomena (e.g., onset times for flame contraction). We also plan to investigate use of Ar as a diluent more extensively, since it will likely change the sooting characteristics of the droplets. The computational model will be extended to combustion of two-component miscible droplets, for which surface-tension gradient effects are expected to be especially significant. In addition, the gravity-level and hydrodynamic-stability analyses will be extended to include gas-phase chemical reactions (combustion).

Acknowledgments

Vedha Nayagam is gratefully acknowledged for providing general project supervision and technical support. Howard Ross is acknowledged for his decision to extend the experimental program and to make the drop tower available for an additional period of time. Special acknowledgments are extended to James Mehlschau, Jerry Dill, Wayne Andrade and Burt Vannucci from the engineering shop at UC Davis for building the rig and offering central design improvements. The invaluable assistance of the personnel at the drop tower - Jack Lekan, Michael Johnston, Charles Traylor, Marlon Richmond and John Jessup made it possible to have a successful program and they are gratefully acknowledged. Jim Simps is acknowledged for providing photolab services. Israel Aharon thanks Brian Borowski for introducing him to the techniques used in the droplet experiments. Finally, gratitude is expressed to NASA for providing financial support.

References

- 1 Wang, C. H., Liu, X. Q., and Law, C. K., "Combustion and Microexplosion of Freely Falling Multicomponent Droplets," *Combustion and Flame*, 56: pp.175-197 (1984).
- 2 Shaw, B. D., and Williams, F. A., "Theory of Influence of a Low-Volatility, Soluble Impurity on Spherically Symmetric Combustion of Fuel Droplets," *International Journal of Heat and Mass Transfer*, 33: pp. 301-317 (1990).
- 3 Shaw, B. D., "Studies of Influences of Liquid-Phase Species Diffusion on Spherically Symmetric Combustion of Miscible Binary Droplets," *Combustion and Flame*, 81: pp. 277-288 (1990).
- 4 Haggard, J. B. and Kropp, J. L., "Development of a Droplet Combustion Experiment for Low-Gravity Operation," paper AIAA-87-0576 presented at the AIAA Twenty-Fifth Aerospace Sciences Meeting.
- 5 Current Address: Sverdrup Technology, Inc., 2001 Aerospace Parkway, Brookpark, Ohio 44142.
- 6 Choi, M. Y. and Dryer, F. L., "A Digital Image Processing Technique for Droplet Burning Data," Mechanical and Aerospace Engineering Report #1875, Princeton University (1989).
- 7 Address: 10696 Parthree Drive, Cupertino, CA 95014.
- 8 Shaw, B. D. and Aharon, I., "Combustion Experiments in Reduced Gravity with Two-Component Miscible Droplets," paper presented at the Second International Workshop on Combustion Science in Microgravity (NASA CP 10113), Cleveland, OH, September 15-17, 1992.
- 9 Shaw, B. D., Dryer, F. L., Williams, F. A. and J. D. Haggard, Jr., "Sooting and Disruption in Spherically Symmetrical Combustion of Decane Droplets in Air," *Acta Astronautica* 17: pp. 1195-1202 (1988).
- 10 Kadota, T., Hiroyasu, H., and Farazandehmer, A., "Soot Formation by Combustion of a Fuel Droplet in High Pressure Gaseous Environments," *Combustion and Flame*, 29, pp.67-75 (1977).
- 11 Yang, J. C., and Avedisian, C. T., "The Combustion of Unsupported Heptane/Hexadecane Mixture Droplets at Low Gravity," Twenty-Second International Symposium on Combustion, The Combustion Institute, pp. 2037-2044 (1989).
- 12 Yang, J. C., Jackson, G. S., and Avedisian, C. T., "Combustion of Unsupported Methanol/Dodecanol Mixture Droplets at Low Gravity," Twenty-Third International Symposium on Combustion, The Combustion Institute, pp. 1619-1625 (1991).

- 13 Mikami, M., Kono, M., Sato, J., Dietrich, D., L., and Williams, F. A., "Combustion of Miscible Binary Fuel Droplets at High Pressure Under Microgravity," *Combustion Science and Technology* 90: pp. 111-123 (1993).
- 14 Beitelmal, A. and Shaw, B. D., "Theory of the Effects of Small Gravitational Levels on Droplet Gasification," paper 95-0144 presented at the 33rd AIAA Aerospace Sciences Meeting, Reno, NV, January 9-12, 1995.
- 15 Aharon, I. and Shaw, B. D., "Hydrodynamic Stability of Multicomponent Droplet Gasification in Reduced Gravity," paper 95-0145 presented at the 33rd AIAA Aerospace Sciences Meeting, Reno, NV, January 9-12, 1995.
- 16 Niazmand, H., Shaw, B. D., and Dwyer, H. A., "Effects of Marangoni Convection on Transient Droplet Evaporation in Reduced Gravity," paper presented at the Fall Meeting of the American Chemical Society, Chicago, Illinois (August 22-27, 1993).
- 17 Niazmand, H., Shaw, B. D., and Dwyer, H. A., "Effects of Marangoni Convection on Transient Droplet Evaporation at Elevated Pressures and With Negligible Buoyancy," paper 93-083 presented at the 1993 Fall Meeting of the Western States Section of the Combustion Institute, SRI International, Menlo Park, CA.
- 18 Niazmand, H., Shaw, B. D., Dwyer, H. A., and Aharon, I., "Effects of Marangoni Convection on Transient Droplet Evaporation," *Combustion Science and Technology* 103: p. 219 (1995).

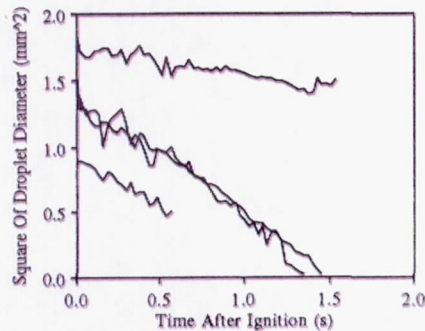


Fig. 1 Droplet diameter histories for heptane/hexadecane mixture droplets (initial hexadecane mass fraction of 0.3) burning in O_2/He environments (35% O_2 molar) at 1 atm.

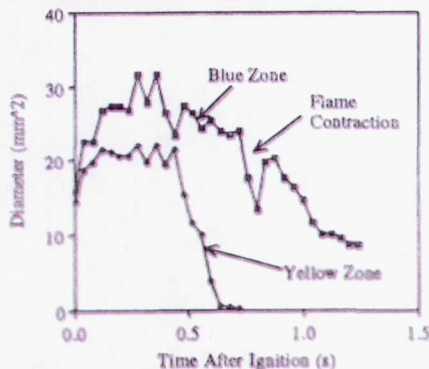


Fig. 3 Blue and yellow flame diameter histories for a heptane/hexadecane mixture droplet (initial hexadecane mass fraction of 0.05) burning in an O_2/He environment (30% O_2 molar) at 1 atm.

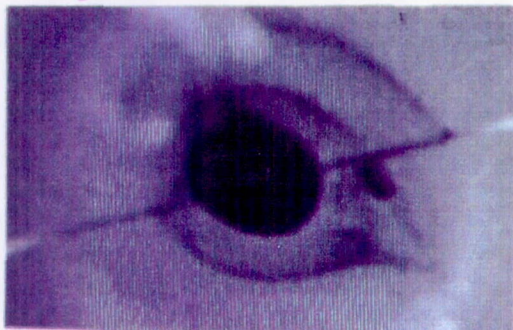


Fig. 5 Double soot shell for a heptane/hexadecane mixture droplet (initial hexadecane mass fraction of 0.4) burning in an $O_2/He/CO_2$ (35% O_2 , 55% N_2 molar) environment at 1 atm. The two soot shells slowly merge into one.

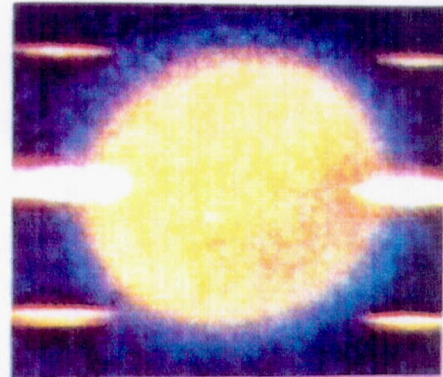


Fig. 2 Flame image of a heptane/hexadecane mixture droplet (initial hexadecane mass fraction of 0.1) burning in an O_2/He environment (30% O_2 molar) at 1 atm.

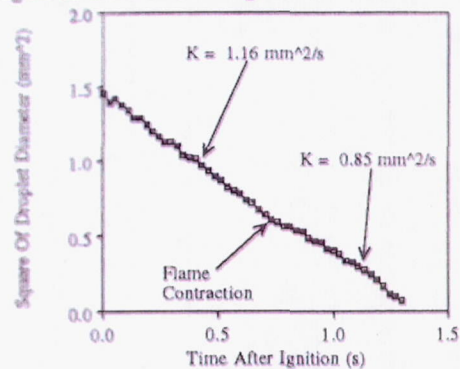


Fig. 4 Droplet diameter history for a heptane/hexadecane mixture droplet (initial hexadecane mass fraction of 0.05) burning in an O_2/He environment (30% O_2 molar) at 1 atm.

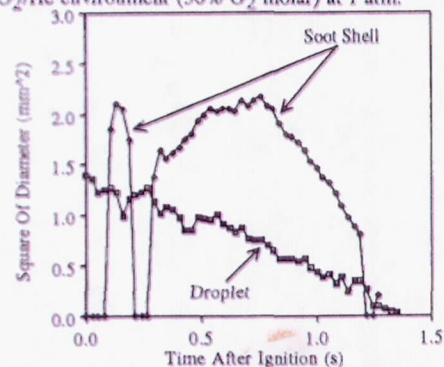


Fig. 6 Soot shell and droplet diameter behaviors for a heptane/hexadecane mixture droplet (initial hexadecane mass fraction of 0.3) burning in an O_2/He environment (35% O_2 molar) at 1 atm.

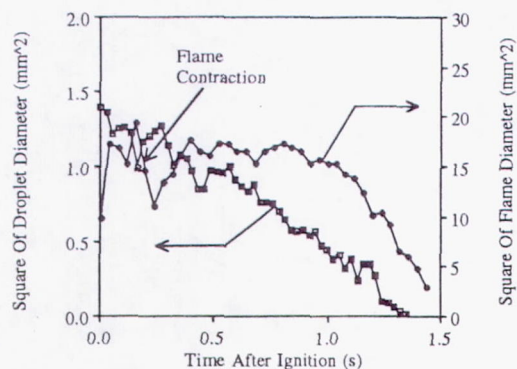


Fig. 7 Droplet and flame diameter behaviors for a heptane/hexadecane mixture droplet (initial hexadecane mass fraction of 0.3) burning in an O_2/He environment (35% O_2 molar) at 1 atm.

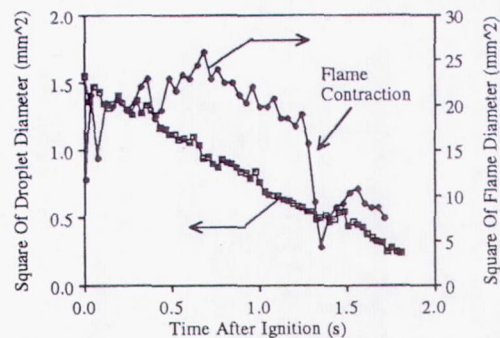


Fig. 8 Droplet and flame diameter histories for a heptane/hexadecane mixture droplet (initial hexadecane mass fraction of 0.05) burning in air at 1 atm.

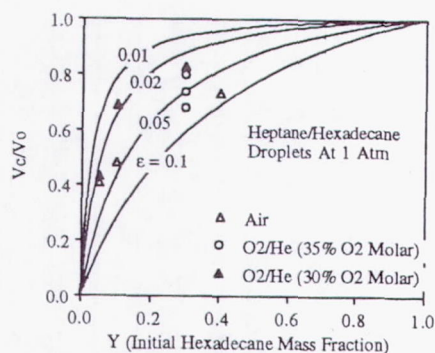


Fig. 9 Comparison of theory and experiment for the droplet diameter ratio at the onset of flame contraction.

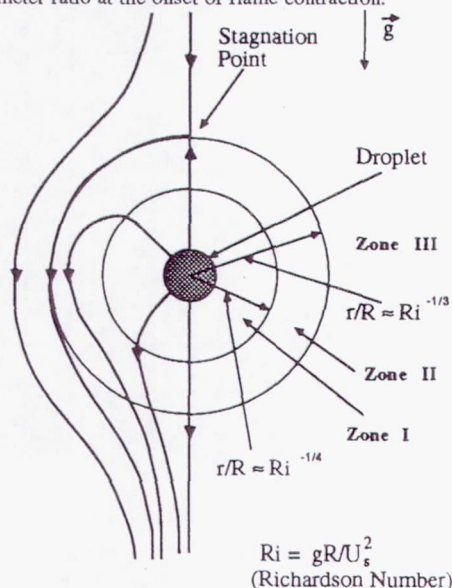


Fig. 11 Qualitative sketch of the flowfield near a gasifying droplet.



Fig. 10 Photo showing the red and blue flames for small droplets ejected from a larger droplet during a microexplosion. The larger droplet was initially composed of heptane/hexadecane (initially 10% hexadecane by mass). The environment is O_2/N_2 (50% O_2 molar).

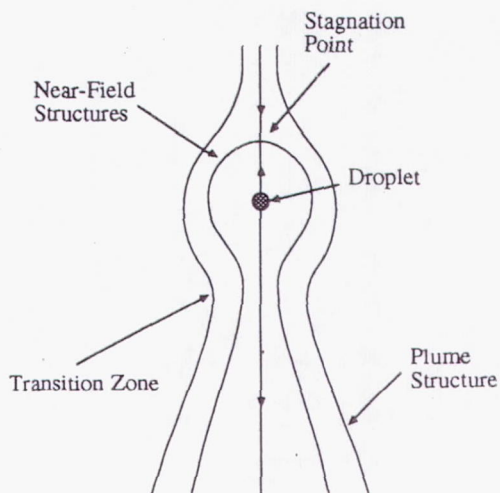


Fig. 12 Qualitative sketch of the flowfield far from a gasifying droplet.

HIGH-PRESSURE COMBUSTION OF BINARY FUEL SPRAYS

Masato Mikami and Michikata Kono
Department of Aeronautics, University of Tokyo
Hongo, Bunkyo-ku, Tokyo 113, Japan

Jun'ichi Sato
Research Institute
Ishikawajima-Harima Heavy Industries Co., Ltd.
Toyosu, Koto-ku, Tokyo 135 Japan

Daniel L. Dietrich
Sverdrup Technology, Inc.
NASA Lewis Research Center, Cleveland, Ohio 44135

and

Forman A. Williams
Center for Energy and Combustion Research
Department of Applied Mechanics and Engineering Sciences 0411
University of California San Diego, La Jolla, California 92093

Introduction

This is a joint research program, pursued by investigators at the University of Tokyo, UCSD, and NASA Lewis Research Center. The focus is on high-pressure combustion of sprays of miscible binary fuels. It involves construction of an experimental apparatus in Tokyo, mating of the apparatus to a NASA-Lewis 2.2-second drop-tower frame in San Diego, and performing experiments in the 2.2-second tower in Cleveland, with experimental results analyzed jointly by the Tokyo, UCSD, and NASA investigators. The project, initiated nearly one year ago, is a follow-on to a project on high-pressure combustion of single binary fuel droplets, initiated in December, 1990, which resulted in clarification of the near-critical three-stage combustion process, as published in ref. 1. The new project has now involved one period of drop-tower testing by Mikami at Lewis, in August, 1994, in which about 30 successful runs of video data were obtained on the combustion of pairs of fiber-supported droplets of mixtures of n-heptane and n-hexadecane, initially about 1 mm in diameter and separated by distances from 4 mm to 8 mm, at pressures up to 4 MPa.

Objective

The ultimate objective of this study is to obtain fundamental information relevant to combustion processes that occur in fuel sprays of practical interest at high pressures in internal combustion engines. Since practical fuels are multicomponent and derived from petroleum, the present work involves the model alkane mixture of n-heptane and n-hexadecane. Since burning droplets in sprays can interact with each other, the present work involves investigation of the effects of this interaction on flame shapes and droplet burning times. The small droplets in practical combustion chambers are not significantly influenced by buoyancy. Since such small droplets are difficult to study experimentally, the present work takes advantage of microgravity to lessen buoyancy and enable information about droplet interactions to be obtained by studying larger droplets. The results are intended to provide fundamental understanding that can be used in improving descriptions of practical spray combustion.

Experimental Apparatus and Procedure

Figure 1 shows a schematic diagram of the experimental apparatus. The pressure chamber has four windows that give two orthogonal views of the combustion process, a black-and-white backlit view from which the droplet sizes as functions of time are obtained and a color view which shows the flame surrounding the droplets. The backlight is in the plane of the droplet support fibers and is focused on the droplet nearest it. During each test, both of these views were recorded on VHS videotape by a fiberoptic link from the test package. Microgravity conditions were attained by dropping the pressure chamber and associated experimental equipment in a drop tower at NASA Lewis Research Center that provides 2.2 seconds of microgravity ($\sim 10^{-5}$ normal).

Before release of the experimental package, fuel droplets were formed at the end of 0.125 mm silica fibers from a high-pressure syringe driven by a stepping motor. Following release, immediately upon entry into microgravity the droplets were ignited. The ignition source was a hot wire (aluminum alloy, 0.2 mm diameter) formed into 2 mm diameter loops that surround the droplets. The hot wire was rapidly removed after ignition, leaving approximately 2 seconds of the 2.2 seconds to observe combustion. All processes, including droplet dispensing and ignition, were controlled by a microcomputer.

The initial droplet size was approximately 1 mm in diameter. This droplet diameter is nearly an order of magnitude larger than that of the suspending fiber, while also being small enough that complete burning could be observed in the available microgravity time. The ambient gas was air at a total pressure ranging from 0.1 MPa to 4.0 MPa. The binary fuel droplets were composed of mixtures of n-heptane and n-hexadecane with mass fractions of hexadecane ranging from 0 (pure heptane) to 1.0 (pure hexadecane). The subject fuels have

critical temperatures and pressures of 540 K, 2.74 MPa and 722 K, 1.53 MPa for heptane and hexadecane respectively. All experiments were performed with the ambient gas and the droplet initially at room temperature.

General Combustion Behavior

Figure 2 shows the flame around two droplets burning side by side at 0.1 MPa. The top photo is at an earlier stage of combustion and the bottom one at a later stage. Figure 3 is the corresponding history of the square of the droplet diameter, as obtained from the backlit camera view orthogonal to that of figure 2. The staged burning found for single droplets and explained previously (ref. 1) continues to exist for these droplet pairs. Resolution of the droplet diameter was achievable only up to 1.0 MPa. Above that pressure, flame radiation from soot washes out the backlight. However, the staged burning is still identifiable from the flame photographs; flame contraction occurs as hexadecane builds up at the droplet surface, then the flame grows again after the hexadecane begins to vaporize and burn. Dilution of the air with nitrogen suppresses soot formation and enables droplet-diameter histories to be resolved to somewhat higher pressures. In previous work with single droplets (ref. 1), such dilution was employed for this purpose.

Total Burning Times

Single-droplet results from previous work (ref. 1) are shown in figure 4. In that figure, X denotes the mole fraction of oxygen in the oxygen-nitrogen atmosphere, and Y_0 is the mass fraction of hexadecane in the liquid fuel. Consider first the results shown in figure 4 for pure heptane ($Y_0 = 0$) and for pure hexadecane ($Y_0 = 1$). For the former, the droplet total burning lifetime decreases with increasing pressure up to 3.0 MPa, but for the latter there is a minimum lifetime at about 2.5 MPa. This behavior is consistent with a minimum lifetime occurring in this atmosphere for pure fuels at pressures somewhat above the critical pressure (2.74 MPa for heptane and 1.53 MPa for hexadecane). A minimum may thus be expected for heptane in figure 4 at a somewhat higher pressure. In theory, the more vigorous the combustion is, the closer to the critical pressure will the minimum lie. This prediction is in agreement with present experimental results on the burning of single droplets of pure heptane in air, as shown in figure 5. In air, the combustion is more vigorous than in the diluted atmosphere, and the minimum total burning time for heptane in figure 5 occurs very near its critical pressure.

Figure 4 shows that in diluted atmospheres the total burning times for mixtures typically exceed those of the pure fuels, and the burning time decreases with increasing pressure, so that if there is a pressure at which the burning time reaches a minimum value, then this pressure is higher than that for the pure fuels. Figure 5 shows that these conclusions continue to apply in

undiluted air. The curve in figure 5 for $Y_0 = 0.33$ suggests that the burning time may achieve a minimum at about 5.0 MPa. At higher values of Y_0 , the minimum may be expected to occur at lower pressures and to approach a value somewhat above 1.53 MPa as Y_0 approaches unity. These results on total burning times of single droplets of binary fuel mixtures are thus exhibiting a consistent pattern.

The effects of droplet spacing on the dependence of droplet burning time on pressure are shown in figures 6 and 7 for two different initial hexadecane mass fractions. It is seen in these figures that droplets separated by eight times their initial diameter burn under microgravity conditions in air almost as if they were single isolated droplets. However, droplets separated by four times their initial diameter burn more slowly as a consequence of the droplet interactions. In addition, the magnitude of the effect of the interaction decreases with increasing pressure. For $Y_0 = 0.33$, at a pressure of 5.0 MPa there is almost no effect of interaction on the total burning time at spacings as close as four times the initial droplet diameter. Further work is needed to explain these observations properly. It may be noted, however, that if effects of interactions are assumed to become noticeable at spacings in fixed proportion to the flame diameter, then in theory at low pressures there is no pressure dependence, while for supercritical burning the spacing for a given magnitude of perturbation should vary inversely with pressure.

Future plans

About 30 successful drops were made in the first series of runs. The parameter space of the problem, however, is too large for significant conclusions to be drawn from so few tests. Two additional series of drops therefore are planned, with about 60 tests in each series. Since the apparatus is now working reliably in the tower, it is anticipated that practically all of these future drops will be successful. The principal parameters to be varied are the droplet spacing, the mass fraction of hexadecane in the fuel, and the pressure. Hexadecane mass fractions of 11% and 33% will be studied at smaller droplet spacings, and measurements will be made at higher hexadecane mass fractions. At pressures of 0.1 MPa, 1.0 MPa, 2.0 MPa, 3.0 MPa, 4.0 MPa and nearly 5.0 MPa, droplet spacings will be varied between about 1 mm and 8 mm. Conditions will be determined under which individual flames surround each droplet and under which one single flame surrounds both droplets, as a function of pressure. In addition, the influence of the droplet separation distance on the burning rate will be measured. Information relevant to testing predictions of cloud burning and of individual-droplet burning thereby will be obtained. Very little data of this type are available at pressures approaching supercriticality. The results should therefore help to improve understanding of spray combustion under conditions of practical interest in engines.

References

1. Mikami, M., Kono, M., Sato, J., Dietrich, D.L., and Williams, F.A., "Combustion of Miscible Binary-Fuel Droplets at High Pressure under Microgravity," Combustion Science and Technology, Vol. 90, pp. 111-123, 1993.

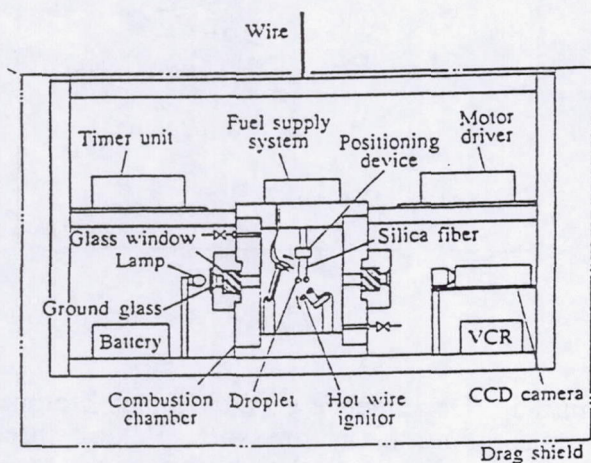


Figure 1 Schematic diagram of the experimental apparatus.

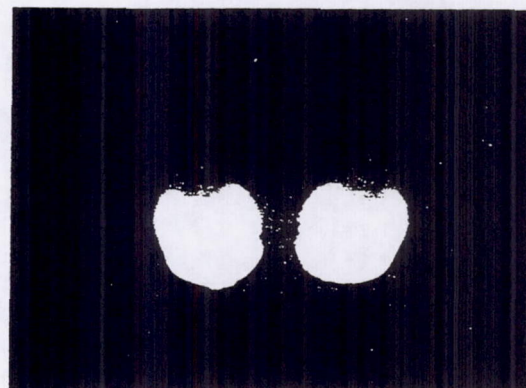


Figure 2 Photograph of a pair of burning droplets with an initial hexadecane mass fraction of 33%, initially 0.93 mm in diameter, separated by a distance of 0.8 mm, burning in air at 0.1 MPa.

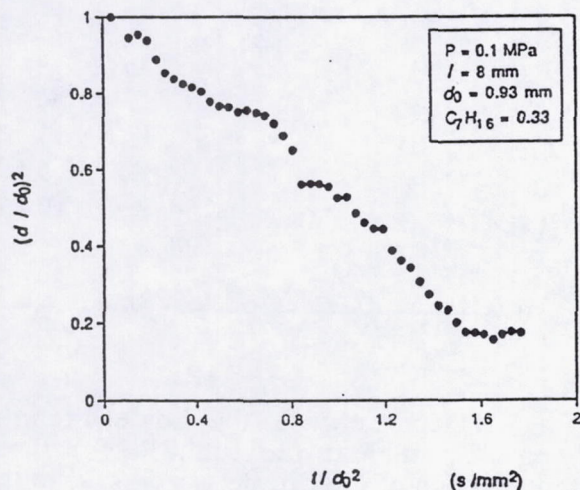


Figure 3 The square of the droplet diameter d as a function of time for the test shown in figure 2.

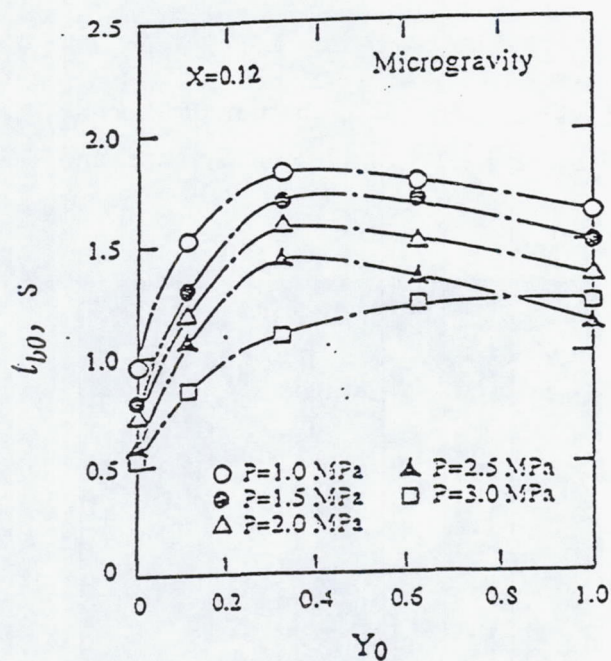


Figure 4 Dependence of the droplet lifetime, t_{b0} , at different ambient pressures on the initial hexadecane mass fraction, Y_0 .

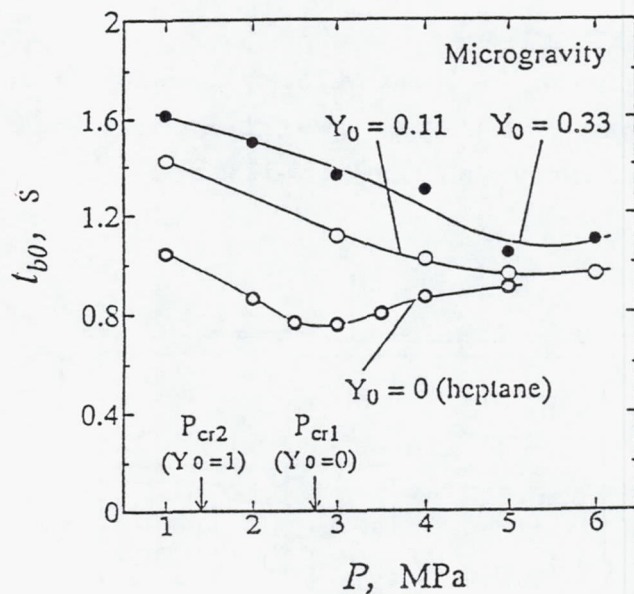


Figure 5 Dependence of the droplet lifetime, t_{b0} , on the ambient pressure, P , for three different values of the hexadecane mass fraction, Y_0 .

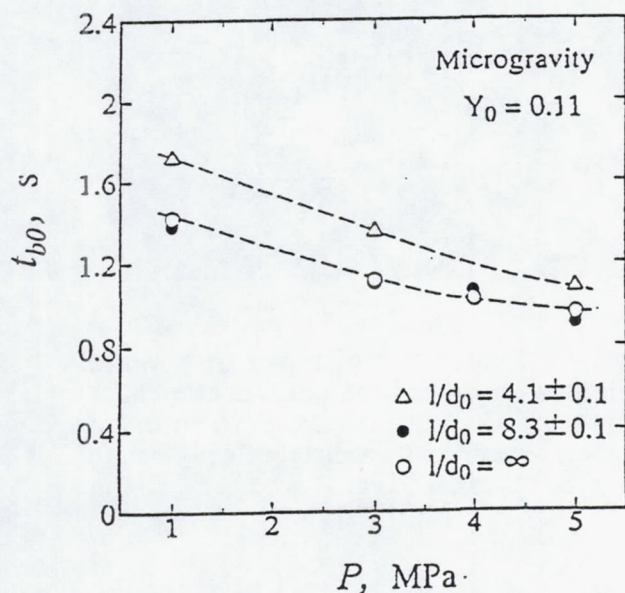


Figure 6 Dependence of the droplet lifetime, t_{b0} , on the ambient pressure, P , for three different ratios of the droplet spacing, l , to the initial droplet diameter, d_0 , for an initial hexadecane mass fraction of $Y_0 = 0.11$.

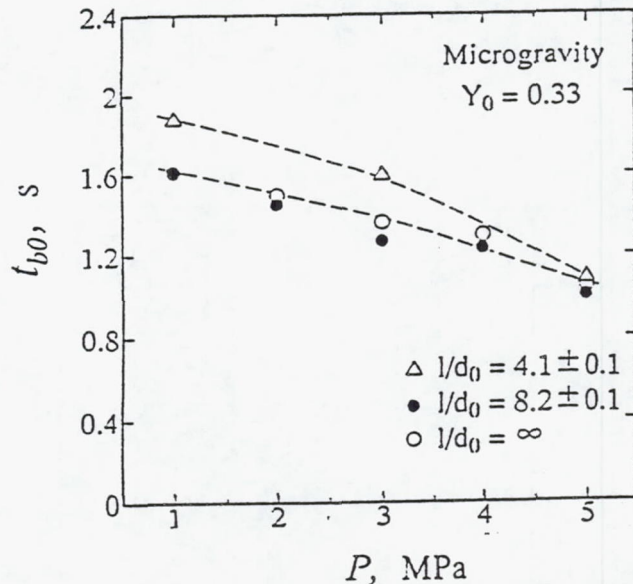


Figure 7 Dependence of the droplet lifetime, t_{b0} , on the ambient pressure, P , for three different ratios of the droplet spacing, l , to the initial droplet diameter, d_0 , for an initial hexadecane mass fraction of $Y_0 = 0.33$.

STUDIES OF DROPLET BURNING AND EXTINCTION

F.A. Williams

Center for Energy and Combustion Research

Department of Applied Mechanics and Engineering Sciences
University of California San Diego, La Jolla, California 92093

Introduction

A project on droplet combustion, pursued jointly with F.L. Dryer of Princeton University, has now been in progress for many years. The project involves experiments on the burning of single droplets in various atmospheres, mainly at normal atmospheric pressure and below, performed in drop towers (e.g., ref. 1) and designed to be performed aboard space-based platforms such as the Space Shuttle or the Space Station and currently manifest for Spacelab in the MSL-1 flight of the Space Shuttle in April of 1997. It also involves numerical computations on droplet burning, performed mainly at Princeton, and asymptotic analyses of droplet burning, performed mainly at UCSD. The focus of the studies rests primarily on time-dependent droplet-burning characteristics and on extinction phenomena.

The presentation to be given here concerns the recent research on application of asymptotic methods to investigation of the flame structure and extinction of alcohol droplets. These theoretical studies are relevant to the second of the proposed space-flight tests and are currently investigating the extent to which combustion of alcohols can be described by four-step reduced chemistry similar to that which has achieved a good degree of success for alkane flames. These studies have progressed to a point at which a number of definite conclusions can now be stated. These conclusions and the reasoning that led to them are outlined here.

Asymptotic Descriptions of Alcohol Diffusion Flames

A mixture fraction Z , defined to be zero in the oxidizer and unity in the fuel, serves as an attractive independent variable for analyses of diffusion-flame structures because its adoption enables the problem to be formulated in a universal manner that does not depend on the specific geometrical configuration. In the mixture-fraction formulation, the simplest asymptotic description is the Burke-Schumann reaction-sheet structure. This limit corresponds to an infinite Damköhler number for one-step, irreversible chemistry and provides the outer, transport-zone solutions to which the reaction-zone solutions are matched. In the reaction zone there is a one-parameter family of solutions, the parameter being χ_{st} , the value at the stoichiometric mixture fraction Z_{st} of the scalar dissipation rate

$$\chi = 2D|\nabla Z|^2, \quad (1)$$

where D is the diffusion coefficient of the outer solutions. As χ_{st} increases, the peak temperature decreases, and eventually an abrupt extinction is approached, at a critical value. For droplet burning, it is found that

$$\chi = \frac{8D}{d_l^2} \left(\frac{[\ln(1-Z)]^2(1-Z)}{\ln(1+B)} \right)^2, \quad (2)$$

where d_l is the droplet diameter, and B is the transfer number for the droplet combustion process, given in an approximation of constant specific heat c_p by

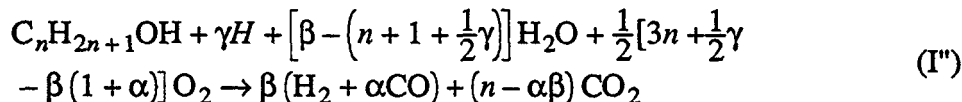
$$B = \{c_p(T_\infty - T_l) + 2QY_{O_{2\infty}} / (3nW_{O_2})\} / L, \quad (3)$$

where T , W , and Y denote temperature, molecular weight, and mass fraction, the subscript ∞ identifies the ambient atmosphere, L is the energy required to vaporize a unit mass of fuel, Q stands for the heat released per mole of gaseous fuel in combustion, and n represents the number of carbon atoms in the alcohol. By use of equation (2) at $Z = Z_{st}$, the droplet diameter at extinction d_{le} , can be obtained from χ_{ste} , the value of χ_{st} at extinction, which has been calculated without reference to the specific geometrical configuration. The calculation employs the reduced chemistry described below.

Reduced Chemistry for Methanol

The starting chemical-kinetic mechanism and the associated rate parameters for methanol are listed in Table 1. The elementary steps and rate parameters given here differ somewhat from those of other studies, since they are based on an evaluation of rate data performed specifically for the present program. In Table 1, CH_2OH stands for the Boltzmann-equilibrated isomers CH_3O and CH_2OH , and the last two sets of rate parameters refer to this mixture. The table represents a minimal set, in the sense that all of the elementary steps shown there are essential.

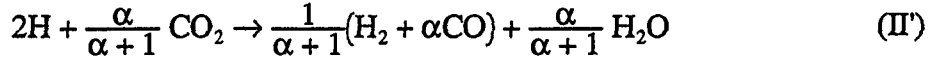
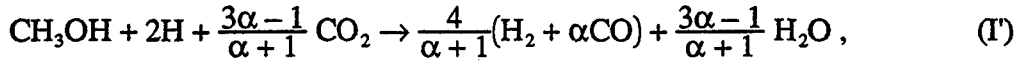
Introduction of steady-state approximations for all radicals except the important H atom results in a four-step reduced mechanism for the alcohols that can be written as



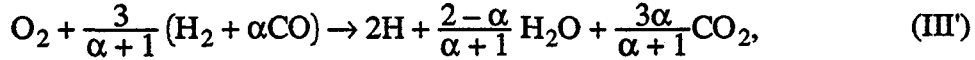
where α is the number of CO molecules produced per H_2 molecule produced, β is the number of H_2 molecules produced per fuel molecule consumed, and γ , a quantity of critical importance, is the number of radicals destroyed for each fuel molecule consumed. For methanol, this four-step description involves introducing steady-state approximations for CH_2OH , CH_2O , CHO , HO_2 , OH and O in Table 1 and results (ref. 2) in $\gamma = 2$, giving a reduced mechanism that can be written as $CH_3OH + 2H \rightarrow 3H_2 + CO$, $CO + H_2O \rightleftharpoons CO_2 + H_2$, $2H + M \rightarrow H_2 + M$ and $3H_2 + O_2 \rightleftharpoons 2H + 2H_2O$, with corresponding rates $k_{14}C_FC_H$, $(k_9/K_3)C_HC_{CO}C_{H_2O}/C_{H_2} - C_{CO_2}K_3/K_9$, $k_5C_MC_HCO_2$ and $k_{17}C_H[CO_2 - (C_H^2C_{H_2O}^2/C_{H_2}^3K_1K_2K_3^2)]$, respectively, where C_i denotes the concentration of species i , subscript F representing the fuel, CH_3OH , and the k 's and K 's are specific reaction-rate constants and equilibrium constants. Here approximations of partial equilibria have been introduced for steps 2 and 3, and the third-body concentration C_M is weighted with the efficiencies given in Table 1, assuming that only N_2 , CO_2 and H_2O are present in significant concentrations in the reaction zone.

Full numerical computations have shown that water-gas equilibrium is an excellent approximation in the reaction zones of these flames, much more accurate than for hydrocarbon

flames, for example. Therefore, the second of the four steps is put into equilibrium, giving $C_{CO} = \alpha C_{H_2}$, where $\alpha \equiv (C_{CO_2} K_3) / (C_{H_2O} K_9)$. There results a three-step mechanism, which can be written as

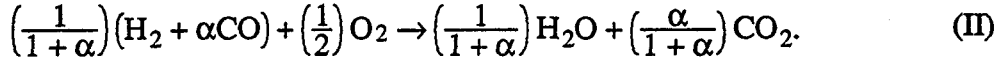
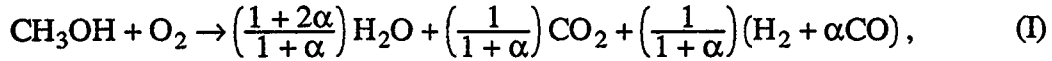


and



with rates $k_{14} C_F C_H$, $k_5 C_M C_H C_{O_2}$ and $k_{1f} C_H [C_{O_2} - C_H^2 C_{H_2O}^2 / (C_{H_2}^3 K_1 K_2 K_3^2)]$, respectively.

If, in addition, a steady-state approximation for H is introduced, then there results the two-step reduced mechanism



The steady-state approximation for H results in

$$C_H = (K_1 K_2)^{1/2} K_3 C_{O_2}^{1/2} (C_{H_2}^{3/2} / C_{H_2O}) [1 - (k_{14} C_F) / (k_{1f} C_{O_2})]^{1/2}, \quad (4)$$

where $k_5 C_M C_{O_2}$ has been neglected in comparison with $k_{14} C_F$ and $k_{1f} C_{O_2}$ because it is quite small in this expression at the pressures considered. The rates of steps I and II are found by reduction of the preceding rates to be

$$\omega_I = k_{14} C_F C_H, \quad \omega_{II} = 2k_5 C_M C_{O_2} C_H, \quad (5)$$

in which equation (4) can be used for C_H . This serves to relate the rates to the temperature and the concentrations of the species appearing in steps I and II, as needed in the analysis. In the three-step mechanism, equation (4) is discarded because C_H becomes an additional dependent variable described by an independent differential equation.

The Flame Structure

The flame structure is analyzed by rate-ratio asymptotics (RRA). In the RRA description, there is a thin fuel-consumption zone on the rich side of a broader but still thin layer of H_2 and CO oxidation. This structure is illustrated in figure 1, where δ and ε are small parameters that measure, in the mixture-fraction coordinate, the thicknesses of the fuel-consumption zone and of the oxidation layer, respectively. The fuel-consumption zone, having peak temperature T^0 , is located at $Z = Z_0$, a value displaced from Z_{st} by the small amount $\varepsilon \xi_0$, where ξ_0 is calculated in the analysis. This structure is quite similar to that previously determined in the present program for alkane flames, such as heptane; essentially the only difference is the chemistry that occurs in the fuel-consumption zone. The methanol flame is in fact simpler than the alkane flames in that water-gas equilibrium is a much better approximation, so that a three-step description suffices.

The RRA analysis yields the peak temperature as a function of χ_{st}^{-1} , as shown in figure 2. These results are essentially the same for both two-step and three-step descriptions. The minimum value of χ_{st}^{-1} identifies the extinction condition. From these minima, equation (2) can

be used to calculate extinction diameters as functions of the oxygen mole fraction in the atmosphere, as shown in figure 3 for three different values of the atmospheric pressure p . Figure 3 applies for pure methanol droplets that have not absorbed water during burning. In fact, water absorption is significant and modifies extinction conditions, as indicated below.

Effects of Water Dissolution

Water is produced in the flame and dissolves in the liquid fuel as it burns. We have completed an analysis of this effect, treating the gas phase as quasisteady. Two limiting cases were analyzed, namely time-dependent liquid-phase diffusion and perfect liquid-phase mixing. Figure 4 shows results of these analyses for the square of the droplet diameter as a function of time.

It is seen from figure 4 that with time-dependent liquid-phase diffusion the d^2 plots are nearly straight lines. This is because the low diffusion coefficient for water in methanol leads to a relatively small amount of water absorption; the water is contained only in a very thin boundary layer at the liquid surface. On the other hand, with perfect liquid-phase mixing, the d^2 plots are curved, illustrating the reduced vaporization rate as water builds up inside the liquid. These curved lines are seen to be in better agreement with experiment. It is therefore concluded that the experiments involved an appreciable amount of liquid-phase mixing. This same conclusion was reached independently by Dryer and co-workers, on the basis of numerical integrations. The agreement in the conclusion from the two different approaches is a strong indication that the conclusion is correct.

The water absorption also influences flame extinction, a further point of agreement with Dryer et al. In the present approach, since the gas phase is quasisteady, calculating extinction conditions entails calculating extinction diameters for droplets consisting of water-methanol mixtures with different percentages of water. For example, figure 5 shows predicted extinction diameters for droplets consisting of 50% water and 50% methanol on a mass basis. These diameters are seen to be appreciably larger than those in figure 3. Figure 6 illustrates how to determine extinction conditions with time-dependent water absorption. Basically, the droplet diameter and the extinction diameter are plotted as functions of time, and extinction occurs when these two diameters become equal. The resulting extinction predictions are in good agreement with experiment.

Future Plans

The research by asymptotics on methanol droplet combustion is essentially completed. It is intended to spend a little time looking at the kinetics of fuel consumption for higher alcohols, to determine the associated values of γ ; the kinetic information needed to do a reasonable job of this has just become available, and so it is a timely investigation. However, most of the future research will involve studying heptane droplet combustion in helium-oxygen atmospheres. This is the system that will be employed in the first flight, MSL-1, and data on this system already are available from preliminary drop-tower tests. Most of the future work, for the next year or two at least, will therefore concentrate on this system. Data on histories of droplet and flame diameters and on extinction conditions will be reduced and compared with our previous theoretical predictions. Data on intensity profiles of emissions in OH bands also will be addressed, to determine what information that data can provide on flame structure, to be compared with theory. The general intent will be to improve understanding of heptane droplet combustion.

References

1. Choi, M.Y., Dryer, F.L., Card, J.M., Williams, F.A., Haggard, J.B., Jr., and Brorowski, B.A., "Microgravity Combustion of Isolated n-Decane and n-Heptane Droplets," AIAA Paper No. 92-242, January 1992.
2. Zhang, B.L., Card, J.M., and Williams, F.A., "Application of Rate-Ratio Asymptotics to the Prediction of Extinction for Methanol Droplet Combustion," Combustion and Flame, to be submitted, 1995.

Table 1
The Starting Chemical-Kinetic Mechanism
and the Associated Rate Parameters
in the form $k = AT^n \exp(-E/R^0T)$

No. ^a	Reactions	A ^a	n ^a	E ^a
Hydrogen-Oxygen Chain				
1f	H + O ₂ → OH + O	3.52 × 10 ¹⁶	-0.7	17070
1b	OH + O → H + O ₂	1.15 × 10 ¹⁴	-0.324	-175
2f	H ₂ + O → OH + H	5.06 × 10 ⁴	2.67	6290
2b	OH + H → H ₂ + O	2.22 × 10 ⁴	2.67	4398
3f	H ₂ + OH → H ₂ O + H	1.17 × 10 ⁹	1.30	3626
3b	H ₂ O + H → H ₂ + OH	6.65 × 10 ⁹	1.30	4352
4f	OH + OH → H ₂ O + O	k = 5.46 × 10 ¹¹ exp (0.00149T)		
4b	H ₂ O + O → OH + OH	k = 4.19 × 10 ⁷ T ^{5.8} exp (0.003T)		
Hydroperoxyl Formation and Consumption				
5 ^b	H + O ₂ + M → HO ₂ + M	6.76 × 10 ¹⁹	-1.4	0
6	HO ₂ + H → OH + OH	1.70 × 10 ¹⁴	0.0	874
7	HO ₂ + H → H ₂ + O ₂	4.28 × 10 ¹³	0.0	1411
8	HO ₂ + OH → H ₂ O + O ₂	2.89 × 10 ¹³	0.0	-497
Water-Gas Shift				
9f	CO + OH → CO ₂ + H	4.40 × 10 ⁶	1.5	-741
9b	CO ₂ + H → CO + OH	4.97 × 10 ⁸	1.5	21446
Formyl Formation and Consumption				
10	CHO + H → CO + H ₂	1.00 × 10 ¹⁴	0.0	0
11 ^c	CHO + M → CO + H + M	2.85 × 10 ¹⁴	0.0	16795
12	CH ₂ O + H → CHO + H ₂	2.26 × 10 ¹⁰	1.05	3278
Fuel Consumption and Formaldehyde Formation				
13	CH ₂ OH + H → CH ₂ O + H ₂	3.00 × 10 ¹³	0.0	0
14	CH ₃ OH + H → CH ₂ OH + H ₂	4.00 × 10 ¹³	0.0	6092

^a Units: mol/lcm³, K, cal/mol.

^b Chaperon Efficiencies: N₂, O₂: 1.0, CO: 1.9, CO₂: 3.8, H₂: 2.5, H₂O: 12.0.

^c Chaperon Efficiencies: same as b except H₂O: 16.3

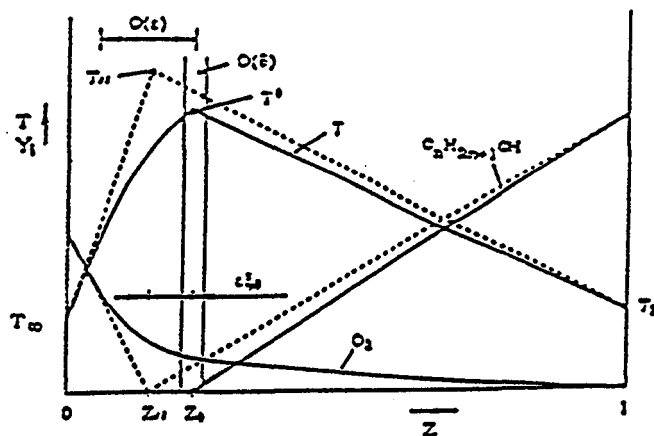


Figure 1 Schematic diagram of the diffusion-flame structure in the mixture-fraction coordinate; dashed lines give the Burke-Schumann structure and solid curves the structure in the two-step approximation.

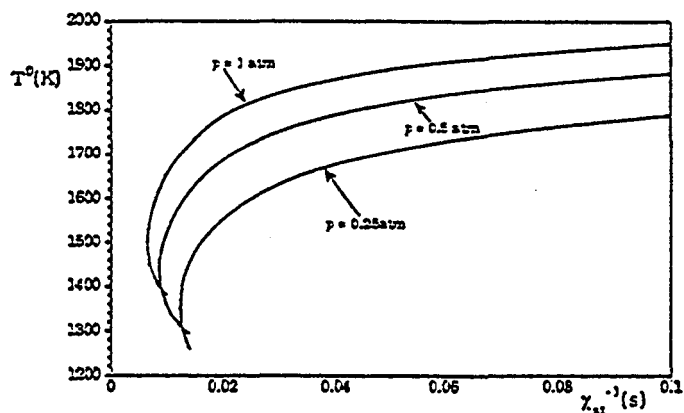


Figure 2 The predicted temperature at the fuel-consumption zone, as a function of the reciprocal of the rate of scalar dissipation at the stoichiometric mixture fraction, for pure methanol droplets burning in air at 300 K, for three different pressures.

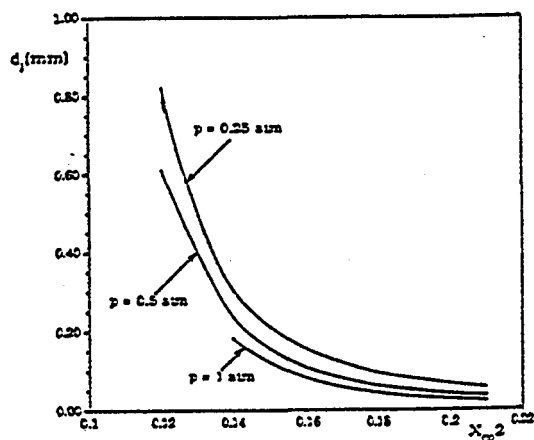


Figure 3 The predicted extinction diameters of pure methanol droplets, burning in oxygen-nitrogen mixtures at 300 K, as functions of the ambient oxygen mole fraction, for three different pressures.

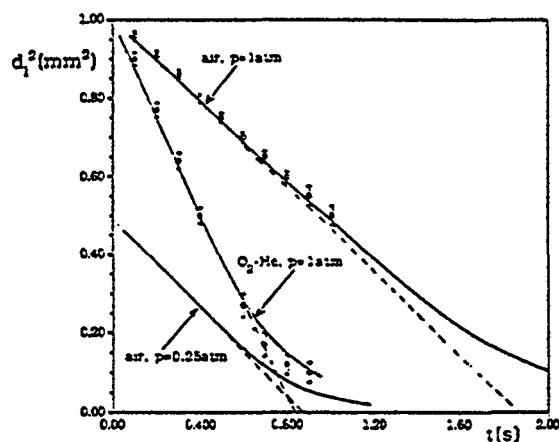


Figure 4 The square of the droplet diameter as a function of time for droplets initially 1 mm in diameter, burning in air at $p = 1$ atm in a helium-oxygen mixture with $X_{O_2} = 0.5$ at $p = 1$ atm, and for a droplet initially 0.7 mm in diameter, burning in air at $p = 0.25$ atm; solid lines are for perfect liquid-phase mixing with the present theory, dashed lines are for time-dependent liquid-phase diffusion with the present theory, and points are data from the literature.

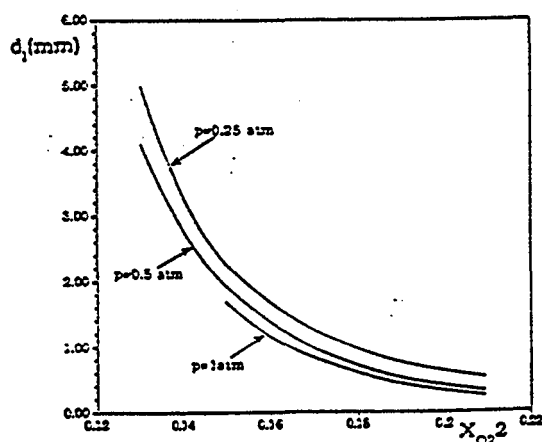


Figure 5 The predicted extinction diameters of droplets composed of 50% methanol and 50% water on a mass basis, burning in oxygen-nitrogen mixtures at 300 K, as functions of the ambient oxygen mole fraction, for three different pressures.

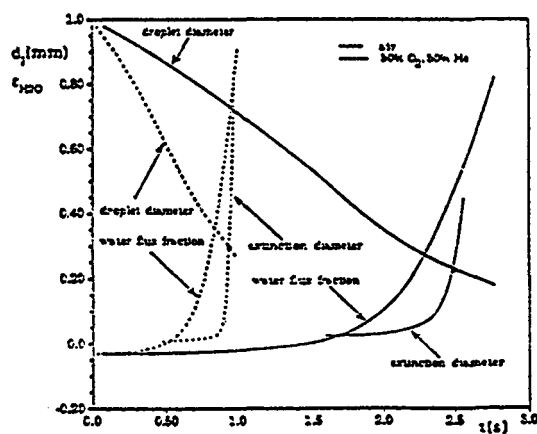


Figure 6 The droplet diameter, the extinction diameter, and the water flux fraction χ_{H_2O} as functions of time with time-dependent water absorption for perfect liquid-phase mixing illustrating how extinction conditions are determined.

COMBUSTION OF A POLYMER (PMMA) SPHERE IN MICROGRAVITY

Jiann C. Yang and Anthony Hamins
Building and Fire Research Laboratory
National Institute of Standards and Technology
Gaithersburg, Maryland 20899

Introduction and Objectives

Since the advent of the manned-space exploration era, fire safety aboard space vehicles including space capsules, the Space Shuttle, and future manned permanent space-stations has been an important and challenging issue. An ideal way to alleviate a portion of the fire hazard is to eliminate completely the use of flammable materials or to replace them with materials with very high fire retardation properties. However, such an approach is not practical or technically feasible at present or in the immediate future. Materials (e.g., paper and plastics) that are flammable under certain conditions will still be used, and they will continue to pose a potential threat to the safety of the crew and the spacecraft. Therefore, the understanding of the combustion characteristics of such materials (e.g., ignitibility, flame spread rates, and burning rates) under different ambient conditions and in a reduced gravity environment is needed.

Polymer combustion is a highly complicated process where chemical reactions may occur not only in the gas phase, but also in the condensed phase as well as at the solid-gas interphase. The chemistry depends strongly on the coupling between the condensed phase and gas phase phenomena. For some polymers, additional complications arise due to the formation of char layers. For others, the behavior of the condensed phase involves swelling, bubbling, melting, sputtering, and multi-stage combustion (refs. 1-3). Some of these features bear resemblance to the phenomena observed in coal particle combustion. In addition to its relevance to spacecraft fire safety, the combustion of polymeric materials is related to many applications including solid and hybrid rocket propulsion, and of recent interest, waste incineration (refs. 4-6).

The burning rate is one of the most important parameters used to characterize the combustion of polymers. It has been used to rank the polymer flammability under the same experimental conditions and to evaluate various modes of inhibiting polymer flammability. The main objective of this work is to measure the burning rates of a polymeric material in low gravity. Because of inherent logistical difficulties involved in microgravity experiments, it is impossible to examine a wide spectrum of polymeric materials. It is desirable to investigate a polymer whose combustion is less complicated, and yet will lead to a better understanding of the burning characteristics of other more complicated materials. Therefore, a typical non-charring polymer is selected for use in this experimental study. PMMA (polymethylmethacrylate) has been chosen because its thermo-physical properties are well characterized. Although the combustion of PMMA has been extensively studied in 1G experiments, only a limited amount of work has been conducted in low gravity (refs. 8-10).

A spherical sample geometry is chosen in this study because it is the simplest configuration in terms of the microgravity hardware design requirements. Furthermore, a burning PMMA sphere in microgravity

represents a one-dimensional flame with *overall* combustion characteristics expected to be analogous to the combustion of a liquid fuel droplet (refs. 1-3), a field with many well-developed theories and models (ref. 7). However, differences can also be expected such as the flame-front standoff ratios and the condensed phase processes occurring during combustion.

Research Approach

It is anticipated that the ignition delay time (on the order of few seconds) of a PMMA sphere will be much longer than that of a liquid fuel droplet. Using a 1G burning rate constant ($2.76 \text{ mm}^2/\text{s}$) from the literature (ref. 1) and assuming the " d^2 -law", the burning time of a PMMA sphere with a given initial diameter can be estimated. For a sphere with initial diameter of 1, 3, 5, and 7 mm, the calculated burning times are 0.36, 3.3, 9.1, and 18 s respectively. Since the burning rate constant is expected to be lower under microgravity conditions, the above calculated values can only be regarded as lower bound estimates on the burning times in microgravity. Thus, the time available to carry out the experiments in both the 2.2 and 5.18 s NASA drop towers may not be adequate for the observation of complete burning histories (from ignition to burnout or extinction, if it occurs), even for a sphere with an initial diameter of 1 mm. Therefore, the experiments will be conducted aboard a NASA DC-9 jet flying a parabolic trajectory in order to achieve longer durations (at least 20 s) of a low gravity environment.

The intent of this work is to use a PMMA sphere which is large enough to allow good photographic resolution for observing the internal behavior of the condensed phase during combustion and at the same time to facilitate deployment of the sphere for the experiments. Two experimental approaches will be used in this study. The first involves the use of a suspended PMMA sphere and the second utilizes an unsupported PMMA sphere. These two techniques and the experimental procedure are discussed below.

A suspended sphere is obtained by using the set-up shown in Figure 1. A thermocouple (Pt/Pt-Rh) is stretched horizontally and heated locally near the thermocouple junction by resistive heating using two fine needles which are connected to four AA batteries and a potentiometer to regulate the current through the thermocouple wire. The sphere which is placed on a three-dimensional translation stage is then slowly positioned toward the heated wire. As the sphere approaches the heated portion of the thermocouple, part of it will become slightly soft so that the thermocouple junction is then easily inserted into the sphere. In this way, the thermocouple junction can be positioned at any location inside the sphere. The thermocouple has two functions; it is used to measure the temperature at one location inside the sphere and to suspend the sphere. Although local heating of the sphere during the embedding of the thermocouple may alter the properties of the sphere slightly, it is believed that the changes will be insignificant if the current through the thermocouple can be controlled in such a way that the temperature of the wire is barely sufficient to locally heat the sphere and if the heated area is very small, which can be achieved by using a fine thermocouple. We have successfully embedded 25, 50, and 75 μm thermocouples. Although working with a 12.5 μm thermocouple is possible, it has not been fruitful because of difficulties associated with the fragility of the wire. The aforementioned technique can also be extended to the suspension of two or more spheres (for studying the interaction between two burning spheres) provided that the wire is strong enough to support the weight of the spheres. Figures 2 and 3 show photographs of a nonburning suspended and two nonburning suspended spheres respectively. In the case of two or more spheres, only one sphere will have the thermocouple junction embedded in it.

Another technique for embedding a thermocouple has been tried but found to be unreliable. This method involved the dissolution of PMMA powder in toluene (a solvent). An initiator (benzoyl peroxide) was then added to the solution which was then cured in an oven until it became highly viscous. While the solution cured, a thermocouple junction was dipped in and out of the solution periodically and rotated slowly to form a nearly spherical bead. There were still many unresolved technical difficulties. Firstly,

the positioning of the junction in the sphere was not possible. Secondly, the shape of the PMMA bead was not completely spherical. Lastly, bubbles were trapped or formed in the PMMA sphere during the fabrication process. Although two other techniques, injection molding and gluing of a sphere onto a quartz fiber, have been used in previous work, they have not been considered in this study based on the following two reasons. Use of injection molding is not practical because it is still very difficult to place a thermocouple junction at the desired location inside the sphere. Attaching a sphere onto a fiber precludes measurement of the temperature inside the sphere, although the technique is the simplest. Having compared the advantages and disadvantages among the four techniques, it is believed that for this study the embedding of a locally heated thermocouple junction in a PMMA sphere offers the best approach to form a suspended sphere. However, the present technique will not work on a thermosetting polymer.

The second experimental configuration that will be used in this work is an unsupported PMMA sphere. Figure 4 shows a (top view) schematic of the set-up which is currently under construction. The design is conceptually similar to the unsupported liquid droplet deployment system currently used in NASA drop tower experiments. Two opposing rods are used to support the sphere initially, and two ignition systems are used subsequently to ignite the sphere in a symmetrical manner. The supporting rods and ignition systems are mounted on four retracting mechanisms (also shown in Figure 4), which consist of springs, sliding blocks, and solenoids. Initially, the spring attached to the sliding block is stretched, the block is held in place by the solenoid plunger. The retracting action occurs when the solenoid is activated and its plunger retracts, and the spring pulls the sliding block away from its original position.

The current ignition method is adopted after other ignition techniques have been tried and found unsuccessful. One technique simply used a spark with very long discharge duration (more than 5 s) to ignite the sphere. Ignition could not be achieved even when the sphere was preheated to a point just before melting of the sphere occurred. The second ignition method was to coat the sphere with a layer of ethanol, followed by spark ignition. This also proved to be unsuccessful because the spark simply ignited the liquid layer and burnt off the liquid fuel without ever igniting the polymer sphere. Ignition, itself, was always successful, using either a match or a small torch. The present ignition system is a modified version of a micro-torch that is evolved from the design of a cigarette lighter and a push-button igniter used on many gas BBQ grills. Figure 5 is a detailed drawing of the present ignition system. It consists of a small stainless steel fuel (liquid butane) reservoir, a needle valve to control the fuel flow, a miniature solenoid valve, a small jet nozzle, and a piezoceramic igniter element to generate a spark for igniting the fuel jet.

PMMA spheres with initial diameters of 3, 5, and 7 mm will be studied. The suspended sphere or the unsupported sphere deployment system together with the ignition system will be housed inside a combustion chamber in which the ambient oxygen concentration can be varied in order to study the effect of oxygen concentration on the burning rate. The ambient oxygen concentration will be varied from 21% (by mole) in nitrogen (simulated air), to 45% and 70%. A vitiated environment (19% oxygen concentration) will also be tested. All the experiments will be conducted at room temperature and 0.101 MPa.

The experimental procedure will involve the following steps. During normal flight paths, a suspended sphere, which is fabricated before flight, is placed in the combustion chamber. In the case of an unsupported sphere, the sphere is manually placed in the deployment mechanism. The ambient conditions in the combustion chamber are then set to the desired oxygen concentration. As soon as the change of G-level occurs, the sphere will be deployed (only for unsupported sphere experiments) and ignited. A high-speed movie camera (Locam) and a CCD camera will be used to record the evolution of the polymer sphere and flame diameter during combustion. The films will be analyzed frame-by-frame using an image

analysis system. Temporal variation of temperatures inside the burning suspended sphere will also be recorded from the thermocouple using a data logger.

The experimental burning rate results will be compared to the predictions from existing liquid droplet combustion theories and polymer sphere burning models (refs. 1-3, 6).

Results to date

This work was started in August, 1994 although the funding was made available in mid June, 1994. The past six months were devoted solely to experimental hardware development. Several techniques for fabricating the thermocouple suspended sphere and for igniting a sphere have been attempted, and the most feasible ones have been identified. A set-up for suspending a PMMA sphere on a thermocouple has been constructed and is operational. The unsupported sphere deployment system is currently under construction, and the ignition system is currently being tested using suspended spheres in 1G conditions.

Some 1G suspended sphere experiments have been performed using commercial grade PMMA spheres with an initial diameter of 4.8 mm. Preliminary observations can be summarized qualitatively as follows. There was an ignition delay of less than 5 s when a single ignition system was used. Upon ignition, the sphere softened, and internal bubbling occurred. The shape of the sphere started to deform, followed by dripping of the molten PMMA. Finally, the deformed, burning sphere fell off the suspended thermocouple wire in less than 10 s after ignition. Thermocouple measurements have not yet been made.

Research Plans

The research plans for the rest of this FY and the next FY will be to finish the construction of the unsupported sphere deployment system, to fabricate the combustion chamber, to assemble the experimental package (rig), and to perform suspended sphere experiments using 3, 5, and 7 mm spheres and four ambient oxygen concentrations (19%, 21%, 45%, and 70%). It is anticipated that the unsupported sphere experiments will require a lot of fine tuning (e.g., coordination of timing of sphere deployment and ignition). Therefore, it is unlikely that a series of unsupported sphere experiments will be performed systematically although some tests are possible.

A flight proposal for using the Space Shuttle Middeck Glovebox (MGBX) Facility to perform a series of supported sphere experiments was submitted to NASA in February, 1995.

References

1. Essenhigh, R.H. and Dreier, W.L., "Combustion Behavior of Thermoplastic Polymer Spheres Burning in Quiescent Atmosphere of Air," *Fuel*, **48** (1969), pp. 330-342.
2. Raghunandan, B.N. and Mukunda, H.S., "Combustion of Polystyrene Spheres in Air," *Fuel*, **56** (1977), pp. 271-276.
3. Waibel, R.T. and Essenhigh, R.H., "Combustion of Thermoplastic Polymer Particles in Various Oxygen Atmospheres: Comparison of Theory and Experiment," *Fourteenth Symposium (International) on Combustion*, The Combustion Institute, Pittsburgh, 1973, pp. 1413-1420.
4. Chung, S.L. and Tsang, S.M., "Soot Control During the Combustion of Polystyrene," *J. Air Waste Manage. Assoc.*, **41** (1991), pp. 821-826.
5. Chung, S.L. and Lai, N.L., "Suppression of Soot by Metal Additives During the Combustion of Polystyrene," *J. Air Waste Manage. Assoc.*, **42** (1992), pp. 1082-1088.
6. Panagiotou, T. and Levendis, Y., "A Study of Combustion Characteristics of PVC, Poly(styrene), Poly(ethylene), and Poly(propylene) Particles under High Heating Rates," *Comb. & Flame*, **99** (1994), pp. 53-74.
7. Williams, F.A., "Combustion Theory," Benjamin-Cummings, Menlo Park, CA, 1985.
8. Melikhov, A.S., Potyakin, V.I., Ryzhov, A.M., and Ivanov, B.A., "Limiting Polymer Combustion Regimes

- in the Absence of Free Convection," *Comb. Expl. & Shock Waves*, 19 (1983), pp. 393-395.
9. Goldmeer, J.S., Urban, D.L., and T'ien, J.S., "An Experimental Study of Solid Diffusion Flame Extinction and Transition to Microgravity," *Eastern States Section of the Combustion Institute, Fall Technical Meeting*, Princeton University, Princeton, NJ, October 25-27, 1993, pp. 441-444.
10. Olson, S.L. and Hegde, U., "Imposed Radiation Effects on Flame Spread over Black PMMA in Low Gravity," *Eastern States Section of the Combustion Institute, Fall Technical Meeting*, Clearwater Beach, FL, December 5-7, 1994, pp.348-351.

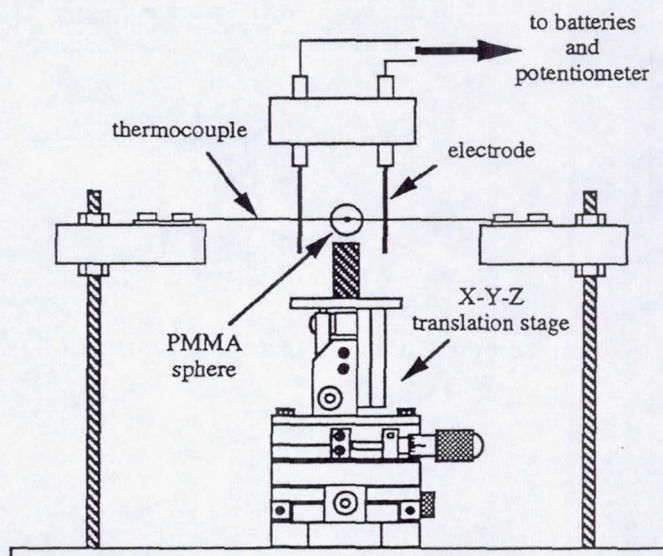


Figure 1.— Schematic of the suspended polymer sphere fabrication set-up.

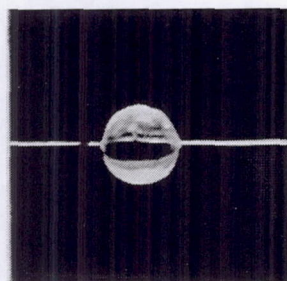


Figure 2.— Photograph of a suspended 4.8 mm PMMA sphere on a 75 μ m thermocouple.

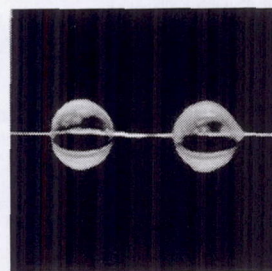


Figure 3.— Photograph of two suspended 4.8 mm PMMA spheres on a 75 μ m thermocouple.

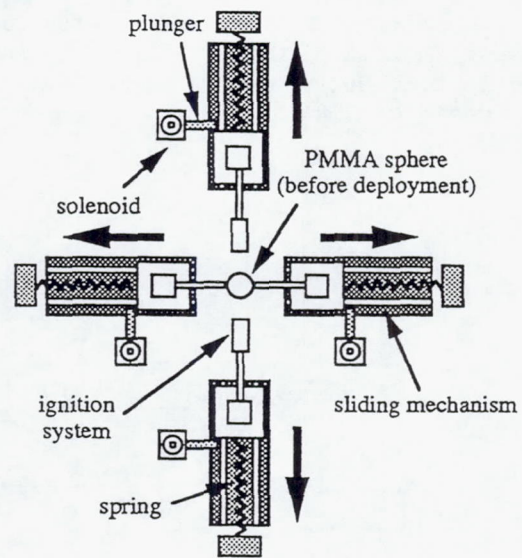


Figure 4.— Schematic of the unsupported sphere experimental set-up.

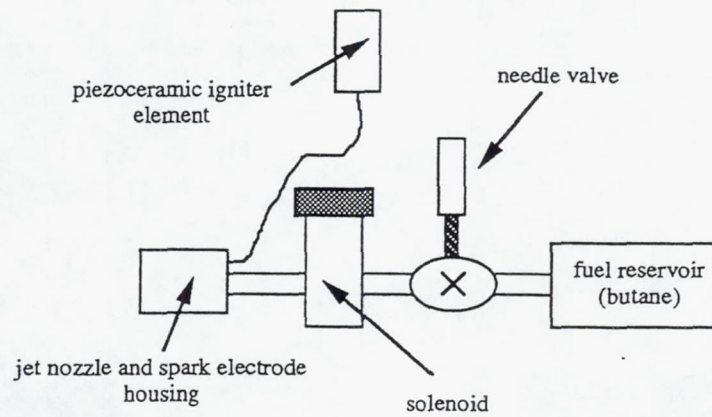


Figure 5.— Schematic of the ignition system.

Metals, Combustion, Synthesis, and Fire Safety

IGNITION AND COMBUSTION OF BULK METALS UNDER ELEVATED, NORMAL AND REDUCED GRAVITY CONDITIONS*

Angel Abbud-Madrid, Melvyn C. Branch, and John W. Daily
Center for Combustion Research
Mechanical Engineering Department
University of Colorado
Boulder, Colorado 80309-0427

Introduction

Although experiments on combustion of metals can be traced back as early as 1782, it was not until violent reactions were observed between titanium (Ti) and oxygen (O₂) in the 1950's that a significant number of studies focused on the compatibility of metals with oxygen (ref. 1). Later, studies focused primarily on metal powders due in part for the use of metal additives in solid rocket propellants. More recently, attention has been given to the flammability properties of bulk, structural metals, due to the large number of accidents involving burning metal components in oxygen systems. In spite of all the investigations conducted on this field to date, there is still a lack of basic understanding of the processes controlling ignition and burning of bulk metals compared to the literature available for gaseous reactions. The difficulty of providing accurate models stems from the variety of complex variables affecting metal-oxygen reactions such as: metal type, phase changes, oxygen pressure and solubility in metals, mechanical and thermal properties of oxide layers, gravitational force, experimental apparatus and configuration, surface tension effects, and sample size to name a few.

This research effort is aimed at providing further insight into this multi-variable dependent phenomena by looking at the effects of gravity on the ignition and combustion behavior of metals. Since spacecraft are subjected to higher-than-1g gravity loads during launch and reentry and to zero-gravity environments while in orbit, the study of ignition and combustion of bulk metals at different gravitational potentials is of great practical concern. From the scientific standpoint, studies conducted under microgravity conditions provide simplified boundary conditions since buoyancy is removed, and make possible the identification of fundamental ignition mechanisms. The effect of microgravity on the combustion of bulk metals has been investigated by Steinberg, et al. (ref. 2) on a drop tower simulator. However, no detailed quantitative work has been done on ignition phenomena of bulk metals at lower or higher-than-normal gravitational fields or on the combustion characteristics of metals at elevated gravity. The primary objective of this investigation is the development of an experimental system capable of providing fundamental physical and chemical information on the ignition of bulk metals under different gravity levels. The metals used in the study, iron (Fe), titanium (Ti), zirconium (Zr), magnesium (Mg), zinc (Zn), and copper (Cu) were selected because of their importance as elements of structural metals and their simple chemical composition (pure metals instead of multi-component alloys to avoid complication in morphology and spectroscopic studies). These samples were also chosen to study the two different combustion modes experienced by metals: heterogeneous or surface oxidation, and homogeneous or gas-phase reaction. The experimental approach provides surface temperature profiles, spectroscopic measurements, surface morphology, x-ray spectrometry of metals specimens and their combustion products, and high-speed cinematography of the heating, ignition and combustion stages of the metal specimen. This paper summarizes the results obtained to date from experiments conducted under normal and high-gravity conditions.

* This work is supported by the National Aeronautics and Space Administration, Lewis Research Center under Grants NAG3-1257 (May 1991 - November 1994) and NAG3-1685 (December 1994 - December 1997).

Experimental Apparatus

The experimental system is shown in Fig. 1. The radiation source consisted of a 1000 W xenon short-arc lamp with 250 W of effective broadband output radiation power. A feasibility study on the use of a continuous radiation short-arc lamp as an ignition source is presented in ref. 3. The light beam from the lamp is focused down by an aspheric lens to a 4 mm spot on the top surface of a metal sample providing a 1.75 MW/m^2 power density. The cylindrical metal specimen is 4 mm in diameter and 4 mm high and it is held in place by an alumina-silica holder. The 4.5 L stainless steel cylindrical chamber permits input radiation through the top quartz window. Optical access for the camera and spectrograph is provided through three fused-silica side windows. An oxygen environment (99.5% min. O_2) is used in all tests at an absolute pressure of 1 atm. The specimen surface temperature is measured with a Type B thermocouple located in the center of the sample at approximately 0.5 mm below the top surface. A 16-mm, high-speed motion picture camera provides a qualitative visual record of the combustion event and an estimate of flame propagation rates. Time-resolved spectral information on reacting species and products of combustion is obtained with a spectrograph/diode-array system. Surface morphology analysis is obtained with a Scanning Electron Microscope (SEM). Quantitative analysis of the chemical composition of quenched samples and combustion products is performed with an Electron Microprobe Analyzer (EMPA). The high-gravity experiments are conducted on a geotechnical centrifuge that is equipped with an onboard computer and signal conditioning system for remote operation. Further details of the various components of the apparatus and the experimental procedures are given in ref. 4.

Normal-Gravity Results

a) Qualitative Observations

High-speed movies of experiments conducted in normal gravity reveal the existence of three important and distinct phases:

i) The heating period, starting when the lamp radiation is applied until metal ignition, exposes the complexity of low-temperature oxidation mechanisms. The fast heating rate applied, 50-150 K/s, encourages metal expansion and rapid oxidation as evidenced by the appearance of spots, blisters, pores or cracks on the surface. Distinct types of oxidation are observed depending on the Pilling and Bedworth ratio of the metal, i.e., the volume of oxide formed/volume of base metal (ref. 5).

ii) The ignition phase is characterized by faster oxidation and a noticeable increase in energy release evidenced by the intense radiation emitted from the reaction zone.

iii) The combustion event varies in nature, speed and strength among the different metals tested. In the case of Fe, Ti, and Zr, a well-defined, self-sustained downward propagation (at 8, 30 and 25 mm/sec, respectively) is followed by a violent exothermic reaction including random outward expelling of small particles. For Mg and Zn the combustion phase evolved much faster with the generation of a fine oxide powder that formed a dust cloud which deposited uniformly on the walls and windows of the combustion chamber. Cu exhibited a smooth combustion phase characterized by a slow regression rate with a low-luminosity reaction zone (ref. 6).

b) Temperature Profiles

Temperature records also reveal uniquely the existence of the heating, ignition and combustion stages. Fig. 2 shows the temperature history of a typical Ti sample being heated at 1 atm under normal gravity. The figure also indicates the most relevant temperatures during the heating and ignition phases, as defined by Glassman, et al. (ref. 7). At the start of the heating period, there is a steep rise in surface temperature in the first second of heating caused by the sudden flux of radiant energy from the light source. After this initial jump, the temperature rise continues monotonically until a change in the slope around 1100 K. This change is caused by the latent heat associated with a crystal structure transformation from an hexagonal to a cubic lattice. A significant increase in the temperature rise follows this phase

transition due to the change in the oxidation mechanism from parabolic to linear. This point corresponds to the transition temperature, T_{trans} , or temperature where the oxide layer becomes a non-protective film and the oxidation rate becomes independent of time. After this point, the temperature continues to increase until a point of inflection is reached in the curve after which the temperature vs. time slope rapidly increases again. This point is identified as the critical temperature, T_{crit} , at which the heat generated by the metal oxidation first exceeds the heat lost through conduction, convection and radiation. Beyond the critical temperature, the metal specimen is driven into a thermal runaway region as a consequence of the exponential dependence of the reaction rate on temperature. After a time delay, the ignition temperature, T_{ign} , is reached. This corresponds to the appearance of a bright, luminous reaction zone. The acceleration of the reaction rate ultimately leads to the exothermic, self-sustained combustion event. At this stage, the temperature drastically increases to values in the range of 3500-4000 K. Similar behavior is observed for Zr and Fe. Temperature profiles for Mg, Zn and Cu vary significantly due to the existence of an intermediate plateau caused by the melting of the metal (ref. 4). Table 1 shows the transition, critical, ignition, and adiabatic flame temperatures at 1 atm of the different metals. All metals appear to be critical-temperature controlled with the exception of Zn, where a critical temperature is not observed. This behavior is typical of transition temperature controlled metals ($T_{\text{trans}} > T_{\text{crit}}$).

c) Spectroscopic measurements

Time-resolved measurements of gas-phase emission spectra have provided a clear, non-intrusive picture of the rapid evolution of reacting species and the formation of oxide products during the ignition and combustion phases of metals burning in a homogeneous flame front. In our experimental set-up the volume immediately above the top surface of the metal sample was focused by two condensing lenses onto a 25-micron wide aperture slit at the entrance of the spectrograph. Different gratings are used to capture broad and narrow spectral regions. Fig. 3 shows the emission spectra from the Mg-O₂ reaction at 1 atm under normal gravity conditions using a 2400 groove/mm grating to highlight the vibrational features of the green B-X system of MgO. The figure shows the time evolution of the gas-phase reaction in 33-ms intervals. The information provided by this figure becomes very important in order to estimate the location and relative abundance of the different species involved as well as the electronic and vibrational temperatures given by the intensity ratios of individual lines or bands. Comparison of time and space resolved spectra will be very useful on determining the effect of gravity-induced convection on the nature and character of ignition phenomena of bulk metals exhibiting gas-phase reactions.

d) Surface Morphology and Chemical Analysis

As illustrated by qualitative observations and by the temperature records, the character of the surface has a major effect on the ignition of metals. A more complete understanding of the ignition mechanism of metals requires monitoring the formation of the various oxide layers and their subsequent physical and chemical transformations. Fig. 4 is an example of the valuable information obtained from metallographic photographs to determine the nature and effect of oxidation processes on bulk titanium ignition. This figure is a SEM photograph showing a 390X magnification of the outer rim of the top surface of a titanium specimen quenched during the heating phase; the lamp was turned off when the specimen reached a temperature of 1550 K. The picture clearly shows the sequence of progressively higher oxides formed. The chemical composition of the main body (shown in the middle of the picture) is Ti+O, i.e. titanium metal with a 25% of oxygen in solution. This indicates that the metal nearly reached the limit of oxygen solubility before the quenching event. The thin (5 μm), intermediate layer has been identified as Ti₂O₃, a white oxide whose porosity and fragility is responsible for the parabolic-to-linear oxidation transition around 1230 K. After the onset of the time independent, linear oxidation process, a yellow-brown oxide layer rapidly starts covering the specimen. This thicker outer oxide coating (60 μm), rutile TiO₂, effectively protects the base metal from direct contact with the oxidizing medium, preventing an explosive reaction. It is this last layer that, after experiencing extreme mechanical stressing on the edges of the upper surface, suddenly breaks up exposing the base metal to the surrounding pure-oxygen

environment, leading finally to self-heating and ignition of the titanium specimen. Since buoyancy-induced free convection alters the advective transport of oxygen towards the metal surface, one can anticipate that the formation and influence of the various oxide layers might be different in other gravity environments.

Elevated-Gravity Results

High gravity experiments were conducted on the University of Colorado Geotechnical Centrifuge Facility. The experiment is subjected up to 130 rpm, an angular speed equivalent to an effective 20 g's acceleration. Fig. 5 shows the temperature histories of Ti samples subjected to different gravity levels.

A computational model of the experiment was developed to explore the effects of gravity and pressure on the heating phase of the metal sample under non-oxidizing conditions (ref. 8). The model includes the effects of conduction, convection and radiation heat transfer in the solid specimen and the surrounding gas. As predicted by this model, based exclusively on heat transfer mechanisms, the 3g's and 5g's temperature curves show a slower heating rate and a progressively longer delay for the ignition time. A higher buoyancy-induced convective flow increases the heat loss from the metal sample keeping the temperature lower than in the normal gravity case. However, this trend seems to reverse after the 5g's temperature curve, leading to faster ignition times for metal specimens subjected to higher gravity loads. This behavior may be explained by the existence of a competing effect between the convective heat loss and heat generation (by oxidation) mechanisms. At high gravity levels increased convection leads to an increase of oxygen transport to the metal surface resulting in higher oxidation rates. Higher heat generation may overcome the heat lost by convection promoting a faster temperature rise. This is specially true at temperatures above the transition temperature where the rate of oxidation of titanium changes from parabolic to linear. Moreover, after 5 g's the convective heat loss term increases only at a very slow rate, due to its $g^{1/4}$ dependence on gravity inside the Grashof number (Gr). With increased oxygen transport and a time-independent linear oxidation, the temperature rises at a faster rate. With an exponential dependence on temperature, the reaction soon becomes self-accelerating and ignition is reached. Fig. 5 clearly illustrates this effect on the 20 g's vs. the 1 g case, where the temperature curves quickly diverge after reaching the transition temperature. After ignition, the burning rates are significantly increased not only by the higher oxygen transport rates, but because the increased gravitational pull on the molten products as well. In the 20 g's case, the gravitational force is increased by twenty times, while the surface tension force exerted on the hot liquid products remains practically unchanged. The significantly larger Bond (Bo) number, i.e., gravitational force/surface tension force, generates massive dripping of molten products that ignite fresh metal ahead of the original reaction front.

Conclusions

An experimental system to study the ignition characteristics of bulk metals has been designed and tested under normal and high gravity conditions. Ignition and combustion tests were performed on Fe, Ti, Zr, Mg, Zn, and Cu specimens. Qualitative observations and temperature profiles have revealed the existence of the heating, ignition and combustion stages. These zones are characterized by well-defined surface structure changes, surface temperature behavior, luminosity and chemical activity. Time-resolved spectroscopic measurements reveal the dynamic evolution of the ignition event. Scanning electron microscope studies and x-ray spectroscopic analysis have given information on the oxide formation process. Preliminary results on the effect of higher-than-normal gravity levels on the ignition of Ti specimens have been obtained. The observed differences between the 1g and the high-g cases may be due to the existence of competing effects between heat transfer and oxidation mechanisms affected by buoyancy-induced free convection. Future work will focus on completing the elevated gravity tests and performing the microgravity experiments onboard the NASA-Lewis DC-9 Aircraft.

References

1. Clark, A. F. and Hust, J. G., "A Review of the Compatibility of Structural Materials with Oxygen," *AIAA Journal*, Vol. 12, No. 4, 1974, pp. 441-454.
2. Steinberg, T. A., Wilson D. B., and Benz, F. J., "Metals Combustion in Normal Gravity and Microgravity," *Proceedings of the Second International Microgravity Combustion Workshop*, NASA Conference Publication 10113, 1993, pp. 273-279.
3. Abbud-Madrid, A., Branch, M. C., Feiereisen, T. J., and Daily, J. W., "Ignition of Bulk Metals by a Continuous Radiation Source in a Pure Oxygen Atmosphere," *Flammability and Sensitivity of Materials in Oxygen-Enriched Atmospheres*, Vol. 6, ASTM STP 1197, 1993, pp. 211-222.
4. Abbud-Madrid, A., Fiechtner, G. J., Branch, M. C., and Daily, J. W., "Ignition and Combustion Characteristics of Pure Bulk Metals: Normal-Gravity Test Results," *32nd Aerospace Sciences Meeting and Exhibit*, Paper AIAA 94-0574, 1994.
5. Kubaschewski, O. and Hopkins, B. E., *Oxidation of Metals and Alloys*, 2nd ed., Academic Press, New York, 1962, pp. 4-12.
6. Branch, M. C., Abbud-Madrid, A., Feiereisen, T. J., and Daily, J. W., "A Study of Ignition Phenomena of Bulk Metals by Radiant Heating," *Proceedings of the Second International Microgravity Combustion Workshop*, NASA Conference Publication 10113, 1993, pp. 265-271.
7. Glassman, I., Mellor, A. M., Sullivan, H. F., and Laurendeau, N. M., "A Review of Metal Ignition and Flame Models," *AGARD Conference Proceedings*, No. 52, 1970, pp. 19-41.
8. Feiereisen, T. J., Abbud-Madrid, A., Branch, M. C., and Daily, J. W., "Gravity and Pressure Effects on the Steady-State Temperature of Heated Metal Specimens in a Pure Oxygen Atmosphere," *Flammability and Sensitivity of Materials in Oxygen-Enriched Atmospheres*, Vol. 6, ASTM STP 1197, 1993, pp. 196-210.
9. Steinberg, T. A., and Wilson D. B., "The Combustion Phase of Burning Metals," *Combustion and Flame*, Vol. 91, 1992, pp. 200-208.

Table 1. Important temperature values of all metals studied at 1 atm, normal gravity.

Metal	Transition Temp. (K) ^a	Critical Temp. (K) ^a	Ignition Temp. (K) ^a	Adiabatic Flame Temp. (K) ^b
Ti	1230	1620	1725	3993
Zr	1225	1555	1690	4278
Fe	1460	1475	1565	3400
Cu	1270	1355	1370	1400
Mg	720	950	975	3432
Zn	970	not observed	1170	2200

^a From this investigation.

^b From Steinberg, et al. (ref. 9), except for the estimated values of Cu and Zn.

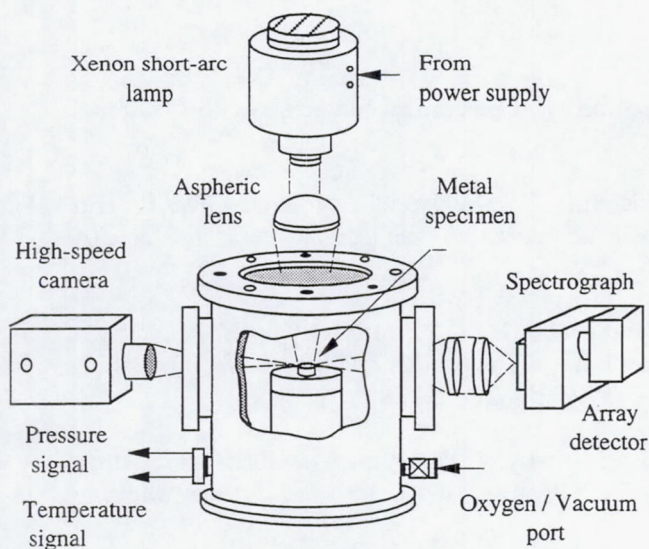


Figure 1. Experimental apparatus

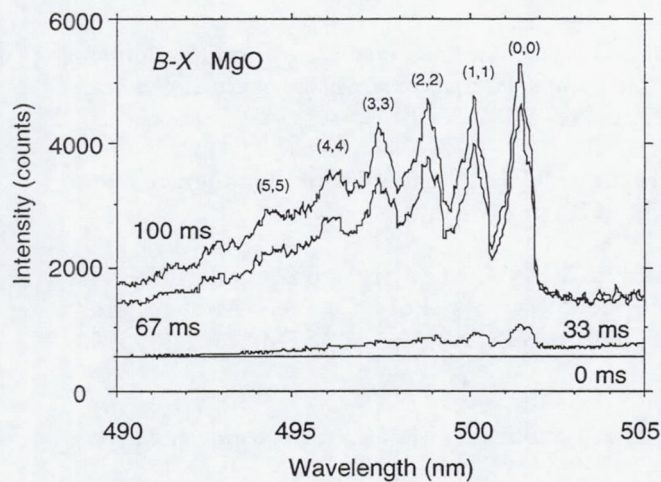


Figure 3. Time-resolved emission spectra from the ignition of a Mg specimen in O_2 at 1 atm.

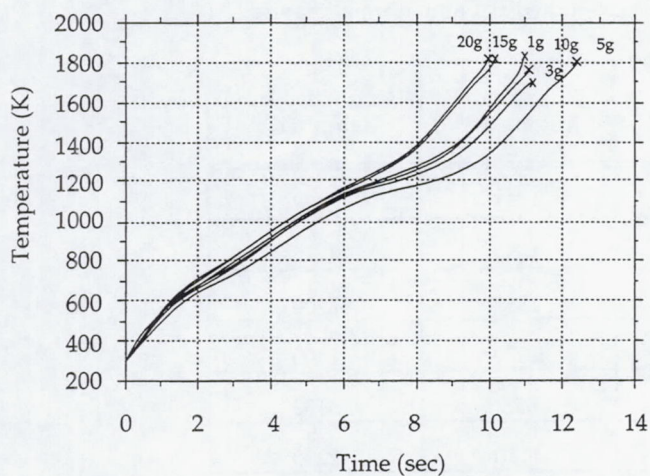


Figure 5. Temperature vs. time behavior of bulk titanium samples subjected to different gravity loads.

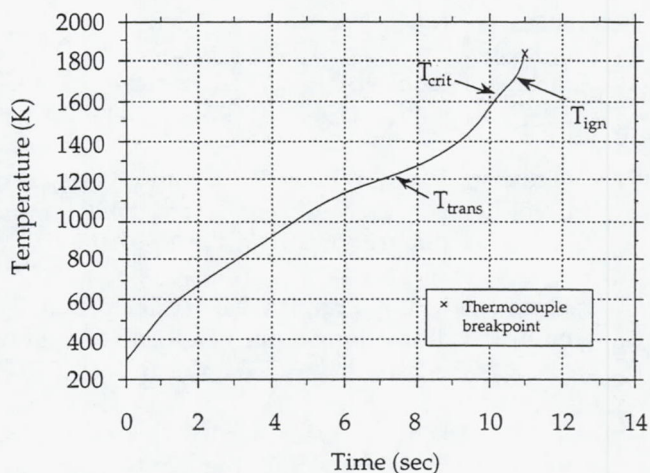


Figure 2. Temperature profile and important temperature values (transition, critical and ignition) of bulk titanium at 1 atm and normal gravity.

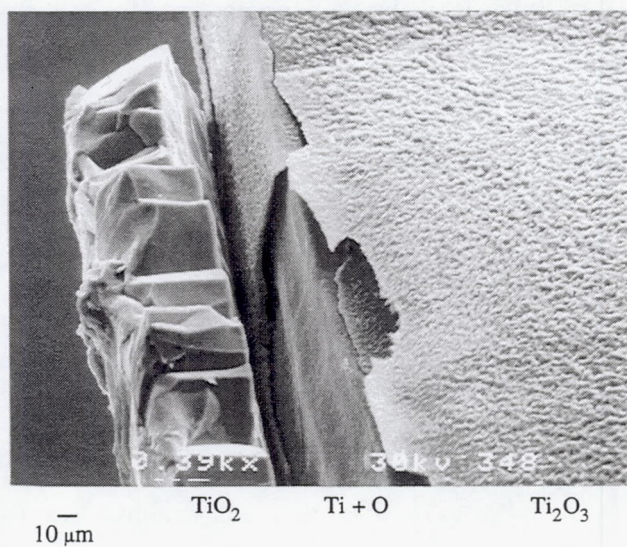


Figure 4. SEM photograph (390X) taken from the outer rim of the top surface of a cylindrical Ti specimen quenched at 1550 K during the heating phase in O_2 at 1 atm under normal gravity.

INTERNAL AND SURFACE PHENOMENA IN METAL COMBUSTION

Edward L. Dreizin

AeroChem Research Laboratories, Inc., Princeton, New Jersey

Irina E. Molodetsky and Chung K. Law

Princeton University, Princeton, New Jersey

Introduction

Combustion of metals has been widely studied in the past, primarily because of their high oxidation enthalpies. A general understanding of metal combustion has been developed based on the recognition of the existence of both vapor-phase and surface reactions and involvement of the reaction products in the ensuing heterogeneous combustion. However, distinct features often observed in metal particle combustion, such as brightness oscillations and jumps (spearpoints), disruptive burning, and non-symmetric flames are not currently understood.

Recent metal combustion experiments using uniform high-temperature metal droplets produced by a novel micro-arc technique (ref. 1-3) have indicated that oxygen dissolves in the interior of burning particles of certain metals and that the subsequent transformations of the metal-oxygen solutions into stoichiometric oxides are accompanied with sufficient heat release to cause observed brightness and temperature jumps. Similar oxygen dissolution has been observed in recent experiments on bulk iron combustion (ref. 4, 5) but has not been associated with such dramatic effects.

This research addresses heterogeneous metal droplet combustion, specifically focusing on oxygen penetration into the burning metal droplets, and its influence on the metal combustion rate, temperature history, and disruptive burning.

A unique feature of the experimental approach is the combination of the microgravity environment with a novel micro-arc Generator of Monodispersed Metal Droplets (GEMMED), ensuring repeatable formation and ignition of uniform metal droplets with controllable initial temperature and velocity. The droplet initial temperatures can be adjusted within a wide range from just above the metal melting point, which provides means to ignite droplets instantly upon entering an oxygen containing environment. Initial droplet velocity will be set equal to zero allowing one to organize metal combustion microgravity experiments in a fashion similar to usual microgravity liquid fuel droplet combustion studies. In addition, the internal compositions of rapidly quenched metal particles will be analyzed using SEM technique. Such compositions are similar to those existing during the combustion and provide new insight on metal combustion processes. The results of this experimental work will be used to model the fundamental mechanisms of metal combustion.

Preliminary experimental results on Al and Zr particle combustion at normal gravity are discussed here. This work was initiated in July, 1994.

Experimental

Metal particle combustion experiments were conducted using the GEMMED described elsewhere (ref. 6). The GEMMED uses a pulsed micro-arc discharge to melt the edge of a consumable wire electrode and separate molten droplets from the wire. Each metal droplet is formed and ignited in a single micro-arc pulse. Repeatability of the duration, current, and voltage of the micro-arc pulses results in reproducible diameters, temperatures, and velocities of the metal droplets formed.

The color temperature histories of the burning droplets were recorded using a three-wavelength pyrometer. The pyrometer included an iris, a fiber optics trifurcated bundle, three interference filters, and three HC120-01 Hamamatsu photo-sensor modules. Different wavelengths of the interference filters were chosen for each metal so that no bands which are observed in the metal-oxygen (or metal-nitrogen) spectra could contribute to the measured signals. The pyrometer was calibrated using a tungsten strip lamp, providing a maximum black body temperature of 2650 K. For any time during the particle trajectory, two color temperatures could be deduced from the three recorded radiation signals. This provided a criterion for the correctness of the temperature measurements, e.g., agreement of the two inferred temperatures showing that the radiation spectrum is that of a gray body, validated the color temperatures.

Spatial resolution of the optical signals produced by the particle and the external luminous zone was achieved using a slot array with equally spaced 0.2 mm wide slots positioned between the burning particle trajectory and the pyrometer (close to the particle trajectory) with the slots perpendicular to the particle velocity vector. The radiation from burning particles moving behind the array was registered as a series of pulses. Each radiation pulse was formed when a particle surrounded with a luminous zone, crossed a single slot. Detailed comparisons of the two temperature-versus-time curves inferred from the three radiation pulses simultaneously measured at different wavelengths were conducted in order to separate particle and stand-off luminous zone radiations and identify the particle temperature. Such analyses showed that a period existed when the two temperatures agreed well for each radiation pulse corresponding to a burning particle crossing a single slot. This period, as expected, was close to the time needed for the particle (excluding the external luminous zone) to cross the slot. Thus, the particle surface temperature could be measured when burning particles crossed the slot, and most of the flame radiation was blocked.

The luminous zone shape was visualized by video-recording of the combustion events using a free running camera at a fast shutter speed (0.5 ms exposure time). Particles were quenched on glass slides at different combustion times, and the shapes of smoke traces surrounding the quenched particles were examined and compared with the video-camera images.

Rapid particle quenching was used to freeze the particle internal compositions which existed during the combustion. The fast cooling rate of a metal droplet provided by its impinging onto a cool metal surface, was utilized in this work. To minimize the particle shape distortion, a thin Al foil was used as a quenching substrate, which resulted in the particle welding into the foil upon collision. The quenched particles were embedded into epoxy and cross-sectioned. An electron probe microanalyzer "Cameca SX50" was used for the cross-section examination, and Energy-Dispersive Spectroscopy (EDS) (Princeton Gamma Tech. detector) as well as Wavelength-Dispersive Spectroscopy (WDS) scan were utilized to determine the particle internal compositions.

Results

Combustion of 80, 120, 165, and 200 μm diameter Al particles and 240 μm diameter Zr particles in room air have been studied.

Video recordings of metal particle combustion events as well as spatially resolved radiation measurements using the slot array consistently showed the existence of luminous zones surrounding burning particles of both Al and Zr. The estimated sizes of the luminous zones correlated well with the sizes of smoke clouds deposited when the particles were quenched on glass slides. For both Al and Zr, the clouds formed upon ignition were spherically symmetric but lost their symmetry later in the combustion. The comparison of the luminous zone (or cloud) shapes with the radiation intensity signals measured in separate channels of the three-wavelength pyrometer indicated that for both metals the zones became non-symmetric after the maxima of radiation were reached.

Pronounced oscillations of radiation intensity caused by the spinning of burning Al particles began simultaneously with the deformation of the originally symmetric external luminous zone. Al droplet combustion also was accompanied by separation of small satellites and often ended with explosions, although smooth particle extinguishing was observed in some cases. Burning Zr particles did not exhibit such noticeable oscillations but their combustion in air always terminated by strong explosions.

Temperature histories of 165 μm diameter Al and 240 μm diameter Zr particles burning in air are shown in Fig. 1. Solid curves in Fig. 1 represent temperature histories determined for single particle combustion events without using the slot array. These temperature histories were very reproducible. For reference, important phase transition temperatures are indicated as dashed lines in Fig. 1. While the two temperatures inferred from the three measured radiation signals were consistent for Al particles (an example of only one of the temperature histories is shown in Fig. 1a), there was some inconsistency between the two temperatures determined for burning Zr particles without the slot array. An example of the temperature history $T_1(t) = f\{(\text{radiation intensity at } 589\text{nm})/(\text{radiation intensity at } 510\text{nm})\}$ of a single Zr particle burning in air is shown in Fig. 1 (solid line) along with the temperatures measured using several (reproducible) Zr particles crossing the slot array (triangles). Each triangle shows where the two temperatures became consistent for different pulses recorded for single particles crossing the slots.

The maximum temperature of burning Al particles, Fig. 1a, was measured during the initial combustion period and exceeded the Al boiling point (2520°C), indicating that particle radiation was shielded by the radiation of spherically symmetric stand-off flame zone. Later on, the temperature stabilized slightly below the Al boiling point (but above the boiling temperature of the saturated Al-O solution, ref. 7), and then decreased close to the solidification point of Al_2O_3 (2050°C) immediately before the extinguishment. Maximum temperatures of Zr particles burning in air were always below the ZrO_2 melting point (2700°C), Fig. 1b and approached the temperature of eutectic αZr and ZrO_2 formation ($\sim 2000^\circ\text{C}$) at the completion of combustion.

EDS and WDS determination of the internal compositions of rapidly quenched Al and Zr particles revealed the presence of oxygen in particle interiors for both metals, while no oxide shells or inclusions were observed. Internal compositions of particles quenched at different times are shown in Fig. 2. Measured atomic concentrations of oxygen in Al particles did not exceed 14%, Fig. 2a, until "oxide caps" started to grow after approximately 2/3 of the entire particle combustion time. The "oxide cap" compositions were close to the stoichiometric Al_2O_3 with some traces of nitrogen, while the composition of the rest of Al particle did not change. The composition of burning Zr particles follows a different path, incorporating both nitrogen and oxygen. Gradual growth of oxygen concentration, approaching stoichiometric ZrO_2 at the combustion end, was observed (see Fig. 2b). Nitrogen concentration in Zr particles was observed to increase up to 20% and then to fall during combustion.

Discussion

According to the existing metal combustion classification, the two metals experimentally examined in this work belong to different groups: Al is a vapor-phase burner, while Zr is known to burn heterogeneously. However, some striking similarities were observed in their burning behavior:

- 1) symmetric stand-off luminous zones formed in both cases and eventually became non-symmetric;
- 2) oxygen dissolved in the burning metal droplets with no observed oxide shell formation;
- 3) disruptive burning occurred with both metals.

The presence of oxygen in the particle interiors and the absence of oxide shells suggest that not only the surface of the burning metal droplets, but also, their entire interiors are actively involved in the combustion processes. It means that metal-gas interactions in the condensed phase should be analyzed in addition to vapor-phase and surface metal-gas interactions in order to elucidate metal particle combustion behavior. Interactions of materials in the condensed phase are usually described using concentration versus temperature phase diagrams. The Al-O and Zr-O phase diagrams suggest that although stoichiometric oxide phases (e.g., liquid Al_2O_3 or solid ZrO_2) are stable as individual phases at the combustion temperatures, no oxides can be formed in a binary metal-oxygen system until a certain limit of oxygen concentration is reached. Thus, while the conventional heterogeneous metal combustion model assumes that an oxide forms as a result of a surface reaction occurring when a clean high-temperature metal surface is exposed to an oxygen-containing environment, the phase diagrams suggest that a metal-oxygen solution forms until the oxygen concentration attains the solubility limit. Then, assuming further oxygen availability, a transition from the saturated solution to the stoichiometric oxide (liquid or solid) can occur. Such a transition is exothermic, but at thermodynamic equilibrium takes place at a constant temperature. However, even at the equilibrium, it can be associated with changes of internal structure and void/crack formation, gas release, etc., which may cause brightness and temperature jumps and particle explosions.

Specifically, the Al-O phase diagram (ref. 7) suggests that liquid Al-O solutions and a vapor-phase form at temperatures from 2240 to 2460°C and at atomic oxygen concentrations below ~14%. Liquid Al₂O₃ starts to form when the 14% limit is attained, and both liquid Al and liquid Al₂O₃ coexist in the temperature range of 2050-2240°C. Thus, the transition from solution to Al₂O₃ can occur when the internal oxygen content is close to 14% and the temperature is in the range of 2240-2460°C. These conditions are in good agreement with the particle temperatures and internal oxygen concentrations measured in Al combustion tests at the transition from the spherically symmetric to non-symmetric combustion mode, associated with disruptive events and particle spinning.

The binary Zr-O system forms liquid solutions at temperatures above 2000°C with the oxygen solubility limit increasing from 40 to 66% (atomic) as the temperature increases up to 2700°C (ref. 7). Solid ZrO₂ forms when the solubility limit is reached, and it co-exists with the saturated solution. Therefore, the transition from solution to oxide can occur if the internal oxygen content exceeds 40% and the temperature is above 2000°C. These conditions, again, correlate well with the Zr particle temperature and composition measured prior to the observed explosions.

Thus, while the possible mechanisms (such as gas release, oxygen penetration into forming voids, or non-equilibrium oxide formation) for the observed phenomena of disruptive burning, explosion, or spearpoint, should be elaborated for each case separately, the generic mechanism actuating these processes apparently is the solution-oxide transformations discussed here. Such transformations actually represent oxidation reactions developing inside burning metal particles and should be added to conventionally considered external (vapor-phase) and surface oxidation processes.

Summary and Plans

Preliminary normal gravity experiments on metal combustion have shown that oxygen dissolves in burning Al and Zr particles. It is suggested that the transformation of a metal-oxygen solution into the stoichiometric oxide results in observed particle brightness and temperature jumps and explosions.

Further work will focus on the experimental apparatus modification for microgravity tests and the design of microgravity experiments. Following experimental tests will elucidate the role of external transport processes on metal particle combustion and, in particular, those processes resulting in non-symmetric luminous zone formation.

Acknowledgements

The research performed at AeroChem and Princeton University were respectively supported by the Microgravity Science and Application Division of NASA (Lewis RC) and by the Office of Naval Research. The authors appreciate the help of Dr. E. Vicenzy of Princeton Material Institute in the SEM sample analyses.

References

1. Dreizin, E.L., Suslov, A.V. and Trunov, M.A., *Combust. Sci. Tech.* **87**:45-58 (1992).
2. Dreizin, E.L., Suslov, A.V. and Trunov, M.A., *Combust. Sci. Tech.* **90**:79-99 (1993).
3. Dreizin, E.L. and Trunov, M.A., *Combustion and Flame*, in press (1995).
4. Steinberg, T.A., Wilson, D.B., and Benz, F., *Combustion and Flame*, **88**:309-320 (1992).
5. Steinberg, T.A., Mulholland, G.P., Wilson, D.B., and Benz, F., *Combustion and Flame*, **89**:221-228 (1992).
6. Suslov, A.V., Dreizin, E.L. and Trunov, M.A., *Powder Tech.*, **74**:23-30 (1993).
7. Levinskiy, Y.V., *P-T-X Binary Phase Diagrams of Metal Systems*, Moscow, Metallurgia, (1990) (In Russian).

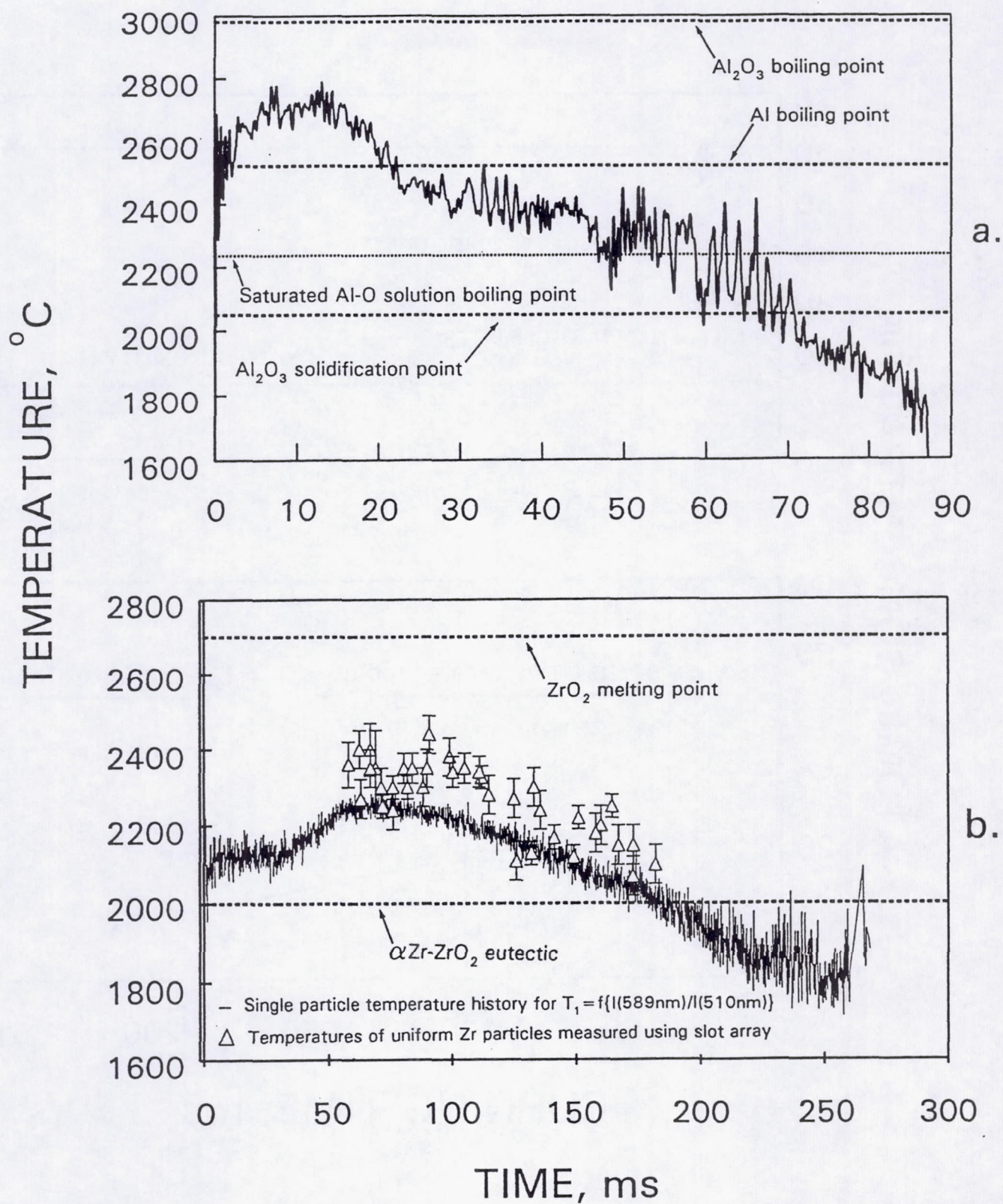


FIGURE 1 TEMPERATURE HISTORIES OF BURNING METAL PARTICLES

- (a) Al, Initial Diameter 165 μm
 (b) Zr, Initial Diameter 240 μm

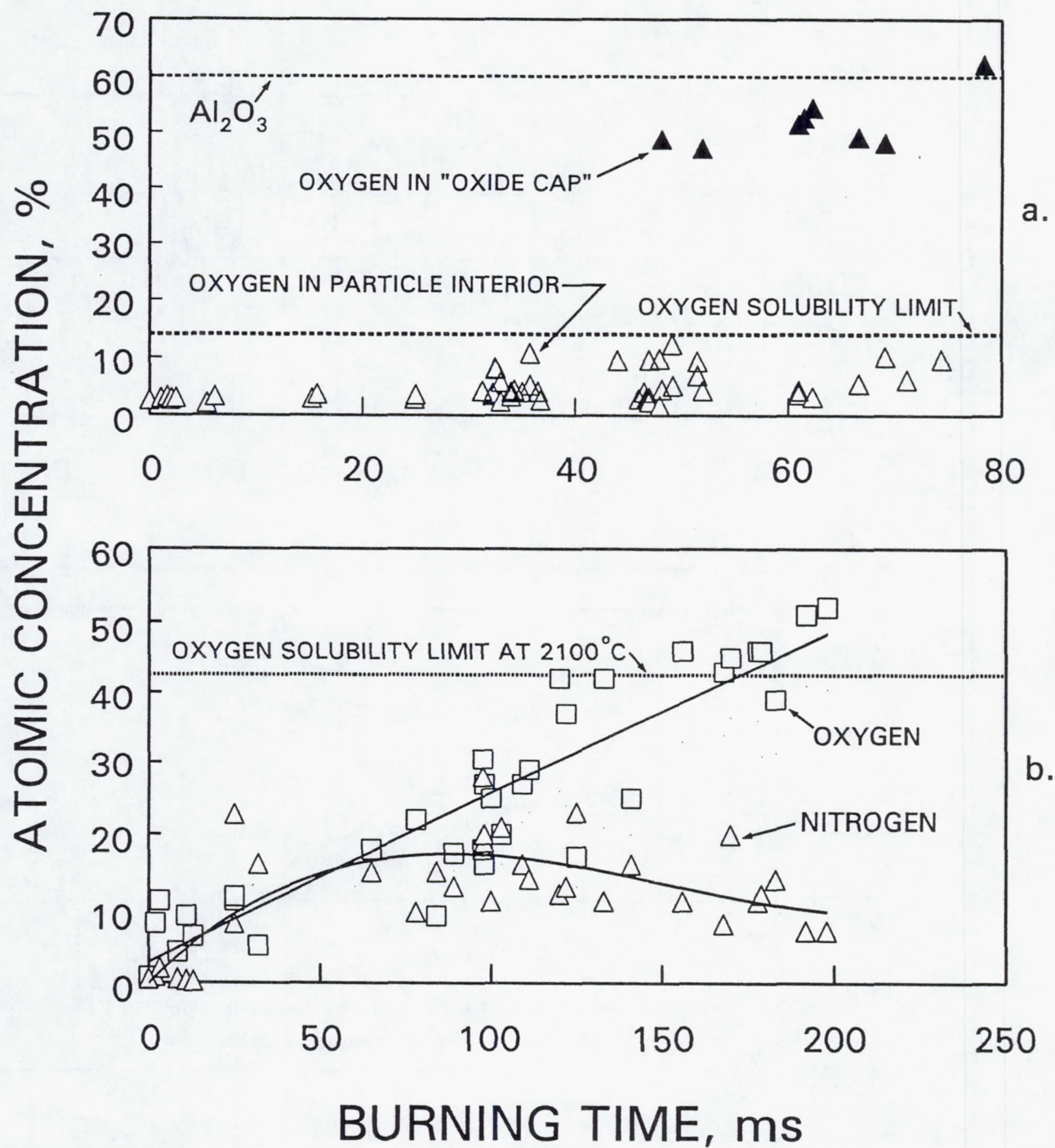


FIGURE 2 INTERNAL COMPOSITION HISTORIES OF BURNING METAL PARTICLES

- (a) Al, Initial Diameter 165 μm
 (b) Zr, Initial Diameter 240 μm

EFFECT OF PRESSURE ON A BURNING SOLID IN LOW-GRAVITY

Jeffrey S. Goldmeer¹, David Urban², and James T'ien¹

1. Case Western Reserve University

2. NASA Lewis Research Center

Introduction

Venting, or depressurization, has been discussed as a possible technique for extinguishing fires on aircraft [1] and spacecraft [2,3]. Fire suppression plans for the International Space Station Alpha (ISSA) discuss the use of depressurization as a method for extinguishing fires [4]. In the case of an uncontrollable fire, the affected compartment would be vented from an initial pressure of 1.0 atm (14.7 psia) to a final pressure 0.33 atm (4.8 psia) within 10 minutes [4]. However, the lack of low pressure flammability data for solid materials in a low-gravity environment presents an uncertainty for the use of the venting technique. There are also transient effects that need to be considered. It is possible that the flows induced by the venting could intensify the fire. This occurred during flammability tests conducted on board Skylab [5]. In addition, the extinction pressure could be a function of the depressurization rate. Studies conducted with solid propellants have shown that if the pressure is reduced quickly enough, the pressure at extinction will be greater than the steady-state extinction limit [6]. This project, which was started in 1992, is examining both the quasi steady-state and transient effects of pressure reduction on a burning solid in low-gravity. This research will provide low-g extinguishment data upon which policies and practices can be formulated for fire safety in orbiting spacecraft.

Hardware & Procedures

Cast polymethyl methacrylate (PMMA) cylinders 1.9 cm in diameter and 2.5 cm in length were burned in these experiments. The cylindrical geometry was selected as a model system because two distinct flow regions exist when cylinders are placed in a flow: a forward stagnation point and a wake (re-circulating) region. The difference between flame stabilization and extinction characteristics in low and high speed flows can be important in venting extinction [7- 11]. The tests were conducted in a 25 cm diameter combustion chamber (50 cm in height) in which a forced flow of air, with velocities ranging from 5 to 20 cm/sec, was generated. (The axis of the cylinders was perpendicular to the flow.) Steel disks (1.9 cm dia) were placed at the ends of the cylinders to prevent end flames. Images were recorded on video tape using two color video cameras. A computer controlled the experiment and sampled pressure, temperature, volumetric flow rates, and acceleration data. Combustion was initiated using a hot wire ignitor.

A thermocouple was inserted along the cylinder axis with the junction at the center of the cylinder. This temperature was used as an indication of the change in the bulk solid temperature. The temperature of a thick solid can influence the flammability limits. In a quasi-steady gas-phase theoretical model [9], which was developed for this problem, a non-dimensional parameter (Φ) was defined to be the ratio of the heat conducted into the solid to that from the gas phase:

$$\Phi = \frac{-\lambda_s \left(\frac{\partial T}{\partial n} \right)_s}{-\lambda_g \left(\frac{\partial T}{\partial n} \right)_g}$$

This term has been demonstrated to be an important parameter determining the flammability of a PMMA cylinder

in zero-gravity with a forced flow of air [9,10]. This model shows that as the solid center temperature increases, the value of Φ decreases. The relationship between the solid center temperature and Φ for a PMMA cylinder (1.9 cm dia) is shown in Figure 1. The solid-phase temperature was computed using a transient heat conduction model for a cylindrical geometry with a step change in the surface temperature: $t < 0$, $T(r) = 300$ K; $t > 0$, $T(r=R) = 700$ K. The gas-phase temperature gradient was calculated using an interface energy balance that included surface radiative loss, latent heat of vaporization, and heat conducted into the solid interior. In the limit of a solid heated to near the vaporization temperature, Φ would be approximately zero.

In these experiments, the sample was ignited, and depressurization was initiated at a pre-determined solid center temperature. (In most cases, this was 320 K.) The rate of depressurization was controlled using a PID controller that monitored the chamber pressure and controlled the outlet valve. The pressure was reduced until the flame was extinguished.

A series of tests was conducted to examine the velocity increase within the combustion chamber during depressurization. In the tests the forced flow velocity ranged from 10 to 18 cm/sec, the depressurization rate was 1.0 atmosphere per minute, the initial pressure was 1.0 atmosphere, and the final pressure was 0.5 atmospheres. The velocity was measured with a hot wire anemometer probe that was inserted into the center of the combustion chamber. During depressurization, the measured velocity increased by less than 2 cm/sec.

Low gravity data at low pressures was obtained on board the NASA Lewis Research Center's Lear Jet. In flight, the aircraft followed a Keplerian trajectory that produced approximately 20 seconds of low-g [12]. Accelerations on the order of ± 0.02 g's were measured during the low-g portion of the trajectory. The periods of low-g were preceded and followed by periods of high-g: + 2 to 3 g's. Because the time needed to establish combustion is longer than the entire low-g period, the samples were ignited in 1g, prior to the low-g trajectory. Reduced pressure on board the aircraft was obtained via an overboard vent line: atmospheric pressure at altitude ($\sim 30,000$ ft.) provided the low pressure source.

Normal Gravity Results

The parameters for these experiments included: forced flow velocity, depressurization rate, and initial pressure. The forced flow was set at 10 or 20 cm/sec and the depressurization rate varied from 0.2 to 1.5 atmospheres per minute. The initial pressures ranged from 1.0 atm down to 0.4 atm.

Figure 2 is a plot of the solid center temperature at extinction and the computed value of Φ (at extinction) versus the extinction pressure. For high initial pressures and low depressurization rates (0.2 atm/min), the resulting temperature at extinction was high (> 500 K; $\Phi < 0.23$). The resulting longer period of burning raised the solid temperature increasing its flammability, as indicated by the decreasing value of Φ . Since the material was more flammable, a reduced pressure (0.07 atm) was required to cause extinction. For tests with a lower initial pressure or a high depressurization rate (≥ 0.5 atm/min), the solid had less time to absorb heat from the flame, so the center temperature was less than 450 K ($\Phi > 0.27$) at extinction. (Extinction pressures varied from 0.1 to 0.3 atm.) Thus, these results provide a flammability boundary dependent on the solid (center) temperature and pressure.

There were distinct changes in the flame shape during the experiments. (Figure 3) Initially, the flame had a tear-drop shape (envelope flame) and a whitish-yellow color. (Figure 3A) As the pressure was reduced, the flame tip length was reduced, and the flame developed an elliptical shape. In addition, the flame color changed to a dim blue. (Figure 3B) As the pressure was reduced further, the flame blew-off at the forward stagnation point. This was followed by a period of oscillations, as the flame tried to re-attach itself. Eventually, the flame receded, forming a wake flame. (Figure 3C) As the pressure was reduced slightly, the flame extinguished.

In this test, the depressurization rate was 0.3 atmospheres/minute. In tests with depressurization rates on the order of 1.5 atmospheres/minute a wake flame did not form after the flame was blown-off the forward stagnation point. In these cases, the short burning times may not have permitted the upper surface temperature profile to increase to the point at which it could sustain combustion.

Low-gravity Results

Two types of experiments were conducted: constant and variable pressure. In both types of experiment, the samples were ignited at pressures ranging from 0.7 to 1.0 atmospheres. In the constant pressure experiments the pressure was reduced to the test condition after ignition, but prior to the beginning of the low-g-interval; the pressure was kept constant during the period of low-g. In the variable pressure tests, the pressure was kept constant until the low-g interval, at which point the combustion chamber was depressurized. The pressure range examined was 1.0 to 0.4 atm, with the lower pressure limit a result of the vent line capacity.

Twenty-six constant pressure extinction tests were conducted with a forced flow of 10 cm/sec in air. During low-g the solid-phase center temperature did not vary significantly, indicating little change in the solid-phase temperature profile. Since the solid-phase thermal diffusion time was on the order of 350 seconds, and the gas-phase time scales (conduction and convection) were on the order of 1 second, these experiments were considered to be quasi-steady. As noted in a previous paper [10], there were distinct changes in the flame's shape from 1g to low-g (Figure 4); at the same pressure (0.8 atm) and with the same forced flow (10 cm/sec), the low-g flame did not have the characteristic 1g plume, and the flame's color changed to a dim blue.

In these experiments, the quasi-steady nature of the flame was disturbed by perturbations about the mean g-level (g-jitter). These perturbations are associated with vibrations in the aircraft due to engine noise, air turbulence, and trajectory control. The perturbations were typically on the order of 10 to 40 milli-g's (10^{-2} to 4×10^{-2} g's). Since the mean g-level during the low-g portion of the trajectory was typically on the order of 1 to 10 milli-g's (10^{-3} to 10^{-2} g's), the perturbations created periods of positive and negative-g. The effect of g-jitter was noticeable in the visible flame thickness at the forward stagnation point. In figure 5, this thickness is plotted with the g-level as a function of time. As the g-level decreased, the flame thickness increased, most likely because changes in the net velocity affected the heat and mass transfer balances within the flame. The flame extinguished after 1.5 seconds of sustained negative-g, as shown in the right edge of the figure. The rapid decrease in the flame thickness denotes extinction.

The pressure and solid center temperature data for these experiments is plotted in Figure 6. Note that there were numerous experiments in which the flame extinguished. In all of these cases, the flame was disturbed by a sustained period of negative-g on the order of 30 milli-g's (3×10^{-2} g's). At this g-level the induced buoyant velocity was on the order of 10 cm/sec. Since the induced velocity opposed the forced flow during a period of negative-g, the local velocity would have approached zero in tests with a forced flow of 10 cm/sec. Previous experiments [13] have indicated that this material is not flammable in air in a quiescent low-g environment. Thus, during negative-g the near zero air velocity weakened the flame. The weakened flame was not able to recover when the g-level began to increase and extinguished as shown in Figure 5.

A method for minimizing the effect of g-jitter would be to increase the forced flow velocity. The induced buoyant velocity would then be a smaller percentage of the forced flow. During a period of negative-g, the induced flow would still oppose the forced flow, however, the local velocity would not approach zero. Work in progress suggests that this method is effective in reducing the effects of g-jitter on the flame.

For cases in which g-jitter did not significantly affect the flames, extinction did not occur. This indicates that the pressures and solid center temperatures tested were above the low-g flammability limit. A recent numerical study agrees with this result [9]. This study examined the burning of PMMA cylinders in low-g with a forced flow and determined that the flammability limit was a function of the solid sub-surface temperature gradient. As the solid center temperature increased, the percentage of energy conducted into the solid interior from the flame (Φ) decreased. Since the solid was at a higher temperature, it required less energy from the flame to create the fuel vapor. Thus, in cases with reduced pressure and increased solid temperatures, the solid was able to produce fuel vapor, even though the reaction rate of the flame was reduced. Because of this, a cylinder at higher bulk temperatures sustained combustion at lower pressures. The limiting case was when the entire solid was near the vaporization temperature: Φ near zero. The low pressure limit with a 10 cm/sec forced flow of air, as reported in the numerical study, was approximately 0.12 atm (1.7 psia) [9].

In the transient experiments, the chamber pressure was reduced during low-g. Six cases were run, with depressurization rates ranging from 0.5 to 1.2 atm/min. The final pressures ranged from 0.67 to 0.42 atm. The

flames were not extinguished during these tests. Additionally, there was no visible intensification or diminishment of the flames.

Conclusions

The 1g experimental results presented in this paper comprise a pressure - temperature flammability boundary for constant % oxygen, forced flow velocity, and g-level. As the bulk solid temperature increased, the low pressure limit decreased. (Figure 2.) When the solid temperature was sufficiently high, as measured by the solid center temperature and Φ , the low-pressure limit was quite low (< 0.1 atm).

The low-g experimental results to date did not produce a flammability boundary, but they illustrate the effects that g-jitter can have on a flame. In these experiments, g-jitter extinguished flames in conditions that have been observed to be flammable without jitter and which were predicted to be flammable [9]. Future experiments will continue to examine methods for limiting the effects of g-jitter.

The inability to determine the low pressure flammability limit in low-g was caused by limitations in the hardware; the lower pressure limit was a result of the vent line capacity. Further low-g experiments at pressures below 0.4 atm (5.9 psia) are planned. The current estimate for the low-g flammability limit with flow is below the final venting pressure for space station (4.8 psia). However, current plans for the ISSA are to turn off forced air circulation, vent to 4.8 psia, and then close the vent valve providing a quiescent low-g environment in which the flame should extinguish. However, during the time required to attain the quiescent condition, the fire may continue to burn.

During the low-g transient experiments, there was no visible intensification of the flames. This was due to the small increase in the velocity due to the venting. An intensification of the flames in the Skylab experiments [5] was due to a large change in velocity during depressurization; the Skylab experiments were conducted in a quiescent chamber with a pressure of 5.2 psia (0.35 atm) and an oxygen concentration of 65% [5]. Thus, during venting of the space station, there may or may not be an intensification of the fire, depending on the flame location and its position relative to the vent port(s).

Acknowledgements

J. Goldmeer would like to acknowledge the funding provided by the NASA Graduate Student Research Program.

References

1. Starrett, P., "Factors Influencing Flame Spread Rates in Solid Materials", Journal of Fire and Flammability, Vol. 8, January 1977, pp. 5-25.
2. Diamant, B., Humphries, W., "Past and Present Environmental Control and Life Support Systems on Manned Spacecraft", Twentieth Intersociety Conference on Environmental Systems, Paper # 901210, July 1990.
3. Friedman, R., Sacksteder, K., "Fire Behavior and Risk Analysis in Spacecraft", NASA TM 100944, 1988.
4. Space Station Program System Specification, SSP-41000, February 1994.
5. Kimzey, J., "Skylab Experiment M-479: Zero Gravity Flammability", Johnson Space Center Report, JSC 22293, 1986.
6. Ciepluch, C.C., "Effects of Rapid Pressure Decay on Solid Propellant Combustion", ARS Journal, Vol 31., 1961, p. 1584.
7. Spalding, D., "The Combustion of Liquid Fuels", Fourth Symposium (International) on Combustion, p. 847.
8. Udelson, D., "Geometric Considerations in the Burning of Fuel Droplets", Combustion & Flame, 1962, Vol. 6, p. 93.
9. Yang, C.T., "Numerical Simulation of the Combustion of a Solid Cylinder in Low Speed Flows", M.S. Thesis, Case Western Reserve University, 1994.
10. Yang, C.T., Goldmeer, J.S., Urban, D.L., and T'ien, J.S., "Combustion of a Solid Cylinder in Low Speed Flows", Fall Technical Meeting of the Eastern States Section of the Combustion Institute, 1994, pp. 47-50.
11. Ferkul, P. and T'ien, J.S., "A Model of Low-Speed Concurrent Flow Flame Spread Over a Thin Fuel", Combustion Science and Technology, 1994, Vol. 99, pp. 345-370.
12. Lekan, J., Neumann, E., and Sotos, R., "Capabilities and Constraints of NASA's Ground-Based Reduced Gravity Facilities", Second International Microgravity Combustion Workshop, NASA CP 10113, 1992, pp 45-60.
13. Goldmeer, J.S., Urban, D.L., and T'ien, J.S., "An Experimental Study of Solid Diffusion Flame Extinction and Transition to Microgravity", Fall Technical Meeting of the Eastern States Section of the Combustion Institute, 1993, pp. 441-444.

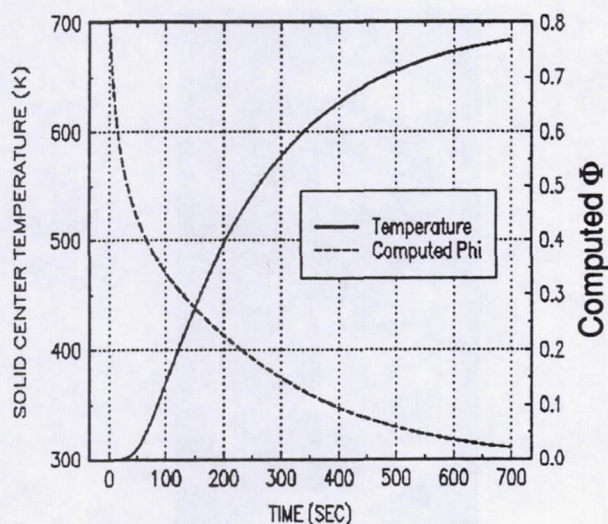


Figure 1 - Computed Solid Center Temperature and Computed Φ vs. Time
(Surface Temperature = 700K)

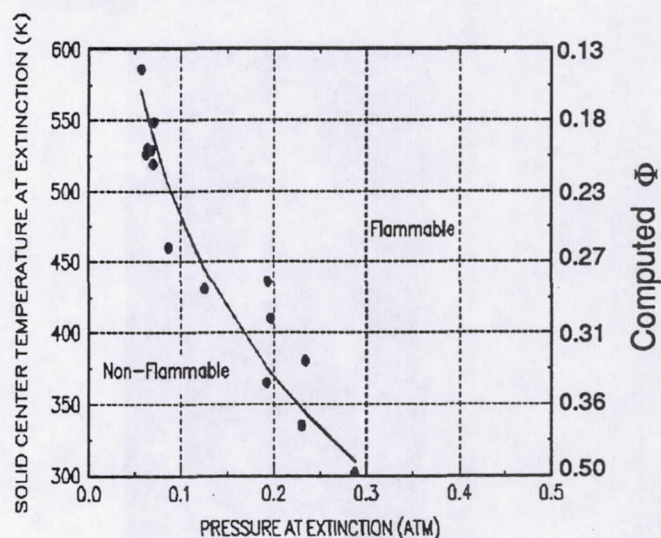
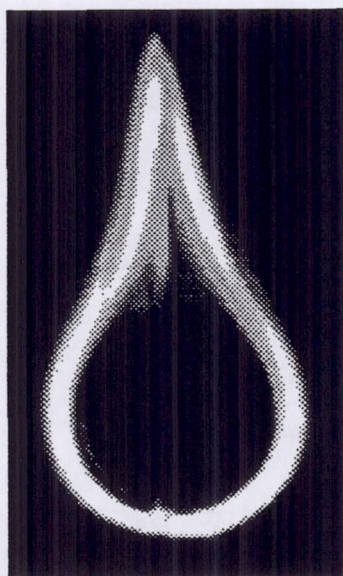
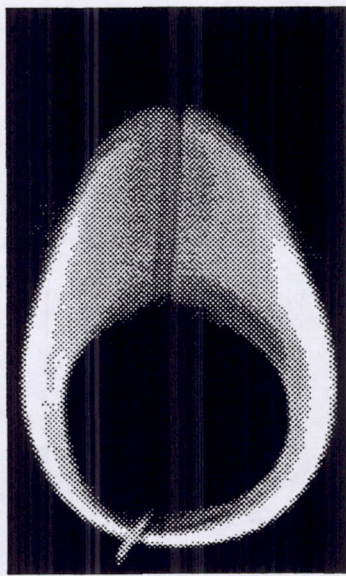


Figure 2 - Solid Center Temperature and Computed Φ vs. Pressure at Extinction in normal gravity
(forced flow of 10 cm/sec in air)



(A) $P = 0.98$ ATM
 $T = 307$ K
 $t = 93$ sec



(B) $P = 0.11$ ATM
 $T = 510$ K
 $t = 301$ sec



(C) $P = 0.07$ ATM
 $T = 526$ K
 $t = 322$ sec

Figure 3 - Visible Flame in normal gravity with a forced flow of 10 cm/sec in air
(ignition occurred at $t = 34$ seconds)

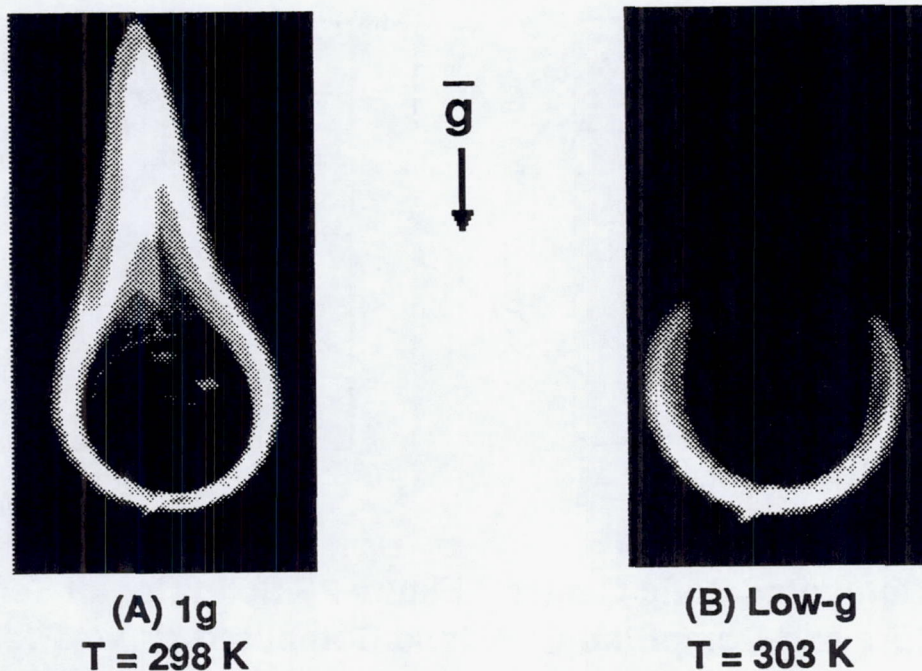


Figure 4 - Comparison of 1g and Low-g Visible Flames
Constant Chamber Pressure (0.8 atm) with a forced flow of 10 cm/sec in air
(Initial Solid Center Temperature = 295 K)

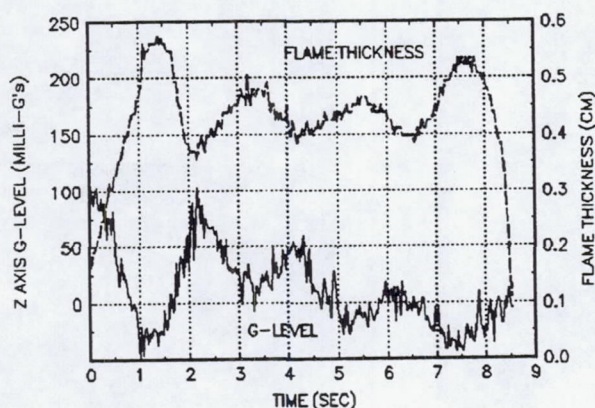


Figure 5
Flame Thickness & G-level vs. Time
Pressure = 0.79 atm
Solid Center Temperature = 303 K

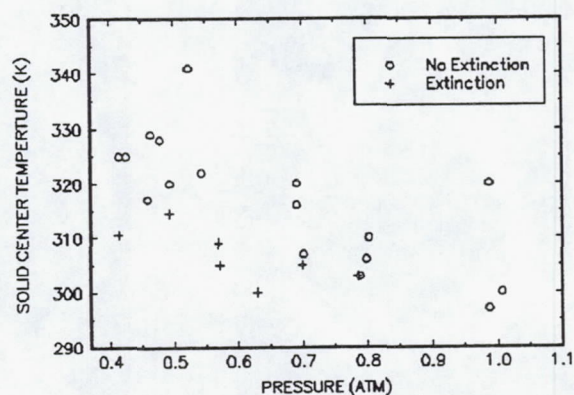


Figure 6
Solid Center Temperature vs. Pressure
in Low-g (Lear Jet) with a
Forced Flow of 10 cm/sec in air
(subject to g-jitter)

MICROGRAVITY COMBUSTION OF DUST CLOUDS. QUENCHING DISTANCE MEASUREMENTS.

S. Goroshin, H. Kleine, J.H.S. Lee, D. Frost

McGill University

817 Sherbrooke St. West, Montreal, Quebec, H3A 2K6, Canada

Introduction

The bulk of current energy production in the industrialized world comes from the burning of fossil fuels, a large part of which is in the form of a solid (e.g., coal) or a heavy liquid (e.g., diesel oil). Such fuels are invariably burnt in an atomized form. Efficient and environmentally clean combustion necessitates a fundamental understanding of the underlying mechanisms of heterogeneous combustion. There is also an inherent danger of dust explosion when combustible dusts are handled in industry. Dust explosions occur in coal mines, in agricultural handling and processing facilities, and in the wood, sugar, metal, paper, chemical, and rubber industries. Processing of ultra-fine and ultra-pure ceramic monosized particles (metal oxides, silicon oxide, carbides) via dust combustion processes (ref. 1) is another example of an important modern technological application of dust combustion.

The current level of physical understanding of dust combustion phenomena is still in a rudimentary state compared with the understanding of gas combustion processes. The reason for such a lack of fundamental understanding is partially based on the complexity of multiphase combustion and the enormous diversity of chemical-physical properties of heterogeneous combustible mixtures but is largely due to difficulties in the experimental investigation of dust combustion. The influence of gravity on a dust suspension is the main reason. First of all, when particulates (either solid particles or liquid droplets) with a characteristic size of the order of tens of microns are suspended, they rapidly settle in the gravitational field. To maintain a particulate suspension for a time duration adequate to carry out combustion experiments invariably requires continuous convection of particulates at or in excess of the gravitational settling velocity. Of necessity, this makes the experiments turbulent in character and makes it impossible to study laminar dust flames. For particle sizes of the order of microns a stable laminar dust flow can be maintained only for relatively small dust concentrations (e.g., for low fuel equivalence ratios) at normal gravity conditions. High dust loading leads to gravitational instability of the dust cloud and to the formation of recirculation cells in a dust suspension in a confined volume (ref. 2 and 3), or to the rapid sedimentation of the dense dust cloud as a whole in an unconfined volume (ref. 4). In addition, many important solid fuels such as low volatile coal, carbon, and boron have low laminar flame speeds (of the order of several centimeters per second). Gravitational convection that occurs in combustion products due to the buoyancy forces disrupts low speed dust flames and, therefore, makes observation of such flames at normal gravity impossible.

The only way to carry out "clean" fundamental experiments in dust combustion over a wide range of dust cloud parameters is in a gravity-free environment. Access to the microgravity environment provided by the use of large-scale drop towers, parabolic flights of aircraft and rockets, and shuttle and space station orbits has permitted now to proceed with a systematic program of dust combustion microgravity research. For example, the NASA-Lewis drop tower and a Lear jet parabolic flight aircraft were used by Ross et al. (ref. 5) and by Berlad and Tangirala (ref. 6) for experiments with lycopodium/air mixtures. The Japan Microgravity Center drop shaft (JAMIC) where a microgravity condition of 10^{-4} g for 10 s is available, was recently used by Kobayashi, Niioka et al. for measuring flame propagation velocities in Polymethyl methacrylate dust/air suspensions (ref. 7).

Microgravity dust combustion experiments were started at McGill University in the early 90's under the sponsorship of the Canadian Space Agency. Several generations of dust combustion platforms permitting dust combustion microgravity experiments to be carried out on board a parabolic flight aircraft (KC-135, NASA) have been designed and tested (ref. 8). The experimental data and experience gained from this research allowed us to design and build in a current phase of this program the microgravity apparatus for the visual observation of freely propagating constant pressure laminar dust flames. Quenching distances in aluminum dust suspensions have been measured in a wide range of dust cloud parameters in ground-based experiments and in recent microgravity experiments (KC-135 parabolic flights, Houston, February 1995).

Microgravity Experimental Set-Up

The microgravity experimental package (see Fig. 1) is assembled in a frame (26"x46"x50") which contains the dust combustion set-up along with flow visualization equipment. The frame is built from standard 1" steel pipe and mounted on a 1/2" thick base aluminum plate which is bolted to the aircraft floor. The dust combustion set-up consists of four major components: the dust dispersion system, the combustion tube assembly, the venting system and optical diagnostics with video and high speed framing cameras.

The dust dispersion system also consists of two parts: a dust feeder and a disperser (Fig. 2). The dust is fed via a syringe-type device which has an internal diameter of 0.5" and a maximum piston stroke of 3". The rate at which the dust is supplied to the flow (and hence the dust concentration in the suspension) is controlled by varying the piston speed with the help of a special electromechanical system (Linear Actuator, Thomson Saginaw, MI). The dust is dispersed at the base of conical chamber through the impact of a high velocity cylindrical jet issuing from an adjustable (20-40 μm) circular slot. A Pyrex flame tube (2" ID) where combustion experiments are performed is connected to the dispersion chamber through an 8° conical diffuser. The diffuser provides expansion and laminarization of the dust flow which is initially turbulent in the dust disperser.

The combustion tube assembly is shown in Fig. 3. The design allows for safe observation of the dust flame as well as for measurement of the quenching distance. This design also allows one to replace the flame tube quickly and store it safely during the flight. A conical nozzle with an opening of about 1" is installed in the upper part of the tube to prevent the appearance of acoustic flame oscillations. An ignition coil made from 0.25 mm tungsten wire is installed in the upper ring of the tube. The lower ring is threaded for fast connection of the tube assembly with the dispersion system. In order to determine the quenching distance a set of thin evenly spaced steel plates (thickness 0.25 mm, L = 50 mm) was installed in the upper section of the flame tube to form a grid aligned with the flow direction. The plates in the set are connected by four thin needles and soldered to form a rigid structure. A second similar set of quenching plates with a smaller gap between the plates of about 3.5 mm is also installed upstream in the lower third of the tube. This set serves as a flame arrester to prevent flashback into the dispersion system and also helps to laminarize the dust flow after it exits the dust disperser.

The venting system provides venting and filtration of the dust flow and combustion products from the combustion tube to the outside of the airplane through the overboard vent. In flight it uses the natural pressure difference between the cabin and the high altitude atmosphere. The venting duct is connected with the combustion tube by a sliding O-ring seal. Four one-way silicon diaphragm valves are installed in the upper ring on top of the tube assembly to prevent the dust flowing into the cabin in case of failure of the venting system. It also provides free access for cabin air in the venting duct at normal conditions, thus ensuring constant-pressure conditions within the combustion tube. A check-flow valve is also installed in the venting duct to prevent ignition and dispersion in the case of a venting system failure.

The filtration system is composed from a two-inch layer of 1/4" stainless-steel balls to provide sufficient cooling of the combustion products and is followed by a 2"-thick glass-wool filter. The filtration system is replaced after each second shot (5 filters are prepared for each flight). The process of flame propagation was monitored by a video camcorder as well as by a high-speed 16 mm camera at a framing rate of about 1,000 frames per second.

Ground-based Experiments

Atomized aluminum powder Ampal-637 (Ampal Inc., NJ), which was used in the ground-based experiments, has an aluminum content of not less than 99.5%. The particles have a spheroidal or nodular shape, and the particle size is found to be $5.4\text{ }\mu\text{m}$ (Sauter mean diameter, d_{32}). The dust concentration is monitored by a light extinctionmeter using an expanded parallel He-Ne laser beam ($d = 8\text{ mm}$) passing through the dust mixture along the tube diameter near its upper rim. The light extinctionmeter was calibrated by the complete aspiration of the dust from the total flow through a set of filters with a vacuum pump. The dust concentration is then determined by dividing the total mass of the collected dust by the volume of gas that flowed through the dispersion system during the same time interval.

The high speed films show that when the flame with a parabolic shape approaches the quenching plates it becomes almost flat. Far from the quenching limit the flame penetrates into all the channels of the quenching section and propagates with almost the same speed in each channel. Sometimes several cycles of flame pulsation can be seen inside the quenching plates with a frequency close to the basic acoustic mode of the tube. If the fuel concentration is close to the quenching limit the flame usually propagates only through the central channel of the quenching section near the tube axis. The quenching distance as a function of dust concentration in dust-air mixtures is shown in Fig. 6. The measured lean limit of the flame propagation in the tube was found to be about 150 g/m^3 . This result is consistent with the value of 160 g/m^3 measured by Ballal for $10\text{ }\mu\text{m}$ atomized aluminum powder in tubes (ref. 9). The minimum quenching distance is found to be about 5 mm , which is close to the value of 4 mm estimated by Ballal from dust ignition experiments (ref. 10), but considerably lower than the value of 10 mm found by Jarosinski for $7.5\text{--}9\text{ }\mu\text{m}$ atomized aluminum powder (ref. 11).

Motivation for Microgravity Experiments

The experimental ground-based results show that the weak dependencies of flame speed and quenching distance on concentration in rich dust mixtures are the most distinguishing features of the dust flame propagation in comparison with premixed homogeneous gas flames. So far it is unknown how far this plateau extends and what the value of the rich limit of dust flame propagation is. This poses one of the most intriguing questions in dust combustion. Obviously, dust clouds with much higher dust concentration than those obtained in ground-based experiments should be produced in order to approach the rich concentration limit. However, in normal gravity this is extremely difficult to achieve experimentally. The results reported by Mason and Wilson (ref. 3) and Green and O'Donnel (ref. 2), as well as our own experiments show that the difficulties of producing laminar dust flows or quiescent dust clouds with high dust concentrations are largely due to the instability of the dust cloud at normal gravity conditions. Green and O'Donnel observed the formation of a chain of large scale vortices in highly loaded dust flows in tubes even at very moderate flow Reynolds numbers and small particle sizes. The tendency towards the formation of large scale vortices at the bottom of the combustion tube was also observed in the present work during attempts to produce flows with dust concentrations higher than 500 g/m^3 . The formation of vortices leads to intensive particle agglomeration and dust deposition on the walls of the combustion tube and the conical diffuser and eventually to the depletion of dust concentration. Only dust combustion experiments in a microgravity environment can alleviate the problem of the gravitational dust cloud instability at high concentrations as well as for large particle sizes.

Microgravity Experiments

The application of the laser light attenuation technique which is used for the dust concentration monitoring in our ground-based experiments is restricted to dusts with relatively small concentrations. We have found that at concentrations higher than 500 g/m^3 , the dust cloud (with a particle size $5.4\text{ }\mu\text{m}$) is almost opaque and the noise from multiple scattering of light decreases the accuracy of the measurements below an acceptable level. In addition, the light absorption technique requires calibration with the same dust and at the same level of dust concentration as in the actual measurements. This inevitably requires that the calibration has to be carried out in the microgravity environment for the high dust concentration and large particle sizes. The dust dispersion system

was calibrated in microgravity conditions to determine the range of attainable dust concentrations. Two flights were reserved for calibration of the dust dispersion system with the 5.4 μm aluminum dust and one flight for calibration with 18 μm aluminum dust (Ampal-611). The calibration was provided by collecting the dust with the help of a stack of fine dust filters. Dust concentration was then determined by dividing the total mass of the collected dust by the known volume of gas which flowed through the dispersion system during the same time interval. The variable parameter was the speed of the piston in the dust feeding system which is proportional to the DC voltage applied to the linear actuator motor. The results of the calibration (see Fig. 4) show that the dust concentration is fairly reproducible and in microgravity the maximum value is more than double the value attainable at normal gravity conditions.

The quenching distance data obtained in microgravity for the 5.4 μm dust (Fig. 6) are in good agreement with the ground-based data for dust concentrations $\leq 600 \text{ g/m}^3$. The microgravity results show that for dust concentrations larger than 600 g/m^3 , the quenching distance continues to decrease and it is probably well below 4 mm (the flame regularly passes through 4 mm quenching plates at concentrations larger than 750 g/m^3). This means that at extremely high concentrations, the quenching distance in dust clouds approaches values that are characteristic of homogeneous gas mixtures. For the first time, quenching distance was also measured for dust clouds formed with comparatively large 18 μm particles - Fig. 6.

Theoretical Analysis

A simple analytical model of a quasi one-dimensional dust flame with heat losses has been developed (details will be published elsewhere). It was assumed that radiative heat transfer in a flame front is negligible, that the aluminum particles are burning heterogeneously and that the particle burning rate in the flame front is controlled by the process of oxygen diffusion. Algebraic equations defining flame speed were obtained in two limiting cases: lean and rich mixtures. The model predicts wide plateaus in the flame speed and quenching distance versus dust concentration plots for rich mixtures - Fig. 5. These plateaus are observed experimentally and calculated values of quenching distances are also in good agreement with experimental data.

The mechanism of flame quenching in a dust-air mixture is similar to that in homogeneous mixtures, i.e., a feedback between flame speed and conductive heat losses. However, because of the diffusive mechanism of particle combustion, a number of significant differences exist. For example, the maximum temperature drop in a homogeneous gas flame before extinction due to the heat loss is known to be not greater than RT_{ad}^2/E , (ref. 12) (i.e., of the order of a few hundreds degrees). In the present case, due to the diffusive particle combustion, the reaction rate is not controlled by Arrhenius kinetics, and the drop of the average gas temperature in a dust flame before extinction is restricted only by the particle ignition temperature. Thus the temperature drop can easily reach more than a thousand degrees. The weak dependence of the particle diffusive combustion rate on temperature can also explain the phenomenon of the weak dependence of the flame speed on dust concentration in rich mixtures. The increase in the dust concentration above stoichiometric only intensifies, due to the larger specific dust surface area, the consumption of oxygen (burning rate). This can compensate for the drop in flame temperature in a broad region of dust concentrations and hence account for wide plateaus in the dependence of the flame speed and quenching distance on the fuel equivalence ratio (dust concentration) in rich mixtures.

This work is supported by the Canadian Space Agency under contract # 04SW.9F007-3-6017. The authors are very grateful to Glen Campbell (CSA) for his substantial assistance in the microgravity experiments.

References

1. Glassman, I., Davis K. A., Brezinsky, K.: *Twenty-Fourth Symposium (International) on Combustion*, The Combustion Institute, 1877-1882 (1992)
2. Green, F.T., and O'Donnell, J.E., *US Bureau of Mines, Report of Investigation OFR 4-83*, (1981).
3. Mason, W.E. and Saunders, K.V., *J. Phys. D: Appl. Phys.*, 8, 1674-1685 (1975)
4. Fuchs, N.A., *The Mechanics of Aerosols*, The Macmillan Company, NY, 1964
5. Ross, H., Facca L., Berlad, A.L., and Tangirala V., NASA Tech. Memo 101371 (1989).
6. Berlad, A.L., Ross, H., Facca, L., and Tangirala, V., *Combust. Flame* 82: 448- (1990).

7. Koboyashi, H., Ono, N., Okuyama, Y., Nioka, T., *Twenty-fifth Symposium (International) on Combustion*, The Combustion Institute, Pittsburgh, (1994).
8. Lee J.H.S., Peraldi, O., Knystautas, R., *2nd International Combustion Workshop*, Cleveland, Ohio, 1992.
9. Ballal, D.R., *Proc. R. Soc. London*. A385:21-51 (1983).
10. Ballal, D. R., *Proc. R. Soc. London*. A369:475-500 (1980).
11. Jarosinski, J., Lee, J.H., Knystautas, R., and Crowley, J.D., *Twenty-first Symposium (International) on Combustion*, The Combustion institute, p.p. 1917-1924 (1986)
12. Zeldovich Ya.B., Barenblatt G.I., Librovich V.D., Makhviladze, G.M., *The Mathematical Theory of Combustion and Explosions*, Consultants Bureau, NY, 1985.

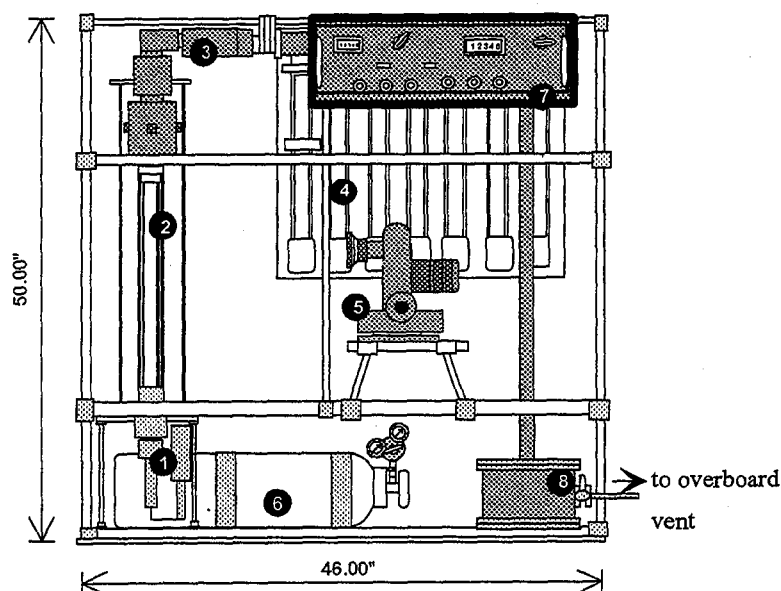


Fig. 1 Microgravity Experimental Package

- 1 - dispersion system, 2 - combustion tube assembly, 3 - flame arrester and filter,
 4 - combustion tube stock, 5 - high speed camera, 6 - compressed air bottle,
 7 - control panel, 8 - vacuum tank.

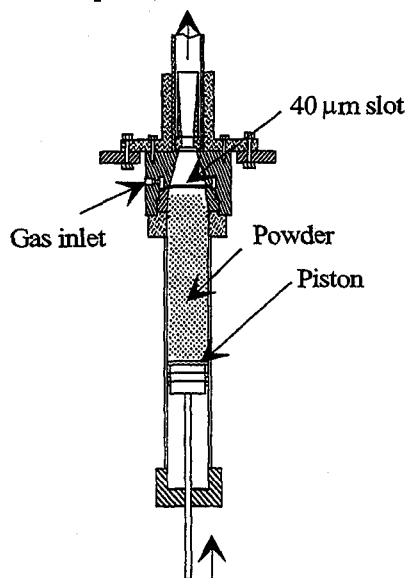


Fig. 2 Dust dispersion system

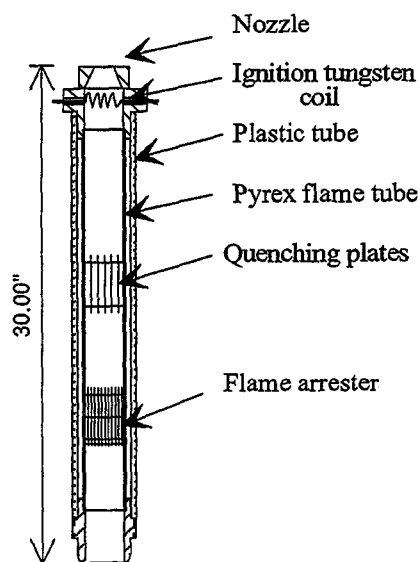


Fig. 3 Combustion tube assembly

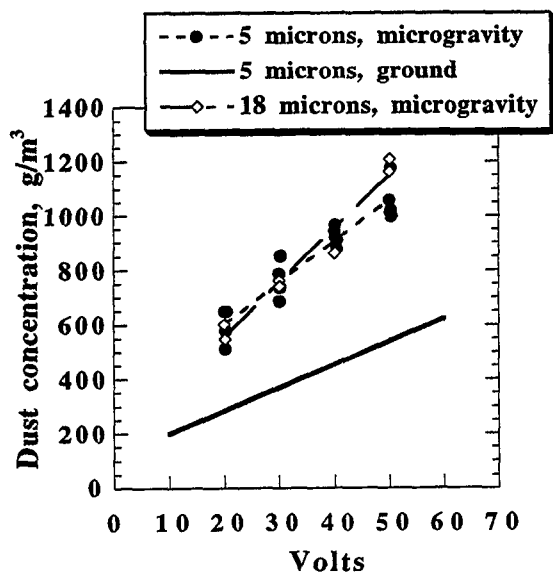


Fig. 4 Results of the dust dispersion system calibration on the ground and in microgravity.

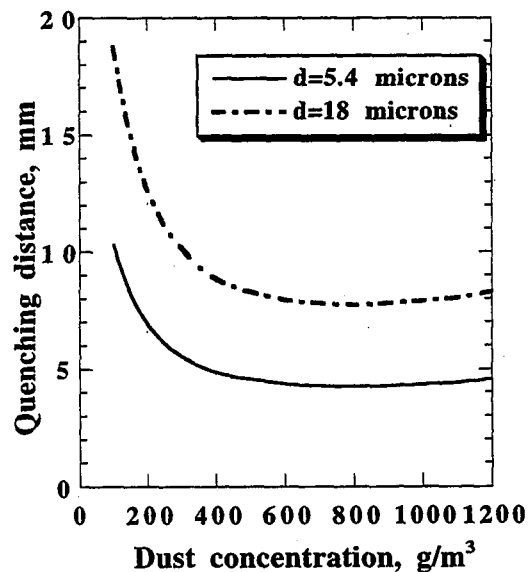


Fig. 5 Effect of aluminum dust concentration on quenching distance (theoretical results).

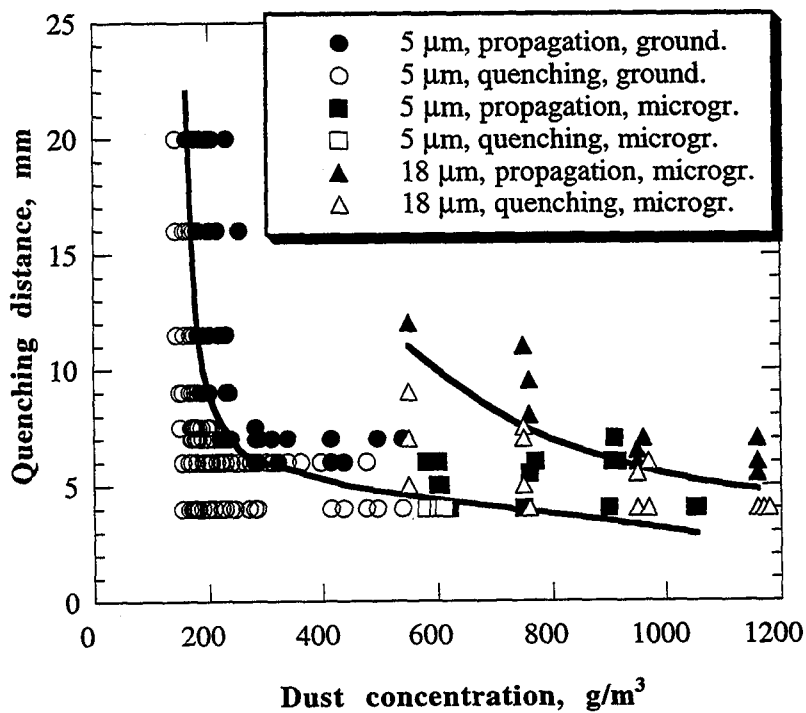


Fig. 6 Quenching distance as function of aluminum dust concentration . Ground-based and microgravity results.

Thermal Degradation of Polytetrafluoroethylene in Tube Reactors

J. Thomas McKinnon and H. M. Duan

*Department of Chemical Engineering and Petroleum Refining
Colorado School of Mines, Golden, CO 80401*

We have studied the thermal degradation of polytetrafluoroethylene (PTFE) in wet air, dry air and nitrogen gas at temperatures ranging from 310°C to 520°C. The principal gas product was tetrafluoroethylene (TFE). The nitrogen experiments yielded only TFE, but experiments in dry and wet air also produced several other minor gas products. The dry air experiments produced the most smoke and the least gas products, with the nitrogen experiments giving no smoke and the highest amounts of gas products. Wet air experiments gave intermediate results for smoke and gas formation. The rate of degradation in wet air showed an apparent activation energy of 103 kcal/mol. We also performed FTIR analyses of the smoke particulate, determining that the particulate formed in dry air is different than that formed in wet air.

Polytetrafluoroethylene (PTFE) is widely used by industry in such applications as electric insulation and coatings. The chemical and thermal stability of PTFE is the primary reason for its widespread use. However, once the PTFE starts to decompose at high temperatures, the gas products and the smoke particulate formed in the degradation are known to be very toxic [1], causing symptoms known as "fume fever" [2-4]. It is believed that much of the toxicity is due to ultrafine particles ($d < 100$ nm) from the degradation process. This problem becomes particularly serious on space craft where no venting is possible [5]. In this paper we present the results of the first part of our ongoing efforts to obtain an understanding of the effect of gravity on the toxicity of ultrafine particles and gas phase materials produced when fluorocarbon polymers are thermally degraded or burned. The motivation for the project is to provide a basic technical foundation on which policies for space craft health and safety with regard to fire and polymers can be formulated.

Figure 1 illustrates the experimental apparatus we constructed to study the pyrolysis and burning of PTFE. Nitrogen, dry air, or wet air flowed into the steel tube of 2.5 cm inner diameter and 80 cm long. The furnace and the Monel tube were preheated to a desired temperature before a glass boat containing 1 gram PTFE powers (Aldrich cat. No. 18,247-8) was put into the center of the furnace. The smoke produced in the reaction was collected by adsorption onto densely-packed glass wool. The gas products were directed to either a cryogenic trap, a mass spectrometer (MS) or a gas chromatograph (GC). The gas flow was ~90 ml/min. In the dry and wet air reaction atmospheres, there was sufficient oxygen in the reactor for the complete oxidation of PTFE.

The experimental temperatures ranged from 310°C to 520°C. Gas products were separated by a 30 meter HP-1 capillary column before entering the flame ionization detector. Figures 2a and 2b show the typical GC results for the gas products. There were major peaks at retention time 0.93 minutes. For reactions in the air atmospheres, several

small peaks were also observed at longer retention times.

Figure 3 shows the major peaks (peaks with retention time 0.93 minutes) for reactions at different temperatures. The areas of the peaks are listed in Table 1. For temperatures lower than 370°C, peak areas are negligible. At temperatures higher than about 370°C, the peak start to be evident. Figure 4a shows the peak area A as a function of the temperature. In figure 4b, a plot of $\log A$ vs. $1000/T$, the data points form a straight line. The slope of the line corresponds to an apparent activation energy of 103 kcal/mol. The value is close, perhaps merely coincidentally, to the bond dissociation energy of a C-F bond.

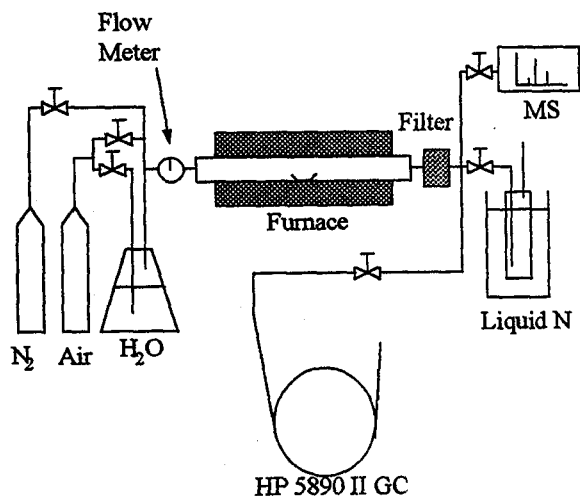


Figure 1: Experimental set up.

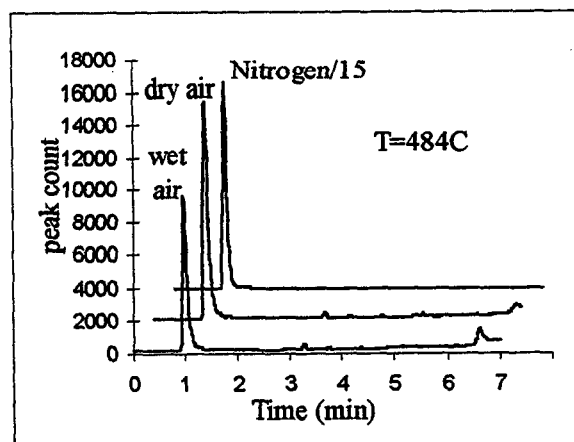


Figure 2a: Gas chromatograms of the gas products. Samples were taken 40 minutes after the PTFE powders were put into the reactor.

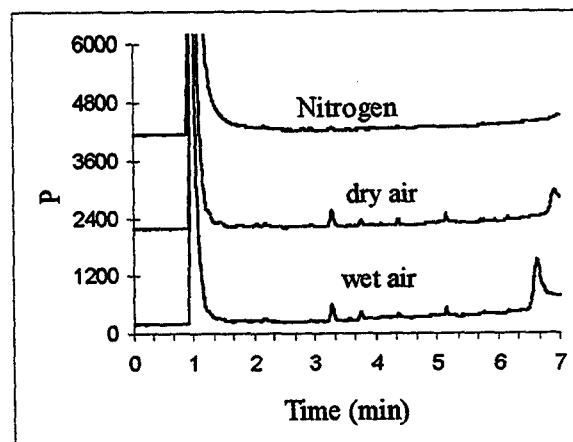


Figure 2b: Peaks other than the major peak are very small. T=484°C.

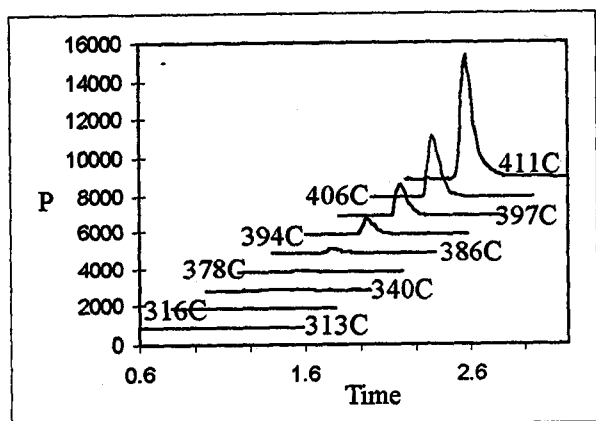


Figure 3: Temperature dependency of the major peaks.

T(°C)	313	316	340	378
Area	trace	trace	trace	497

	386	394	397	406	411
	1308	4418	8945	16863	36503

Table 1: Areas of the major peak at various temperatures.

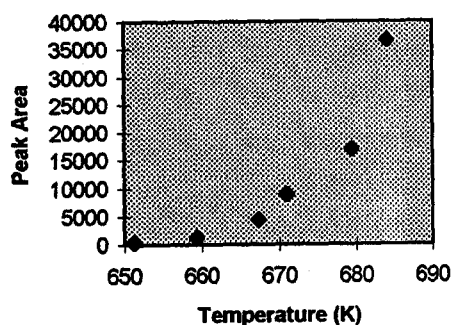


Figure 4a: Temperature dependency of the peak areas.

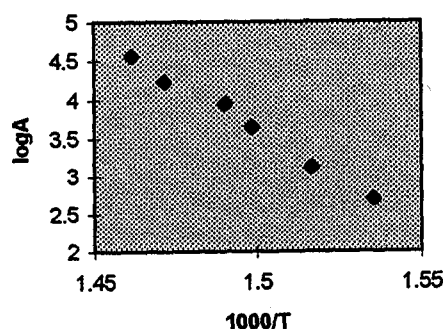


Figure 4b: The data point follows Arrhenius relation with $E_a=103\text{kcal/mol}$.

Gas products from reactions in wet air were analyzed by mass spectrometry. Figure 5 shows one of the spectra. There is no peak above 100 amu, the mass of C_2F_4 molecule. So the concentrations of chemicals having fragments heavier than 100 amu (such as C_3F_4 , C_2F_6) are negligible. Table 2 lists the mass peaks (less those peaks contributed by air). All fragments in Table 2 correspond to fragments of C_2F_4 . We therefore believe that the gas appearing at 0.93 minutes in the gas chromatograms is C_2F_4 .

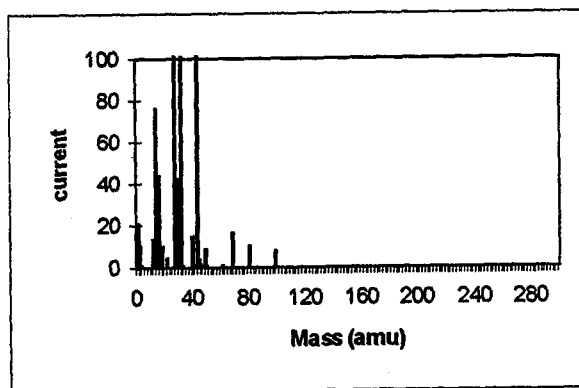


Figure 5: MS of the gas products. No mass heavier than 100 amu was seen ($T=510^\circ\text{C}$).

fragment	C	CF	CF_2	CF_3	C_2F_3	C_2F_4
mass	12	31	50	69	81	100
$1000 \cdot I/I(31)$	325	1000	205	405	250	195

Table 2: The fragments of the gas products.

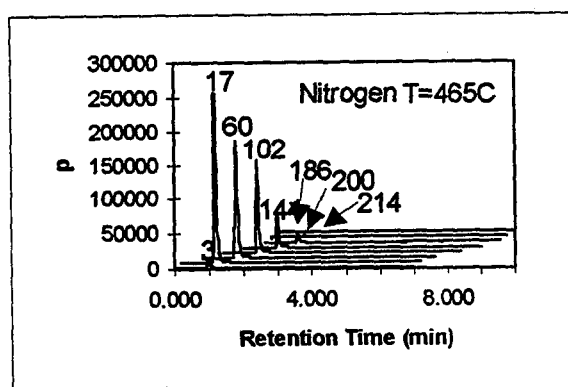


Figure 6a: Chromatogram of the emission from reaction of 1 gram PTFE powder in pure nitrogen. The numbers denote the minutes after the sample was put into the reactor.

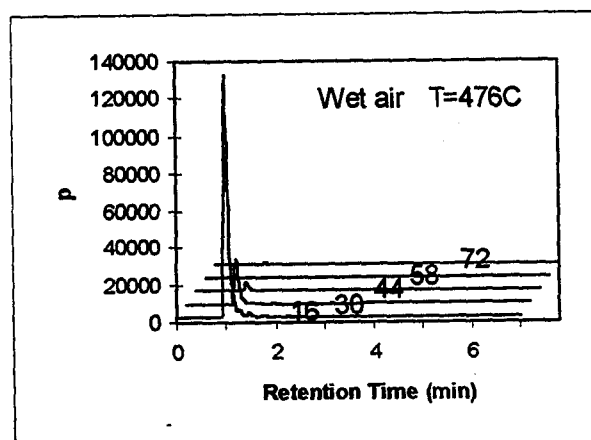


Figure 6b: Chromatogram of the emission from reaction of 1 gram PTFE powder in wet air. The numbers denote the minutes after the sample was put into the reactor

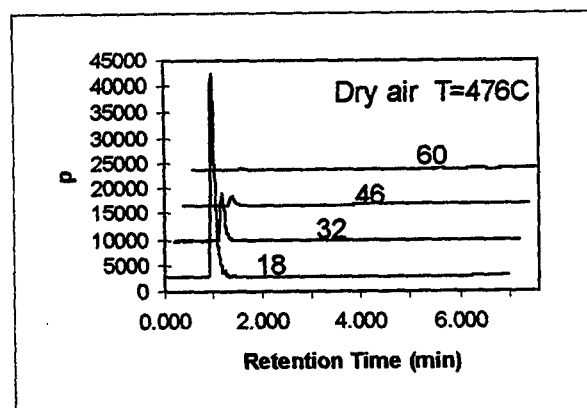


Figure 6c: Chromatogram of the emission from reaction of 1 gram PTFE powder in dry air. The numbers denote the minutes after the sample was put into the reactor

The formation of C_2F_4 was very sensitive to the reaction atmosphere. In pure nitrogen gas, no smoke was formed and C_2F_4 was the only degradation product. The reaction lasted longer and the concentration of C_2F_4 gas in the emission was higher for the nitrogen environment than for the wet air or dry air environments (see figures 6a, 6b, and 6c). Degradation in dry air yielded the least C_2F_4 gas, but the most smoke. Visual observations indicated that the amount of smoke formed by reactions in dry air was much higher than that formed in wet air.

Figures 7a, 7b, and 7c show the results of FTIR analyses of pure PTFE and the smoke powders formed by reactions in wet and dry air atmospheres. The three IR spectra are clearly different. Pure PTFE powder has two relatively sharp peaks around 1212 cm^{-1} and 1156 cm^{-1} . The IR spectrum for powder formed by reaction in wet air has a major peak at about 1101 cm^{-1} , with several smaller peaks located at 1637 cm^{-1} , 1421 cm^{-1} , 934 cm^{-1} , and 805 cm^{-1} . The IR spectrum for the powder formed by reaction in dry air has very large peaks at 1101 cm^{-1} and 768 cm^{-1} . These results show that the chemical formula of the powder formed by

reaction in wet air is different from that of the powder formed by reaction in dry air.

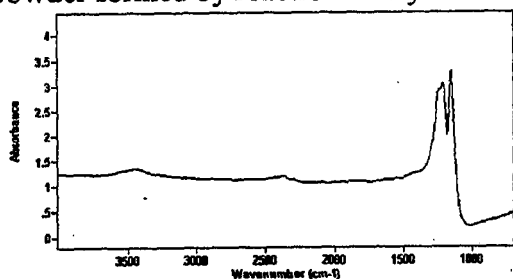


Figure 7a: IR spectrum of pure PTFE powder.

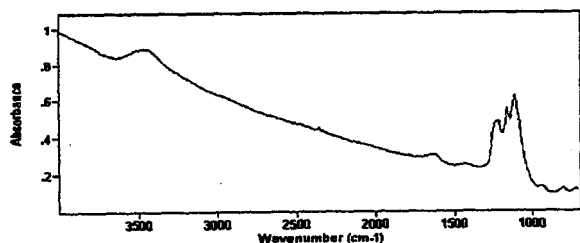


Figure 7b: IR spectrum of powder formed by PTFE reaction in wet air.

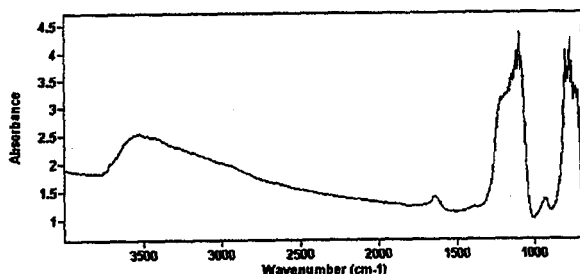


Figure 7c: IR spectrum of powder formed by PTFE reaction in dry air.

In summary, we have studied the thermal degradation of PTFE in pure nitrogen gas, wet air, and dry air at temperatures ranging from 310°C to 510°C. The primary gas product is C_2F_4 . The reaction rate follows the Arrhenius formula $r = Ae^{-E_a/RT}$, with $E_a \sim 103$ kcal/mol. The nitrogen experiments yielded the highest C_2F_4 concentrations, the longest reaction times, and no observable smoke. The dry air experiments gave the

lowest C_2F_4 concentrations, the shortest reaction times, and large amounts of smoke. Wet air experiments gave results intermediate to the nitrogen and dry air experiments. IR spectra indicate differences between smoke formed in wet air and dry air environments.

We are in the process of obtaining more information on the mechanisms of the formation of smoke. Various experiments, including measurements of smoke concentration, reaction at higher temperature, TEM and SEM experiments, C_nF_{2n+2} ($n=6, 7$, and 8) thermal degradation and computer simulations will take place in the near future.

We thank NASA for supporting this research under contract number NAG3-1628.

References:

1. B. B. Baker and M. A. Kaiser, *Analytical Chemistry* **63**, 79A-83A (1991)
2. G. Oberdoster, J. Ferin, Gelein and R. S. Soderholm, *Environ. Health Perspectives*, (1991)
3. G. Oberdoster, J. Ferin, J. Finkelstein, P. Wade and N. Corson, *J. Aerosol Sci.* **21**, 384-387 (1990)
4. G. Oberdoster, J. Ferin, J. Finkelstein, R. Baggs, D. M. Stavert and B. E. Lehnert, 22nd International Conference on Environ. Systems, Seattle, WA, July 1992, Paper 921388, SAE International, Warrendale, PA
5. H. D. Ross, Overview of NASA's microgravity combustion science and fire safety program. 2nd International Microgravity Workshop, Sept. 15-17, 1992, NASA CP-10113.

FILTRATION COMBUSTION: SMOLDERING AND SHS

Bernard J. Matkowsky ¹
Northwestern University
Evanston, Illinois

Introduction: Filtration Combustion

Smolder waves (see ref. 1) and SHS (self-propagating high-temperature synthesis) waves (see refs. 2,3) are both examples of combustion waves propagating in porous media. When delivery of reactants through the pores to the reaction site is an important aspect of the process, it is referred to as filtration combustion. The two types of filtration combustion have a similar mathematical formulation, describing the ignition, propagation and extinction of combustion waves in porous media. The goal in each case, however, is different. In smoldering the desired goal is to prevent propagation, whereas in SHS the goal is to insure propagation of the combustion wave, leading to the synthesis of desired products. In addition, the scales in the two areas of application may well differ. For example, smoldering generally occurs at a relatively low temperature and with a smaller propagation velocity than SHS filtration combustion waves. Nevertheless, the two areas of application have much in common, so that mechanisms learned about in one application can be used to advantage in the other. In this paper we discuss recent results in the areas of filtration combustion.

Smolder waves

Smoldering combustion is important for the study of fire safety. Smoldering itself can cause damage, its products are toxic and it can also lead to the more dangerous gas phase combustion which corresponds to faster propagation at higher temperatures. Examples of porous substances that can sustain smoldering combustion are cotton, dusts, polyurethane foams, thermal insulation materials, wood, etc. Smolder sometimes occurs on the surface of a sample and sometimes in its interior. We describe results obtained as well as plans for future studies of smolder combustion through a porous sample in a series of five papers, which include two papers to appear in *Combustion and Flame* on forced smolder, corresponding to (i) forward and (ii) reverse, or opposed flow filtration, in which gas is forced into the sample in the same direction as, or opposite to, the direction of propagation of the smolder wave, respectively. We have also begun work on gravity induced buoyant (iii) downward smolder, and (iv) upward smolder, and we plan to consider (v) smolder in microgravity. Finally, we plan to consider the problem of surface smolder.

We considered a simple one-step reaction in which solid and gaseous reactants produce solid and gaseous products and release heat. This one-step reaction represents the rate limiting step in a more complex reaction scheme. Specifically, smolder is generally thought to proceed in two stages. In the first stage the solid fuel decomposes through endothermic pyrolysis, releasing gases and solid char as products. The char then oxidizes in a highly exothermic process and is converted to ash. Our reaction scheme models the second stage so that we capture the heat producing mechanism. We believe that the first stage, which somewhat increases the width of the front where heat is absorbed, has only a minor qualitative impact on solution structure. Heat transfer between the solid and the gas is assumed

¹NASA Grant NAG3-1608, beginning 6-1-94.

to be sufficiently fast that the gas and solid phases are in local thermodynamic equilibrium, so that a single temperature model is used to describe both the solid and gaseous phases. The solid phase is considered to be stationary and nondeforming. The activation energy is considered to be large so that the reaction occurs in a narrow region. The sample is assumed to be highly porous so that the characteristic length scale of pressure variations is much larger than that for thermal variations. In addition, the ambient pressure is assumed to be larger than the hydrostatic pressure drop over the length of the sample as is generally the case in normal gravity.

The model consists of equations describing balances of energy, gas mass, oxygen mass, solid reactant mass, and gas momentum using Darcy's law, as well as an equation of state, and appropriate boundary and initial conditions. The incoming gas flux m^i and the concentration Y^i of the oxidizer in the gas are prescribed at the open end of the sample. We consider the adiabatic problem which does not account for heat loss to the environment.

For forward smolder we found two different structures possible, referred to as a reaction leading structure and a reaction trailing structure, respectively. The temperature profile for a reaction leading solution exhibits three regions in which the temperature is essentially constant. The sample is cool ahead of the reaction site, hot immediately behind the reaction zone, and cool again where the sample is cooled by the incoming gas. The initial and final temperatures need not be the same if the incoming gas is at a different temperature than the initial sample. Connecting these regions of constant temperature are two transition layers in which the temperature changes rapidly. These two layers, which in general move at different velocities, are referred to as the combustion layer and the heat transfer layer. In reaction leading solution structures the combustion layer precedes the heat transfer layer. In fact, there are two types of reaction leading structure depending on the oxygen mass flux $Y^i m^i$: stoichiometric and kinetically controlled solutions. Reaction leading stoichiometric solutions occur when the rate of oxygen supply is slow compared to the reaction rate and the reaction must wait for oxygen to arrive in order to proceed. This mode of propagation can be identified by the linear dependence of the smolder speed on $Y^i m^i$. When the supply of oxygen is sufficiently high that the rate of consumption limits the speed of propagation the solution is said to be kinetically controlled. Smolder velocity is determined by reaction kinetics. Increasing Y^i affects the smolder velocity weakly through the reaction rate increase due to a higher concentration of oxygen at the reaction site. Varying m^i , however, affects the smolder velocity by changing the burning temperature, which has a large effect on the propagation velocity.

In addition to the reaction leading structure, we also described a reaction trailing structure, which is similar to the reaction leading structure, except that the heat transfer layer now precedes the combustion layer. Incoming inert gas carries the heat rapidly from the combustion layer into the unburned region where it preheats the solid reactant. As in the reaction leading structure, there are two types of solution with the reaction trailing structure. The reaction trailing stoichiometric solution is similar to the reaction leading stoichiometric solution in that the smolder velocity is proportional to the oxygen influx $Y^i m^i$, and the burning temperature is affected by Y^i and not by m^i . However, the structure of the wave is very different in that all the heat from the reaction is carried ahead of the reaction front. Kinetically controlled reaction trailing structures occur when the incoming gas absorbs heat sufficiently fast that the solid is cooled before it is completely converted. This solution differs from the reaction leading kinetically controlled solution in its dependence on the oxygen influx because the final depth of conversion of solid and thus the total heat released in the reaction is determined by the oxygen influx. The incoming gas and in particular the incoming oxygen affect the smolder velocity and the burning temperature. Solutions with reaction leading and trailing structures were found in refs. 4,5. Those results are extended in our work. We describe regions in parameter space where each type of structure is to be expected. In particular, we find that in smoldering, reaction trailing stoichiometric structures are generally encountered.

We found that both reaction leading and trailing structures in forced forward smolder exhibit super-adiabatic burning temperatures, which are achieved because the energy released in the reaction remains in the localized high temperature region between the two layers and thus travels with the wave. In the reaction leading structure, we think of the gas extracting heat from the hot solid product, and carrying it toward the reaction site. In this sense, the gas can be said to be preheated, i.e. the

gas is heated to the burning temperature before it reaches the combustion layer. In the reaction trailing structure, the gas, which is heated while passing through the reaction zone, heats the solid reactant so that the solid reactant can be said to be preheated. The magnitude of the super-adiabatic effect is determined by the relative velocities of the heat transfer and combustion layers. Reaction trailing (leading) structure solutions occur for Y^i less (greater) than a critical value, and for a given Y^i , kinetically controlled (stoichiometric) solutions occur for large (small) incoming mass flux. We compare our results to the experimental works of Ohlemiller and Lucca (ref. 6) who observe reaction trailing stoichiometric structures, Torero et. al. (ref. 7) who observe reaction leading stoichiometric structures, and Voice and Wild (ref. 8) who observe the transition from one structure to the other by varying the oxygen fraction in the incoming gas flux.

For the forced opposed flow smolder problem we find two types of solutions. Gas deficient solutions, in which the oxidizer is consumed in the reaction and solid conversion is incomplete, and solid deficient solutions, in which conversion of the solid reactant is complete. The most interesting results for opposed flow smolder involve extinction limits. The extinction limits considered are adiabatic extinction limits in the sense that they are not due to heat losses to the external environment. Rather, extinction is due to heat transferred from the reaction to the gas passing through it. Extinction occurs when the heat lost to the inert exceeds a critical value. We compute an explicit expression for the extinction limit in terms of the parameters of the problem.

The model predicts that in the environments where smoldering is usually studied, i.e. at moderate oxygen concentrations and with reaction rates which do not vary too strongly with the degree of conversion, extinction occurs when solid conversion is complete. Extinction can occur within the solid deficient regime or at stoichiometry which corresponds to the limit of the solid deficient regime. In some cases, when the reaction rate exhibits a strong kinetic dependence on the solid fuel, extinction can occur in the gas deficient regime. We compare our results to the experimental works of Ohlemiller and Lucca (ref. 6) who observe gas deficient smolder waves as well as dependencies on parameters in agreement with ours, and Torero et. al. (ref. 9) who appear to observe solid deficient extinction, though some points remain to be resolved in this comparison. We also compare our results to Dosanjh et. al. (ref. 10) whose theoretical work we extend.

We next initiated studies of smolder in a gravitational field. We consider gravity induced buoyant downward and upward smolder, which correspond to ignition at the top and bottom of the sample, respectively. In contrast to the problem of forced smolder, in which the gas influx is prescribed, here the gas influx is determined by the combustion process itself. Specifically, in the downward configuration, gravity causes the hot gases at and above the reaction zone to rise and exit the top of the sample, so that cool fresh gases are pulled in through the bottom. Downward buoyant smolder is thus similar in configuration to the forced opposed flow smolder configuration, described above. Buoyancy driven smolder is a slower process than forced smolder. Thus, in contrast to forced smolder, heat losses can no longer be neglected. We therefore determine the structure of the combustion wave in both the adiabatic and nonadiabatic cases. In the nonadiabatic case the temperature profile exhibits a preheat region in which the temperature rises from its initial value to the burning temperature, followed by a high temperature region at the burning temperature, followed by a cooling region in which the temperature decays due to heat losses. In the adiabatic case there is no cooling region. Only if the heat losses are sufficiently strong so that the high temperature region is localized to lie entirely within the sample, can there possibly be a traveling wave solution which propagates with constant velocity, unchanged in shape. In the adiabatic case or if heat losses are not sufficiently strong for localization, the combustion wave is quasi-steady or slowly varying. We determine the characteristics of the quasi-steady wave and of the traveling wave, when it exists. As in forced opposed flow smolder we expect extinction if the gas influx is sufficiently strong. We derive explicit extinction criteria in terms of the parameters of the problem, including the dependence on gravity, in particular. The strength of the gas influx depends on the combustion process through the density and temperature of the gas in the sample. There is an interesting feedback mechanism which arises since the filtration strength determines the burning temperature, which in turn determines the buoyant filtration strength. The problem of ignition is more interesting and more difficult to achieve for buoyant downward smolder than for, say, forced

smolder, since the amount of heat required for the former exceeds that for the latter. Specifically, in addition to the heat necessary to preheat the sample, extra heat must be supplied to the wave in the initial stages of propagation, to insure buoyant convection of the product gases, which induces the buoyancy driven flow of fresh gas to the reaction site. The upward smolder configuration can be similarly seen to resemble the forced forward smolder configuration. Thus, we expect to study the possible structures of the combustion wave, in terms of the parameters of the problem, including, in particular, the effect of gravity. Finally, we will investigate smolder in microgravity. In this case, after an initial period in which reactant gas is consumed in the reaction zone and inert gas accumulates there, gas no longer enters the sample by convection, but rather by diffusion. That is, we no longer deal with forced smolder or gravity induced forcing, but rather with diffusion controlled smolder. We therefore expect that the combustion velocity will be significantly smaller. Furthermore, in contrast to the faster forced processes, heat losses to the environment are expected to be significant. By controlling which end of the sample is open or closed we can arrange for forward or reverse smolder. We will study the propagation of, and see if there are extinction criteria, for diffusion controlled smolder.

SHS Waves

We consider filtration combustion of a porous solid sample, consisting of a finely ground powder mixture of reactants. The sample is ignited at one end and a high temperature thermal wave, having a frontal structure, propagates through the sample converting reactants to products. The SHS technology appears to enjoy a number of advantages over the conventional technology, in which the sample is placed in a furnace and "baked" until it is "well done". The advantages include shorter synthesis times, greater economy, in that the internal energy of the reactions is employed rather than the costly external energy of the furnace, purer products, simpler equipment and no intrinsic limitation on the size of the sample to be synthesized, as exists in the conventional technology.

The SHS process is often accompanied by melting of one or more components of either the initial mixture or of the products, either intermediate or final. This is due to the considerable exothermicity and high combustion temperatures for most mixtures. Melting with subsequent spreading of the melt increases the surface-to-surface contact between reactants which significantly promotes the reaction.

We formulated and analyzed a model describing the combustion of porous condensed materials in which a reactant melts and spreads through the pores of the sample (ref. 11). This is the situation that occurs in the experiments of Feng et.al. (ref. 12). Our model describes the cases when the melt either fills all the pores or when some gas remains in the pores. In each case the melt occupies a prescribed volume fraction of the mixture. We employed both analytical and numerical methods to find uniformly propagating combustion waves, to analyze their stability and to determine behavior in the instability region. One of the conclusions of this analysis is that the flow of the melted component can result in nonuniform composition of the product. Unlike models which do not take into account the relative motion of the components, this model exhibits a dependence of the structure of the product on the mode of propagation of the combustion front, in accord with experimental observations. We also consider combustion waves in which the liquid melt does not occupy the entire product region, but rather, only a part of the product adjacent to the reaction front. The remaining part of the product remains porous and contains no liquid. This situation was observed in experiments (refs. 12,13).

We are also considering the case that the melting is so appreciable that the porous structure is destroyed and we have a liquid bath of reactant *A* containing a suspension of particles *B*, either liquid or solid. That is, we study the structure of a combustion wave propagating under the influence of a gravitational field, through a heterogeneous powder mixture which initially forms a hard matrix. The matrix is destroyed by the propagating combustion wave, due, e.g., to melting of some of the components of the mixture. Thus, a liquid bath is formed, in which processes such as heat and mass transfer as well as chemical reactions determine the structure of the combustion wave, its propagation velocity and the composition of the reaction product. The liquid bath may contain a suspension of particles, either liquid or solid, which may either be reactive or inert. This is the situation that occurs in the experiments of Lee et. al. (ref. 14). Combustion waves in such condensed systems are

distinguished from condensed combustion systems in which the matrix is preserved, and which are referred to as "solid flames". Here we deal with so-called "liquid flames". Whether or not combustion waves are able to propagate in such systems depends not only on the characteristics of the initial components, such as their melting temperatures, but also on the experimental conditions such as initial temperature, heat exchange with the environment, etc.

Earlier studies of the combustion of powder mixtures considered the mixture to be either a nonporous solid or a porous solid with no flow through its pores. Later models considered porous solids with gas or liquid flowing through its pores. In the latter class of models there is a single unknown velocity, that of the gas or liquid flowing through the pores, which is to be determined during the course of solving the relevant model. In the model considered here, destruction of the porous matrix allows for two unknown velocities, that of the liquid bath and that of the particles suspended in it, each of which must be determined during the course of solution of the model. Thus, there exists the possibility of relative motion of the individual components of the mixture. This may result in separation of the components under the influence of an external force field, such as gravity, if the densities of the components differ from one another. Separation is opposed by a friction force. The phenomenon of separation does not occur in the relatively well studied case of "solid flames". We discuss the possible consequences of separation. We observe that separation is more pronounced when (i) the viscosity of the bath is small, (ii) the difference in the densities of the species forming the bath and the particles suspended in it, is large. In addition, since the gravitational force is proportional to the weight of the particles, and therefore to their volume, while the friction force is proportional to the particle's surface area, separation is expected to be large if the dimensions of the suspended particles are large. Separation may be easily observed if the mixture is placed in a centrifuge. In contrast, microgravity conditions are appropriate if the relative motion of the components is undesirable and should be suppressed.

To gain an understanding of the phenomena associated with relative motion and separation during the propagation of the combustion wave, topics which heretofore have not been considered, we formulate and analyze a relatively simple mathematical model of "liquid flame" combustion in a gravitational force field. We describe uniformly propagating combustion waves and determine explicit expressions for the combustion temperature and velocity as well as profiles for temperature and composition. For a certain range of parameters we find multiplicity of solutions. We also study nonsteady waves whose dynamics are determined by the relationship between the characteristic times t_R of reaction and t_S of separation of the components due to gravity. In addition, we find shock type solutions which exhibit jumps in composition, thus describing "settling" of components.

Finally, we have initiated a study of deformation of samples in SHS systems in a gravitational field. It is often desired to produce materials which are very dense (very low porosity), or alternatively to produce highly porous materials. Clearly, it is better to achieve densification (expansion) of the sample during the combustion synthesis process itself, rather than by post processing the sample. To control this process we previously introduced a model (ref. 15) in which the porosity of the sample is not fixed, as in all other models, but rather, the porosity varies dynamically as the combustion synthesis front propagates. We will now consider deformation in the presence of a gravitational field. In particular, we wish to explain the experimental observations of Shteinberg et. al. (ref. 16) and Feng et. al. (ref. 17) who considered samples (i) oriented with gravity, (ii) oriented perpendicular to gravity (resulting in a lower gravitational force), and (iii) in microgravity. They observed that increased (decreased) gravity acts to densify (expand) the sample. To accurately describe their results, and to determine parameter dependencies it will be necessary to modify our previous model to fit the experimental conditions.

References

1. Ohlemiller, T.J. *Modeling of smoldering combustion propagation*, Prog. Energy Comb. Sci. 11 (1985), pp. 277-310.

2. Merzhanov, A.G. *Self-propagating high-temperature synthesis: twenty years of search and findings*, In: Combustion and Plasma Synthesis of High-Temperature Materials, Munir, Z.A., Holt, J.B. (Eds.), VCH, 1990, pp. 1-53.
3. Munir, Z.A., and Anselmi-Tamburini, U. *Self-propagating exothermic reactions: the synthesis of high-temperature materials by combustion*, Material Science Reports, A Review Journal **3** (1989), pp. 277-365.
4. Aldushin, A.P., and Seplyarsky, B.S. *Propagation of waves of exothermal reaction in porous medium during gas blow-through*, Soviet Physics Doklady **23** (1978), pp. 483-485.
5. Aldushin, A.P., and Seplyarsky, B.S. *Inversion of the structure of a combustion wave in a porous medium during blow-through of gas*, Soviet Physics Doklady **24** (1979), pp. 928-930.
6. Ohlemiller, T.J., and Lucca, D.A. *An experimental comparison of forward and reverse smolder propagation in permeable fuel beds*, Combustion and Flame **54** (1983), pp. 131-147.
7. Torero, J.L., Kitano, M., and Fernandez-Pello, A.C. *Forward smoldering of polyurethane foam*, Presented at the Combustion Institute, Western States Section, Fall Meeting, Boulder Co., March 1991, Paper 91-27.
8. Voice, E.W., and Wild, R. *Importance of heat transfer and combustion in sintering*, Iron and Coal Trades Review, **175** (1957), pp. 841-850.
9. Torero, J.L., Fernandez-Pello, A.C., and Kitano, M. *Opposed forced flow smoldering of polyurethane foam*, Comb. Sci. and Tech. **91** (1993), pp. 95-117.
10. Dosanjh, S.S., Pagni, P.J., and Fernandez-Pello, A.C. *Forced cocurrent smoldering combustion*, Combustion and Flame **68** (1987), pp. 131-142.
11. Aldushin, A.P., Matkowsky, B.J., Shkadinsky, K.G., Shkadinskaya, G.V., and Volpert, V.A. *Combustion of porous samples with melting and flow of reactants*, Comb. Sci. and Tech. **99** (1994), pp. 313-343.
12. Feng, H.J., Moore, J.J., and Wirth, D.C. *Combustion synthesis of ceramic-metal composite materials: the $TiC-Al_2O_3-Al$ system*, Metallurgical Transactions A **23** (1992), pp. 2373-2379.
13. Feng, H.J., Moore, J.J., and Wirth, D.C. *Combustion synthesis of $TiB_2-Al_2O_3-Al$ composite materials*, In: Developments in Ceramic and Metal-Matrix Composites, Upadhyay, K (Ed.) The Minerals, Metals and Materials Society, 1991, pp. 219-239.
14. Lee, J.H.S., and Goroshin, S. *SHS processing of ZnS in microgravity*, Proc. Third IUMS Int'l. Conf. on Adv. Materials (Tokyo 1993), Eds. Masumoto, T., Doyama, M., Kuribayashi, K., and Kishi, T., (1994), pp. 653-658.
15. Shkadinsky, K.G., Shkadinskaya, G.V., Matkowsky, B.J., and Volpert, V.A. *Self-contraction or expansion in combustion synthesis of porous materials*, Comb. Sci. and Tech. **88** (1992), pp. 271-292.
16. Shteinberg, A.S., Shcherbakov, V.A. Martynov, V.V., Mukhoyan, M.Z., and Merzhanov A.G. *Self-propagating high-temperature synthesis of high-porosity materials under weightlessness*, Soviet Physics Doklady **36** (1991), pp. 385-387.
17. Feng, H.J., Moore, J.J., and Wirth, D.C. *The combustion synthesis of $B_4C-Al_2O_3-Al$ composite materials*, Mat. Res. Soc. Symp. Proc. **249** (1992), pp. 529-535.

COMBUSTION AND STRUCTURE FORMATION IN SHS PROCESSES UNDER MICROGRAVITY CONDITIONS (SHS Plans for Microgravity Experiments)

A.G. Merzhanov
Institute of Structural Macrokinetics (ISMAN)
Russian Academy of Sciences
Chernogolovka, Moscow region, 142432 Russia

This paper outlines ISMAN suggestions for the joint NASA-RSA project "Combustion and Structure formation in SHS Processes under Microgravity Conditions". The basic ideas of this work naturally follow from our almost 30-year experience in the field of SHS [refs. 1 and 2]. As a matter of fact, we have already obtained some results in the following two directions closely related to the microgravity problem.

One is the studies on SHS processes in the field of centrifugal forces conducted by the group of Prof. Yuxhvid [refs. 3 and 4]. These studies aimed at the intensification of gravity-sensitive SHS processes in multicomponent highly caloric systems forming melts at high overloads (up to 2000 g). In other words, these studies had the objectives that are inverse to those in the microgravity studies. Basically, the following results have been obtained. Combustion velocity U was found to increase with increasing overload $n=a/g$ (Fig. 1). This was explained by the gravity-induced impregnation of the melt formed in the combustion zone into the mixture of starting reactants. This intensifies the longitudinal mass transfer in the combustion wave, thus elevating the burning velocity. Combustion yields two- or multicomponent melts. Within these melts, the gravity-sensitive processes also take place. In the gravitation field, heavy products precipitate whereas light fractions come to the surface: the so-called phase separation takes place. In experiments, the extent of phase separation η_{ph} is normally measured (Fig. 2). In some systems, two ultimate limiting cases can be observed -- complete phase separation and its complete absence. Within the intermediate range, the functionally gradient structures are formed. Overload intensifies the process of phase separation (Fig. 3). In the absence of phase separation, the cast composite materials are formed. The higher is the difference between the density of constituent components, the more difficult is to obtain cast composite materials even under the conditions of normal gravity. In view of this, microgravity may turn out to be the only tool to obtain these materials (Fig. 4).

The second group of results directly relates to the microgravity problem and the project under consideration. These experiments played the important role in establishing links between SHS and microgravity. In 1990, Prof. Shteinberg and his coworkers [ref. 5] carried out the first SHS experiments on

the board of the plane during its parabolic flight: the microgravity conditions were sustained for 30 s. The experiment aimed at obtaining a foam material and its retention in the absence of gravity-induced damage of foam. The data obtained were promising: under the microgravity conditions, we obtained the foam titanium carbide with a porosity of 97% (Fig.5). Another important result is that homogeneous porous materials can be obtained only under the microgravity conditions (Fig.6). This was the only our work on microgravity. However, it turned out to be the first one that stimulated further interest in SHS microgravity studies.

Of great importance is a proper selection of the systems to be studied. This can predetermine a success of the project as a whole. For this reason, preliminary screening of numerous known systems seems to be necessary to perform. Some systems that may turn out suitable are listed in Table I, although some others can be found in the course of further studies. In investigating the processes of foam formation, the use will be made of gasifying agents.

Table 1. Systems to be studied

Synthesis of foam materials	Synthesis of fine-grained composites
foam carbides: Ti-C; Zr-C; Ti-Ni-C; Ti-Fe-C foam borides: Ti-B; Zr-B; Ti-Ni-B; Ti-Fe-B foam silicides: Ti-Si foam nitrides: multicomponent mixtures yielding nitrides foam intermetallics: Ni-Al; Co-Al; Ni-Co-Al; Ti-Ni-C; Ni-Al-B-Ti foam composites: $\text{Cr}_2\text{O}_3\text{-TiO}_2\text{-Fe}_2\text{O}_3\text{-Al-C}$; FeO-Al-C ; NiO	$\text{W}_2\text{O}_3\text{-Al}$; $\text{MoO}_3\text{-Al}$; $\text{Nb}_2\text{O}_3\text{-Al}$; Ni-Al-Ti-C; FeO-Al-C ; $\text{Cr}_2\text{O}_3\text{-TiO}_2\text{-Fe}_2\text{O}_3\text{-Al-C}$

The experimental setup for first experiments is presented in Fig.7. The main point here is the angle between the vectors of combustion velocity and force of gravity. The most important cases: (1) these vectors coincide, (2) the vectors are opposite, and (3) they are oriented normally. In spite of the fact that the project has not been officially approved, we have carried out some preliminary experiments. (Table 2).

Table 2. Same preliminary results

System	$U \downarrow g \downarrow$		$U \uparrow g \downarrow$		$U \perp g \downarrow$	
	$U, \text{cm/s}$	$\frac{\Delta l}{l}$	$U, \text{cm/s}$	$\frac{\Delta l}{l}$	$U, \text{cm/s}$	$\frac{\Delta l}{l}$
Ti+C	0.60	6	0.60	7	0.60	4
$\text{Fe}_2\text{O}_3\text{+Al+Al}_2\text{O}_3$	0.45	2	—	—	0.20	1
Ni+Al	3.20	1	3.20	1	2.20	1

For the Ti+C system, the sample elongation was found to be orientation-dependent. The maximum (7-fold) elongation was achieved in the case of opposite orientation. At normal orientation, the elongation never exceeded a value of four.

Another possibility is the dependence of combustion velocity on the angle between the U and g vectors found in the $\text{Fe}_2\text{O}_3\text{+Al+Al}_2\text{O}_3$ system. Burning velocity is largest when the angle is equal to zero and smoothly decrease with increasing angle. Quite different behavior is observed for the Ni+Al system. Minimum burning velocity is obtained when sample is oriented horizontally. Even these preliminary results seem to be fairly promising

Fig.8 shows the experimental setup for the study of combustion mechanisms under high overload ($n = 2-10$). This is a centrifugal machine (up to $10g$) specially designed for a given project. Its manufacturing will get started immediately after real financial support. Special attention was paid to provide a possibility of experiments at both positive and negative overloads. Centrifugal studies are needed for the extrapolation of the data to be obtained to the microgravity conditions. Our approach – the use of positive and negative overloads – allows us to reduce the extrapolation problem to the interpolation one, thus making the solution more reliable. An expected result is illustrated in Fig. 9. It cannot be ruled out that, under the antigravity conditions (negative overload), SHS may turn out promising and competitive in solving some special problems.

Expected behavior of various SHS systems at gravity and microgravity conditions is illustrated in Table 3. Some effects have already been discussed above.

Table 3. Behavior of SHS systems at microgravity conditions (preliminary data)

Characterization of SHS system	Behavior at normal gravity	Expected behavior at microgravity conditions	Microgravity applications
1. Solid flame	Weak effects at high overload	No effects	–
2. Melted reactants, solid product	Effect of centrifugal impregnation	Purely conductive combustion of melts	–
3. Melted reactants, liquid (melted) multiphase product	The same as for Item 2. Coalescence of drops, phase separation in melt Melt shaping	The same as for Item 2. No drop coalescence and phase separation in melt, formation of fine-grained materials Controlled shape formation (by the forces of surface tension), spheroid products	Producing of cast fine-grained heterogeneous materials Producing of cast spheres
4. Partial gasification of components with melt in the combustion zone; added gasifying agents	Sample elongation, pore formation	Formation of highly porous materials	Synthesis of foam materials on the spacecraft board for <i>in situ</i> applications

In this context, we have selected the following two problems: (1) the formation of pores and foam and (2) the formation of fine-grained pore-free materials upon crystallization of multicomponent melts as well as the related microgravity effects.

Objectives of the Project:

1. Fundamental studies

- Dynamics and mechanism of the gravity, "antigravity", and microgravity effects on the combustion and structure formation in SHS systems during the formation of pores and foam in the combustion wave
- Formation of fine-grained structures upon crystallization of multicomponent melts

2. Research and Development

- Synthesis of foam materials (borides, carbides, nitrides, silicides, intermetallics, and composites) on the spacecraft board for *in situ* applications
- Preparation of cast fine-grained composites

Principal Stages

1st Stage: Laboratory-Scale Experiments

- 1.1. Selection of the systems to be studied by screening
- 1.2. The effects of the charge composition, charge structure, and environment on the SHS parameters under the conditions of gravity ($U \downarrow g \downarrow$; $U \uparrow g \downarrow$; $U \leftarrow g \downarrow$)
- 1.3. Centrifugal studies at $n=a/g=\pm 10$ followed by the interpolation to microgravity conditions
- 1.4. Model experiments with elementary heterogeneous cells
- 1.5. Mathematical modeling of combustion and structure formation at microgravity conditions
- 1.6. Detailed studies on the properties and structure of selected SHS products prepared under optimum conditions
- 1.7. Designing the reactors for space experiments

2nd Stage: Experiments at Artificial Microgravity -- to check the data obtained at Stage 1.

3rd Stage: Experiments at Natural Microgravity (on the board of spacecraft)

In conclusion, I would like to note that we found the points of mutual interest with Prof. Moore of the Colorado School of Mines in the SHS+microgravity problem and agreed to unify our efforts. Partially, the above tasks are to be solved within the frame of another project that has no special financial support. I believe that this cooperation will be useful for the project under consideration. I would like to note that we are open for cooperation with all those who are interested in.

Acknowledgments

The author is grateful to Dr. H.Ross for his kind invitation for me to come to this workshop, Dr. A.S.Mukas'yan for his help in preparing the materials of the project and this communication, Dr. Yu.B.Scheck for his translating the text into English, and Mrs. O.B.Trushnikova for her performing the artwork.

References

1. Merzhanov A.G., and Borovinskaya I.P. Self-propagating high-temperature synthesis of inorganic compounds. Dokl. Akad. Nauk SSSR, vol.204, no.2, 1972, pp.366-369.
2. Merzhanov A.G. Self-Propagating High-Temperature Synthesis: Twenty Years of Search and Finding. In: Combustion and Plasma Synthesis of High-Temperature Materials, ed. Z.Munir and J.B.Holt, VCH Publ.Inc., New York, 1990, pp. 1-53.
3. Yuxhvid V.I. Modifications of SHS Processes. Pure Appl. Chem., vol.64, no. 6, 1992, pp. 965-97.
4. Merzhanov A.G., and Yuxhvid V.I. The Self-Propagating High-Temperature Synthesis in the Field of Centrifugal Forces, Proc. I US-Japanese Workshop on Combustion Synthesis. January 11-12, Tsukuba. National Research Institute for Metals, Tokyo, Japan, 1990, pp. 1-21.
5. Shteinberg A.S., Shcherbakov V.P., Martynov V.M., Mukhoyan M.Z., and Merzhanov A.G. SHS of Highly Porous Materials at Zero Gravity Conditions, Soviet Physics Doklady, vol.36, no.5, 1991, pp.385-387.

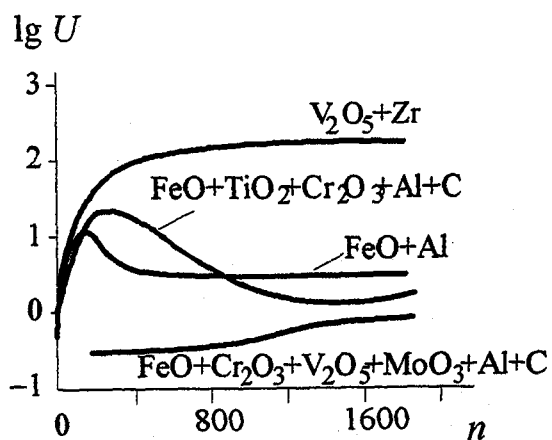


Figure 1. Combustion of SHS systems of gravity overload (some results)

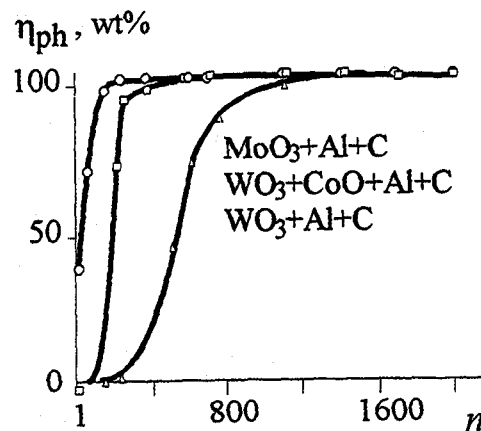


Figure 2. Effects of overload on phase separation

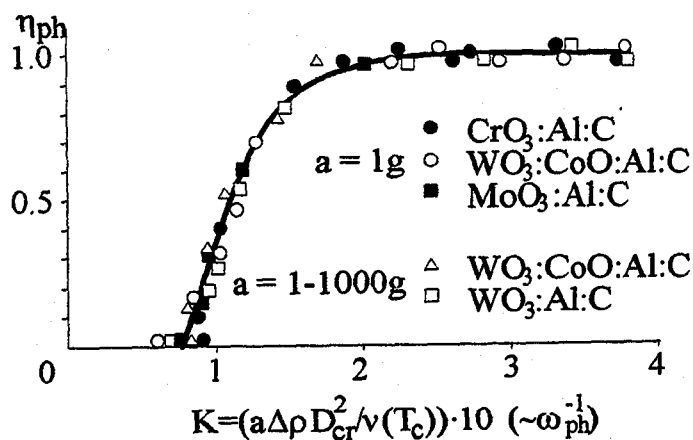


Figure 3. Generalized curve of phase separation

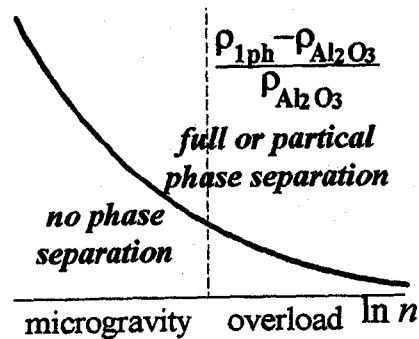


Figure 4. Expected microgravity effect

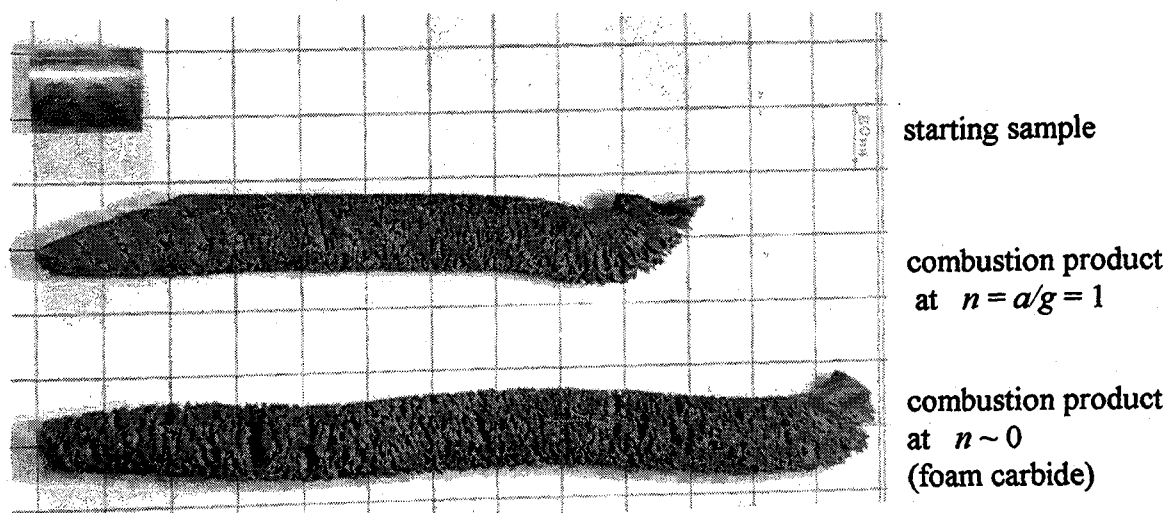


Figure 5. Photograph of samples.

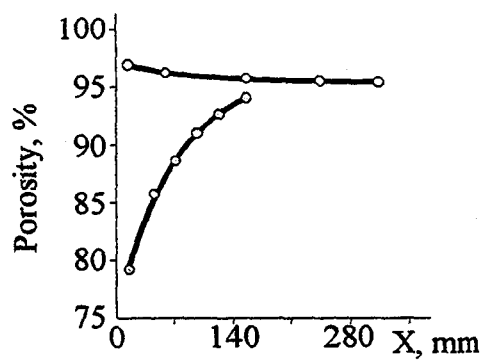


Figure 6. Porosity distribution along the sample length after combustion

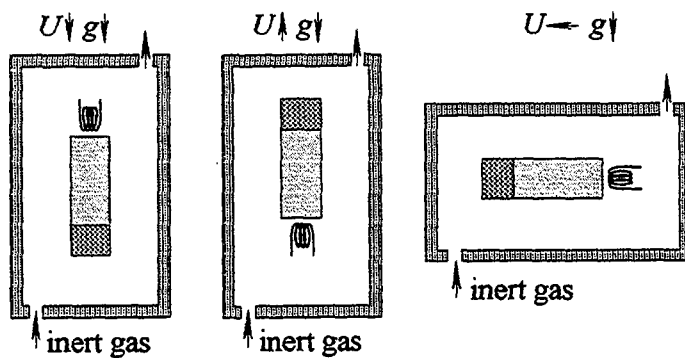


Figure 7. Experimental setup for testing the system to be studied

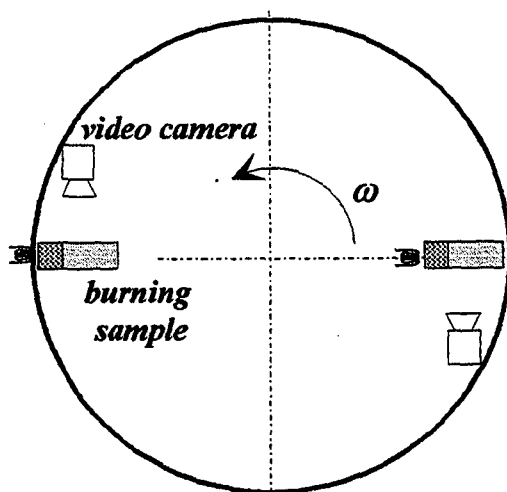


Figure 8. Schematic diagram of centrifugal experiment

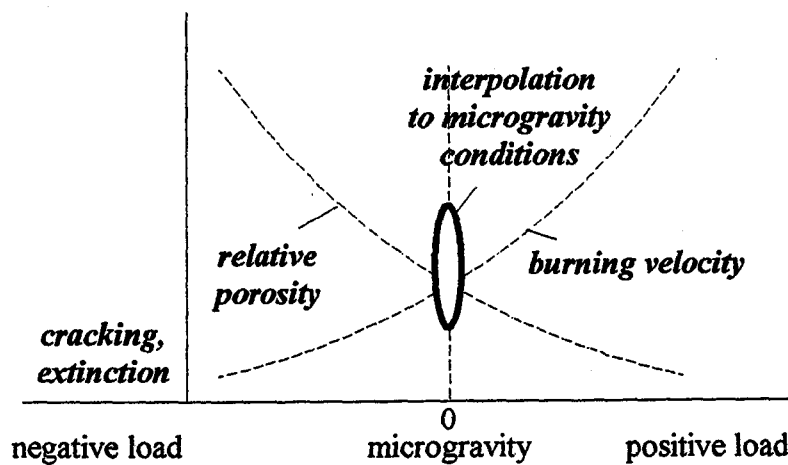


Figure 9. Expected results

COMBUSTION SYNTHESIS OF CERAMIC-METAL COMPOSITE MATERIALS IN MICROGRAVITY

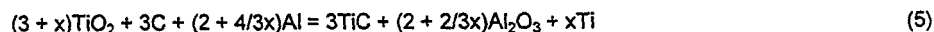
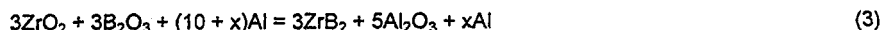
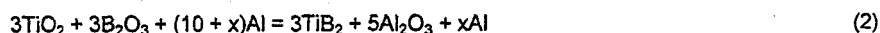
John Moore, Colorado School of Mines
Grants: NCC3-215, (8/1/91 to 18/1/95), and
NAG3-1698, (1/19/95 to 1/18/98)

Introduction:

Combustion synthesis¹⁻³, self-propagating high temperature synthesis (SHS) or reactive synthesis provides an attractive alternative to conventional methods of producing advanced materials since this technology is based on the ability of highly exothermic reactions to be self sustaining and, therefore, energetically efficient. The exothermic SHS reaction is initiated at the ignition temperature, T_{ig} , and generates heat which is manifested in a maximum or combustion temperature, T_c , which can exceed 3000K. Such high combustion temperatures are capable of melting and/or volatilizing reactant and product species and, therefore, present an opportunity for producing structure and property modification and control through liquid-solid, vapor-liquid-solid, and vapor-solid transformations

Experimental Reaction Systems

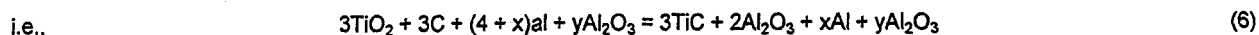
Several model ceramic-metal composite SHS reaction systems have been investigated in which an excess amount of metal, e.g., (xAl), is used both as a reductant in the SHS reaction and as the metal component of the ceramic-metal composite.⁴ These model reaction systems are given below:



These reaction systems were selected on the basis of generating a liquid (e.g. Al) and/or a gas (e.g., B_2O_3 gas) at, and ahead of, the reaction front. The main focus of this research is to investigate the effect of gravity on these reactant species and on the resultant composite microstructure and properties.

The research concerned with conducting these reactions in the propagating mode was presented at the Second International Microgravity Combustion Workshop. Therefore, this paper will provide the main conclusions and observations of the research work conducted over the past two years.

Reaction systems (1) and (4) were examined in more detail under 1g, microgravity ($\pm 0.2\text{g}$) and 2g (in the NASA Lear Jet) under the propagating mode of combustion synthesis. A modification of reaction (1) was also investigated using the combined simultaneous combustion plus pressing (SC-HP) process under 1g conditions in order to establish the criteria for producing dense ceramic-metal composites⁵ in which Al_2O_3 is used as a diluent to control T_c and therefore, product microstructure,



Applying a consolidating load of 33 MPa as soon as the exotherm was recorded on the thermocouple in the die, and maintained for ten minutes at 1600°C, resulted in significantly improved densities compared with those produced in the propagating mode without pressing (Figure 1). The compressive strengths achieved in these composites are given in Figure 2 for reaction (6) as a function of x when y = 0 and as a function of y when x = 0 respectively, and the corresponding microstructures are presented in Figure 3.

The large plate of Al_2O_3 observed in Figure 3(a) indicates that the combustion temperature, when x = 0, exceeded the melting point of Al_2O_3 (2050°C). The excellent distribution of a fine Al network between the fine TiC and Al_2O_3 particles [Figure 3(b)] is clearly evident in the $3\text{TiC}-2\text{Al}_2\text{O}_3-4\text{Al}$ (x = 4, y=0) ceramic-metal composite. Increasing xAl has decreased T_{ad} to below 2050°C producing fine $1\mu\text{m}-3\mu\text{m}$ Al_2O_3 particles. Increasing the relative density of the composite from 83% to 96% produced a considerable increase in compressive strength and decrease in scatter of the data (Figure 2), even though the volume fraction of the soft ductile aluminum has increased. The terraced appearance of the fractured surface of the samples tested in the compression tests [Figure 3(c)] indicates a potential for increased toughness. A K_{1c} fracture toughness value of $9\text{MPa m}^{1/2}$ and a modulus of rupture (MOR) of 320 Mpa have recently been achieved in these TiC- Al_2O_3 ceramic composites. A more detailed examination of this SC-HP approach for producing ceramic-matrix composites has been provided elsewhere.⁵

Conducting reactions (1) and (6) under microgravity conditions produced a much more uniform distribution of porosity and excess Al, (Figure 4).⁸

The compressive strengths of the $3\text{Ti}-2\text{Al}_2\text{O}_3-x\text{Ti}$ for reaction (5) were found to increase with increase in excess Ti ($x\text{Ti}$), (Figure 4).

Another variation of the same approach is presented by reaction (4) in which the combustion temperature (1500-1900°C) was sufficient to generate a large volume of high pressure (>1 atm.) B_2O_3 gas, but very little, if any Al gas. This high pressure, high volume B_2O_3 gas is able to push or expand the reactant materials ahead of the combustion front in the vertical direction, thereby, producing an expanded or foamed ceramic-metal composite which exhibited $\geq 65\%$ uniform porosity and an expansion of 230% ($x = 0\text{ Al}$) and 210% ($x = 3\text{ Al}$) (Figure 5). Conducting these reactions under microgravity in the NASA Lear Jet resulted in expansion of over 300% while an expansion of only 150% was achieved at 2g, (Figure 5).

In a separate investigation, reaction (2) was investigated using the propagating mode under 1g and microgravity and also the elemental SHS reaction system:



In each of these reaction systems, a higher T_c and, therefore, larger product grain sizes were obtained under microgravity conditions compared with 1g. The minimization of heat losses when conducting SHS reactions under microgravity conditions is thought to be the cause for these higher T_c values.

Summary and Conclusions

This research has clearly demonstrated that gravity can substantially influence combustion synthesis (SHS) reactions with respect to the control of the micro- and macrostructure, and therefore, the properties of the combustion synthesized materials. This conclusion has been particularly strengthened when liquid and/or gaseous species are generated at, and/or ahead of, the propagating SHS reaction front. Some examples that have recently been observed of the effect of gravity on the control of SHS reactions are given below.

Subjecting a liquid phase, generated by the SHS reaction, to gravity-driven fluid flow has been clearly shown to result in severe segregation of the product phases. Conducting the same reaction in a microgravity environment, i.e., NASA Lear Jet, has resulted in a minimization of segregation of the liquid phase and a more uniform distribution of the synthesized product phases. This will be particularly important in the combustion synthesis of metal-matrix composites in which a slurry, consisting of fine, solid, ceramic particles, is generated in a large volume of liquid metal.

The minimization of heat losses, when conducting SHS reactions under microgravity environments, has resulted in a maximum combustion temperature, T_c , that is much closer to that predicted by adiabatic conditions than when conducting the reaction under normal 1g conditions. The higher T_c has resulted in an increased grain size of the synthesized materials. Therefore, variation of gravity may provide a means by which product grain size can be controlled in SHS reactions.

The generation of a large volume of gaseous specie(s) at, and/or ahead of, the reaction front has resulted in the formation of expanded or foamed ceramic materials. This expansion has been found to increase when a highly fluid liquid is simultaneously generated together with the gas, so the gas can be readily transported through the fluid liquid, establishing a highly porous network. Conducting the SHS reaction in the propagating mode of combustion generally results in an expansion of the material in the vertical direction, e.g., 250-300%, with very little expansion in the lateral direction. However, conducting the SHS reaction in the simultaneous combustion (or thermal explosion) mode has resulted in near equal three dimensional expansion of the product material. Conducting these SHS reactions under microgravity conditions in the propagating mode has resulted in increased expansions, e.g., 350-400%, in the vertical direction, while an expansion of only 150% was achieved when conducting the same SHS reaction under 2g conditions in the NASA Lear Jet. Therefore, variation of gravitational forces may provide a practical means of controlling porosity, surface area, and expansion in this type of SHS reaction.

There is likely to be an increased demand in the future for such expanded or foamed ceramic and composite materials in such applications as filters, catalyst support materials, precursors for ceramic-metal composites, and ultra lightweight structural materials. The latter material may find particular applications as future space station materials. The mechanical and physical properties of these foamed materials are essentially unknown and may provide interesting new combinations of material properties, especially if the distribution and morphology of the porosity, micro- and macrostructures can be controlled.

Future Research Program

Although the limited research work conducted to date on the effect of gravity on SHS reactions has indicated some interesting trends, a more fundamental, multidisciplinary, and interactive research program is needed in order to clearly identify the controlling mechanisms by which gravitational forces can be used to advantage in the control of combustion synthesis reactions that could be used in the production of new advanced materials. Such a program is currently being planned at CSM.

There are two combustion synthesis research programs currently funded by NASA at CSM. One of these programs (CSM¹) is funded through the Microgravity-Combustion Science Program with Dr. J.J. Moore as the Principal Investigator and Dr. Suleyman Gokoglu (NASA Lewis Research Center) as the NASA Program Manager. This research program is concerned with developing a fundamental understanding of the role of gravity in synthesizing (a) uniformly porous ceramic composites and (b) dense metal-matrix composites. The second program (CSM²) is funded through the Microgravity-Materials Science Program with Dr. J.J. Moore and Dr. D.W. Readey as Co-Principal Investigators and Mr. Tom Glasgow (NASA Lewis Research Center) as the NASA Program Manager. This research program is concerned with developing a fundamental understanding of the role of gravity on SHS reactions conducted in inert and reactive gas conditions, the effect of gas pressure and the effect of the density of small amounts of liquids generated at, and/or ahead of, the propagating SHS reaction front.

A joint NASA-CSM-ISMAN (Russia) research proposal has been submitted in the recent NASA-RSA initiative and is aimed at pooling the existing expertise and resources from these three sources to establish a fundamental research program. The overall combustion synthesis research program will, therefore, couple the two NASA Microgravity Sciences research programs at CSM with those proposed by ISMAN in the NASA-RSA proposal.

Also, a joint research program between CSM and Guigne International Ltd. (GIL) in Newfoundland has recently been established on the NASA-Microgravity-Combustion Science Program (CSM¹) in which the containerless processing facilities of GIL and the SHS facilities and expertise of CSM have been coupled to investigate containerless microgravity combustion synthesis reactions. GIL, under the direction of their president, Dr. Jacques Guigne, has recently developed a new, unique acoustic levitation system capable of levitating 80 gram, golf ball size, samples. Therefore, the joint interaction and cooperation between NASA-CSM-ISMAN-GIL will provide considerable leveraging of the total research program.

A further interaction on these NASA research programs has also been established between the CSM group and that of Professor Matkowsky's NASA funded group at Northwestern University. Dr. Matkowsky's research group will use CSM's data in the development of their mathematical models. In addition, Dr. Mark Linne, a professor at CSM with an expertise in heat transfer modeling, will be part of the CSM team that will establish heat transfer experiments and modeling of selected SHS reactions under 1g, low and high gravity conditions.

References

1. Z.A. Munir and U. Anselmi-Tamburini, "Self-Propagating Exothermic Reactions: The Synthesis of High-Temperature Materials by Combustion", Mater. Sci. Report 3 (1989), 227-365.
2. H.C. Yi and J.J. Moore, "Self-Propagating, High Temperature (Combustion) Synthesis (SHS) of Powder Compacted Materials", J. Mater. Sci., 25 (1990), 1159.
3. J.J. Moore, "An Examination of the Thermochemistry of Combustion Synthesis Reactions", Processing and Fabrication of Advanced Materials, III, (Tms, Warrendale, PA, 1994) Ed. V.A. Ravi, T.S. Srivatsan and J.J. Moore, 813-817.
4. H.J. Feng, K.R. Hunter and J.J. Moore, "Combustion Synthesis of Ceramic and Metal-Matrix Composites", J. Mat. Synth. Proc., 2-2 (1994), 71-86.
5. H.J. Feng and J.J. Moore, "In-Situ Combustion Synthesis of Dense Ceramic and Ceramic-Metal Interpenetrating Phase Composites", Submitted to Met. and Mat. Trans.
6. H.J. Feng, J.J. Moore and D.G. Wirth, "Combustion Synthesis of Ceramic-Metal Composite Materials: The $ZrB_2-Al_2O_3-Al$ System", Int. J. Self Prop. High Temp. Synth. 1, 2 (1992), 228-283.
7. N.R. Perkins, J.J. Moore and D.W. Readey, "Synergistic Effects of Coupled Combustion Synthesis and Vapor Phase Transport in the Synthesis of Advanced Materials", Advanced Synthesis of Engineered Structural Materials, (ASM Int. Materials, Park, OH, 1992), Ed. J.J. Moore, E.J. Lavernia, F.H. Froes, 7-23.
8. K.R. Hunter and J.J. Moore, "The Effect of Gravity on the Combustion Synthesis of Ceramic and Ceramic-Metal Composites", Accepted for publication in J. Mat. Synth. and Proc.

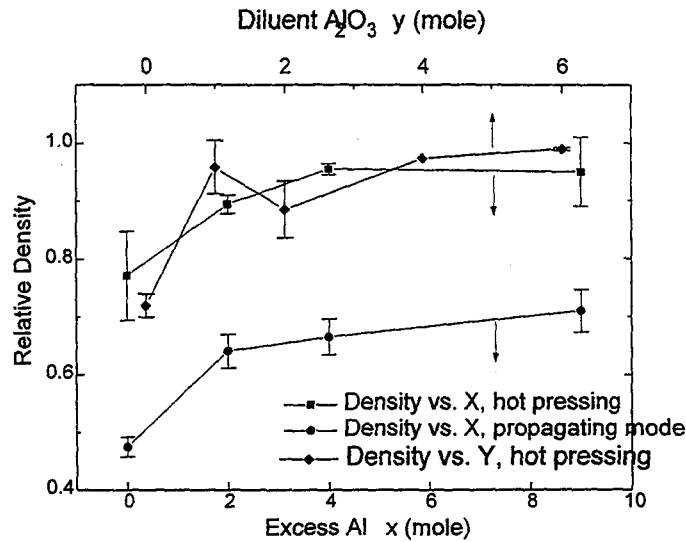


Figure 1 - The effect of excess Al (xAl) with no Al_2O_3 diluent ($y = 0$), (■), and Al_2O_3 diluent ($y\text{Al}_2\text{O}_3$) with no excess Al ($x = 0$), (◆), on the relative density of the $\text{TiC-Al}_2\text{O}_3\text{-Al}$ ceramic-metal composite using the simultaneous combustion mode and a pressure of 24.8 MPa (3600 psi) applied to the reaction system (6) in a graphite die for ten minutes and maintained at 1600°C once the SHS reaction had been initiated. These data are compared with similar data obtained for the SHS reaction (1) conducted in the propagating mode without pressure, (●).

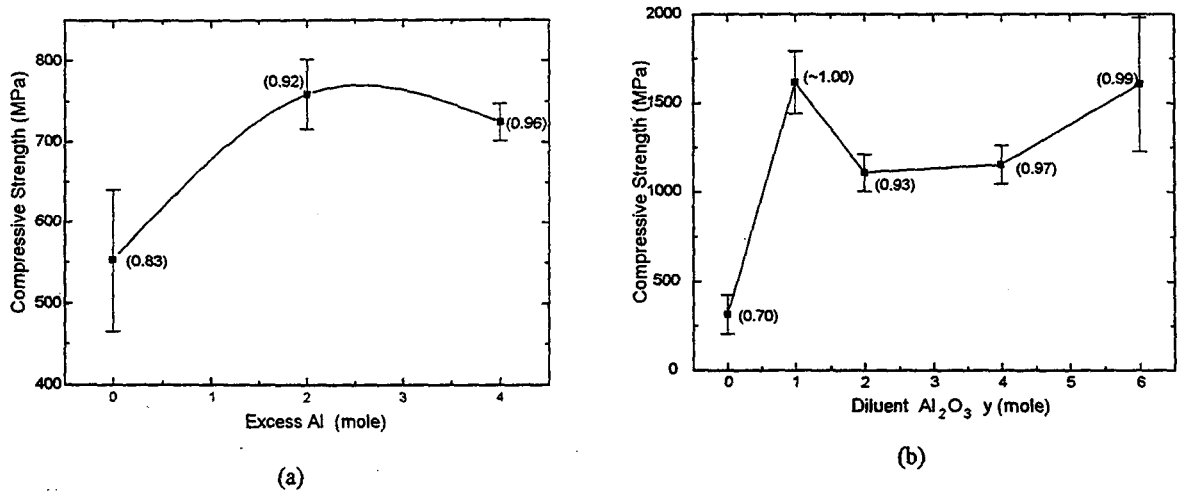


Figure 2 - (a) The Effect of excess Al on compressive strength for $\text{TiC-Al}_2\text{O}_3\text{-Al}$ ceramic-metal composites produced by simultaneous combustion synthesis and pressing in a graphite die, for reaction (6) for $y = 0$. (b) The effect of excess Al_2O_3 (diluent) in reaction system (6) when $x = 0$, (no excess Al) on the compressive strength for $\text{TiC-Al}_2\text{O}_3$ composites produced by simultaneous combustion synthesis and pressing in a graphite die. The figures in parentheses indicate the relative density of the samples tested.

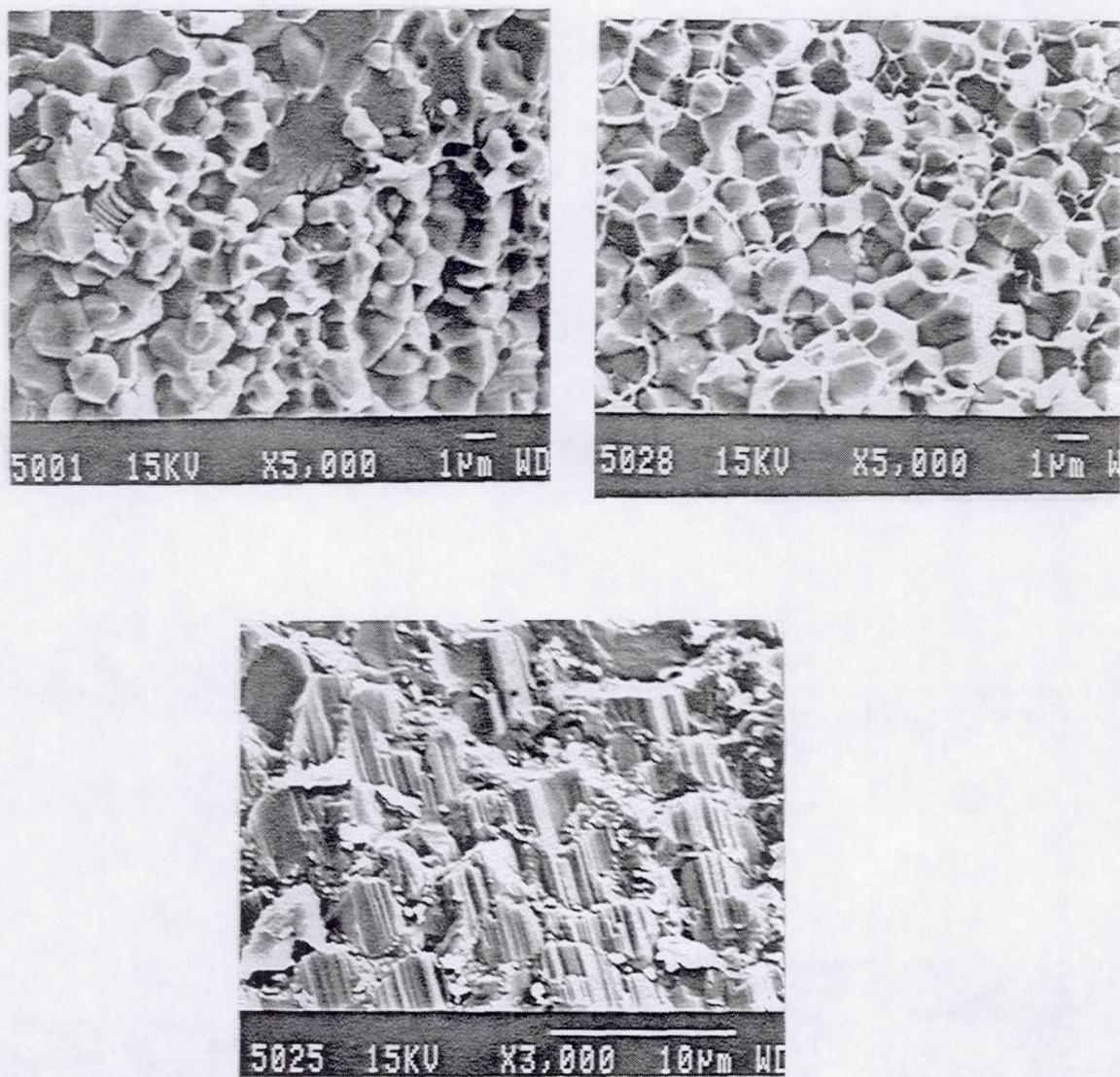


Figure 3 - SEM photomicrograph of (a) $3\text{TiC}-2\text{Al}_2\text{O}_3$ ($x = 0$, $y = 0$). Note the large plate of Al_2O_3 at top center, (b) $3\text{TiC}-2\text{Al}_2\text{O}_3-4\text{Al}$ ($x = 4$, $y = 0$), (c) fractured surface of $3\text{TiC}-2\text{Al}_2\text{O}_3-4\text{Al}$ ($x = 4$, $y = 0$) samples tested in compression test.

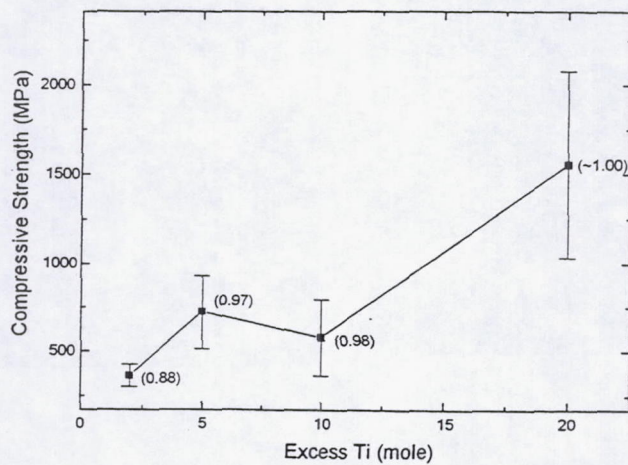


Figure 4 - Effect of excess Ti (xTi) and relative composite densities (figures in parenthesis) on compressive strengths of composites produced from reaction (5).

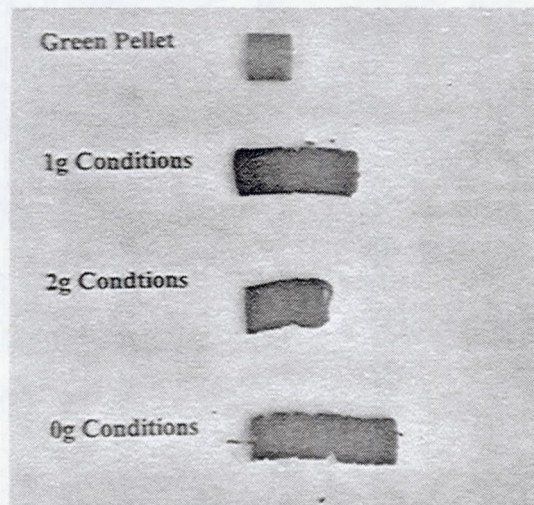
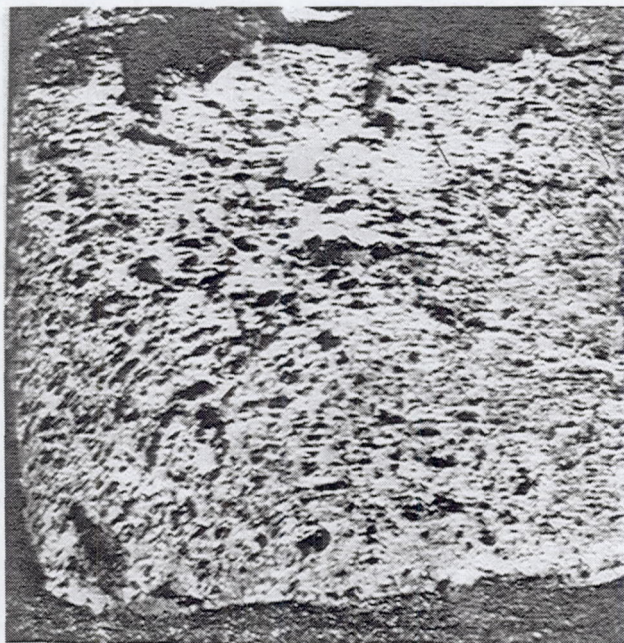


Figure 5 - Photographs of green pellet for reaction (4) with reaction stoichiometry $x = 0$, and reacted samples of this same green pellet conducted under microgravity (0.01g), normal gravity (1g) and elevated gravity (2g) conditions.



(a)



(b)

Figure 6 - Microstructures of products for reaction (1) for a reaction stoichiometry $x = 9Al$: (a) reacted in propagating mode under microgravity conditions; (b) reacted under propagating mode under normal gravity conditions. Note the increased Al segregation at bottom of Figure 6(b), indicated by arrow.

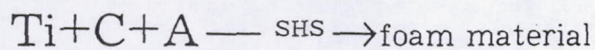
Self-Propagating High-Temperature Synthesis of High Porosity Foam Materials in Microgravity

Alexander S. Shteinberg
and

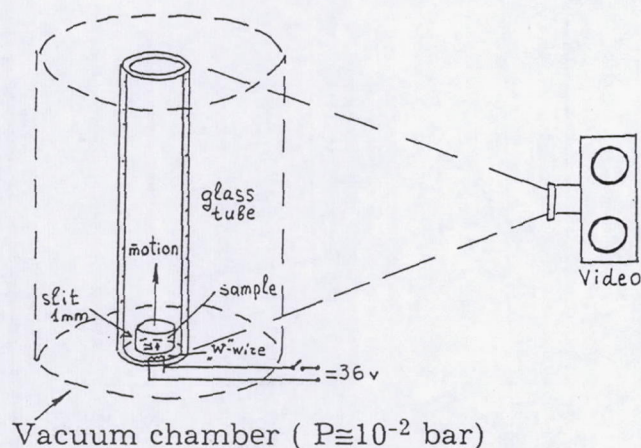
Vladimir A. Scherbakov
Institute for Structural Macrokinetics
Russian Academy of Sciences

Ceramic and metalloceramic foam materials are important construction, building, and thermal insulation materials for space stations of the 21st century. Delivery of these materials from Earth to space using rockets is not profitable due to the low density of these materials. Production of foam materials in space using traditional methods requires large energy consumption. Using SHS in space solves this problem!

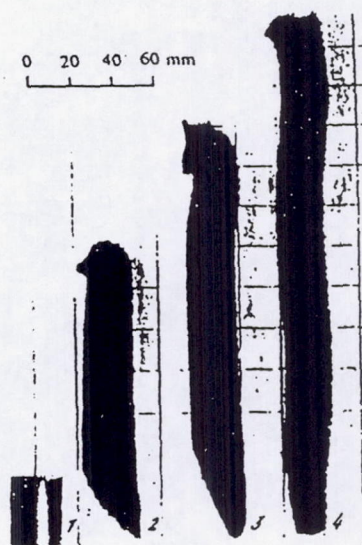
Method of experiments



↑
a gasifying additive



Vacuum chamber ($P \approx 10^{-2}$ bar)
Time of microgravity ≤ 30 sec
 $d = 10 \dots 50$ mm
 $h = 20$ mm



Photograph of samples. 1) Initial; 2) burned on Earth, in vertical position; 3) burned on Earth, in horizontal position; 4) burned under weightlessness.

Important features of SHS foam materials in space conditions: ignition of the mixture with endothermic dissociation of additive in vacuum is difficult. Reasons: low temperature of the equilibrium dissociation of the additive; intensive thermal losses due to vacuum dissociation.

2 Vacuum Chambers

Small

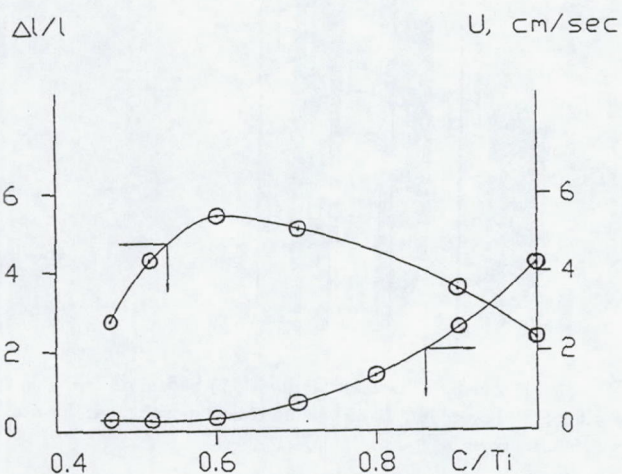
D=12cm
L=80cm
n=1 sample

Big

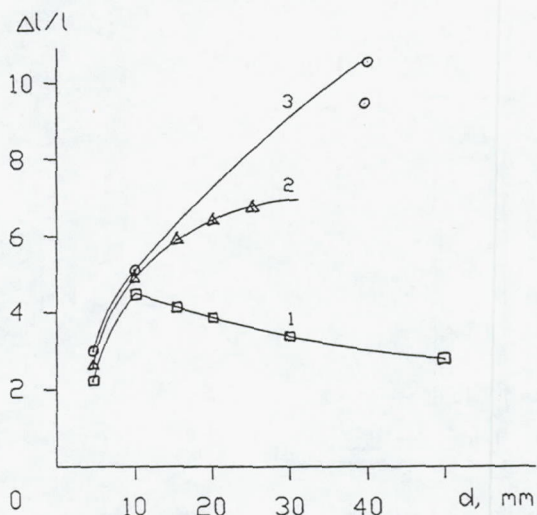
D=60cm
L=100cm
n=10 samples

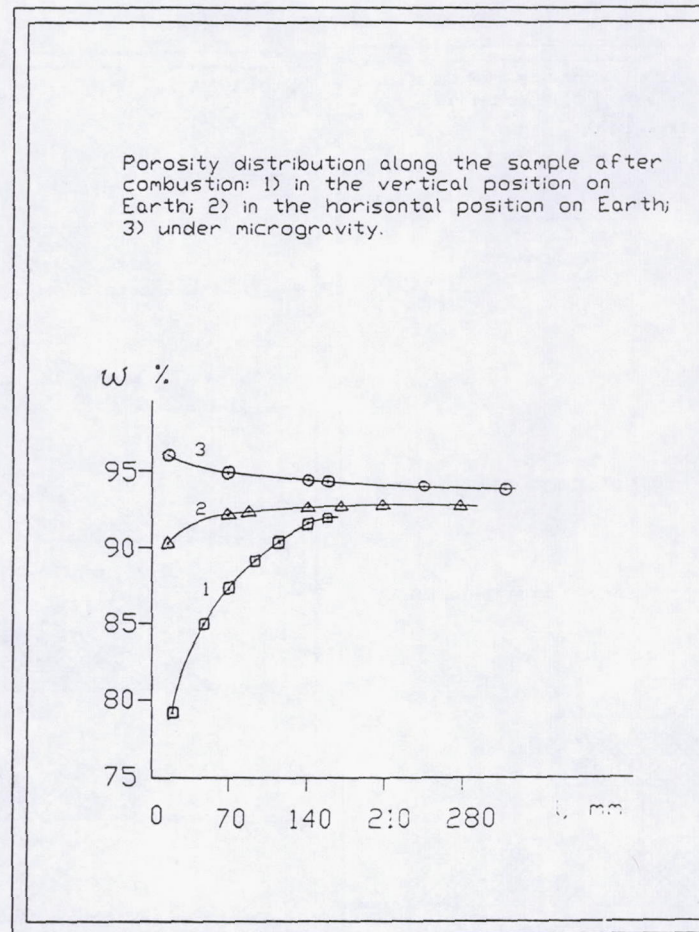
Results of experiments: 1. During combustion the diameter of the sample remains constant; length increases severalfold. 2. Burned sample is in the form of an "extended accordion", consisting of plates arranged in a stack; the micropores take on a disk-like shape.

Dependence of the degree of elongation of the sample (1) and of combustion (2) on the titanium/carbon ratio.



The degree of elongation of the sample during the combustion as a function of the diameter of the initial sample under combustion: 1) in the vertical position on Earth; 2) in the horizontal position on Earth; 3) under microgravity.





The mechanism and structural macrokinetics for the foamforming (the increasing in the length of the sample).

Two main processes: 1. Melting of one reagent and capillary flow along the particles of the other components-- in this case the material in the reaction zone becomes much more plastic. 2. Decomposition of the gasifying additive; an increase in the gas pressure in the pores of the sample causes them to grow larger and, hence, the volume of the entire sample to increase.

$$\tau_{\text{comb}} = \frac{\Delta x}{u};$$

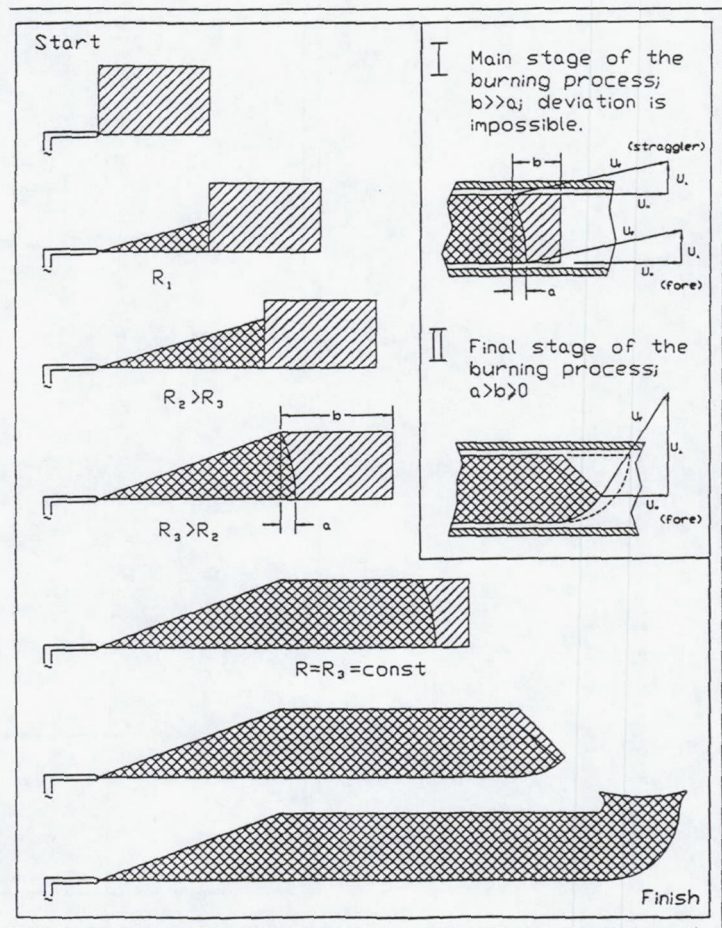
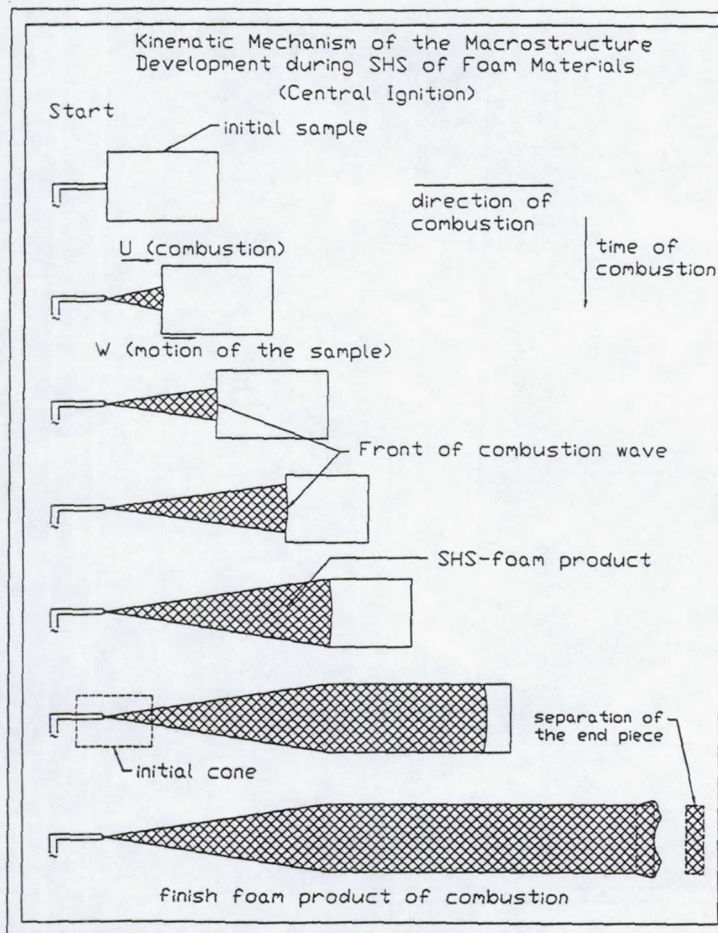
Δx - size of the reaction zone
 u - rate of combustion

$$\tau_{\text{def}} = \eta / (P_g - P_\infty)$$

η - viscosity;
 P_g - gas pressure in the pores;
 P_∞ - gas pressure in the ambient medium

Elongation $\Delta l/l$:

$$\Delta l/l \sim \tau_{\text{comb}} / \tau_{\text{def}} = [(\eta / (P_g - P_\infty)) * \Delta x / u]$$



From this data we can predict much more accurately the multiplex form and the realization potential of the combustion products.

If the angle between the axis of the cylindrical sample and the axes of the igniting surface (ellipse or circle) equal:

- 1) $\alpha = 90^\circ$
 $\beta = 90^\circ$ We have the finished product in a cylindrical form.
- 2) $\alpha = 0-180^\circ$
 $\beta = 90^\circ$ We have the finished product in a circular form.
- 3) $\alpha = 0-180^\circ$
 $\beta = 0-180^\circ$ We have the finished product in the form of a spiral (a ceramic spring)

If we are changing α and β we can change the diameter and step of the spring.

SMOKE DETECTION IN LOW-G FIRES

David L. Urban

DeVon W. Griffin

NASA Lewis Research Center
Cleveland, OH

Melissa Y. Gard

NASA Marshall Space Flight Center
Huntsville, AL

Michael Hoy

NASA Johnson Space Center
Houston, TX

Introduction

Fires in spacecraft are considered a credible risk (Refs. 1-3). To respond to this risk, NASA flew fire detectors on Skylab and the Space Shuttle (STS) and included them in the design for International Space Station Alpha (ISSA). In previous missions (Mercury, Gemini and Apollo), the crew quarters were so cramped that it was not considered credible that the astronauts could fail to observe a fire. The Skylab module included approximately 20 UV fire detectors. The space shuttle has 9 ionization detectors in the mid deck and flight deck and Spacelab has six additional ionization detectors. The planned detectors for ISSA are laser-diode, forward-scattering, smoke or particulate detectors. Current plans for the ISSA call for two detectors in the open area of the module and detectors in racks that have both cooling air flow and electrical power. Due to the complete absence of data concerning the nature of particulate and radiant emission from low-g fires, all three of these detector systems were designed based upon 1-g test data.

As planned mission durations and complexity increase and the volume of spacecraft increases, the need for and importance of effective, crew independent, fire detection grows significantly. This requires more knowledge concerning low-gravity fires and how they might be detected.

To date, no combustion-generated particulate samples have been collected for well-developed microgravity flames. All of the extant data come from drop tower tests and therefore only correspond to the early stages of a fire. The fuel sources were restricted to laminar gas-jet diffusion flames and rapidly overheated wire insulation. These gas-jet drop tower tests indicate, through thermophoretic sampling, (Ref. 4) that soot primaries and aggregates (groups of primary particles) in micro-g may be significantly larger than those in normal-g (n-g). This raises new scientific questions about soot processes as well as practical issues for particulate detection/alarm threshold levels used in on-orbit smoke detectors. Furthermore, it is widely speculated but unverified that the aggregates will grow to very large scales in a microgravity fire of longer duration than available on the ground. Preliminary tests in the 2.2 second drop tower suggest that particulate generated by overheated wire insulation will also be larger in microgravity than in normal gravity (Ref. 5). TEM grids downstream of the fire region in the WIF experiment (Ref. 6) as well as visual observation of long string-like aggregates, further confirm this suggestion. The combined impact of these limited results and theoretical predictions is that direct

knowledge of low-g combustion particulate as opposed to extrapolation from 1-g data is needed for a more confident design of smoke detectors for spacecraft.

Background

Although optical detectors (responding to fire's radiant emission rather than particulate emission) were used in the Skylab module and were considered for use on ISSA, their implementation has been hampered by the facts that they require a line-of-sight to the area to be monitored and the lack of knowledge of radiant signatures for low-g fires. Consequently, smoke detection has typically been favored for spacecraft applications and will be the focus of the rest of this paper. Low-g smoke detection has several challenges that make direct application of 1-g technology inappropriate. These issues include: dust discrimination, sampling in the absence of buoyant flows, lack of a knowledge base of low-g fire signatures, lack of knowledge of appropriate alarm levels. Different portions of spacecraft raise unique problems. Inside equipment racks, a likely location for fires given the presence of power and heat-producing devices, free volume is limited and tortuous, however avionics return air may be available (both as an oxidant source and smoke gathering mechanism). Outside the racks, in the crew space, free volume is much less limited and potential ignition sources are less frequent but potential fuel is more common (e.g. paper, clothing, and trash materials). In addition, residence times for the air in the ventilation system are long (tens of minutes in some portions of the shuttles). Future operation plans for the ISSA suggest that modules will have systems powered up but no human occupants present. In situations such as this, adequate fire/smoke detection systems for both the racks and the crew space are needed.

Well-established normal-gravity fires emit small particulate of the size range to which ionization detectors are more sensitive than optical detectors (Ref. 7). Less well-established or smoldering fires will produce larger particulate, owing to the large amount of condensed, unoxidized fuel pyrolysis products and the incomplete soot oxidation. For this type of fire, light scattering/obscuration detectors are more appropriate. However, for materials heated slowly as in the very early stages of some fires, the particulate can be very small, favoring ionization detectors (Ref. 8). This analysis was used by Brunswick Defense in their decision to pursue an ionization detector for the STS. (Fig. 1) The design consists of a dual-chamber ionization detector that is in the flow path created by a vane pump. This vane pump provides some active sampling capability and also provides flow for an inertial separation system which is designed to make the detector insensitive to particulate larger than 1 micron. These advantages are offset by a fairly large power consumption (9 Watts), fan noise, and limited life due to the moving parts. The design developed for ISSA by Allied Signal (Fig 2) consists of a 2 pass laser diode obscuration system that also has a photo-diode positioned to sense forward scattered light (30 degrees) on the return path. The system is designed to alarm based on the magnitude of the scattered light signal. Dust discrimination is based on frequency analysis of the scattered light signal. The system is less sensitive to particles smaller than the wavelength of the laser (near IR) than it is to larger particles but is relatively low power (1.5 W) and has a long operational life.

The performance of these two detectors has been compared in normal gravity (Refs. 9 & 10). Consistent with theory, the ISSA detector alarmed more rapidly in cases where large particles were expected (punk smoke) while for smaller particle size sources (over heated wire) the ISSA detector generally responded last. For punk smoke, despite the difference in the time to alarm, the time to initial response was roughly equivalent for both detectors. The implementation (alarm threshold selection) of both of these systems in microgravity is hampered by the lack of knowledge of their performance against low-gravity combustion generated particulate. To address this problem, an experiment (Comparative Soot Diagnostics (CSD)) is in final development that would take advantage of a Glovebox (GBX) Facility. It will provide the first test of these detectors against low-gravity smoke sources. The design of the experiment was constrained by the GBX power and size constraints; in addition toxicity was a significant constraint since one of the most likely spacecraft smoke sources is overheated wire insulation which usually contains fluorine.

Description of Apparatus

The CSD experimental hardware consists of two modules named the Near-Field Module and Far-Field Module as shown in figure 3. The Near-Field Module will be installed inside the glovebox and will contain the sample and the near field diagnostics. The Far-Field module will be external to the glovebox and will contain two spacecraft smoke detectors, exactly matching the STS detector and the prototype ISSA detector. Products from the near field tests will be transported to the far-field box and subsequently back into the glovebox via teflon hoses. These hoses will enter the glovebox through ports in the airlock door. All of the combustion products will be contained in either the glovebox or the far field module; by the time the experiment terminates, all of the products will have been returned to the glovebox.

A schematic of the Near-Field Module is shown in figure 4. It consists of a small test chamber fitted with a sample carrier that holds the sample being tested. Air is blown into the chamber from the right side by a small fan, and flows past the sample, exiting on the left side where it enters the hose to the Far-Field Module. The sample is ignited or overheated by a resistively heated Kanthal wire. The smoke particulate produced is sampled by a rake of thermophoretic probes. The particulate volume fraction measurements are made using two laser light obscuration systems.

Thermophoretic sampling has been used previously in the drop tower for gas jet diffusion flames and for overheated wires (Refs. 4 & 5). For the overheated wire and silicone rubber tests we expect a weak thermal gradient and consequently will leave the probe in place for a longer time (several seconds) than in the case of the much hotter candle flame where we will leave the probe in for 10 to 20 ms. When the probes are returned to earth, the grids will be removed and analyzed in a TEM to determine the primary particle and aggregate size distribution.

In the Near-Field Module, a custom-built laser-light extinction system will measure the volume fraction of the produced particulate in two locations along the axis of the flame. At each location a low-power laser diode with associated collimating optics is directed through a beam splitter. The intensity of one beam is measured by a photodiode to supply a reference signal and the other beam is expanded to approximately 1 cm in diameter and will pass across the chamber perpendicular to the chamber axis to where the beam is imaged on another photodiode. The particulate scatters and absorbs some of the light (extinction) causing a reduction in the signal from the detector. This signal change will be used with particle size information from the thermophoretic probes to calculate the volume fraction occupied by particulate.

The Far Field Module (figure 5) consists of a box containing a duct through which the smoke-containing air from the Near Field Module is drawn by a fan. The two spacecraft smoke detectors are attached to the duct and monitor the smoke in the air that passes through it. It is important to note that the detectors are very sensitive and consequently, the tests are designed to generate a very small amount of smoke particulate. It is anticipated that for some of these tests, no visible smoke will be produced, however it should be detectable by all of the near and far-field diagnostics. The signals from the near field extinction photodiodes, sample temperature thermocouple and the two far field smoke detectors will be displayed on digital readouts on the Far Field Module. These readouts will update at 1 Hz and are to be recorded by a glovebox video camera for subsequent analysis.

Tests have been conducted with the engineering version of the hardware both in 1-g and on the Lear Jet and the KC-135. These tests were designed to allow determination of the correct sample size and heater geometry to produce acceptable signal levels at the detectors and to keep the total particulate emission low enough that there are no safety concerns. To achieve detectable particulate at the detectors in the Far Field Module, mass losses of approximately 2 mg are needed. The samples are designed so that repeatable mass losses can be achieved at different heating rates by varying the amount of igniter wire in contact with the sample and the temperature and activation time of the ignitor. Typical conditions are 60 seconds activation time with an approximately 350 C igniter wire temperature for slow heating rate cases and 15 to 30 seconds activation time with an approximately 500 C igniter for the high heating rate cases.

These conditions will be refined in the future when the flow duct in the engineering hardware is updated to match the flight hardware.

The first detector in the Far Field Module will be the ISSA prototype duct smoke detector designed by Allied Signal, the second detector is the STS smoke detector designed by Brunswick Defense.

Flight Execution

After installing the near field hardware in the glovebox and attaching the far field module to the glovebox, the operator runs the self diagnostic procedures on the two smoke detectors and activates the GBX video camera, turns on the ignitor for a defined period of time and initiates the thermophoretic soot samplers when the flame is well developed. The actual duration of the combustion event will be of the order of five minutes or less. After the experiment, the operator will stow and reload the soot samplers, the test sample, and the filters at the end of the return line from the Far Field Module. At this point the operator either stows the modules or initiates another run.

Test Matrix

The exact flow and power levels will be determined based on ground based testing with the engineering version of the flight hardware. However, the tests will consist of testing a coflow ventilated candle at three coflow velocities and overheating four materials, (paper, silicone rubber, and teflon and kapton coated wires) at three heating rates. Candles were selected because their particulate will be primarily soot and varying the flow velocity should influence the soot production level and the soot residence time in the flame. Varying the heating rate for the other materials will affect the particle size distribution. The silicone rubber was selected because it is a particle-generation technique developed for testing the STS smoke detectors. While this technique produces almost no visible smoke, its particle generation was studied in 1-g by Brunswick Defense. The wire insulations are from spaceflight rated wire (TFE and Kapton) and were selected because overheated wires are the most credible fire risk on space craft and detection of their smoke emission is an important concern. Paper was selected for the last sample because paper is ubiquitous on spacecraft, the paper being tested is used in flight data files.

References

1. Friedman, R., 1992. Fire Safety Practices and Needs in Human-Crew Spacecraft. *Journal of Applied Fire Science*, 2:243-259.
2. Friedman, R., K. Sacksteder and D. Urban. 1991. *Risks, Designs and Research for Fire Safety in Spacecraft*. NASA TM 105317.
3. Friedman, R., and D. Dietrich, 1991. *Fire Suppression in Human-Crew Spacecraft*. NASA TM 104334.
4. Ku, J.C., D.W. Griffin, Greenberg, P.S., and J. Roma. 1992: Buoyancy-Induced Differences in Soot Morphology. *Combustion and Flame*, submitted.
5. Paul, M., F. Issacci, G.E. Apostolakis and I. Catton. 1993. The Morphological Description of Particles Generated from Overheated Wire Insulations in Microgravity and Terrestrial Environments. *Heat Transfer in Microgravity System-1993*, S.S. Sadhal and A. Hashemi eds. ASME-HTD Vol 235:59-66.
6. Greenberg, P.S., K.R. Sacksteder and T. Kashiwagi. 1995. Wire Insulation Flammability Experiment: USML-1 1 Year Post Mission Summary. *Joint Launch + one Year science Review of USML-1 and USMP-1 with the Microgravity Measurement Group*. NASA CP 3272 V II.
7. Bukowski, R.W. and G.W. Mulholland. 1978. *Smoke Detector Design and Smoke Properties*. NBS Technical Note 973.
8. Chuan, R.L. and H.D. Chen. 1986. Aerosol Characterization in an Incipient Fire. Second International Aerosol Conference, Berlin, Sept.
9. Steisslinger, H.R., D.M. Hoy, J.A. McLin and E.C. Thomas. 1993. Comparison Testing of the Space Shuttle Orbiter and Space Station Freedom Smoke Detectors. SAE Paper 932291, Warrendale, PA, 23rd Intl. Conference on Environmental Systems, Colorado Springs, CO, July.
10. McLin, J. 1993. Smoke Comparison Test Report Doc # 93-05902, Allied Signal Aerospace.

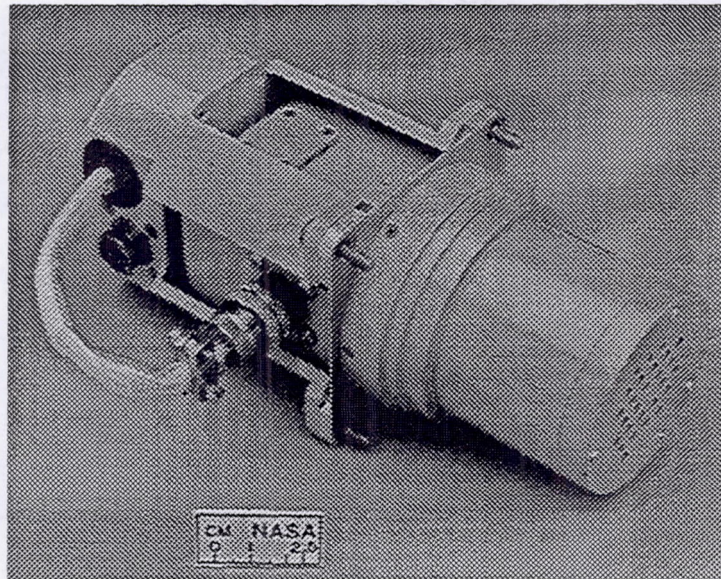


Figure1: Space Shuttle (STS) Smoke Detector (Brunswick Defense). Inlet is on right and outlet from pump is behind small plate on top left.

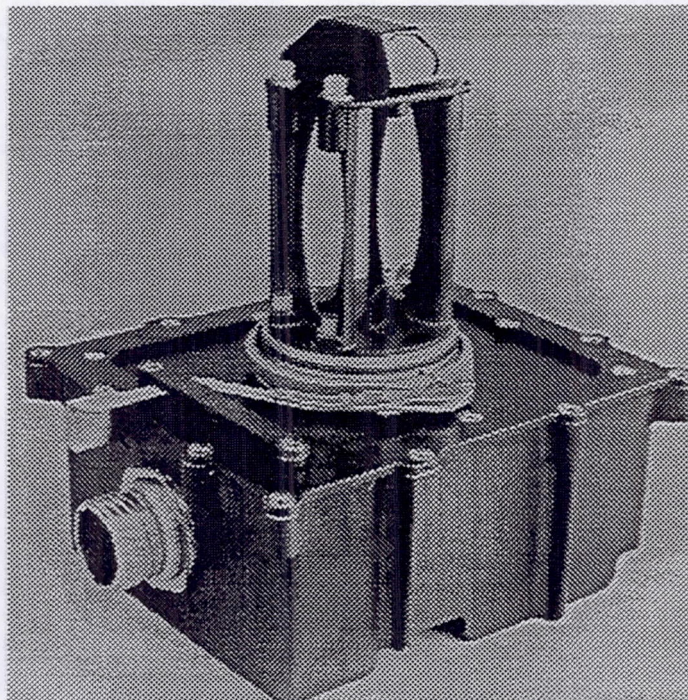


Figure 2: International Space Station Alpha (ISSA) Prototype Smoke Detector (Allied Signal). Laser beam path originates in base reflects off two mirrors on top and returns to the base. The back of one of the mirrors is visible on the top.

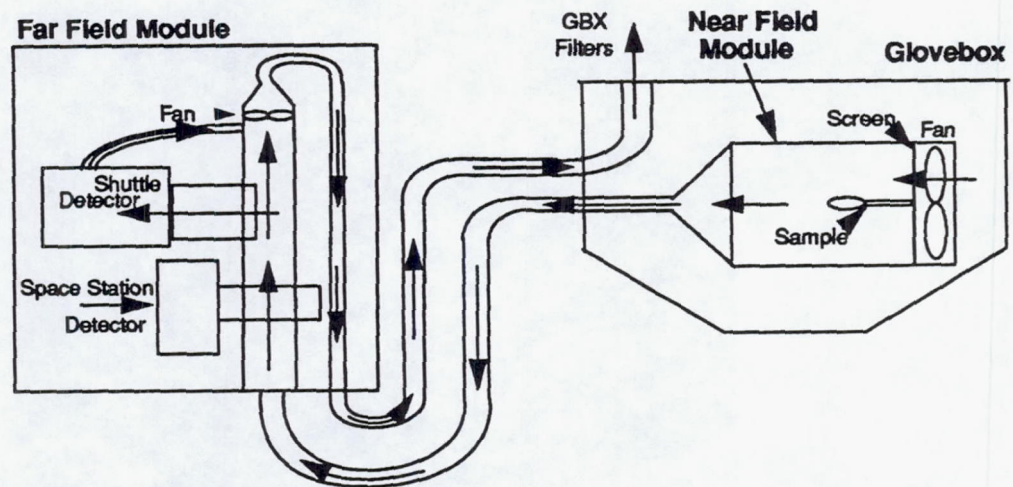


Figure 3: CSD System Schematic

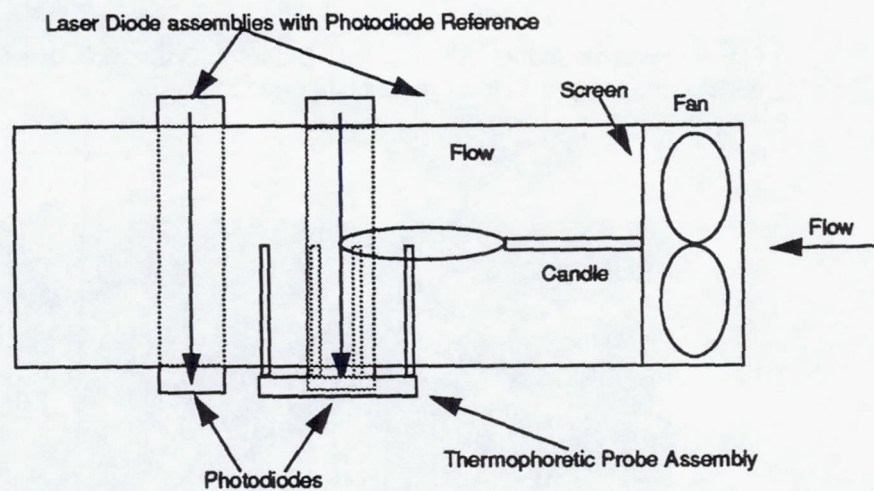


Figure 4: Near Field Module Schematic

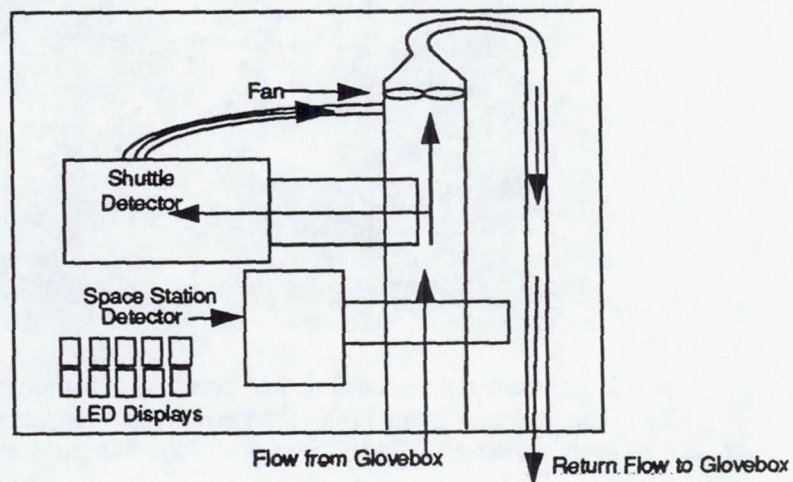


Figure 5: Far Field Module Schematic

THE EFFECT OF GRAVITY ON THE COMBUSTION SYNTHESIS OF Ni-Al AND Ni₃Al-TiB₂ COMPOSITES FROM ELEMENTS

Arvind Varma*, Hu Chun Yi, and Paul J. McGinn
University of Notre Dame
Notre Dame, IN 46556

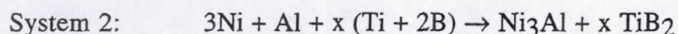
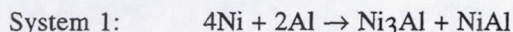
Introduction

Previous studies on the combustion synthesis of advanced materials indicate that combustion and structure formation mechanisms involve several stages including melting of reactants and products, spreading of the melt, droplet coalescence, diffusion and convection, buoyancy of solid particles, and densification of the liquid product. Most of these processes are affected by gravity. Conducting the combustion synthesis under microgravity conditions is expected to help elucidate the reaction mechanisms.

Although there have been a number of publications examining the role of gravity in materials processing [1-4], there is only limited work dealing with the effect of gravity on combustion synthesis. Hunter and Moore [5] recently compared the combustion synthesis of a number of ceramic-metal composites under both 1g and μ g conditions. While both the combustion temperature and wave velocity changed relatively little, they found that a more uniform microstructure resulted from the μ g condition.

Experiment

Two systems were examined. The first involves Ni/Al clad particles, which is an ideal system to examine the individual particle and liquid flow before combustion occurs. For comparison, elemental Ni and Al powders with the same stoichiometry as that of the clad particles were also used in some experiments. The reactant powders used in the present work are listed in Table I. Figure 1 shows a photomicrograph of the clad particles used in this investigation, which correspond to a composition of Ni(67.6 at%)-Al(32.3 at%). The second system was the Ni₃Al-TiB₂ composite in which the Ni₃Al ($-\Delta H_f^\circ = 153.1$ kJ/mol) phase melts during reaction enabling us to examine settling of the liquid phase. The amount of liquid phase was controlled by varying the TiB₂ ($-\Delta H_f^\circ = 323.8$ kJ/mol) content which generates the additional heat. The overall reactions for the two systems can be expressed as follows.



For the first system, pellets were pressed directly from the clad particles, at green densities about $77 \pm 3\%$ of theoretical value. For the second, the pellets were prepared by mixing the elemental reactant powders in the required stoichiometry by ball-milling and then pressing uniaxially at green densities about $70 \pm 3\%$ of theoretical. The pellets were cylindrical in shape, 10 mm in diameter and length typically 20-30 mm.

The pellet samples were reacted in UHP Argon (1 atm) using the experimental setup and procedure described previously [6]. After reaction, the samples were sectioned axially in order to conduct the microstructural analysis in the longitudinal direction. The phase composition of the reacted product was determined by X-ray diffraction (XRD) and the microstructure was analyzed using scanning electron microscopy (SEM) along with energy dispersive X-ray spectrometry (EDX).

* Author to whom correspondence should be addressed.

Results and Discussion

System 1: Ni/Al

Combustion of pellets pressed from clad particles was extremely complex and exhibited features that have never been reported before. It was found that such pellets were more difficult to ignite than those pressed from elemental Ni and Al powders. Therefore, the section close to the ignition coil was always heated to a higher temperature than the remainder of the pellet before combustion started, which implies that the reaction was actually ignited from an elevated rather than room temperature. In fact, a pre-combustion wave, possibly corresponding to aluminum melting, was observed in many cases and the combustion started afterwards. Then a stable combustion occurred initially due to the preheating described above. When the combustion wave reached the less preheated part, it changed to an unstable and rather complex mode (combination of spin and oscillating, see also [7]). In some cases, the ignition either started from some distance away from the ignition coil, or started from the opposite end if the sample was short, and then propagated in a complex mode. In other cases, the combustion wave stopped during its progress. In yet other cases, the reaction started stable (preheating part) and propagated (unstable) downward to about 2/3 of the sample length and then stopped. Surprisingly, the reaction did not terminate at that point, but reinitiated from the opposite end after ~ 15 seconds and then propagated upward with a lower velocity. Visual observations revealed that the brightness of the reinitiated combustion was less as compared to the upper part. Examination of the sample after combustion showed that the lower part had a lower density. These facts indicate that the combustion temperature of the lower part was apparently lower.

The pellets were then combustion synthesized at elevated temperatures by preheating the green pellets using another W-coil placed around the pellet. For preheating temperatures over 200°C, the above described complex combustion did not occur. However, the combustion front was still quite irregular. Figure 2 shows the plots of combustion propagation velocity and combustion temperature (T_c) versus pre-heating temperature. It can be seen that the velocity increases only slightly with increase of preheating temperature above 200°C, while the combustion temperature shows a larger degree of variation.

The combustion of pellets from elemental Ni and Al powders does not have the complex features described above. When ignited at room temperature, the combustion wave propagates in a spin mode. Preheating above 200°C not only changes combustion to a stable one, but also increases the wave propagation velocity considerably, particularly above 300°C as shown in Fig. 2. This may be compared with results for clad particles where relatively small velocity increment was observed. The same trend also holds for the combustion temperature, as shown in Fig. 2. Note that both the velocity and combustion temperature behave similarly in this case, indicating that a close relation exists between the two.

The product was examined by XRD and microscopy. It was found that the reacted product for both pellets, pressed from clad particles or pressed from elemental Ni/Al powders, contained the same phases: NiAl, Ni₃Al and possibly Ni₅Al₃. An optical photomicrograph from a fully reacted part of a sample with clad Ni/Al particles, is shown in Fig. 3. Figure 4 shows a SEM photomicrograph of the reaction front of a sample ignited at room temperature, which stopped in the middle of the pellet. At the reaction front, the NiAl phase formed between the clad particles and indicates that the nickel shell broke up, molten aluminum flowed out, which then wet, spread, and reacted with nickel. This was also confirmed by in-situ observation of heating loose clad particles using a high-speed video camera.

In the combustion synthesis of nickel aluminides from elemental powders, ignition and wave propagation usually result from melting and spreading of Al [8]. In these cases, once the Al melts, it immediately wets and spreads over the Ni, leading to product formation. However, for pellets pressed from clad particles, the Ni shell reduces the wettability of liquid Al before it cracks, and the combustion rate is controlled by the outflow of liquid aluminum from inside the nickel shell. During heating up, the Al core melts first and liquid Al reacts immediately with solid nickel within the shell, forming NiAl₃ as observed by SEM and confirmed by EDX. However, this reaction is not responsible for the self-sustained combustion wave, which instead is caused by the outflow of Al from cracked Ni shell as stated above. Gravity may play a role in this process and future experiments conducted under microgravity will clarify this issue. Since the Ni shell reduces the wettability of molten Al, it is expected that the combustion rate for clad particles is lower than that for elemental powders, leading to smaller propagation velocities as observed in Fig. 2.

System 2: Ni₃Al-TiB₂

Figure 5 shows the measured combustion temperature (along with theoretical adiabatic temperature) and wave velocity as a function of the amount of TiB₂ formed. Both combustion temperature and wave velocity increased dramatically with the TiB₂ content owing to the increased exothermicity of reaction. For samples containing more than 20 wt%TiB₂, the combustion temperature was higher than the melting point of Ni₃Al (1395 °C) so that a fully liquid phase was formed. For the 5 wt%TiB₂ sample, the combustion proceeded in an oscillatory and spin mode whereas for the 20 wt%TiB₂ sample, it propagated in a spin mode. For all samples with more than 40wt% TiB₂, a stable combustion was observed, although the wave front was not planar. It should be noted that the temperature measurement for samples containing more than 60 wt%TiB₂ was not accurate since the thermocouples (0.25 mm diameter, C-type) often broke during the combustion. However, Fig. 5 does show that the measured wave velocity had a trend similar to the adiabatic temperature. The combustion characteristics of the system are summarized in Table II, where the data are averages of two or more samples.

The XRD spectra showed complete reactions for all samples except the 5 wt% TiB₂, where traces of unreacted Ni and Al were also present. Figure 6 shows the morphology of the 40 wt% TiB₂ composite, indicating a relatively uniform distribution of the TiB₂ ceramic particles dispersed in the Ni₃Al matrix. Figure 7 shows some typical SEM photomicrographs of the same sample at different locations. It can be seen that the microstructure is non-homogenous. Apart from the uniform Ni₃Al-TiB₂ structure, there are also Ni₃Al islands of size 0.05-0.5 μ m. Liquid settling clearly occurred at the bottom of the sample (Fig. 7c) and on the upper side of pores (Fig. 7b).

In order to further investigate the effect of gravity, the 40 wt% TiB₂ samples were also ignited from the bottom (placed vertically) and from the side (placed horizontally). While there was no substantial difference in the combustion temperature, the wave velocity was higher in both cases than when ignited from the top. Hunter and Moore [5] also observed similar results and attributed them to the preheating effect by the ignition coil. In the present work, the higher combustion velocity for the horizontal orientation was likely due to the fact that the pellet was placed in a semi-cylindrical quartz boat which may have decreased heat loss. The SEM examinations of the reacted products showed similar microstructure as in Figs. 6 and 7.

The terminal velocity of a spherical particle in a liquid medium under ideal conditions is described by the well-known Stoke's equation:

$$V_t = \frac{2}{9} \frac{g (\rho_s - \rho_l)}{\mu} R^2 \quad (1)$$

where g is the gravitational acceleration (9.81 ms^{-2} at 1 g and 9.81×10^{-3} at μ g), ρ_s the density of the solid TiB₂ particle (4310 kgm^{-3}), ρ_l the density of the liquid Ni₃Al (6500 kgm^{-3}), and μ the dynamic viscosity (4.7×10^{-3} Pas). The last two properties were estimated from their elemental constituents assuming ideal mixing. Since the density of the liquid is larger than that of the solid particles, the liquid phase is expected to settle down. From the SEM photomicrographs shown in Fig. 6, the size of most TiB₂ particles ranges from 2-5 μ m. Taking the average size as 3.5 μ m, we have $V_t = 12.4 \text{ }\mu\text{m/s}$. From the temperature profile recordings, the Ni₃Al phase stays in liquid state for 9.1 seconds for this particular sample. Hence, the settling of the liquid Ni₃Al phase should be about 113 μ m. Measurements on different parts of the sample showed that the settling was between 10-30 μ m. The measurements are comparable to the calculated values, especially given the numerous phenomena which would contribute to modifying eq. (1), including unsteady state, dynamics of particle formation, their non-spherical shape and large population. Under microgravity conditions, the settling effect would be greatly diminished (three orders of magnitude less).

Unstable convection may also play a role in this system. This phenomenon occurs when a fluid held in a container is heated from below, and the Rayleigh number defined as

$$Ra = \frac{\beta g \Delta T L^3 C_p \mu}{\nu^2 k} \quad (2)$$

exceeds a critical value which depends on the shape and dimensions of the container [4,9]. Here, ΔT is the temperature difference, L a characteristic length, β the liquid volumetric expansion coefficient, ν the kinematic viscosity, C_p the specific heat and k is the thermal conductivity. Owing to complications of the geometry and the heterogeneous nature, it is difficult to evaluate the critical Rayleigh number for the present system. However, it is

clear that unstable convection is more likely to occur when the sample is ignited from the top, rather than from the bottom or the side. This issue is still under investigation. In any case, from eq. (2), it appears almost certain that unstable convection would not play a role under microgravity conditions.

Acknowledgement

This work was supported under NASA grant NAG3-1644.

References

1. Sharma S C, Narayanan P R, Sinha P P, Nagarajan K V, "Processing characteristics of Al/W composite under 1g conditions", J. Mater. Sci., **29**, (1994), 5719-24.
2. Froyen L, Deruyttere A, "Melting and solidification of metal matrix composites under microgravity", in 5th European Symposium on Material Sciences under Microgravity, Edited by Guyenne T D and Hunt, J J, Schloss Elmau, Germany (1984), 69-78.
3. Laxmanan V, Studer A, Wang L, Wallace J F, Winsa E A, "Gravitational macrosegregation in binary Pb-Sn alloy ingots", Low-Gravity Sciences, Edited by Koster J N, American Astronautical Society (1987), 119-48.
4. Ostrach S, "Convection phenomena of importance for materials processing in space", in Materials Sciences in Space with Application to Space Processing, Edited by Steg L, Progress in Astronautics and Aeronautics, **52**, (1977), 3-32.
5. Hunter K R and Moore J J, "The effect of microgravity on the combustion synthesis of ceramics and ceramic-metal composites", J. Mater. Syn. Proc. (in press).
6. Lebrat J -P, Varma A, and Miller A E, "Combustion synthesis of Ni₃Al and Ni₃Al-matrix composites", Metall. Trans. **23A**, (1992), 69-76.
7. Wenning L A, Lebrat J -P, and Varma A, "Some observations on unstable self-propagating high-temperature synthesis of nickel aluminides", J. Mater. Syn. Proc., **2** (3), (1994), 125-32.
8. Lebrat J -P, Varma A, and McGinn P J, "Mechanistic studies in combustion synthesis of Ni₃Al and Ni₃Al-matrix composites", J. Mater. Res., **9** (5), (1994), 1184-92.
9. Ostrach S, Pnueli D, "The thermal instability of completely confined fluids inside some particular configurations", Trans. ASME, series C, **85**, (1963), 346-54.

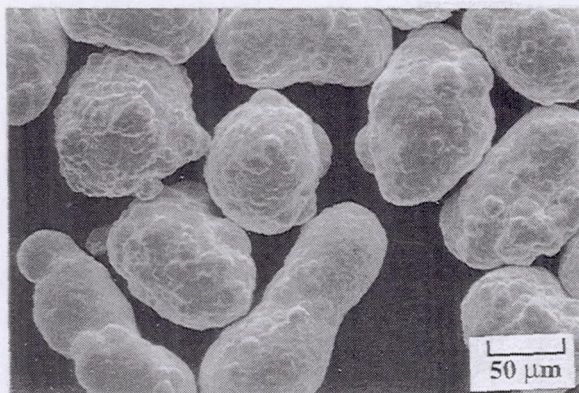
Table I. Characteristics of the Reactant Powders

Powder	Size, μm	Purity, %	Vendor
Ni	25 - 44	99.9	Cerac
Al	< 44	99.5	Aesar
Ti	< 44	99.5	Cerac
B (amorphous)			
Cladded Ni/Al	44 - 90	99.5	Sheritt Gordon
Ni	< 7	99.9	Aesar
Al	52 - 75	99.0	Aesar

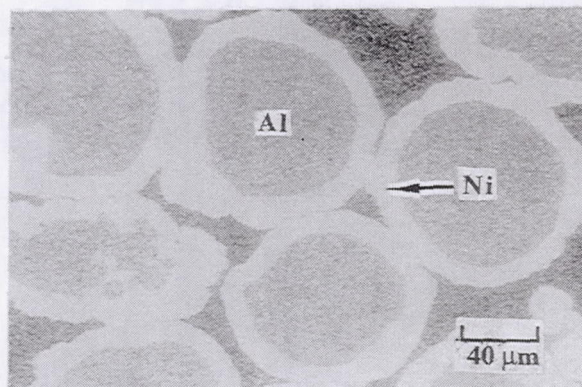
Table II. Combustion Characteristics of the Ni₃Al-xTiB₂ system

Composition (wt%TiB ₂)	T _c (°C)	Velocity (cm/s)	Propagation Mode
5	1351	-	Oscillatory
20	1384	1.2	Spin
40	1921 [†] 1932 1970*	3.6 [†] 3.2 4.1*	Stable
60	-	6.4	Stable
80	-	6.4	Stable

[†] Ignited from bottom. * Ignited horizontally.



(a)



(b)

Figure 1 - Cladded Ni-Al particles. (a) Morphology and (b) Cross-section.

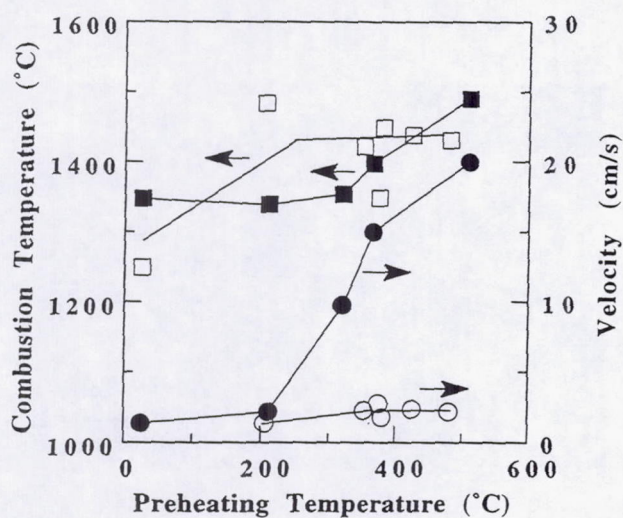


Figure 2 - Plot of combustion temperature and velocity versus preheating temperature for pellets from cladded (□,○) and elemental (■,●) Ni/Al powders.

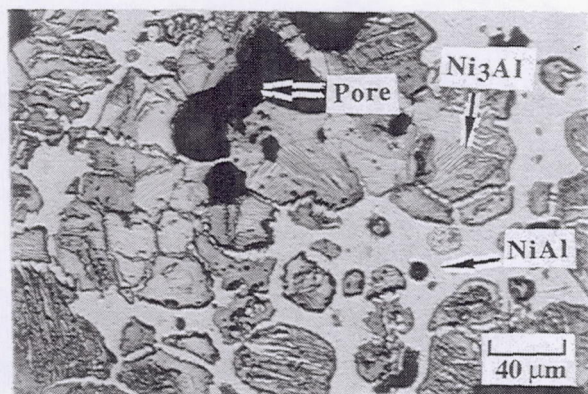


Figure 3 - Optical photomicrograph of the reacted pellet from cladded Ni/Al particles, showing the multiphase structure.

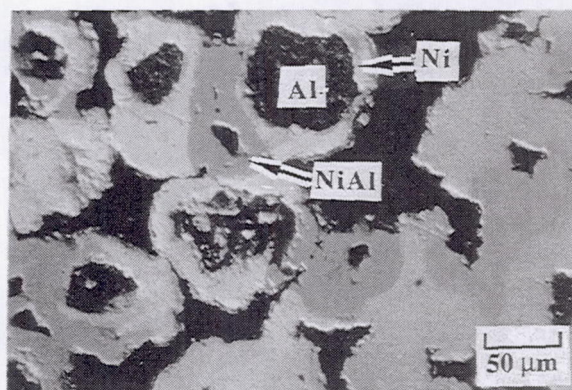


Figure 4 - Back-scattered SEM photomicrograph of reacted pellet from cladded Ni/Al particles, showing the reaction front.

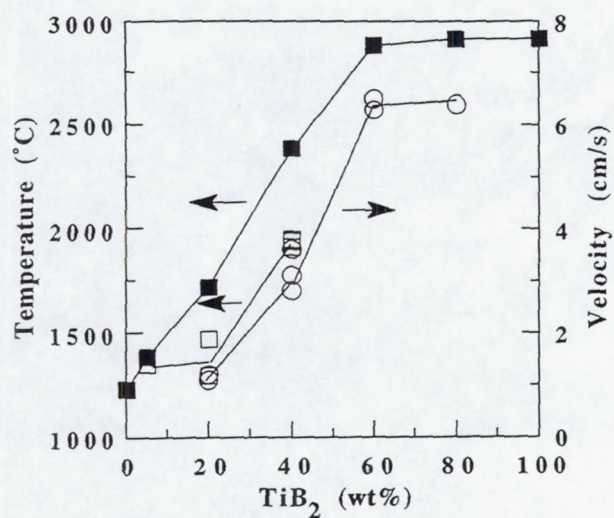


Figure 5 - Plot of measured combustion (\square) and theoretical adiabatic (\blacksquare) temperatures and velocity (\circ) versus TiB_2 amount.

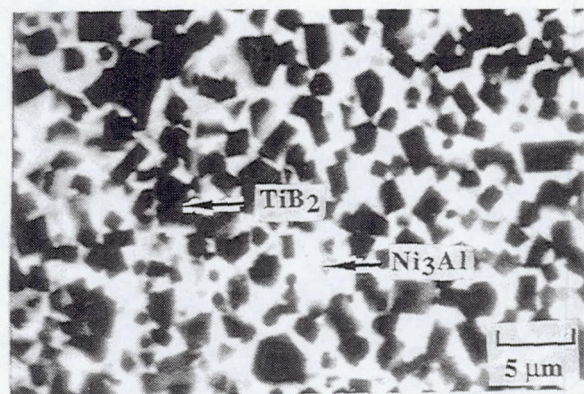
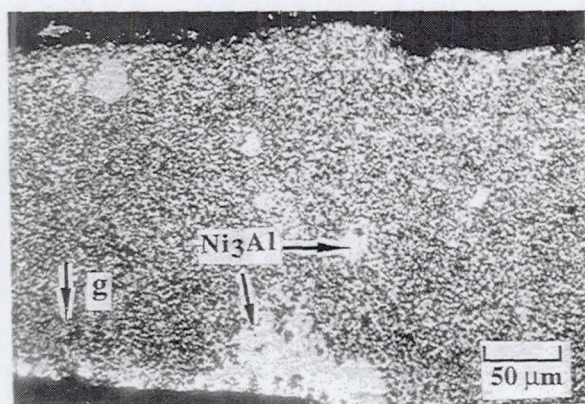


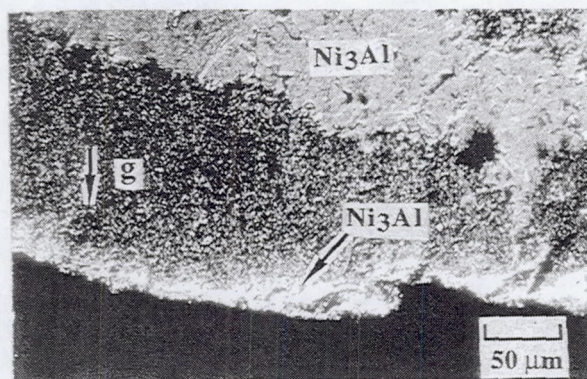
Figure 6 - Back-scattered SEM photomicrograph of a Ni_3Al -40wt% TiB_2 sample showing the size of TiB_2 particles.



(a)



(b)



(c)

Figure 7 - Back-scattered SEM photomicrographs of the same sample shown in Fig. 6, indicating settling of the Ni_3Al phase. (a) top part, (b) middle part, and (c) bottom part.

Ignition and Flame Spread

Low Velocity Opposed-Flow Flame Spread in a Transport-Controlled Environment DARTFire

Jeff West, Pete Thomas, Ruian Chao, and Subrata Bhattacharjee
Department of Mechanical Engineering
San Diego State University, San Diego, CA 92182-0191

Lin Tang and Robert A. Altenkirch
Department of Mechanical Engineering and NSF/ERC for Computational Field Simulation
Mississippi State University, Mississippi State, MS 39762

Sandra L. Olson
NASA Lewis Research Center
Cleveland, OH 44135

Introduction

Opposed-flow flame spread over a solid fuel is a fundamental combustion problem with applications to fire safety. The forced or free convection configuration for the situation where the opposing oxidizer flow velocity, \hat{V}_r , is large compared to the flame spread rate, \hat{V}_f , has been subjected to substantial investigation (see for example Refs. [1-3]). Reasonable agreement exists on the physics of the process for $\hat{V}_r / \hat{V}_f \gg 1$. In this limit, the flame propagates by transferring heat by conduction to the unburnt fuel ahead of it to raise the fuel temperature from \hat{T}_∞ to the vaporization temperature \hat{T}_v . This produces gas-phase fuel to feed the gas-phase flame with species diffusion taking place in the presence of the relatively strong convective bulk oxidizer flow.

While the physics of the flame spread process for $\hat{V}_r / \hat{V}_f \gg 1$ are reasonably clear, such is not the case for \hat{V}_r / \hat{V}_f of unit order. This situation may arise in the absence of any externally supplied forced flow in the reduced-gravity environment of spacecraft where natural convection is suppressed. Consequently, our focus in the DARTFire project is on flame spread at reduced or microgravity in an effort to delineate those aspects of the physics of the problem that must be included in flame spread modeling. Modeling efforts are important to spacecraft fire safety issues because, unlike usual experimentation in Earth-bound laboratories, it is difficult to obtain substantial amounts of experimental data under reduced-gravity conditions that have direct application to space travel.

As \hat{V}_r is made close to \hat{V}_f , radiation cannot be ignored [4]. For flames spreading into a low-velocity flow or a quiescent environment that can be obtained in microgravity, we anticipate behavior then that is different from that obtained at the higher velocities where radiation is unimportant and transport is relatively fast.

Objectives

The overall objectives of the DARTFire project are to uncover the underlying physics and increase understanding of the mechanisms that cause flames to propagate over solid fuels against a low velocity of oxidizer flow in a low-gravity environment. Specific objectives are 1) to analyze experimentally observed flame shapes, measured gas-phase field variables, spread rates, radiative characteristics, and solid-phase regression rates for comparison with previously developed model prediction capability that will be continually extended, and 2) to investigate the transition from ignition to either flame propagation or extinction in order to determine the characteristics of those environments that lead to flame evolution. To meet the objectives, a series of sounding rocket experiments has been designed to exercise several of the dimensional,

controllable variables that affect the flame spread process over PMMA in microgravity, i.e, the opposing flow velocity (1-20 cm/s), the external radiant flux directed to the fuel surface (0-2 W/cm²), and the oxygen concentration of the environment (35- 70%). Because radiative heat transfer is critical to these microgravity flame spread experiments, radiant heating is imposed, and radiant heat loss will be measured. These are the first attempts at such an experimental control and measurement in microgravity. Other firsts associated with the experiment are 1) the control of the low velocity, opposed flow, which is of the same order as diffusive velocities and Stefan flows; 2) state-of-the-art quantitative flame imaging for species-specific emissions (both infrared and ultraviolet) in addition to novel intensified array imaging to obtain a color image of the very dim, low-gravity flames.

UV-Visible Imaging

As part of the DARTFire sounding rocket experiment, an intensified array video camera is used to image the flame. This technique has the advantage of increased sensitivity over film (equivalent film ASA numbers can be as high as 180,000 [5]) and therefore can enable direct visualization of radical species by incorporating appropriate filters. It has the disadvantage, however, of imaging only in black and white due to its operational characteristics. Because a color image is strongly desired, in part for comparison with previous film images, a multispectral intensified array camera was obtained that could image with red, green, and blue additive filters (RGB) as well as narrow-bandpass filters for specific excited species. The RGB filtered images can be combined to obtain a 24-bit color composite image of the flame as part of the post-mission image processing.

The intensified array camera (Xybion ISG 240, 768 x 493 pixel array) includes a filter wheel with 6 filters. The rotation rate of the filter wheel is 300 rpm, providing 5 frames per filter per second. Color filters include a red additive dichroic filter with 80% transmission above 610 nm, a green additive dichroic filter with 80% transmission from 505-575 nm, and a blue additive dichroic filter with 80 % transmission below 480 nm. A neutral density filter with 70% transmission is also used to obtain a total intensity measure. Chemiluminescent emissions are imaged through 20 nm bandwidth OH and CH filters at 310 nm and 430 nm. The camera utilizes peak mode to avoid saturation of the bright flames against the dark background and optimizes exposure time for each filter image independently.

Infrared Imaging

Infrared emissions from the combustion products will also be monitored during the DARTFire experiment. A multispectral PtSi detector camera (Inframetrics, Inc. Model Infra-Cam PtSi FPA (256x256 pixel array)) was modified to include a 6-filter internal wheel. Filters include 1.87 μm (H₂O), 4.3 μm (CO₂), 3.4 μm (MMA vapor), 4.8 μm (CO), and two soot filters at 1.6 and 3.8 μm . The filter wheel rotates 1 rev/s, providing 1 image per filter per second, which is recorded for later image processing. The gain is fixed for all filters, so each image must be balanced to provide a similar brightness.

Ground-Based Experiments

Laboratory and low-gravity tests aboard the NASA Learjet have been performed using the cameras. The UV-visible imaging provides very good color reproduction provided the rate of change in the image is slow relative to the 5 Hz framing rate so that proper overlap of the images can be obtained upon recombination. Fortunately, in low gravity, most of the changes occur over significantly longer times. Images from the free radical chemiluminescence show that the peak intensity zone from both excited CH and OH occurs at the same approximate distance from the fuel surface. Excited OH is more evenly distributed across the visible flame than excited CH, which is more localized, and thus, presumably, gives a better idea of where the highest reaction rate zones occur.

Infrared imaging has provided a first glimpse into the species fields in the experiment. Because the image is generated due to the combined influence of the concentration and temperature, accurate modelling of the gas-phase radiation greatly helps interpretation of the results. Results to date indicate that MMA fuel vapor is indeed localized near the surface. CO appears over a fairly thick region in low gravity whereas it occurs over a

thin region in normal gravity. Water and CO₂ extend into the oxidizer side of the flame, but CO₂ extends farthest. This could be due to condensation of the water vapor as it moves into cooler regions, because stoichiometric water concentrations are at least six times the dew point at ambient temperatures.

Imaging of the gaseous species is more straightforward than soot because stoichiometry dictates to a large degree the concentration ranges of the gaseous species. Soot concentration, however, is a very strong function of experimental conditions (especially gravity) and can span several orders of magnitude, so determining the right filters for the soot requires high quality ground-based testing prior to the sounding rocket flights. DARTFire will be flying the sounding rocket hardware on the DC-9 this spring in order to finalize these filter choices.

DARTFire Modeling

The DARTfire experiment is supported by, and results interpreted in concert with, a comprehensive modeling effort that is both analytical and computational, e.g., [6,7].

Model Sweep: A model sweep is carried out in Fig. 1, where the computed spread rate corresponding to various mathematical models is presented for a particular environmental condition for flame spread over a thick slab of PMMA in a fully developed channel flow configuration, i.e., similar to the DARTFire configuration. On the very left of the abscissa (model #1), the spread rate matches (within 99.9%) with the exact solution of de Ris [1], and on the extreme right (model #14) is the experimental result of Fernandez-Pello et al. [2], with the intermediate points being the computational results with the assumptions in the thermal theory of de Ris, i.e., zero hang distance (#2), approximate velocity boundary condition (#3), Oseen flow (#4), constant gas density (#5), no wall blowing (#6), infinite-rate chemistry (#7), known vaporization temperature (#8), constant transport properties (#9), no gas or surface radiation (#10-#12), no radiation feedback (#13), removed one by one. It is immediately noticeable that the Oseen flow assumption, i.e., the assumption of a slug flow for the opposing flow field, is the crudest of all assumptions at both high and low \hat{V}_g .

EST: An Extended Simplified Theory (EST) [6] has been developed that gives a closed form approximate solution for the spread rate and the flame structure corresponding to model # 6. In the simplified formulation, the conservation equations are parabolized, \hat{V}_g is replaced with an equivalent velocity $\hat{V}_{eqv} = v_{hyd} \hat{V}_g$ to overcome the drawbacks of the Oseen approximation, and a new boundary condition is introduced for

$\phi_2 = \frac{\beta_2}{\beta_4} [y_F - \beta_1(y_o^* - 1)]$, the second Schvab-Zeldovich coupling function, such that at the vaporizing surface,

$\phi_2 = v_{lift} \phi_{2,f} = v_{lift} \frac{\beta_1 \beta_2}{\beta_4}$ where v_{lift} and v_{hyd} are unknown coefficients and $\beta_1 \dots \beta_6$ are known parameters

$(\frac{y_{o,\infty}}{s}, \frac{\Delta h_c^o}{c_g T_\infty}, \frac{\Delta h_v^o}{c_g T_\infty}, \frac{T_v}{T_\infty}, \frac{\lambda_s}{\lambda_g}, \frac{\hat{p}_s \hat{C}_s}{\hat{p}_g \hat{C}_g})$. This results in a modified expression for the spread rate:

$$\beta_{thick,EST} \equiv \beta_6 \frac{\hat{V}_{f,EST}}{\hat{V}_g} = \gamma_{hyd} \frac{F'^2}{\beta_5} \quad \text{where, } F' \equiv \frac{T_{f,ad,EST} - \beta_3}{\beta_3 - 1}, \quad T_{f,ad,EST} = 1 + \beta_1 \left(\beta_2 - \frac{\gamma_{lift} \beta_4 B}{\ln(1+B)} \right). \quad (1)$$

For $v_{hyd} = v_{lift} = 1$ the spread rate expression of Eq. (1) reduces to the de Ris formula. \hat{V}_{eqv} should be the velocity at the flame leading edge at a distance $\hat{L}_g = \frac{\hat{\alpha}_g}{\hat{V}_g}$ from the surface [8,9]. Depending on the geometry under consideration, γ_{hyd} for the fully developed channel (FDC) and flat-plate (FP) configuration can be evaluated.

$$\gamma_{hyd,FDC} \sim \left(\frac{\hat{\alpha}_g}{\hat{H}\hat{V}_g} \right)^{\frac{1}{2}} = c_{h,FDC} \left(\frac{\hat{\alpha}_g}{\hat{H}\hat{V}_g} \right)^{\frac{1}{2}}, \quad \gamma_{hyd,FP} \sim \left(\frac{\hat{\alpha}_g}{\hat{x}_d \hat{V}_g \text{Pr}} \right)^{\frac{1}{4}} = c_{h,FP} \left(\frac{\hat{\alpha}_g}{\hat{x}_d \hat{V}_g \text{Pr}} \right)^{\frac{1}{4}} \quad (2)$$

In order to obtain a functional relationship between γ_{lift} and the parameters of the problem, we note that the flame stand-off distance depends on this coefficient. From the one-dimensional solution, it can be shown [1] that the stand-off distance depends on the parameter $\frac{\ln(1+B)}{\beta_1}$. Therefore, we expect γ_{lift} to be a function of

$\frac{\ln(1+B)}{\beta_1}$. The hydrodynamic constants, $c_{h,FDC}$ and $c_{h,FP}$ as well as the functional relationship between γ_{lift}

and the blowing parameters are obtained through a series of numerical case studies, resulting in:

$$\gamma_{lift} = 1 + c_{lift} \frac{\ln(1+B)}{\beta_1}, \text{ where, } c_{lift} = 0.09, \text{ and, } c_{h,FDC} = 2.22, c_{h,FP} = 0.57. \quad (3)$$

To test the flame spread expression from the EST thoroughly, computations were carried out for two different flow configurations, different oxygen levels ($\gamma_{O,\infty}$), a wide range of opposing velocity (\hat{V}_g), different ambient pressures (\hat{P}_∞), different channel heights (\hat{h}), and different plate lengths up to the leading edge (\hat{x}_d). To present the results on the same plot, we note that Eq. (1) can be written as:

$$\hat{V}_{f,EST} = \gamma_{hyd} \hat{V}_g \frac{F'^2}{\beta_5 \beta_6} = \hat{V}_{eqv} f(\beta_i, c_{lift}) \quad (4)$$

The function $f(\beta_i, c_{lift})$ carries with it all the chemical information, and \hat{V}_{eqv} carries the hydrodynamic effects. A plot of $\hat{V}_{f,comp} / f(\beta_i, c_{lift})$ vs. \hat{V}_{eqv} in Fig. 2 collapses all the computed data onto a single line described by Eq. (4). The spread rate data [2] at different oxygen levels are similarly plotted in Fig. 3. Except for relatively high or low \hat{V}_g , where the bounds of the thermal regime are crossed, the data agree well with the prediction of the EST.

The Microgravity Regime:

When the opposing flow velocity is reduced, radiation plays a more important role. This is evident from the model sweep of Fig. 1, where at $\hat{V}_g = 1$ cm/s the introduction of radiation (model #10 to model #13) reduces the spread rate by almost 70%.

The Pseudo-Steady Hypothesis: For a forced opposing flow over a flat plate, the spreading flame encounters a progressively stronger flow due to the thinning of the boundary layer. As a result, even after the ignition transients subside, the flame behavior changes with time for all three regimes of flame spread: In the thermal regime, V_f increases as γ_{hyd} increases; in the blow-off extinction regime, V_f decreases as the effective residence time decreases [2,3]; and, in the microgravity regime, V_f increases as the radiative effects decline [7].

In Fig. 4, we explore this unsteadiness by comparing a series of steady-state computations for the spread rate with unsteady computations for an evolving flame spreading over a thick fuel bed against an opposing flow velocity of 1 cm/s. In the steady computations the fuel pyrolysis length and the flow development lengths are altered to match the instantaneous values of the evolving flame. After the ignition transients subside, the spread rate decreases because of an increase in the flame length resulting in a weakening influence of the flame trailing edge on the forward heat conduction. As the boundary layer effect becomes established, V_f starts to increase as expected. It is evident from this figure that the application of a quasi steady-state model is reasonable after the initial ignition transients are over.

Spread Rate Predictions of the DARTfire Matrix: The steady-state model as well as the predictions from the de Ris formula and the EST are tabulated in Table 1 for the DARTFire experimental matrix. Because the flame spread rate is dependent on the location of the flame leading edge, the values tabulated correspond to an instant when the flame is at the leading edge of the sample, i.e., 4 cm from the entrance of the tunnel and 2 cm from the ignition source. Note that the EST predicts a spread rate very close to the computations for high \hat{V}_g while the de Ris formula, unable to capture the hydrodynamic effects, overpredicts the spread rate by almost an order of magnitude. The discrepancy between the EST and numerical model computations grows as \hat{V}_g is reduced and radiation effects become dominant, radiation being absent in the EST. With the external radiative flux imposed, V_f jumps as can be expected, the jump providing an indication of the level of importance of radiation, which can be directly compared to experiment.

Infra-red Images: The radiation code developed that is incorporated in the computational model is capable of producing a spectral view of the flame from any given angle. An example is given in Fig. 5 where the side-view intensity contours in the $4.5 \mu\text{m}$ band are plotted for comparison with future IR images. Comparisons at different bands are expected to provide valuable insight into the species and temperature fields in the spreading flames.

Ox. Level	\hat{V}_g	Radiative Power (W)	Spread Rate, (mm/s)		
	(cm/s)		de Ris	EST	Steady-state Computations
35%	15	0	3.84	0.32	0.36
	5	0	1.75	0.21	0.17
	1	0	0.43	0.1	0.04
	1	1	-	-	0.29
	1	2	-	-	0.52
50%	1	0	0.64	0.15	0.09

Table 1. Spread rate predicted by different methods for the experimental matrix.

ability to model radiative effects in flame spreading. Comparison of spread rate behavior as the controllable variables, including the radiative field, are exercised, and spectral images of the flame with model prediction will provide insight into the important physics of low-velocity, opposed-flow flame spread, the importance of radiative and transport effects, and delineate those conditions under which ignition evolves to flame spreading and/or extinction.

Acknowledgments: This work was supported by NASA through Contract NCC3-221.

References

1. de Ris, J. N., Twelfth Symp. (Int) on Comb., The Comb. Inst., Pittsburgh, (1969), pp. 241-252.
2. Fernandez-Pello, A.C., Ray, S.R., and Glassman, I., Eighteenth Symposium (International) on Combustion, The Combustion Institute, Pittsburgh, PA, p. 579, (1981).
3. Altenkirch, R.A., Eichhorn, R., and Rizvi A.R, Combust. Sci. and Tech., Vol. 32, pp. 49-66, (1983).
4. Altenkirch, R.A., Olson, S.L., and Bhattacharjee, S., "Science Requirement Document for DARTFire", NASA Lewis Research Center, May 1994.
5. Weiland, K.J. AIAA-92-0240, 30th Aerospace Sciences Meeting & Exhibit, Jan. 6-9, 1992, Reno.
6. Bhattacharjee, S., West, J., and Dockter, S. "A Simplified Theory for de Ris Flame Spread over Thermally thick and Thin Fuel", Combustion and Flame, Accepted for Publication, 1995.
7. Bhattacharjee, S., and Altenkirch, R.A., Twenty-Third (Int) Symp. on Combustion, pp. 1627-1633, The Combustion Institute, Pittsburgh, (1990).
8. Bejan, A., "Convection Heat Transfer", John Wiley and Sons, Inc., 1982.
9. Williams, F.A. Sixteenth Symp. (Int.) on Comb., The Comb. Inst., Pittsburgh, (1976), pp. 1281-1294.
10. West, J., Bhattacharjee, S., Thomas, P., Ramirez, B., and Altenkirch, R.A. 1994, ASME Summer Conference, Colorado Springs, CO pp.29-36.

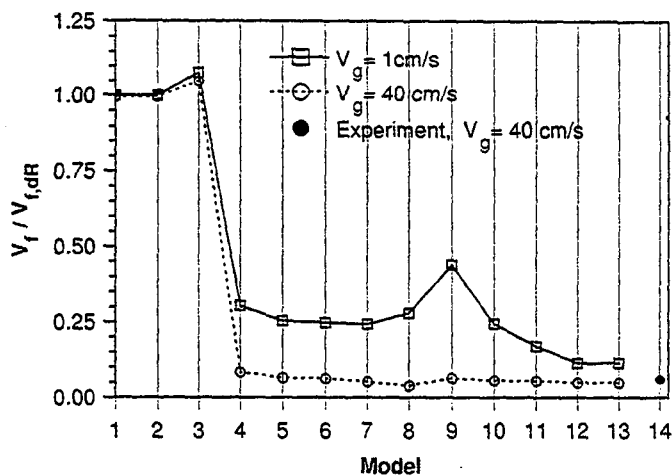


Fig. 1. Computed spread rates for different models. Models on the right are progressively more comprehensive. FDC configuration, $\hat{V}_g = 40$ cm/s, 1 cm/s, $\gamma_{O,\infty} = 0.533$, $\hat{P}_\infty = 1.0$ atm.

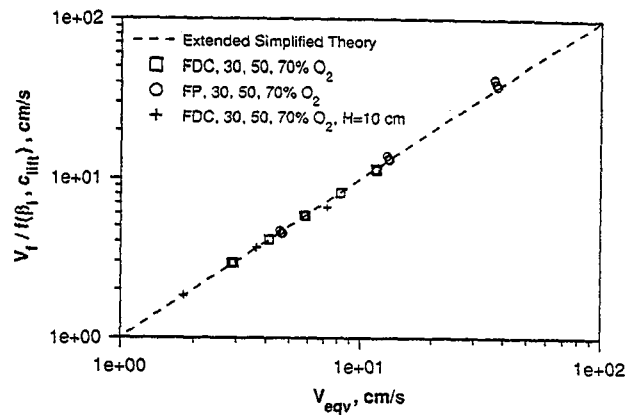


Fig. 2. Computed and EST-predicted spread rates for different flow configurations and ambient conditions.

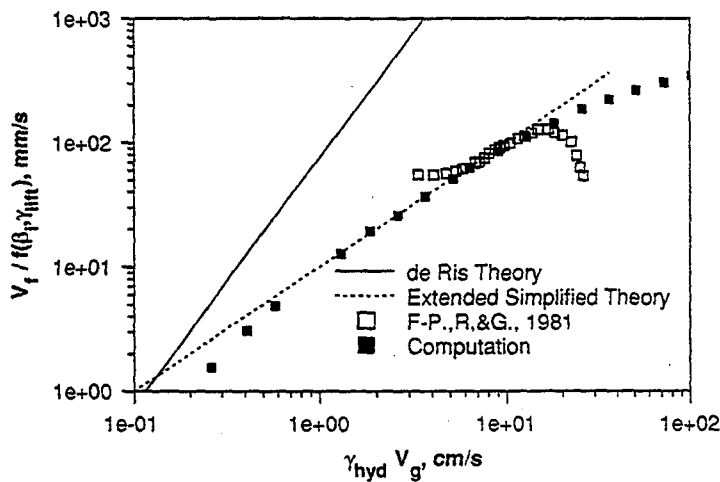


Fig. 3. Experimental data [2] vs. the prediction of EST.

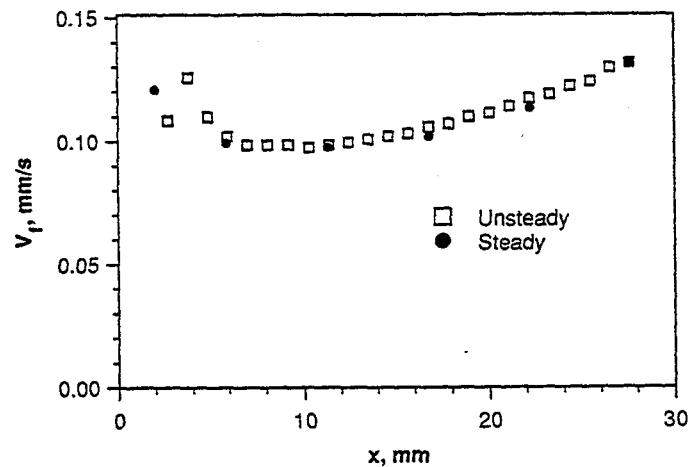


Fig. 4. Spread rate predicted by the steady and the unsteady codes for $\hat{V}_g = 1$ cm/s, $\gamma_{O,\infty} = 0.533$, $\hat{P}_\infty = 1.0$ atm.

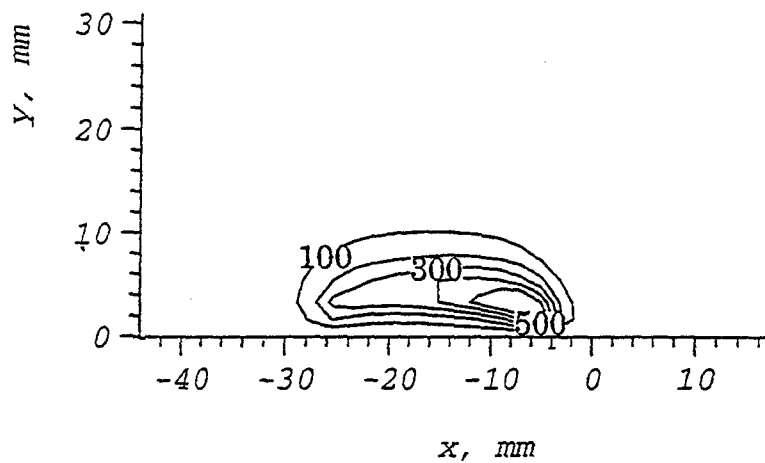


Fig. 5. Intensity contours ($W/m^2.sr$) for the 4.5 micron band for a particular case of the experimental matrix.

FIRE SAFETY EXPERIMENTS ON "MIR" ORBITAL STATION

Egorov S. D., Belayev A. Yu., Klimin L. P., Voiteshonok V. S., Ivanov A. V.

Keldysh Research Institute of Thermal Processes
Russia, Moscow

and

Semenov A. V., Zaitsev E. N., Balashov E. V., Andreeva T. V.

RKK "Energia"
Russia, Moscow Region

Introduction

The actuality of investigating combustion of various substances under microgravity is related to increasing fire hazard probability on spacecrafts. Higher power levels of onboard power systems of long-life space station under development, first of all of the International Space Station (ISS) "Alpha", and fulfillment of scientific experiments and technological operations employing high temperatures, require additional measures on preventing fires. The main trends of investigations, required for solution of this problem, were discussed at IAF-94 in Moscow [1].

The process of heterogeneous combustion of most materials under zero-g without forced motion of air is practically impossible. However, ventilation is required to support astronauts' life and cool equipment. The presence of ventilation flows in station compartments at accidental ignition can cause a fire. An additional, but exceedingly important parameter of the fire risk of solid materials under zero-g is the minimum air gas velocity at which the extinction of materials occurs. Therefore, the conception of fire-safety can be based on temporary lowering the intensity of ventilation and even turning it off.

To substantiate the conception suggested, quantitative data are required. Short-time realization of microgravity on drop towers and flying laboratories not always enables obtaining of reliable results. It is expedient to study the limiting conditions of combustion by this way only in the case of gas-phase burning of solid materials. If combustion occurs on the surface of materials, then laboratory simulation of microgravity not limited by time seems to be a more effective approach.

The essence of the approach consists in suppression of free convection that is practically absent in the case of microgravity. The intensity of free convection in combustion of a sample with the characteristic dimension d is characterized by the Grashof number:

$$Gr = g\beta\rho^2 d^3 \Delta T / \mu^2 = g\rho^2 d^3 \Delta T / \mu^2 T.$$

It follows from the Grashof number expression that convection can be suppressed on the ground by reducing the air density ρ , i.e. the pressure value. Besides, the influence of free convection can be decreased additionally by placing a burning sample between two horizontal plates. To simulate the process of combustion in forced motion of gas, the experiment should be performed at the same Reynolds number and oxygen concentration as on the orbital station. To realize the approach described, a

laboratory experimental device was developed on which experiments are being currently performed. As an example, Fig. 1 shows results obtained from investigation of gas-phase combustion of acrylic plastic (PMMA) on a drop tower and simulation of diminished gravitation on the laboratory device. The range of the applicability of these approaches can be determined only through space experiments.

Therefore, the information on the limiting conditions of combustion under natural conditions is needed from both scientific and practical points of view. It will enable to judge about the reliability of results of ground-based investigations and develop a conception of fire safety of inhabited sealed compartments of space stations to be provided by means of nontraditional and highly-effective methods without both employing large quantities of fire-extinguishing compounds and hard restrictions on use of polymers.

In this connection, an experimental installation was created to study the process of heterogeneous combustion of solid non-metals and to determine the conditions of its extinction under microgravity [2]. This installation was delivered to the orbital station "Mir" and the cosmonauts Viktorenko and Kondakova performed initial experiments on it in late 1994.

Experimental Installation and Procedure of Experiments

The experimental installation is shown in Fig. 2. The installation consists of a combustion chamber with an electrical systems for ignition of samples, a device for cleaning air from combustion products, an air-suction unit, air pipes and a control panel.

The combustion chamber is the basic component of the installation, it is a channel of rectangular section (150 by 80 mm) which is 320 mm in length. The chamber has two rotatable devices in the form of drums on which experimental samples are attached, six samples on each drum. The chamber has two rectangular windows to visualize the process and record it on a video tape. They are arranged on its lateral surfaces, perpendicular to each other. At the inlet of the combustion chamber, a safety mesh and removable metallic shutter are installed. The igniter is a spiral electric heater. There are two igniters in the combustion chamber, one of which is reserval.

The air-suction unit is a suction fan with a flow regulator; it provides preset velocities of the incoming flow. The installation employs a so-called open scheme, i.e. the gas mixture leaving the chamber is filtered and enters the habited compartment of the space station. The installation is controlled from the control panel.

The whole experiment is controlled by telemetry and recorded with two video cameras located at two different places. Besides the picture, parameters are recorded to determine the velocity of the air flow incoming to the samples, the time points of switching on/off the devices, etc. The combustion chamber temperature is also controlled.

An experiment is conducted as follows. The shutter is removed from the combustion chamber. The sample to be tested is installed along the centerline of the chamber with the rotatable devices. Power is supplied to the control panel. The suction-fun is turned on and air motion in the chamber required for ignition is established. Then, the ignition system is turned on and the hot spiral is brought to the sample. When flame appears, it is removed and a required flow regime is established by means of the air-suction unit. The velocity of the incoming flow can be changed in experiment from its maximum value of 20 cm/s down to zero. When the combustion of sample is over, the combustion chamber is ventilated with the maximum air flow rate. After that, a similar procedure is performed with the next sample, etc.

The experimental procedure described was developed on the ground with an analogue of the space installation.

Objectives of Investigation

In the initial series of experiments, 12 samples were burnt. On one of the drums, 6 samples of cotton (which is a representative of smouldering materials) were fixed, and on the other, 6 samples of PMMA (burning in a gas-phase regime) were fixed. The PMMA samples were plates of 1 by 8 by 60, 2 by 8 by 60 and 3 by 8 by 60 mm dimensions. The cotton samples were cords with metallic bases inside.

The main objectives of experiments of this series were as follows:

- a) verification of the reliability of the installation in orbital flight;
- b) verification of the experimental procedure;
- c) investigation of combustion of two types of materials under microgravity at various velocities of the incoming air flow.

Tentative experimental results

Experiments with each smouldering material sample were conducted at fixed velocities of the incoming flow. Results were obtained for the velocities of 20, 12, 5, 3 and 2 cm/s.

In the experiment with the last (sixth) sample, it had been planned to turn the suction-fan off after its ignition, i.e. to reduce the velocity of the incoming flow down to zero; however, this plan failed for some technical reasons. Tentative results of the tests are given in Table 1.

Table 1

Smouldering material test results

Sample number	1	2	3	4	5	6
Air flow velocity, cm/s	20	12	5	3	2	?
Ignition time, s	3	2	4	3	3	2
Combustion time, s	14	18	20	21	21	22
Burning rate, mm/s	4.3	3.3	3.0	2.9	2.9	2.7

Experiments with the first two PMMA samples of 1 mm thickness were performed with constant velocities of the incoming air flow of 3 and 2 cm/s. In experiments with the remaining four samples of 2 and 3 mm thickness, the velocity was reduced from 2 cm/s down to zero. After the samples became charred half of their lengths at the constant velocity of the incoming air flow of 2 cm/s, the suction-fan was turned off. In doing so, the flame changed for about 10 to 15 s. It became spherical and changed its color from yellow-orange to light-blue. Before the flame extinction, flashes on a background of fading light-blue fluorescence were observed. Tentative results of the tests are given in Table 2.

Table 2

PMMA test results

Sample number	1	2	3	4	5	6
Air flow velocity, cm/s	3	2	2 → 0	2 → 0	2 → 0	2 → 0
Ignition time, s	8	4	8	4	2	5
Total combustion time	82	146	89	101	153	49
Combustion time at preset flow velocity, s		131	39	70	122	-
Extinction-out time, s	-	-	15	10	7	49
Burning rate, mm/s					0.03	
Sample thickness, mm	1	1	2	2	3	3

The tests were performed at the air pressure in the compartment of about 660 mm mercury. The oxygen partial pressure of 152 mm mercury corresponded to its 23 % concentration.

The results presented in this work will be refined and analyzed after the video tapes are returned to earth and the video recording of the experiments is treated by computer.

Conclusion

The aims of the pilot experiments on combustion of materials aboard the "Mir" space station has been mainly achieved. The installation has demonstrated its suitability for conducting investigations of combustions of non-metal structural materials under microgravity. The results obtained show that combustion of materials ceases when the velocity of forced flow diminishes, i.e. there is a limiting admissible velocity of ventilation flows at which arising combustion zone extinguishes. The work accomplished is a substantiation to proceed experiments on investigation of parameters of combustion of non-metal structural materials on both the existing "Mir" space station and the ISS "Alpha" under development.

References

1. Egorov S. D., Belyaev A. Y., Ivanov A. V. et al. "Main Trends of Investigation of Material Combustion in Reduced Gravity for Orbital Station Fire Assurance" - Proceeding of International Aerospace Congress, August 15 - 19, 1994, Moscow, Russia.
2. Patent RF № 2006841.
3. Melikov A. S. et al. "On Limiting Conditions of Polymer Combustion in the Absence of Free Convection" - Fizika gorennya i vzryva, № 4, 1983 (in Russian).

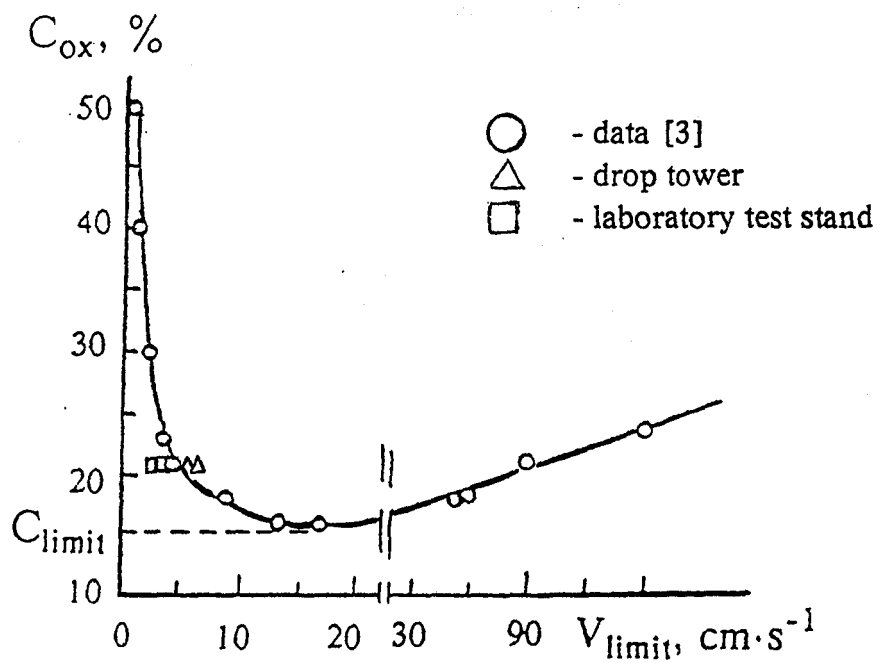


Fig.1. Limiting flow velocity for PMMA combustion versus oxygen concentration

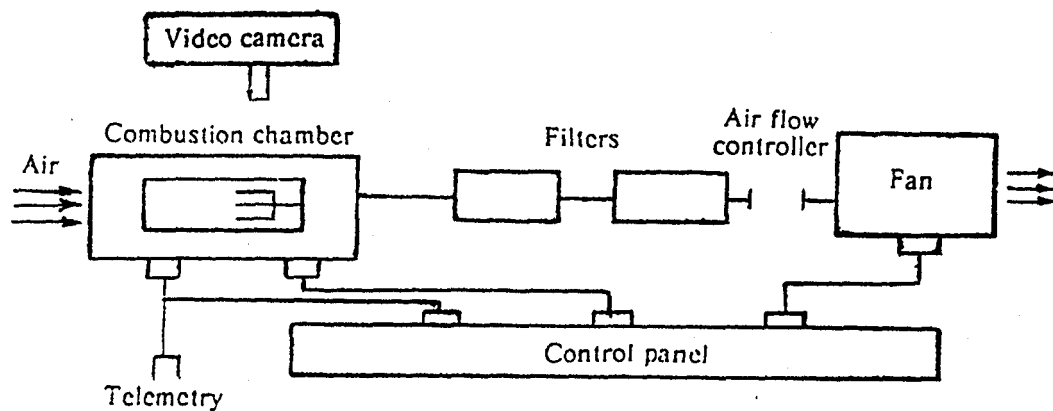


Fig.2. Space experimental installation

RESEARCH ON IGNITION AND FLAME SPREAD OF SOLID MATERIALS IN JAPAN

Kenichi Ito and Osamu Fujita
Hokkaido University
Sapporo, Japan

Introduction

Fire safety is one of the main concerns for crewed missions such as the space station. Materials used in spacecraft may burn even if metallic. There are severe restrictions on the materials used in spacecraft from the view of fire safety. However, such restrictions or safety standards are usually determined based on experimental results under normal gravity, despite large differences between the phenomena under normal and microgravity. To evaluate the appropriateness of materials for use in space, large amount of microgravity fire-safety combustion data is urgently needed.

Solid material combustion under microgravity, such as ignition and flame spread, is a relatively new research field in Japan. As the other reports in this workshop describe, most of microgravity combustion research in Japan is droplet combustion as well as some research on gas phase combustion.

Since JAMIC, the Japan Microgravity Center, (which offers 10 seconds microgravity time) opened in 1992, microgravity combustion research is robust, and many drop tests relating to solid combustion (paper combustion, cotton string combustion, metal combustion with Aluminum or Magnesium) have been performed (ref.1). These tests proved that the 10 seconds of microgravity time at JAMIC is useful for solid combustion research.

Some experiments were performed before JAMIC opened. For example, latticed paper was burned under microgravity by using a 50 m drop tower to simulate porous material combustion under microgravity (ref.2). A 50 m tower provides only 2 seconds microgravity time however, and it was not long enough to investigate the solid combustion phenomena.

Current Research Activities

Some theoretical and numerical approaches on ignition and flame spread of paper sheet have been performed by the Nagoya University group (ref.3). They have described the events occurring during paper preheating, ignition, and flame spread at various oxygen concentrations.

A research program titled 'Combustion properties of solid materials' and supported by JSUP under an agreement for the international collaboration between NEDO and NASA under the research project 'Advanced Combustion Science Utilizing Microgravity Combustion Research', has been started in 1994. Prof. Ito of Hokkaido University and Prof. Hirano of the University of Tokyo participate in the program on the Japanese side. From NASA, Ms. Sandra L. Olson, LeRC, and Dr. Takashi Kashiwagi, NIST, participate. According to the agreement, microgravity experiments of paper combustion were performed using the JAMIC facilities in March, 1995. A summary of this experiment will be reported in this workshop by the US side. This program will continue for 3 years.

The Hokkaido University group is investigating flame propagation phenomena with two types of solid materials. The first is flame spread on wire insulation which is heated up to 125 °C by an inner wire electric current. The flame spread rate is measured under various oxygen concentrations and pressures. The second is flame propagation of a porous material using polystyrene foam. Polystyrene foam beads of ϕ 2-3 mm are two-dimensionally arranged to simulate a porous material in ignition and flame spread. This research has been performed by using the 10 second drop shaft and a 1.2 second (10 m) drop tower.

This report describes the experimental results from these two kinds of solid material combustion tests.

Wire Insulation Combustion

A nichrome heated coil was used as the ignitor. The sample wire was placed at the center of the ignition coil. A schematic diagram of the experimental apparatus is shown in Fig 1. The motion of the flame was recorded by a Hi8 video camera. The shape of the molten insulator and products from the insulator were visualized by Schlieren images and also recorded by 8mm video camera. Wire tension was provided by a tension spring to avoid slackening during the combustion. The dimensions of the samples are listed in Table 1.

A part of the experimental results are shown in Fig 2. In microgravity, the flame becomes spherical 1 or 2 seconds after the capsule release. The flame moves at constant speed during the drop. The pressure dependency of the flame spread is shown in Fig.3 with the results under normal gravity. In addition, results without current were shown in the figure. Under microgravity, in the heated condition, the flame spread rate decreases with increasing pressure. However, the effect of the pressure is not so large. A pressure change of 4 times (1.6/0.4) results in a 30% decrease in the flame spread rate. Without current, we can estimate almost the same results. Compared with normal gravity, the flame spread rate is remarkably slow. Roughly, the spread rate at 1 g is 2.5 times that under microgravity.

Porous Material Combustion

Porous materials are considered as a model of many flammable real solids, such as waste paper, accumulated room dust, cloth, and buffer materials. In this experiment, an array and two-dimensional arrangements of beads of polystyrene foam (PSF) were used as a model of porous materials. PSF contains air in the order of 60 or 80 times of the solid volume. PSF beads shrink

immediately by radiation from flames, and the rate of shrinkage is faster than the burning time of the bead. Consequently, we can estimate the heat flux radiated from the surrounding flames by the shrinkage rate or mass-loss of the beads. This particular characteristics of polystyrene foam makes it possible to use the beads of polystyrene foam simultaneously as combustible material and heat flux detector.

In a part of the microgravity experiments, we used the new 10 m drop tower, shown in Fig.3, at Hokkaido National Industrial Research Institute (HNIRI). A linear motor breaking system is employed and the pay load is 100 kg.

Single arrays of beads and two kinds of two-dimensional arrangements were examined. The diameter of beads, the distance between beads, and oxygen concentration were varied. A model of the combustion process is shown in Fig.4. Both auto-ignition and gas phase propagation were observed. The effects of the oxygen concentration with a single array is shown in Fig.5. Figure 6 is a record of the flame position from the ignition point. The distance between beads was increased from 2.5mm to 5.5 mm. Above 5.5 mm, there is no flame spread.

The results with the two-dimensional arrangement are shown in Figs 7 and 8. Ignition was at the center. It is evident that shrinkage occurs at first and then ignition follows. In the case of a square lattice, the flame spread towards 45 degrees is slower than that at right angles. For the hexagonal arrangement, there are still differences in the flame spread in different directions.

Conclusions and Future Plans

The studies conducted to date in Japan have provided new information on the behavior of solid flame spread under microgravity. In 1995, a series of microgravity experiments on flame spread of materials will be conducted by NASDA using the MGLAB drop shaft which was completed in February, 1995. The University of Tokyo and IHI Research Institute will participate in the experiment. The Hokkaido University group is planning to use parabolic flights of the MU-300 airplane. Flame spread rate of un-heated materials will be measured. Up to now, there is no research project on solid ignition in Japan. But, we consider the necessity of high energy ignition studies under microgravity for future crewed space activities essential.

References

1. Ito, K., Fujita, O., Tazumi, M., Ito, H. and Tagashira, T. : Preliminary experiments on solid combustion in microgravity at JAMIC drop tube, Proceedings of the 18th International Symposium on Space Technology and Science, 1992, pp. 2295-2302.
2. Ito, K., Fujita, O., and Ito, H.: Observation of fire spreading over porous materials under microgravity, 29th Symposium (Japanese Section) on Combustion, 1991, pp. 16-18.
3. Nakamura, U., Kushida, G., Yamashita, H. and Takeno, T.: Numerical analysis on paper combustion mechanism under microgravity environment, 32nd Symposium (Japanese Section) on Combustion, 1994, pp. 221-223.

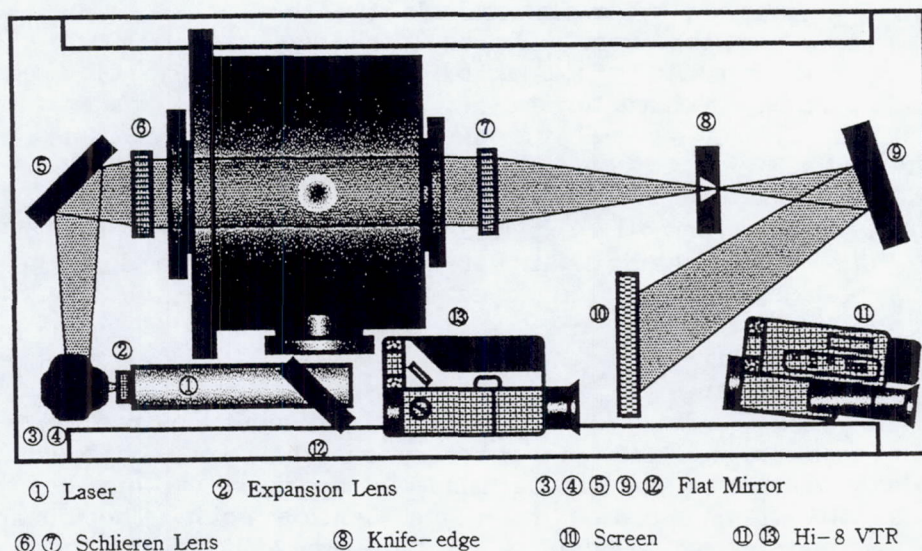
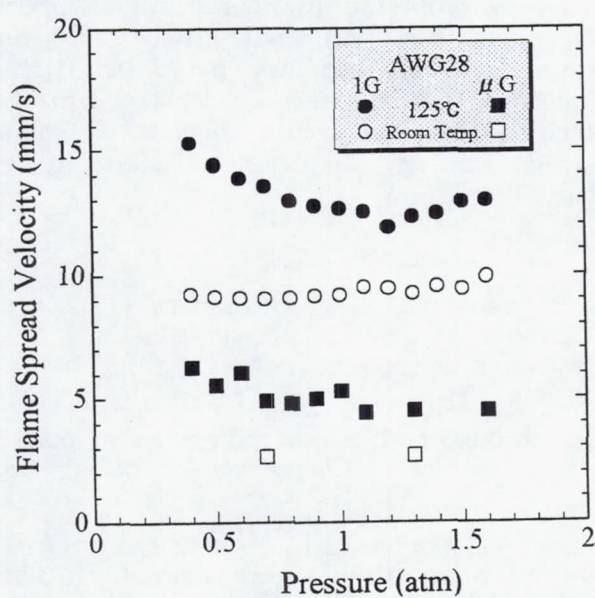


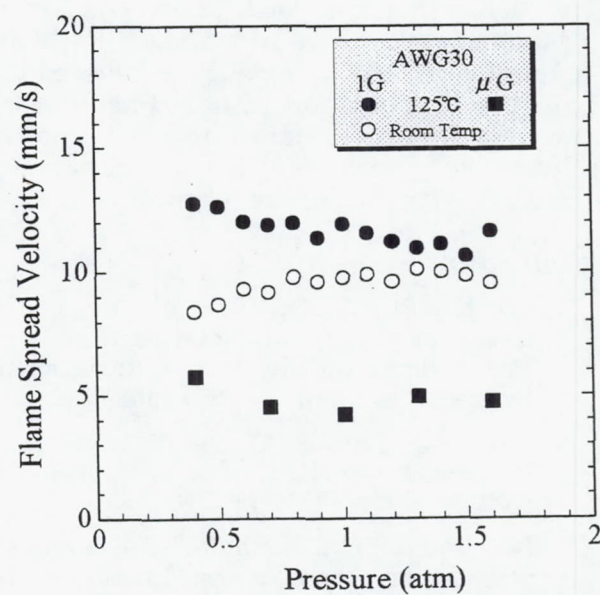
Fig. 1 Experimental Set-up for Wire Insulation Combustion

Table 1 Wire dimensions

sample	wire diameter d_s	sample diameter d	insulator thickness Δ
AWG-24	0.45(mm)	1.20(mm)	0.875(mm)
AWG-28	0.30	0.60	0.15
AWG-30	0.25	0.55	0.15



(a) AGW28



(b) AGW30

Fig. 2 Effects of pressure on flame spread rate (a) AGW28, and (b) AGW30
 (O_2 30 %)

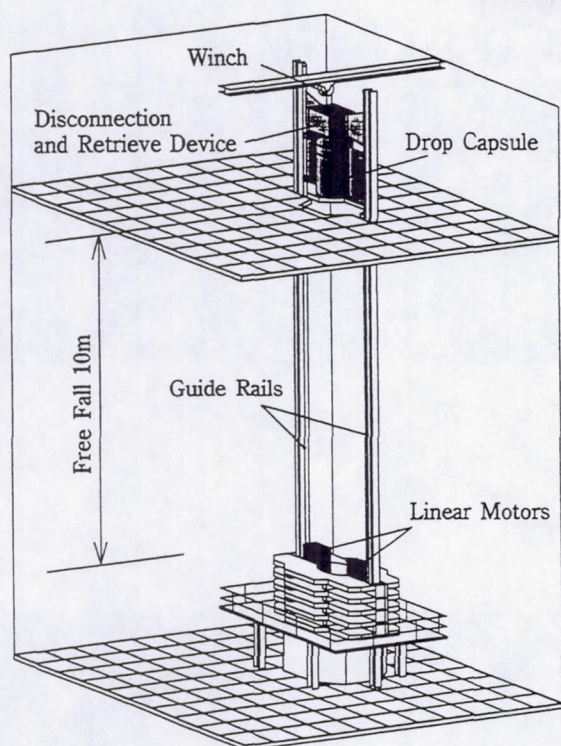


Fig. 3 10 m drop tower in HNIRI

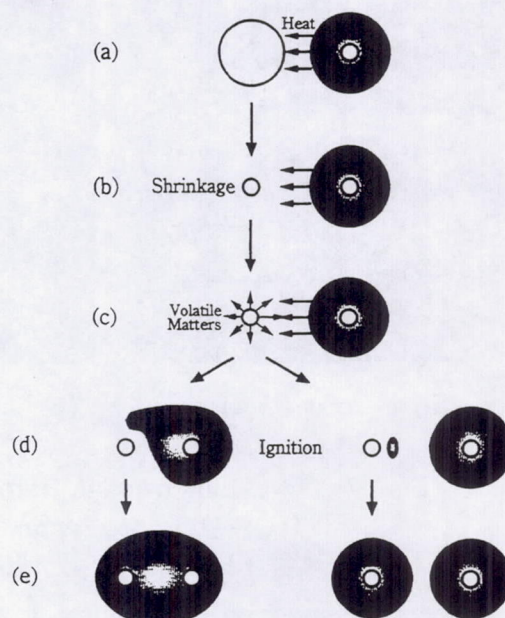


Fig. 4 Combustion process of polystyrene foam

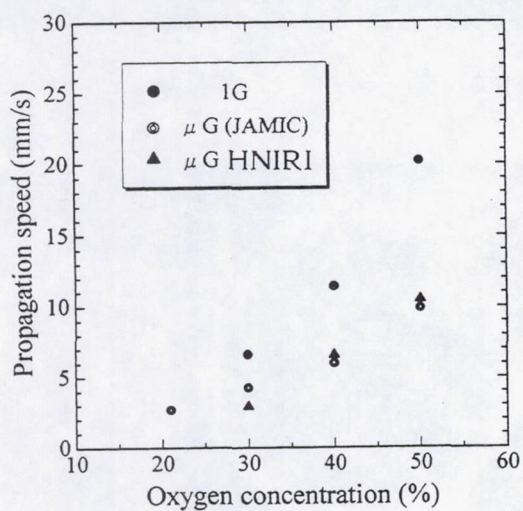


Fig. 5 Propagation speed of single array (ϕ :2.5mm,space:2.5mm)

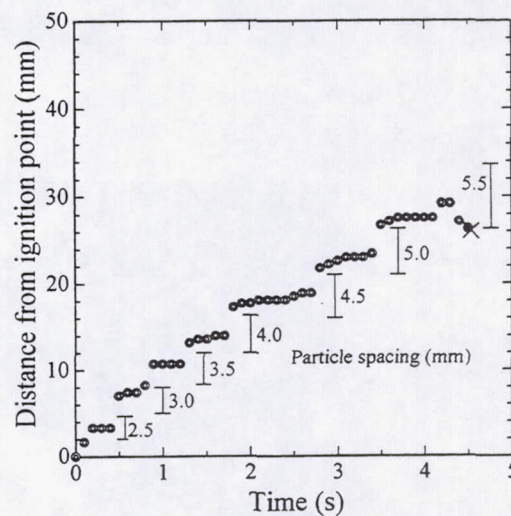
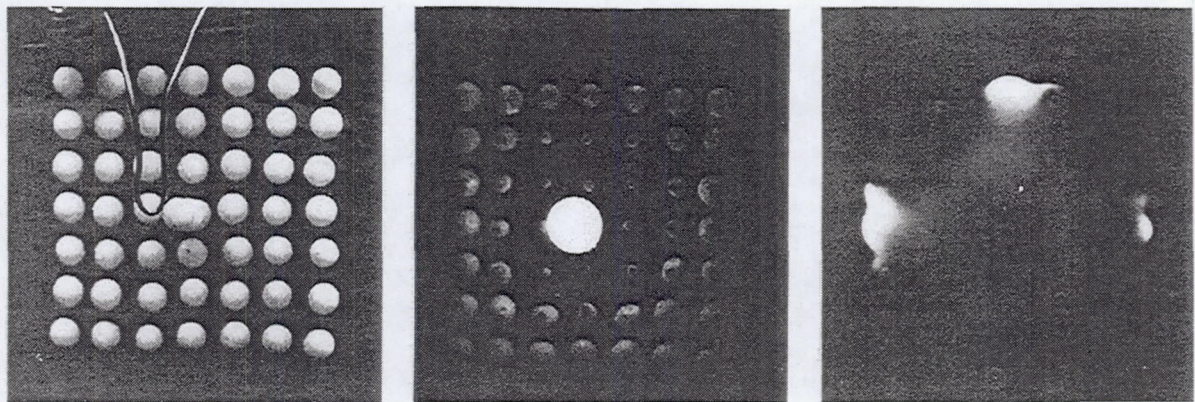


Fig. 6 Records of flame position (O_2 40%, ϕ :2.5 mm)

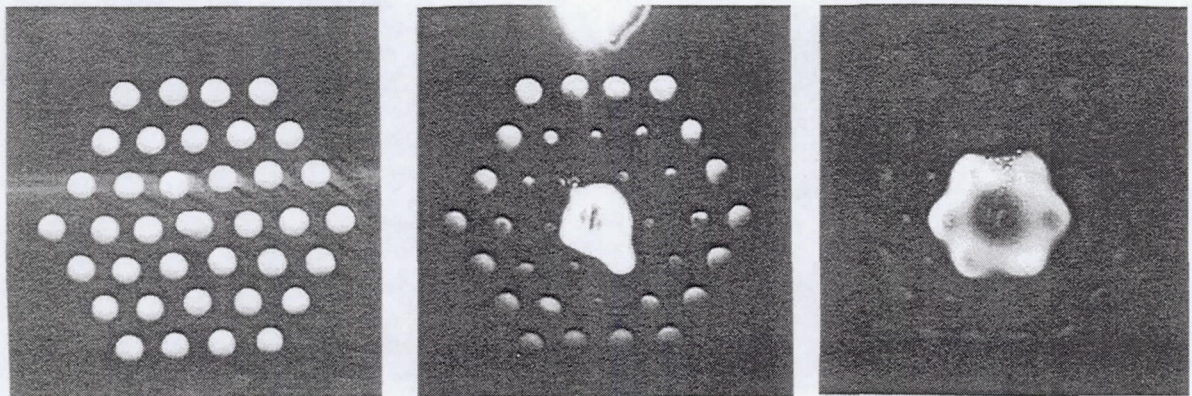


(a) before ignition

(b) 1.0 s after ignition

(c) 3.6 s

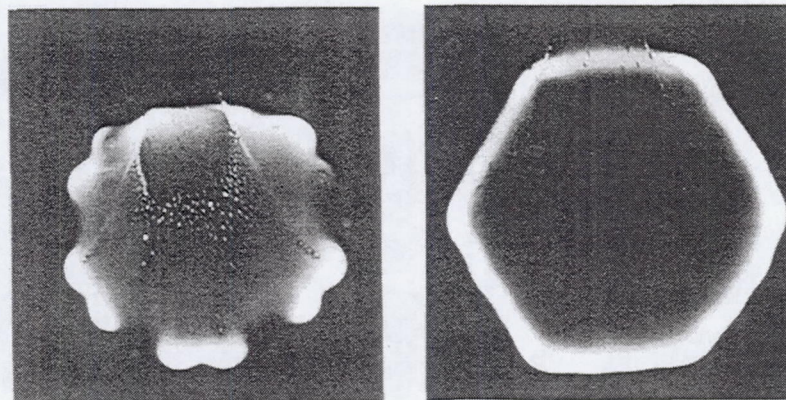
Fig. 7 Two-dimensional flame spread; Square lattice arrange
(O_2 40%, ϕ :2.5mm,space:3.5mm)



(a) before ignition

(b) 1.1 s after ignition

(c) 1.6 s



(d) 2.9 s

(e) 4.0 s

Fig. 8 Hexagonal lattice arrange (O_2 40%, ϕ :2.5mm,space:4.5mm)

IGNITION AND SUBSEQUENT TRANSITION TO FLAME SPREAD IN A MICROGRAVITY ENVIRONMENT

Takashi Kashiwagi, Kevin McGrattan and Howard Baum
Building and Fire Research Laboratory
National Institute of Standards and Technology
Gaithersburg, Maryland 20899

Introduction

The fire safety strategy in a spacecraft is (1) to detect any fire as early as possible, (2) to keep any fire as small as possible, and (3) to extinguish any fire as quickly as possible. This suggests that a material which undergoes a momentary, localized ignition might be tolerable but a material which permits a transition to flame spread would significantly increase the fire hazard. Therefore, it is important to understand how the transition from localized ignition to flame spread occurs and what parameters significantly affect the transition. The fundamental processes involved in ignition and flame spread have been extensively studied, but they have been studied separately. Some of the steady state flame models start from ignition to reach a steady state, but since the objective of such a calculation is to obtain the steady state flame spread rate, the calculation through the transition process is made without high accuracy to save computational time.

We have studied the transition from a small localized ignition at the center of a thermally thin paper in a microgravity environment [2]. The configuration for that study was axisymmetric, but more general versions of the numerical scheme have been developed by including the effects of a slow, external flow in both two and three dimensions. By exploiting the non-buoyant nature of the flow, it is possible to achieve resolution of fractions of millimeters for 3D flow domains on the order of 10 centimeters. Because the calculations are time dependent, we can study the evolution of multiple flame fronts originating from a localized ignition source. The interaction of these fronts determines whether or not they will eventually achieve steady state spread. Most flame spread studies in microgravity consider two-dimensional flame spread initiated by ignition at one end of a sample strip with or against a slow external flow [4]. In this configuration there is only one flame front. A more realistic scenario involves separate, oppositely directed fronts in two dimensions, or a continuous, radially directed front in three dimensions.

Results and discussion

We present here some results of both the two and three dimensional codes. Unless otherwise noted, the ambient oxygen concentration for the simulations is nominally 30%. The gas phase reaction parameters were chosen to roughly match the experiments of Olson; it is not our intention to fine-tune the parameters to agree with the data exactly but rather to assess qualitative trends.

The spatial resolution for both the 2D and 3D codes is the same; grid cells for the finite difference scheme are 1 mm in length in the directions parallel to the surface and about 0.25 mm in the normal direction, expanding to about 1 mm farther away. The increased resolution in the normal direction is intended to capture large gradients at the surface. For this grid resolution, the 2D calculations require less than an hour of CPU time on a typical workstation, while the 3D calculations require several tens of hours. Increasing the resolution in the 2D simulations did not effect the results appreciably, thus the resolution was chosen to match the 3D cases for consistency. Obviously, most of the parameter studies were conducted with the 2D code, reserving the 3D code for examination of special geometric effects.

The effect of a slow external flow on the transition period is considered first. A strip is ignited in the middle in order to generate two flames at the same time. An external wind of 2 cm/s is imposed along the length of the strip. Fig. 1 displays the evolution of the two flames during the transition period. The wind blows from left to right. The upwind flame (left) successfully makes the transition to flame spread and propagates into the wind at about 1.5 cm/s. The downstream flame, however, does not survive the transition, as it lifts off from the surface and a clear flame front does not appear. Not only does the upwind flame survive, but it is about twice as strong as a flame spreading in the absence of wind as measured by the peak gas phase reaction rate. The quiescent flame propagates at about 1.2 cm/s.

The experiments of Olson [5] for this configuration show the flame propagating at about 1.95 cm/s while the quiescent counterpart spreads at about 1.8 cm/s. The downstream flame in these experiments is reportedly much weaker, much sootier, and in the short test time likely to extinguish. The dependence of the upstream flame spread rate on flow velocity has been attributed to oxidizer transport effects [5], or radiative loss effects [1]. Both of these theories is supported by the numerical simulations. The experiments and numerical simulations both show a strengthening of the upstream flame due to increased oxidizer transport in the presence of a slow external wind. Also, reduced radiative loss from the sample surface in front of the flame leads to faster flame spread. It is difficult to judge which is the more important effect due to the uncertainty about the gas phase kinetics, which for this model is described by a one step global reaction of fuel and oxygen.

The weakness and extinction of the downstream flame of the sample strip seems to be due to lack of available oxygen. Clearly in the two flame case, the upwind flame robs the downstream flame of the oxygen needed to survive the transition. To show this, a few single flame simulations are performed using the same sample strip as before, except that no fuel is present upwind of the ignition point. For an imposed wind of 2 cm/s, where no upwind flame is present, the downstream flame is weak, but unlike before it survives the transition period. Fig. 2 displays the computed oxygen mass fraction contours, along with the gas phase reaction zones, of three other single flames under different wind speeds. The case of no wind represents an opposed flow, because in flame fixed coordinates the flame encounters a flow equal to its spread rate. The case of a 5 cm/s wind represents a concurrent flow, because the wind speed is faster than the spread rate. The 1 cm/s case is neither concurrent nor opposed because the wind speed is about the same speed as the flame spread rate (at least before the flame dies out). It is clear from the oxygen contours why the 1 cm/s case extinguishes — the oxygen concentration gradients are the least steep among the three cases and the oxygen is unable to reach the reaction zone in sufficient concentration to maintain combustion. The flame exposed to a 5 cm/s external wind is strengthened by increased convective transport of oxygen due to the wind, and by the preheating of the sample, again due to the wind. As seen by Ferkul and T'ien [3], the overall flame length increases with increasing wind speed.

Olson reports an experiment in 30% oxygen (Ref. [5]) in which a wind is directed in the same direction as the flame spread, and the wind speed is slightly slower than the flame speed (characteristic relative velocity is 0.1 cm/s). She notes that the flame is very sooty, and propagates more slowly than the opposed flow counterparts. The numerical simulation in which the flame is neither concurrent nor opposed shows this flame dying out, but again this is due to the choice of the gas phase reaction parameters.

It has been pointed out by Bhattacharjee *et al.* [1] that for low speed flame spread heat loss in front of the flame has a significant impact on the steady state spread rate. This effect is also seen in the transition period between ignition and flame spread. If the distribution of the radiative ignition source is spread out, it takes longer for ignition to occur, and the accumulation of fuel vapors then generates a larger flame and increases the heat feedback rate during the transition. In effect there is greater preheating of the sample in front of the developing flame front. Fig. 3 shows the effect of varying the initial flux profile, while fixing the total energy delivered to the sample. Ignition is triggered most rapidly by a sharp radiative flux distribution with a high peak flux (20 W/cm^2). However, for a wider distribution with lower peak flux (5 W/cm^2), the preheating of the sample in front of the flame causes it to propagate at a higher rate of speed during the transition period. Also, its overall width is wider than that of the flame ignited with a sharp radiant flux profile (or a pilot wire). Bhattacharjee *et al.* note that more preheating of the sample surface in front of the flame causes an increase in flame speed and a widening of the overall flame.

Next, we examine some calculations of the transition to flame spread in three dimensions. Fig. 4 shows the evolution of a flame ignited at the center with an axially symmetric radiative flux in the presence of a 2 cm/s wind. The umbrella-shaped flame appears initially due to the expansion of hot gases. Then it changes to a horseshoe-shaped flame propagating upwind. The downwind part is extinguished, as was seen in the 2D simulations. This simulation clearly shows the effects of a slow wind on the transition.

Fig. 5 shows a 3D simulation of a quasi-2D experiment, that of the ignition of a 5 cm wide strip with a 2 cm/s wind blowing along the length (which has been discussed above). For the short duration of the simulation (3 seconds) the centerline flame profile was similar to the 2D counterpart. However, the downstream flame at the edge of the strip is stronger than the upstream flame and propagates more rapidly due to the increased supply of oxygen there. Fig. 6 displays the flow vectors for this simulation near the sample surface. Note the higher velocities near the edge. The three dimensional nature of the flow field cannot be ignored. Indeed, it has been observed when comparing the 2D and the 3D simulations of the strip ignition that the downstream flame in the 2D simulation dies out before the 3D counterpart (measured at the strip centerline). This difference is mainly due to the lateral transport of oxygen, both convective and diffusive, which occurs over a few seconds.

Conclusion

It has been seen in the experiments that a slow external wind strengthens the upstream, while weakening the downstream flame. The numerical simulations agree qualitatively, and a close examination of gas phase fuel and oxygen concentrations near the flame fronts offer explanations as to the cause of the strengthening/weakening. It has been observed in the two simultaneous flame configuration that the downstream flame which are viable on their own cannot survive the transition when an upstream flame is present to rob the oxygen.

For low speed flame spread, heat losses from the sample have a great effect on the flame spread. This has also been seen in the transition process when radiative sources of various widths have been used to heat the samples. Wider sources generate more preheating in front of the flame, and the flame spreads more rapidly during the transition. Ultimately, the flame spread rate is independent of how ignition is achieved.

We are presently conducting studies of the transition to flame spread in three dimensional configurations. In addition to providing us with a useful tool to consider problems that were considered intractable before, the 3D runs also point out the limitations of 2D simulations of experiments which use relatively narrow sample strips. Experiments are presently underway in a 10 second drop tower at the Japan Microgravity Center and some of the experimental results will be presented and compared with the calculated results at the meeting.

Acknowledgments

We would like to thank Sandra Olson of the Lewis Research Center for her support and advice.

References

- [1] Bhattacharjee, S. and Altenkirch, R.A., "The Effect of Surface Radiation on Flame Spread in a Quiescent Microgravity Environment," *Combust. Flame*, Vol. 84, 1991, pp. 160-169.
- [2] Nakabe, K., McGrattan, K.B., Kashiwagi, T., Baum, H.R., Yamashita, H., and Kushida, G., "Ignition and Transition to Flame Spread Over a Thermally Thin Cellulosic Sheet in a Microgravity Environment", *Combust. Flame*, Vol. 98, 1994, pp. 361-374.
- [3] Ferkul, P.V. and T'ien, J.S., "A Model of Low-Speed Concurrent Flow Flame Spread Over a Thin Fuel," *Comb. Sci. Tech.*, Vol. 99, 1994, pp. 345-370.
- [4] Olson, S.L., Ferkul, P.V., and T'ien, J.S., "Near-Limit Flame Spread Over a Thin Fuel in Microgravity," *Twenty-Second Symposium (International) on Combustion*, The Combustion Institute, Pittsburgh, 1988, pp. 1213-1222.
- [5] Olson, S.L., "Mechanisms of Microgravity Flame Spread Over a Thin Solid Fuel: Oxygen and Opposed Flow Effects," *Comb. Sci. Tech.*, Vol. 76, 1991, pp. 233-249.

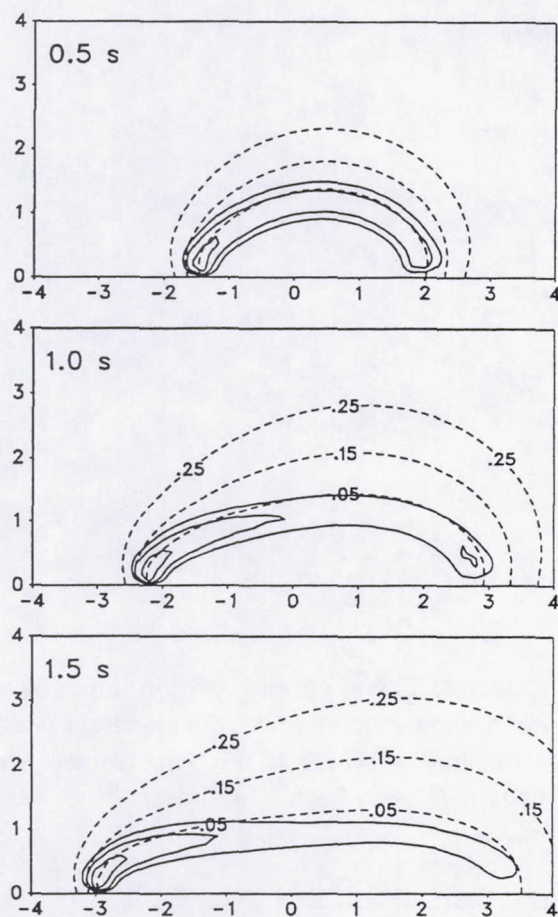


Figure 1: Transition period for a flame in the presence of a 2 cm/s wind blowing from left to right. Dashed lines indicate oxygen concentration, solid lines indicate the gas phase reaction rate.

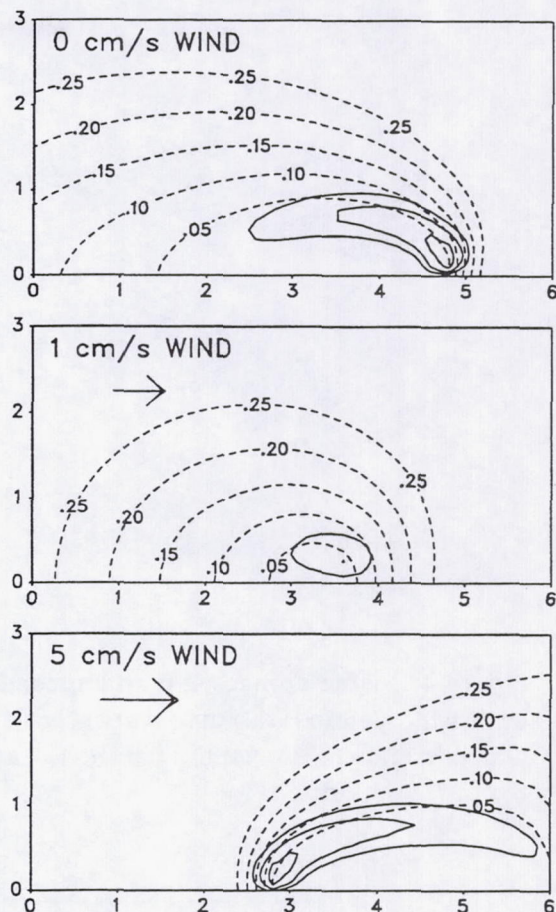


Figure 2: Three single flames with three different wind speeds 3 s from ignition.

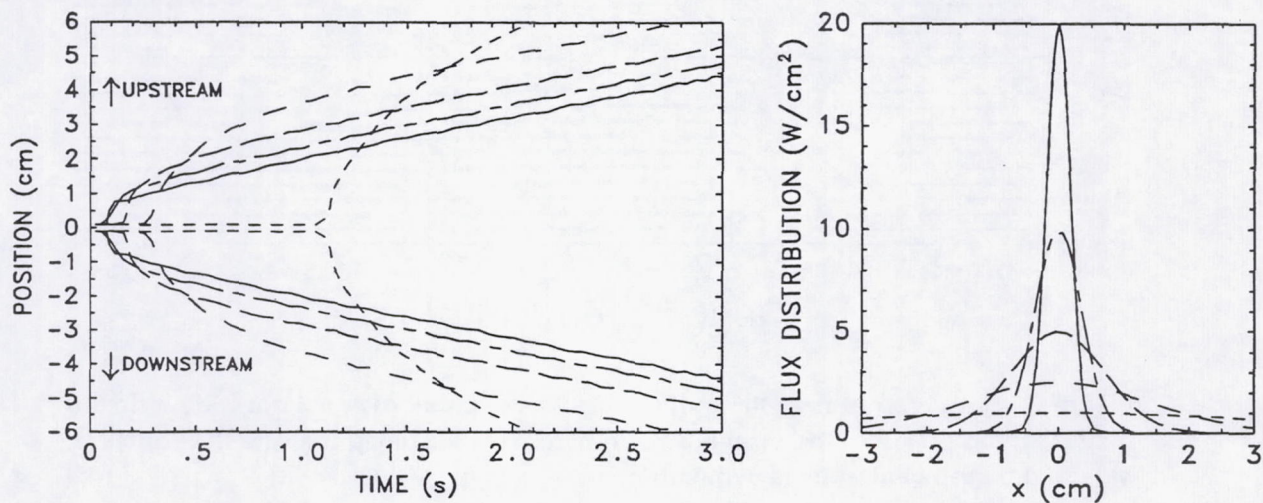


Figure 3: Flame front trajectories (left) for various radiative source distributions (right), all of which have the same integrated heat flux. The oxygen concentration is 30%; there is no external wind.

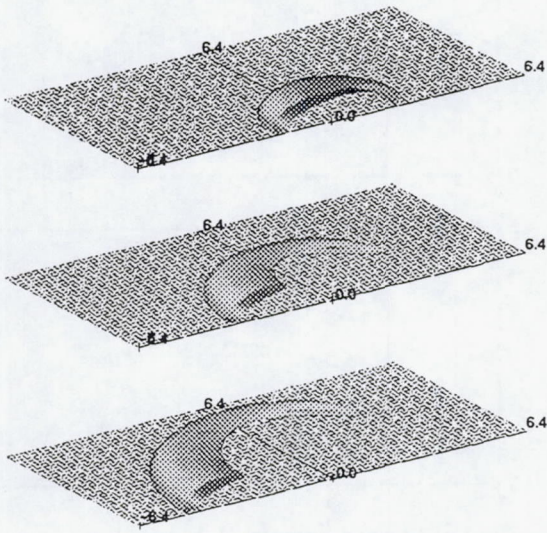


Figure 4: Flame spread with an imposed 2 cm/s wind (left to right) over a sheet, half of which is shown. Shown are flames 1, 2 and 3 s past ignition.

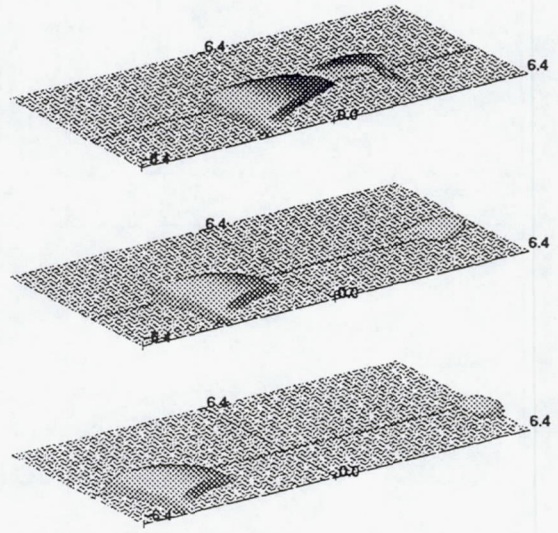


Figure 5: Flame spread with an imposed 2 cm/s wind (left to right) over a 5 cm wide strip, half of which is shown. Shown are flames 1, 2 and 3 s past ignition.

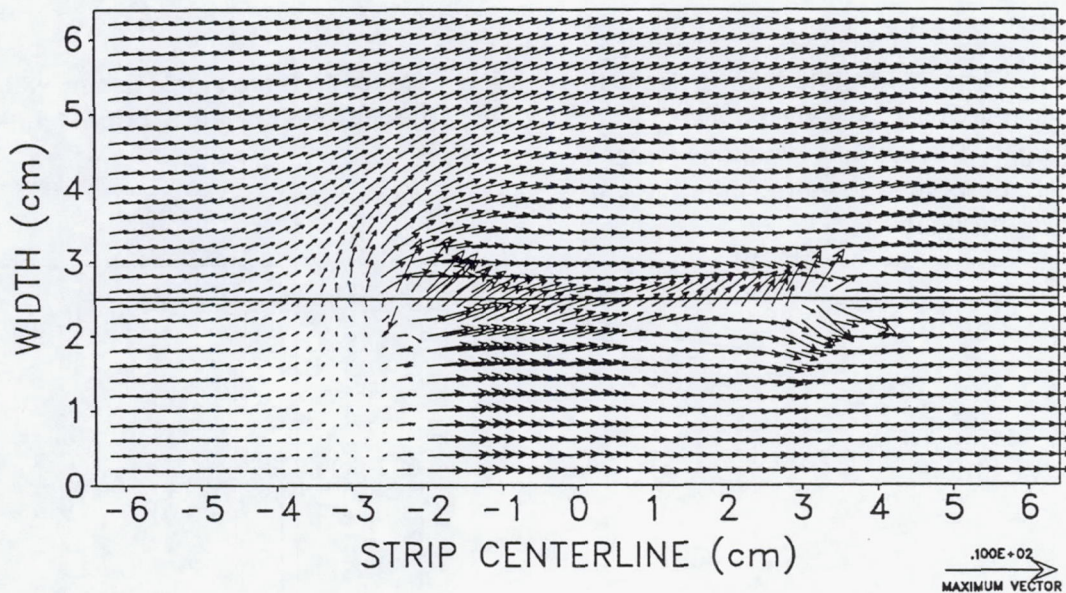


Figure 6: Flow vectors near the surface for flame spread over a 5 cm wide strip 1.0 s after ignition. Half of the strip is shown here. It is assumed that the flow on each side of the strip centerline is symmetric.

Premixed Atmosphere and Convection Influences on Flame Inhibition and Combustion (PACIFIC)

Paul D. Ronney

Department of Mechanical Engineering,
University of Southern California, Los Angeles, CA 90089-1453

Objective

Under NASA-Lewis Grant NAG3-1611, starting date 6/1/94, a three-year experimental and theoretical study of the effects of ambient atmosphere on the properties of flame spread over thin and thick solid fuel beds has been initiated. In particular the effect of the type of inert gas, which affects the Lewis numbers of fuel and oxidant, and the effect of the addition of sub-flammability-limit concentrations of gaseous fuels to the oxidizing atmosphere will be studied. The effect of convection will be studied through one-g and μ g experiments with and without a forced flow. Moreover, the influence of thermal radiation, whose effect is known to be markedly different depending on the convection level, will be addressed.

Approach

The emphasis of this study is on thermally thin fuels because of the limited μ g test time available in ground-based facilities, but preliminary scaling analyses suggest that it may be possible to study thermally thick fuels as well when gaseous fuel is added to the oxidizing atmosphere.

The experiments will be conducted in a combustion chamber in which a convective flow of a few cm/sec can be imposed in the direction opposite the flame spread. The oxidizing atmosphere will be mixed by the partial pressure method. For tests of Lewis number effects, the inert gases He, Ne, N₂, CO₂ and SF₆ will be used since they provide Lewis numbers from about 0.3 to 1.4. CO and CH₄ will be used for the gaseous fuels. Thin fuel samples will be ashless filter paper and thick fuel samples will be PMMA. Fuel samples of varying thickness will be ignited by the heat generated by a current passed through a coiled nichrome wire coated with nitrocellulose.

The primary diagnostics are video and an array of fine-wire thermocouples to measure the temperature simultaneously at several locations. The video records provide information on the spread rate and flame shape. The thermocouples give an independent check of the spread rates and the existence (or lack thereof) of a

separate flame front in the case of added gaseous fuel. The temperature data may also be used to determine the heat flux from the gas phase to the fuel bed, which can be related to the spread rate.

Significance

The understanding and control of accidental fires is a critical safety issue in both terrestrial and space-borne environments. The proposed work would provide insight that could be used to assess the fire hazards associated with non-standard atmospheres that might be employed in future manned spacecraft. Also, fires in enclosures produce a considerable amount of unburned vaporized fuel and partially combusted gases such as CO. One-g experiments have shown that the addition of combustible gases such as CO to the oxidizing atmosphere may increase the flame spread rate substantially. This study could provide information to improve models of fire development and spread in enclosures at one-g and μ g.

The influence of weak forced convection is particularly important for studies of flame spread at μ g because there is very little buoyancy-induced flow at μ g. Experiments by Olson and collaborators shows that the presence of forced convection currents (for example due to ventilation systems in manned spacecraft) can have a profound effect on the spread rate and extinction conditions. Consequently, the understanding of these effects is critical to understanding how fires might start, spread, and be extinguished at μ g conditions.

Progress

To improve the sensitivity of the video imaging system for the very weak near-extinction flames, a shearing interferometer (Fig. 1) has been designed and is being constructed for evaluation. The shearing interferometer has no parts that have critical alignment requirements, and thus may be especially suitable for drop tests. The interferometric measurements may also be useful to supplement the thermocouple temperature measurements. A system has been constructed and bench-tested and has been found to provide excellent resolution and sensitivity for flame spread experiments (Fig. 2). Both finite fringe spacing and infinite fringe spacing configurations have been tested. The infinite fringe spacing configuration has been selected for the drop apparatus because it appears to be easier to quantify the recorded images from the infinite fringe system to obtain temperature information. The system is sensitive enough to detect temperature differences of only a few degrees Kelvin in air, though sensitivity of this level is not required to image flames. This system is now being integrated into our drop-tower flame spread experiment. All optical components and cameras have been obtained, and the mounting system is being fabricated.

A graduate student has built a new test chamber and flame spread apparatus to supplement the PT's existing apparatus. The test combustion chamber is based on Lewis's now-standard layout for 2.2 second drop tower experiments. The new chamber and apparatus provides improved fuel sample mounting, optical access for direct photography and interferometry, a rapid ignition system and an updated

Tattletale-based data acquisition system. This equipment is now being integrated into a standard 2.2 Second drop tower frame. Preliminary one-g tests have been conducted to verify previous results in the PI's laboratory and elsewhere. Initial μg experiments are planned for the summer of 1995.

The PI's existing computer-controlled partial pressure gas mixing system has reconfigured for the planned experiments. An undergraduate student has re-written the partial pressure gas mixing software using a nonlinear least-square fit algorithm to obtain successively improved estimates of the final pressure after gas is added to the chamber, to minimize the total time required to mix the gases and maximize the accuracy of the final mixture. This gas mixing system is now operational.

While the focus of this study is on opposed-flow flame spread, corresponding to downward flame spread at one-g, it is useful to compare these results to concurrent-flow flame spread, corresponding to upward flame spread at one-g. It is found (Fig. 3), as expected, that the spread rate is higher for upward flame spread because heat transport is in the same direction as the spread. However, what has not been shown previously is that upward flame spread over thin fuels can be steady, but only for sufficiently narrow samples and/or sufficiently tall samples. This is sensible considering that the early stages of upward flame spread, the spread rate is accelerating due to the fact that the flame length is increasing and thereby the rate of heat transfer to the fuel surface is increasing. When the flame length has grown to the point where transverse losses match the rate of heat generation by the flame, a steady spread rate is observed. Since the transverse losses will be greater for smaller sample widths, the spread rate will be smaller for narrow samples. Moreover, because these considerations are absent for downward flame spread, the downward spread rate is nearly independent of the sample width.

An analytical study has been initiated in conjunction with Dr. Mike Delichatsios of Factory Mutual Research Corporation in Norwood, MA. The goal of the work is to extend his exact solution of flame spread over a pyrolyzing fuel bed to consider the effects Lewis number, finite-rate chemistry, and gaseous fuel addition on flame spread rate. A preliminary theory of Lewis number effects on flame spread over thin fuel beds, including finite-rate chemistry, has been obtained and compared with prior one-g data from Zhang et al (1992). The results (Fig. 4) are in reasonable agreement except for SF_6 -diluted mixtures, which have the lowest oxygen Lewis number (≈ 0.30); current theoretical efforts are aimed at trying to understand the unusual behavior of SF_6 .

Publications/Presentations:

Delichatsios, M. A., Ronney, P. D., "Horizontal and Lateral Flame Spread on Solids: Closure and Diffusional Lewis Number Effects," Fall Technical Meeting, Combustion Institute, Eastern States Section, Dec. 5-7, 1994, Clearwater Beach, FL.

Liu, J. B., Ronney, P. D., "Robust Interferometer System for Drop Tower Experiments," SPIE International Symposium on Optical Science, Engineering, and Instrumentation, July 9-14, 1995, San Diego, CA (to be presented).

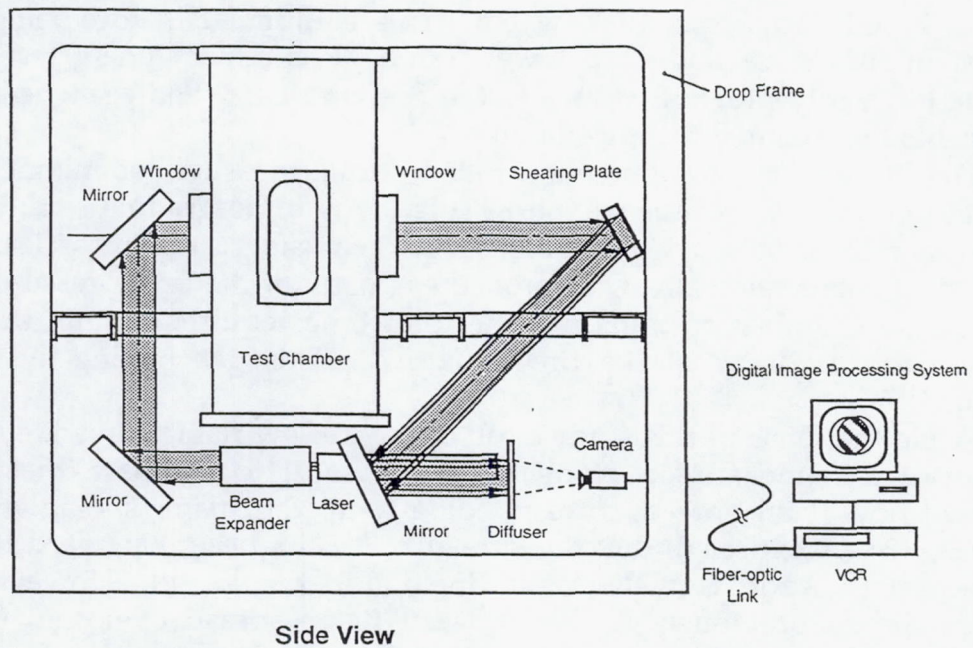


Figure 1. Schematic diagram of laser shearing interferometer system for 2.2 second drop tower.

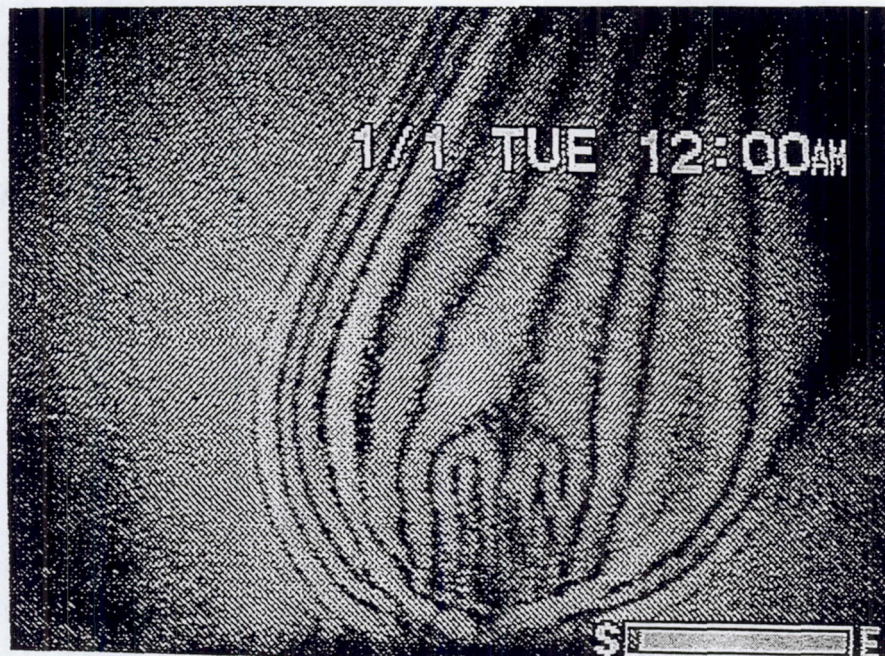


Figure 2. Digitized image of the plume above a burning paper match obtained from the shearing interferometer system.

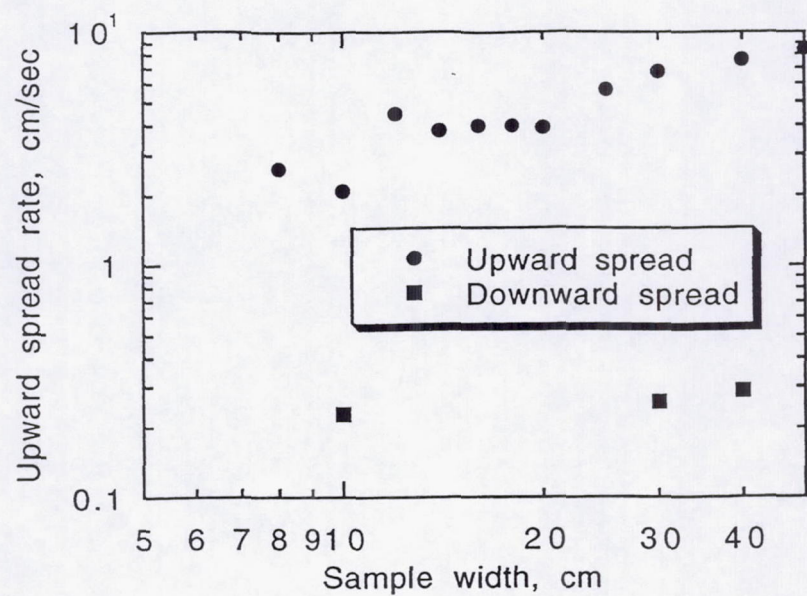


Figure 3. Observed spread rates for upward and downward spread over a thin solid fuel as a function of sample width

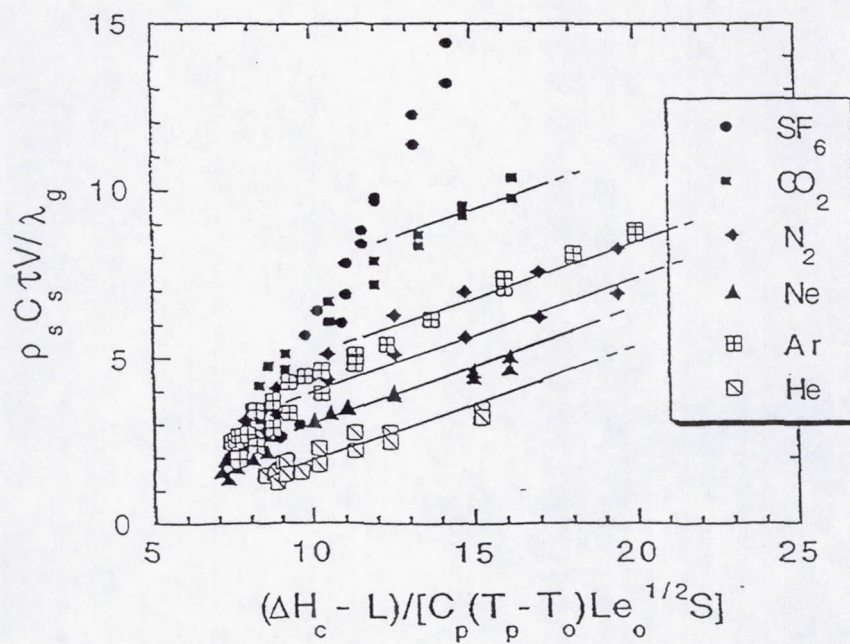


Figure 4. Comparison of model of spread rate over thin solid fuels with Lewis number effects to experimental results.

FLAME SPREAD OVER SOLID FUEL IN LOW-SPEED CONCURRENT FLOW

James S. T'ien,^{*} Kurt R. Sacksteder,⁺ Paul V. Ferkul,[#] Paul S. Greenberg,⁺
Ching-Biau Jiang,^{*} and Richard D. Pettegrew^{*}

^{*}Case Western Reserve University, Cleveland, Ohio 44106

⁺NASA Lewis Research Center, Cleveland, Ohio 44135

[#]Analex Corporation, Brookpark, Ohio 44142

Introduction

This research program is concerned with the effect of low speed flow on the spreading and extinction processes of flames over solid fuels. Primary attention is given to flame propagation in concurrent flow - the more hazardous situation from the point of view of fire safety. Support for the theoretical modeling effort and ground-based experiments was awarded in 1990. In 1994, the project was awarded flight experiment definition status.

Concurrent-Flow Flame Spread Modeling with Gas-Phase Radiation

In a recent paper,^[1] a model of flame spread and extinction over thin solid fuel in concurrent flow was described that uses an elliptic formulation in the leading-edge, flame-stabilization zone and includes a solid surface radiative loss. This model was used to study flame spreading characteristics and detailed flame profiles in low-speed forced flow. In addition, a flammability boundary which consists of a low-speed radiatively quenched branch and a high-speed residence-time-limited blowoff branch was established.

More recently gas-phase radiation was introduced into the flame spreading model.^[2, 3] The radiation model considers gray emitting, absorbing, and non-scattering medium (CO_2 and H_2O). The equation of radiative transfer is solved numerically by the S-N discrete ordinates method. A two-dimensional S_4 (12 ordinates) scheme is adopted based on a balance of numerical accuracy and computational cost after extensive numerical testing. The major results of this model computation include:

- 1) Radiative heat flux is multi-dimensional in nature, and the S-N discrete ordinates method provides a net-radiative-flux vector field in the gas phase. In fig. 1, for example, the net-radiative-flux vectors are shown for a flame spreading over a thin cellulosic fuel in a 5 cm/sec concurrent flow of a mixture of 15% oxygen-85% nitrogen. To model flame spread, an accurate directional radiative flux field is needed to evaluate the radiative interaction between the gas phase and the fuel surface.
- 2) Using fuel properties of a thin cellulosic fuel, the radiative flux from the gas phase to the surface is always smaller than the surface emissions, as illustrated in fig. 2 (same conditions as fig. 1.) Ultimately, because the flame is optically thin, the net radiative flux from the solid surface is lost to the surroundings.
- 3) Gas-phase radiation losses lower the flame temperature for flames in low-speed flows, especially in the downstream flame zone. Lower temperatures shorten the reaction zone and the visible flame. The shorter flames compare better with experimental results than predictions obtained without the gas-phase radiation loss.^[4]
- 4) Gas-phase radiation influences the behavior of concurrent flow flame spreading from the low-speed quenching limit to the high-speed blowoff limit. Figure 3 shows a comparison of flame spread rates with and without gas-phase radiation. In the low-speed limit radiative losses from the gas phase cause the quenching limit to occur at a higher flow velocity than with surface losses alone, but the high-speed blowoff limit occurs at essentially the same velocity with or without gas-phase radiation. Extinction is controlled by processes occurring in the flame-stabilization zone, where the flow first meets the flame.^[5] Here the relative importance of gas-

phase radiation increases with decreasing flow velocity. At low speeds gas-phase radiation reduces the flame temperature, eventually quenching. At higher speeds gas-phase radiation is not important in this zone and flame stabilization is determined by reactant residence times. Hence, there is little difference in the two predicted blowoff limits. Flame spread rates in concurrent flow, however, depend on the integrated heat flux to the fuel over the preheating and pyrolysis zones. As pyrolysis and preheating lengths increase with flow speed, the volume of radiating species (in our case, CO_2 and H_2O) increases, amplifying the radiative feedback to the solid. The effect of increased heat transfer to the fuel overpowers the effect of radiative reductions in the flame temperature, producing a net increase in spread rate. As shown in fig. 3, for free-stream velocities above 5 cm/sec, the spread rate is higher with gas-phase radiation. Hence, unlike flame spread in opposed flows,^[6, 7] where gas-phase radiation is important only at lower speeds, flames in concurrent flows can be influenced by gas-phase radiation throughout the flammable flow velocity range.

- 5) A U-shaped flammability map using oxygen fraction and flow velocity has been constructed for concurrent-flow flame spreading. The shape of the boundary is similar to the one determined by^[1] based on surface radiative loss alone, but quantitatively the boundary is shifted because of the effects of gas-phase radiation.
- 6) With gas-phase radiation included in the model, steady-state flame propagation can always be achieved in low-speed flows (fig. 4). With surface radiation alone, the flame spread rate increases quickly as surface emissivity is decreased. At this time, numerical difficulty prevents us from determining if steady spread is possible for the adiabatic case.

Droptower Experiments

The first experiments on concurrent-flow flame spread over a thin solid fuel (Kimwipe tissue) were performed in 5-second droptower tests using a fuel-sample translation device.^[4] In this series of experiments, direct photographs of visible flames provided the only basis for validating the numerical model. These tests showed that steady state was not obtained during the 5-second test time. While we cannot do much about the transient state of the flames in the droptower, a number of new features were subsequently added for a second set of tests to improve the procedure and the scope of data recorded:^[8]

- 1) A new fuel-sample translation device driven by a stepping motor. This change improves the control of the sample translation speed (and the equivalent relative flow speed).
- 2) The camera is mounted on the translation device and follows the flame, improving the quality of the image.
- 3) A blinking light in the chamber illuminates the sample providing images of the pyrolysis and burnout fronts. The two-dimensionality of these features can be checked to verify the comparison to the two-dimensional model.
- 4) Gas-phase and surface temperatures were measured using thermocouples in several tests.
- 5) The performance of two ignition methods were studied: one using a serpentine heated wire and the other using a straight heated wire augmented with a nitrocellulosic doped strip.

The second test-series results show that the serpentine ignitor produces a uniform pyrolysis and burnout front while the nitrocellulosic strip produces a nonuniform pyrolysis front at ignition that evolves toward uniformity, but only in higher speed flows. The time history of pyrolysis and burnout fronts confirms the earlier conclusion that steady state is not reached in these experiments. The thermocouple (0.076mm wire) distorts the flame front for this thin fuel, because of heat loss to the thermocouple.

The temperature measurements are affected by the thermocouples' proximity to the ignition source (unavoidable since the flame spreads only a short distance in 5 seconds). Nevertheless, the temperature data are consistent with the model's predictions indicating peak measured flame temperatures in the flame stabilization zone

near the solid burnout point. Measured and calculated peak temperatures are well below the adiabatic flame temperature, consistent with the predicted importance of radiative heat loss.

Glovebox Experiments

The Forced Flow Flame-Spread Test (FFFT) is a Glovebox experiment for studying concurrent-flow flame spreading being prepared for both the United States Microgravity Payload Mission (USMP-3) and the Shuttle-Mir Science Project (PRIRODA). In these space-flight experiments, the time limitation encountered in the drop-tower tests is eliminated. However, the fixed atmospheric environment in the Glovebox (cabin air) and the limited diagnostic and data acquisition capability constrain the scope of these tests. The objective of these tests will be to observe the effect of flow velocity and bulk fuel temperature on the flammability, ignition, flame growth and spreading behavior, in preparation for a more complete space-flight experiment program described below.

The FFFT flight hardware consists of a miniature low-speed wind tunnel (derived from the Wire Insulation Flammability experiment that was flown aboard the Shuttle spacelab in 1992) a control box and replaceable test samples, all shown in fig. 5. The test module provides flow control and conditioning, bulk velocity measurements, thermocouple temperature displays and optical access for photography. The front window of the module contains the temperature and anemometer displays to be included in the video images with the flames, and the window opens for replacing fuel samples.

Two types of fuel will be flown during the USMP-3 mission: flat paper samples lying in a plane parallel to the flow will be ignited in various air-flow velocities, and cylinders of cellulose formed around an electrically-heated ceramic core will be ignited at different bulk-fuel temperatures. The cylindrical geometry minimizes the mass of fuel required for heated samples and provides a simple method of uniform sample heating.

For the MIR/PRIRODA mission, four flat paper samples of different thickness will be tested. According to computed results for thermally thin fuels,^[3] there is a critical fuel thickness, τ_c , above which the flame structure is independent of thickness and where spread rate varies inversely with thickness. Below τ_c , flames shrink and finally quench when the fuel becomes too thin. This series of tests is intended to validate some of these predictions.

Space Flight Experiment Hardware Definition

The proposed space flight experiment SIBAL (Solid Inflammability Boundary At Low-Speed) is intended to observe the flammability boundary and flame-spreading characteristics of thin solid fuel (paper sample) in low-speed, forced-concurrent flow. In order to determine the extinction limit efficiently, a solid fuel delivery system/wind tunnel device has been conceived that continuously feeds solid fuel to maintain the burnout location of a lengthy fuel sample (and therefore the flame) at a fixed location in the wind tunnel. The spreading flame, fixed with respect to the laboratory, will facilitate diagnostic measurements, save space, and make it possible to conduct a series of experiments quickly without changing fuel samples.

To demonstrate the feasibility of this concept, a prototype device was constructed (see fig. 6). This device is operated inside an existing apparatus providing atmospheric control, rainbow-schlieren imaging, data acquisition, and experiment control capabilities.^[9] The first reduced-gravity tests of the prototype were completed in a recent NASA KC-135 low-gravity flight campaign. The solid-fuel feeding mechanism successfully maintained flames at a fixed location, indicated by the schlieren photograph, shown in fig 7., of a flame spreading over an ashless filter paper sample in a 5cm/sec flow of a 18% oxygen/82% nitrogen mixture. As is often the case in parabolic aircraft experiments at reduced gravity, the flame was disturbed by the unsteady acceleration environment (g-jitter), limiting the completeness of comparisons with the theoretical results. Nevertheless, to illustrate the type of comparison that can be made using the proposed SIBAL experiment results, fig.7 includes a

contour plot of density gradients, directly related to the schlieren imagery, computed for the same conditions of 18% oxygen, 5cm/sec.

Future Plans

During the next year we will pursue several parallel efforts: 1) Continue the improvement and extension of the modelling effort including consideration of cylindrical geometry and transient calculations, 2) complete the hardware development and perform the FFFT Glovebox experiments aboard the Shuttle (USMP-3) and the MIR Space Station; 3) continue the development of prototype hardware for the SIBAL flight experiment; and 4) prepare and complete a Science Concepts Review for the SIBAL flight experiment.

References

1. Ferkul, P. V. and T'ien, J. S., "A Model of Low-Speed Concurrent Flow Flame Spread Over a Thin Fuel," *Combustion Science and Technology*, 99, 4-6, pp.345-370, (1994).
2. Jiang, C.-B. and T'ien, J. S., "Numerical Computation of Flame Spread Over a Thin Solid in Forced Concurrent Flow with Gas-Phase Radiation," Fall Technical Meeting, Eastern States Section of The Combustion Institute, Clearwater Beach, Florida, December 5-7 (1994).
3. Jiang, C.-B., "A Model of Flame Spread Over a Thin Solid in Concurrent Flow with Flame Radiation," Ph.D. Thesis, Dept. of Mechanical and Aerospace Engineering, Case Western Reserve Univ., May, 1995.
4. Grayson, G. D., Sacksteder, K. R., Ferkul, P. V., and T'ien, J. S., "Flame Spreading Over a Thin Fuel in Low Speed Concurrent Flow: Droptower Experimental Results and Comparison with Theory," *Microgravity Science and Technology*, VII/2, pp.187-195, (1994).
5. T'ien, J. S., "The Flame Front Problem: Combustion in Low-Reynolds-Number Flow," ASME Paper 86-WA/HT-49 (1986).
6. Altenkirch, R. A. and Bhattacharjee, S., "Opposed-Flow Flame Spread with Implications for Combustion in Microgravity," *AIAA Prog. Astro. Aero.*, 130, pp.723-740, (1990).
7. Chen, C. H. and Cheng, M. C., "Gas-Phase Radiative Effects on Downward Flame Spread in Low Gravity," *Combustion Science and Technology*, 97, pp.63-83, (1994).
8. Pettegrew, R. D., "Ignition and Transient Effects of Flame Spread Over a Thin Fuel in Low-Speed Concurrent Flow Using Droptower Facilities", M. S. Thesis, Dept. of Mechanical and Aerospace Engineering, Case Western Reserve Univ., May, 1995.
9. Sacksteder, K. R., and T'ien, J. S., "Buoyant Downward Diffusion Flame Spread and Extinction in Partial Gravity Accelerations," *Twenty-Fifth Symposium (International) on Combustion*, to appear (1995).

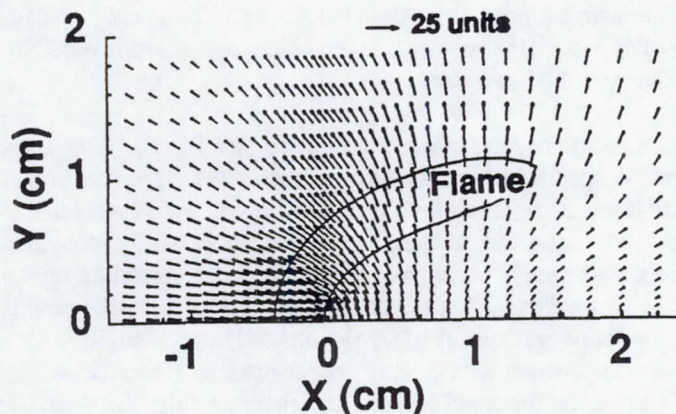


Fig. 1. Nondimensional radiative flux vectors at 15% O_2 and $U_\infty = 5$ cm/s (1 unit = $\sigma T_\infty^4 = 0.011$ cal/cm²/s).

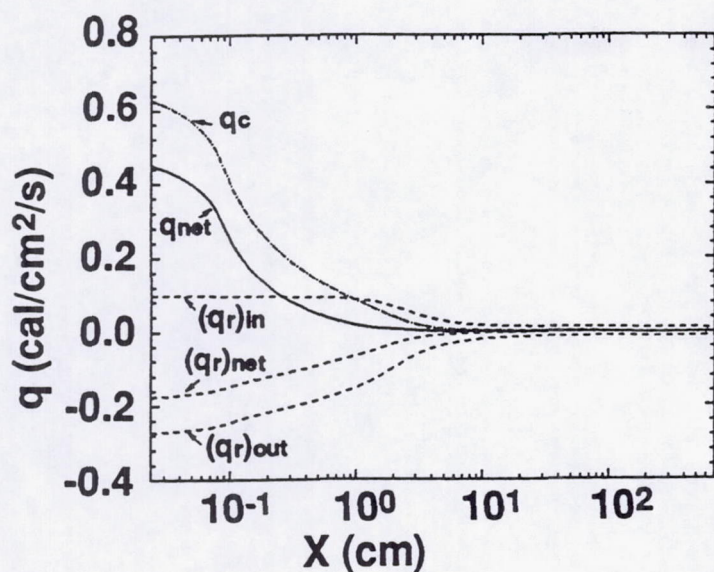


Fig. 2. Heat fluxes on the solid including conductive flux q_c , incoming gas radiative flux $(q_r)_{in}$, outgoing surface radiative flux $(q_r)_{out}$, net radiative flux $(q_r)_{net}$, and net heat flux q_{net} at 15% O_2 and $U_\infty = 5$ cm/s.

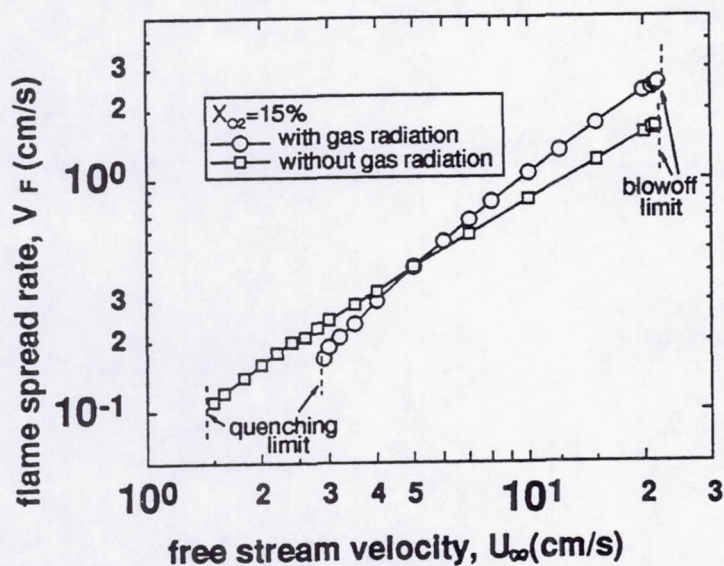


Fig. 3. The effect of gas radiation on flame spread rate at 15% O_2 .

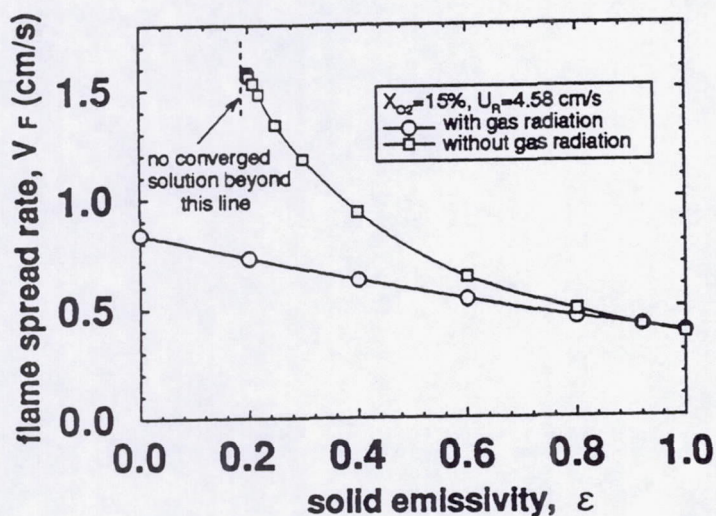


Fig. 4. The effect of solid fuel emissivity on flame spread rate for the corresponding cases with and without gas radiation at 15% O_2 and $U_R = 4.58$ cm/s.

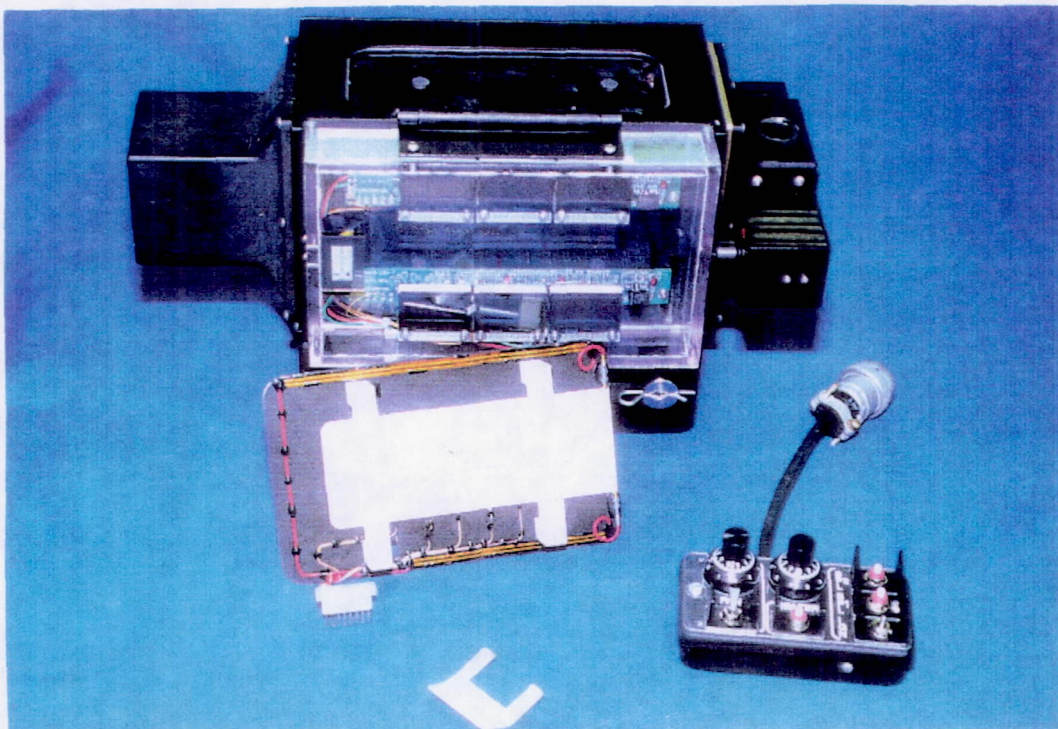


Fig. 5. FFFT (Forced Flow Flamespread Test) Glovebox Hardware

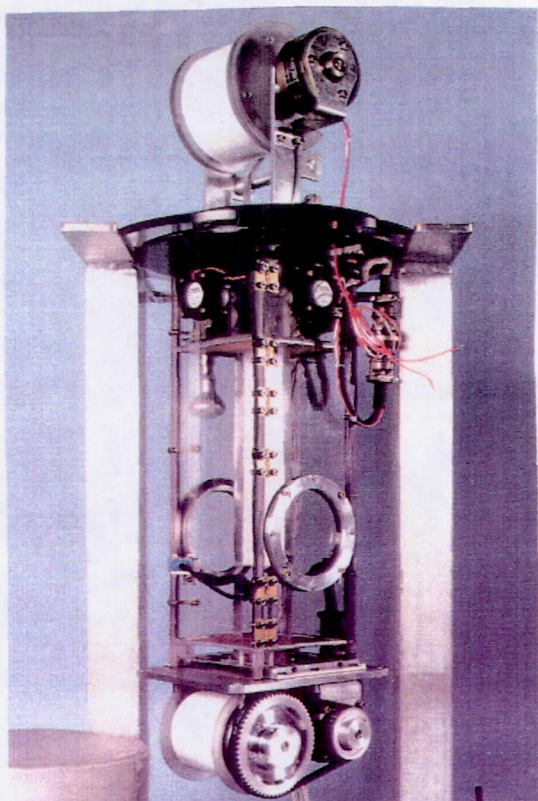


Fig. 6. Solid Fuel Delivery System prototype. Fuel advances to maintain the burnout location in the centered circular rainbow schlieren window.



Fig. 7. Comparison of experimental rainbow schlieren image of refractive index gradients and computed contours of density gradients (18% O_2 , 5 cm/s).

ON THE EFFECT OF PRESSURE, OXYGEN CONCENTRATION, AIR FLOW AND GRAVITY ON SIMULATED POOL FIRES

J. L. Torero, J. M. Most and P. Joulain
Laboratoire de Combustion et Détonique
UPR 9028 au CNRS
Université de Poitiers - ENSMA
BP 109 - 86960 Futuroscope Cedex
FRANCE

Introduction

The initial development of a fire is characterised by the establishment of a diffusion flame over the surface of a the condensed fuel and is particularly influenced by gravity, with most of the gaseous flow induced by natural convection. Low initial momentum of the fuel vapour, strong buoyant flows induced by the hot post-combustion gases and consequently low values of the Froude number (inertia-gravity forces ratio) are typical of this kind of scenario. An experimental study is conducted by using a porous burner to simulate the burning of a horizontal combustible surface. Ethane is used as fuel and different mixtures of oxygen and nitrogen as oxidiser. The magnitude of the fuel injection velocities is restricted to values that will keep the Froude number on the order of 10^{-5} , when calculated at normal gravity and pressure, which are characteristic of condensed fuel burning. Two different burners are used, a circular burner (62 mm diameter) placed inside a cylindrical chamber (0.3 m diameter and 1.0 m height) and a rectangular burner (50 mm wide by 200 mm long) placed in a wind tunnel (350 mm long) of rectangular cross section (120 mm wide and 90 mm height). The first burner is used to study the effect of pressure and gravity in the absence of a forced flow parallel to the surface. The second burner is used to study the effect of a forced flow parallel to the burner surface as well as the effect of oxygen concentration in the oxidiser flow. In this case experiments are also conducted at different gravity levels (micro-gravity, $0.2 g_0$, g_0 and $1.8g_0$) to quantify the relative importance of buoyancy.

The Effect of Gravity

The gravity level was varied systematically to observe the effect of gravity on the flame characteristics. Experiments were performed in reduced and micro gravity conditions in an aircraft (Caravelle) following a parabolic trajectory. The aircraft provides up to 20 sec. of $10^{-3}g_0$ per parabola. By performing special manoeuvres, 20 sec. of reduced gravity ($0.2g_0$) were also obtained. Tests in over gravity conditions are conducted in a centrifuge facility and experiments were conducted for 3, 6, 9 and 12 normal earth gravity conditions. The maximum value of the ratio of the velocities induced by coriolis and centrifugal accelerations and the hot products

Preceding Page Blank

velocity is of the order of 10^{-2} at $3g_0$, decreasing as the g-level increases, thus their effect is neglected.

At normal gravity the flames examined show the three main zones characteristic of buoyant diffusion flames [1]. Close to the burner surface edge, the flame presents a luminous annular zone around a fuel rich central region. The flame appears to be laminar with a light blue colour. Most of the chemical reactions occur in the luminous zone, due to the availability of oxidiser brought by buoyant air entrainment. The large heat release induces a drastic increase in the gas velocity and temperature in this region. Downstream (second zone) the flame has an intermittent character and turns yellow as the temperature maximum reaches the burner axis. Above the visible flame tip is the buoyant plume (third zone), which is characterised by decreasing gas velocities and temperatures.

It was observed from the video images that by increasing gravity the flame behaviour is clearly modified. As gravity is increased above normal level, the flame colour in the second zone changes from yellow towards blue (at $12g_0$ the whole flame is blue). Also the flame becomes compact, its neck is less visible, its height decreases, and its fluctuation increases. In reduced gravity, at $0.2g_0$, the flame is compact cylindrical, yellow and stable. During the micro-gravity period, a flattened flame is seen to float over the burner, periodically moving outward towards the air side, apparently seeking fresh air. The observed flame behaviour as the gravity is increased is interpreted as being the result of the increase in the air entrainment with gravity. A larger air entrainment results in better mixing and shorter residence times, both of which tend to reduce soot formation [2]. Furthermore, the soot particle pathlines and velocity distributions as well as the soot production regions are also affected by buoyancy [2]. The pathlines are wider, the velocities lower, and the soot containing volumes are broader as gravity is decreased. All these effects tend to reduce soot formation and increase soot oxidation as gravity is increased, and consequently to change the flame colour from yellow to blue.

The measured variation of the flame length (L_f) with gravity is presented in Figure 1. The flame height presented corresponds to the boundary of visible gas emission and is related either to the end of soot oxidation or the hydrocarbon radicals burning. It is obtained from the processing of 120 video images and is defined by the 50% flame tip appearance rate. The results show that the flame height has a $-1/3$ power law dependence on the gravity vector, g , from $0.2g_0$ to $12g_0$, i.e.

$$L_f \propto g^{-1/3} \quad (1)$$

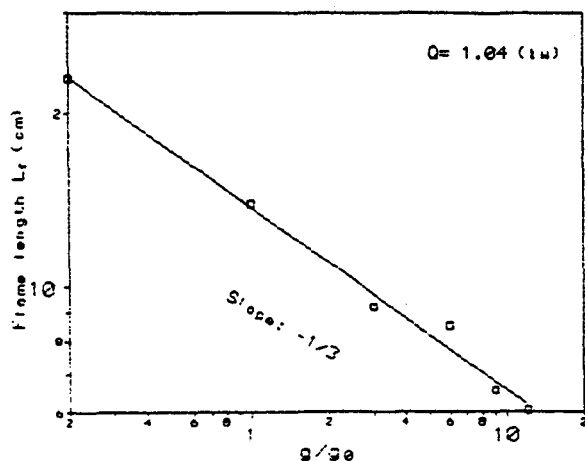


Figure 1
Variation of the flame length with gravity

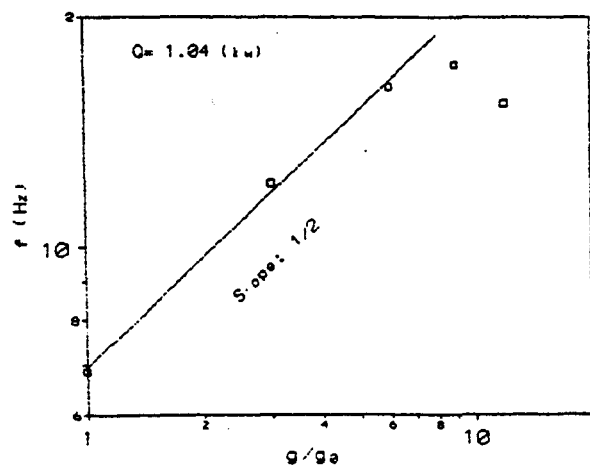


Figure 2
Variation of the pulsation frequency with gravity

These results agree well with the flame height predictions of the fire plume dimensionless analysis of Quintere [3]. The results are also in agreement with the experimental correlation of Zukoski et al. [4] and the work of Altenkirch et al. [5].

The flame pulsation frequencies are obtained from the flame video recordings by applying fast Fourier transformation of the analog output signal of a photo detector placed on the video monitor screen. The measured variation of the flame pulsation frequency with gravity is presented in Figure 2. For gravity levels smaller than $8g_0$, the results of Figure 2 give a $1/2$ power law dependence of the flame pulsation frequency on gravity. For gravity levels larger than $8g_0$, limitations a significant deviation from this power law is observed and might be due to limitations in the video sweeping rate. Theoretical derivation of this $1/2$ power dependence was previously conducted by Baum and McCaffrey [6] and independently by Bejan [7]. If the velocity at the surface is negligible the equation proposed by Baum and McCaffrey [6] can be simplified to

$$f \propto \sqrt{g/D} \quad (2)$$

For normal gravity the results of numerous experimental studies for various fuels and pool diameters are well correlated with equation (2) [8].

Other parameters studied are the maximum temperature as measured by a $75\mu\text{m}$ diameter Cr/Al thermocouple and the radiative heat flux.

The Effect of Pressure

The effect of pressure was studied by changing the pressure inside the cylindrical chamber from 0.03 to 0.3 MPa. All tests were conducted at normal gravity. It was observed that pressure had a significant effect on the flame physical appearance, temperature and pulsation frequency.

Video images of the flame were obtained by using a CCD camera and from these images it could be observed that as the pressure is increased above atmospheric levels the flame turns yellower and its height and width decrease. Small eddy structures appear and the soot formation increases visibly. Heat transfer to the vessel wall is drastically intensified. When decreasing the pressure below atmospheric levels, the flame turns blue and becomes more laminar, the central fuel rich zone grows, and the flame height decreases. These observations agreed qualitatively with those of Faeth et al. [2], for the effect of pressure on jet diffusion flames. It is interesting to note that the effect of pressure on soot formation in these types of flames is opposite to that of gravity. Since increasing pressure increases buoyancy, one would expect that according to the above arguments soot formation should decrease rather than increase as observed experimentally. This result seems to be due to the stronger effect of pressure on the soot formation reaction rate (a square power law dependence on pressure [2]), than on the other soot formation factors (soot residence time, pathway, containing volume).

Concerning the variation of the flame height with pressure, the results of Figure 3 show that for pressures below 0.08 MPa, the flame height increases with pressure according to a 0.16 power law. However, for pressures above 0.08 MPa, the flame height decreases with pressure, according to a -0.5 power law. The pressure at which the height maximum is observed (0.08 MPa) is higher than that observed by Hirst and Sutton [9] in experiments with a liquid pool fire of small diameter. At low pressures air entrainment is small, thus, transport of oxidiser to the reaction zone is mainly by diffusion, as pressure increases air entrainment becomes dominant over diffusion. For the former a Burke-Schumann [6] applies and for the latter an analysis such as the one of Quintere [3] is more convenient. The Burke-Schumann analysis predicts that for a

diffusion dominated flame the flame length will increase with pressure, instead the buoyant analysis predicts that the flame length will decrease with pressure according to a $-2/3$ power law. The experimental results have a qualitative similarity with the theoretical predictions but quantitatively they differ significantly. Both diffusion and buoyancy seem to be significant transport mechanisms for all conditions studied therefore the opposing dependencies on pressure seem to explain the differences between the experimental results and the predictions derived by neglecting one of the effects.

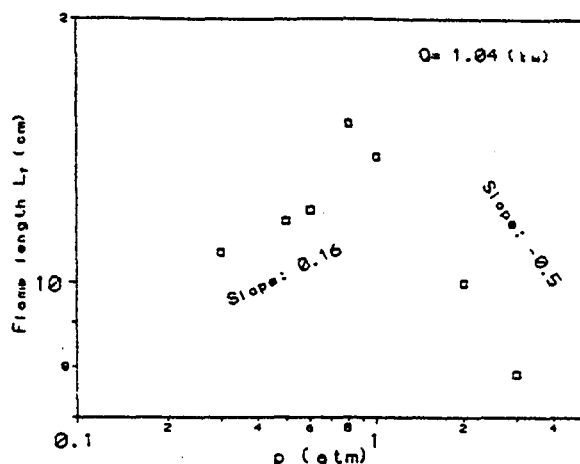


Figure 3
Variation of the flame length with pressure

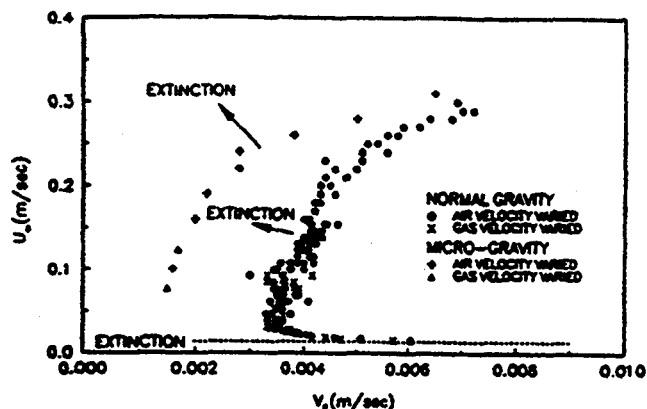


Figure 4
Effect of the oxidiser flow and fuel injection on the stability of the flame

The Effect of Oxygen Concentration and a Forced Flow Parallel to the Surface

The results presented above attempt to explain the effect that gravity and pressure have upon a flame established in a quiescent environment. This kind of environment is seldom found in real situations, in general, a forced flow is always present parallel to the burning surface. The objective of this work is to try to improve the knowledge on fire safety as related to micro-gravity environments therefore the effect of a forced flow of magnitude comparable to those induced by a spacecraft ventilation system (in spacecraft the ventilation system generates a flow of the order of 0.1 m/s) was systematically studied. The effect of oxidiser concentration on fire safety is also of great importance when determining the atmosphere of a spacecraft, thus, experiments were conducted with oxidiser flows ranging from 18% to 62% oxygen concentration.

The geometry of the experimental set up was changed to the above mentioned rectangular burner and a forced oxidiser flow was generated inside a wind tunnel. The burner geometry was changed to keep the two dimensional approach used when analysing the previously explained experiments. Video recordings of the flame allowed the observation of the flame geometry and extinction limits and six 75 μ m diameter Cr/Al thermocouples provided estimates of the flame temperature.

To study on the effect of gravity on the extinction limits, the flame was established and then the air flow velocity (U_{∞}) was increased until extinction occurred. For low air flow velocities, the fuel injection velocity (V_F) was varied until the flame extinguished. The results are

presented in Figure 4, the data points represent the values of air and fuel velocities at which extinction occurred. In normal gravity, for $U_{\infty} < 0.03$ m/s all flames extinguished. Close to the extinction limit the flames were almost vertical and very close to the leading edge of the plate. For $0.03 \text{ m/s} < U_{\infty} < 0.1 \text{ m/s}$ flames extinguished at an almost constant value of V_F . For $U_{\infty} > 0.1 \text{ m/s}$ the extinction limit depends on both fuel and oxidiser velocity, with the dependence on the former becoming less significant as U_{∞} increases. The extinction curves, in normal and micro-gravity, are similar with the latter significantly displaced towards the left. It is important to note that the difference between normal and micro-gravity extinction limits decreases as U_{∞} increases. For $U_{\infty} < 0.07 \text{ m/s}$, perturbations in the gravity level become important rendering the micro-gravity extinction limits unreliable.

As mentioned before, oxygen concentration, oxidiser flow velocity and injection velocity were systematically varied. The influence on the flame geometry and appearance was observed. In normal gravity the flame consisted of two distinctive zones, a first zone, close to the leading edge, where a boundary layer flame can be observed and a second zone, further upstream, where a buoyantly induced plume is present. The first zone is characteristically blue and the second zone yellow.

Changing the oxygen concentration in the oxidiser flow has a significant effect on the appearance of the flame. As the oxygen concentration increases the flame becomes more stable and brighter. The first zone remains blue and the second yellow, but both colours become more intense. The distance from the leading edge at which the plume appears remains constant with the oxygen concentration, but the size of the plume decreases significantly.

The fuel injection velocity also exerts a significant effect on the appearance of the flame. There is a minimum injection velocity that will sustain a flame (as described before). For very low injection velocities the flame appears close to the burner and is very unstable. Almost the entire flame is blue and only slight traces of yellow can be observed. As the fuel injection velocity increases the plume increases in height and the presence of a yellow zone becomes more evident. The distance from the leading edge at which the plume becomes evident remains almost invariable with the fuel injection velocity.

The oxidiser forced flow velocity has an effect on the stability, stand-off distance and colour of the flame. The relative importance of the boundary layer and plume zones is also affected by the forced flow velocity. Increasing the forced flow velocity results in a bluer and more unstable flame. The flame appears closer to the burner, the plume becomes smaller and the size of the boundary layer zone increases with the plume appearing further downstream.

In micro-gravity three distinctively different flames can be observed. For low fuel injection velocities the flame adopts a parabolic geometry. The stand-off distance and the colour of the flame can be varied by changing the oxidiser flow velocity and oxygen concentration. The shape of the flame can be varied by increasing the fuel injection velocity. Far away from the leading edge, a change in the geometry of the flame can be observed when the injection velocity increases. The parabolic flame turns linear towards the end of the plate. A further increase on the injection velocity increases the presence of the linear flame. Finally, a third type of flame can be observed for high injection velocities, this flame is almost entirely linear and a curved flame is only present very close to the leading edge. The colour and stand off distance for the last two flames follow the same pattern as for the first type of flame.

It was also observed that all flames are blue on the lean side and yellow on the rich side and that there is a significant effect of the ceiling on the flame shape. The ceiling reflects the flame, when it gets too close, generating a point of maximum stand-off distance. The geometrical

limitation of the chamber has a significant effect downstream but no observable effect upstream of the point of maximum stand-off distance.

For low oxygen concentrations significant three dimensional effects could be observed, this effects along with the influence of the lateral walls are extensively discussed in the work of Torero et al. [10] and will not be treated here.

Conclusions and Perspectives

The influences of gravity, pressure, oxygen concentration and wind have been studied experimentally on a small scale simulated pool fire, conclusions regarding several fundamental parameters have been drawn from mainly video images and thermocouples. Verification of existing dimensionless laws has been accomplished and phenomena such as blow-off limits has been explored. Numerical simulations and theoretical analysis are being developed and comparison with the experimental results should be expected for the near future. Further experiments with gas burners as well as liquid and solid fuels have been planned for different gravity levels. Comparison between the idealised cases and the more realistic ones should shed further light on the fundamental mechanisms controlling pool fires.

Acknowledgements

This work was supported by the European Space Agency, the Centre National d'Etudes Spatiales, the Centre National de la Recherche Scientifique, the University of Poitiers and the Ministère de la Recherche et de la Technologie. The authors wish to Drs. J.Chen and L. Bonneau for conducting some of the experiments and to Prof. A.C. Fernandez-Pello for extensive contribution on the interpretation of the experimental results.

References

1. McCaffrey, B.J., NBSIR 79-1910, National Bureau of Standards, Washington D.C., U.S.A., 1979.
2. Faeth G.M., Sunderland, P.B., Koylu, U.O. and Urban, D.L., *Proc. Int. Symp. Aero. Fluid Sci.*, Sendai, Japan, 1993.
3. Quintiere, J.G., *Fire Safety Journal*, 15, 3-29, 1989.
4. Zukoski, E.E., Cetegen, B.M. and Kubota, T., *Twentieth Symposium (International) on Combustion*, The Combustion Institute, 361-366, 1984.
5. Altenkirch, R.A., Eichorn, R., Hsu, N.N., Brancic, A.B. and Cevallos, N.E., *Sixteenth Symposium (International) on Combustion*, The Combustion Institute, 1165-1174, 1976.
6. Baum, H.R and McCaffrey, B.J., *Proc. 2nd Int. Symp. Fire Safety Sc.*, 1989.
7. Bejan, A., *Journal of Heat Transfer*, 113, 261-263, 1991.
8. Pagni, P.J., *App. Mech. Rev.*, 43, 8, 153-170, 1990.
9. Hirst R. and Sutton D., *Combustion and Flame*, 5, 319, 1961.
10. Torero, J.L., Bonneau, L., Most, J.M. and Joulain, P., *Twenty-fifth Symposium (International) on Combustion*, The Combustion Institute,(in press) 1994.

INTERACTIONS BETWEEN FLAMES ON PARALLEL SOLID SURFACES

David L. Urban
NASA Lewis Research Center
Cleveland, Ohio
Program Began 1994

Introduction

The interactions between flames spreading over parallel solid sheets of paper are being studied in normal gravity and in microgravity. This geometry is of practical importance since in most heterogeneous combustion systems, the condensed phase is non-continuous and spatially distributed. This spatial distribution can strongly affect burning and/or spread rate. This is due to radiant and diffusive interactions between the surface and the flames above the surfaces. Tests were conducted over a variety of pressures and separation distances to expose the influence of the parallel sheets on oxidizer transport and on radiative feedback.

Owing largely to their practical importance, flame interactions have been an area of active research, however microgravity research has been largely limited to candles (Ref. 1) and droplets, (Refs. 2 & 3). Consideration of parallel solid surfaces has been limited to 1-g studies (Refs. 4 - 9). Of these works, (Refs. 4, 6 and 7) considered flame spread.

Emmons and Shen (Ref 4.) studied horizontal flame spread over an array of vertically oriented paper sheets. The flame spread rate was found to be proportional to the fuel sheet aspect ratio (height/separation) for small and large values of the aspect ratio. However, the proportionality was different in these two cases and, at intermediate values, the correlation broke down. Using a simple model for the energy transport ahead of the flame and a value for the burning zone width estimated from the data, acceptable agreement was obtained with the experimental data.

Kim, De Ris and Kroesser (Ref. 5) performed a theoretical and experimental analysis of the downward burning rate between two parallel fuel surfaces. Assumptions similar to those in the work of De Ris (Ref. 10) were made (unity Lewis number, infinite gas phase reaction rate and insignificant radiative transport). Burning rate was found to be controlled by the product of the Grashof number and the channel aspect ratio (b/l (channel half width/length)). Good agreement was found between the theoretical formulation and the burning rate for methanol-soaked slabs. The selection of methanol as the test fuel increased the suitability of the assumption that radiation could be neglected since methanol flames produce little soot and consequently the radiative transport from the flames can be expected to be small. Three burning regimes were found depending upon the ratio l/b^4 . For small values of l/b^4 , the burning rate was independent of b ; for larger values, the burning rate is independent of l but proportional to the b^3 . At intermediate values a simple parameter dependence was not observed.

Ohlemiller and Villa (Ref. 11) and Ohlemiller (Ref. 12) suggest the importance of considering the radiant interaction between two surfaces in NASA's flammability assessment of materials. The current flammability standard for materials to be used on spacecraft (Ref. 13) is an upward burning test with a single sheet of material. As Ohlemiller (Ref. 12) suggests, this is a geometry that is not necessarily the worst case it is intended to be. Without radiant preheating of the unburned material, the flammability hazard is lower than with modest radiative feedback. The radiant interaction between surfaces is also very important in terrestrial fire safety; the classic example is wood, which is nonflammable as a single large sheet but very flammable if multiple pieces are arranged to allow radiant interaction.

Experiment Description

The tests were conducted for downward flame spread over parallel sheets of paper. The fuel was stored in a desiccator and the chamber filling process exposed the fuel to vacuum or dry air for at least two hours. The low gravity tests were conducted in the NASA LeRC 2.2 second drop tower in a 45 liter quiescent chamber. The normal gravity tests were either conducted in the 45 liter chamber or a new 27 liter chamber. The fuel was Kimwipe™ laboratory wipes, selected because of their uniform thickness and low mass/area (1.9 mg/cm^2). The sample frame opening was 5 cm wide and the flame spread rate and flame structure were observed using a color video camera on the edge view. The oxidant was either mixed in the chamber using partial pressures or supplied directly from a gas bottle, in either case the mixture error was less than 0.5 mole %. The bulk of the low gravity tests were conducted at 30% oxygen because a value within the quiescent microgravity flammability range for Kimwipe™ was desired, while the normal gravity tests were conducted at 21% oxygen. The diluent was either helium or nitrogen. Test pressures ranged from 100 to 1000 Torr, with the majority conducted at 760 Torr, and separation distances varied from 6.4 to 50 mm. Unlike single sheet tests, it was learned that the ignition process must be carefully controlled to prevent the ignition products from filling the gap between the fuels, thereby preventing development of internal flame(s).

The experiment imaging was recorded in S-VHS video format. After the tests, the video frames were digitized using a frame grabber and the flame spread rate was determined using object tracking software which stepped through the video images and determined the position of the leading edge of the flame. The spread rates were very stable throughout the tests with correlation coefficients greater than 0.99. Where there was a flame between the sheets of paper (internal flame), the reported spread rates are the average of the spread rates of the internal and external flames on at least one of the sheets. The camera was centered on the edge of one of the sheets to provide optimum imaging of one pair of flames. At large separation distances the flames on the second sheet were sufficiently distorted that they were not trackable; for these cases the spread was determined from only the sheet aligned with the camera.

In process of these tests, numerous deficiencies were observed in the 20 year old generic combustion drop package that was being used. The most important of these was inflexibility concerning sample size and separation distances. In addition, it was found to be unsuitable for normal gravity testing due to the support hardware needed to support the samples impeding buoyant air flow. A new drop package was designed and fabricated. It was used for limited normal gravity testing and is now ready for use in the drop tower. This apparatus allows more systematic sample configuration variation and also improves the quality of the recorded images.

Results and Discussion

It was found that flame interactions occur in a manner similar to that reported for normal gravity downward spread. The microgravity flames, however, exhibit greater interaction for a given separation distance, the difference being attributed to the influence of the buoyant flow. Similar to the normal gravity case, the interaction displays four phases as separation distance is increased (Fig. 1): 1. no flame between the sheets of paper (internal flame), 2. an unstable internal flame, 3. a single internal flame which becomes more deeply notched with separation distance, 4. individual internal flames on each surface which in the limit of large separation become independent of each other. These results are similar to those reported for normal gravity flames by Kurosaki, Ito and Chiba (Ref. 6) who reported, as separation distance was reduced, a progression from independent flames through increasing flame interaction to ultimate extinguishment of the internal flame. The range of separation distances over which the interaction was apparent was much greater than that seen in normal gravity tests where separate flames are observed at 10 mm separation while the low-g flames were still connected at 40 mm separation. (Fig 2.)

Figure 3 contains the low-gravity spread rates for parallel sheets at various separation distances with helium and nitrogen diluents. As expected, the spread rate is higher for helium for all cases; this is consistent with the thin fuel spread model of De Ris (Ref. 10) which shows linear dependence on gas phase thermal conductivity. The greater dependence on separation distance for the helium case is also consistent with helium's larger thermal diffusivity, which was also evident in the fact that the helium flames were much larger than the corresponding nitrogen flames, and interacted over greater separation distances. The tendency of the internal flame to extinguish at larger separations for helium is most likely due to increased conductive losses to the paper. The limited change in the spread rate with nitrogen diluent is surprising given the evident interaction in the video record.

Kurosaki, Ito and Chiba (Ref. 6), in similar normal gravity tests, reported that as separation was increased, after passing through a maximum value, the spread rate decreased asymptotically to the single sheet value. In this work, for nitrogen, the spread rate for multiple sheets was very close to that of the single sheet; for the case of helium diluent, test chamber limitations prevented increasing the separation distance enough to see the low-gravity spread rate return to the single sheet values. The flames were largely blue and therefore the radiant contribution is likely to be low, however at this point it is not possible to determine whether the increased spread rate was due to the increased radiant transport due to the higher flame temperature or due to the increased thermal conductivity of the helium diluent. In their work Kurosaki, Ito and Chiba (Ref. 6) found (by analysis) that radiation from the ember section of the opposing sheet was of the same order as conduction; their fuel was computer cards which can be expected to produce a more significant ember section than the thin paper used in these tests. Their results showed that the interaction increased with sample width (consistent with radiation view factors). Due to access limitations, the sample width could not be significantly varied in the old drop rig, however the new drop rig will accommodate a variety of sample sizes and this parameter will be varied in future tests.

The change in spread rate as a function of pressure is presented in figure 4. At pressures greater than atmospheric, the limited change in spread rate with pressure is consistent with thin fuel flame spread theory. However, below atmospheric pressure (600 to 700 Torr), there is a dramatic change in the pressure dependence. In these cases, the internal flame does not extinguish until well below the transition point. However, in some cases below the transition point, oscillation was seen in the internal flame. Similar tests were conducted for 1-g flames (Fig. 5). In this case there was also a

pressure below which spread rates dropped off, however the change in slope was less abrupt. In 1-g the internal flame was the last to extinguish. This effect was attributed to the chimney effect of the sheets of paper providing enhanced air flow.

In this work, an unstable region was observed in low-g flames for 30% oxygen in helium at 760 Torr for 15 mm separation. The flame between the sheets pulsed six times during the drop, alternating between small pulsations and very large pulsations that filled the entire region between the sheets behind the flame leading edge. The frequency was 2.5 to 3 Hz and the duration of the pulsations was 0.1 to 0.2 s. All of the pulsations involved a flame propagating back from the leading edge toward the ignitor. In another case, with nitrogen diluent (30% oxygen at 645 Torr, 10 mm separation), an unstable internal flame was also observed, however in this case it was a flame bubble that oscillated in both directions as it trailed behind the leading edge of the external flames. In addition to the instability causing the flame oscillation down the channel, it also appeared that the instabilities were alternately starting at the near and far (with respect to the camera) edges of the flame. With a single camera view, it is impossible to confirm this; further study of this phenomenon will require 2 orthogonal camera views. Instability was found in normal gravity near the low pressure extinction limit, however in this case the internal flame would pulse forward (opposite to the low-g pulsations). The frequency was again approximately 3 Hz but the duration was approximately 0.03 seconds, much briefer than the low-g pulsations. Kurosaki, Ito and Chiba (Ref. 6), reported an intermittent internal flame in their tests in 1-g but little detail was provided.

Instabilities (cellular flames) for flames spreading over single sheets of paper have been reported for low Lewis numbers (Ref. 14), however these instabilities were small scale flamelets meandering across the burning edge of the fuel. In their helium dilution case (Lewis number of 1.4) instabilities were not observed. A pulsating mode has been suggested for high Lewis number cases by Joulin and Clavin (Ref. 15), with the critical Lewis number for pulsations decreasing with increasing heat loss. The difference between this work and the work of Zhang, Ronney et al. (Ref. 14) may be the increased heat loss due to the opposing sheets of paper. More work is needed to confirm this effect and to determine whether the pulsations reported here are a Lewis number effect or an artifact of the sample geometry.

Conclusions

Interactions between flames spreading over parallel surfaces have been demonstrated in low-gravity. There is an expanded spatial scale over which the flames interact compared to the normal gravity case. These interactions change the response of the flame spread to pressure variation and cause instabilities that have not been observed for normal gravity flames. Further work is needed with a variety of sample geometries and sizes to clarify these results.

References

1. Dietrich, D.L., H.R. Ross, and J.S. Tien. 1993. On the Sustained Burning of a Candle in Microgravity. submitted to *Science*.
2. Dietrich, D.L. and J.B. Haggard. 1992. Combustion of Interacting Droplet Arrays in a Microgravity Environment. *Second International Microgravity Combustion Workshop*, NASA CP 10113, 317-323.
3. Mikami, M., H. Kato, J. Sato, and M. Kono. 1994. Interactive Combustion of Two Droplets in Microgravity. Presented at 25 Symposium (International) on Combustion, Irvine CA.

4. Emmons, H.W., and T. Shen. 1971. Fire Spread in Paper Arrays, *Thirteenth Symposium (International) on Combustion* 917-926.
5. Kim, J.S., J. De Ris, and F.W. Kroesser. 1974. Laminar Burning Between Parallel Fuel Surfaces. *International Journal of Heat and Mass Transfer* 17:439-451.
6. Kurosaki, Y., A. Ito and M. Chiba. 1979. Downward Flame Spread Along Two Vertical, Parallel Sheets of Thin Combustible Solid. *Seventeenth Symposium (International) on Combustion* 1211-1220.
7. Itoh, A., and Y. Kurosaki. 1985. Downward Flame Spread along Several Vertical, Parallel Sheets of Paper. *Combustion and Flame* 60:269-277.
8. Tamanini, F. and A.N. Moussa. 1980. Experiments on the Turbulent Burning of Vertical Parallel Walls. *Combustion Science and Technology* 23:143-151.
9. Toong, T.Y. 1961. A Theoretical Study of Interactions Between Two Parallel Burning Fuel Plates. *Combustion and Flame* 5:221-227.
10. De Ris, J.N. 1969. Spread of a Laminar Diffusion Flame. *Twelfth Symposium (International) on Combustion* 241-252.
11. Ohlemiller, T.J., and K.M. Villa. 1991. *Material Flammability Test Assessment for Space Station Freedom*. NISTIR 4591, NASA CR-187115, NIST, Gaithersburg, MD.
12. Ohlemiller, T.J. 1992. *An Assessment of the NASA Flammability Screening Test and Related Aspects of Material Flammability*. NISTIR 4882, NASA CR-189226, NIST, Gaithersburg, MD.
13. NHB 8060.1C. 1991. *Flammability, Odor, Offgassing, and Compatibility Requirements for Material in Environments the Support Combustion*. NASA OSMQ.
14. Zhang, Y. P.D. Ronney, E.V. Roegner and J.B. Greenberg. 1992. Lewis Number Effects on Flame Spreading Over Thin Solid Fuels. *Combustion and Flame* 90:71-83.
15. Joulin, G. and P. Clavin. 1979. Linear Stability Analysis of Nonadiabatic Flames: Diffusional-Thermal Model. *Combustion and Flame* 35:139-153.

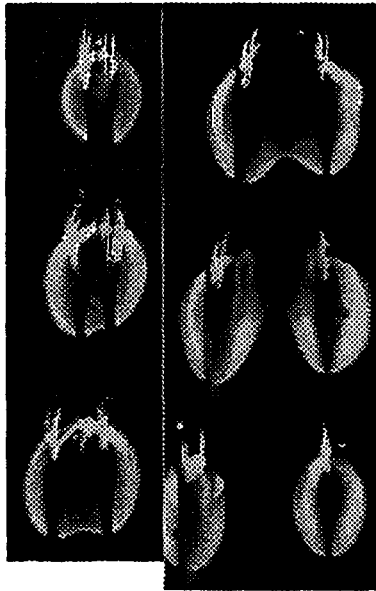


Figure 1. Edge view of flames propagating in microgravity over parallel sheets of Kimwipe at different separation distances in 30% oxygen, balance nitrogen, at 760 Torr. Separation distances in order (top to bottom, left to right) are 6.4, 10, 20, 30, 40 and 50 mm. At 40 mm separation, the flames are nearly separate with slight interaction. At 30 mm the flames have merged, producing a notched blue flame compared to the more luminous external flame. The internal flame is nearly flat at 20 mm and in the 10 mm case the flatness is slightly skewed by slightly delayed ignition for the left sheet. By 6.4 mm the internal flame has extinguished and the fuel burns only on the outer surfaces.

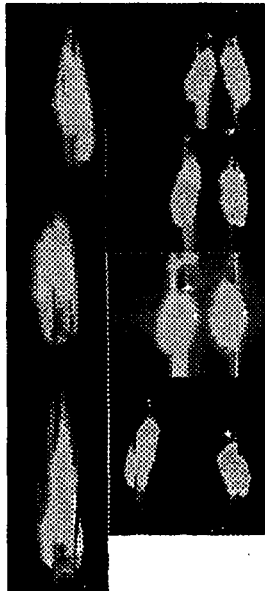


Figure 2. Edge view of flames propagating in normal gravity over parallel sheets of Kimwipe at different separation distances in dry air at 760 Torr. Separation distances in order (top to bottom, left to right) are 3 mm, 4.7, 6.4, 10,

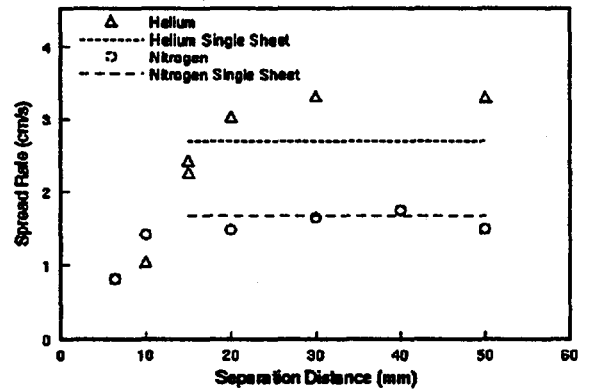


Figure 3. Flame spread rate versus separation distance for two parallel sheets in microgravity in 30% oxygen, balance helium or nitrogen at 760 Torr. Single sheet values are shown as dashed lines. The sharp slope change below 20 mm separation for helium and 10 mm for nitrogen, is a result of the extinction of the internal flame.

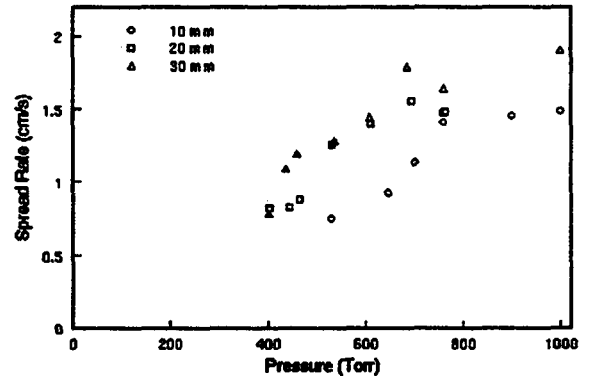


Figure 4. Flame spread rate versus pressure for two parallel sheets at 10, 20 and 30 mm separation distances in 30% oxygen, balance nitrogen, in microgravity.

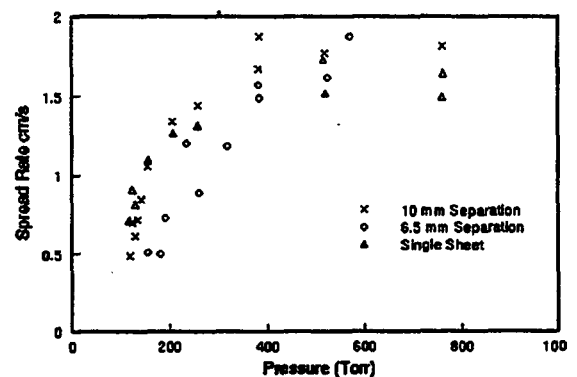


Figure 5. Flame spread rate versus pressure for single sheets and parallel sheets 6.5 and 10 mm separation distances in dry air in normal gravity. Flames were propagating downward.

TRIPLE FLAMES IN MICROGRAVITY FLAME SPREAD

Indrek S. Wichman
Michigan State University
East Lansing, Michigan

Introduction

It has become apparent from recent work, for both opposed and coflow flame spread (refs. 1-4), that the flame tip controls much of the subsequent flame spread dynamics. The "flame anchoring region" or "lean-limit zone" or "weakly premixed flame foot zone" of the late 1970s and early 1980s has acquired a definite theoretical structure, commonly referred to as the "triple flame". Though its existence is unquestionably acknowledged, its importance in practical situations of flame attachment, flame spread, etc. has not been clearly established.

The purpose of this project is to examine in detail the influence of the triple flame structure on the flame spread problem. It is with an eye to the practical implications that this fundamental research project must be carried out. The microgravity configuration is preferable because buoyancy-induced stratification and vorticity generation are suppressed. A more convincing case can be made for comparing our predictions - which are zero -g - and any projected experiments.

Our research into the basic aspects will employ two models, both of the general kind illustrated in Fig. 1. In one, flows of fuel and oxidizer from the lower wall are not considered. In the other, a convective flow is allowed, see Fig. 1. The non-flow model allows us to develop combined analytical and numerical solution methods that may be used in the more complicated convective-flow model.

Zero-Flow Model:

A preliminary analysis of this model is found in ref. 5. We are presently developing a more comprehensive version. The difficult part occurs in the construction of the outer solution, which must be matched to the inner flame-zone solution. The forward flame zone, in which the reaction rate is a maximum, is the elliptic (2-D) triple point region. Downstream of this is the trailing diffusion flame (DF). The elliptic, non-linear triple-point-zone equation must possess spatial boundary conditions on all of its four sides. The top side is straightforward, the two lateral sides are more difficult. The bottom side is by far the most difficult. Here, the nonlinear elliptic triple-point-zone equation must match to the homogeneous quenching-zone solution (there

is no reaction here). But this region itself cannot be solved unless a suitable set of boundary conditions at its top edge is found (see Fig. 2). An iterative solution method must be employed. A "reasonable" boundary condition is postulated for the top of the quench zone. Then the quench equation is solved. The inner-zone equation is matched to this and the other outer-zone solutions. A new and more accurate temperature distribution across the lower zone is obtained, the quench zone equations are solved and the process is repeated. The solution can be compared with the full numerical solution for the quenching distance and the quenching temperature, as well as heat fluxes to the solid boundaries.

Convective-Flow Model:

Most of our effort on this project has centered on the convective flow case. We have developed a numerical solution code with variable meshes and other numerical refinements. The model problem is identical to the zero-flow case except for the presence of the constant convective flow from the lower reservoirs. A somewhat artificial zero-infiltration boundary conditions is applied, as in the zero-flow case [i.e., neither species can diffuse into the other stream prior to its arrival through the exit plane]. By numerical experimentation, we have determined that the triple flame structure is most clearly evident when both the nondimensional activation energy β and the Damköhler number D are large. As D increases, the flame tip moves closer to the cold wall. This can be offset by increasing the flow rate ϵ . When the increases of ϵ and D are coordinated in order to keep the stand-off (or quenching) distance constant, the triple flame structure becomes prominent. In our notation, D and ϵ are independent of one another, since length scales are measured with the burner width. Hence, an increase of ϵ for fixed D merely shifts the entire structure further downstream, whereas an increase of D (for fixed ϵ) moves it closer to the cold surface while simultaneously shrinking it laterally. In neither of these cases is the triple flame structure prominent. We can compare the sequences of figures given by Figs. 3.a-c, 4.a-c, 5.a-c. See also the full plots of temperature and fuel and oxidizer mass fractions in Figs. 6.

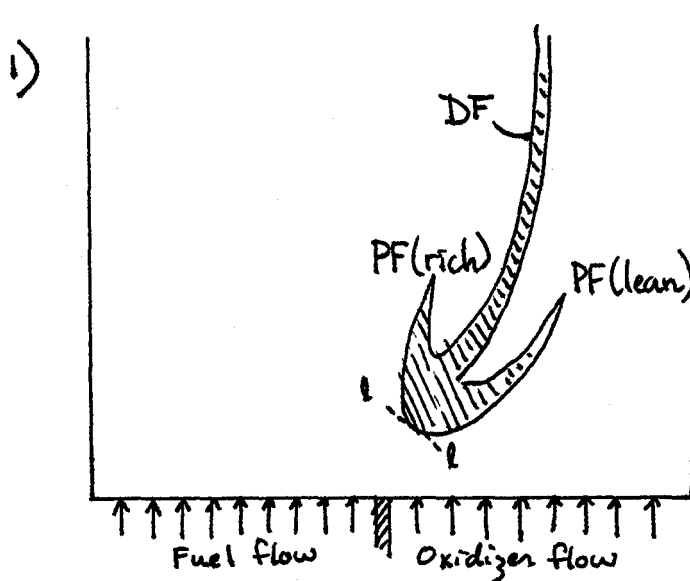
Once the fundamental details of the zero-flow model are clarified, similar methods may be applied to the convective flow model.

Simplified Flame Spread Model

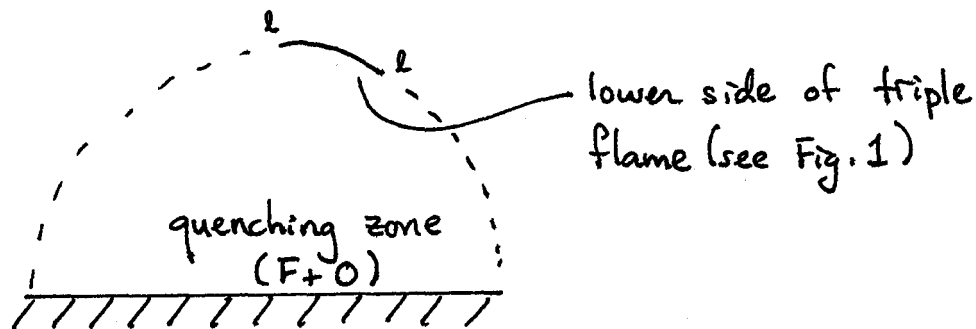
Here we examine a simple solution for the mixture fraction, Z , for the case of a model configuration that resembles the flame spread problem. A discussion, and some results, for this simple model are given in ref. 6. Once the Z contours are calculated (we vary the input of fuel from the fuel wall, see Fig. 7), we choose a constant- Z flame contour (see Fig. 7) onto which we superpose the flame quenching information from the two previous model problems and the flame-shape information. In this way, a set of hypothetical flame shape plots can be made, as shown in Fig. 7. These can be used to aid in the prospective experimental visualization of triple flame structures in actual flames. It may also provide clues for why these structures are very difficult to see in practice for flame spread over solid fuels. For liquid fuels, triple flame structures can actually be observed, see ref. 7.

References

1. Agrawal, S., and Atreya, A., "Wind-Aided Flame Spread over an Unsteadily Vaporizing Solid," Twenty Fourth Symposium (International) on Combustion, The Combustion Institute, Pittsburgh, PA, 1992, pp. 1685-1693.
2. Wichman, I.S., and Agrawal, S., "Wind-Aided Flame Spread over Thick Solids," Combustion and Flame, 83, 1991, pp. 127-145.
3. Bhattacharjee, S., "A Comparison of Numerical and Analytical Solution of Creeping Flame Spread over Thermally Thin Material," Comb. and Flame, 93, 1993, pp. 434-444.
4. Delichatsios, M. A., "Comments on 'A Comparison of Numerical and Analytical Solution of Creeping Flame Spread over Thermally Thin Materials' by S. Bhattacharjee," Comb. and Flame, 95, 1993, pp. 336-339.
5. Wichman, I.S., "On the Quenching of a Diffusion Flame Near a Cold Wall," Combust. Sci. Tech., 64, 1989, pp. 295-313.
6. Wichman, I.S., "Theory of Opposed Flow Flame Spread," Prog. Energy Combust. Sci., 18, 1992, pp. 553-592.
7. Ross, H. D., "Ignition of and Flame Spread over Laboratory-Scale Pools of Pure Liquid Fuels," Prog. Energy Combust. Sci., 20, 1994, pp. 17-63.



2)



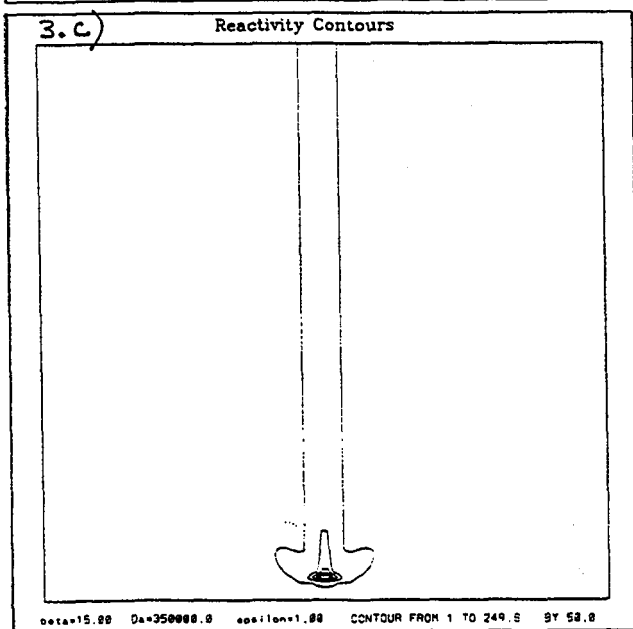
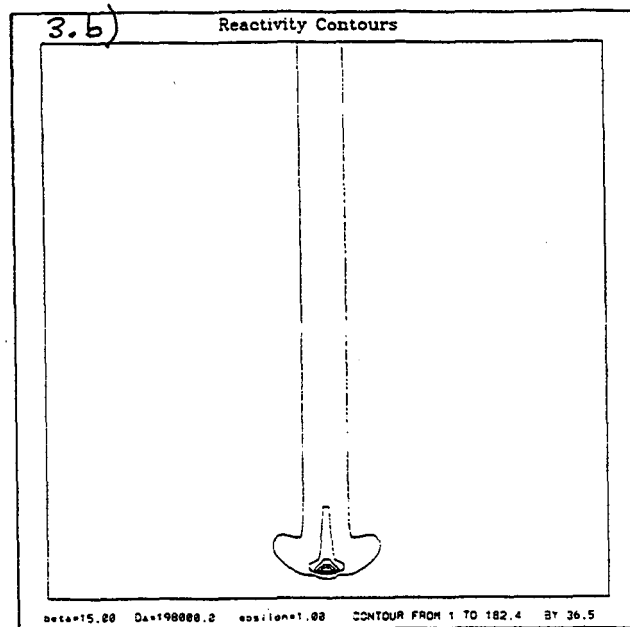
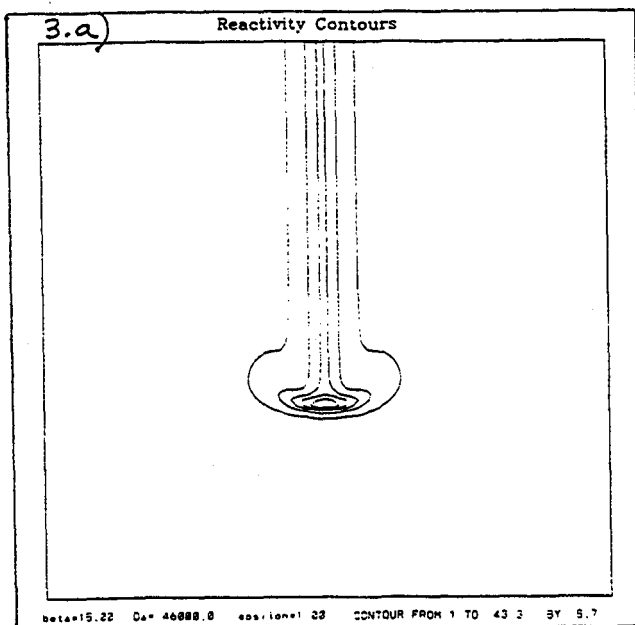


Fig. 3.a, b, c. Fix β , fix ϵ , vary D from 46,000 to 350,000.

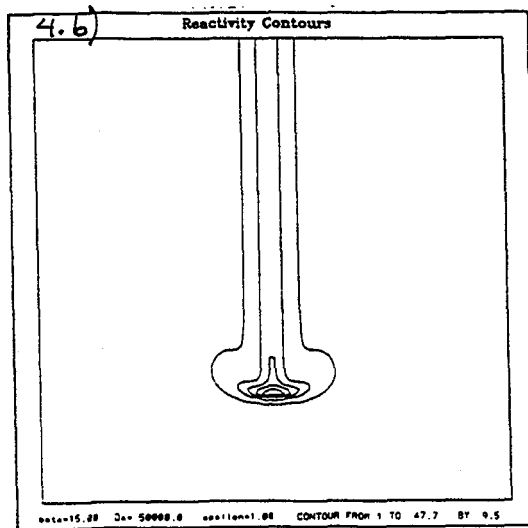
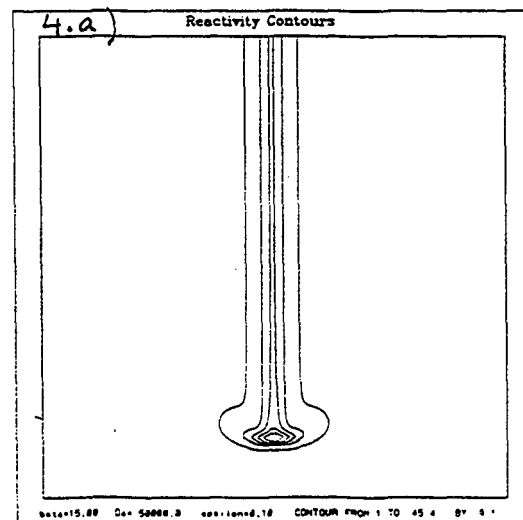
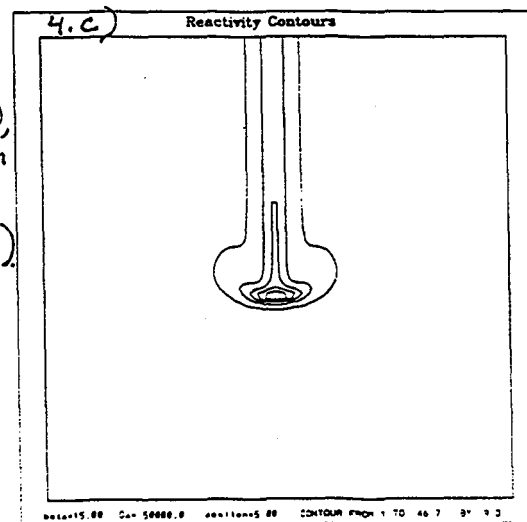


Fig. 4.a, b, c.
Fix β , fix D ,
vary ϵ from
0.1 to 5.0
($\epsilon=0.1, 1.0, 5$)



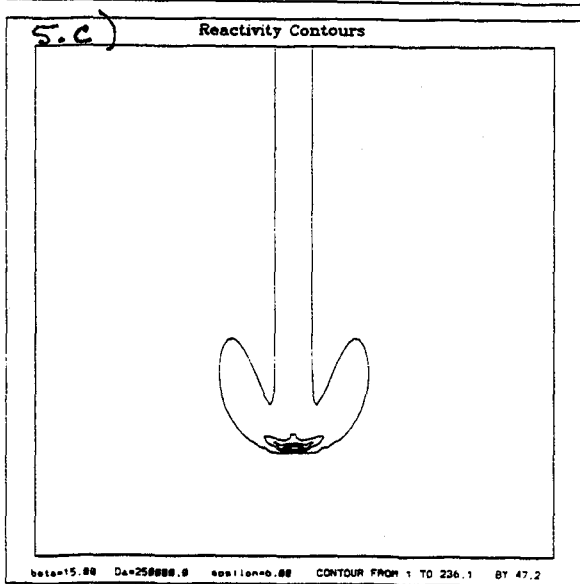
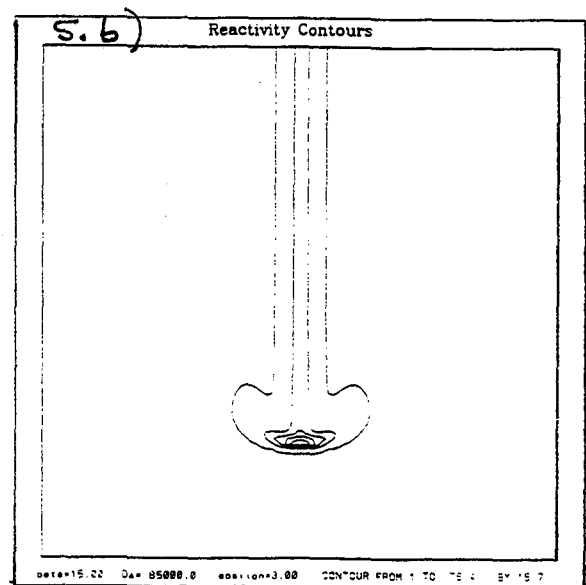
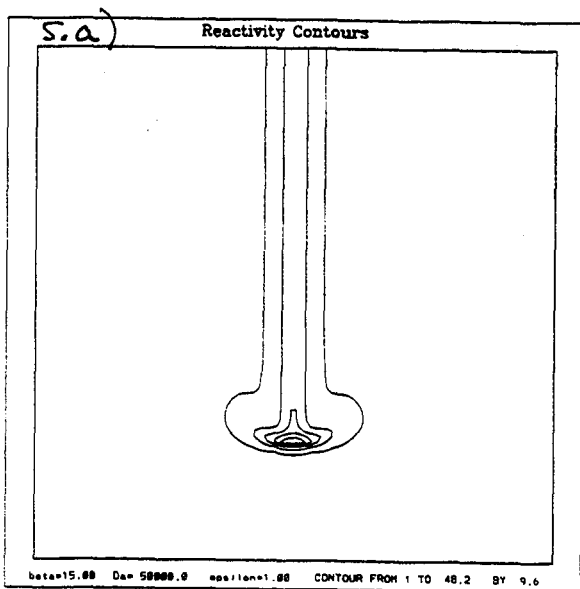


Fig. 5.a,b,c: Fix $\beta=15$, vary ϵ and D so that stand-off distance is fixed.

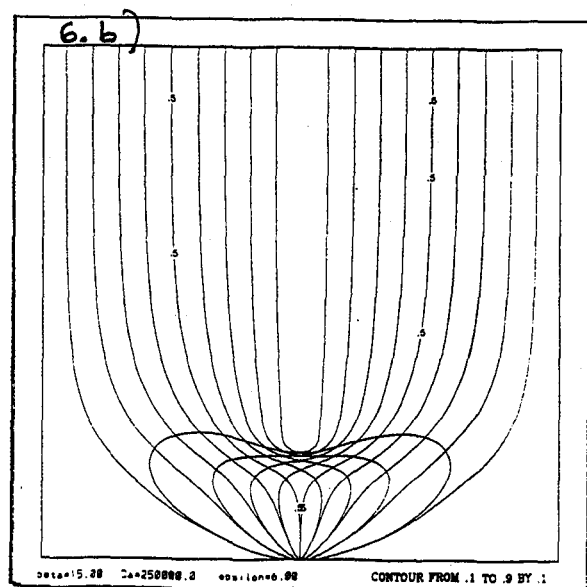
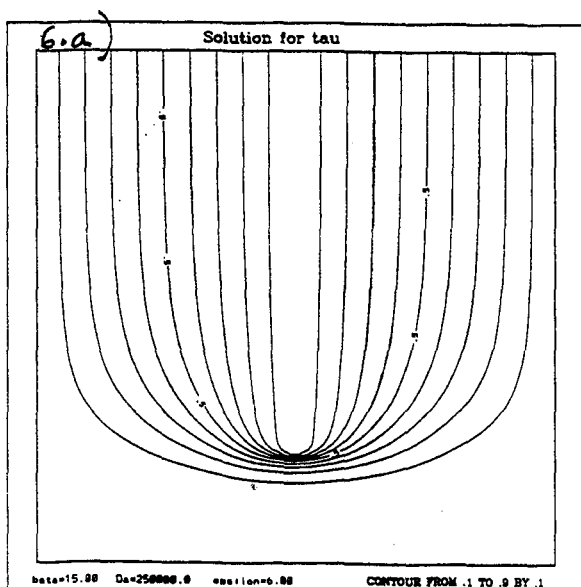


Fig. 6.a,b: Contours of constant τ , y_0 , y_F .

7)

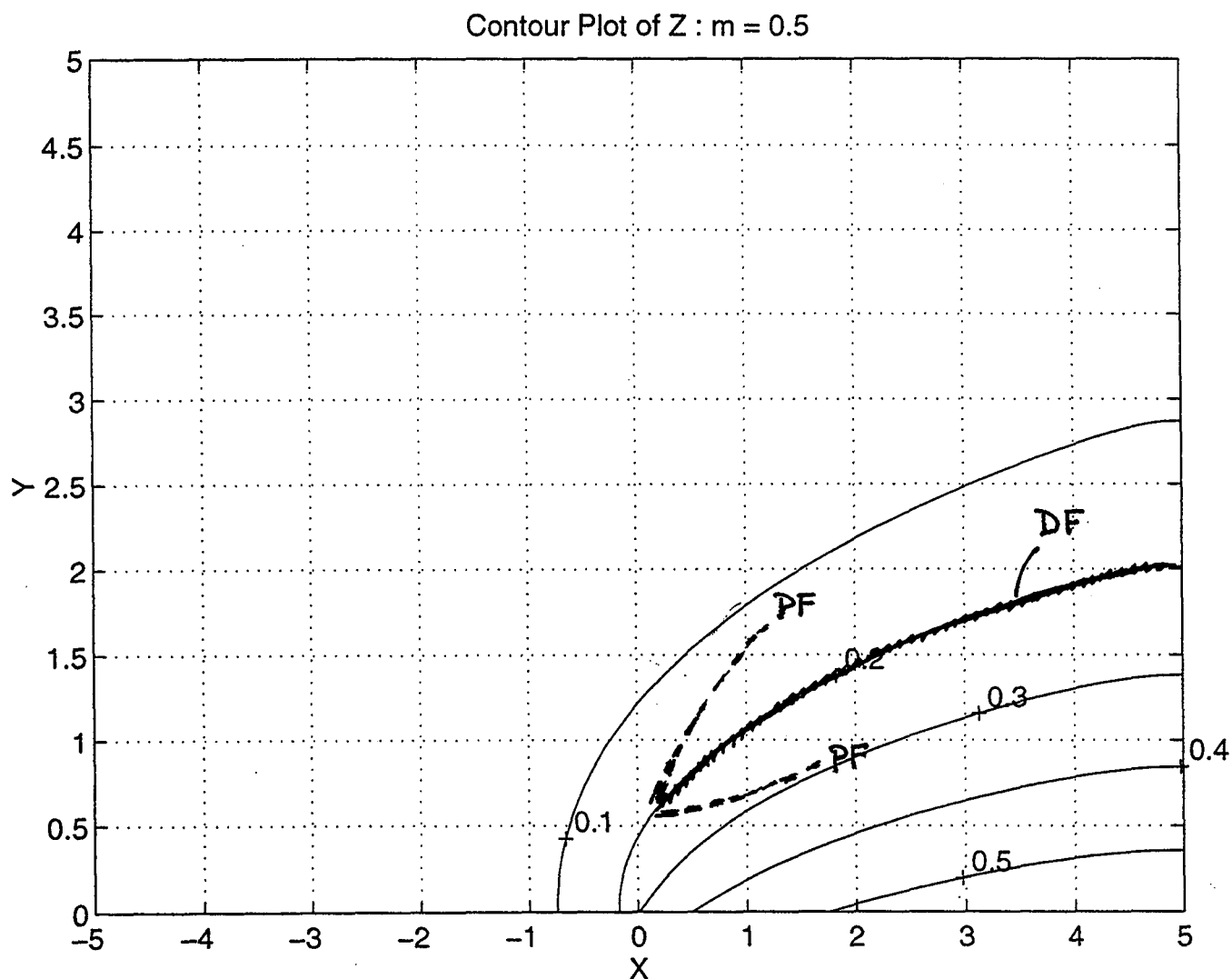


Fig. 7 : Contours of $Z = \text{constant}$ for a mock flame-spread problem, onto which is superposed a flame structure ($Z = 0.2$).

Combustion Diagnostics

LASER DOPPLER VELOCIMETRY AND FULL-FIELD SOOT VOLUME FRACTION MEASUREMENTS IN MICROGRAVITY

Paul S. Greenberg
NASA-Lewis Research Center
Cleveland, Ohio

Laser Doppler Velocimetry

Since its introduction in the mid-sixties,¹ laser doppler velocimetry (LDV) has become one of the most widely used methods for the measurement of flows. Its remote and essentially non-intrusive nature provides an invaluable tool for a variety of difficult measurement situations which would be otherwise inaccessible. The high spatial resolution and rapid temporal response afforded by this technique are well suited to the determination of spatial and temporal details of flow fields, as well as characterization of turbulence. Advances in the understanding of the properties of LDV signals, accompanied by technological advances in coherent laser sources, detectors of high sensitivity and low noise, optical fabrication techniques and high-speed digital signal processing architectures have resulted in systems of increased accuracy and flexibility. As will be shown, recent progress in solid-state lasers and photo-detectors have been beneficial insofar as the compatibility of this method with the unique and severe constraints inherent in microgravity combustion science experiments.

In brief, LDV relies on the doppler shift of optical radiation imparted by the velocity of the fluid flow.² Generally, this requires the introduction of small seed particles into the flow to serve as optical scattering centers. The size and mass of these seed particles must therefore be carefully considered to insure that their velocities are suitably indicative of the velocity of the fluid medium in which they are entrained. This property is usually expressed as the aerodynamic or hydrodynamic diameter of the particle³ and is defined as the diameter of a unit density sphere possessing the same settling velocity as the particle in question. For the case of spherical particles, this expression simplifies to $d_a = a(\rho)^{1/2}$, where a is the actual diameter and ρ is the mass density. The frequency response of this equivalent particle is then evaluated for its ability to respond to flow-field accelerations. The relatively low velocities, moderate turbulence intensities, and large spatial scales in most microgravity combustion phenomena allow the use of larger particles. The result is large scattering cross sections, and thus acceptable signal-to-noise ratios in the presence of compact, low power laser sources and modest optical collection efficiencies. As an example, for a band-limited turbulent spectra of 10^4 Hz., a 1.0 micron particle yields a value of $(v_p/v_a) = 0.98$, where v_p is the particle velocity and v_a is the actual velocity of the fluid flow. At a maximum frequency of 10^3 Hz., this ratio is still achievable by the use of 5.0 micron particles.

Rudimentary analysis of a laser doppler signal demonstrates that the frequency of the incident radiation is doppler shifted by an amount $\Omega = \mathbf{K} \cdot \mathbf{v}$, where $\mathbf{K} = \mathbf{k}_s - \mathbf{k}_i$, where \mathbf{v} is the velocity of the entrained particle, the latter quantities representing the wave vectors of the scattered and incident radiation, respectively. The most common physical realization of an LDV system is the so called dual-doppler, or fringe configuration. This is shown schematically in figure 1. The net result of the two incident beams can be thought of as producing a set of periodic fringes throughout the spatial volume defined by their intersection. Particles passing through this intersection region and traveling transverse to the orientation of these fringes produce a scattered signal whose periodicity is given by: The signal resulting from the passage of a single particle is referred to as a doppler burst; a burst produced from a

Preceding Page Blank

$$f = [\vec{v} \cdot \vec{K}] / |\vec{K}| \lambda_i \quad (1)$$

typical LDV system is shown in figure 2. For most systems encountered in practice, the fringe spacing results in observed dual-doppler frequencies on the order of 10^5 to 10^6 Hz./meter/second.

The system represented in figure 1 is configured in a coaxial, backscatter arrangement. This affords two principal advantages: 1) the system is single-ended (i.e. the transmission and detection optics are on the same side of the test section), and 2) it is easier to maintain alignment of the transmission and detection sample volumes. The latter is attributable both to the more compact geometry and to the fact that the incident and scattered light traverse the same optical path. This eliminates problematic beam steering effects produced by refractive index gradients that are often present in the flow-field itself. The disadvantage of a coaxial backscatter configuration arises from the fact that differential scattering cross sections are peaked in the forward direction, thus overall collection efficiency is reduced. Again, for the velocity fields typical of microgravity combustion phenomena, this is not outweighed by the advantages of a backscatter configuration.

As previously indicated, technological advances in solid-state laser diodes and avalanche photo-detectors (APD's) have recently been utilized to construct compact, mechanically robust LDV systems. Such systems offer extremely modest electrical power consumption as well. Diode laser sources possessing reasonable coherence and geometric radiation properties are now routinely available on a commercial basis. Active temperature control circuitry is required, however, to provide modal stability. In contrast, more conventional LDV systems that use gas discharge lasers are too large, fragile, and consume too much power for reduced gravity applications.

High performance APD's and associated preamplifiers are now similarly available. Although photomultiplier tubes (PMT's) provide higher absolute gains, APD's are shown to be more suitable for this purpose due to their substantially larger quantum efficiencies (QE) ($\approx 80\%$ for an APD vs. $\approx 14\%$ for a PMT). Because photon noise is given by $(n/QE)^{1/2}$, where n is the mean photon arrival rate, APD's provide a superior excess noise factor in this application, providing a three-fold improvement in signal to noise for peak scattered fluxes approaching 100 microwatts. APD's also require high voltage power supplies; incorporating this into a compact package while providing the necessary degree of shielding and isolation requires careful consideration. Additional improvement in signal to noise ratio is achieved by cooling the detector. Compact LDV systems of this type are presently being utilized in the Microgravity Combustion Diagnostics Development Laboratory at the NASA-Lewis Research Center. Shown in figure 3 is velocity field data from a non-reacting gas jet obtained with such a device. The doppler burst shown in figure 2 was also obtained with this system. The particular device used to collect this data measures 65 mm in diameter and 200 mm in length, and consumes approximately 12 watts of electrical power. Contained within this package are the diode laser source with active temperature control circuitry, the APD with the required high voltage DC-DC converter, a low noise preamplifier, and a 50 ohm line driver.

The relatively modest f numbers associated with these compact systems ($\approx f/6$) decreases the spatial resolution of the sample volume in the axial direction. The axial extent of the sample volume is on the order of 1.5 mm for present systems, limiting the ability to perform measurements in close proximity to test section walls or other boundaries. Seasholtz, et al⁴ demonstrated that considerable improvement can be obtained in this regard through improvements in the transmitting optics, and confocal masking.

Significant advances have also been made in the area of dedicated signal processors. To provide on-line estimates of velocity spectra at bandwidths typical of LDV signals, early counter-type processors relied on zero-crossing signal detection. Over the past several years, high speed digital signal processing architectures have enabled the calculation and subsequent parameter estimation of complete spectra, either in the form of Fourier spectra or temporal autocorrelation functions. Processors of this type have yielded a ten-fold improvement in the accuracy of the resulting velocity estimates, and are able to operate at lower overall signal to noise ratios.⁵ A system of this type is being utilized in microgravity combustion science research at the Lewis Research Center, and provides several

unique features relevant to this application. Specifically, this processor has been configured in the form of two 16-bit ISA cards for use in a conventional personal computer. This affords convenience and flexibility for utilization in the LeRC drop tower and aircraft facilities; it is also anticipated to be advantageous for space flight applications. Also included is the capability to function as a digital transient recorder. This is extremely valuable for drop tower and aircraft studies, allowing raw data to be acquired and archived for subsequent post-processing.

Soot Volume Fraction Imaging

Soot is of fundamental interest from the standpoint of fuel and combustor efficiency, hardware longevity, and its relationship to public health. A comprehensive understanding of soot formation, aggregation, and oxidation mechanisms is, however, far from complete. Details concerning precursor chemistry, morphology, and overall production rates (i.e. volume fractions) remain active areas of study. For more than a decade, optical extinction methods have been utilized as an important tool for the determination of soot volume fractions in combustion applications.^{6,7} More recently, investigations have focused on providing detailed, spatially resolved measurements of soot particle concentration fields.^{8,9} These techniques have benefitted from the availability of coherent, monochromatic sources (i.e. lasers), owing to their well defined spectral properties, critical to interpreting the spectrally dependent properties of carbonaceous soot itself and to the advantages afforded in optical beam conditioning and manipulation.

The analysis of optical extinction data involves the determination of local soot volume fractions from a set of integrated line-of-sight measurements. Assumptions required to validate the inversion of this data include parallel, chord-like ray trajectories, negligible refraction effects, no significant absorption or scattering from media other than soot particles, an absence of radiant emissions corresponding to the wavelength of the laser source, and a knowledge of the spectrally dependent scattering and absorption properties of the soot itself, and the optical path length through the soot-containing medium. The latter is usually handled by the selection of a combustion phenomenon possessing axisymmetry. Well known Abel transformation equations may then be invoked.

Given the above assumptions, the extinction of optical radiation due to the presence of soot may be expressed as:

$$\frac{dI_{\lambda}}{ds} = -k_{e\lambda} I_{\lambda} \quad (2)$$

where $k_{e\lambda}$ is the optical extinction coefficient evaluated at the wavelength of the source. Integration of equation (2) along chord-like paths through the flame yields the relation:

$$\ln(I_{\lambda 0}/I_{\lambda}) = \int_{-\infty}^{+\infty} k_{e\lambda} ds \quad (3)$$

In the Rayleigh scattering limit, the volume fraction is then related to the extinction coefficient by:

$$f_v = \lambda k_{e\lambda} / (6\pi E(m)) \quad (4)$$

where $E(m) = -\text{Im} (m^2 - 1)/(m^2 + 2)$, m being the complex refractive index for soot particles. Spatially localized values of f_v are then obtained from equations (3) and (4) via tomographic inversion.

To date, studies have relied on sequential point-by-point interrogation of the soot field. Such methods are not well suited to investigations involving nonrepeatable time dependent or transient phenomena. In the context of microgravity combustion science, where constraints on overall experiment duration and/or available expendable resources are often encountered, this limitation can be difficult to overcome.

To address this need, a full-field, or image based technique was developed.¹⁰ It provides the capability to perform measurements at 2.5×10^5 simultaneous spatial locations at a refresh rate of 30 Hz. The total field of view corresponding to this sample set is determined by the receiving optics. An appreciation for the benefits of this enhanced capability is immediate when viewed in the context of aircraft or drop tower tests; by using a point measurement technique, it would be difficult to obtain more than a few selected data points during the overall experiment run time. Given the desire to reach some reasonable approximation of steady-state conditions, the validity of temporal correlations between these individual data points would be questionable. Additionally, the value of an image of the complete soot field to qualitative understanding is immense.

Soot volume fraction data corresponding to a 3.85 cc/sec laminar ethylene diffusion flame is shown in figure 4. In this case, the burner is stabilized with an annular co-flow of air. Data obtained with this method are observed to be in close agreement with previously published experimental results obtained via pointwise measurements.⁸ The present limitation of this technique is absolute sensitivity. The high temporal bandwidths required to sustain the described data rate of 7.5 megabytes per second provides a large noise equivalent power (NEP) as well. If overall data rate is preserved, a signal to noise ratio of one corresponds to a line-of-sight extinction value of roughly two percent.

Apparatus to perform soot volume fraction imaging has also been implemented within the relatively confined volume of a 2.2 second drop package. This does not include the provision for on-line data storage, which is presently accommodated by telemetric link. A comparison of soot volume fractions corresponding to a 1.5 mm laminar gas jet diffusion flame with a 50/50 [partial pressure] acetylene/nitrogen mixture operating under both normal and reduced gravity conditions is shown in figures 5 and 6. It can be readily observed that the soot shell occurs at significantly larger radii, and that the maximum value of volume fraction is approximately twenty percent larger under reduced gravity. Under these same conditions, the transmittivity is reduced by over forty percent, indicating a significant increase in overall soot production.

References

1. Yeh, Y., and Cummins, H. Z., "Localized Fluid Flow Measurement with a He-Ne Laser Spectrometer," *Applied Physics Letters*, Vol. 4, No. 10, 1964, pps. 176-178.
2. Edwards, R.V., Angus, J. C., French, M. J., and Dunning, J. W., "Spectral Analysis of the Signal from the Laser Doppler Flowmeter: Time-Independent Systems," *Journal of Applied Physics*, Vol. 42, No. 2, 1971, pps. 837-850.
3. Agarwal, J. K., and Fingerson, L. M., "Evaluation of Various Particles for Their Suitability as Seeds in Laser Velocimetry," *Laser Velocimetry and Particle Sizing, Proceedings of the Third International Workshop on Laser Velocimetry*, Purdue University, Hemisphere Publishing Corporation, 1978.
4. Seasholtz, R. G., Oberle, L. G., and Weikle, D. H., "Optimization of Fringe-Type Laser Anemometers for Turbine Engine Component Testing," *AIAA/SAE/ASME 20th Joint Propulsion Conference*, Cincinnati, OH, June 11-13, 1984.
5. Hepner, T. E., "State-of-the-Art Laser Doppler Velocimeter Signal Processors: Calibration and Evaluation," *AIAA 32nd Aerospace Sciences Meeting*, Reno, NV, January 10-13, 1994.
6. Haynes, B. S., and Wagner, H. G., "Soot Formation," *Progress in Energy and Combustion Science*, 7, 1981, pps. 229-273.
7. T'ien, C. L., and Lee, S. C., "Flame Radiation," *Progress in Energy and Combustion Science*, 8, 1982, pps. 41-59.
8. Santoro, R. J., Semerjian, H. G., and Dobbins, R. A., "Soot Particle Measurements in Diffusion Flames," *Combustion and Flame* 51, 1983, pps. 203-218.
9. Gore, J. P., and Faeth, G. M., "Structure and Radiation Properties of Turbulent Ethylene/Air Diffusion Flames," *Twenty-First Symposium (International) on Combustion*, The Combustion Institute, 1986, pps. 1521-1531.
10. Greenberg, P. S., Ku, J. C., Lin, K. -C., Köylü, Ü. Ö., and Faeth, G. M., "Soot Volume Fraction Imaging," manuscript in preparation.

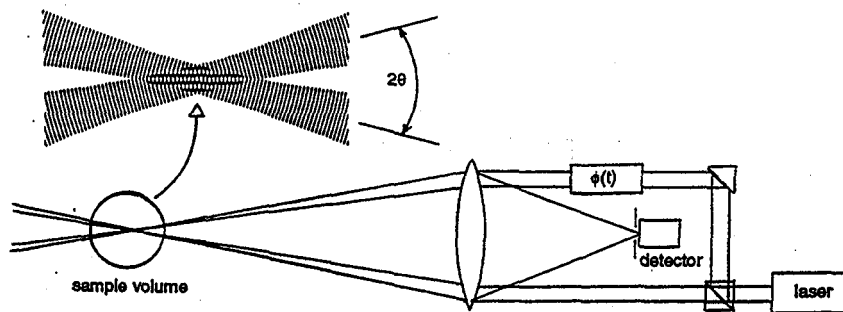


Figure 1: Schematic of dual-doppler LDV in backscatter configuration

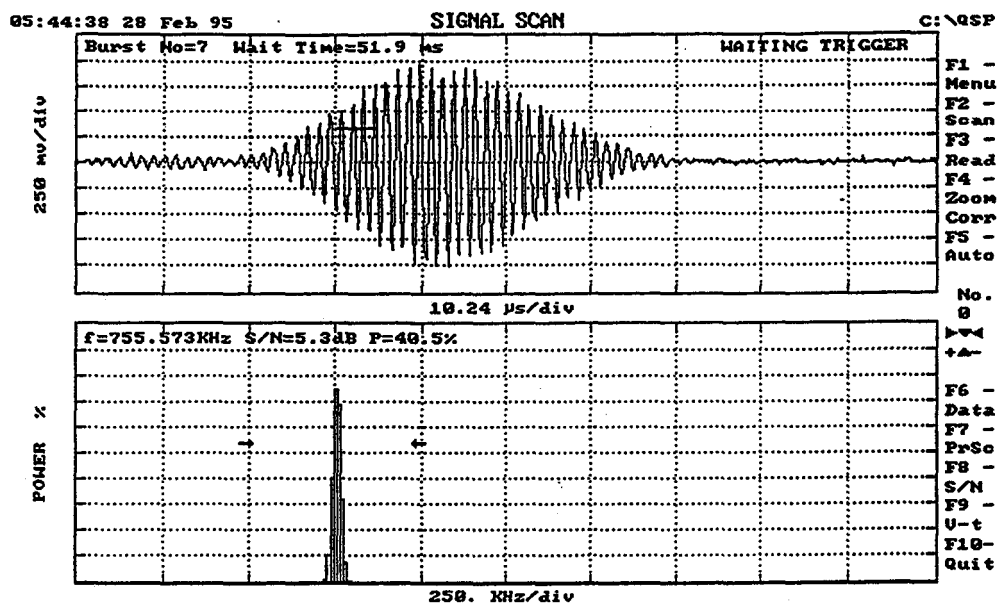


Figure 2: Single Doppler Burst from Compact, Solid-State LDV

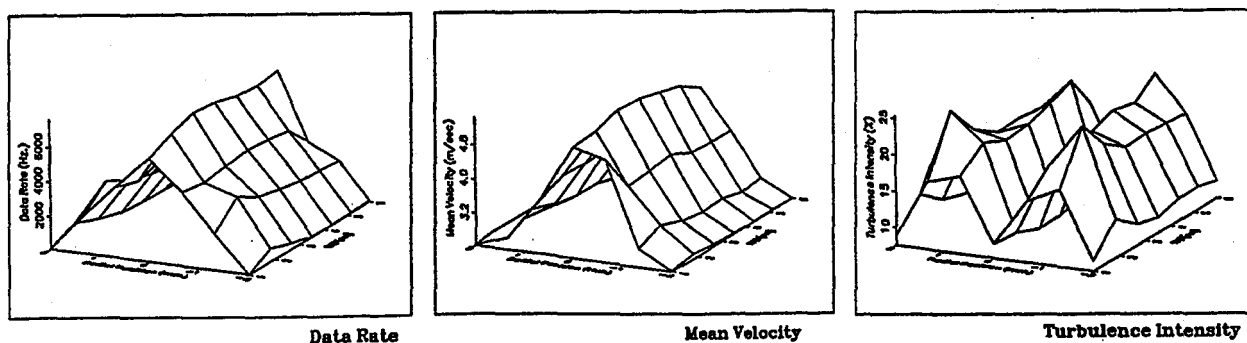


Figure 3: Velocity Field of Re 1438 Non-reacting Jet

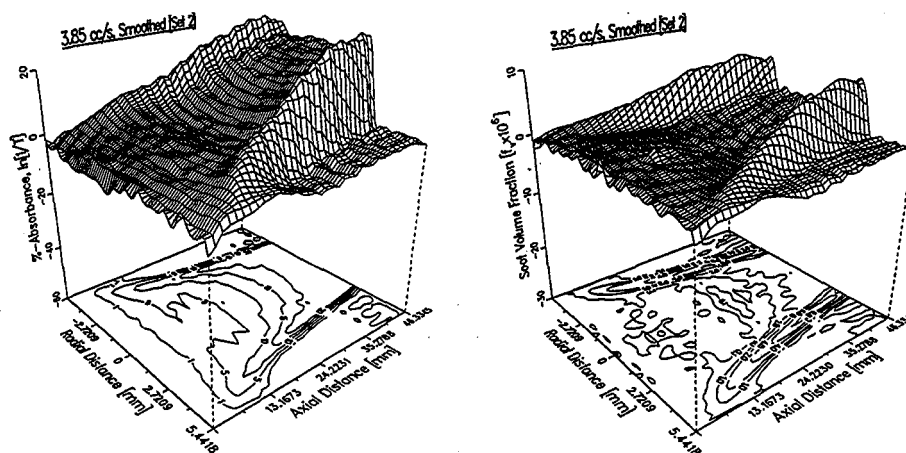


Figure 4: Absorbance and Soot Volume Fractions: 3.85 cc/sec laminar ethylene diffusion flame

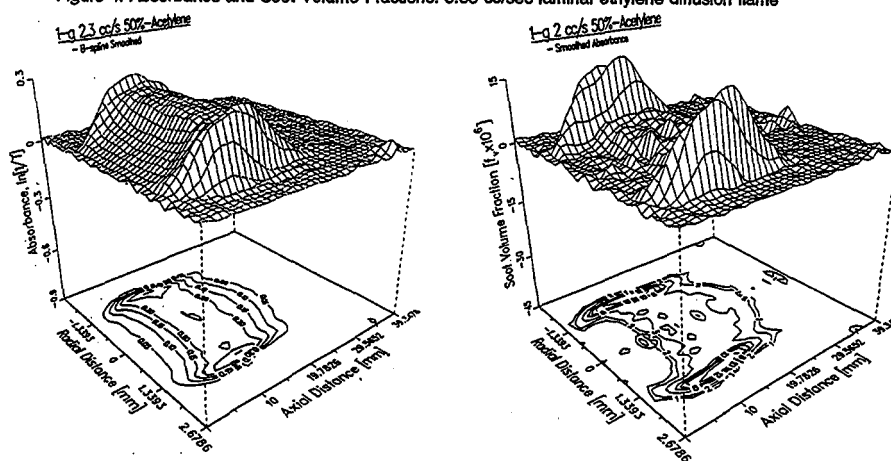


Figure 5: Absorbance and Soot Volume Fractions: 2.3 cc/sec laminar acetylene/nitrogen diffusion flame; Normal Gravity

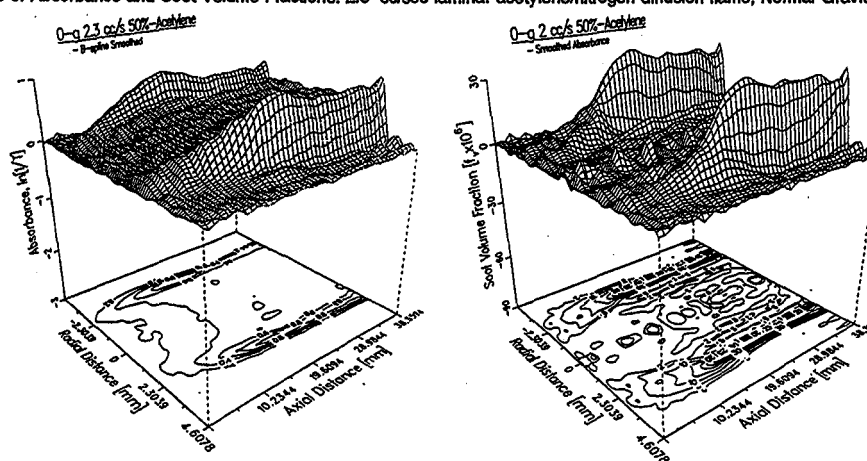


Figure 6: Absorbance and Soot Volume Fractions: 2.3 cc/sec laminar acetylene/nitrogen diffusion flame; Reduced Gravity

Full Field Gas Phase Velocity Measurements in Microgravity

DeVon W. Griffin
NASA Lewis Research Center
Cleveland, OH

and

William Yanis
NYMA, Inc.
Cleveland, OH

Introduction

Measurement of full-field velocities via Particle Imaging Velocimetry (PIV) is common in research efforts involving fluid motion. While such measurements have been successfully performed in the liquid phase in a microgravity environment [1,2], gas-phase measurements have been beset by difficulties with seeding and laser strength. A synthesis of techniques developed at NASA LeRC exhibits promise in overcoming these difficulties.

Olson [3] used a pulsed smoke- wire technique to measure flow velocities over a solid fuel sample in microgravity. In this method, current was periodically passed through wire coated with an oil that produced smoke at low temperatures. The result was a series of smoke puffs, the velocity of which was assumed to match the local flow velocity. Data from flow velocities between 5 and 40 cm/sec were compared with plug flow velocities from rotameter measurements and found to agree well. Additionally, the technique was used to measure boundary layer velocities across the sample holder and were found to be within 3% of that predicted by Blasius theory.

While useful to characterize flows in that particular application, typical implementation of PIV involves forming the light from a pulsed laser into a sheet that is some fraction of a millimeter thick and 50 or more millimeters wide. When a particle enters this sheet during a pulse, light scattered from the particle is recorded by a detector, which may be a film plane or a CCD array. Assuming that the particle remains within the boundaries of the sheet for the second pulse and can be distinguished from neighboring particles, comparison of the two images produces an average velocity vector for the time between the pulses. If the concentration of particles in the sampling volume is sufficiently large but the particles remain discrete, a full field map may be generated.

Light Source

PIV systems often use pulsed lasers, generally Nd:YAG, that provide between 50 and 200 mJ per pulse. Such lasers, however, are currently incompatible with reduced gravity facilities, due to power consumption, size and lack of ruggedness [4]. To overcome those constraints, Big Sky Technologies developed for this project a Nd:YAG laser that pulses continuously at 30 Hz and in a burst mode where 4 pulses separated by 1 ms are produced every second. In the continuous mode, pulse energies may be as high as 42 mJ whereas 50 mJ is possible in the burst mode; typical pulse lengths are on the order of 12 ns. With these parameters and assuming a 50 mm wide light sheet, velocities between 3 and 1666 cm/sec may be measured. Efforts at LeRC have concentrated on the sub-buoyant region between 5 and 40 cm/sec.

Physically, the laser head is 318 mm long, 127 mm wide and 76 mm deep. Plumbing and electrical connections on the end add another 100 mm to the length. The cooling system and all electronics are housed in a rack of typical width and a total depth of 635 mm. The entire system is rated to +3 and -0.1 G and is operated on 10 amps of 110 VAC.

Based on those specifications, the entire unit may be flown on reduced gravity aircraft. At this date, hardware is being developed to support operation of this laser on NASA LeRC's DC-9 airplane. Current plans envision using one platform to support the laser and associated optics while fuel handling and ignition are provided by existing hardware. An enclosed beam path between the two rigs will prevent accidental exposure to the beam of this Class

IV laser. We are currently working with a vendor to determine if a tapered fiber could replace the lenses and tube as a beam delivery system. If the fiber meets the manufacturer's claims, it may also be implemented in NASA LeRC's 2.2 second drop tower, as is currently done with optical communications fiber.

Seed Particles and Delivery

Apocryphal stories abound concerning the need to periodically shock seeding chambers to insure a steady supply of seed to the flow of interest. While such procedures are easily implemented in normal gravity facilities, tending operation is not always possible in reduced gravity experiments on platforms such as sounding rockets. Therefore, we attempted to design a seeder that would be self-supplying. The seeder we developed features an inlet with a diameter of 0.1 mm and an outlet that can be as large as 6.3 mm. The device was made of extruded acrylic tubing to view the seed bed, thus facilitating rapid development of the seeder design. Depending on the gas, Reynolds numbers developed within the chamber are equal to or greater than 2000. The turbulent mixing, combined with an interior funnel, generate a seed bed that is continually agitated and generates a large seeding density within the chamber.

Current efforts are directed at velocity measurements in gas jet diffusion flames. To provide adequate measurement of the jet's flow velocity, seed particles must faithfully retrace the flowlines and be easily entrained. The particles that we have found that work best for this application are MicroSpherical Feathers sold by Osaka Gas America.[5] These SiO_2 particles are specifically engineered to be spherical and not agglomerate. The specific gravity is also low and on the order of 0.45 grams / cm^3 . Unfortunately, they presently cost \$1500 for 100 grams with a minimum order of 500 grams. We have tried three different diameters in our experiments with the 75 micron particles the optimal size for our application since they resist agglomeration better than the small 2.7 micron variety and are much more easily entrained than those with a diameter of 150 microns. Compared to other powders that may be used for such applications, such as 10 micron diameter TiO_2 , or similarly-sized SiO_2 , MicroSpherical Feathers agglomerate less and appear to follow the flow much better.

Experiment Design

The light scattering physics underlying PIV was elucidated by many but is most often attributed to Gustav Mie [6]. To avoid *ad hoc* determination of system parameters such as laser power, detector sensitivity and lens speed, we have assembled a collection of computer codes that simplify this process. The first, developed by Edward Hovenac of NYMA, Inc. for use at LeRC in icing research calculates components of the scattering matrix using Mie theory. These results, when combined with propagation distance, can provide the irradiance level on the surface of the collecting lens. Additionally, integration of the data from Hovenac's program using software written by one of us (Griffin), produces the scattering cross section.

Before the illumination on the detector can be calculated, the irradiance at the object plane must be known. This requires knowledge of a combination of the laser energy/pulse, pulse duration and area over which the beam is spread. Design of the optics that produce a light sheet is required before the area is known. As before, avoidance of experimental determination of the correct optical prescription requires a computer code that models the optical path to sufficient precision. While most commercial lens design codes claim features for calculation of Gaussian beam parameters, they are typically based on the method of Kogelnik and Li [7] which masks a second solution to the Gaussian propagation equation. The net result is that the codes may not adequately represent beams used in light sheet systems. Therefore, a code based the equations of Seasholtz [8] was developed that allows the user to interactively search for parameters to produce the desired light sheet. Given the interactive nature of the formalism and program, at least one configuration can typically be found for almost any set of cylindrical lenses.

Data Reduction

Data reduction may be accomplished either via correlation of the two image fields or using the Particle Displacement Tracking method (PDT) developed at LeRC that was described previously [4,9]. Enhancements to the latter technique have allowed the use of only two frames to generate a velocity field. This software package also controls the acquisition of the image files for later analysis.

Planned Experiment Demonstration

A gas jet diffusion flame has been selected for the initial low-g demonstration. It will be located inside of a combustion chamber with the seeder previously described forming the base of the burner. When operating, light from the Big Sky laser enters the chamber through a window and illuminates the particles. Synchronization of the experiment is based on the 60 Hz timing pulse from a Xybion CID camera. This pulse is fed to a divide-by-2 circuit and then into a delay generator. Following the adjustable delay, a pulse is sent to the laser, causing it to fire. A notebook computer equipped with an expansion station and an Epix frame-grabber board uses the software previously described to grab every other field, coincident with the firing of the laser. Up to a 25 field sequence can thus be recorded, corresponding to almost 1 second of data. After the images are written to the hard drive, the experiment may be repeated immediately. By operating in this manner, a large data set may be collected and analyzed at a later time.

References

1. Ross, H., Miller, F., Schiller, D. and Sirignano, W.A., Third International Microgravity Combustion Conference, (1995).
2. Kamotani, Y., Ostrach, S. and Pline, A., *Physics of Fluids A*, **6**, 3601-3609 (1994).
3. Olson, S.L., *Combustion Science and Technology*, **76**, 233-249 (1991).
4. Greenberg, P.S., NASA CP 10113, pp. 61-66 (1992).
5. Ikeda, Y., Nishigaki, M., Ippommatsu, M., Hosokawa, S. and Nakajima, T., Sixth International Symposium on Applications of Laser Techniques to Fluid Mechanics, S32-2 (1993).
6. Mie, G., *Ann. Physik*, **30**, 59 (1908).
7. Kogelnik, H. and Li, T., *Applied Optics*, **5**, 1550-1567 (1966).
8. Seasholtz, R.G., NASA TN D-8297 (1977).
9. Wernet, M.P. and Edwards, R.V., *Applied Optics*, **29**, 3399-3417 (1990).

DIAGNOSTICS IN JAPAN'S MICROGRAVITY EXPERIMENTS

Toshikazu Kadota
University of Osaka Prefecture
Sakai, Osaka Japan

Introduction

The achievement of the combustion research under microgravity depends substantially on the availability of diagnostic systems. The non-intrusive diagnostic systems are potentially applicable for providing the accurate, realistic and detailed information on momentum, mass and energy transport, complex gas phase chemistry, and phase change in the combustion field under microgravity. The non-intrusive nature of optical instruments is essential to the measurement of combustion process under microgravity which is very nervous to any perturbation. However, the implementation of the non-intrusive combustion diagnostic systems under microgravity is accompanied by several constraints. Usually, a very limited space is only available for constructing a highly sophisticated system which is so sensitive that it is easily affected by the magnitude of the gravitational force, vibration and heterogeneous field of temperature and density of the environments. The system should be properly adjusted prior to the experiment. Generally, it is quite difficult to tune the instruments during measurements. The programmed sequence of operation should also be provided. Extensive effort has been toward the development of non-intrusive diagnostic systems available for the combustion experiments under microgravity.

This paper aims to describe the current art and the future strategy on the non-intrusive diagnostic systems potentially applicable to the combustion experiments under microgravity in Japan.

Raman Scattering

Raman scattering has the unique advantage of being able to provide spatially resolved measurements of temperature and all major species using only a single incident laser light without the need for tuning. It is essentially an instantaneous process occurring within a time of 10^{-12} s or less. The Raman spectrum is species specific, temperature sensitive and linearly proportional to the species number density. Unfortunately, the scattered signal is very weak, hence it is usually difficult to assure the high signal interference ratio. Raman scattering is suited to combustion diagnostics in clean flame. Preliminary experiments under normal gravity include the thermometry of propagating flame(1) and species concentration and temperature measurements in the wake flame formed behind a pair of small porous spheres(2) and jet diffusion flame. The application of this technique to the microgravity

experiments is now under consideration.

Rayleigh Scattering

Rayleigh scattering has been of interest since its cross section is approximately three orders of magnitude stronger than the one for vibrational Raman scattering. Since the Rayleigh scattering is an elastic process, the scattered light is unshifted in frequency, and hence not species specific. The employment of Rayleigh diagnostic is restricted to the measurements in a very clean environments free of particulate. Preliminary experiments carried out under normal gravity include the thermometry of propagating premixed flame(1) and turbulent jet diffusion flame, and the measurement of the fuel vapor concentration profile around a pair of spheres evaporating in a uniform stream of air(3), planar Rayleigh scattering for the visualization of the fuel concentration field in an unsteady and a steady circular turbulent jets(4). These experiences suggest that it is not so far ahead for this technique to be employed for probing species concentration and temperature in the combustion environments under microgravity. The high power laser and the highly sensitive optical detector are recommended in the installation of diagnostic system.

Mie Scattering

Mie scattering is also an elastic scattering of light from particulate of which diameter is so large that $d/\lambda \ll 1$ does not hold. The intensity of the scattered light is a complicated function of various physical parameters such as the number density, the optical size, the complex refractive index and the angle of observation. The comprehensive analysis has provided a library of scattering function for spheres and other geometries. Mie scattering is applicable to soot diagnostics in flame. Figure 1 shows the planar laser Mie scattering system(5) developed for two dimensional visualization of soot concentration field in a droplet flame under microgravity inside a drop tower. The optical system is consisted of a frequency doubled Nd-YAG laser to irradiate an envelope flame formed around a fuel droplet, an interference filter and a CCD camera. Mie scattering is also available for the droplet sizing in fuel spray flame. It has been proposed to employ a small angle forward scattering technique(6) for the measurements of droplet size and number density in a spray flame under microgravity.

Laser Induced Fluorescence

Laser induced fluorescence(LIF) is the spontaneous emission of radiation from an upper energy level which has been excited by incident laser light. For the most flame radicals and minor species, the excitation to electric upper level requires a tunable laser light radiation with the wave length ranging from 200 to 600 nm which is conveniently accessed by tunable dye lasers or others either directly or via some readily available frequency conversion scheme. LIF possesses the capability of detecting the flame radicals and minor species at the level of ppm or less and hence has received a considerable attention. Fluorescence spectra are in general shifted in frequency from the incident laser light and hardly influenced by the interference from the spuriously scattered incident laser light and Mie scattering. The spectra are species specific. This technique requires the correction for the quenching that is the decay of the excited state of species to obtain the quantitative

data. Several attempts have been done to apply planar laser induced fluorescence (PLIF) for the combustion experiments under normal gravity. These include two dimensional visualization of radical concentration in flame(7)(8), fuel vapor concentration in isothermal mixing process and liquid density in a spray(9). These efforts have resulted in the development of the PLIF based combustion diagnostic system under microgravity as shown in Fig. 2. It has already been constructed and now available for the measurements of radicals in a various kinds of flames. Liquid phase thermometry in the droplet flame has been successfully done by using exciplex based fluorescence under normal gravity(10). Figure 3 shows the schematic diagram of the apparatus which is now being utilized for the remote probing of burning droplet temperature under microgravity inside a drop tower. A fuel droplet doped with a trace of naphthalene and TMPD is subject to the nitrogen laser excitation and the resultant fluorescence spectrum from the droplet is measured with an optical multichannel analyzer. Since the fluorescence spectra are temperature sensitive, droplet temperature is determined from the measured results of the spectra.

Interferometry and Schlieren

Interferometric and Schlieren techniques have been widely employed for the visualization and the quantitative analysis of combustion processes, for flame geometry determination and for the measurements of density and temperature field in combustion. Michelson interferometry has been employed for the experimental study of autoignition of fuel droplet under microgravity. Figure 4 shows the experimental apparatus to visualize and quantify the instantaneous temperature field formed around a droplet which was subject to the hot ambient gas(11). Interferometric image is stored by a 8 mm video tape and analyzed by a high speed image analyzing system. Instrumentation of Schlieren is rather flexible and simple, hence most appropriate for the visualization of the heterogeneous density field due to temperature or concentration difference in the gaseous medium in a limited space. It has been employed for the study of turbulent burning velocity in a closed vessel under microgravity(12). The special attention has been paid to prevent the doubling of the image and to keep the long optical pass.

Emission Spectroscopy

Instantaneous two dimensional concentration profile of OH around the array of fuel droplets during autoignition in high temperature gaseous environment was visualized under microgravity(13) by using a CCD camera with an image intensifier and an interference filter. The flame color could give us some data available for understanding combustion process. It has been reported the the flame color is well correlated with some kinds of experimental parameters under normal gravity(14). It has been attempted to extend its use to the combustion experiments under microgravity.

Velocimetry

Both particle image velocimetry (PIV) and laser doppler velocimetry (LDV) are available for probing the flow field in the combustion environments under microgravity. PIV is preferential and the system which is similar to the one as shown in Fig. 2 has been constructed. Liquid phase PIV is based on either Mie scattering or fluorescence of droplets

which is subject to the irradiation of a sheet of frequency doubled or quadrupled Nd-YAG laser. Seed material is added to the gaseous medium as a scattering center in gas phase PIV.

References

1. Ujiie, Y., Tsukamoto, T. and Kono, M., Temperature Measurement of Spherically Propagating Flames Using Rayleigh and Raman Scattering Methods, *Trans. JSME*, Vol.55, No.513(1989), 1444-1447.
2. Kadota, T., Sumida, K., Tsuzaki, H. and Tsue, M., Raman Scattering Probing of the Species Concentration and Temperature in the Wake Flame behind Spheres, *Proc. of the 2nd Asian-Pacific Int. Symp. on Combustion and Energy Utilization*, (1993), 833-838.
3. Kadota, T., Kadowaki, K. and Tsue, M., Rayleigh Scattering for Probing the Fuel Vapor Concentration Profile around a Pair of Evaporating Spheres, *Proc. of IUTAM Symposium on Mechanics and Combustion of Droplets and Sprays*, (1994), 231-240.
4. Tsue, M., Inoue, K., Nakamae, T., Hattori, H. and Kadota, T., Planar Rayleigh Scattering Method for the Visualization of Concentration Field in a Gaseous Jet, *Proc. of the 2nd JSME-KSME Thermal Engineering Conference*, Vol.2(1992), 453-458.
5. Tsue, M., Yamasaki, H., Miura, S., Hamaya, H. and Kadota, T., Measurements of Soot Concentration Profile for Microgravity Droplet Combustion, *Prepr. of JSME*, No. 940-30(1994), 359-361.
6. Hayashi, S., A Laser Small-Angle Scattering Instrument for the Determination of Size and Concentration Distribution in Sprays, *ASTM Tech. Pub.* 1083(1990), 77-92.
7. Hirano, A. and Tsujishita, M., Visualization of CN by the Use of Planar Laser-Induced Fluorescence in a Cross Section of an Unseeded Turbulent CH₄-Air Flame, *Applied Optics*, Vol.33, No.33(1994), 7777-7780.
8. Fujita, O., Itoh, K., Fukuda, T., and Tanaka, K., Non-Contact Measurement of Formaldehyde Distribution in Methanol Laminar Flames by Using LIF Method, *Proc. of the 2nd JSME-KSME Thermal Engineering Conference*, Vol.1(1992), 187-192.
9. Tsue, M., Hattori, H., Saito, A. and Kadota, T., Planar Fluorescence Technique for Visualization of a Diesel Spray, *SAE Paper* 922205(1992), 1-12.
10. Kadota, T., Tsue, M. and Miyoshi, K., Laser-Induced Fluorescence Thermometry of Burning and Evaporating Fuel Droplets, "Non-Intrusive Combustion Diagnostics", Begell House, (1994), 87-97.
11. Tanabe, M., Kono, M., Sato, J., Koenig, J., Eigenbrod, C., Dinkelacker, F. and Rath, H.J., Two Stage Ignition of n-Heptane Isolated Droplets, 25th Symposium on Combustion to appear
12. Kawakami, T., Okajima, S. and Inuma, K., A Study of Turbulent Burning Velocity in a Closed Vessel by Zero-Gravity Method, *Archivum Combustionis*, Vol.10, No.1-4(1990), 161-171.
13. Niioka, T., Kobayashi, H. and Mito, D., Ignition Experiments on Droplet Array in Normal and Microgravity Environments, *Proc. of IUTAM Symposium on Mechanics and Combustion of Droplets and Sprays*, (1994), 367-377.
14. Ito, K., Ihara, H., Tatsuta, S. and Fujita, O., Quantitative Characterization of Flame Color and Its Application, *JSME Int. Journal*, Ser. 2, Vol.35, No.2(1992), 287-292.

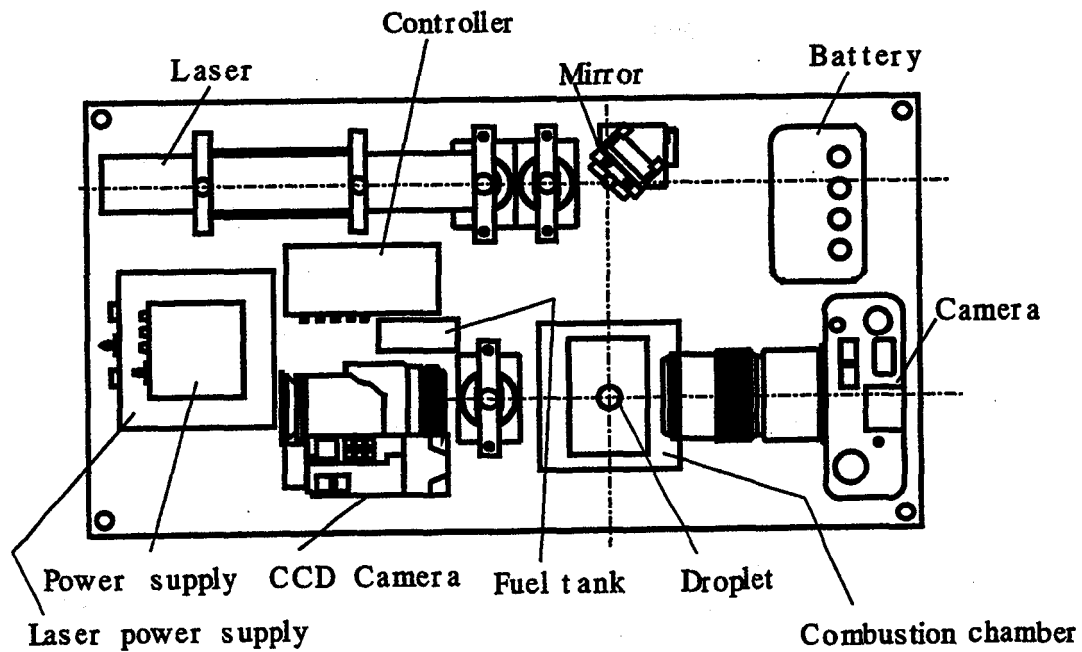


Fig.1 Planar Mie scattering for soot diagnostics

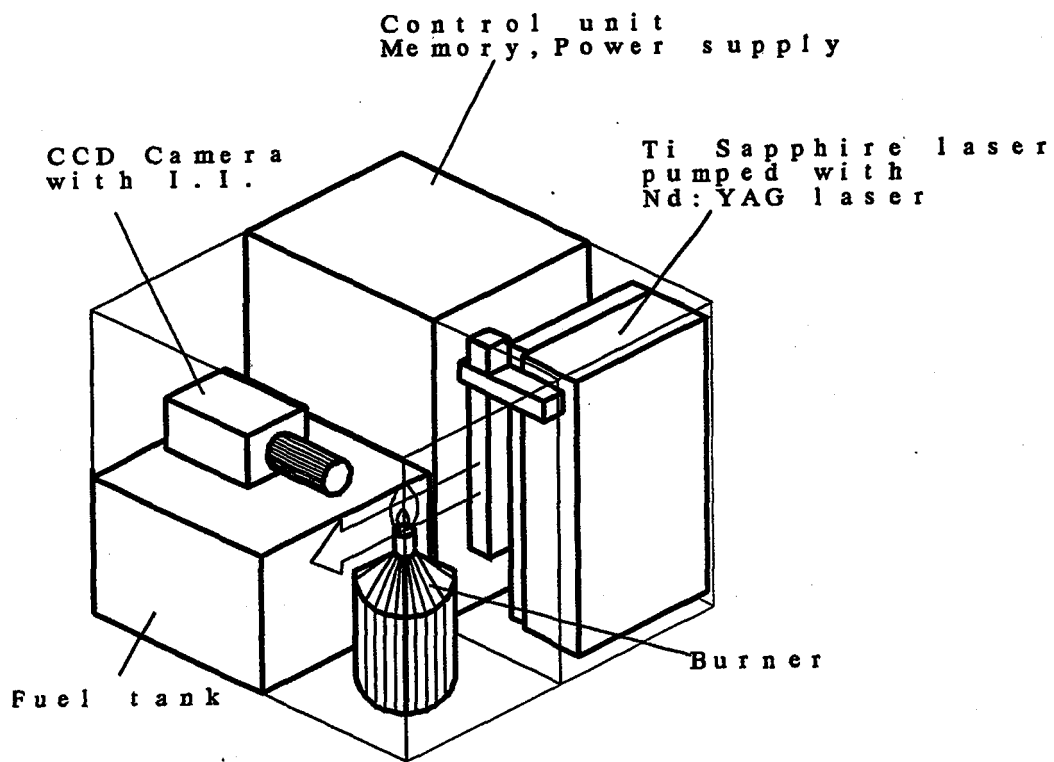


Fig.2 PLIF and PIV

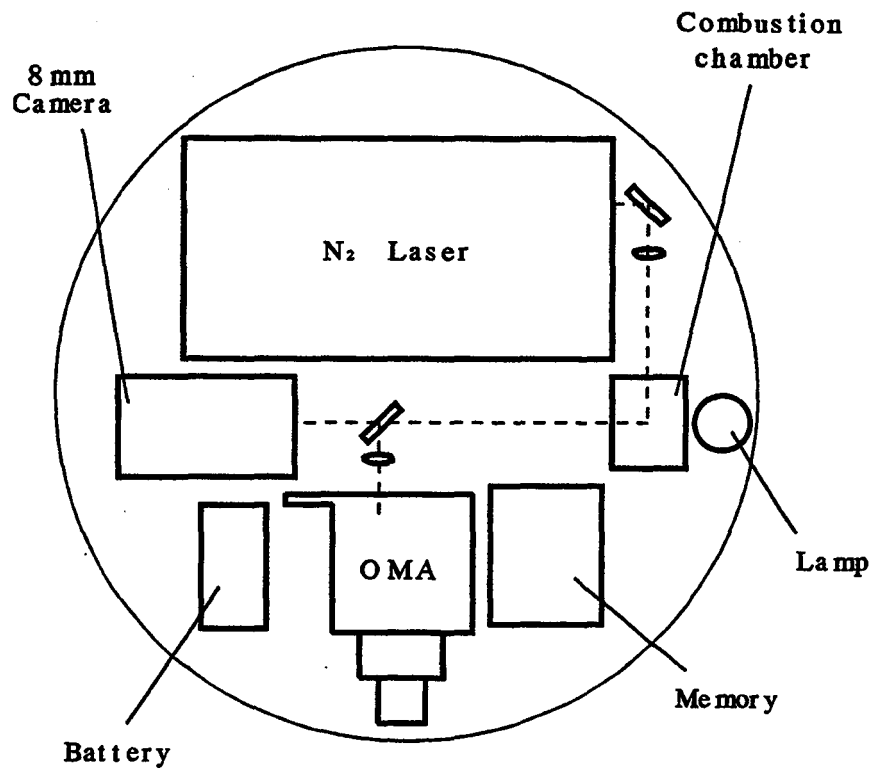


Fig.3 LIF thermometry

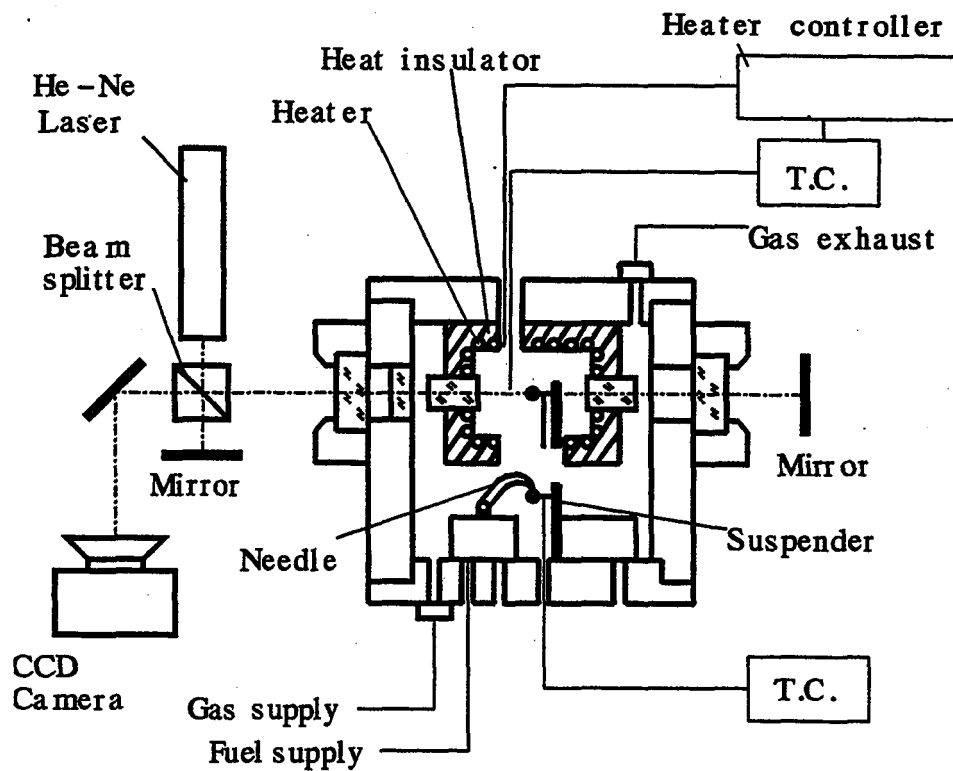


Fig.4 Michelson interferometry

AN INNOVATIVE APPROACH TO THE DEVELOPMENT OF A PORTABLE UNIT FOR ANALYTICAL FLAME CHARACTERIZATION IN A MICROGRAVITY ENVIRONMENT

Mark A. Dubinskiy, Mohammed M. Kamal, and Prabhakar Misra*

Laser Spectroscopy Laboratory
Department of Physics and Astronomy
Howard University
Washington, D.C. 20059

Introduction

The availability of manned laboratory facilities in space offers wonderful opportunities and challenges in microgravity combustion science and technology. In turn, the fundamentals of microgravity combustion science can be studied via spectroscopic characterization of free radicals generated in flames.

The laser-induced fluorescence (LIF) technique is a noninvasive method of considerable utility in combustion physics and chemistry suitable for monitoring not only specific species and their kinetics (ref. 1), but it is also important for imaging of flames (ref. 2). This makes LIF one of the most important tools for microgravity combustion science. Flame characterization under microgravity conditions using LIF is expected to be more informative than other methods aimed at searching for effects like pumping phenomenon that can be modeled via ground level experiments (ref. 3). Importance of LIF for two-dimensional temperature and species measurements, and for visualization and imaging of flames in microgravity was especially emphasized at the Second International Microgravity Workshop (ref. 4). However, it was noted that the lack of reliable, portable lasers tunable in the UV, based most probably on solid-state active media, was a major constraint for conducting actual microgravity experiments.

A primary goal of our work consisted in working out an innovative approach to devising an LIF-based analytical unit suitable for in-space flame characterization. It was decided to follow two approaches in tandem:

- (i) use the existing laboratory (non-portable) equipment and determine the optimal set of parameters for flames that can be used as analytical criteria for flame characterization under microgravity conditions; and
- (ii) use state-of-the-art developments in laser technology and concentrate some effort in devising a layout for the portable analytical equipment.

This paper presents an up-to-date summary of the results of our experiments aimed at the creation of the portable device for combustion studies in a microgravity environment, which is based on a portable UV tunable solid-state laser for excitation of free radicals normally present in flames in

* Author to whom correspondence should be addressed

detectable amounts. A systematic approach has allowed us to make a convenient choice of species under investigation, as well as the proper tunable laser system, and also enabled us to carry out LIF experiments on free radicals using a solid-state laser tunable in the UV.

On the proper choice of analytical species and precursors

The hydroxyl (OH) radical is an important species for combustion studies due to many reasons. According to recognized experts in combustion science: (i) the OH radical is convenient for study in a flame environment because its spectrum is easily characterized (unlike, say NO_2) and excited (ref.5), (ii) agreement between the experimental and calculated OH profiles is excellent (ref. 6), which makes OH an appropriate analytical candidate for flame-profile characterization under microgravity conditions. Compared to other radicals born in flames, the LIF signal from OH radicals is very strong and no complications associated with their detection occur. Therefore, the requirements for the UV tunable laser output energy are not so stringent; as well as requirements for the high voltage applied to the photomultiplier tube (PMT) normally used for LIF detection are more flexible. Thus, by choosing the OH radicals as the species for microgravity combustion studies, the weight-dimension characteristics of the analytical unit (including the tunable UV laser and the PMT-detection system) can be minimized, which is extremely important for airborne measurements in flight and aboard spacecraft.

A second important issue for in-flight and/or drop tower microgravity combustion experiments is a proper choice of precursors to obtain OH radicals. Part of our efforts has been devoted to the search for molecular precursor species that would be appropriate for investigation of combustion processes in flight (space) microgravity experiments. Another goal of these experiments has been to search for appropriate laser excitation regions that would yield data sensitive to a range of experimental conditions, so that besides being suitable for visualization and imaging of flames, we can also expect it to be appropriate for the search of gravity-sensitive features in laser-induced fluorescence excitation spectra recorded during flight experiments. Based on considerations of availability, the alkane family of gases - methane (CH_4), ethane (C_2H_6) and propane (C_3H_8), in order of increasing molecular weight and complexity - were chosen for burning. One expects a measure of commonality in free radical formation from the above gases due to their chemical similarity. This expectation was confirmed for air flames, when we studied laser-induced fluorescence excitation spectra for three alkane gases, recorded using a monochromator (employed at this stage as a variable narrowband UV filter) set at different wavelengths in a wide region of fluorescence from free radicals produced under air-combustion conditions. Fluorescence was detected using a R-1477 type PMT attached to the exit slit of a low-resolution ($f=100$ mm; $F/3.5$ aperture) H-10 type monochromator. The choice of this particular type of PMT was determined by its reduced sensitivity to the direct light from an open flame in the spectral region of registration (chosen to be 320 - 500 nm for OH radicals under consideration). The subject of study was the flame from a regular burner (without any premixing of gases) placed just in front of an entrance slit of the monochromator. No optics were used to image the flame on the entrance slit of the monochromator. Experimental set-up for these measurements is sketched in Fig. 1. Excitation of the OH radicals born in the combustion process was accomplished by a slight focusing of the tunable UV laser radiation (output radiation spectral bandwidth of 0.07 nm) in the 305-311 nm wavelength region within the flame. The excitation region corresponded to the $\text{A } ^2\Sigma^+ - \text{X } ^2\Pi (0,0)$ OH-absorption band. Tunable radiation in this part of our work was obtained in a traditional manner, using a tunable dye laser in the visible region of the spectrum, with subsequent frequency-doubling (described elsewhere, e.g., ref. 2, 5, 6). The lifetime of observed fluorescence was short and could not be measured very precisely within the time response limitations of our detector system used for these preliminary experiments.

The preliminary conclusions drawn from the series of experiments performed are as follows:

- For the three alkane gas-air flames, LIF excitation spectra recorded at the same registration wavelength are very similar. Since, analytically there appears to be no preference, the choice of

an appropriate species for burning may very well be made taking into account flame stability, price of starting materials and weight-dimension considerations relevant to a flight experiment. According to our data, the ethane-air combustion provides an example of the so-called fluctuation flame even under ambient conditions, which makes it inappropriate for studying important microgravity combustion features such as the pumping phenomenon (ref. 3). On the other hand, if we compare methane and propane, their flames are equally stable. At this point, propane seems to be the most appropriate, because it is available in a condensed state at room temperature and at relatively low pressure, and will occupy less space aboard an aircraft.

- LIF spectra of alkane-air flames excited in the region of the $A^2\Sigma^+ - X^2\Pi(0,0)$ OH-absorption band are sensitive to changes in experimental conditions (i.e., spectra are temperature-sensitive and positionally-sensitive in the flames). Also noticeable is their sensitivity to a particular wavelength of registration. As an example (because the results obtained with other studied alkane-air flames are qualitatively the same), Fig.2 shows LIF excitation spectra of a propane-air flame recorded at a registration wavelength of 330 nm (a) and 324 nm (b), respectively. The registration spectral bandwidth was $\text{FWHM} = 4$ nm. A comparison of Fig.2 (a) and (b) indicates a drastic change in the appearance of the excitation spectra with a change in registration wavelength by only 6 nm; and to the left and to the right of the spectral point around 327 nm there is no qualitative change in the spectra over a range of 60 nm. The reasons for such behavior are still under consideration, but it is quite clear that such anomalous alkane-air flame features may be useful for studies under microgravity conditions.

Analytical Application of the $\text{LiCaAlF}_6:\text{Ce}^{3+}$ Laser for Combustion Studies

As mentioned above, the main problem that one faces trying to devise a portable unit for flame characterization via UV laser induced fluorescence (LIF) analysis in space is that conventional (commercially available) UV tunable lasers are extremely cumbersome and energy-consuming devices that are not suitable for in-flight experiments. Indeed, such lasers, in addition to a pumping source (usually a YAG:Nd laser with an attached nonlinear frequency-doubler) need a tunable dye laser in the orange-red region of the spectrum and should be provided with a dye circulation system, as well as a system for frequency-doubling of the dye laser radiation with a servo-tuning system to follow the wavelength changes ("Autotracker") and also a system for separation of the visible and UV beams emanating from it ("Frequency Separator" in Fig. 1). Proceeding from state-of-the-art developments in quantum electronics, a reasonable way to overcome the problem is to use an all-solid-state tunable UV laser that employs direct pumping of the UV-active medium by UV harmonics from a YAG:Nd laser, and with no frequency transformation after the tunability stage (ref. 7). This emerging laser technology, which is only two years old, may allow the overcoming of drawbacks characteristic of traditional tunable UV laser systems. Promising results in this field have been demonstrated on the $\text{LiCaAlF}_6:\text{Ce}^{3+}$ (LiCAF:Ce) laser developed recently by M.Dubinskiy and co-workers (ref. 7-9) and the $\text{LiSrAlF}_6:\text{Ce}^{3+}$ (LiSAF:Ce) laser developed at the Naval Research Laboratory (ref. 10) and the Lawrence Livermore National Laboratory (ref. 11). To demonstrate the feasibility of our approach we have carried out preliminary experiments and succeeded in obtaining first positive results studying LIF of free radicals under the LiCAF:Ce UV tunable laser excitation at Howard University's Laser Spectroscopy Laboratory. Our considerations relevant to the choice of the source, a discussion of its advantages for applications such as flame characterization in space, and the results themselves, are summarized below.

Well-studied free radicals (that are also well-described theoretically and are therefore good combustion model subjects) are hydroxyl (OH) (ref. 12) and methoxy (CH_3O) (ref. 13, 14), which have analytically convenient excitation bands located in the 280 - 298 nm spectral region. Analytical equipment for routine LIF experiments with these radicals comprises usually an excimer laser delivering over 0.1 J of energy for photolyzing the precursor and a tunable ultraviolet laser consisting of a dye laser and a doubling stage for excitation of the fluorescence from the free radicals (ref. 15). As was emphasized above, it is hardly possible to use such equipment in space

because it is extremely cumbersome and energy-consuming. To the best of our knowledge, there have been no attempts to devise a portable all-solid-state unit suitable for spectroscopic measurements on free radicals in space. Such a development could promote significantly microgravity combustion science and applications.

The key-factor governing the design of a portable tunable UV laser for LIF excitation is a proper choice of "pumping source - active medium" combination so as to (i) avoid complications and energy consumption relating to the dye solution circulation and photochemical instability, (ii) to use the same efficient laser source for photolyzing the reaction species and for pumping the active medium, and (iii) to provide as high as possible "wall-plug" conversion efficiency for the device as a whole. Given the number of state-of-the art possibilities, we chose to use the newly discovered solid-state tunable UV laser based on the $\text{LiCaAlF}_6:\text{Ce}^{3+}$ (LiCAF:Ce) single crystal pumped by the quadrupled output of a Q-switched YAG:Nd laser (ref. 7-9). Our choice is based on the following considerations:

- (i) - LiCAF:Ce laser is extremely efficient (most recent data - up to 30% slope efficiency (ref. 11) and photochemically stable (ref. 7,8,11) ;
- (ii) - its available tunability (281 - 297 nm)(ref. 7,10) covers the region of excitation of OH and CH_3O free radicals ;
- (iii) - 266-nm pumping radiation is efficient enough for photolyzing the precursor species, if necessary (ref. 16);
- (iv) - LiCAF:Ce laser is the first known all-solid-state UV tunable device with direct pumping so that the portable unit devised will be compact.

For our first experiments we chose the methoxy radical, because its LIF is not so easy to observe, and thus observation of LIF using an all-solid-state tunable laser would be better proof of feasibility of approach, than say observation of OH fluorescence.

Fig. 3 represents the experimental arrangement for recording the excitation spectra of free radicals in the 291.5 - 296.5 nm spectral region based on the LiCAF:Ce tunable laser pumped by the fourth harmonic of the Q-switched Nd-YAG laser. The 266 nm output (about 10 mJ) was split into two beams of equal intensity, one of which was used for photolyzing the precursor and the other was used to pump the laser crystal. Pulse repetition rate of the computer-controlled device was 10 Hz; the LiCAF:Ce tunable laser output had a spectral bandwidth of 0.15 cm^{-1} , and the speed of spectral scanning was 0.5 nm/min. Tunability of the LiCAF:Ce laser was provided by a step-motor-driven Littrow-mounted diffraction grating. An optical scheme with counterpropagating photolyzing and excitation beams focused by fused silica lenses into the reaction vacuum chamber was employed. Fig. 4 represents a typical excitation spectrum of the methoxy (CH_3O) radical in the spectral region 291.5 - 296.5 nm obtained using the above-cited arrangement with CH_3ONO precursor and a time delay of 8 μs between the photolysis and probe pulses.

Thus, the laboratory experiment shows that the idea of using the LiCAF:Ce laser as an excitation source, in conjunction with a 266 nm pumping laser as a means for photolysis of the precursor species, provides a reliable solution for routine analytical investigations of combustion processes in space under microgravity conditions.

Acknowledgment

Financial support from the NASA Lewis Research Center (Grant #NAG3-1677) is gratefully acknowledged.

References

1. Crosley, D., "Collisional effects on laser-induced fluorescence flame measurements," *Optical Engineering* **20**, August 1981, pp. 511-521.
2. Allen, M., Hanson, R., "Planar laser-induced-fluorescence monitoring of OH in spray flames," *Optical Engineering* **25**, December 1986, pp. 1309-1311.

3. Durox, D., Bailott, F., Scoufflaire, P., Prud'homme, R., "Some effects of gravity on the behaviour of premixed flames," *Combustion and Flame* **82**, August 1990, pp. 66-74.
4. Weiland, K., "Visualization and imaging methods for flames in microgravity," *Proceedings of the Second International Microgravity Combustion Workshop*, Sept. 1992, pp. 135-140.
5. Smith, G., Dyer, M., Crosley, D. "Pulsed laser optoacoustic detection of flame species," *Applied Optics* **22**, December 1983, pp. 3995-4003.
6. Fleming, J., Burton, K., Ladouceur, H. "OH and CH profiles in a 10 Torr methane/oxygen flame: experiment and flame modeling." *Chemical Physics Letters* **175**, December 1990, pp. 395-400.
7. Dubinskii, M., Semashko, V., Naumov, A., Abdulsabirov, R., Korableva, S., "Ce³⁺-Doped Colquiriite - a New Concept of All-Solid-State Tunable Ultraviolet Laser," *J. Mod. Opt.* **40**, January 1993, pp.1-5 .
8. Dubinskii, M., Semashko, V., Naumov, A., Abdulsabirov, R., Korableva, S., "Spectroscopy of a New Active Medium of a Solid-State UV Laser with Broadband Single-Pass Gain," *Laser Physics* **3**, January 1993, pp. 216-217.
9. Dubinskii, M., Semashko, V., Naumov, A., Abdulsabirov, R., Korableva, S., "Active Medium for All-Solid-State Tunable UV Laser," *OSA Proc. on Adv. Solid-State Las.*, A.Pinto and T.Fan, eds. (Opt. Soc. of Amer., Wash. DC, October 1993), v.15, pp. 195-198.
10. Pinto, J. , Rosenblatt, G., Esterowitz, L., Castillo, V., Quarles, G., "Tunable Solid-State Laser Action in Ce³⁺:LiSrAlF₆," *Electron. Lett.* **30**, February 1994, pp. 240-241.
11. Marshall, C., Payne, S., Speth, J., Krupke, W., Quarles, G., Castillo, V., Chai, B., In: 1994 OSA Proceedings on Advanced Solid-State Lasers, (Optical Society of America, Washington, D.C., 1994), vol. **20**, pp. 389-394.
12. Misra, P., Zhu, X., Nur, A., "Laser Induced Fluorescence Spectroscopy of the Hydroxyl Radical," *Spectr. Lett.* **25** (4), 547 - 557 (1992).
13. Misra, P., Zhu, X., Hsueh, C.-Y., Halpern, J., "Laser Excitation and Emission Spectroscopy of the Methoxy Radical in a Supersonic Jet," *Chem. Phys.* **178**, 377-385 (1993).
14. Williams, B., Fleming, J., "LIF Detection of Methoxy in CH₄/O₂/NO₂N₂ Flames," *Chem. Phys. Lett.* **221**, April 1994, pp. 27-32.
15. Misra, P., Zhu, X., Nur, A., "Rotationally-Resolved Excitation Spectroscopy of the Methoxy Radical in a Supersonic Jet," *Spectr. Lett.* **25** (5), 639-649 (1992).
16. Nur, A., "Laser Induced Fluorescence Spectroscopy of the Hydroxyl and Methoxy Radicals," M.S.Thesis, Howard University, Washington, D.C., 1991.

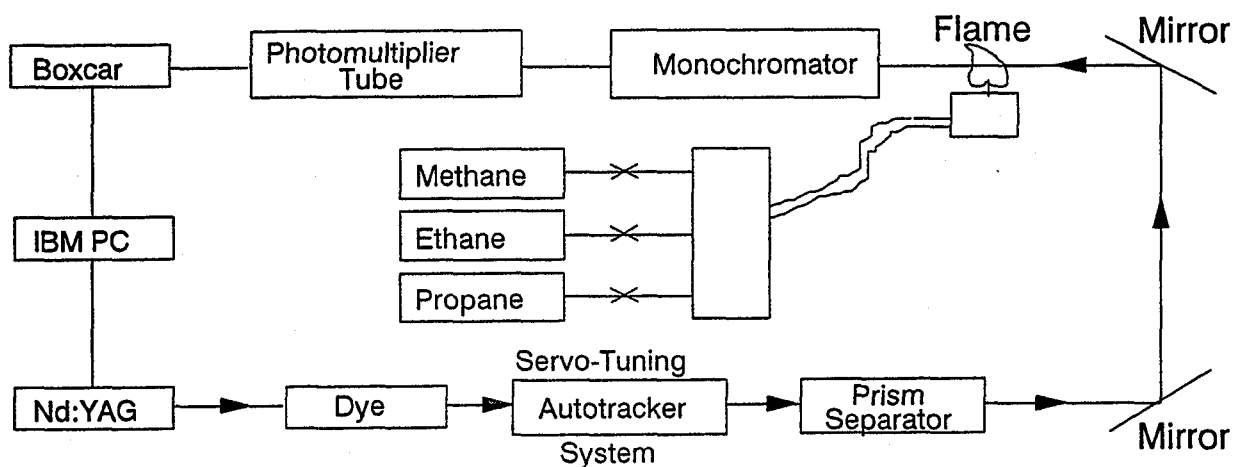


Figure 1: Experimental arrangement for recording laser excitation spectra of free radicals in alkane-air diffusion flames.

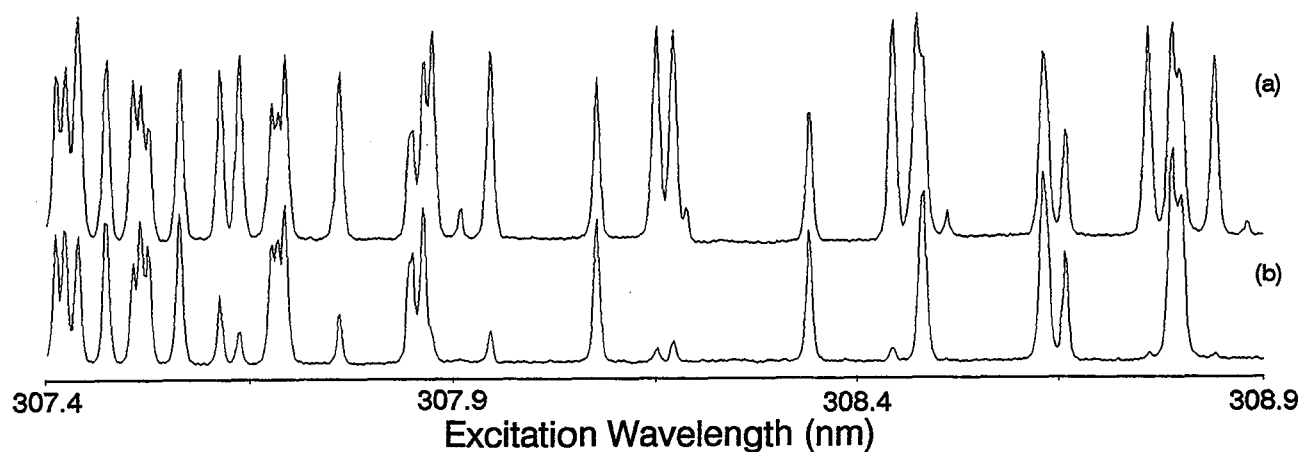


Figure 2: LIF excitation spectra of propane-air flame: (a) Registration wavelength 324 nm; (b) Registration wavelength 330 nm.

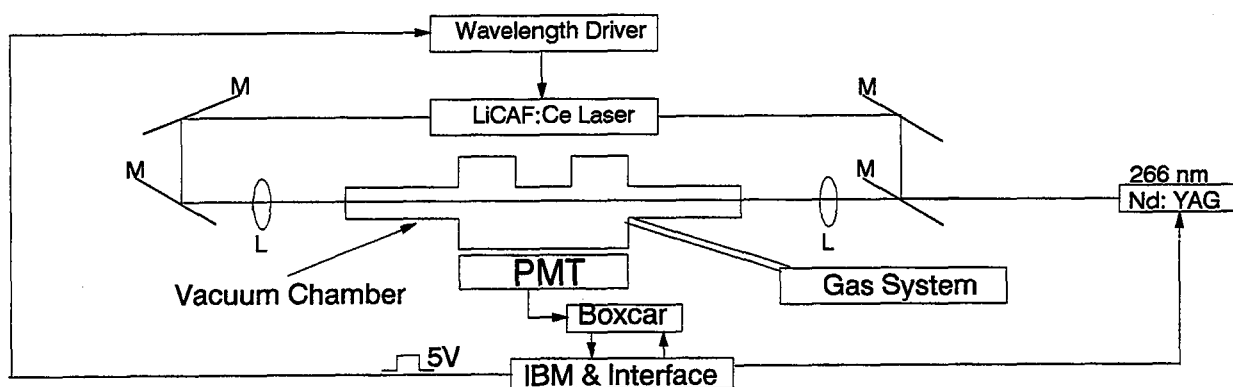


Figure 3: Experimental set-up for recording the UV excitation spectra of free radicals using a tunable all-solid-state LiCAF:Ce laser.

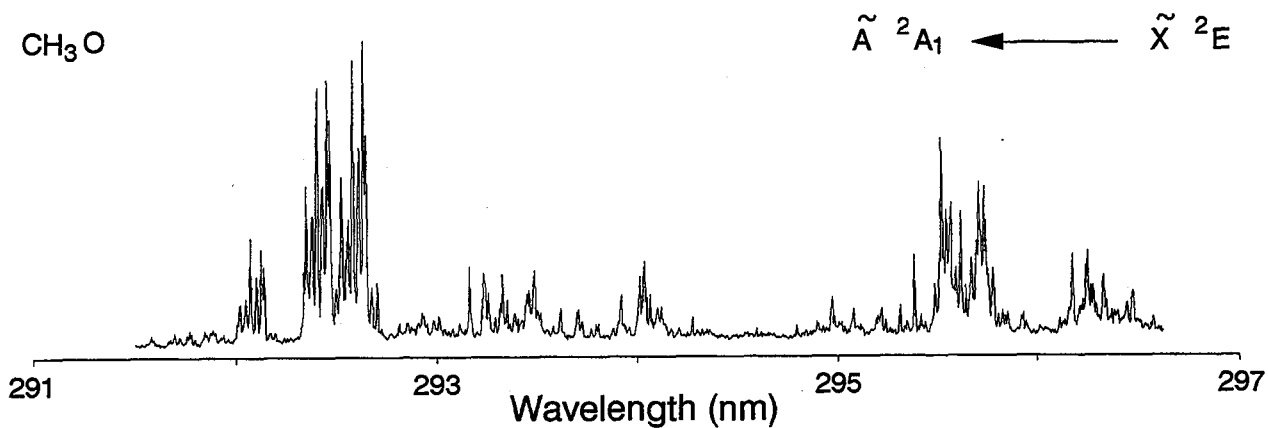


Figure 4: Laser excitation spectrum of the methoxy (CH_3O) free radical.

DEVELOPMENT OF ADVANCED DIAGNOSTICS FOR CHARACTERIZATION OF BURNING DROPLETS IN MICROGRAVITY

Subramanian V. Sankar, Dale H. Buermann, and William D. Bachalo
Aerometrics, Inc.
Sunnyvale, California

1. Introduction

Diagnostic techniques currently used for microgravity research are generally not as advanced as those used in earth-based gravity experiments. For example, most microgravity tests involving single burning droplets make use of imaging techniques for determining the droplet size, and hence, the droplet vaporization/burning rate. The measurement resolution of these cameras are generally not very good (order of 100 microns), and since typical TV cameras have a frame rate of only 30 fps, the amount of data that can be collected during the short period of low-gravity achievable in drop tests and flight tests is small. Furthermore, diagnostic techniques for measuring the instantaneous radial temperature profile (or temperature gradients) within the burning droplet do not exist.

Over the past few years, Aerometrics has been researching and developing a *rainbow thermometric* technique for measuring the droplet temperatures of burning droplets. This technique has recently been integrated with the *phase Doppler interferometric* technique to yield a diagnostic instrument that can be used to simultaneously measure the size, velocity, and temperature of burning droplets in complex spray flames [1]. Also, the rainbow thermometric technique has been recently integrated with a *point-diffraction interferometric* technique for measuring the instantaneous gas phase temperature field surrounding a burning droplet [2]. These research programs, apart from being very successful, have also helped us identify other innovative techniques for the characterization of burning droplets. For example, new techniques have been identified for measuring the instantaneous regression rate of burning droplets. Also, there is the possibility of extracting the instantaneous radial temperature distribution or the temperature gradients within a droplet during transient heating.

What is important is that these diagnostic techniques have the potential for making use of inexpensive, light-weight, and rugged devices such as diode lasers and linear CCD arrays. As a result, they can be easily packaged for incorporation into microgravity drop-test and flight-test facilities. Furthermore, with the use of linear CCD arrays, data rates as high as 10-100 kHz can be easily achieved. This data rate is orders of magnitude higher than what is currently achievable.

2. Program Objectives

In this research and development program, a compact and rugged diagnostic system will be developed that can be used to measure instantaneous fuel droplet diameter, droplet regression rate, and the droplet internal temperature profiles or gradients at very high data rates in microgravity experiments. This is a one year R&D program that commenced toward the end of August 1994. The principle behind the measurement of each of these parameters is briefly described in the following sub-sections.

Rainbow Thermometry

The occurrence of rainbows can be understood with the help of the simple geometrical optics based theory proposed by Descartes several hundred years ago. Using geometrical optics assumptions, the scattering of light by spherical

particles can be described as a combination of diffraction, external reflection, refraction, and refraction occurring after multiple internal reflections. Furthermore, adopting van de Hulst's notation [3, $p=0$ refers to externally reflected light, $p=1$ refers to refracted rays, $p=2$ refers to rays that emerge from the droplet after undergoing one internal reflection, and so on. For each order scattered ray, the scattering angle bears a definite relationship to the incident angle. The location of the primary rainbow can then be understood to correspond to that scattering angle at which the angular relationship for $p=2$ goes through an extremum. At the rainbow angle, the scattered intensity achieves a local maximum. To one side of the rainbow angle is a shadow region into which no rays emerge and to the other side is a lit region. Similarly, the secondary rainbow corresponds to the scattering angle extremum for $p=3$ rays. For example, for water droplets, the primary and the secondary rainbows occur at scattering angles of 137.9° and 128.8° , respectively. The dark region between the primary and the secondary rainbow is historically known as Alexander's dark band. Rainbows of order greater than $p=3$ can also be present, but in general, are very weak in intensity.

Several characteristics of the rainbow cannot be adequately explained with the geometrical optics based theory, for example, the presence of supernumerary arcs on the lighted side of the primary and secondary rainbows. They occur as a result of interference between two different rays of the same order emerging in the same direction. Thus, at any given angle slightly greater than the rainbow angle, the scattered light includes rays that have followed two different paths through the droplet. To further complicate the situation, the interference of the internally reflected rays with externally reflected ($p=0$) rays gives rise to high frequency intensity oscillations that are superimposed upon the supernumerary fringes. Over the years, several theories have been developed to explain such rainbow characteristics. These theories include Airy's theory [4], the Lorenz-Mie theory [3], the complex angular momentum theory [5,6] which provides an approximation to the Lorenz-Mie theory, and a theory based on Huygen's principle [7]. Of these, only the Lorenz-Mie theory provides an exact solution for the scattering of electromagnetic waves by a spherical particle.

Rainbow thermometry takes advantage of the fact that the rainbow angle is a function of the refractive index of the droplet. Therefore, by measuring the rainbow location with the help of a linear array detector such as a CCD, the refractive index of the droplet can be determined. Since refractive index varies with temperature, the droplet temperature can also be inferred if the relationship between the refractive index and temperature is known *a priori*. A typical measured (using a linear CCD array) dependence of the rainbow location on the droplet refractive index is presented in Fig.1.

In describing the principles of rainbow thermometry we have so far assumed that the droplet is homogeneous. However, during the transient heating period, the droplet is inhomogeneous and exhibits a radial temperature distribution. Theoretical light scattering studies [8] have shown that during the transient droplet heating period, the rainbow position actually moves in a direction opposite to the expected direction of motion. This could lead to erroneous measurements. The measured variation of the rainbow location during the transient heating period of a burning *n*-heptane droplet is presented in Fig.2. Recent experimental and theoretical studies in this area also suggest that the rainbow angle is a direct measure for the refractive index gradients (temperature gradients) near the surface, as long as the gradients are practically linear in the outer region of the droplet [9]. In the current research and development program we are attempting to use the fully digitized time dependent rainbow signature, in conjunction with theoretical light scattering models for inhomogeneous droplets, for reconstructing the temporal evolution of the droplet internal temperature profile or gradient.

Drop Size Measurement

The spatial frequency of the supernumerary fringes that can be observed in the rainbow signature is a function of the droplet diameter. Therefore, in this research program the droplet size information will also be obtained from the time dependent rainbow signature.

Droplet Regression Rate Measurement

As mentioned earlier, the interference of internally reflected rays with external reflections gives rise to high frequency oscillations that are superimposed upon the supernumerary fringes. These high frequency oscillations are extremely sensitive to small changes in the droplet diameter. A typical example of resonance scattering by spherical

particles is presented in Fig.3. The dotted line in Fig.3 was computed using the Lorenz-Mie theory for droplet diameters between 60.0 to 61.0 μm and having a refractive index of 1.354. The computed scattered intensities correspond to a point detector placed at a scattering angle of 142.5°. The solid line in Fig.3 is the result of applying a FFT-based digital filter to the raw signal. The presence of a dominant resonant frequency is obvious in the presented result. In this research program, the measured rainbow signature will also be used to observe the time dependent variation of the high frequency oscillations which will subsequently be used to extract the instantaneous droplet regression rates.

3. Progress to Date

Optical System Development

The development of a breadboard/prototype optical system has been completed. A photograph of the developed optical system is shown in Fig.4. The optical transmitter basically consists of a He-Ne laser beam which is focused to form a measurement probe volume using an appropriate lens. The optical receiver is placed in the backscatter direction at a scattering angle of approximately 145° depending upon the refractive index of the fuel that is being studied, Fig.5. A schematic of the rainbow receiver system is presented in Fig.6. It consists of a front lens for collecting and collimating the scattered light in the backscatter direction and a second lens for focusing the collimated light on to a slit which acts a spatial filter. A third lens is placed behind the slit to image the collected light on to a linear CCD array camera. The other important components of the rainbow receiver include two photomultipliers. PMT#1 is used in conjunction with an automatic exposure control circuitry for the CCD, and PMT#2 is used along with an independent gating circuitry.

Electronics/Opto-electronics System Development

The major components of the electronics/opto-electronics system are presented in Fig.7. It includes an imaging board for housing the CCD array, a gate controlling system, and a data acquisition/signal processing module for the rainbow signal. Prototype, printed circuit boards have been developed and tested for this purpose. The imaging board is located in the rainbow optical receiver and houses a 2048 pixel linear CCD array. As per the manufacturer specification, the maximum clock rate is 60 MHz. However, for the current research program a clock rate of 20 MHz is being used. This yields an effective data rate of approximately 10,000 per second. To increase the dynamic range of the rainbow system, an automatic exposure control circuitry has also been built into the gate control electronics. The automatic exposure control system integrates the output of PMT#1 and compares the integrated value to an adjustable exposure level for determining the optimal CCD exposure time for each droplet. This not only helps in preventing CCD saturation but also ensures uniform output signal levels for droplets of different size.

The CCD output is then sampled and digitized by a dedicated rainbow signal processor, Fig.7. As discussed earlier, the rainbow signals contain high frequency components which would be undesirable if the rainbow peaks are to be determined directly. However, these may be minimized by using a suitable digital filter. The rainbow signal processor has a digital peak detector which can accept either the ADC output or the digital filter output. The rainbow peak location and intensity of the rainbow are available for transfer to the data acquisition computer for further analysis and post processing. The rainbow signal processor also provides a digital output of each CCD pixel. The digital output can be interfaced to a frame grabber so that large amounts of rainbow signals can be fully digitized and saved for further post-processing.

Droplet Temperature Measurement

The performance of the developed optical/electronic system has been tested by using it to measure the temperature of heated kerosene droplets. For these experiments, a drop-on-demand generator was modified such that fuel droplets could be generated at elevated temperatures. The liquid (within the drop-on-demand cavity) was raised from room temperature (24 °C) to about 100 °C in increments of about 5 °C. The measurements were performed at approximately 3 cm below the drop-on-demand nozzle. The CCD pixel number corresponding to the measured rainbow peak is presented in Fig.8 as a function of the cavity temperature. The data presented in Fig.8 shows a measurement uncertainty of $\pm 5^\circ\text{C}$. This uncertainty results from the high frequency oscillations that ride on the

rainbow signal. By digitizing the complete rainbow signal and filtering out the high frequency oscillations, the measurement accuracy can be significantly improved.

Drop Size Measurement

The developed system has also been used to demonstrate the feasibility of measuring the droplet size from the supernumerary fringe pattern. A drop-on-demand generator was used to create water droplets of unknown size but in the range of about 150 - 200 μm . The digitized rainbow signal for this case is shown in Fig.9. The presence of low frequency and high frequency oscillations can be clearly observed in this figure. The effect of applying a low pass FFT filter to this signal is shown in Fig.10. The high frequency oscillations have been completely eliminated. The measured data is compared to a theoretically computed, low pass filtered, rainbow signal for a 185 μm water droplet. The agreement between the measurements and theoretical predictions is excellent suggesting that the diameter of the experimentally generated droplet is 185 μm .

Sensitive Measurement of the Change in Drop Size

Preliminary measurements have also been conducted to examine and demonstrate the feasibility of using morphology dependent resonances as a sensitive means for measuring small changes in the drop size. For the droplet combustion studies, this information can be used to measure the instantaneous droplet regression rates, and hence, the droplet vaporization rates. During the course of this program it was observed that the voltage applied to the drop-on-demand generator could be varied to cause small changes in the droplet diameter. Therefore, in this study, the voltages were slowly varied to examine whether it would produce a measurable change in the high frequency pattern. A high pass FFT filter was applied to the rainbow signal to extract the high frequency oscillations from the measured data, see Fig.11. In Fig.12, the extracted high frequency oscillations for two slightly different voltage settings are compared. In order to visually detect any differences in the pattern, we have zoomed in to a region in the neighborhood of the main rainbow. The data presented in Fig.12 shows that the two wave patterns are approximately 90° out of phase. Using the Lorenz-Mie theory calculations, it was determined that this phase shift corresponds to a change in droplet diameter of approximately 0.05 μm . This clearly shows that the high frequency waveform can be used as a sensitive means of measuring the droplet regression rates in droplet combustion experiments. On the other hand, Fig.13 compares the low frequency oscillations for the same two voltage settings. The two patterns are identical which suggests that the low frequency oscillations cannot be used to measure small changes in the droplet diameter.

Theoretical Modeling

One of the planned tasks for this program involves enhancing the currently available Lorenz-Mie theory to account for light scattering by radially inhomogeneous particles using the algorithm developed by Wait [10]. As a first step toward this end, we have developed a model to describe the light scattering by a two layered spherical particle. The model makes use of the algorithm developed by Toon and Ackermann [12]. This model has been used to determine regions of the droplet that actually contribute to the rainbow signature. Our simulations suggest that the inner 50% of the droplet radius does not contribute to the rainbow signature. It is only the rays that pass through the top 50% (from the surface) that influence the rainbow. To demonstrate this, the theoretically simulated rainbow signal for 100 μm homogeneous water droplet has been compared with that of a 100 μm stratified droplet (inner 50% has a refractive index of 1.40 and the outer 50% has a refractive index of 1.33). The rainbow signatures computed for the two cases are identical as shown in Fig.14. These results are also important because in flight testing the fuel droplet is suspended by a tether which includes a bead of about 100 μm in diameter. It is important to know how the presence of the tether influences the measurement. The stratified sphere light scattering model can be used as a first approximation to study this effect.

4. Planned Work for the Future

As mentioned earlier, the primary objective of this program is to develop a compact and rugged diagnostic system that could be in microgravity experiments involving droplet combustion. It is anticipated that the developed diagnostic can be used to extract valuable information such as droplet size, droplet regression rate, and internal temperature profiles/gradients. With data rates as high as 10 kHz, large amounts of data can be obtained that will enable detailed studies of the transient heating characteristics of different fuels during the combustion process. Such

information is important in the development and validation of reliable theoretical drop combustion models. To achieve this objective we have planned work in several different areas during the coming months. Improved light scattering models to describe the scattering by inhomogeneous droplet and the data acquisition and post-processing software have to be developed and tested. Detailed measurements will be undertaken with various evaporating and burning droplets. Since flight testing of the developed instrument is also planned, a suitable optical system will need to be designed, developed, and tested.

Acknowledgement

This work has been supported by the NASA Lewis Research Center under Contract NAS3-27261.

References

1. Sankar, S.V., Ibrahim, K.M., Buermann, D.H., Fidrich, M.J., and Bachalo, W.D., "An integrated phase Doppler/rainbow refractometer system for simultaneous measurement of droplet size, velocity, and refractive index, *3rd Intl. Congress on Optical Particle Sizing*, Yokohama, Japan, August 23-26, 1993.
2. Sankar, S.V., Buermann, D.H., Ibrahim, K.M., and Bachalo, W.D., "Application of an Integrated Phase Doppler Interferometer/Rainbow Thermometer/Point Diffraction Interferometer for Characterizing Burning Droplets," *25th Symposium (Intl.) on Combustion*, Irvine, California, August 1994.
3. van de Hulst, "Light scattering by small particles," Dover Publications, Inc., New York 1981.
4. Airy, G.B., "On the intensity of light in the neighbourhood of a caustic," *Trans. Camb. Phil. Soc.* 6 (1838) 379.
5. Nussenzveig, H.M., "High frequency scattering by a transparent sphere. II. Theory of the rainbow and glory," *J. Math. Phys.* 10 (1969) 125-176.
6. Khare, V. and Nussenzveig, H.M., "Theory of the rainbow," *Phys. Rev. Lett.* 33 (1974) 976-980.
7. Mobbs, S.D., "Theory of the rainbow," *J. Opt. Soc. Am.* 69 (8) (1979) 1089-1092.
8. Schneider, M., Hirleman, E.D., Saleheen, H., Chowdhury, D.Q., and Hill, S.C., "Rainbows and radially-inhomogeneous droplets," *3rd Intl. Congress on Optical Particle Sizing*, Yokohama, Japan, August 23-26, 1993.
9. Anders, K., Roth, N., and Frohn, A., "Theoretical and experimental studies of the influence of internal temperature gradients on rainbow refractometry," *4th International Congress on Optical Particle Sizing*, Nurnberg, Germany, March 21-23, 1995.
10. Wait, J.R., "Electromagnetic scattering from a radially inhomogeneous sphere," *Applied Scientific Research* 10 (1963) 441-450.
11. Toon, O.B. and Ackerman, T.P., "Algorithm for the Calculation of Scattering by Stratified Spheres," *Applied Optics*, Vol. 20, pp. 3657-3660, 1981.

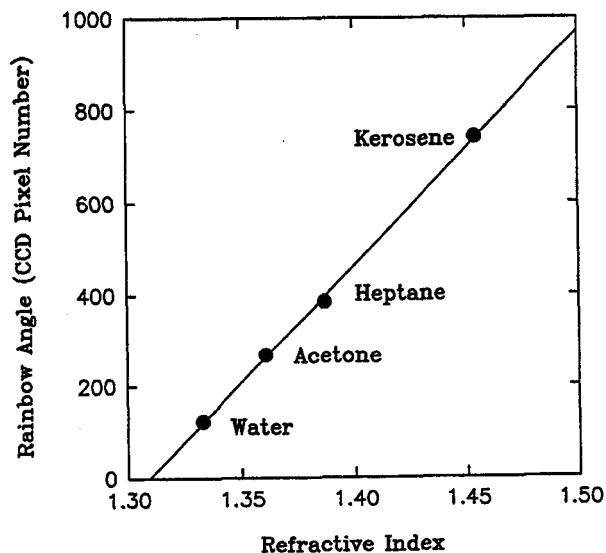


Figure 1: Calibration of the rainbow refractometer. Droplets (approximately $120\ \mu\text{m}$ in diameter) were generated using a monodisperse droplet generator. The CCD pixel number is a direct measure of the rainbow angle.

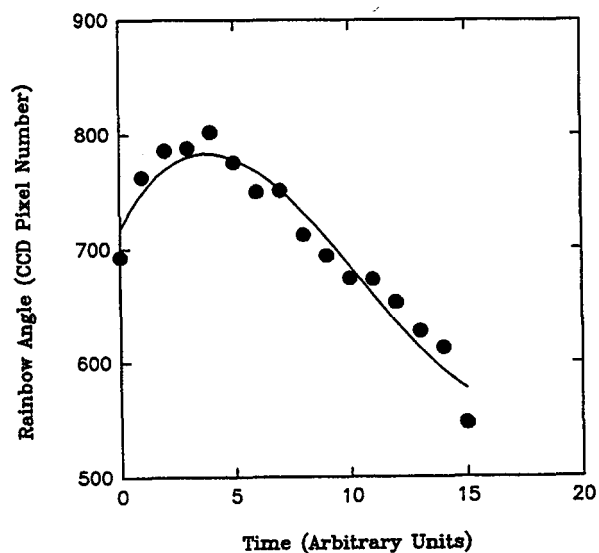


Figure 2: Measured variation of the rainbow position during the transient heating of a n-heptane droplet.

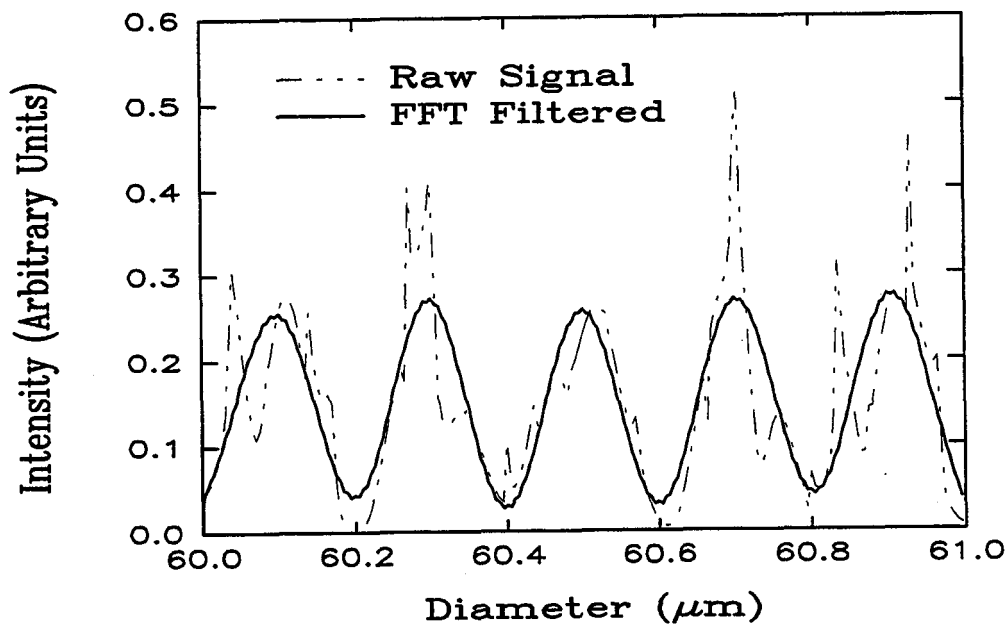


Figure 3: Computed and digitally filtered resonance structure exhibited by spherical particles ($m=1.354$) in the size range 60.0 to $61.0\ \mu\text{m}$. The measurements were performed assuming a point detector is placed at a scattering angle of 142.5° .

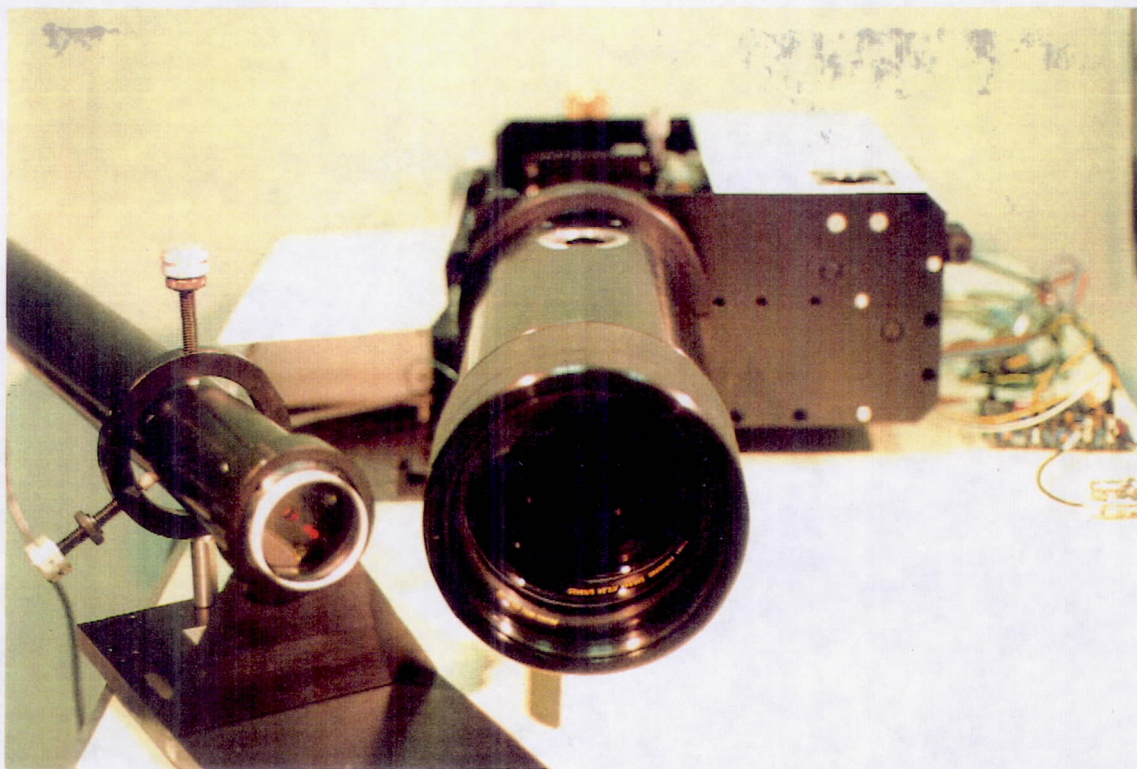


Figure 4: Photograph of the developed prototype diagnostic system.

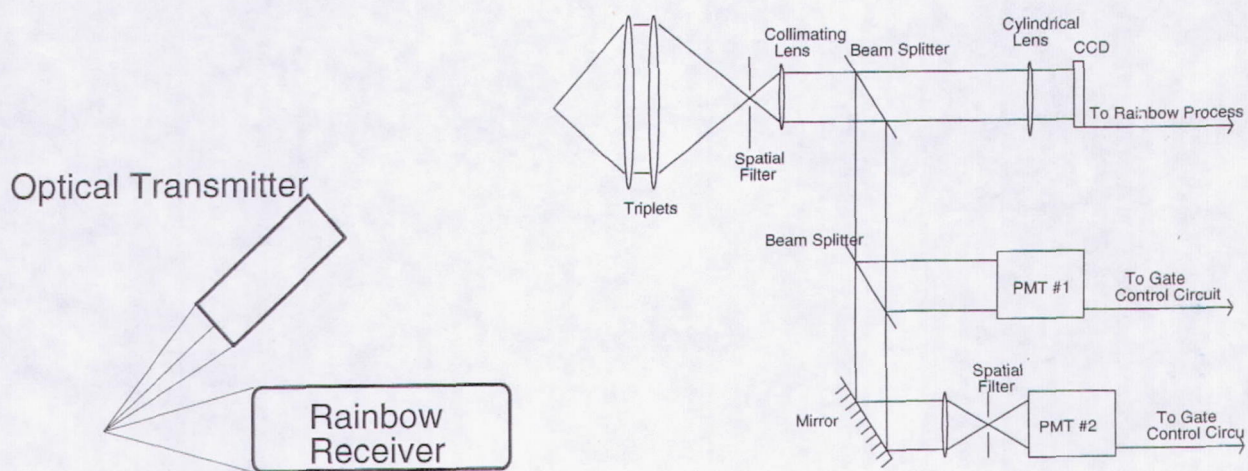


Figure 5: Schematic of the optical system layout.

Figure 6: Schematic of the rainbow receiver

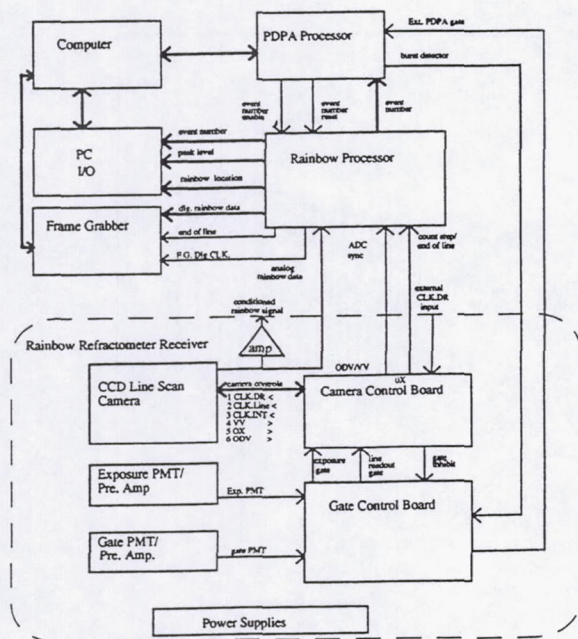


Figure 7: Schematic of the electronics/electro-optics system of the integrated diagnostics.

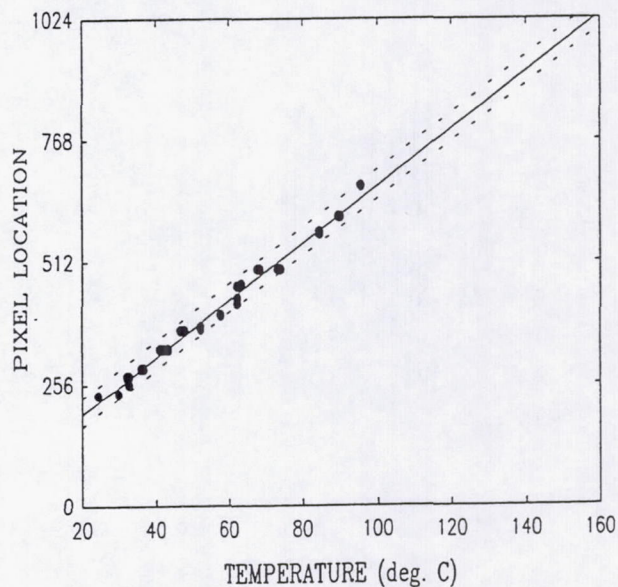


Figure 8: Variation of the measured rainbow location with temperature.

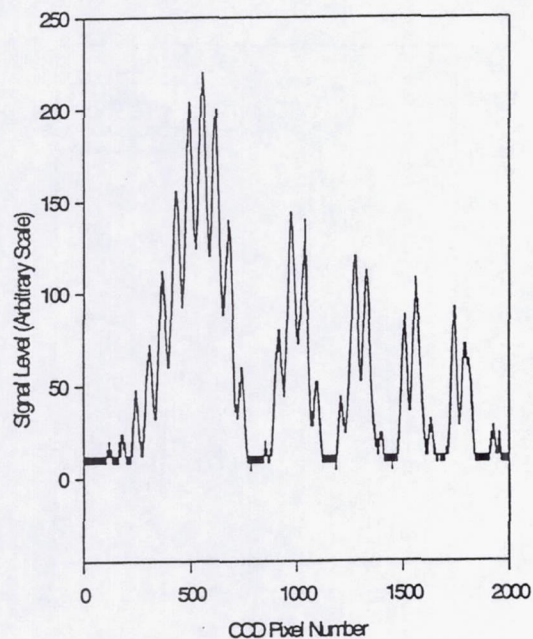


Figure 9: Measured rainbow signal for a water droplet.

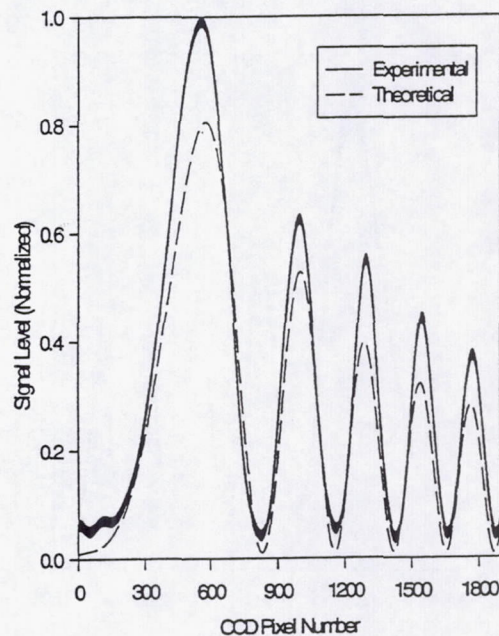


Figure 10: Comparison of experimental and theoretical rainbow signature for a 185 μm water droplet.

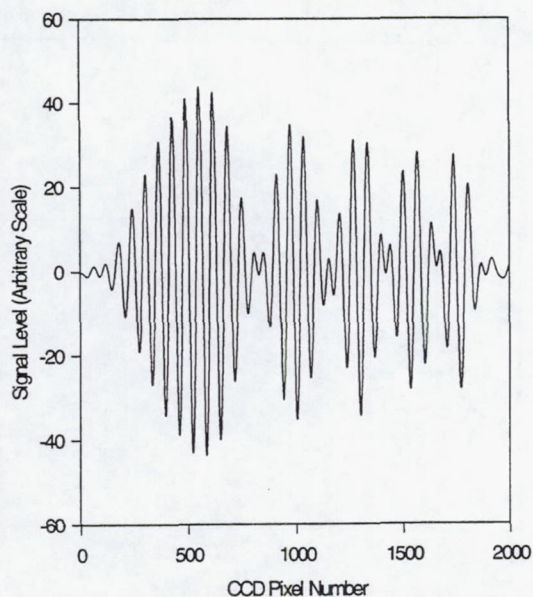


Figure 11: High pass filtered experimental rainbow signal.

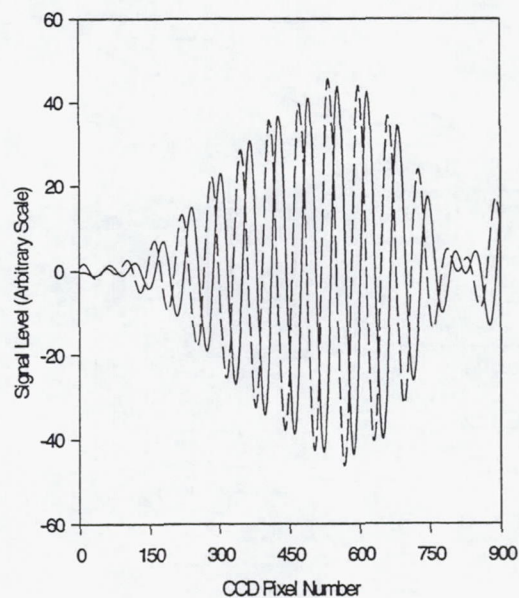


Figure 12: High pass filtered rainbow signal for two different voltage settings on the drop-on-demand generator.

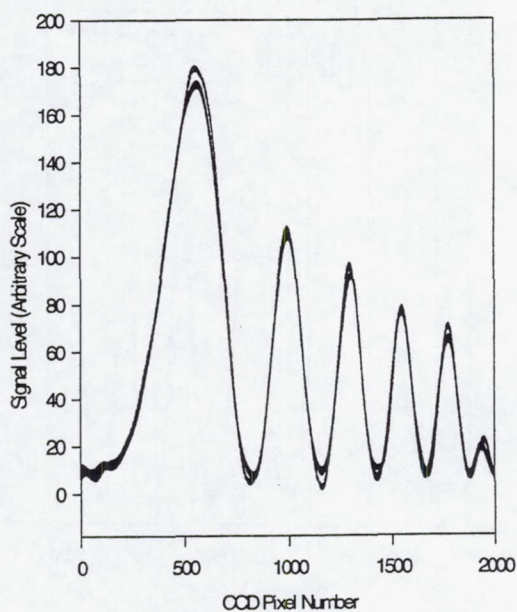


Figure 13: Low pass filtered rainbow signal for the two different voltage settings on the drop-on-demand generator.

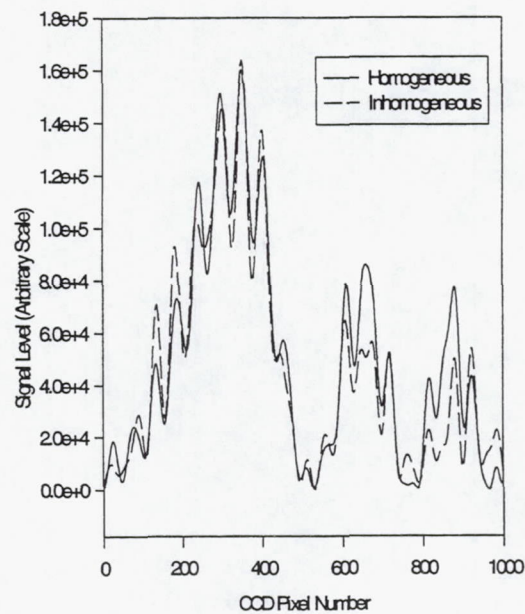


Figure 14: Computed rainbow signals for a homogeneous water droplet and for a stratified droplet for which the outer 50% shell is assumed to have a refractive index of 1.33 and the inner 50% core is assumed to have a refractive index of 1.40. The outer diameter is 100 μm in both cases.

QUANTITATIVE MEASUREMENT OF OXYGEN IN MICROGRAVITY COMBUSTION

Joel A. Silver
Southwest Sciences, Inc.
Santa Fe, New Mexico

Introduction

A low-gravity environment, in space or in ground-based facilities such as drop towers, provides a unique setting for studying combustion mechanisms. Understanding the physical phenomena controlling the ignition and spread of flames in microgravity has importance for space safety as well as for better characterization of dynamical and chemical combustion processes which are normally masked by buoyancy and other gravity-related effects. Due to restrictions associated with performing measurements in reduced gravity, diagnostic methods which have been applied to microgravity combustion studies have generally been limited to capture of flame emissions on film or video, laser Schlieren imaging and (intrusive) temperature measurements using thermocouples. Given the development of detailed theoretical models, more sophisticated diagnostic methods are needed to provide the kind of quantitative data necessary to characterize the properties of microgravity combustion processes as well as provide accurate feedback to improve the predictive capabilities of the models. When the demands of space flight are considered, the need for improved diagnostic systems which are rugged, compact, reliable, and operate at low power becomes apparent.

This research builds on our earlier work¹ and combines two innovations in an experimental system which should result in a new capability for quantitative, nonintrusive measurement of major combustion species. Using a newly available vertical cavity surface-emitting diode laser (VCSEL) and an improved spatial scanning method, we plan to measure the temporal and spatial profiles of the concentrations and temperatures of molecular oxygen in a candle flame and in a solid fuel (cellulose sheet) system. The required sensitivity for detecting oxygen is achieved by the use of high frequency wavelength modulation spectroscopy (WMS).²⁻³ Measurements will be performed in the NASA Lewis 2.2-second Drop Tower Facility.

The objective of this research is twofold. First, we want to develop a better understanding of the relative roles of diffusion and reaction of oxygen in microgravity combustion. As the primary oxidizer species, oxygen plays a major role in controlling the observed properties of flames,

Program Starting Date: 28 June 1994.

including flame front speed (in solid or liquid flames), extinguishment characteristics, flame size and flame temperature. The second objective is to develop better diagnostics based on diode laser absorption which can be of real value in microgravity combustion research. We will also demonstrate diode lasers' potential usefulness for compact, intrinsically-safe monitoring sensors aboard spacecraft. Such sensors could be used to monitor any of the major cabin gases as well as important pollutants.

Experimental Approach

A schematic of the experimental setup is shown in Fig. 1. The output of the diode laser is focussed onto an optical scanning mirror positioned at the focus of an off-axis paraboloidal (OAP) reflector. Since all light rays emanating from this point are reflected along parallel paths by the OAP, this results in a collimated laser beam (~1 mm dia.) which linearly traverses the flame region as the mirror is scanned. A second OAP refocuses the beam onto a single detector. The mirror pair is configured so that the total optical path at any transverse position is nearly constant.

This arrangement permits a temporal map of concentration and temperature of O_2 to be obtained during the microgravity experiment. In a typical run, the mirror is dithered back and forth at a rate of 20 Hz, so that the laser samples a 4 cm wide region encompassing the flame. As the mirror is moved, an absorption spectrum is recorded at 1 mm spatial resolution. The laser wavelength sweeps across two adjacent absorption lines. From these data, the temperature and concentration of O_2 can be recovered for each spatial element as a function of drop time. For the candle flame experiments, where the profiles of interest are radially distributed from the flame center, Abel inversion techniques are used to convert the measured projection spectra to radial profiles for selected heights in the flame.^{1,4}

In our prior work,¹ an eight line-of-sight fiber optic system measured water vapor mole fractions in the NASA Lewis 2.2-sec Drop Tower. The electronic modulation and detection circuitry developed in that program will be used here. The spatial scanning mechanism now used has the advantage that much higher spatial resolution is achieved with a concurrent simplification in complexity and size of the detection electronics. A single detection channel sequentially records all spatial information, which avoids problems associated with multiple detection channels (relative calibrations, drift, cost, etc.) A commercial state-of-the-art digital signal processing (DSP) data acquisition board is used to generate both the mirror dithering and laser ramp waveforms, as well as acquire, pre-process, and store all the data. This board will be controlled by a stand-alone 486 computer board. All of the electronics (including the computer) will be housed in a small enclosure which will be mounted on the drop rig.

This program utilizes a new type of diode laser. Vertical cavity surface-emitting lasers, which are now available at selected wavelengths below 1 μm , are true single-mode devices. Unlike the Fabry-Perot GaAlAs lasers typically used in this spectral region, VCSEL lasers can be scanned without mode-hopping over a relatively large wavelength range (3 nm). We have obtained custom VCSEL lasers at 760.3 nm, chosen to access a pair of O_2 rotational lines in the $b^1\Sigma-X^3\Sigma$ electronic transition.

Wavelength Modulation Spectroscopy

In traditional absorption measurements, the spectral lineshape is obtained by subtracting the signal transmitted through the absorbing medium from a reference (no absorber) spectrum. The factor limiting detection sensitivity is source noise, and limits of 10^{-3} fractional absorption are common. High frequency wavelength modulation absorption spectroscopy allows the measurement of much weaker optical absorbances by shifting the detection band to high frequencies where excess laser source noise becomes unimportant. For WMS, a small sinusoidal modulation is superimposed on the diode laser injection current. This current modulation produces a modulation of the laser wavelength. Typically, the amplitude of the current modulation is chosen so that the induced wavelength modulation is comparable to the width of the spectral feature under study. Phase-sensitive electronics are then used to detect the signal at the second harmonic of this frequency.

Diode laser intensity noise power per unit frequency has been found to decrease rapidly at higher frequencies. Therefore, improved sensitivity is attained by modulating the laser wavelength at megahertz frequencies. In this way we have achieved fractional absorption sensitivities at the near shot-noise limit ($\sim 10^{-7}$) for both near- and mid-IR diode lasers.³ For the greatest sensitivity, WMS (or lower frequency harmonic detection) has usually been implemented using a "sweep and fit" approach. The laser is modulated and scanned in wavelength across the absorption feature; the entire $2f$ WMS spectrum is recorded. By numerical fitting techniques (multilinear regression, matched filtering, etc.) the measured $2f$ lineshape is compared to a calibrated value so as to determine the absolute sample concentration.

Given the flexibility of the data acquisition system, both in-phase and quadrature components of the phase-sensitive detector output will be recorded. Thus the detection phase does not have to be preset and can be optimized during data analysis. Also, the dc photocurrent will be acquired as well. This signal is proportional to the laser intensity (I_0) and is used to account for all variations in alignment, beam attenuation, etc.

Measurement of Oxygen Mole Fraction and Temperature

The absolute absorber concentration N is related to the WMS signal by

$$\text{Signal} = C \cdot \alpha \cdot f_{WMS}, \quad \text{where} \quad \alpha = \sigma Nl, \quad (1)$$

and C is a system electronic calibration constant, f_{WMS} is a factor relating the WMS signal to the direct absorption peak value (approximately 0.6), α is the absorbance, σ the absorption cross section and l is the absorption path length. Given the system temperature and pressure, the absolute concentration is linearly proportional to the measured signal and is readily obtained.

The optimum spectral lines for use in simultaneously measuring temperature and concentration (or mole fraction) of O_2 have been determined. Our goal is to use two closely spaced, but not overlapping, lines where the composite numerical factor which is used to convert signal to mole fraction should be very sensitive to temperature for one of the lines, and insensitive for the other, over the flame temperature range of interest. In this manner we can use a single line to get mole

fraction without accurately knowing the temperature profile, or we can use the signal peak ratios to obtain temperature.⁵ We have identified four pairs of lines which exhibit these characteristics. These pairs lie in the 759 to 761 nm wavelength range. The best pair shows a temperature sensitivity of 47% ratio change per 100 K in the range 1300-1800 K. The best temperature independent line in this region has a constant conversion factor ($\pm 5\%$) between 1000 and 1650 K. Since we should be able to measure signal height ratios to better than 5%, the expected temperature accuracy (assuming we have an accurate knowledge of all spectral parameters) is ± 25 K.

Results

At this point in the program, we have tested a benchtop layout of the optics. It appears that the dither scanner can readily move a collimated beam of diameter ~ 1 mm back and forth across the required 40 mm range at 20 Hz. The laser power on the detector was flat to better than 2% during these scans (although any variations will be accounted by measurement of I_0). The DSP board has been programmed to generate both laser and scanning waveforms and can acquire the $2f$ spectra. We have received and are now characterizing the VCSEL lasers. We plan to begin preliminary benchtop candle flame measurement shortly.

References

1. J.A. Silver, D.J. Kane and P.S. Greenberg, "Quantitative Species Measurements in Microgravity Flames With Near-IR Diode Lasers, Appl. Opt. (in press, 1995).
2. J. Silver, "Frequency Modulation Spectroscopy for Trace Species Detection: Theory and Comparison Among Experimental Methods," Appl. Opt. **31**, 707-717 (1992).
3. D.S. Bomse, A.C. Stanton and J.A. Silver, "Frequency Modulation and Wavelength Modulation Spectroscopies: Comparison of Experimental Methods Using a Lead-Salt Diode Laser," Appl. Opt. **31**, 718-731 (1992).
4. C.J. Dasch, "One-Dimensional Tomography: A Comparison of Abel, Onion-Peeling, and Filtered Backprojection Methods," Appl. Opt. **31**, 1146-1152 (1992).
5. M.P. Arroyo, S. Langlois, and R.K. Hanson, "Diode-Laser Absorption Technique for Simultaneous Measurements of Multiple Gasdynamic Parameters in High-Speed Flows Containing Water Vapor," Appl. Opt. **33**, 3296-3307 (1994).

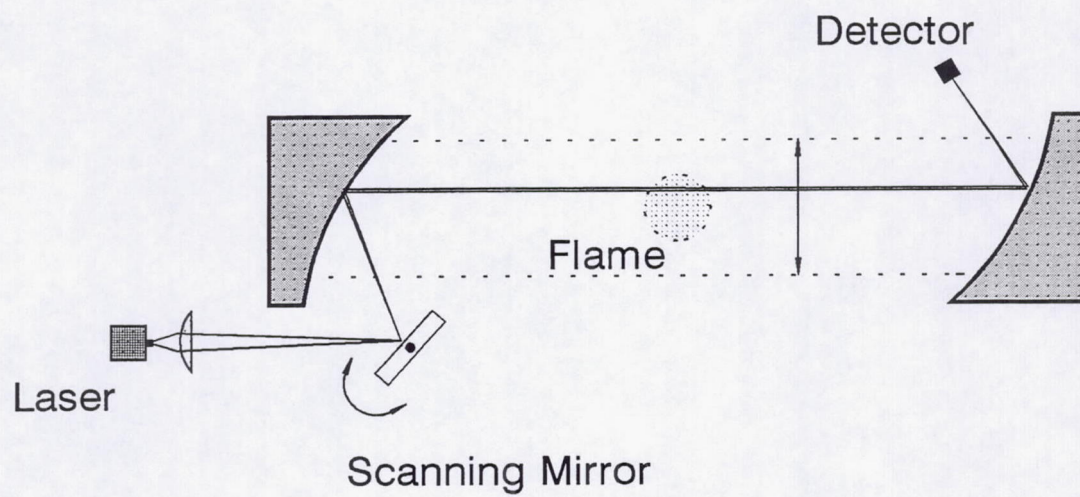


Figure 1 - Schematic of Optical Setup.

DEVELOPMENT AND APPLICATIONS OF LASER-INDUCED INCANDESCENCE

Randy L. Vander Wal and Daniel L. Dietrich
(Nyma Inc.) (NASA-Lewis)
@ NASA-Lewis
Cleveland, Ohio

and

Zhiquang Zhou and Mun Y. Choi
University of Illinois at Chicago
Chicago, Illinois

Introduction

Presently, several NASA-funded investigations currently focus on soot processes and radiative influences of soot in diffusion flames given their simplicity, practical significance and potential for theoretical modelling. Among the physical parameters characterizing soot, soot volume fraction, f_v , a function of particle size and number density, is often of chief practical interest in these investigations, as this is the geometrical property that directly impacts radiative characteristics and the temperature field of the flame and is basic to understanding soot growth and oxidation processes. Diffusion flames, however, present a number of challenges to the determination of f_v via traditional extinction measurements.

Soot in diffusion flames is often confined to narrow spatial regions with steep concentration gradients limiting the accuracy of inversion methods based on single line-of-sight extinction measurements. Additionally, such inversion techniques have only been demonstrated for axisymmetric systems. An absorption measurement requires a known path length, often made by visualization of the flame, which is imprecise and presents a difficulty for dim flames. In turbulent flames and droplet combustion, both the small spatial scales and time-varying processes have impeded 'instantaneous' measurement of f_v in these systems. Scattering contributions to an extinction measurement are difficult to account for, particularly for time-varying systems and large soot aggregates, hence are often neglected leading to overestimation of the inferred f_v .

By comparison, laser-induced incandescence (LII) possesses several advantages compared to line-of-sight extinction techniques for determination of f_v . Since LII is not a line-of-sight technique, similar to fluorescence, it possesses geometric versatility allowing spatially resolved measurements of f_v in real time in nonaxisymmetric systems without using deconvolution techniques. The spatial resolution of LII is determined by the detector and imaging magnification used. Neither absorption by polycyclic aromatic hydrocarbons (PAH's) nor scattering contributes to the signal. Temporal capabilities are limited only by the laser pulse and camera gate duration, with measurements having been demonstrated with 10 ns resolution. Because of these advantages, LII should be applicable to a variety of combustion processes involving both homogeneous and heterogeneous phases. Our work has focussed on characterization of the technique as well as exploration of its capabilities and is briefly described here.

Description of LII

Laser-induced incandescence uses a pulsed high energy laser to heat soot to incandescent temperatures. For 8-10 nsec. laser pulses, energy balance equations indicate that the energy addition rate greatly exceeds the loss rate

from thermal conduction and radiation[1-5]. For example, the temperature of a soot particle is predicted to rapidly rise to the vaporization temperature of carbon, roughly 4300 K, for laser intensities of 1×10^7 W/cm² or greater. Calculations by Eckbreth[1] show that equilibration of the absorbed energy within the particle occurs rapidly, on the time scale of the laser pulse, but heating of the medium surrounding the particle occurs on a longer time scale. In accord with the Planck radiation law, the particle thermal emission at these elevated temperatures increases and shifts to the blue compared to the non-laser-heated soot and flame gases. Theoretical analysis predicts the LII signal to be nearly proportional to soot volume fraction.[2-5] Qualitatively, large and small LII signals represent high and low soot volume fractions, respectively. Several recent applications of LII involve gas-jet diffusion flames[6-9], premixed flames[6], both fiber-supported and freely falling droplet combustion[10-12] and engine research[13-14].

Figure 1 is a general experimental schematic of our experiments using LII. Major equipment items are the pulsed laser, flame system and detection system. Pulsed laser light from a Nd:YAG laser at either 1064 or 532 nm heats the soot to incandescence temperatures. 'Point' and one-dimensional measurements are performed by aperturing the beam while a laser sheet is formed to obtain two dimensional LII images. For 'point' measurements, various lenses and/or mirrors direct the incandescence signal into a monochromator with a photomultiplier as detector. A gated intensified array camera preceded by various filters and a UV lens often fitted with an extension tube is used to obtain LII images. LII images are captured digitally using a frame-grabber with 16 MByte of on-board memory while natural flame images are captured on SVHS tape using a second gated intensified array camera. Digital delay generators control the timing of the firing of the laser, camera gate(s), data acquisition hardware and if applicable, the initiation of the combustion process. As shown in Fig. 1, we have examined a variety of combustion processes such as premixed and diffusion flames[6], turbulent flames[16] and fiber-supported burning droplets.[10,12]

Characterization/Applications of LII

We have tested the dependence of the LII signal upon f_v , both within a flame[6] and in the post-flame gases well above the flame.[16] In-situ tests were performed in a premixed rich flame of ethylene/air supported on a McKenna burner. A flat steel plate above the burner stabilized the flame. As the C/O ratio varies from 0.76 to 0.9, f_v changes by over an order of magnitude. At each of two detection wavelengths, 425 and 550 nm, excellent agreement between the LII signal and f_v , previously determined by line-of-sight extinction was observed as illustrated in Fig. 2. The dependence of the LII signal upon f_v in post-flame gases was performed in a chimney placed on the McKenna burner burning a rich mixture of C₂H₂/air. The chimney consisted of a meter-long steel tube with a pyrex top consisting of four side ports for optical access. Addition of N₂ to the post-flame gases in a tangential direction created a swirling action while a tripper plate within the chimney inhibited direct flow, thus homogenizing the soot containing post-flame gases. Through the technique of gravimetric sampling, f_v 's from 0.035 to 1.5 ppm were measured, produced by varying the C/O ratio from 1.53 to 2.49. As before, the linearity between the LII signal and f_v , determined through gravimetric sampling of the N₂ diluted post-flame gases is shown in Fig. 3 at each of two detected wavelengths of 450 and 550 nm. The excellent linearity between the LII signal and f_v , within and outside of a flame greatly simplifies interpretation of LII images with regions of high intensity corresponding to regions of high f_v , while regions of low intensity correspond to regions of low f_v .

Demonstration of the geometric versatility of LII was performed in an ethylene/air diffusion flame surrounded by an air coflow as described in reference 6. Figure 4a is an LII image of f_v , obtained with the laser sheet oriented vertically. Figures 4b-d show a sequence of LII images obtained at heights of 16.9, 14.1 and 10.0 millimeters above the burner, respectively in which the laser sheet was oriented in a horizontal plane with the LII image collected by means of a mirror placed above the non-smoking diffusion flame. The thin peripheral region containing soot is typical of laminar diffusion flames with soot converging toward the central axis at higher positions within the flame as illustrated in Fig. 4a.

As illustration of the spatial and temporal capabilities of LII, Fig. 5 shows single laser shot LII images of the soot field within the chimney illustrating the instantaneous spatial and temporal variations. Although N₂ is added to the post-flame gases to achieve mixing and uniformity of f_v , fluctuations still occur. Such characterization of the gravimetric device for different N₂ addition rates and C/O ratios of the flame was readily performed by LII.

Such images reveal several capabilities of LII as a diagnostic technique for measuring f_v . First, only with the temporal and spatial resolution capabilities of LII could such nonuniformities be observed and quantified in real time without the need for deconvolution techniques. Second, the soot within the chimney is well-removed from the flame environment and illustrates the capability of LII to reveal regions of 'cold soot' (the temperature within the pyrex top was roughly 430 K) which would not be discernable via an emission measurement, thus being complementary to that technique.

Laser-induced incandescence (LII) is ideally suited for obtaining high temporally and spatially resolved measurements of soot volume fraction in transient combustion phenomena. To further demonstrate and test the spatial and temporal capabilities of LII, f_v 's were determined within a turbulent ethylene/air diffusion flame. With identical laser intensities and detection optics, the LII signal from a $Re = 5000$ flame was calibrated via comparison to the LII signal from the chimney described above. The image in Fig. 6a is a single laser-shot beginning at 14.5 cm above the nozzle with Fig. 6b a contour plot of the LII image, the contours representing f_v in ppm. Noteworthy about this calibration method is the elimination of uncertainties in soot optical properties in the calibration of the LII signal.

Droplet combustion, with its associated small spatial scales and transient nature, typifies difficulties associated with line-of-sight extinction measurements for f_v . Natural flame luminosity, a path-integrated quantity, dominated by oxidizing soot, does not reveal the spatial distribution of soot within a flame nor f_v . Figure 7 illustrates the differences between the natural flame luminosity and LII images (Fig. 7b and 7d) for both decane and 1-chloroheptane. Image pairs 7a, 7b and 7c, 7d were each obtained approximately 2.5 seconds after ignition. Superimposed on each LII image is a picture of a ruler placed in the LII object plane prior to flame measurements. The LII image of decane, while being similar in appearance to the corresponding natural flame image, clearly reveals the soot as being concentrated in a conical region centered above the burning fuel droplet. This spatial distribution of the soot above the droplet is obscured in the natural flame image of Fig. 7a. The closed tip nature of the decane flame is also evident in Fig 7b; no soot was ever found via LII in a location above the closed tip. The LII image of 1-chloroheptane (Fig. 7d) starkly differs from the corresponding natural flame image (Fig. 7c). While both the natural flame and LII images reveal an open tipped flame, the LII image illustrates the extent of soot escape through the flame. This soot emission was easily visible by eye and some of the soot coated the optical fiber supporting the droplet. For highly sooting fuels such as monochlorinated alkanes, the natural convective flow enhances the soot emission by transporting the soot particles in the downstream direction. At sufficiently high concentration, quenching of the flame by radiative emission occurs thus opening the flame tip and allowing soot escape.[15]

These LII images of decane and chloroheptane clearly reveal the spatial and temporal capabilities of LII in measuring f_v . We have performed LII measurements on a variety of fuels to measure their relative sooting tendencies. Figure 7d further demonstrates the potential for delineating regions of cold or nonoxidizing soot by LII. Comparison between the LII and natural flame images shows the LII signal to be free from emission from excited state flame species such as C_2 , CH and OH, and can provide information complementary to chemiluminescence measurements.

Other Applications

Through the use of pulsed lasers, beam-controlling optics, and time-gated detection, LII possesses high spatial and temporal resolution in both point and planar measurements in a variety of applications. Other potential applications of LII include measurement of f_v within engine exhaust or in other pollution control situations. Other manufacturing processes require knowing the carbon content of an aerosol independently of PAH content such as in the manufacture of carbon black or carbon fibers. These applications are ideal in that detection methods as simple as photodiodes or ordinary video cameras could be used since rejection of natural flame luminosity in these applications is not an issue. Since 'point' measurements are often sufficient to characterize a reaction process or relative concentration versus time, data collection and systems need not be elaborate. Other applications of LII potentially include measurement of f_v of aerosols other than soot.

Future Plans

We are presently completing a series of detailed spectral and temporal characterization measurements of LII using different excitation wavelengths, intensities and alternative signal detection methods in order to optimize strategies for excitation and signal collection. Laser-induced spectral interferences may have little relation to f_v . Excitation intensities must also be appropriately chosen, as low intensities may not uniformly heat the soot while high intensities may result in photochemical interferences and in significant changes in the soot morphology.[17]

Our goal is to support this diagnostic technique aboard the reduced-gravity aircraft of NASA-Lewis. Both the pulsed laser system and gated intensified array camera will be compatible with a reduced-gravity environment. Plans for an aircraft rig supporting the laser and a variety of combustion experiments will be formulated this coming year. Selected laboratory measurements will identify optimal LII strategies and flame systems best suited to this reduced-gravity environment.

Acknowledgements

This program is funded through the Advanced Technology Development Program of the Microgravity Sciences and Development Program of NASA. RVW acknowledges support through contract no. NAS327-186. The official starting date for this project was Sept. 1993.

References

1. Eckbreth, A.C. J. Appl. Phys., 48:4473-4483, (1977).
2. Dasch, C.J. Appl Opt., 23:2209-2215 (1984).
3. Melton, L.A. Appl. Opt., 23:2201-2208 (1984).
4. Tait, N.A. and Greenhalgh, D.A. Proceedings of the "Optical Methods and Data Processing in Heat Transfer and Fluid Flow", Conference, London, April, (1992).
5. Hofeldt, D. L. SAE Technical Paper 930079, International Congress and Exposition, San Francisco, California, Feb.-March, (1993).
6. Vander Wal, R.L. and Weiland, K.J., J. Appl. Phys. B, in press, (1994).
7. Quay, B., Lee, T.W., Ni, T. and Santoro, R.J., Comb. and Flame 97:384-396, (1994).
8. Shaddix, C.R., Harrington, J.E. and Smyth, K.C., Twenty-Fifth Symposium (Int'l) on Combustion, The Combustion Institute, in press, (1994).
9. Cignoli, F., Benecchi, S. and Zizak, G., Appl. Opt. 33:5778-5782 (1994).
10. Vander Wal, R.L. and Dietrich, D. J., Appl. Opt., 34:1103-1107 (1994).
11. Gupta, S.B., Ni, T. and Santoro, R.J., "Spatial and Time Resolved Soot Volume Fraction Measurements in Methanol/Toluene Droplet Flames", Presented at the Technical Meeting of the Eastern States Section of the Combustion Institute, Clearwater Beach, FL, (1994).
12. Vander Wal, R.L., Dietrich, D.L. and Choi, M.Y., "Relative Soot Volume Fraction in Droplet Combustion via Laser-Induced-Incandescence", Presented at the Technical Meeting of the Eastern States Section of the Combustion Institute, Clearwater Beach, FL, (1994).
13. Dec, J. E., zur Loye, A. O., Siebers, D. L., SAE Technical Paper 910224, International Congress and Exposition, Detroit, Michigan, Feb.-March, (1991).
14. Pinson, J. A., Mitchell, D. L., Santoro, R. J. and Litzinger, T. A., SAE Technical Paper 932650, Fuels and Lubricants Meeting, Philadelphia PA, Sept. 18-21, (1993).
15. Randolph, A.L. and Law, C.K., Comb. and Flame, 64:267-284 (1986).
16. Vander Wal, R.L., Zhou, Z. and Choi, M.Y., "Laser-Induced Incandescence Calibration via Gravimetric Sampling", Presented at the Technical Meeting of the Central/Western States and Mexican Section of the Combustion Institute, San Antonio, TX, (1995).
17. Vander Wal, R.L., Choi, M.Y. and Lee, K.O., "The Effects of Rapid Heating of Soot: Implications When Using Laser-Induced-Incandescence for Soot Diagnostics", Comb. and Flame, submitted, (1994).

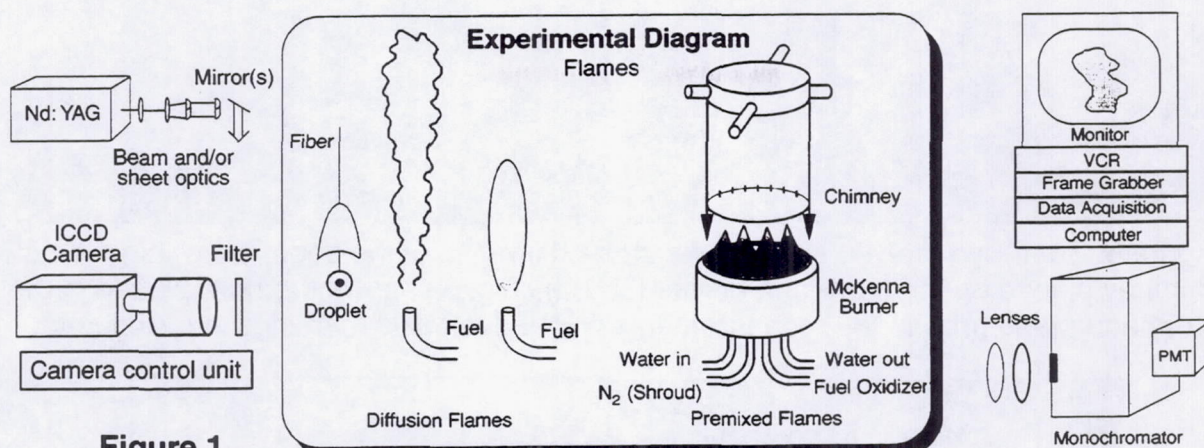


Figure 1.

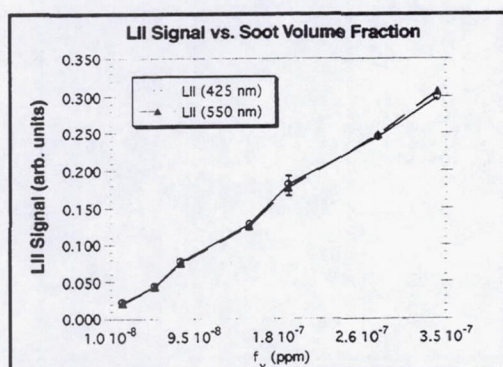


Figure 2.

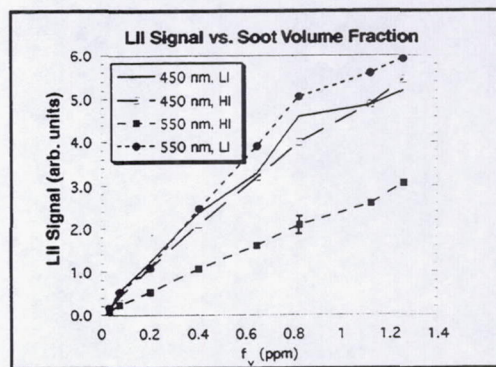


Figure 3.

Figure 2. Dependence of LII signal upon f_v within the flame using an excitation intensity of $\sim 1 \times 10^8 \text{ W/cm}^2$ with the signal detection at 425 and 550 nm. A spectral detection bandpass of 1 nm was used.

Figure 3. Dependence of LII signal upon f_v at laser intensities of 2.9×10^7 (LI) and $5.7 \times 10^7 \text{ W/cm}^2$ (HI) with detection at wavelengths 450 and 550 nm using a 1 nm spectral detection bandpass.

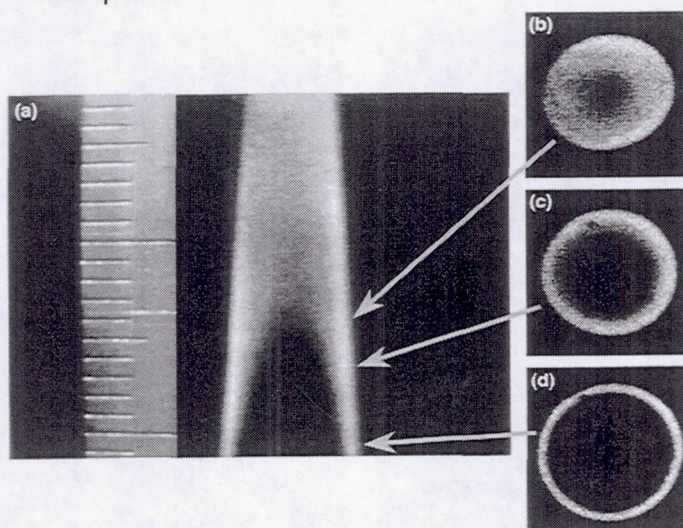


Figure 4. LII images of an ethylene diffusion flame surrounded by an air coflow. Fig. 4a was obtained with the laser sheet oriented vertically, while Fig. 4b-4d were obtained with the laser sheet oriented horizontally at heights of 10, 14.1, and 16.9 mm above the burner at the positions indicated by the arrows on Figure 4a.

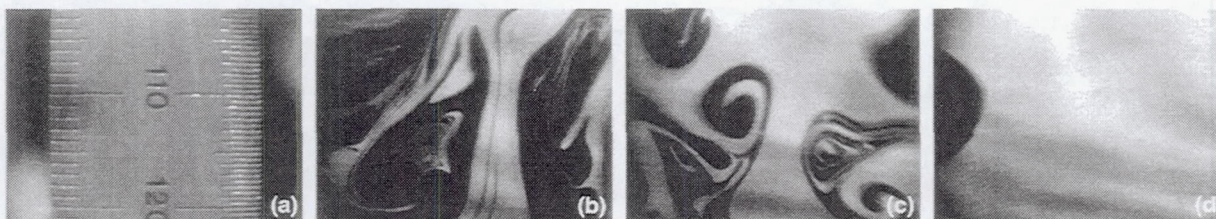


Figure 5. Spatially resolved single laser-shot LII images of the soot field within the chimney placed on the McKenna burner (5b-5d). Fig. 5a shows the ruler placed in the LII image plane prior to the measurements with the left axis markings in millimeters.

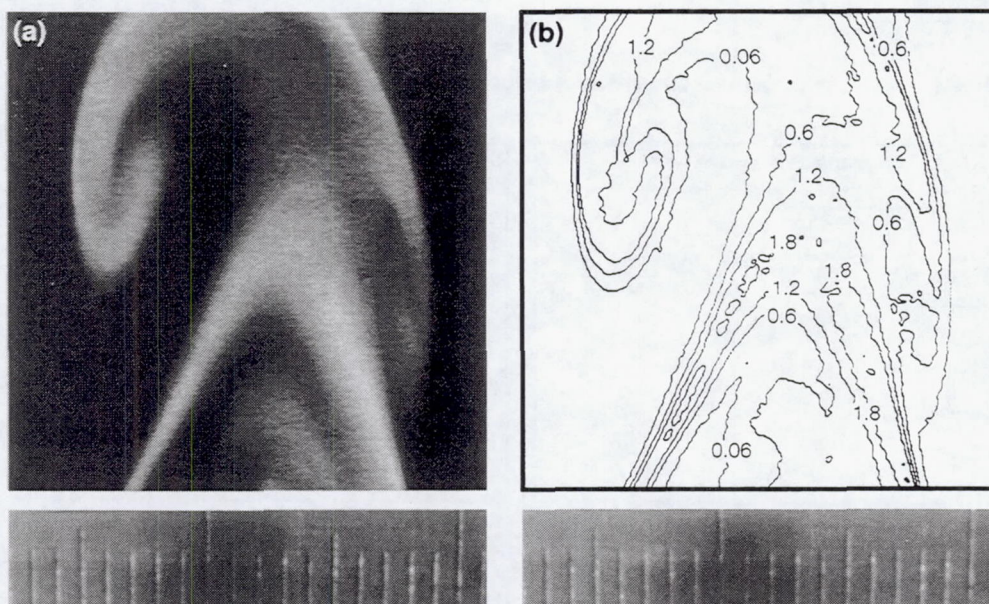


Figure 6. LII image of the $Re=5000$ turbulent gas-jet diffusion flame with the lower edge starting at 14.5 mm above the nozzle (Fig. 6a). The ruler tick marks are in millimeters. Fig. 6b is a contour plot of Fig. 6a giving f_v in ppm, determined as described in the text.

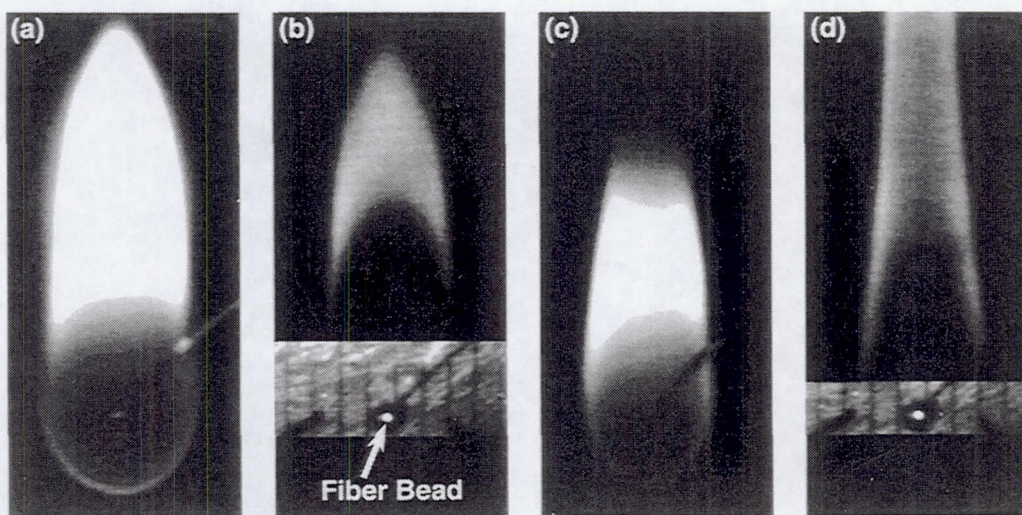


Figure 7. Simultaneous natural flame luminosity and LII images of decane (Fig. 7a-7b) and chloroheptane (Fig. 7c-7d) each obtained ~ 2.5 seconds after ignition. See text for details.

QUALITATIVE AND QUANTITATIVE IMAGING IN MICROGRAVITY COMBUSTION

Karen J. Weiland
NASA Lewis Research Center
Cleveland, Ohio

Introduction

The study of combustion often begins by asking simple questions such as these: Is there a flame? What color is it? What is its spatial extent and structure? What is its reaction rate? Does it vary with time? How long does it persist? How fast does it spread? Asking these types of questions is especially appropriate in microgravity combustion, where the effects of the removal of buoyancy often produce unexpected and dramatic changes. Images of the flame provide the answers to these questions and an overall view of the time and length scales of combustion processes, and guide the application of other diagnostics. In addition, flame imaging is often the easiest non-intrusive diagnostic to implement, especially in microgravity combustion where physical constraints limit the diagnostics able to be used.

This paper provides an overview of the imaging techniques implemented in the laboratory and reduced-gravity facilities by researchers in the in-house and external microgravity combustion program. Examples of each technique demonstrate the variety and extent available. For a more complete description of the experiment and combustion results, the reader is invited to refer to the references and to the other papers in this conference proceedings. Techniques under further development are also mentioned.

Visible and Ultraviolet Imaging

The use of commercial monochrome and color video cameras for imaging in both drop tower and aircraft experiments is routine. Recording of images on S-VHS, Hi-8 mm, 8 mm, or Betacam tape and/or direct digitizing by a frame grabber depends on the specific experimental requirements. A comparison of monochrome signals digitized directly from a camera compared to those digitized from the Betacam recorder shows that the digitized signals at each pixel are identical to 8 bits of resolution, even when the recorder is in digital pause mode. This provides great advantages for users requiring quantitative data at 30 frames per sec for extended lengths of time. During the recent upgrade of the NASA Lewis 2.2 sec drop tower facility, a dual channel, high bandwidth (6 MHz) frequency modulated fiber optic video transceiver system was installed to provide low loss signals especially suited for quantitative imaging such as for rainbow schlieren or laser light extinction. In the future, a color digitizer at the top of the 2.2 sec drop tower with network capabilities to transfer data may be available. In the NASA Lewis Zero Gravity facility, two 8-mm video recorders reside on each drop bus to record images from the users' cameras. Aboard the NASA reduced-gravity aircraft, S-VHS and Hi-8 mm video recorders have been used by many investigators.

In many studies of microgravity combustion phenomena, systems lie near the limits of flammability, ignition, or stability, and typically have a dim flame. The use of intensified array cameras reduces many of the difficulties in imaging these flames. The intensifier acts as a photon amplifier, thereby allowing

the imaging of flames too dim to be detected by film or standard video cameras. The first application of this type of camera to microgravity experiments was in the study of weakly luminous flames spreading across ashless filter paper samples aboard the NASA Learjet (ref. 1). The problem of how to set the camera gain to provide the correct exposure was noted, as many of the images were saturated when the gain was adjusted by observing the monochrome image on a monitor during the experiment. Soon after, an intensified array camera was used in the study of lean, premixed hydrogen flames at low Lewis numbers. The camera could image the flames without any colorant added, as was required for movie film imaging in 2.2 sec drop tower tests. New, unpredicted flame structures and behaviors were observed aboard the NASA KC-135A (ref. 2). This type of camera is scheduled for use in a spaceflight experiment in the spring of 1997 to study the long-term behavior of these flames in microgravity. A wide field of view of 30 cm x 22.5 cm, depth of field of 30 cm, and spatial resolution on the order of several mm are accommodated by a custom lens. The gain of the camera will be set by digitizing the video signal, applying a false color look-up-table, and displaying the false color signal on a monitor. The operator observing the false color signal will adjust the camera gain to insure the image is just below saturation.

In another spaceflight experiment, the study of droplet combustion (ref. 3), plans for spaceflight include the use of an intensified array camera having sensitivity in the ultraviolet. Demonstration of the intensified array camera in the drop facilities yielded OH chemiluminescence images of burning isolated heptane droplets by using a bandpass filter centered at 310 nm. The field of view and depth of field were 4 cm x 4 cm and 3.3 cm, respectively. The camera gain was adjusted so that the profile of the digitized image of the flame was not saturated. Additionally, the experiment used a high speed (80 frames per sec), 35 mm movie film camera to obtain high resolution images of a backlit droplet view. The field of view and depth of field were 3.3 cm x 3.3 cm and 3 cm, respectively. The spatial resolution was 18 microns. The movie film was scanned at a resolution of 5080 dots per inch into a TIFF file. The high resolution enables accurate measurement of droplet extinction diameters as small as 100 microns.

A more sophisticated approach is being taken in a sounding rocket experiment to study influences of radiative heat transfer on flame spread over polymethylmethacrylate (ref. 4). An intensified array camera is equipped with a rotating wheel having six filters: red, green, blue, OH (310 nm), CH (430 nm), and clear. A recording rate of five images per second for each filtered image is achieved by rotating the wheel at 30 Hz in synchronization with the framing rate of the camera. The gain of the intensified camera is fixed for all the frames throughout the experiment, and the exposure time is varied for each filter automatically by the camera operating in a peak mode. The camera response will be calibrated with the filters in place using a gray scale and other charts. The field of view of the system is 1 x 2 cm; the spatial resolution is better than 100 microns. The red, green, and blue images can be used to reconstruct a color image of the flame using an appropriate algorithm based on the calibration. Although the flames are expected to be mostly blue in color, detection of soot, if any is present, is desirable. The intensities of the OH and CH images will be treated as qualitative measures of the strength of the reaction. The camera was tested in NASA Learjet flights in which the images were recorded onto videotape and later digitized for analysis and color reconstruction.

High speed, intensified video cameras were used in the laboratory to study the behavior of high-Lewis number premixed flames in tubes (ref. 5). New phenomena, such as spiral waves and radial pulsations, were observed that are not visible to the naked eye or at standard video rates of 30 frames per second. Others employed such a camera to track particles floating on a liquid fuel surface ahead of a spreading flame and found liquid motion in regimes where it had not previously been seen (ref. 6). High speed video framing rates of monochrome images can be acquired at up to 1000 frames per second for a full frame, or up to 6000 frames per second for 1/6 of a frame. The length of time of the recording depends upon the amount of storage for either tape (30,000 frames) or electronic memory (as high as 4600 frames). These cameras have also been used for other aerospace applications.

Infrared Imaging

Two-dimensional infrared cameras, based on platinum silicide, indium antimonide, or other infrared materials, have recently been used in reduced-gravity experiments. Such cameras image spectral regions of infrared emissions. For some systems, the use of narrow bandpass filters permits selected species to be detected. For others, the infrared images can be used as a surface temperature measurement.

An infrared camera, along with a rotating filter wheel, will be used to obtain species-specific radiation levels for the burning polymethylmethacrylate experiment mentioned above. The filters correspond to carbon dioxide (4.2 micron), water (1.8 micron), carbon monoxide (4.8 micron), methylmethacrylate vapor (3.4 micron), and soot (1.6 and 3.8 micron). The bandwidth of each filter is selected to match the signal sizes in each band and minimize saturation of the camera signal based on aircraft tests and model predictions. The camera will be calibrated against a black-body source so that the images can be quantitatively compared. For this experiment, the camera field of view is 3 x 2 cm for each of two images; the array is 256 x 256 pixels.

A system capable of obtaining spatially- and spectrally-resolved images is being built under a Phase II Small Business Innovative Research program contract. The initial instrument will have a bandpass between 2.4 and 3.2 microns dispersed by a grating across a 128 x 128 indium antimonide focal plane array. A scan mirror sweeps across the object of interest and the fore optics image a vertical slit onto the grating. For each video frame, the focal plane array detects a dispersed spectrum in the x-direction and position in the y-direction. A data cube consists of x, y, and wavelength (128 x 128 x 128) and can be taken once every 1.5 seconds. Data collection and storage is accomplished using a personal computer and a specialized I/O board. Data analysis will be conducted on a UNIX workstation using software written to use a commercial visual data analysis program.

Temperature measurements of the surface of a liquid pool ahead of a spreading flame were recorded with an infrared camera (ref. 6). The camera is sensitive to wavelengths between 3 and 12 microns, but for this case, a filter restricts the wavelength range to between 8 and 12 microns. The alcohol fuel is essentially opaque in this wavelength region so that the radiant emission reaching the camera comes from the surface layer, not the bulk fuel. The camera records monochrome images at normal video framing rates onto videotape. The temperature span chosen on the camera depends on the expected range of temperatures. During data analysis, the images are converted to false color and an absolute temperature scale is determined. This system has been used successfully aboard a sounding rocket.

Fluorescence Imaging

Although laser-induced fluorescence, LIF, imaging of radical species such as OH and CH is highly desirable, to date, this has not been performed in microgravity primarily because of the size and power limitations of the excitation laser sources. As the size of laser systems continues to decrease, radical species imaging becomes more feasible. Experiments in the laboratory using a new, solid-state laser source based on titanium:sapphire showed that laser-induced fluorescence point measurements on CH radicals can be made. As a step in making fluorescence measurements in microgravity, laser-induced fluorescence imaging of sodium doped into a burning droplet was performed on the NASA Learjet (ref. 7). The output of a small nitrogen-pumped dye laser at 589.6 nm was imaged into a thin sheet and directed across the top of a droplet. An LIF image was collected by an intensified CCD camera and, simultaneously, a second CCD camera detected the natural flame luminosity. Both video signals passed through time code generators to allow for a frame-by-frame comparison of the LIF and natural flame luminosity images.

Schlieren Imaging

The schlieren method is one of the oldest and simplest methods for visualizing refractive index inhomogeneities, such as those arising from temperature and species distributions. The refractive index gradients cause light rays in the test section to undergo angular deviations which are encoded by a suitable spatial filter into a detectable change in intensity, color, or other parameter. Schlieren has been employed primarily as a qualitative visualization tool, but with the development of the rainbow schlieren technique, quantitative measurements of the refractive index distribution may be made.

Gray-scale laser schlieren with video recording and subsequent digitizing and image processing was used (ref. 8) in the study of premixed laminar and turbulent flames in normal and reduced gravity. A 5 milliwatt HeNe laser was expanded to fill a 75 mm field of view. A compact monochrome CCD camera with a fast shutter speed detected the laser light after a 1.5 mm diameter dark field spot. Only the regions of light deflected by a refractive index gradient in the flame cone pass around the stop and were detected as bright regions on a black background. An Abekas-based editing facility at Lewis digitized the frames to have 512 x 512 pixel resolution. Since each video frame was captured in individual fields at 1/60 of a second, the frames were broken apart into odd and even fields having 512 x 256 pixel resolution. Several standard image processing techniques such as time sequencing, line representation, and Fast Fourier Transform, were used to further analyze the data to extract information such as gross features and flame flickering frequencies.

Quantitative schlieren measurements are based upon having a known relationship between the refractive index distribution and the angular ray deflections. For systems possessing simple or axisymmetric geometries, inversion of the data to obtain the refractive index distribution from the measured ray deflections is straightforward. The use of a continuously graded color filter, or rainbow filter, along with a stable light source and CCD camera minimizes the problems of nonuniform absorption, shadowgraphy, diffraction of the source image around a hard schlieren stop, and inherent nonlinearities in film recorders. The angular ray deflections are encoded as shifts in color attributes, specifically the hue, which can be reliably and accurately detected in an automated fashion (ref. 9). Quantitative laboratory calibration and demonstrations of the schlieren system were performed on a gas wedge, optical flat, and radiantly heated liquid pool.

In reduced gravity aboard the NASA KC-135A, rainbow schlieren systems were used to study flame spread across thin solid surfaces and isolated droplet combustion. More recent are sounding rocket studies of the flame spread across liquid pools and 2.2 sec drop tower studies of nonsmoking diffusion flames. The liquid pool experiment system has a field of view of 100 mm. The color filter has a continuous hue variation in the horizontal direction across a span of 10 mm. Liquid temperature gradients over a 2 cm path length of $\pm 20^\circ\text{C}/\text{cm}$ were resolved; the smallest resolvable gradient is $0.07^\circ\text{C}/\text{cm}$. The data can be integrated to obtain a map of the temperature distribution in the liquid or gas. The study of nonsmoking hydrogen diffusion flames determined the near-nozzle flow structures of these extremely dim flames.

Imaging of Soot

A measurement of significant interest is that of the total amount of soot in the flame, or the integrated soot volume fraction. Traditionally, single line-of-sight absorption measurements using a narrow light source, such as a laser, and a single-element detector are used with traversal over the flame. A new method more suitable for microgravity where space and time are limited is based on imaging absorption of a laser light source with a CCD camera (ref. 10). Light from a low power HeNe is expanded, collimated, and directed through the test section. A lens and camera detect the light through a bandpass filter that rejects the flame

luminosity and transmits the laser light. The amount of light absorbed or scattered by the soot in the flame is measured by comparison to a reference frame taken without the flame. A deconvolution algorithm based on the Abel transform is used to invert the data for axisymmetric systems. The minimum absorptivity seen in a laminar diffusion flame in practice to date is approximately 2%. A study of different laser beam configurations, smoothing algorithms and kernels, and camera integration periods was undertaken to understand and minimize the effects of spatial noise and beam steering.

An alternate way to measure the soot volume fraction is by the use of laser-induced incandescence, LII. This process occurs when intense laser light heats the soot to temperatures far above the background. In accord with the Planck radiation law, the particle thermal emission at these elevated temperatures increases and shifts to the blue compared to the non-laser-heated soot and flame gases. Measurements in the laboratory show that the LII signal is linearly proportional to the soot volume fraction and may be easily interpreted as a relative measure of soot volume fraction (ref. 11). Absolute calibration of the technique may be made by *in situ* comparison of the LII signal to a system with a known soot volume fraction. LII offers high temporal resolution by obtaining signals induced by a single laser pulse. The laser may be formed into a sheet for imaging measurements. In the laboratory, one- and two-dimensional imaging measurements of premixed flames, gas jet diffusion flames, and isolated burning droplets were performed using a gated, intensified array camera.

Most nonintrusive measures of soot temperatures using multiline emission methods are based upon points in the flames being studied by traversal of the light source and detector. A new method uses a CCD camera system to image the entire flame, in this case a laminar diffusion flame, and with deconvolution procedures, alleviates the need for moving parts. Evaluation by comparing soot temperatures measured using three separate line pairs and by comparing the multiline temperature distribution with conventional thermocouple temperature measurements made in nearby soot-free regions of the flame showed that with the CCD system there was good agreement between the average of the three line pairs and each of the three line pairs, and that the best results were obtained when the line pairs were separated by more than 150 nm. This system is being implemented into a 2.2 sec drop rig and also is scheduled for a spaceflight experiment in 1997 to study sooting processes in laminar diffusion flames.

Image Processing and Tracking

An image processing and tracking workstation has been set up at NASA Lewis to assist in the data analysis of objects on recorded film or video tape. System components include film and video tape transports, personal computer, frame grabber, laser disk drive, high resolution video monitor, hard copy devices, and access to the Internet for file transfer to remote sites. Images on 16 and 35 mm film, S-VHS or Hi-8 mm video tape, laser disk, or TIFF and other image files can be analyzed. For film digitizing, a digital camera having a resolution of 1280 x 1024 pixels images the film directly. A 2:1 optical zoom enables imaging of a sub-region to an equivalent resolution of 2560 x 2048. A frame grabber digitizes and displays up to 1280 x 1024 pixels, with 8 bits each in the red, green, and blue colors. Image processing is performed on an area of interest which includes the desired object to be tracked to aid in the process. The processing algorithms include filtering, edge detection, thresholding, histogram equalization, and correlation. Recent examples of investigations using this workstation include the tracking of flames spreading between parallel solid surfaces, flame spread across liquid pool surfaces, candle flames, solid surface combustion of paper, and measuring the relative droplet-to-gas velocities during free float periods in microgravity.

Summary

An overview of the imaging techniques implemented by researchers in the microgravity combustion program shows that for almost any system, imaging of the flame may be accomplished in a variety of ways. Standard and intensified video, high speed, and infrared cameras, and fluorescence, laser schlieren, rainbow schlieren, soot volume fraction, and soot temperature imaging have all been used in the laboratory and many in reduced-gravity to make the necessary experimental measurements.

References

1. Weiland, K. J., "Intensified Array Camera Imaging of Solid Surface Combustion Aboard the NASA Learjet," *AIAA Journal*, Vol. 31, 1993, p. 786-788.
2. Ronney, P. D., Whaling, K. N., Abbud-Madrid, A., Gatto, J. L., and Pisowicz, V. L., "Stationary Premixed Flames in Spherical and Cylindrical Geometries," *AIAA Journal*, Vol. 32, 1994, p. 569-577.
3. Williams, F. A. and Dryer, F. L., "Science Requirements Document for the Droplet Combustion Experiment," 1994.
4. a. Altenkirch, R. A., Olson, S. L., and Bhattacharjee, S., "Science Requirements Document for the Diffusive and Radiative Transport in Fires Experiment," 1994.
b. Melikian, S., "Intensified True Color Imaging," NASA TM in preparation.
5. a. Pearlman, H. G. and Ronney, P. D., "Self-organized spiral and circular waves in premixed gas flames," *Journal of Chemical Physics*, Vol. 101, 1994, p. 2632-2633.
b. Pearlman, H. G. and Ronney, P. D., "Near-limit behavior of high-Lewis number premixed flames in tubes at normal and low gravity," *Physics of Fluids*, Vol. 6, 1994, p. 4009-4018.
6. Miller, F. J. and Ross, H. D., "Liquid-Phase Velocity and Temperature Fields During Uniform Flame Spread over 1-Propanol," *Eighth International Symposium on Transport Phenomena*, San Francisco, CA, 1995 (submitted).
7. Winter, M., "Laser Diagnostics for Microgravity Droplet Studies," AIAA Paper 94-0431, 32nd Aerospace Sciences Meeting & Exhibit, January 10-13, 1994, Reno, NV.
8. Kostiuk, L. W. and Cheng, R. K., "Imaging of premixed flames in microgravity," *Experiments in Fluids*, Vol. 18, 1994, p. 59-68.
9. Greenberg, P. S., Klimek, R. B., and Buchele, D. R., "Quantitative Rainbow Schlieren Deflectometry," *Applied Optics*, Vol. 34, 1995 (in press).
10. Greenberg, P. S. and Ku, J., "Soot Volume Fraction Imaging," *Applied Optics*, in preparation.
11. a. Vander Wal, R. L. and Weiland, K. J., "Laser-Induced Incandescence: Development and Characterization Towards a Measurement of Soot Volume Fraction," *Journal of Applied Physics B*, 1995, (in press).
b. Vander Wal, R. L. and Dietrich, D. L., "Laser-Induced Incandescence Applied to Droplet Combustion," *Applied Optics*, Vol. 34, 1995, p. 1103-1107.

LASER DIAGNOSTICS FOR MICROGRAVITY DROPLET STUDIES

Michael Winter
United Technologies Research Center
East Hartford, Connecticut

Introduction

One of the most fundamental distinctions in combustion is whether a flame is a premixed or non-premixed flame. Condensed-phase materials usually serve as reactants in practical combustion devices, either through direct injection of a condensed-phase fuel into a combustor or the initial presence of a condensed-phase fuel within the combustor. These fuels generally burn as non-premixed flames. Additionally, most hazardous flames are multi-phase diffusion flames as well. Several of these combustion systems involve burning liquid-phase fuels which are comprised of numerous individual droplets.

Basic understanding is best advanced by well-controlled experiments and simplified calculations. A great deal of attention has been paid to studying the combustion of individual droplets,^{1,2} which is the simplest example of non-premixed combustion. These single-droplet flames provide an idealized geometry for investigating the interaction of the physical and chemical processes involved. The importance of droplet vaporization and combustion was recognized as early as 1953,^{3,4,5} and several reviews^{1,6-10} describe the progression of this work. A significant means of simplifying droplet combustion is to approach the phenomena in a microgravity environment. A great deal of activity is ongoing in this area, including calculations, drop towers, the Droplet Combustion Experiment (DCE), and glove-box experiments aboard the space shuttle. Drop tower data have shown deviations from calculated results, suggesting that the experimental conditions may differ from the idealized assumptions used.

Optical diagnostics offer several advantages over physical probes because they permit nonintrusive multi-point measurements. Nonintrusive measurements are of particular importance for droplet combustion and transport in microgravity environments, where physical contact would introduce an unacceptable level of perturbations. The resolution of these diagnostics can also isolate transport to length scales much smaller than the droplet diameter. These techniques can be configured to instantaneously map an entire flow field in two and three dimensions, providing either qualitative or quantitative information on the distribution of a desired scalar or vector quantity.

The classic model of droplet combustion in the absence of gravity assumes the inner core contains the liquid fuel. Beyond a diameter d_l , there is a symmetric vapor cloud. Around the fuel exists an envelope flame at radius d_f . Energy is radiated both toward and away from the droplet center while combustion products flow out and oxidizer flows inward. Other assumptions include spherical symmetry, an isolated droplet in a quiescent medium, diffusion controlled rates, a single component fuel, and thin reaction zones.

Discrepancies between model predictions and experimental data have been observed in steady burning, convective transport, and microexplosions, to name just a few. These observations can be linked to the hypothesized responsible mechanisms including:

1. Unsteady or quasi-steady flame front position,
2. relative droplet/gas phase motion,
3. transport and condensation of pyrolytic products onto the droplet surface, and
4. convective transport within the droplet.

Approach

Flame Front and Velocimetry

A research requirement would be detailing the gas-phase flow field and position of the flame front. This can be achieved using PLIF of OH^1 or another flame front marker which is typically performed by tuning a laser to the molecular absorption and recording the emitted radiation with a two-dimensional detector. Laser sources and detection systems capable of operating under the power and shock environments typical of flight conditions are now available. An alternative approach, which is reported here is to obtain LIF from a diagnostic seed included in the liquid-phase fuel; it would be consumed at the flame front. The main advantage to this approach is that it is easier to choose the wavelength of the molecular absorption which coincides with convenient laser wavelengths rather than finding lasers which can be configured to access OH. Our present method uses a nitrogen-pumped dye laser tuned to a sodium absorption and addition of small concentrations of NaCl to the fuel. This will be described in more detail below.

PIV is a laser-based technique which has recently had its practicality greatly enhanced by the development of high-resolution CCD cameras and the increase in speed and capacity of computer systems. With this technique, a seeded flow is illuminated with a double-pulsed laser sheet to generate a double exposure image on a film or CCD camera. Computer analysis of the image is used to determine the particle velocity vectors and, thus, the gas velocity within the plane of the laser sheet. Our current experiment uses PIV for measuring relative droplet gas-phase velocities in a parabolic flight environment.

Experimental Methods and Design

UTRC under contract with NASA beginning in October of 1992, has designed and built an apparatus for performing measurements aboard the NASA Learjet, DC-9 and KC-135 aircraft facilities. An integrated diagnostic unit, capable of performing these measurements has been assembled. A new ND:Yag laser is currently being incorporated into the system. The system remains operational and flight ready; low gravity testing was performed.

Package

An overview photograph of the apparatus is shown in Fig 1. The system currently contains a nitrogen pump laser, tunable dye laser, two camera systems-one intensified, two time code generators, two VCRs, a Macintosh IIfx computer with image digitization hardware and experiment control software, timing electronics, and power distribution. The package also contains a windowed combustion vessel capable of a wide range of pressures.

Controls

Droplet combustion occurs within the combustion vessel that houses the remote control systems on an internal multi-level platform consisting of triangular sections and threaded rod. In the center

resides a fiber droplet holder surrounded by the droplet deployment and ignition hardware. The multi-level platform is complete with servo-actuators capable of deployment of a droplet onto a fiber, removing the deployment needle, introducing and energizing the igniter, igniting the droplet, and retracting the ignitor, all through remote operation via the control system joysticks and switches on the control box. A CCD video camera is used to monitor the procedure, and the images are displayed on a 2 in. LCD monitor attached to the control box. A second 2 in. LCD monitor is attached to the control box to display the images from the intensified CCD camera recording the PLIF or PIV data. In order to comply with power, size weight and cost budgets, the monitors used are commercial-grade miniature color television sets that have been modified. The controls box joysticks and actuators are modified radio controlled airplane equipment. The control system box can be seen in the top of Fig. 1.

A second multi-level combustion platform is available that includes a levitator. This module is a direct replacement to the original and can be replaced in a matter of minutes between tests. The design relies on electrodynamic levitation and the electrostatic levitation electrode are passive. While this increases the difficulties associated with 1-g testing, it significantly increases the optical access and precludes flame interferences at 0-g where the flame stand off distances are much greater. Plans for flying the levitator module aboard parabolic aircraft have been initiated.

Laser/Camera

Advanced laser diagnostics involving imaging of fluorescence fields, typically rely on high-power lasers, and sophisticated and extremely sensitive camera systems. The current NASA/UTRC flight apparatus uses a pulsed nitrogen laser that produces 0.3 mJ at 337 nm in a 3 ns pulse. This laser is used to pump a tunable dye laser providing a 30% pumping efficiency into a visible wavelength. The current experiment uses the laser system to provide either one pulse at 589 nm for PLIF of sodium, or, two pulses in sequence for PIV using elastic scattering from seed particles.

Two camera systems are currently housed in the flight apparatus. One is an intensified, cooled CCD capable of external triggering. Maximum data readout is 30 Hz, however, the system is operated at 20 Hz to achieve synchronization with the laser pulsing frequency. For PIV the intensifier is gated twice for every CCD frame readout event. A second CCD camera is used for observing droplet loading and ignition, and recording the flame luminosity during a burn. Both cameras are provided with microscopic optics to resolve both the droplet and surrounding flow field. The images from both camera are passed through synchronized time code generators which superimpose a time code signal on the images. This allows later comparison between the luminosity and the PLIF signals on a frame by frame basis. This can be important since all previous measurements of the flame behavior in microgravity droplet combustion relied on recording the flame luminosity. The time coded images are then recorded on highband 8 mm videocassettes for later analysis. The PLIF signals are also recorded through a frame grabber resident in the Macintosh IIfx included in the flight rig.

Results and Discussions

PLIF from burning droplets under microgravity conditions was extremely successful. The nitrogen-pumped dye laser was formed into a sheet $<250\text{ }\mu\text{m}$ wide and directed across the top of the droplet. The dye laser was tuned to 589 nm to pump sodium as described above. The laser-induced fluorescence was recorded in two-dimensions. Figure 2 shows a comparison of the laser-induced fluorescence image along with the luminosity image from the exact same instant in time. The luminosity image displays the full spherical envelope flame around the droplet while the PLIF image only provides flame position information over the droplet. The PLIF image however, only corresponds to a 3 ns instant in time corresponding to the laser pulse duration while the luminosity image is temporally integrated over the video frame time.

Video imaging of the flame luminosity gives a spatially integrated view, of the outside limit of the reaction zone. While the temporal resolution provided by a video camera frame time might be adequate under droplet combustion conditions, the lack of spatial resolution in such a measurement can be misleading. The video image will record the projection of this flame shell in two dimensions. The outermost position of the flame front is ascertained based on the region with the highest intensity, which may or may not correspond to the great circle, or equator of the droplet. Using the position of the highest intensity may also be misleading because for all locations other than the great circle, the camera will record two flame front positions, one in front of and one behind the actual circle of interest. In fact only at the one location which is of primary interest along that great circle will the luminosity be under represented, leading to an underprediction of flame diameter.

Using laser-induced fluorescence the spatial resolution into and out of the plane of the image corresponds to the thickness of the laser sheet. In our experiment a thin ($\sim 250\ \mu\text{m}$) laser sheet is directed across the top of the droplet at precisely the greatest diameter, (i.e. the equator). The information relating to flame front position from sodium fluorescence can only correspond to that spatial position regardless of the depth-of-field of the imaging system. It further eliminates the ambiguities associated with assuming the highest intensity marks the flame position.

PIV was also attempted and early data analysis suggests that these experiments were less successful in combustive environments. Adequate seeding densities were achieved using $.9\ \mu\text{m}$ silica particles. The particles were entrained into the flow ~ 15 seconds prior to initiating a trajectory by providing pulses of air through the chamber. Prior to ignition and in the absence of combustion, double exposures of the particles were recorded corresponding to two laser pulses. These data have been processed to provide the gas-phase flow field. Upon ignition the heat release and corresponding gas expansion propels the PIV seeds out of the measurement volume. When the droplet combustion is complete the particles immediately return to the measurement volume. From this we conclude that while PIV is applicable in general to microgravity studies and can successfully be applied in this environment, it may not be appropriate as a microgravity combustion diagnostic. This can be contrasted with one-g combustion where PIV has successfully been applied since the dominant flow mechanism is convection, which carries the PIV seed particles into the region of interest. Another interpretation of this result might be that radial outflow dominates droplet combustion.

Successful radical chemiluminescence, PLIF and visible flame luminosity images were obtained. Initial analysis indicates that the broadband visible flame luminosity and radical chemiluminescence agree well in mapping the flame front position. The resulting data were processed to provide information on droplet regression rate and flame diameter as a function of time. These data are shown in Fig. 3 where the results are shown for d^2 as a function of time for these luminosity, radical emission at 308 nm, and sodium PLIF. Similar behavior is seen for each. However, the luminosity consistently over predicts the flame diameter relative to the radical emissions and PLIF data. The flame position as determined from the PLIF is self consistent with the radical emissions. Future efforts will be directed at recording PLIF from OH radicals directly.

Conclusions

An instrument has been designed, built, and tested for performing laser diagnostic measurements of droplet combustion in low gravity flight aircraft. The results show successful application of PLIF relative to luminosity and radical emission near 308 nm. PIV results are less successful due to gas thermal expansion deflecting the seed particles away from the measurement volume. PIV is

applicable for measurements in the absence of combustion. Further analysis and alternate seeding schemes are being explored.

The flight instrument embraces many new actuation and control schemes that proved successful in flight. The system has been designed for various other diagnostic measurements. Further experiments will investigate these as well as a range of droplet fuels and combustion under a range of pressure situations.

Acknowledgement

I would like to thank Jason S. Wegge for his expert technical assistance. His contributions to the design and assembly of the experimental apparatus were extremely valuable. I would also like to thank Dr. Alan Eckbreth, Dr. Howard Ross, Professor Fred Dryer and Professor Forman Williams for their encouragement and useful discussions. We appreciate the efforts and assistance of the staff at the NASA LeRC Flight Research Laboratory. We also would like to acknowledge many useful discussions and contributions by Dr. Randy Vander Wal. His technical contributions, suggestions and guidance was particularly valuable. His on-sight support of our effort at NASA LeRC was also essential in achieving our success.

References

1. Law, C. K., *Recent Advances in Droplet Vaporization and Combustion*, Prog. Energy Combust. Sci. 8, 171-201 (1982).
2. Sanders, B. R. and Bergen, N. E., *Workshop on Mass, Momentum, and Energy Exchange in Combusting Sprays: Droplet Studies*, Report SAND89-8442, Sandia National Laboratories, Livermore, CA (28-29 March 1988).
3. Godsave, G. A. E., 1953, *Studies of the Combustion of Drops in a Fuel Spray - The Burning of Single Drops of Fuel*, Fourth Symposium (International) on Combustion, Williams and Wilkins Co., Baltimore, pp. 818-830.
4. Hall, A. R. and Diederichsen, J. D., 1953, *Experimental Study of the Burning of Single Drops of Fuel in Air at Pressures up to Twenty Atmospheres*, Fourth Symposium (International) on Combustion, Williams and Wilkins Co., Baltimore, pp. 837-846.
5. Spalding, D. B., 1953, *The Combustion of Liquid Fuels*, Fourth Symposium (International) on Combustion, Williams and Wilkins Co., Baltimore, pp. 847-865.
6. Williams, A., 1976, *Fundamentals of Oil Combustion*, Progress in Energy and Combustion Science 2, pp. 167-179.
7. Faeth, G. M., 1977, *Current Status of Droplet and Liquid Combustion*, Progress in Energy and Combustion Science 3, pp. 191-224.
8. Law, C. K., 1982, *Mechanisms of Droplet Combustion*, Proceedings of the Second International Colloquium on Drops and Bubbles, edited by le Croisette, D. H., JPL Publication 82-7, Jet Propulsion Laboratory, Pasadena, pp. 39-53.
9. Williams, F. A., 1985, *Diffusion Flames and Droplet Burning*, Chapter 3 of Combustion Theory, Second Edition, Benjamin/Cummings Publ. Co., Menlo Park, California, pp. 52-91.
10. Law, C. K., 1989, *Some Recent Advances in Droplet Combustion*, Proceedings of the Third International Colloquium on Drops and Bubbles, edited by Wang, T. G., Vol. 197 of AIP Conference Proceedings, American Institute of Physics, New York, pp. 321-337.
11. Hanson, R. K.; 1986: Twenty-First Symposium (International) on Combustion, p. 1677.

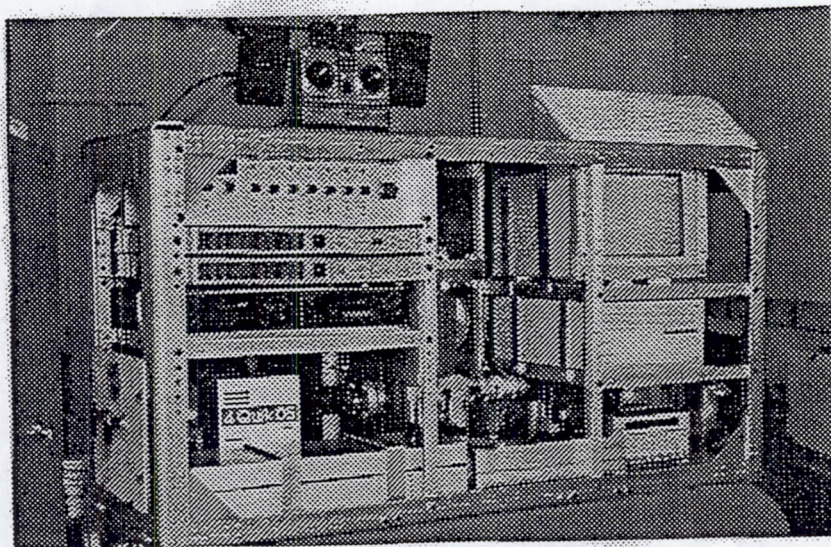


Figure 1. Photograph of the UTRC/NASA laser diagnostics for microgravity droplet combustion apparatus.

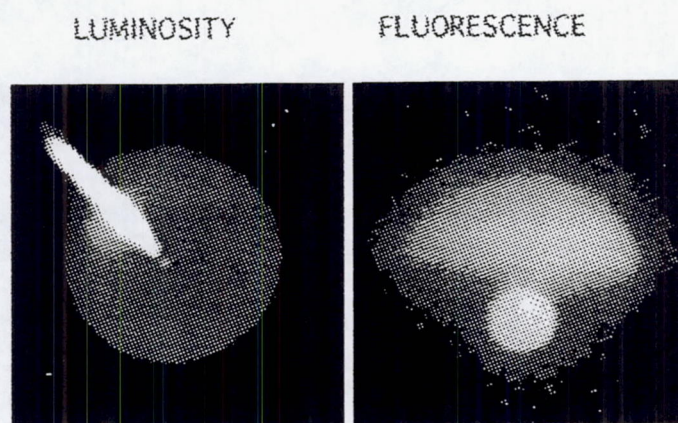


Figure 2. Comparison of PLIF of sodium and flame luminosity.

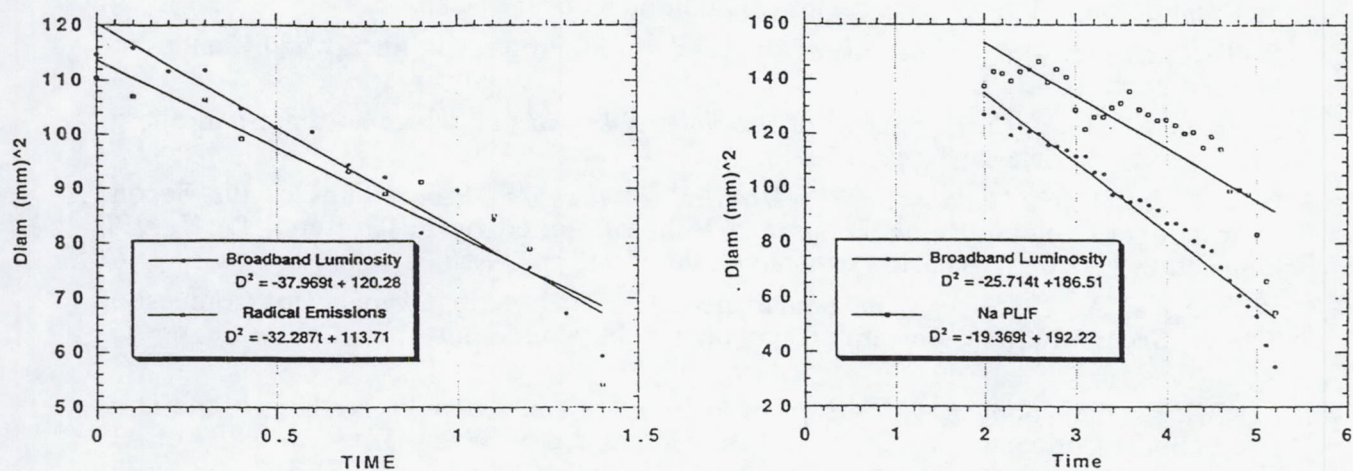


Figure 3. D^2 fit to broadband luminosity, radical emissions and sodium PLIF.

AN IMAGING SPECTROMETER FOR MICROGRAVITY APPLICATION

Wallace K. Wong
SSG, Inc.
Waltham, Massachusetts

Introduction

Flame structure is the result of complex interaction of mechanisms operating in both unwanted fires and controlled combustion systems. The scientific study of gas-jet diffusion flames in reduced-gravity environment is of interest because the effects of buoyancy on flow entrainment and acceleration are lessened. Measurements of flames have been restricted to cinematography, thermocouples, and radiometers. SSG, Inc. is developing an MWIR Imaging Spectrometer (MIS) for microgravity flame measurements. The device will be delivered to NASA Lewis at the end of this project to demonstrate flame measurements in the laboratory. With proper modifications, the MIS can be used to monitor a gas-jet flame under microgravity on an NASA Learjet or DC-9.

Instrument Concept

The MIS is a spatially scanned imaging spectrometer. Figure 1 illustrates the spectrometer concept. The instantaneous field of view (IFOV) of the instrument is defined by a slit behind an objective lens. This slit is imaged onto the central column of the FPA for the central wavelength, and on the end columns for the minimum and maximum wavelengths respectively. The FPA consists of 128 x 128 Indium Antimonide (InSb) photodiodes. Each detector column corresponds to the y-orientation and each detector row corresponds to 128 spectral components of the pixel corresponding to the crossing column. The scan mirror is synchronized with the FPA start of frame so that the footprint of the slit will advance by one footprint width on successive frames. After 128 FPA frames, a square image is collected. Post processing of the data block can produce an image of various spectral aggregates or a spectrum for part of the image. Figures 2 and 3 are compiled from the breadboard MIS developed during Phase I of this project.

Design Characteristics

The MIS design is optimized for flame measurements under microgravity on an NASA airplane. The parameters are tabulated on Table 1. Figure 4 shows the optical configuration. The mechanical package has been designed to be used with another instrument on an existing NASA free-floating rig. Figure 5 shows the hardware and the overall layout. The scan mirror is placed 30.5 cm (12.0 inches) from the flame at the center of a combustion chamber.

The Amber Engineering, Inc. Model 4128C camera system consists of a 128 x 128 InSb FPA packaged in a liquid nitrogen dewar; and the Amber Electronics. The dewar is custom modified with aluminum foam and burst disk and pressure relief valve for Learjet or DC-9 microgravity use. The hold time is more than six hours with 0.3 liters of liquid nitrogen. The Amber Electronics converts the analog at-dewar Trans-Impedance Amplifier (TIA) signals into a 12-bit digital video format. The 12-bit digital signal is first conditioned, then stored in the random access memory (RAM) of the Pentium PC. The fastest reliable frame rate is 109 Hz.

For a square image, 128 frames are collected as a 128 x 128 x 128 data cube. Each data cube is approximately 4 megabytes. The scan efficiency is approximately 75%. Therefore, successive data cubes are collected every 1.6 seconds. The MIS computer has 64 megabytes of RAM that can store 15 data cubes during a data collection period of 24 seconds. For reference, the NASA Model 25 Learjet can provide 22 to 25 seconds of reduced gravity.

During a typical experimental scenario, the MIS would be set up and held at the Stand-By Mode. When Zero-G condition is approaching, the operator will ignite the flame and press the MIS data collection TTL trigger switch to start data collection. After the data run, the data in RAM can be copied with header information to the hard disk memory. After multiple trails, the data is transferred from the disk to an 8-mm tape cartridge of an internal tape drive.

Operation and Software

The MIS Software has three modules: ImSet, ImDat and ImSpec. ImSet and ImSpec are applications under MS Windows; ImDat must run under MS DOS.

ImSet: This is the programmable experiment setup routine which allows the user to set parameters for the next data set. The ImSet has simple user interfaces, such as experimental configurations, that can be read from the hard disk. The configuration file includes the camera and frame grabber I/O board setup parameters. Header information can also be tagged to the data block to support subsequent quick look data identification.

ImDat: The user must reboot the PC prior to running this software. A TTL trigger switch provides synchronization with the ignition of the flame. The pointing mirror will move back and forth to perform the spatial scanning function. Successive spatial/spectral data are collected with the mirror scanning in opposite directions. No data is collected during the overscanned intervals. On average, the stepper motor moves two steps for each FPA readout frame. The stepper motor is synchronized with the master clock internal to the Amber Electronics.

ImSpec: This data visualization and analysis software is developed under Interactive Data Language (IDL) for MS Windows. The array processing capability of IDL allows simple arithmetic on data cubes such as coaddition and background subtraction. Figure 6 illustrates the main screen functions. The image can be recompiled to display a narrower aggregate of spectral components. The data range graphically illustrates the band center position and bandwidth. Other menu functions are provided to ease data visualization and analysis. SSG will also provide NASA with IDL for a UNIX Workstation. The ImSpec software will be modified for use on a UNIX computer.

Status and preliminary results

SSG is developing a laboratory MWIR imaging spectrometer instrumentation for microgravity applications. The data acquisition rate is once every 1.5 seconds for a $128 \times 128 \times 128$ data cube. Our MIS instrument is designed with Learjet microgravity flights in mind. The operation of this instrument on the bench will be demonstrated at NASA Lewis by late spring of 1995.

Acknowledgements

This work is sponsored by NASA Lewis Research Center under a Phase II SBIR, Contract No. NAS3-26554. The NASA technical monitor is Dr. Karen Weiland. Stewart Radiance Laboratory in Bedford, Massachusetts provides subcontractual support to this project.

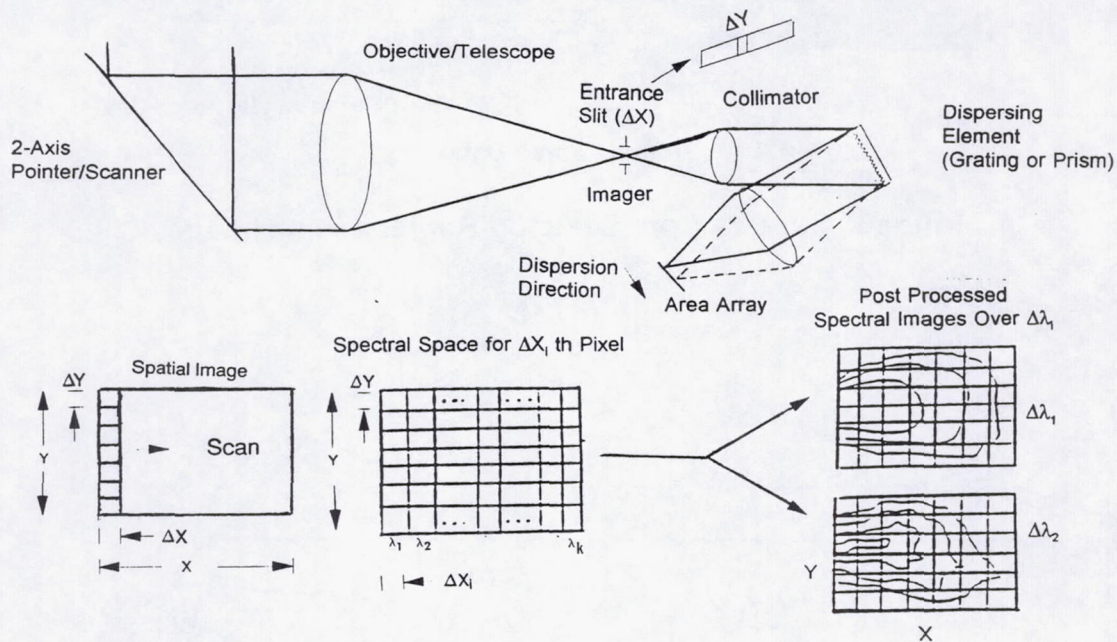


Figure 1. Spatially Scanned Imaging Spectrometer Concept

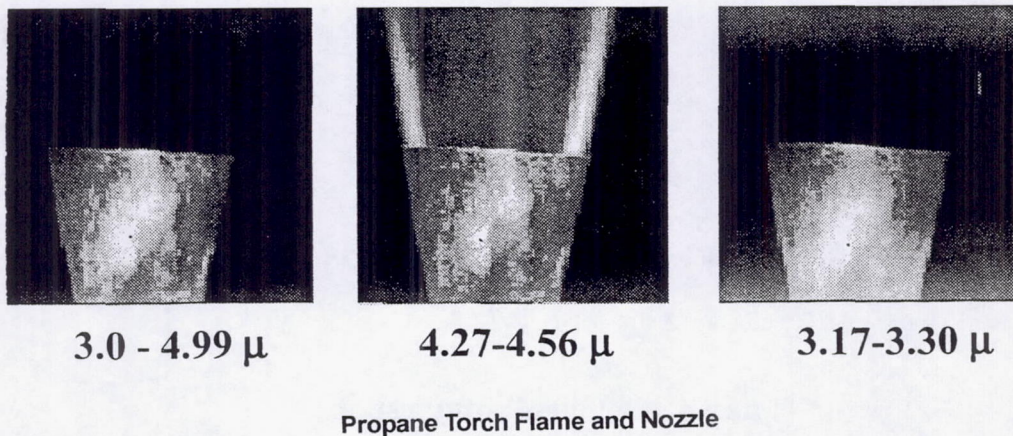
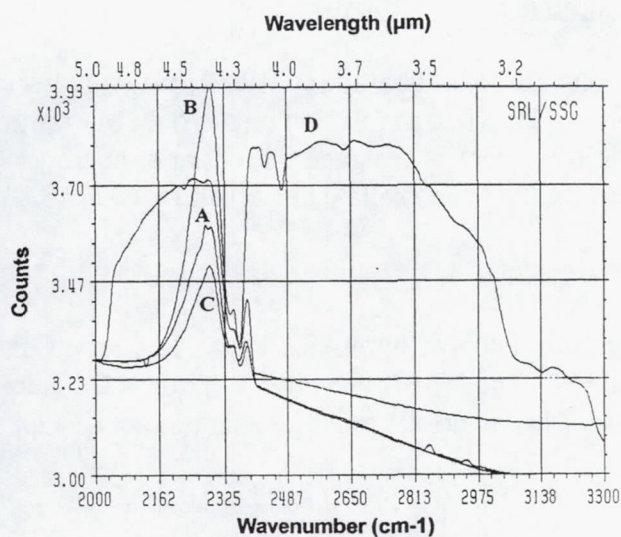
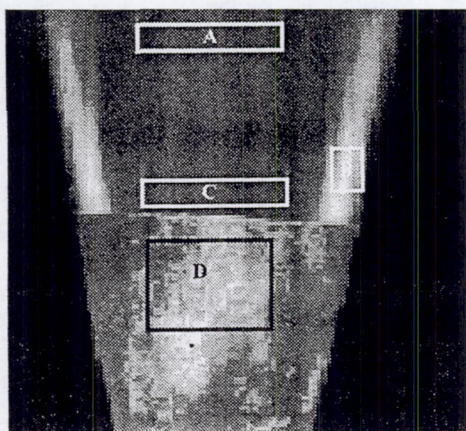


Figure 2. In-Band Images from One Scan



NASA Lewis Spectrometer Torch Data

Propane Torch Data

Figure 3. Spectra from Selected Regions in an Image

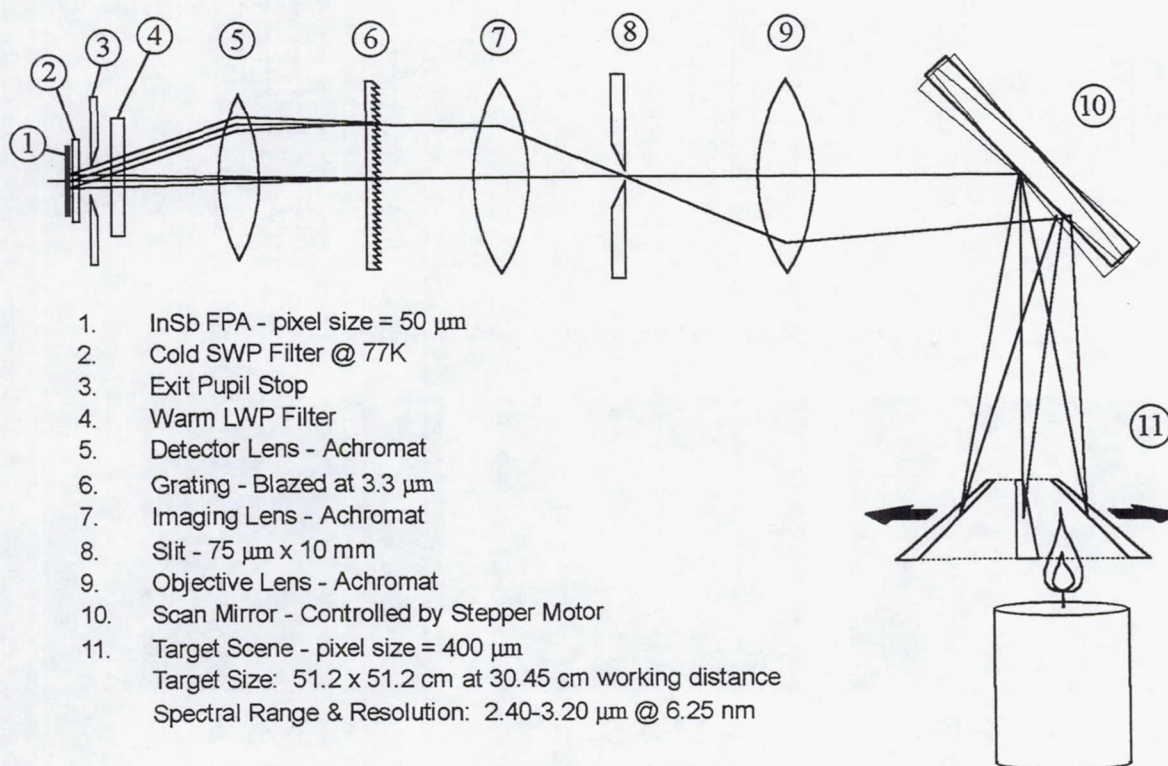


Figure 4. Optical Configuration

Table 1. Instrument Optical Characteristics

PARAMETER	UNIT	DESIGN VALUES	NOTES
Spectral Range	micron	2.4 - 3.2	FPA / optics / grating
Spectral Components	-	128	Limited by 128 X 128 FPA
Spatial Resolution		128	Limited by 128 X 128 FPA
Detector Material		InSb	Amber 4128 camera
FPA Format		128 x 128	Multiplexed digital output
Detector Pitch	micron	50.0 x 50.0	~43 x ~43 active area
Slit width x height	micron	75 x 6400	1 x 128 IFOVs
Demagnification		8	
Spatial Resolution	micron	400	distance of 40 cm between lens and flame!
Spatial Coverage	mm	0.4 x 51.2	1 x 128 IFOVs
Final F-number		2.3	at Detector
Optics type		achromats	3, at ambient temperature
Achromats coating		AR	2 - 5 micron
Grating	groove/mm	120	reflector, blazed at 3.25 μ m
SWP Filter - cold	micron	cutoff @ 3.5	inside dewar
LWP Filter - warm	micron	cuton @ 1.9	outside dewar window
dewar window material		Silicon	2 - 5 micron AR coated
Dewar	°K	77	alum.foam, Abs. press.relief valve, burst disk, hold ~ 7 hr.
Digitization		12	4096 levels
Data Acq. System			Pentium microprocessor based PC
Data Acq. Rate	Mbyte/s	10	Matrox Frame Grabber
Data Cube Collection Rate	second	1.6	Data Cube: > 128x128x128x2 Byte
NESR	W/cm ² -str- μ m	5.6e-6	calculated

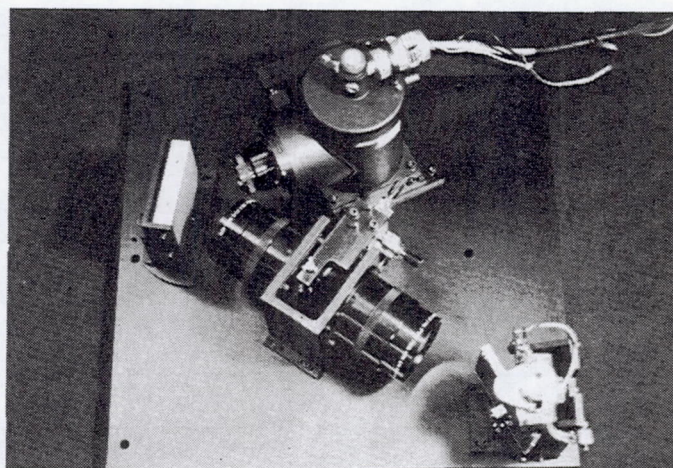
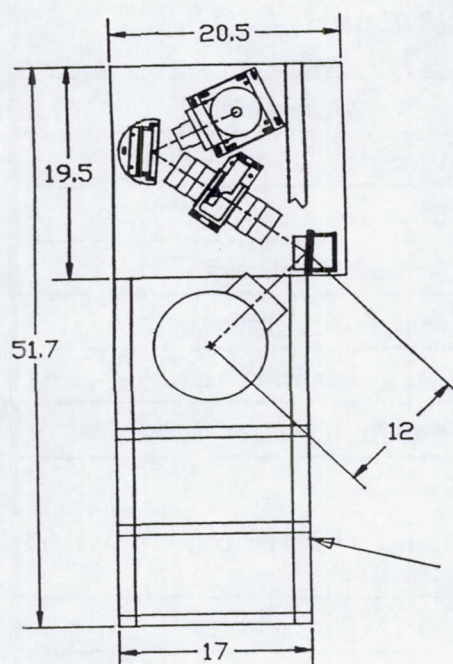


Figure 5. Optical Hardware and Overall Layout

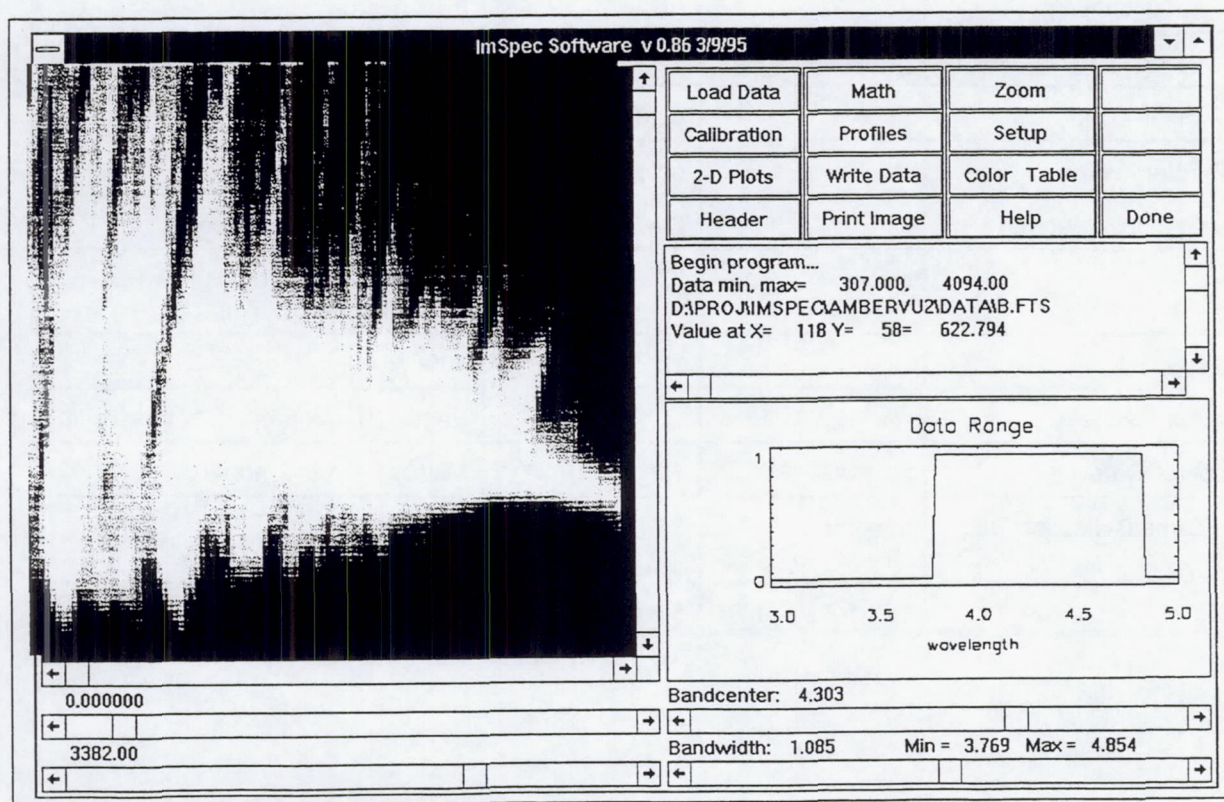


Figure 6. Main Screen Functions

Gaseous Diffusion Flames

EFFECTS OF ENERGY RELEASE ON NEAR FIELD FLOW STRUCTURE OF GAS JETS¹

Ajay K. Agrawal and Subramanyam R. Gollahalli
School of Aerospace and Mechanical Engineering
University of Oklahoma, Norman, OK

DeVon Griffin
NASA Lewis Research Center, Cleveland, Ohio

Introduction

The interaction of flames and flow structures in combustion systems has been the subject of several investigations in recent years [1-6]. The phenomena occurring in the near-field of a gas jet determine the burning characteristics and pollutant generation from its diffusion flame. The diffusion of the oxidizer near the nozzle exit governs the flame stability and flame lift-off. Entrainment of the oxidizer into the fuel jet is controlled by the Kelvin-Helmholtz instabilities in the shear layer between the fuel jet and ambient fluid, and by the buoyancy driven instabilities outside the flame. The jet growth and fuel-air mixing rates depend upon these near-field fluid dynamics which could be modified to alter the energy release and pollutant emission characteristics of diffusion flames. Thus, an understanding of the near-field structures of jet flames and physico-chemical factors affecting them is important for improving the combustion characteristics of diffusion flames.

Figure 1. taken from Savas and Gollahalli [3] shows the schlieren photographs of nonburning and burning propane jets at the same nozzle exit Reynolds number of approximately 13,000. These photographs clearly show that the flame inhibits coalescence of small scale coherent structures and hence, suppresses the radial growth of the shear layer. The lengthening of the coherent structures has been attributed to the changes in the jet fluid viscosity [1], volumetric expansion [7], and the stretching effect of buoyancy [8]. The buoyancy associated with ground experiments has prevented a clear identification of the mechanisms responsible for this effect. The buoyancy also generates vortical structures outside the flame resulting in the flame flicker [9].

The primary objective of this research is to understand how buoyancy affects the structure of the shear layer, the development of fluid dynamic instabilities, and formation of the coherent structures in the near-nozzle regions of gas jets. The secondary objectives are to study the role of buoyancy in lifting and reattachment process of diffusion flames, to evaluate the scaling behavior of diffusion flames, and to aid development and/or validation of theoretical models by providing quantitative data in the absence of buoyancy. Fast reacting hydrogen or hydrogen-inert fuels are used in this study to isolate the effects of buoyancy on fluid dynamics without masking the flame behavior by soot and radiative heat transfer. This choice of fuel also permits an evaluation of simulating low gravity in low pressure ground experiments because the similarity constraints are relaxed for the fast reacting, nonsooting diffusion flames. The diagnostics consists primarily of a color schlieren system coupled with computer generated rainbow filters, video recording and image analysis.

The project involves (i) drop tower experiments (ii) ground experiments, and (iii) theoretical analysis. The following sections describe the work accomplished to-date and the plans for future work of this project.

¹ This project was started in June 1994

Drop Tower Experiments

The apparatus for this series of experiments, shown in Figure 2, was developed by Griffin and Greenberg [10]. This consists of a color schlieren system mounted on a drop module for studies in the 2.2 second drop-tower at NASA Lewis Research Center. The schlieren system is based on 75 mm diameter, off-axis parabolic mirror optics. The white light is provided by a fiber-optics cable connected to the light source either within the module or outside at the control platform. The light emerging from a 50 micron slit is collimated by a 300 mm focal length lens and decollimated by a 3000 mm focal length lens combination. A computer generated rainbow filter is used at the light source image to color code the ray deflections. The schlieren image is captured by a CCD color camera and transmitted fiber optically to a S-VHS video recorder and a TV monitor at the control platform.

The fuel supply system consists of a 75 ml fuel tank at 5 bar, a flow meter, a solenoid activated flow control valve, associated tubing, and an interchangeable fuel-tube. The fuel was ignited prior to the drop by a retractable hot-wire. The apparatus was controlled either manually or by an inboard computer. Prior to the drops a pre-burn was done to ensure proper functioning of the system. The schlieren images were recorded during the main run at both the normal and low gravity conditions.

Ground Experiments

The ground tests consist of experiments at atmospheric and sub-atmospheric pressures. Penner [11] found that no practical combustion process can be exactly modeled in a strict sense of similarity. This prompted Spalding [12] to suggest partial modeling where only a select few of the similarity restrictions are followed. Mortzavi et al [13] used scaling approach to obtain weakly-buoyant flames simulating low-gravity by exploiting the fact that the buoyancy scales with p^2g in laminar flames where p =pressure and g =gravitational acceleration. The finite rate reactions, soot formation and radiative heat transfer in hydrocarbon flames studied by these authors impose severe similarity constraints. Because of the fast reactions, the absence of soot and the lack of significant radiation in hydrogen flames, similarity constraints are considerably relaxed in the present study.

Figures 3 and 4 show, respectively, the schematic and a photograph of the test chamber. This 0.75m high stainless steel combustion chamber has a square cross-section (0.3m x 0.3m). The hydrogen or hydrogen/inert mixture is supplied to a fuel-tube at the center of the chamber. Because of the large chamber volume, the influence of side walls on the jet flow characteristics is expected to be negligible. Optical access is provided by glass windows (0.2m x 0.60m and 10 mm thick) on two parallel side walls. An access door to facilitate changing of the burner and a retractable spark-igniter are provided on other side walls. Upstream and downstream ends of the chamber connect, respectively, to a diffuser and a nozzle with flow smoothening honeycombs. The downstream end is connected to a vacuum pump rated to provide 0.055 m³/s (117 cfm) at up to 0.0033 bar absolute pressure. The vacuum pump is driven by a 3-phase 7.5 HP electric motor. The entire chamber is mounted on a swiveling bracket to facilitate orienting the flow direction at any angle with the gravity vector.

The burner is mounted in the collimated optical path of a color schlieren system set up on an optical rail. The schlieren system consists of a halogen light source with fiber-optics, a 50 micron aperture, and 63 mm diameter, 490mm focal length collimating and decollimating lenses. A computer generated rainbow filter is used at the light source image. The schlieren images are captured by a 3-chip CCD color video-camera connected to a microcomputer through a frame grabber. The real time schlieren images can be viewed on the computer screen and the frame sequences can be digitized and stored for post processing.

Theoretical Analysis

The analysis follows the recent investigations to simulate effects of heat release on flow structures [6,8,14-15]

by solving time-dependent conservation equations of the mixture mass, species mass fraction, momentum and energy. These equations in cylindrical polar coordinates have the following general form:

$$\frac{\partial}{\partial t}(\rho\phi) + \nabla \cdot (\rho\vec{v}\phi - \Gamma_{\phi}\nabla\phi) = S_{\phi} \quad (1)$$

where ϕ stands for the dependent variable. Γ_{ϕ} and S_{ϕ} are, respectively, the diffusion coefficient and generation rate of the variable ϕ . ρ is the density and \vec{v} is the velocity vector. The dependent variables are pressure, radial and axial velocities, sensible enthalpy, and species mass fractions. The transport equations are solved by a commercial computational fluid dynamics code, PHOENICS modified to include chemical kinetics and transport properties computed by the chemical kinetics code CHEMKIN.

Results and Discussion on the Work Completed

The first series of drop tower experiments were conducted at low fuel flow rates because of the safety concerns with releasing hydrogen in an unconfined environment. Figures 5 and 6 show schlieren pictures obtained from video recordings at a cold jet Reynolds number of 90 for two different fuel-tubes. Figure 5 pertains to the tube inside diameter of 0.58 mm, tube wall thickness of 0.15mm and the average exit velocity of 16m/s while the corresponding values in figure 6 are 1.19mm, 0.23mm, and 8m/s. The rainbow filter was one-half of the symmetric filter shown in figure 7. Figures 5 and 6 indicate that the flame widens in the absence of gravity. Video recordings also indicated low gravity flames were more stable compared to their normal gravity counterparts. These results agree with previous experiments with diffusion flames, for example, by Bahadori et al [16]. Figures 5 and 6 also show that the difference in flame width at normal and low gravity depended upon the fuel flow rate. At the same cold jet Reynolds number, the normal gravity flame was 12% wider at the higher fuel flow rate while the corresponding low gravity flame was 55% wider. The flame anchored upstream of the fuel tube exit at both normal and low gravity. This upstream distance of 2 OD at normal gravity increased to approximately 6 OD at low gravity. Similar observations were made by Haggard and Cochran [17] who used black and white infrared film to photograph the low gravity flames.

The ground experiments were conducted at atmospheric pressure for various fuel tubes and flow rates. Figure 8 shows schlieren pictures at different Reynolds numbers for a 0.58mm ID tube. These pictures were obtained using a symmetric rainbow filter shown in figure 7. The flame appears laminar at a Reynolds number of 540 (figure 8a). At higher Reynolds numbers the laminar and turbulent zones are distinguished by the flame necking. The necking distance decreases with increasing Reynolds number as the flame becomes fully turbulent, lifts-off and eventually blows-off.

The experiments at low pressures will be conducted after the validation tests on the vacuum chamber facility are completed. The analytical procedure has been used for a different project to predict ignition of natural gas [18]. This procedure is currently undergoing validation for use in the present configuration.

Future Plans

Future experiments in the drop tower will be conducted at higher Reynolds numbers. The ground experiments will be conducted for cold jets and flames at various pressures and Reynolds numbers. A high power strobing white light source will be used to capture details of the flow structures. The schlieren images will be processed to yield refractive index and temperature distributions. The analytical effort will focus on numerical simulations of the cold jets and flames studied experimentally.

Acknowledgments

This project is sponsored by the NASA Microgravity Science and Application Division grant NAG3-1594. We wish to acknowledge P.S. Greenberg and F. Miller for the helpful discussions on the rainbow schlieren system. We wish to thank R. Turley for his meticulous and hard work in fabricating and setting up the vacuum chamber facility.

References

1. Yule, A.J., Chigier, N.A., Ralph, S., Boulderstone, R., and Ventura, J., 1981, "Combustion Transition Interaction in a Jet Flame," *AIJA Journal*, vol. 19, pp. 752-760.
2. Eickoff, H., Lenze, B., and Leuckel, W., 1986, "Experimental Investigation on the Stabilization Mechanism of Jet Diffusion Flame, 20th Sym. (Int.) on Combustion, pp. 311-318, The Combustion Institute, Pittsburgh, PA.
3. Mungal, M.G., Dimotakis, P.E., and Broadwell, J.E., 1984, "Turbulent Mixing and Combustion in a Reacting Shear Layer," *AIJA Journal*, vol. 22, pp. 797-800.
4. Savas, O., and Gollahalli, S.R., 1986, "Flow Structure in the Near-Nozzle Region of Gas Jet Flames," *AIJA Journal*, vol. 24, pp. 1137-1140.
5. Chen, L.-D., Seaba, J.P., Roquemore, W.M., and Goss, L.P., 1988, "Buoyant Diffusion Flames," 22nd Sym. (Int.) on Combustion, pp. 677-684, The Combustion Institute, Pittsburgh, PA.
6. Davis, R.W., Moore, E.F., Roquemore, W.M., Chen, L.-D., Vilimpoc, V., and Goss, L.P., 1991, "Preliminary Results of a Numerical-Experimental Study of the Dynamic Structure of a Buoyancy Jet Diffusion Flame," *Combustion and Flame*, vol. 83, pp. 263-270.
7. Chen, L.-D., Roquemore, W.M., Goss, L.P., and Vilimpoc, V., 1991, "Vorticity Generation in Jet Diffusion Flames," *Combustion Science and Technology*, vol. 77, pp. 41-57.
8. Katta, V.R., and Roquemore, W.M., 1993, "Role of Inner and Outer Structures in Transitional Jet Diffusion Flame," *Combustion and Flame*, vol. 92, pp. 274-282.
9. Buckmaster, J., and Peters, N., 1986, "The Infinite Candle and Its Stability-A Paradigm for Flickering Diffusion Flames," 21st Sym. (Int.) on Combustion, pp. 1829-1836, The Combustion Institute, Pittsburgh, PA.
10. Griffin, D.W., and Greenberg, P.S., 1992, "Selected Microgravity Combustion Diagnostic Techniques," *Proc. of the 2nd Int. Microgravity Comb. Workshop*, pp. 141-148, NASA CP-10113.
11. Penner, S.S., 1955, "Similarity Analysis and the Scaling for Liquid Fuel Rocket Engines," *Combustion Researches and Reviews (AGARD)*, Chap. 12, Butterworths.
12. Spalding, D.B., 1963, "The Art of Partial Modeling," 9th Sym. (Int.) on Combustion, pp. 833-843, The Combustion Institute, Pittsburgh, PA.
13. Mortazavi, S.M., Sunderland, P.B., Jurng, J., and Faeth, G.M., 1992, "Structure and Soot Properties of Buoyant and Non-Buoyant Laminar Round-Jet Diffusion Flames," *Proc. of the 2nd Int. Microgravity Comb. Workshop*, pp. 101-114, NASA CP-10113.
14. Ellzey, J.L., and Oran, E.S., 1990, "Effects of Heat Release and Gravity on an Unsteady Diffusion Flame," 23rd Sym. (Int.) on Combustion, pp. 1635-1640, The Combustion Institute, Pittsburgh, PA.
15. Katta, V.R., Goss, L.P., and Roquemore, W.M., 1994, "Numerical Investigations of Transitional H_2/N_2 Jet Diffusion Flames," *AIJA Journal*, vol. 32, pp. 84-94.
16. Bahadori, M.Y., Stocker, D.P., Vaughan, D.F., Zhou, L., and Edelman, R.B., 1992, "Effects of Buoyancy on Laminar, Transitional, and Turbulent Gas Jet Diffusion Flames," *Proc. of the 2nd Int. Microgravity Combustion Workshop*, pp. 91-106, NASA CP-10113.
17. Haggard, J.B., and Cochran, T.H., 1973, "Hydrogen and Hydrocarbon Diffusion Flames in a Weightless Environment," *NASA TN D-7165*, 29pp.
18. Bi, H., and Agrawal, A.K., 1995, "Influence of Fluid Dynamics on Ignition of Natural Gas at Diesel Environments," *Paper No. 95-S-092*, Joint Technical Meeting, San Antonio, TX.

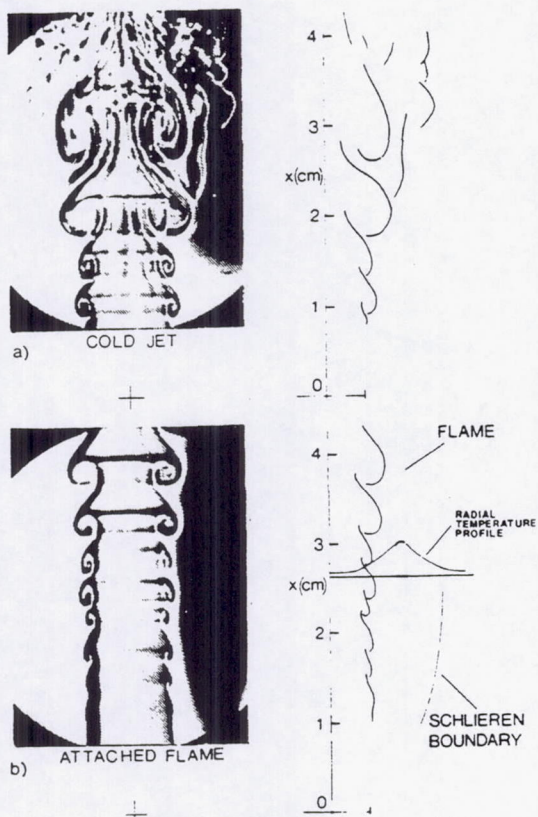


Fig. 1 Schlieren Photographs of propane cold jet and flame at $Re=13000$

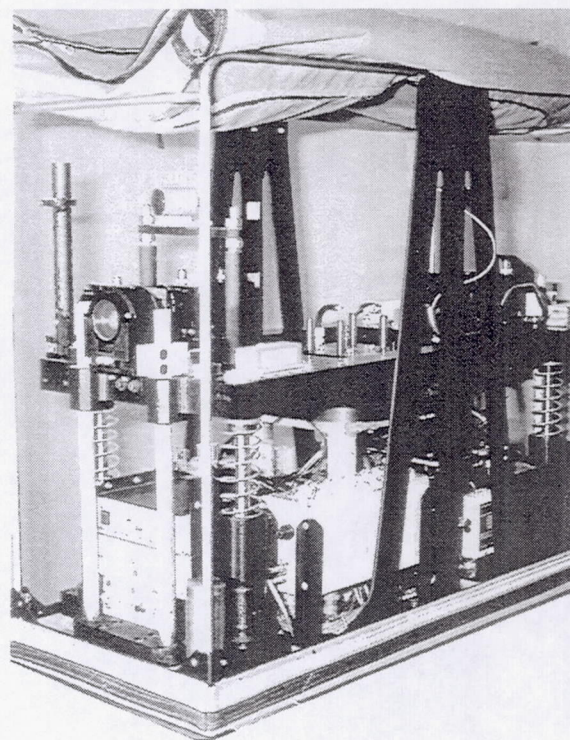


Fig. 2 The Drop Tower Test Rig

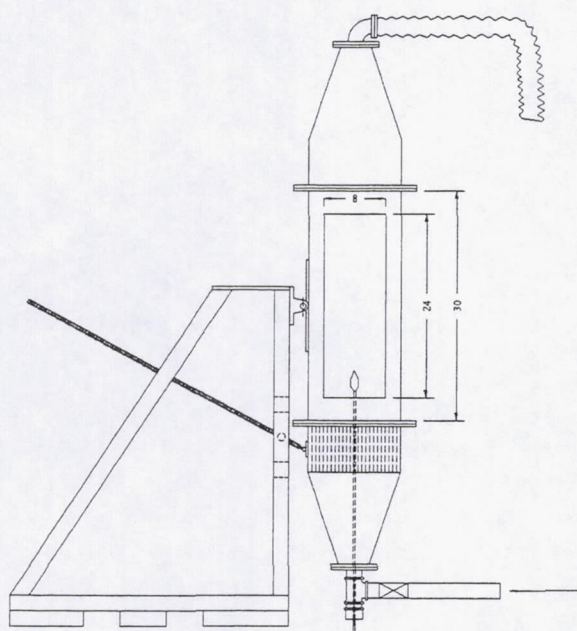


Fig. 3 Schematic of the Combustion Chamber

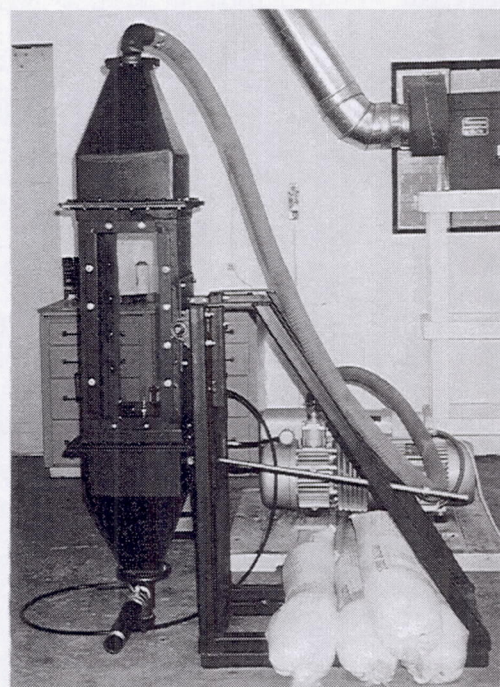


Fig. 4 A view of the Combustion Chamber

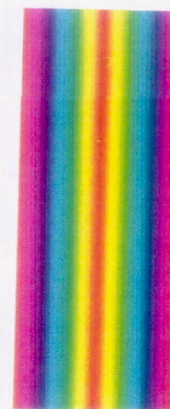
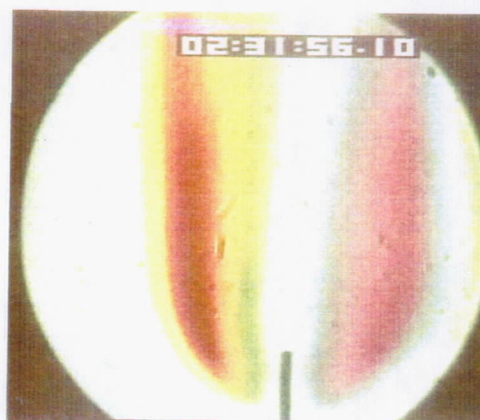
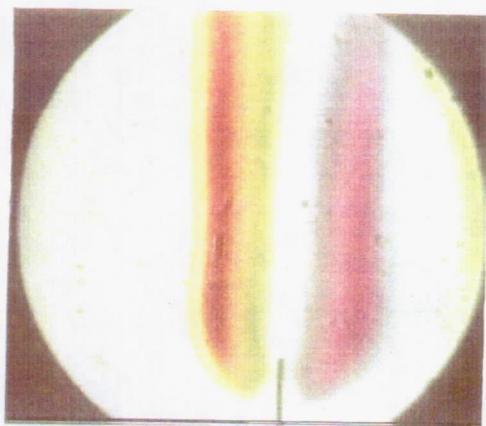
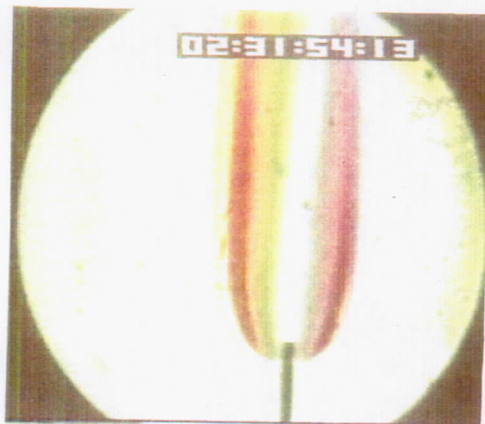
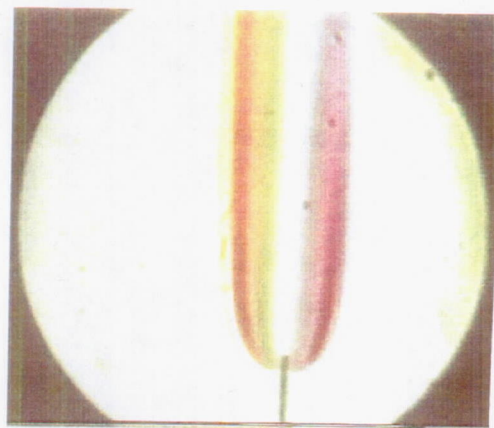


Fig. 5 Schlieren Photographs of Hydrogen Flame at $Re=90$, 0.58mm ID Fuel Tube; top) Normal Gravity, bottom) Low Gravity

Fig. 6 Schlieren Photographs of Hydrogen Flame at $Re=90$, 1.19mm ID Fuel Tube; top) Normal Gravity, bottom) Low Gravity

Fig. 7 Symmetric Rainbow Filter



a) $Re=540$

b) $Re=1200$

c) $Re=1800$

d) $Re=2400$

Fig. 8 Schlieren Photographs of Hydrogen Flame at Normal Gravity, 0.58mm ID Fuel Tube

RADIANT EXTINCTION OF GASEOUS DIFFUSION FLAMES

Arvind Atreya, Sanjay Agrawal, Tariq Shamim & Kent Pickett
University of Michigan; Ann Arbor, MI 48109

Kurt R. Sacksteder
NASA Lewis Research Center; Cleveland, OH 44135

Howard R. Baum
NIST, Gaithersburg, MD 20899

INTRODUCTION

The absence of buoyancy-induced flows in microgravity significantly alters the fundamentals of many combustion processes. Substantial differences between normal-gravity and microgravity flames have been reported during droplet combustion[1], flame spread over solids[2,3], candle flames[4] and others. These differences are more basic than just in the visible flame shape. Longer residence time and higher concentration of combustion products create a thermochemical environment which changes the flame chemistry. Processes such as flame radiation, that are often ignored under normal gravity, become very important and sometimes even controlling. This is particularly true for conditions at extinction of a μg diffusion flame.

Under normal-gravity, the buoyant flow, which may be characterized by the strain rate, assists the diffusion process to transport the fuel & oxidizer to the combustion zone and remove the hot combustion products from it. These are essential functions for the survival of the flame which needs fuel & oxidizer. Thus, as the strain rate is increased, the diffusion flame which is "weak" (reduced burning rate per unit flame area) at low strain rates is initially "strengthened" and eventually it may be "blown-out." Most of the previous research on diffusion flame extinction has been conducted at the high strain rate "blow-off" limit. The literature substantially lacks information on low strain rate, radiation-induced, extinction of diffusion flames. At the low strain rates encountered in μg , flame radiation is enhanced due to: (i) build-up of combustion products in the flame zone which increases the gas radiation, and (ii) low strain rates provide sufficient residence time for substantial amounts of soot to form which further increases the flame radiation. It is expected that this radiative heat loss will extinguish the already "weak" diffusion flame under certain conditions. Identifying these conditions (ambient atmosphere, fuel flow rate, fuel type, etc.) is important for spacecraft fire safety. Thus, the objective of this research is to experimentally and theoretically investigate the radiation-induced extinction of diffusion flames in μg and determine the effect of flame radiation on the "weak" μg diffusion flame.

RESEARCH APPROACH

To investigate radiation-induced extinction, spherical and counterflow geometries are chosen for μg & 1-g respectively for the following reasons: Under μg conditions, a spherical burner is used to

produce a spherical diffusion flame. This forces the combustion products (including soot which is formed on the fuel side of the diffusion flame) into the high temperature reaction zone and may cause radiative-extinction under suitable conditions. Under normal-gravity conditions, however, the buoyancy-induced flow field around the spherical burner is complex and unsuitable for studying flame extinction. Thus, a one-dimensional counterflow diffusion flame is chosen for *I-g* experiments and modeling. At low strain rates, with the diffusion flame on the fuel side of the stagnation plane, conditions similar to the μg case are created -- the soot is again forced through the high temperature reaction zone. The *I-g* experiments are primarily used to determine the rates of formation and oxidation of soot in the thermochemical environment present under μg conditions. These rates are necessary for modeling purposes. Transient numerical models for both μg and *I-g* cases are being developed to provide a theoretical basis for the experiments. These models include soot formation and oxidation and flame radiation and will help quantify the low-strain-rate radiation-affected diffusion flame extinction limits.

RESULTS

Significant progress has been made on both experimental and theoretical parts of this research. This may be summarized as follows:

- 1) Experimental and theoretical work on determining the expansion rate of the μg spherical diffusion flame. Preliminary results were presented at the AIAA conference (Ref. 5).
- 2) Theoretical modeling of zero strain rate transient diffusion flame with radiation (Ref. 6).
- 3) Experimental and theoretical work for determining the radiation from the μg spherical diffusion flame. Preliminary results were presented at the AIAA conference (Ref. 7).
- 4) Theoretical modeling of finite strain rate transient counterflow diffusion flame with radiation (Ref. 8).
- 5) Experimental work on counterflow diffusion flames to determine the soot formation and oxidation rates (Ref. 9).

The above experimental and theoretical work is briefly summarized in the remainder of this section.

Experimental Work: The μg experiments were conducted in the 2.2 sec drop tower at the NASA Lewis Research Center and the counterflow diffusion flame experiments (not described here) were performed at UM. For the μg experiments, a porous spherical burner was used to produce nearly spherical diffusion flames. Several experiments, under ambient pressure and oxygen concentration conditions, were performed with methane (less sooty), ethylene (sooty), and acetylene (very sooty) for flow rates ranging from 4 to 28 cm³/s. These fuel flow rates were set by a needle valve and a solenoid valve was used to open and close the gas line to the burner upon computer command. Two ignition methods were used for these experiments: (i) The burner was ignited in *I-g* with the desired fuel flow rate and the package was dropped within one second after ignition. (ii) The burner was ignited in *I-g* with a very low flow rate of H₂ and the flow was switched to the desired flow rate of the given fuel in μg just after the commencement of the drop. Following measurements were made during the μg experiments:

- i) The *flame radius* was measured from photographs taken by a color CCD camera. Image processing was used to determine both the flame radius and the relative image intensity. Sample photographs are shown in Photos E1 to E3 for ethylene and A1 to A3 for acetylene.
- ii) The *flame radiation* was measured by the three photodiodes with different spectral absorptivities. The first photodiode essentially measures the blue & green radiation, the second photodiode captures the yellow, red & near infra-red radiation, and the third photodiode is for infra-red radiation from 0.8 to 1.8 μm .
- iii) The *flame temperature* was measured by two S-type thermocouples and the sphere surface temperature was measured by a K-type thermocouple. In both cases 0.003" diameter wire was used. The measured temperatures were later corrected for time response and radiation.

It is interesting to note that for both ethylene and acetylene (see the progressive flame growth in the Color Photos) initially the flame is blue (non-sooty) but becomes bright yellow (sooty) under μg conditions. Later, as the μg time progresses, the flame grows in size and becomes orange and less luminous and the soot luminosity seems to disappear. A possible explanation for this observed behavior is suggested by the theoretical calculations of Ref. 6 & 8. The soot volume fraction first quickly increases and later decreases as the local concentration of combustion products increases. Essentially, further soot formation is inhibited by the increase in the local concentration of the combustion products and soot oxidation is enhanced [Ref.9,10]. Also, the high temperature reaction zone moves away from the already present soot leaving behind a relatively cold (non-luminous) soot shell. (A soot-shell is clearly visible in the ethylene Photo E2.) Thus, at the onset of μg conditions, initially a lot of soot is formed in the vicinity of the flame front (the outer faint blue envelope in the photographs) resulting in bright yellow emission. As the flame grows, several events reduce the flame luminosity: (i) The high concentration of combustion products left behind by the flame front inhibits the formation of new soot and promotes soot oxidation. (ii) The primary reaction zone, seeking oxygen, moves away from the soot region and the soot is pushed toward cooler regions by thermophoresis. Both these effects increase the distance between the soot layer and the reaction zone. (iii) The dilution and radiative heat losses caused by the increase in the concentration of the combustion products reduces the flame temperature which in turn reduces the soot formation rate and the flame luminosity.

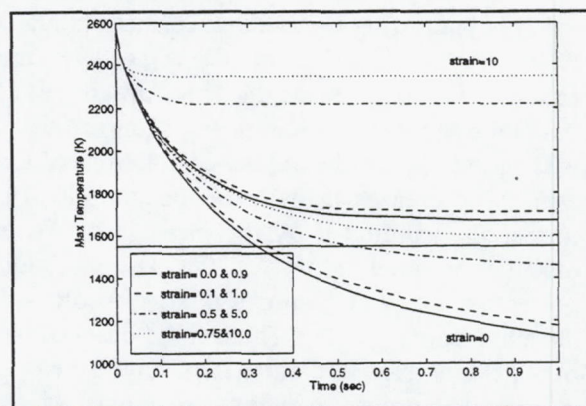
Upon further observation, we note that the ethylene flames become blue toward the end of the μg time while the acetylene flames remain luminous yellow (although the intensity is significantly reduced as seen by the photodiode measurements in Figure 2). This is because of the higher sooting tendency of acetylene which enables soot formation to persist for a longer time. Thus, acetylene soot remains closer to the high temperature reaction zone for a longer time making the average soot temperature higher and the distance between the soot and the reaction layers smaller. Eventually, as is evident from Figure 2, even the acetylene flames will become blue in μg . From Figure 2 we note that the peak radiation intensity occurs at about 2.5 cm flame radius which corresponds to a time of about 0.2 seconds. This is almost the location of the first thermocouple whose output is plotted in Figures 3 & 4 as $T_{gas}(1)$. From the temperature measurements presented in Figures 3 & 4, we note that: (i) The flame radiation significantly reduces the flame temperature (compare the peaks of the second thermocouple with those of the first for both fuels) by approximately 300K for ethylene and 500K for acetylene. (In fact, the acetylene flame seems to be on the threshold of extinction at this instant.) (ii) The temperature of the acetylene flame is about 200K lower than the ethylene flame at the first thermocouple location. (iii) The final gas temperature is also about 100K lower for the acetylene flame, which is consistent with larger radiative heat loss.

The data from the photodiodes is further reduced to obtain the total soot mass and the average temperature of the soot layer. This is plotted in Figures 5 & 6. These figures show that the average acetylene soot layer temperature is higher than the average ethylene soot layer temperature. The total soot mass produced by acetylene peaks at 0.2 seconds which corresponds to the peak of the first thermocouple, explaining the large drop in temperature. Also, the acetylene soot layer is cooling more slowly than the ethylene soot layer which is consistent with the above discussion regarding the photographic observations. Thus, for ethylene the reaction layer is moving away faster from the soot layer than in the case of acetylene. This is also consistent with the fact that ethylene soot mass becomes nearly constant but the acetylene soot mass reduces due to oxidation. Finally, the rate of increase in the total soot mass (i.e. the soot production rate) should be related to the sooting tendency of a given fuel. This corresponds to the slope of the soot mass curve in Figures 5 & 6. Clearly, the slope for acetylene is higher.

The flame radius measurements, presented in Figure 1, show a substantial change in the growth rate from initially being roughly proportional to $t^{1/2}$ to eventually (after significant radiative heat loss) being

proportional to $t^{1/5}$. In Ref. 5, we had developed a model for the expansion rate of non-radiating flames which is currently being modified to include the effects of radiant heat loss.

Theoretical Work: Due to lack of space, only our most recent theoretical work is summarized here. In this work, to quantify the low-strain-rate radiation-induced diffusion flame extinction limits, a computational model has been developed for an unsteady counterflow diffusion flame. So far, only the radiative heat loss from combustion products (CO_2 and H_2O) have been considered in the formulation. The computations show a significant reduction in the flame temperature due to radiation. The adjacent figure shows the time variations of the maximum flame temperature for various values of the strain rates. This plot shows that for flames with strain rates less than 1 s^{-1} , the effect of gas radiation is sufficient to cause extinction. These results agree with our earlier study [6] at zero strain rate where gas radiation was also found to be sufficient to cause extinction. Clearly, additional radiation due to soot will extinguish the flames at higher strain rates.

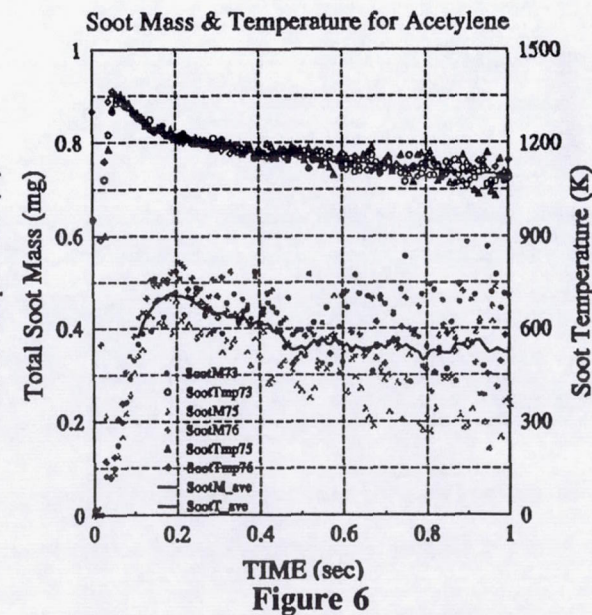
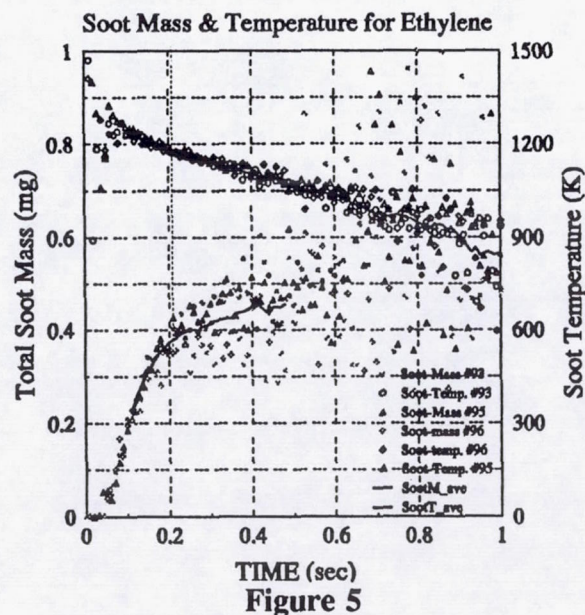
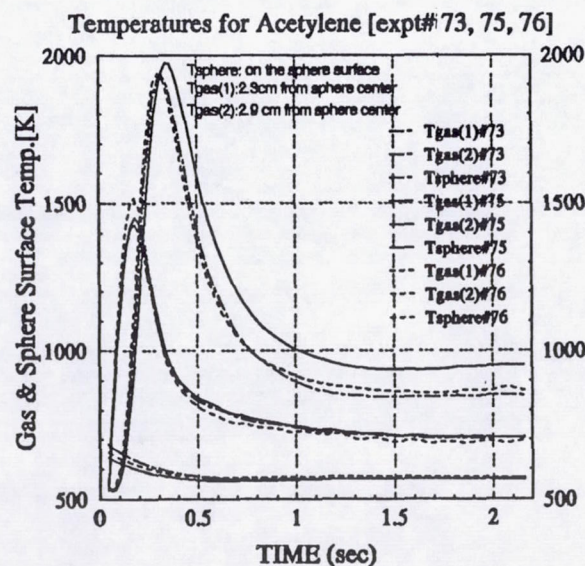
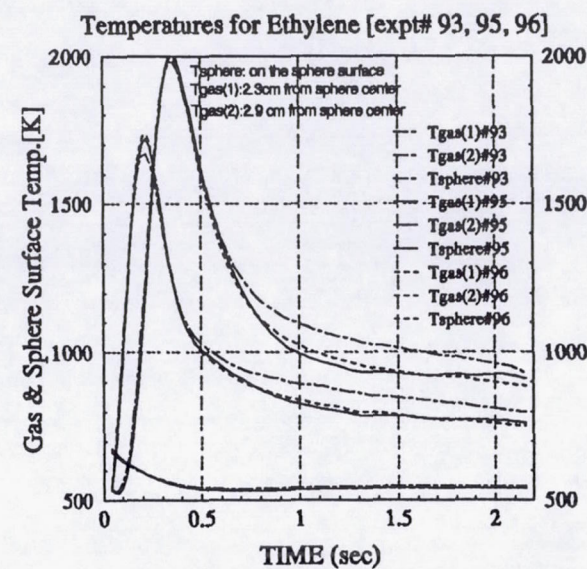
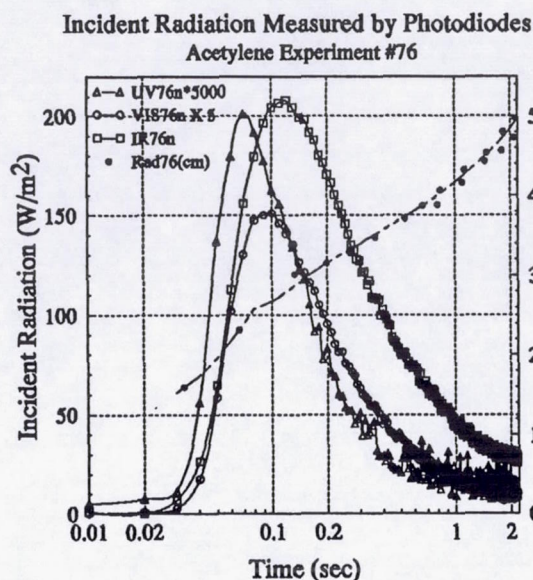
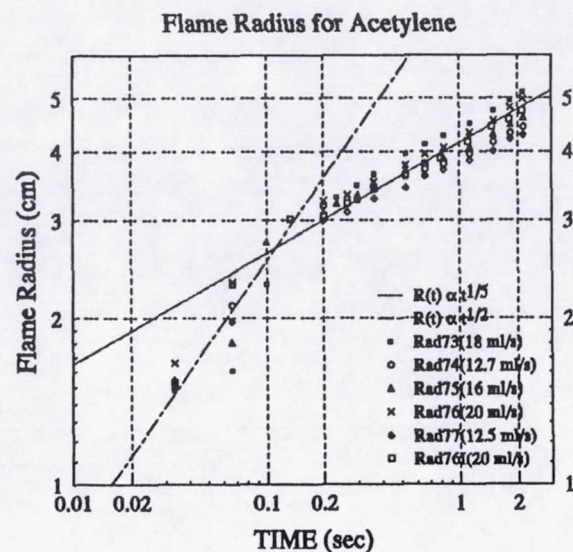


Reduction in Maximum Flame Temperature with Radiation ($T_\infty=295\text{K}$, $Y_{\text{Foc}}=0.125$, $Y_{\text{Ooc}}=0.5$)

Acknowledgements: This project is supported by NASA under contract no. NAG3-1460.

REFERENCES

1. Jackson, G., S., Avedisian, C., T. and Yang, J., C., Int. J. Heat Mass Transfer., Vol.35, No. 8, pp. 2017-2033, 1992.
2. T'ien, J. S., Sacksteder, K. R., Ferkul, P. V. and Grayson, G. D. "Combustion of Solid Fuels in very Low Speed Oxygen Streams," Second International Microgravity Combustion Workshop," NASA Conference Publication, 1992.
3. Ferkul, P., V., "A Model of Concurrent Flow Flame Spread Over a Thin Solid Fuel," NASA Contractor Report 191111, 1993.
4. Ross, H. D., Sotos, R. G. and T'ien, J. S., Combustion Science and Technology, Vol. 75, pp. 155-160, 1991.
5. Atreya, A., Agrawal, S., Sacksteder, K., and Baum, H., "Observations of Methane and Ethylene Diffusion Flames Stabilized around a Blowing Porous Sphere under Microgravity Conditions," AIAA paper # 94-0572, January 1994.
6. Atreya, A. and Agrawal, S., "Effect of Radiative Heat Loss on Diffusion Flames in Quiescent Microgravity Atmosphere," Accepted for publication in Combustion and Flame, 1993.
7. Pickett, K., Atreya, A., Agrawal, S., and Sacksteder, K., "Radiation from Unsteady Spherical Diffusion Flames in Microgravity," AIAA paper # 95-0148, January 1995.
8. Shamim, T., and Atreya, A. "A Study of the Effects of Radiation on Transient Extinction of Strained Diffusion Flames," Central States Combustion Institute Meeting, 1995.
9. Atreya, A. and Zhang, C., "A Global Model of Soot Formation derived from Experiments on Methane Counterflow Diffusion Flames," in preparation for submission to Combustion and Flame.
10. Zhang, C., Atreya, A. and Lee, K., Twenty-Fourth (International) Symposium on Combustion, The Combustion Institute, pp. 1049-1057, 1992.
11. Atreya, A., "Formation and Oxidation of Soot in Diffusion Flames," Annual Technical Report, GRI-91/0196, Gas Research Institute, November, 1991.



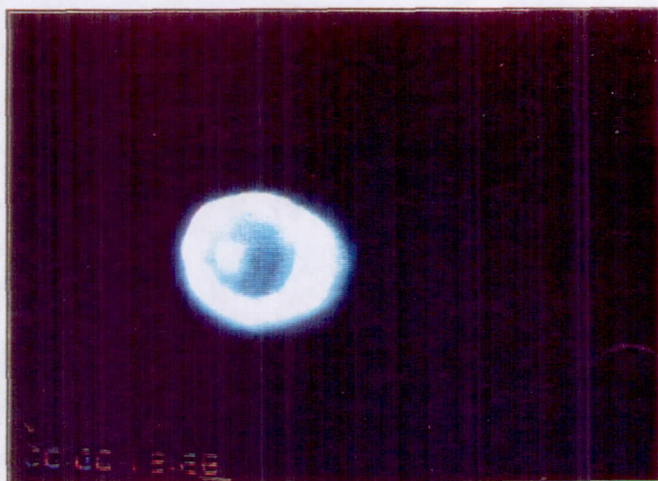


Photo E1. Ethylene flame at 0.067 sec μ g time.
(Flow rate: 20 ml/sec)

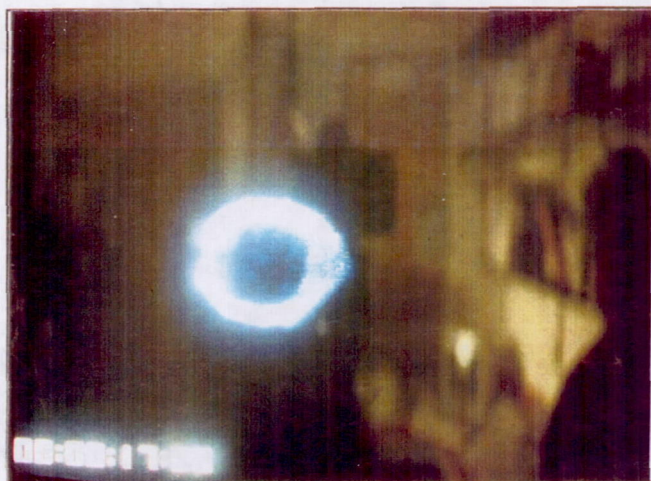


Photo A1. Acetylene flame at 0.067 sec μ g time.
(Flow rate: 20 ml/sec)

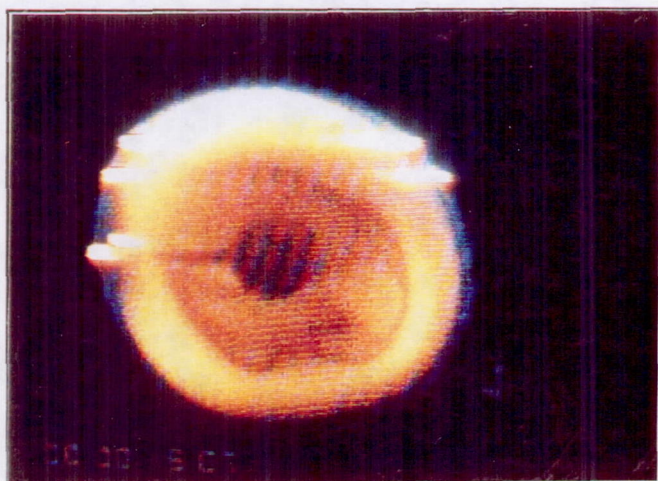


Photo E2. Ethylene flame at 1.37 sec μ g time.
(Flow rate: 20 ml/sec)

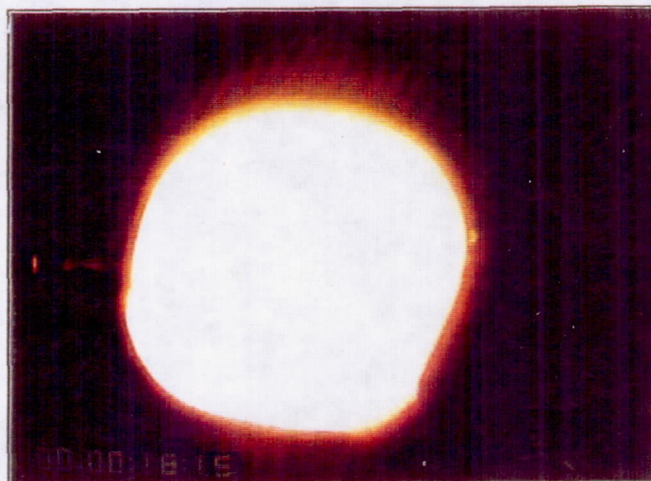


Photo A2. Acetylene flame at 0.50 sec μ g time.
(Flow rate: 20 ml/sec)



Photo E3. Ethylene flame at 1.80 sec μ g time.
(Flow rate: 20 ml/sec)

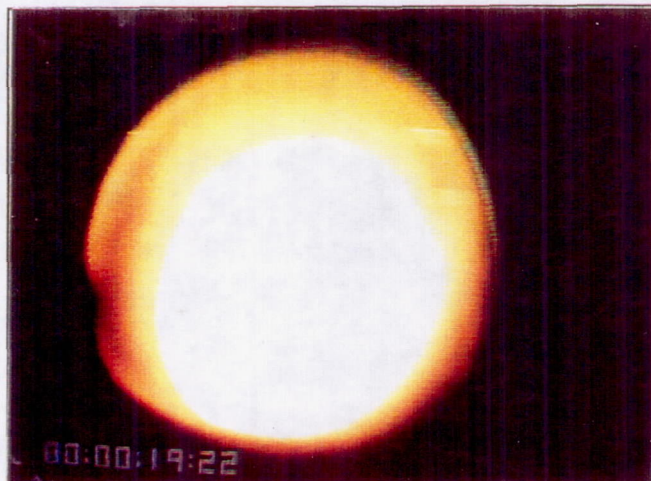


Photo A3. Acetylene flame at 1.90 sec μ g time.
(Flow rate: 20 ml/sec)

CHARACTERISTICS OF TRANSITIONAL AND TURBULENT JET DIFFUSION FLAMES IN MICROGRAVITY*

M. Yousef Bahadori[†] and James F. Small, Jr.
Science Applications International Corporation
Torrance, California 90501

Uday G. Hegde,[‡] Liming Zhou,[§] and Dennis P. Stocker
NASA Lewis Research Center
Cleveland, Ohio 44135

Introduction

This paper presents the ground-based results obtained to date in preparation of a proposed space experiment to study the role of large-scale structures in microgravity transitional and turbulent gas-jet diffusion flames, by investigating the dynamics of vortex/flame interactions and their influence on flame characteristics. The overall objective of this effort is to gain an understanding of the fundamental characteristics of transitional and turbulent gas-jet diffusion flames. Understanding of the role of large-scale structures on the characteristics of microgravity transitional and turbulent flames will ultimately lead to improved understanding of normal-gravity turbulent combustion.

Ground-based experiments conducted in this program have revealed significant differences between normal-gravity and microgravity flames (e.g., refs. 1 and 2). For example, microgravity transitional and turbulent flames are dominated by the formation and convection of large-scale structures and their interaction with the flame. Although large-scale structures are an integral part of turbulent flames in normal gravity as well, their evolution and interaction with the flame is completely different. In particular, buoyant acceleration in normal gravity promotes the formation of small scales, even at low cold-jet Reynolds numbers, which interact with the flame and with the large-scale structures. In microgravity, buoyantly induced formation of small scales is absent. Hence, microgravity gas-jet diffusion flames are dominated by large-scale structures over a significant range of Reynolds numbers. This does not imply that these flames contain a single, well-defined turbulent scale. Nor does it imply that the dynamics of disturbances are non-random. In fact, observations to date from drop-tower tests conducted in this program show that the transitional and turbulent microgravity flames contain randomly generated large-scale structures which exhibit symmetric and/or asymmetric characteristics, and therefore, have multiple instability modes. The effects of microgravity on transitional and turbulent flames is to increase the size of the smallest scales (i.e., the Kolmogorov scale) compared to the normal-gravity case (ref. 2). However, even in microgravity, the problem of multiple, interacting large scales and modes persists. In order to understand the cause of the observed behavior of transitional and turbulent diffusion flames in microgravity, one approach is to separate the effects of these interacting modes and scales by studying the response of a microgravity flame to a single mode with one time scale and one length scale.

The proposed space experiment is aimed at the effects of the structure parameters (e.g., frequency, amplitude) responsible for the observed characteristics of transitional and turbulent gas jet diffusion flames. In order to achieve this objective, large-scale, controlled disturbances are imposed on a well-defined microgravity laminar diffusion flame. Similar techniques have been used in the past in order to study the characteristics of transitional and turbulent shear layers, and to understand the interaction of vortical structures with the flame (e.g., ref. 3). A normal-gravity, laminar gas-jet diffusion flame cannot be utilized for this purpose due to buoyantly induced hydrodynamic instabilities which cause flame oscillations and introduce additional length and time scales (e.g., ref. 4). Implicit in most normal-gravity combustion models is the assumption that the behavior of the smallest scales of turbulence can be related in a specific and universal way to correlations obtained from the characteristics of large-scale structures (ref. 5). In normal-gravity, however, as Grashof number estimates clearly show (ref. 6), buoyancy profoundly influences the large scales whereas it has no effect on the smallest scales (smaller than approximately 100 microns; see ref. 6). On the other hand, in microgravity, there is no buoyant influence on the large scales. Therefore, modeling of the small scales of turbulence based on the properties of the large scale structures in microgravity will not be contaminated by buoyancy, leading to improved turbulent combustion models applicable in normal gravity.

* Paper presented at the Third International Microgravity Combustion Conference, April 11-13, 1995, Cleveland, Ohio. This work is supported by NASA Lewis Research Center under Contract NAS3-25982 (start date: November 11, 1991) with SAIC.

[†] Author for correspondence; Thermal Sciences Division, 21151 Western Avenue.

[‡] NYMA, Inc., NASA Lewis Research Center Group, Brook Park, Ohio.

[§] Analox Corp., NASA Lewis Research Center Group, Brook Park, Ohio.

Laminar/Transitional/Turbulent Flames in Microgravity

The classical behavior of laminar/transitional/turbulent gas-jet diffusion flames in normal gravity is shown by Hottel and Hawthorne (ref. 7). References 1 and 2 show that fundamental differences, such as flame height behavior with Reynolds number, onset of instabilities, extent of the transitional regime, and blow-off limit characteristics exist between the normal-gravity and microgravity flames. Thus, a major finding of this work is that buoyancy has a significant effect on these gas-jet flames regardless of the Reynolds number regime (Fig. 1). The microgravity experiments were conducted at the 2.2-second Drop Tower at the NASA Lewis Research Center. Several hydrocarbon fuels were employed with fuel being injected into quiescent air at atmospheric pressure through a nozzle of 0.45 to 1.65 mm in diameter. The cold-jet Reynolds number, based upon the nozzle diameter and inlet velocity, covered the entire range of laminar, transitional, and turbulent (up to $Re = 9000$). Both the normal-gravity and microgravity laminar flames exhibit a linear increase in luminous height with increasing jet momentum and Reynolds number. However, the microgravity flame is taller and wider than the corresponding normal-gravity flame for all regimes. Furthermore, the microgravity flames are less luminous, but due to the larger size and accumulation of hot products, they radiate up to an order of magnitude more than flames in normal gravity (ref. 8).

The transitional regime in normal gravity jet diffusion flames is characterized by the appearance of instabilities at the flame tip (at $Re \sim 2300$; see Fig. 1). The location of the onset of instability moves upstream toward the nozzle as the jet Reynolds number is increased, with the lower part of the flame maintaining its laminar characteristics. In addition, the height of the flame starts to decrease due to the enhancement of mixing caused by instabilities. Thus, the flame becomes wrinkled, increasing in surface area which increases the total transport per unit length of the flame, thereby shortening the overall flame length. Microgravity flames have been observed to be laminar for Reynolds numbers up to ~ 2000 (ref. 9). Transition in the observed microgravity flames (refs. 1 and 2) is characterized by the appearance of intermittent, naturally occurring disturbances which are generated near the flame base and are convected downstream (in contrast to the normal-gravity flames where disturbances are first observed at the flame tip). Between two successive disturbances, the flame appears laminar and undisturbed. As the jet Reynolds number increases, the frequency of occurrence of the disturbances increases. Above Reynolds number of approximately 3000, a continuous train of disturbances is formed and is convected downstream along the flame (see Fig. 1). The disturbances distort the flame as they move downstream. An important effect is their influence on the flame tip. In the laminar regime, microgravity propane flames exhibit (apparent) open tips. However, the tip tends to close when the disturbances arrive at the tip. When there is a continuous train of disturbances (i.e., in the turbulent regime), the tip closing is permanent. The height of the transitional and turbulent microgravity flames continues to increase with injection Reynolds number until near-blowoff conditions, although at a slower rate compared to the variation in the laminar regime. Note that at the higher Reynolds number (3500 and above), the normal-gravity flame height is almost constant, indicating that turbulent conditions have been achieved, whereas the microgravity flame height is still increasing (see Fig. 1). The decrease in the normal-gravity flame height as transition to turbulence commences is believed to be caused by increased turbulent transport which opposes the tendency for increased flame height due to increased jet momentum.

The correlation for turbulent flame height, H , has been traditionally established by using the laminar flame relation $H_L \sim Q/D$ and substituting the turbulent diffusivity, D_{eff} , for the molecular diffusivity D . Here, H_L is the laminar flame height and Q is the fuel volume flow rate. Furthermore, D_{eff} is assumed (ref. 10) to be proportional to the product of nozzle diameter, d , and jet exit velocity, u_o , i.e., $D_{eff} \sim u_o d$. This leads to the conclusion that the flame height in the turbulent regime is independent of the fuel flow rate and is linearly proportional to the nozzle diameter alone, that is, $H \sim d$. It would be expected that as the injection Reynolds number increases, the relative importance of forced convection would increase and the dependence on buoyancy would decrease. Thus, defining the Froude number (in terms of the injection velocity u_o , flame height H , and gravitational acceleration g) by $Fr = u_o^2/gH$, which denotes the ratio of forced convection and buoyant convection, it may be expected that as Fr becomes large, gravity effects become small. However, our studies show that the behavior of normal-gravity turbulent flames with Froude numbers in excess of 100 remains substantially different than the behavior of their microgravity counterparts. In particular, the continual increase in the microgravity flame height in the transitional and turbulent Reynolds number ranges indicates that any increased transport due to the effect of the naturally occurring disturbances does not fully overcome the effects of increased jet momentum, as in normal gravity. An estimate of the effective diffusivity in the microgravity transitional/turbulent regime may be obtained by assuming that the laminar-flame relation $H_L \sim Q/D$ holds with D replaced by the effective diffusivity D_{eff} . This yields the result that D_{eff} for the normal-gravity flames is approximately three times the value of D_{eff} for the microgravity flame (ref. 2). One reason for this difference in the values of D_{eff} in microgravity and normal gravity is due to the preferential generation of smaller scales in normal gravity compared to microgravity. Large scales are not very effective in the fine-scale mixing process (required to enhance combustion rates and reduce flame height for a given flow rate) since their action is primarily to move packets of fluid from one location to another. Small scales, on the other hand, enhance local mixing, thereby increasing the effective diffusivity of fuel and oxidizer at the flame.

Additionally, in the normal-gravity turbulent flames, the base lifts off the nozzle tip, and air entrainment creates a premixed region at the base of the flame, resulting in flame stabilization at a standoff location where the flame velocity balances the local flow velocity (see Fig. 1). As the jet momentum increases beyond a critical value, this balance is no longer sustainable, resulting

in flame blowoff. For turbulent microgravity flames, our studies (ref. 1) have shown that flame standoff distance is approximately 50% of that for the corresponding normal-gravity flame. This suggests that even at the base of the flame, buoyancy plays an important role in determining flame characteristics. Closely related to flame standoff is the blowoff limit. For microgravity flames, the blowoff Reynolds number is substantially higher than that of the flames in normal gravity (see Fig. 1). Near the blowoff Reynolds number, the microgravity standoff distance begins to increase, and the flame takes on a premixed appearance, and flame height begins to decrease, as shown in Fig. 1. Further increase in the Reynolds number results in blowoff in microgravity.

Vortex-Flame Interactions in Microgravity

The proposed space experiment utilizes the interaction of controlled disturbances with a laminar gas jet diffusion flame in microgravity in order to understand the fundamental vortex-flame interactions and their effects on the observed behavior of microgravity transitional and turbulent flames. The basis for this approach lies in the connection between the imposed and naturally occurring disturbances (see ref. 2), where spatial instability theory is applicable to a jet under the action of both types of disturbances for arbitrary Reynolds numbers. Therefore, imposing a harmonic disturbance on a microgravity laminar gas jet diffusion flame creates effects similar to those occurring naturally in transitional and turbulent diffusion flames observed in microgravity; this has been discussed in detail elsewhere (ref. 2).

A sinusoidally-driven iris is used to provide well-defined and controlled disturbances to interact with the flame. The plane of the iris is mounted approximately 5 mm above the nozzle tip, with its center coincident with the nozzle axis. Harmonic axisymmetric disturbances are obtained by periodically opening and partially closing the iris at 0-10 Hz. The difference between the maximum and minimum diameters of the iris (2.2 and 1.2 cm) during the pulsing is a measure of the amplitude of the disturbance. The average iris opening, amplitude and oscillation frequency define the shear-layer pulsations that are imposed on the jet flow. These disturbances have been characterized by LDV measurements under isothermal (non-reacting) conditions.

The disturbance technique has been tested on flames in the Zero-G Facility with satisfactory results. In these 5.18-second, microgravity tests, propane (at 2 cc/sec and $Re \approx 350$, based on nozzle diameter and cold-jet properties) is injected in quiescent air, and then ignited by a hot wire. The experiment chamber is equipped with thermocouples, both slice and global radiometers, a pressure transducer, a retractable ignitor, and two cameras.

Modeling

Modeling is an integral part of the program, and is needed to interpret the experimental results and improve our understanding of the fundamental mechanisms that occur in microgravity diffusion flames. The proposed space experiment utilizes a pulsed laminar flame in microgravity. Hence, a linearized analytical model is developed for the effects of imposed pulsations on the flame. Extensions to the linearized model to include non-linear terms are underway. In addition, a transient Navier-Stokes numerical model is utilized to predict the characteristics of microgravity flames under the effects of imposed pulsations.

The analytical model of the pulsed laminar flames in microgravity treats the effects of a harmonic source localized at the flame base. This simulates the naturally occurring disturbances observed to originate at the base. However, in contrast to the transitional and turbulent flames which exhibit a multiplicity of scales, the pulsed laminar flame is subjected to a disturbance of single characteristic length and time scales, in accordance with the proposed space experiment. Using this approach, the effects of the parameters of the disturbance on flame behavior can be studied. Once the effects of a single-type disturbance are identified, the model will be extended for multiple-disturbance types with arbitrary modes and scales. The analytical model is comprised of linearized, time-dependent conservation equations. It allows for both radial and axial variations of the mean velocity and temperature. The disturbances may be axisymmetric or asymmetric, and are characterized by their frequency and amplitude. A closed-form representation of the time-dependent flame shape variation is obtained by invoking the flame sheet approximation. Results are obtained for instantaneous flame shape under the action of an axisymmetric disturbance near the base of the flame, as shown in Fig. 2. As seen, the wavelength of the disturbance decreases as it is convected downstream. This is due to the higher velocities near the base of the flame and lower velocities downstream for microgravity flames, as predicted elsewhere (ref. 11). The analysis will be modified to include non-linear, second-order effects (such as mode-mode interactions).

A comprehensive transient, Navier-Stokes model is utilized to predict the characteristics of the flame under the influence of disturbances. The model provides pressure, velocity, temperature, and species fields in the presence of convective, conductive, and radiative heat transfer. Predictions such as the following will be compared with experimental data and observations to validate the model: (i) both time-averaged and oscillatory flame shapes; (ii) convection velocity of the structures; (iii) size variations of the structures along the flame; (iv) both time-averaged and oscillatory temperature fields. Once the model is validated, it will also be used to determine the effects of oscillations on radiation and effective transport properties for flames in the presence of a disturbance.

Results and Discussion

Unpulsed Flame: The centerline temperature of microgravity flame drops with increase in axial distance (see Fig. 3) in contrast to normal-gravity flames where the temperature drops only beyond the tip. Predictions have confirmed this behavior, as shown in Fig. 4. The temperatures in the downstream portion of the flame in Fig. 3 were still increasing at the end of the drop with those near the tip registering an increase at the rate of approximately 75 K/sec. Whereas the thermocouple closer to the nozzle exit has shown steady-state temperature data, the thermocouple near the flame tip has indicated that the upper part of the flame is still in transient state.

Tests were conducted with the global radiometers placed at different axial locations above the nozzle tip. The radial location in all cases was 10 cm from the nozzle centerline. Figure 5 plots the radiometer signals at four locations ($x = 2, 4.5, 9.5$, and 12 cm) during the last 1.5 seconds of the drop. It is seen that the highest signal is obtained at $x = 4.5$ cm which corresponds to x/L of approximately 0.45. Good agreement between predictions and data (from the last instant of the drop) for the global radiometer measurements is obtained (see Fig. 6). The predicted flame radiation shown in Fig. 6 indicates that the optimum axial location for the global radiometer in terms of the signal strength is between $0.40 < x/L < 0.55$ for the microgravity case where L is the flame length. The calculations assumed that the radiometer was located at a radial distance of 10 cm from the flame centerline consistent with the design of the proposed flight experiment. The optimum signal strength occurs a little below half-height of the flame due to the drop in flame temperature with axial distance when radiation is taken into account. The discrepancy between measurements and predictions in the upper half of the flame in Fig. 6 is due to the transient nature of radiation (see Fig. 5), as discussed below, since the predicted values are from the steady state model. Clearly, the observed increase which persists after 5 seconds of microgravity in these signals is due to increasing amounts of hot gases in the field of view of the radiometers. Estimates based upon radial diffusion suggest that the near-field of the flame will approach steady conditions after about 15 seconds of burning. However, the continuous accumulation of products may begin to affect oxidizer transport to the flame, particularly near the tip region. If this occurs, combustion near the tip may be reduced, resulting in a possible drop in thermal radiation as the production of hot gases is reduced. Pulsing and consequent increased entrainment of oxidizer into the flame may reverse this effect.

The unpulsed flame studies show the following: (a) Temperatures near the flame tip are increasing by 75 K/sec at the end of the drop (not shown here); (b) Global radiometer signals are increasing at a rate of 15% per second at the end of the drop, see Fig. 5; (c) Slice radiometer signals (not shown here) are increasing at a rate of 5% per second at the end of the drop; (d) Optimum location of the global radiometer is verified to be at $x/L \sim 0.45$, which is consistent with numerical calculations, see Fig. 6; (e) Temperature drop along the centerline of the microgravity flames is verified both experimentally (see Fig. 3) and numerically (see Fig. 4); and (f) Microgravity times longer than 5 seconds are needed to approach steady conditions in the near-field of the flame.

Pulsed Flame: The pulsed-flame studies in the Zero-G Facility were conducted for iris frequencies of 2.5, 5.0, and 7.5 Hz, with fuel flow rate of 2 cc/sec. Figure 7 shows the oscillatory centerline temperature at two axial locations for $f = 2.5$ Hz during the last two seconds of the drop. Sinusoidal variations in temperature data are obtained, since the iris is pulsed sinusoidally in this experiment. Temperature oscillations are strongest near the base of the flame. The oscillatory temperature data at different radial locations (at the centerline and near the flame) for the same axial location are shown in Fig. 8 for $f = 2.5$ Hz during the last two seconds of the drop. The data show that temperature oscillations are out of phase at the two locations due to vortex dynamics. The slice radiometer signals display the sinusoidal nature of these oscillations, as shown in Fig. 9 for two axial locations of the radiometer at $f = 2.5$ Hz during the last two seconds of the test. The centerline temperature autospectra show that the dominant frequency is the iris pulsation frequency. In addition, it is found that the centerline temperature-oscillation amplitude is smaller at higher frequencies and drops in the axial direction. Temperature coherence and slice radiation-temperature coherence of 0.95 to 1.00 are obtained from these tests.

The pulsed microgravity flame studies can be summarized as follows: (a) Iris pulsing leads to sinusoidal temperature and radiation oscillations, see Figs. 7-9; (b) Centerline temperature amplitude decreases with axial distance, which indicates damping of the disturbances; see Fig. 7; (c) Increasing the pulse frequency (results not shown here) decreases the amplitude of the centerline temperature oscillations; (d) Temperature oscillations near the centerline are 180° out of phase with oscillations near the flame sheet, which is consistent with vortex dynamics, see Fig. 8; (e) Near-perfect coherence of ~ 1 between both temperature and radiation oscillations are observed over the flame length (results not shown here), which is not observed in normal gravity; (f) Time-averaged data do not reach near-steady state in 5 seconds of microgravity, see, e.g., Fig. 7; and (g) 5 seconds of microgravity does not provide enough time to obtain statistically stationary data.

Conclusion

The microgravity tests conducted for the laminar, transitional and turbulent regimes show significant differences compared to flames in normal gravity. These include flame height behavior with Reynolds number, onset of instabilities, extent of the transitional regime, and flame stand-off and blow-off behavior. In order to gain a better understanding of characteristics of these flames, microgravity tests in preparation of a space flight experiment were conducted on the effects of imposed disturbances on a laminar diffusion flame. The tests provided data such as flame centerline temperature distribution, optimum radiometer location, temperature and radiation oscillations due to flame/disturbance interactions, and effects of imposed oscillation frequency on flame properties. The results also show that 5 seconds of microgravity is not sufficient to approach near-field steady conditions in the unpulsed or (time-averaged) pulsed flames, and to obtain statistically stationary data for the pulsed case.

References

1. Bahadori M.Y., Stocker D.P., Vaughan D.F., Zhou L., and Edelman R.B. (1993), Modern Developments in Energy, Combustion, and Spectroscopy, pp. 49-66, (F.A. Williams, A.K. Oppenheim, D.B. Olfe, and M. Lapp, eds.), Pergamon Press, New York.
2. Hegde U.G., Zhou L., and Bahadori M.Y. (1995), Combust. Sci. Tech., in press.
3. Markstein G.H. (1949), Third Symposium on Combustion, pp. 162-167, Williams and Wilkins Co., Baltimore, Maryland.
4. Strawa A.W. and Cantwell B.J. (1985), Phys. Fluids, 28 (8), 2317-2320.
5. Peters N. (1986), 21st Symposium (International) on Combustion, pp. 1231-1250, The Combustion Institute, Pittsburgh, Pennsylvania.
6. Faeth G.M. (1991), Homogeneous premixed and nonpremixed flames in microgravity: a review. AIAA/IKI Meeting, Moscow, USSR. American Institute of Aeronautics and Astronautics.
7. Hottel H.C. and Hawthorne W.R. (1949), Third Symposium on Combustion, pp. 254-266, Williams and Wilkins Co., Baltimore, Maryland.
8. Bahadori M.Y., Edelman R.B., Sotos R.G., and Stocker D.P. (1991), Radiation from gas-jet diffusion flames in microgravity environments. Paper AIAA-91-0719, AIAA 29th Aerospace Sciences Meeting, Reno, Nevada.
9. Zhou L., Hegde U.G., and Bahadori M.Y. (1992), Reduced-gravity observations of high-momentum laminar diffusion flames. Western States Meeting of The Combustion Institute, Berkeley, California.
10. Hawthorne W.R., Weddell D.S., and Hottel H.C. (1949), Third Symposium on Combustion, pp. 266-288, Williams and Wilkins Co., Baltimore, Maryland.
11. Edelman R.B. and Bahadori M.Y. (1986), Acta Astronautica, 13, 681-688.

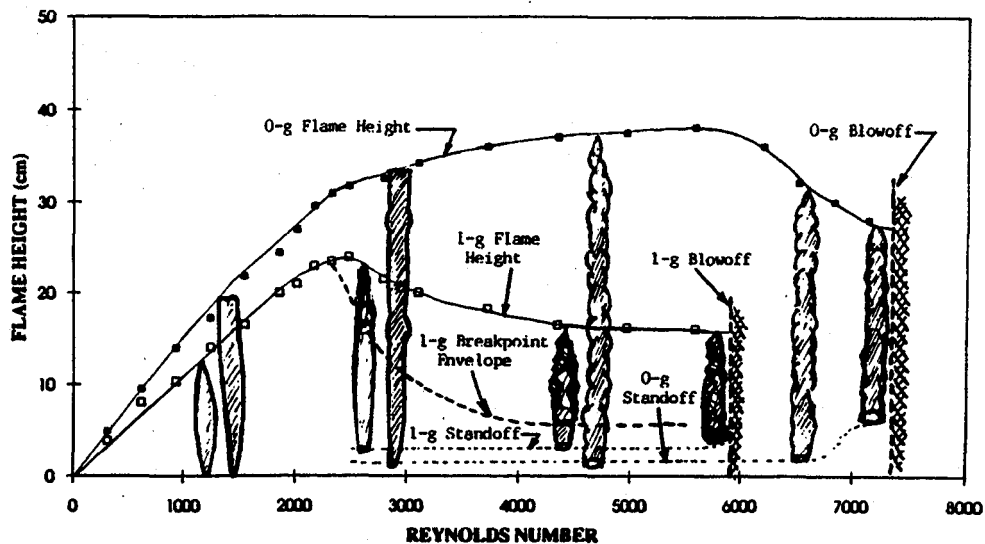


Fig. 1. Microgravity and normal-gravity heights of propane flames burning in quiescent air at 1 atm, as a function of the jet Reynolds number (based on fuel properties and nozzle diameter); nozzle diameter = 0.8 mm.

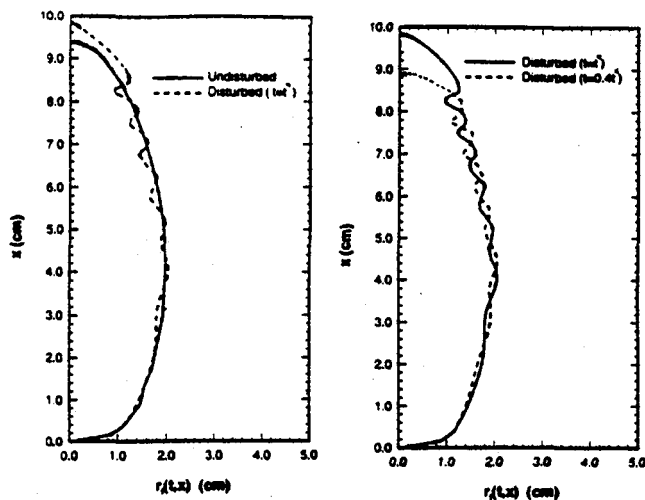


Fig. 2. Predicted instantaneous flame shape under the action of an axisymmetric disturbance mechanism located near the base of the flame. Flame shapes are shown for disturbed ($t = t^*$ and $t = 0.4 t^*$) and undisturbed cases.

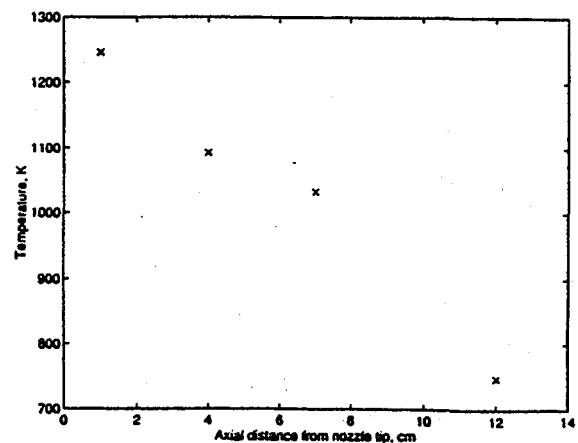


Fig. 3. Axial variation of centerline temperature for undisturbed microgravity flame of propane at 2 cc/sec. Note that the thermocouple signal for $x = 1$ cm saturated due to a limitation of the data acquisition system in the zero-g drop rig. Hence, the temperature at this location is higher than shown. The luminous flame height was between 10-11 cm.

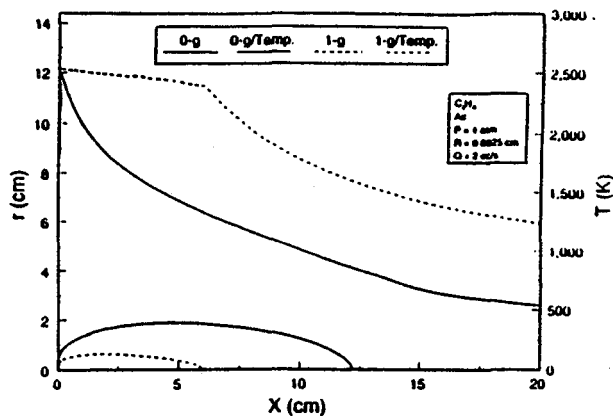


Fig. 4. Predicted flame shape and centerline temperature for both normal-gravity and microgravity flames of propane.

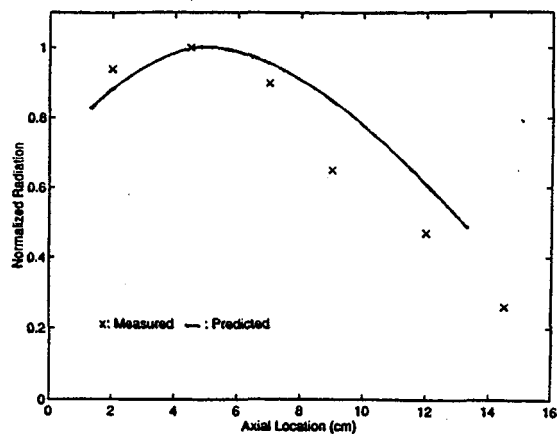


Fig. 6. Measured and predicted flame global radiation as a function of radiometer axial location for a radial location of 10 cm. The microgravity propane flame has a volume flow rate of 2 cc/sec.

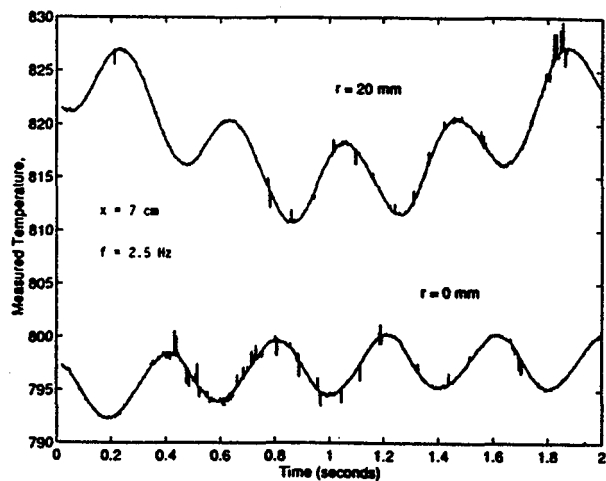


Fig. 8. Temperature during the last two seconds of the drop for two radial locations (i.e., centerline and near the flame) at axial location of 7 cm; microgravity propane flame at 2 cc/sec; iris frequency = 2.5 Hz.

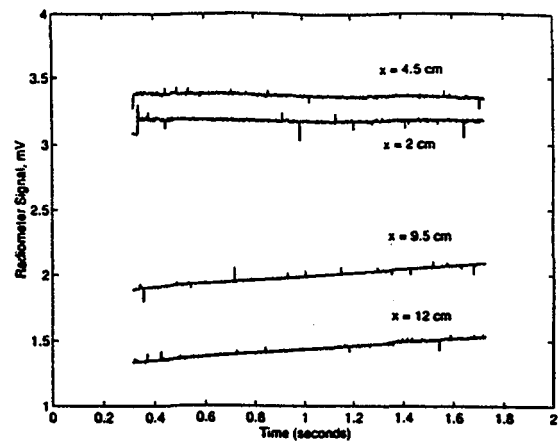


Fig. 5. Measured global radiometer signals during the final 1.5 seconds of the drop for different axial locations. The radial location is 10 cm from the flame centerline. Time $t = 0$ in the plot corresponds to 3.3 seconds after commencement of the drop.

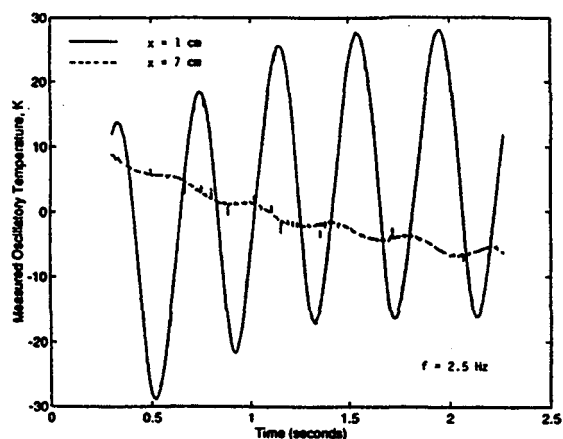


Fig. 7. Oscillatory component of centerline temperature at two axial locations for a microgravity propane flame at 2 cc/sec. The iris frequency was 2.5 Hz. The data is for the final 2 seconds of the drop.

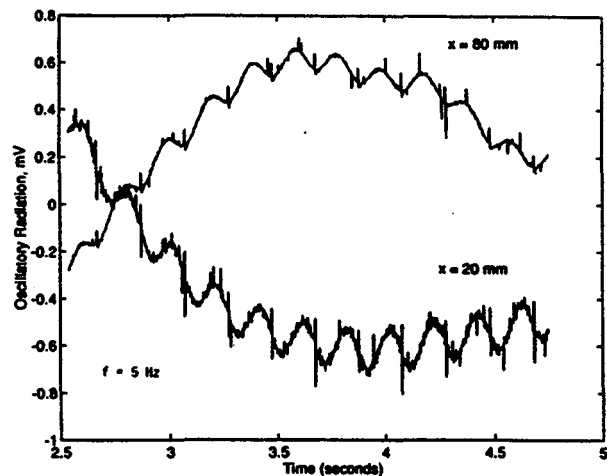


Fig. 9. Oscillatory component of slice-radiometer signal at two axial locations for a radial location of 10 cm; microgravity propane flame at 2 cc/sec; iris frequency = 5.0 Hz.

DYNAMIC RESPONSE OF A PULSED BURKE-SCHUMANN DIFFUSION FLAME

Jyh-Cherng Sheu
Dep. of Mech. Eng., The University of Iowa
Iowa City, Iowa 52242

Dennis P. Stocker
NASA Lewis Research Center
Cleveland, Ohio 44135

Lea-Der Chen
Dep. of Mech. Eng., The University of Iowa
Iowa City, Iowa 52242

Introduction

Turbulent flames are often envisioned as an ensemble of random vortices interacting with the combustion process. A better understanding of the vortex-flame interactions therefore would be useful in improving the modeling of turbulent diffusion flames. Substantial simplification may be made by investigating controlled interactions in a laminar flame, as opposed to random interactions in a turbulent flame [1]. The general goals of the research project are to improve our understanding of (A) the influence of buoyancy on co-flow diffusion flames, and (B) the effects of buoyancy on vortex-flame interactions in co-flow diffusion flames. As a first step toward Objective (B), we conducted a joint experimental and numerical investigation of the vortex-flame interaction. Vortices were produced by mechanically pulsing the fuel flow at a low frequency, e.g., 10 Hz.

Experiments were conducted using a non-flickering Burke-Schumann [2] flame in both microgravity (μg) and normal gravity (1g) as a means of varying the buoyant force without modification of the pressure (i.e., density). The effects of buoyant convection may then be determined by a comparison of the μg and 1g results. The μg results may also reveal the important mechanisms which are masked or overwhelmed by buoyant convection in 1g. A numerical investigation was conducted using a validated, time-accurate numerical code to study the underlying physics during the flame interaction and to assist the interpretation of the experimental results.

Numerical Model

The mathematical formulation was based on the Burke-Schumann flame sheet model [2]. The time-dependent, axisymmetric Navier-Stokes equations coupled with the continuity and mixture fraction equations were solved by a semi-implicit scheme, which was modified from that reported in [3], by application of a flux-corrected transport (FCT) term [4] to the QUICK-based convective flux and a second-order central differencing to the diffusional flux. The projection method was retained to solve the velocity and pressure coupling through a direct solver. Two computational grid distributions, 180 (axial) by 80 (radial) and 120 by 60, were employed to cover a computational domain of 20.1 cm (axial) by 2.33 cm (radial), matching the chimney of the experimental burner. The fuel jet diameter was set to 0.56 cm, matching the inner diameter of the experimental burner. The two different grid distributions predicted the same dynamical characteristics but the denser grid produced a better resolution for isotherm and vorticity images. Steady-state solutions were obtained for the non-pulsed case and used as the initial condition for the simulation. The computation was done using a computer Workstation (RISC-based CPU-50 MHz) or a Personal Computer (486-66 MHz, DX2). With the 120 by 60 grids, the CPU times for each time step (0.2 ms) are 5.1 s and 10.5 s for the Workstation and PC, respectively.

Modeling Results

The BSDF studied in this paper does not exhibit flickering in 1g (normal gravity) or 0g (zero gravity) for both the simulation and experimental results. In 0g, the predicted flame (stoichiometric boundary) is wider and slightly shorter than in 1g, in qualitative agreement with [5]; the luminous region of experimental μg diffusion flames were slightly taller than the 1g flames, however. To simulate the experimental pulsation of the fuel jet due to opening and closing of a solenoid valve, a sine-wave forcing with an amplitude of 80% of the mean fuel-jet velocity (u_j) was imposed on the fuel jet inlet boundary condition. The simulation shows that the imposed sine-wave perturbation results in periodic flame oscillation, responding to the imposed forcing and with a phase lag of between the maximum flame height and the maximum u_j during one forcing cycle. No tip cutting is seen at low velocity, e.g., $u_j = u_a$ (coflow air velocity) = 5 cm/s. The cutting occurs at higher velocities.

When the fuel-jet velocity is increased, flame-tip cutting (i.e., pinching and separation of the flame tip) is predicted for $u_j = u_a = 18$ cm/s, in both 0g and 1g, cf. Fig. 1. The flame contours at ten phase angles separated by 10 ms (or phase angle of 36 degrees) are shown. The 18 cm/s emulates the non-perturbed 20 cm/s condition in test 3 (cf., Table I). The arbitrarily chosen reference time, i.e., $t = 0$ ms, has a nearly matched flame shape at $t = 50$ ms for the 0g and 1g flames. The flame-tip cutting for the 1g flame occurs at $10 \text{ ms} < t < 20 \text{ ms}$, whereas in 0g, the flame tip detaches at $20 \text{ ms} < t < 30 \text{ ms}$. Unlike the 0g flame, the detached flame parcel in 1g disappeared within the 10 ms interval. The flame-tip cutting is a result of an enhanced local mixing which leads to a local mixture fraction below the stoichiometric value. This enhanced mixing can be attributed to the vortex-flame interaction in a 1g pulsed methane-air diffusion flame [6], in which the vortex was formed due to the buoyancy acceleration. The present simulation and experiments showed a similar tip-cutting in BSDF in μg . The predicted flow-field isotherm, vorticity, and velocity contours revealed a large vortex outside the flame in the BSDF with $u_j = u_a = 18$ cm/s for both the 0g and 1g conditions. The pulsation of the fuel jet was responsible for the formation of an initial vortex near the fuel nozzle. The tip cutting was seen to coincide with the formation of a new vortex near the flame tip in 1g, and below the instantaneous half flame-height in 0g.

Experiment

Tests in the 2.2-second Drop Tower at the NASA Lewis Research Center [7] were conducted by pulsing the fuel flow in a laminar BSDF. The nitrogen-diluted fuel (CH_4/N_2 50% by mole) was used to reduce the sooting since sooting obscures the true flame shape as determined from the video image. Dry air was the oxidizer, and all tests were performed at approximately 0.98 atm. The small cylindrical burner consisted of a glass chimney (i.d. of 4.66 cm and length of 20 cm) surrounding a thin-walled (0.04 cm) stainless-steel tube (i.d. of 0.56 cm), with a fuel-to-oxidizer tube diameter ratio of 0.12 [3]. Flow restrictions and straighteners were used to produce a flat velocity profile at the entrance of the annulus. The fuel tube had a straight length with a length-to-i.d. ratio of approximately 27, presumably having a parabolic flow at the exit. A single layer of fine wire mesh was placed across the outlet of the chimney to keep sand (the drop tower deceleration material) out of the burner.

The tests were performed with u_j in the range of 10 to 30 cm/s, measured with a mass flowmeter and without the pulsation. The fuel flow was pulsed at a low frequency in the range of 6.7 to 12.5 Hz by opening and closing a solenoid valve (specified response time of 5-10 ms) in the fuel supply line. The solenoid valve was closed for approximately 10 ms and then held open for the remainder of the cycle. Two particle filters (valve coefficient of 0.15) were positioned between the solenoid valve and the burner inlet to produce a small pressure drop, and thus limit the amplitude of the pulsating inlet velocity. The annular air velocity was nominally set to be equal to the non-perturbed fuel velocity. Regrettably, after cessation of these tests (due to a shutdown of the Drop Tower for rehabilitation) a noticeable leak in the oxidizer system between the flow meter and the burner was discovered. Even with the leak, the air velocity was such that the flame did not flicker when the fuel flow was not perturbed.

The flames were ignited in 1g prior to the drop, with a hot-wire ignitor which was retracted (about 1 cm) out of the flame following ignition. In a typical test, the flame was allowed to develop without pulsations for 2 s, and then pulsed for 3 s in 1g. After a pulsation-free period of 5 to 7 s, the flame was dropped and the pulsations were resumed (at 0.1 s into the drop) for 2 s in μg . Although 1g ignition leads to residual buoyant flows, the gas velocities were such that buoyant effects should be convected away in less than 1 s (e.g., a flame-zone velocity of 40 cm/s would convect buoyant effects from the 20-cm chimney in 0.5 s). Furthermore, the experiments of [8] showed that flames ignited in 1g will more quickly reach (nearly) steady conditions during the drop test, than

flames ignited in μg .

For the present investigation, the instrumentation was strictly photographic with a color video camera recording the flame's side view at 30 frames per second (or 60 fields per second) [3]. The flame response to the flow pulsations was quantified by a measurement of the flame height as a function of time, using an image-processing and object-tracking workstation at NASA Lewis [9]. When the tip cutting occurred, the detached flame parcel was included in the flame height determination [3].

Table I: Summary of Test Results.

Test	Test Conditions		Flame Response, ϕ , (and tip cutting)		Flame Height (cm)		
	Forcing Frequency (Hz)	Fuel Velocity (cm/s)	1g	μg	1g,	Mean (and std. dev.)	
					without pulsations	with pulsations	
						1g	μg
1	10	10	1 (n)	1 (n)	1.2	0.9 (0.1)	0.7 (0.1)
2	10	15	3 (n)	1 (n)	2.1	1.9 (1.1)	1.5 (0.2)
3	10	20	2 (y)	2 (n)	2.7	2.9 (2.0)	2.3 (0.7)
4	10	25	2 (y)	2 (y)	3.4	4.1 (2.6)	3.3 (1.3)
5	10	30	1 (y)	2 (y)	4.3	5.0 (2.1)	4.2 (1.8)
6	6.7	20	2 (n)	1 (n)	2.6	2.4 (1.5)	2.3 (0.8)
7	8.3	20	2 (n)	1 (n)	2.6	2.6 (1.7)	2.3 (0.6)
3	10.0	20	2 (y)	2 (n)	2.7	2.9 (2.0)	2.3 (0.7)
8	12.5	20	2 (y)	3 (y)	2.7	2.5 (1.8)	2.1 (1.0)

Experimental Results

The video recording showed that the flames pulsated in response to the flow perturbations, and tip cutting was sometimes observed. When the flow was pulsed, the flames appeared to be strongly flickering, although the oscillations were the result of the forced perturbations and not buoyancy-generated instabilities. In addition to the fundamental frequency (i.e., showing the perturbation frequency in the response), the flame also exhibited a subharmonic response which varied with the gravity level, frequency, and flow rate. The subharmonic flame response can be seen in the photographs reported in [3]. For example, when the fuel jet with a mean velocity of 18 cm/s and pulsed at 10 Hz (as in Fig. 1), the flame responded subharmonically at 5 Hz in both μg and 1g as shown by the flame-height plots in Fig. 2; the flame-tip cutting was observed in 1g but not in μg . In other tests, however, the flame responded differently in μg and in 1g. A summary of the test results is shown in Table I.

A flame frequency response parameter, ϕ , can be defined to be the ratio of (*number of fuel-flow-cycles imposed*) to (*number of flame-shape-oscillations in response*) to describe the dynamic characteristics. For example, ϕ is equal to 2 for both gravity levels shown in Fig. 2. As seen in Table I, the mean flame heights were slightly greater in 1g than μg , in contrary to the steady-state predictions of [10-12] or earlier observations of non-perturbed BSDF [5, 8, 10, 11] in which the μg flames were slightly taller than the 1g flames. However, the observation of the mean flame height being slightly less in μg is in agreement with the numerical predictions presented in this paper.

The flame height as a function of fuel flow is shown in Fig. 3. For both 1g and μg conditions, the mean flame height increased linearly proportional to the fuel flow rate (as measured when it was not perturbed). The perturbed flows were not measured; thus, the figures can be misleading because the mean perturbed flow is lower than the non-perturbed value. For this reason, the height of the non-perturbed 1g flame was included in the figures. In general, the flame-height oscillation amplitude increased with increasing flow rate, and the relative position of the mean height within the amplitude range appeared to be related to ϕ .

The variation in forcing frequency over the range of 6.7 to 12.5 Hz had a limited effect on the flame response in 1g. All four flames in Table I (i.e. with four different u_j values) responded bimodally (i.e., $\phi_{1g} = 2$), and since the fuel flow was approximately fixed, the flame height oscillations were also fairly similar in the observed maximum, mean, and minimum heights. The test procedure resulted in a reduction in fuel flow with increased frequency, because the flow rate was set under no perturbations and a constant valve closure time for each cycle

was used for all frequencies (i.e., 10 ms). The most significant effect of the forcing frequency was on the tip cutting, which was apparent in the video record for the high frequencies but not the low frequencies. However, it was also possible that the flame tip cut between video frames because the tip often pinched partially when cutting was not apparent. In μg , the flame response becomes increasingly subharmonic as the forcing frequency was increased. Other than the change in ϕ , the height oscillation of the μg flames was only moderately affected by the forcing frequency (with test 8 at $\phi_{\mu\text{g}} = 3$ showing the most dramatic change, cf. Table I). The flame frequency response, ϕ , generally increased with increasing fuel flow and forcing frequency in μg ; but ϕ varied non-monotonically with fuel flow and it was not affected by the forcing frequency in 1g. However, the tip cutting occurrence increased in both 1g and μg with increasing fuel flow or forcing frequency.

The predicted flame heights at different fuel-jet velocities are also shown in Fig. 3. The predicted mean flame height increased linearly with increasing u_j , similar to the trend observed in the experiments. The predicted mean flame heights were longer than the experimental data, but the discrepancy decreased as the fuel-jet velocity was increased. The predicted mean flame length regresses to zero at $u_j = 0$ while there is an offset for the experimental data. The offset is due to the perturbation technique which diminished the flow rate from that reported. The predictions also showed $\phi = 1$ for all the conditions examined; the experiments, however, had different ϕ values, cf. Table I.

Discussion

The flow characteristics during the tip cutting can be deduced from numerical visualization based on the predicted isotherms and vorticity. For example, in 0g and 1g flames, large vortical structures (or concentrated vorticities) were formed outside the stoichiometric surface. These concentrated vorticities were caused by the sharp velocity gradient adjacent to the injector wall, and first appeared near the fuel nozzle and were then convected downstream. In 0g, the vorticity strength decayed rapidly when the vortex was convected downstream, but this rapid decay was not observed in 1g. In 1g, the downstream maximum-vorticity was found to be comparable to (or even slightly higher than) the maximum at the fuel jet exit. Both the buoyancy acceleration and volumetric expansion significantly affected the species transport (i.e., the mixture fraction). For example, the 1g flame length continued to increase beyond the phase angle or the time instant of the maximum fuel-jet velocity at nozzle exit because of buoyant convection of the stoichiometric surface. The volumetric expansion, however, appeared to "hold up" the flame tip at certain phase angles during the forcing. In 0g, the predicted tip cutting was located at below half of the instantaneous flame height at a phase angle having a zero fuel-jet velocity at the nozzle exit. In 1g, the tip cutting occurred near the flame tip at a phase angle before the zero fuel-jet velocity was reached. The unsteady flow due to the pulsation of the fuel jet was responsible for the high vorticity value at the nozzle exit and responsible for the vortex-flame interaction. The buoyant acceleration in 1g enhances the downstream convection of combustion products, and the vortex growth. In 0g, the volumetric expansion in the fuel-lean region appeared to be a sink term in the vorticity budget; whereas in 1g, the buoyant acceleration was a source term in the fuel-lean region. The observation was consistent with theoretical analysis of the vorticity equation of a jet diffusion flame reported in [13].

The numerical simulation predicted the BSDF tip-cutting in response to the periodic forcing of the fuel jet. The simulation, however, did not predict the experimentally observed bimodal or trimodal response. On the other hand, the current numerical model was able to predict the subharmonic frequency (resulting from vortex merging) of the flame flicker for the condition reported in [14]. Thus, a parametric study was conducted to assess such effects on the flame response as different velocities, fuel-jet velocity (spatial) profile, driving waveform and driving frequency. Decreasing u_a to half or one-third of the fuel-jet velocity (i.e., to 9 or 6 cm/s) was used to simulate the leak in the experiments, but it yields only a slight decrease in flame length and the tip cutting was still predicted. The predicted ϕ value, however, did not change. Using a uniform or parabolic velocity profile at the fuel-nozzle exit did not change the prediction of ϕ either. A slightly longer maximum flame-height was predicted when the parabolic profile was used.

Three waveforms were used as the fuel-jet boundary condition in an effort to evaluate the effects due to the perturbed fuel-jet velocity profile since the profile was not quantified in the experiments. None of these waveforms, however, predicted a bimodal or trimodal response, nor a $\phi \neq 1$ response. The waveforms evaluated included (A) using a zero velocity for the initial 10 ms and followed by 20 cm/s for the remaining 90 ms of a 100 ms forcing cycle, (B) a zero velocity for the initial 10 ms, 32.5 cm/s for next 5 ms, and 19.27 cm/s for the remaining 85 ms, and (C) a zero velocity for the initial 10 ms, 53 cm/s at 10 ms and followed by an exponential

decay to preserve the averaged flow rate. The predicted flame length varied with these different waveforms; for example, the tip-cutting was not predicted. It was also observed that higher harmonic frequencies in the flow field were predicted with a 1-Hz or 2-Hz forcing of the fuel jet, when a higher-order scheme was used (i.e., the current FCT scheme). This higher harmonic frequency response, however, was not predicted when a lower-order scheme (e.g., an upwind) when the same grid resolution was used. Thus, a higher-order scheme is required for accurate prediction of dynamic response of the chemically reactive flow investigated in this paper.

To assess the effects due to the model assumptions on the prediction of flame response (or the failure in the prediction of the bimodal or trimodal response), the finite-rate chemistry, equal diffusion, and unity Lewis number assumptions were relaxed. The simulation based on the one-step global kinetics of Westbrook and Dryer [15], differential diffusion of different species, and with the non-unity Lewis number effect accounted for in the energy equation predicted essentially the same flame response, i.e., only with $\phi = 1$. The results suggested that the flame dynamics were dominated by convective flow, and the transport properties and finite rate chemistry played a secondary role. It should also be mentioned that the differential pressure across the solenoid valve was measured and there was no evidence to suggest that a sub-harmonic response existed in the valve opening and closing. Therefore, the failure to predict the bimodal or trimodal response was not due to the numerical model assumptions, nor was it due to the presence of a subharmonic response in valve characteristics. Further investigation is needed to resolve the discrepancy.

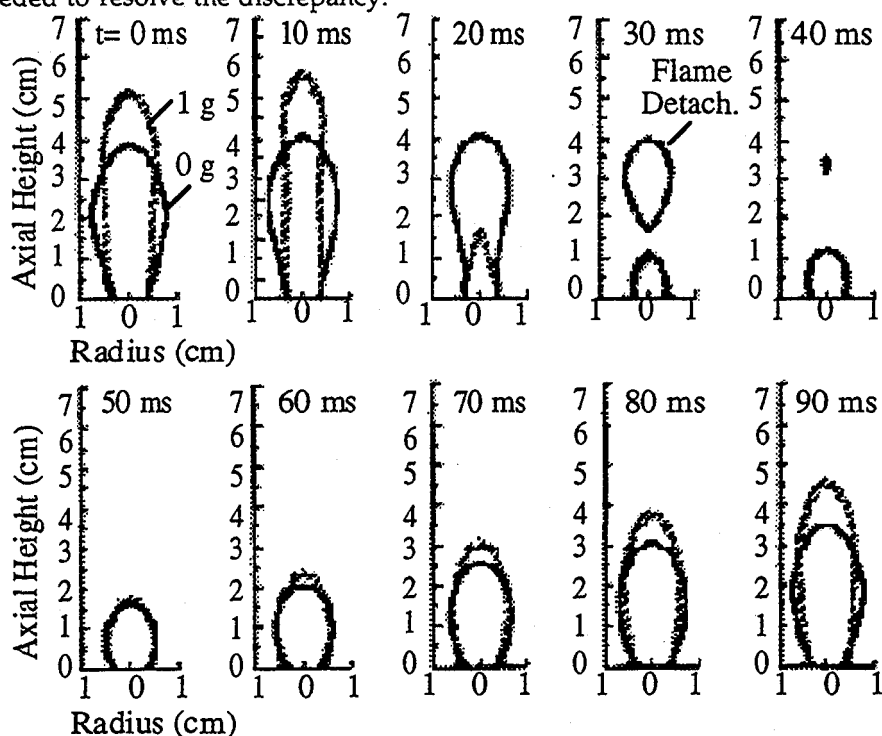


Figure 1. Predicted time evolution of flame shape with a 10-Hz driving (test 3, Table I).

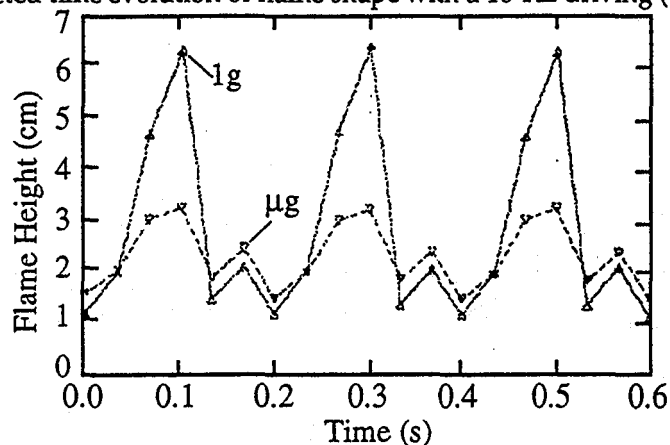


Figure 2. Observed flame height vs. time in 1g and μ g with a 10-Hz driving (test 3, Table I).

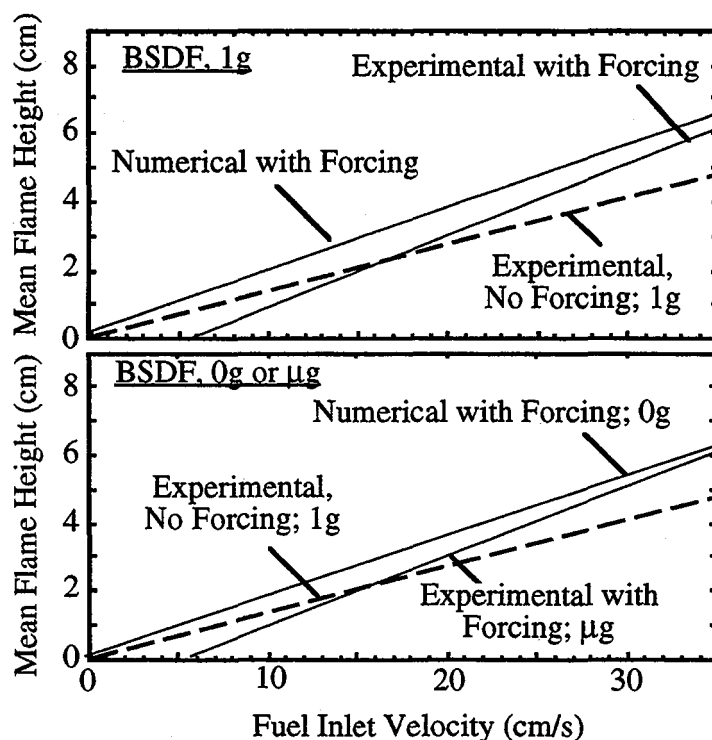


Figure 3. Flame height vs. non-perturbed fuel-jet inlet velocity; detached flame parcels are included and ϕ values are shown for fuel-jet inlet velocities of 5, 10, 20, 25 and 30 cm/s.

Acknowledgment

This research was supported by NASA Microgravity Science and Applications Division, Code UG, under Grant No. NAG3-1592.

References

1. Markstein, G.H. (1949). Third Symposium on Combustion, Flame and Explosion Phenomena Williams and Wilkins Co., Baltimore, Maryland, p. 162.
2. Burke, S.P., and Schumann, T.E.W. (1928). Ind and Engineer. Chem., Vol. 20, p. 998.
3. Stocker, D.P., Sheu, J.-C. and Chen, L.-D. (1993). Paper 93-065, 1993 Fall Meeting of the Western States Section, The Combustion Institute.
4. Zalesak S.T. (1979). J. of Comput. Phys., Vol. 31, p. 335.
5. Stocker, D.P. (1991). Paper No. 15 and No. 16, the 1991 Spring Technical Meeting of the Central States Section of The Combustion Institute, Nashville, Tennessee, April 22-24.
6. Strawa, A.W. and Cantwell, B.J. (1985). Phys. Fluids, Vol. 28, p. 2317.
7. Lekan, J. (1989). AIAA Paper No. 89-0236, (also appears as NASA TM-101397).
8. Stocker, D.P. (1990). Paper No. 42, the 1990 Spring Technical Meeting of the Central States Section of The Combustion Institute, Cincinnati, Ohio, May 20-22.
9. Klimek, R.B. and Paulick, M.J. (1992). Color Image Processing and Object Tracking Workstation. NASA TM 105561
10. Hegde, U. and Bahadori, M.Y. (1992). AIAA Paper No. 92-0334.
11. Hegde, U. and Bahadori, M.Y. (1992). An Analytical Model for Gravitational Effects on Burke-Schumann Flames. The 1992 Fall Western States Meeting of The Combustion Institute.
12. Hyer, P.V., Stocker, D.P., and Clark, I.O. (1993). AIAA Paper No. 93-0707.
13. Chen, L.-D., Roquemore, W.M., Goss, L.P., and Vilimpoc, V. (1991). Combust. Sci. Technol., Vol. 77, p. 41.
14. Chen, L.-D., Vilimpoc, V., Goss, L. P., Davis, R. W., Moore, E. F. and Roquemore, W. M. (1992). 24th Symp. (Internat.) on Combust., P. 303.
15. Westbrook, C.K. and Dryer, F.L. (1981). Combust. Sci. Technol., Vol. 27, p. 31.

FLAME-VORTEX INTERACTIONS IMAGED IN MICROGRAVITY

James F. Driscoll, Werner J.A. Dahm, Martin Sichel

Department of Aerospace Engineering
University of Michigan, Ann Arbor MI

The scientific objective of this program is to obtain high quality color-enhanced digital images of a vortex exerting aerodynamic strain on premixed and nonpremixed flames with the complicating effects of buoyancy removed. The images will provide universal (buoyancy free) scaling relations that are required to improve several types of models of turbulent combustion, including KIVA-3, discrete vortex, and large-eddy simulations. The images will be used to help quantify several source terms in the models, including those due to flame stretch, flame-generated vorticity, flame curvature and preferential diffusion, for a range of vortex sizes and flame conditions. The experiment is an ideal way to study turbulence-chemistry interactions and isolate the effect of vortices of different sizes and strengths in a repeatable manner [1-5]. A parallel computational effort is being conducted which considers full chemistry and preferential diffusion [6].

The status of the project, which began eight months ago is as follows.

- a) The Flame-Vortex Experiment to be dropped in the NASA 2.2 second drop tower has been constructed and has been transported to NASA Lewis for a safety inspection; a final safety clearance is pending. Drops are scheduled to begin in one month.
- b) One-g baseline tests have been conducted which have yielded one hundred high resolution PIV images showing the time history of the velocity field for ten different vortex conditions; considerable improvements to the PIV diagnostics also were made. The flame-generated vorticity was imaged and some determinations of flame stretch rates were made.
- c) A two-color white light PIV system that is suitable for the drop experiment was designed and is being tested. A second experiment to study nonpremixed flames is being designed; results will be compared to new modeling approaches developed by Dahm, et al. [7].
- d) The numerical simulation effort has begun [6]; a graduate student (Fernando Costa) spent several months at The Naval Research Laboratory using the code FLAME1D

-DFLM93 to identify the effects of full chemistry and differential diffusion on unsteady diffusion flames. Plans have been made by Dr. Kailasanath to simulate some of the experiments.

The one-g baseline test results will be compared to the drop tower results in order to quantify the complicating effects of buoyancy, including the generation of baroclinic torques and the buoyancy-induced stabilizing mechanisms that inhibit flame wrinkling. The factors that are of primary interest are the unsteady physics of a vortex passing through the flame, and the flame curvature that is caused by the wrinkling process. It is now known that aerodynamic strain/stretch effects are not simply of academic interest but cause large, measurable changes in the burning velocity, local extinction, and the production of CO, NO and soot.

The Experimental Apparatus

The flame-vortex experiment to be dropped in the NASA 2.2 sec Drop Tower next month is shown in Fig. 1. The experiment is a rectangular tube of dimensions 10 cm by 10 cm by 60 cm. All four walls have Lexan shockproof windows. The chamber is filled with a lean premixed fuel air mixture; fuels to be used are methane, propane and hydrogen. A loudspeaker is pulsed to create a toroidal laminar vortex ring and the ignitor near the upper wall creates a flat, non-wrinkled laminar flame. There is sufficient time available during the 2.2 sec drop to observe the 90 millisecond interaction. The following diagnostic techniques will be employed for the premixed flame studies.

- (i) Temperature Field 2-D Images -to determine temperature profiles across the flames, heat losses, and to identify local quenching- using an array of 50 Thin Film Pyrometers and video camera
- (ii) Flame Shape, Curvature Images -using Mie scattering from oil drops, a white light sheet, a CCD camera; flame emission is imaged on a 16 mm movie camera
- (iii) PIV Images of Strain Field and Vorticity Field - using two pulsed white light sources to create red and green light sheets, imaged on 35 mm film
- (iv) Conserved Scalar (nonpremixed flame) - by seeding the fuel with alumina particles

In the later stages of the project, the feasibility of OH PLIF imaging will be investigated. Such measurements are not critical to the success of the work, but would provide important information about the flame chemistry during an unsteady stretch process. In year three it is planned to add a fuel spray into the nonpremixed experiment in order to determine the effect of vortex-induced motion on spray boundaries and the spray flame. The spray flame results will be compared to the analysis of Shiah and Sichel [8].

A computational effort [6] is being conducted in parallel with the experimental effort. Under the present plan, researchers at NRL will simulate the premixed flame-vortex interactions with full chemistry for the case of hydrogen-air flames. The simulation of heat losses, preferential diffusion, and unsteady effects are important in the understanding of the problem. For the case of nonpremixed flames, the approach has been to first simulate an unsteady 1-D diffusion flame with full chemistry and realistic diffusion coefficients; this type of simulation later will be combined with a simulation of the velocity field induced by a vortex.

Of particular interest in the nonpremixed case is the way in which a vortex creates pockets of unburned fuel or air. Such pockets may not burn completely due to strain effects, leading to excessive levels of CO and soot. The numerical code developed to date simulates the burning of strips and bubbles of fuel which are surrounded by unsteady diffusion flames. The FLAME1D/DFLM93 code developed at NRL was used. A vectorized kinetics solver (VSIAM) is employed, and a method to treat open boundaries uses an implicit Lagrangian calculation. An asymptotic coupling method is applied in conjunction with time step splitting, in order to couple the chemical kinetics and the other physical processes.

Some numerical simulations are shown in Figure 3 for the unsteady diffusion flame. Results quantify the importance of including full chemistry and preferential diffusion effects. Comparisons were made with solutions obtained assuming single step chemistry and constant diffusion coefficients.

ACKNOWLEDGMENT

This research is supported by NASA Microgravity Contract NAG3-1639.

REFERENCES

1. Driscoll, J.F., Sutkus, D., Roberts, W., Post, M. and Goss, L. "The Strain Exerted by a Vortex on a Flame", Combust.Sci.Technol. 96,213, 1994.
2. Roberts, W.L., Driscoll, J.F., Drake, M.C. and Ratcliffe, J. "OH Fluorescence Images of the Quenching of a Premixed Flame by a Vortex", Twenty-Fourth Symposium (International) on Combustion, pp. 169-176, Sydney Australia, (1992).
3. Roberts, W. and Driscoll, J.F. "A Laminar Vortex Interacting With a Premixed Flame: Formation of Pockets of Reactants", Combustion and Flame 87:245-256, 1991.
4. Roberts, W.L., Driscoll, J. F., Drake, M.C. and Goss, L.P. "Quenching of a Flame By a Vortex - To Quantify Regimes of Turbulent Combustion", Combust. Flame 94, 58, 1993.
5. Wu, M.S. and Driscoll, J. F. "Simulations of a Premixed Flame-Vortex Interaction Using a SLIC Interface Algorithm", Combustion and Flame 91:310-322, 1992.
6. Costa, F. S., Kailasanath, K., and Sichel, M., "Analysis of Unsteady 1-D Diffusion Flames", submitted for conference presentation.
7. Buch, K., Dahm, W.J. A., Dibble, R.W. and Barlow, R.S., "Structure of Equilibrium Reaction Rate Fields in Turbulent Jet Diffusion Flames" Twenty-Fourth Symposium (International) on Combustion, 1992, p. 295.5.
8. Shiah, S.M., and Sichel, M., 1993, "On the Interaction of a Dense Spray Diffusion Flame and a Potential Vortex", AIAA paper No. 93-0901.

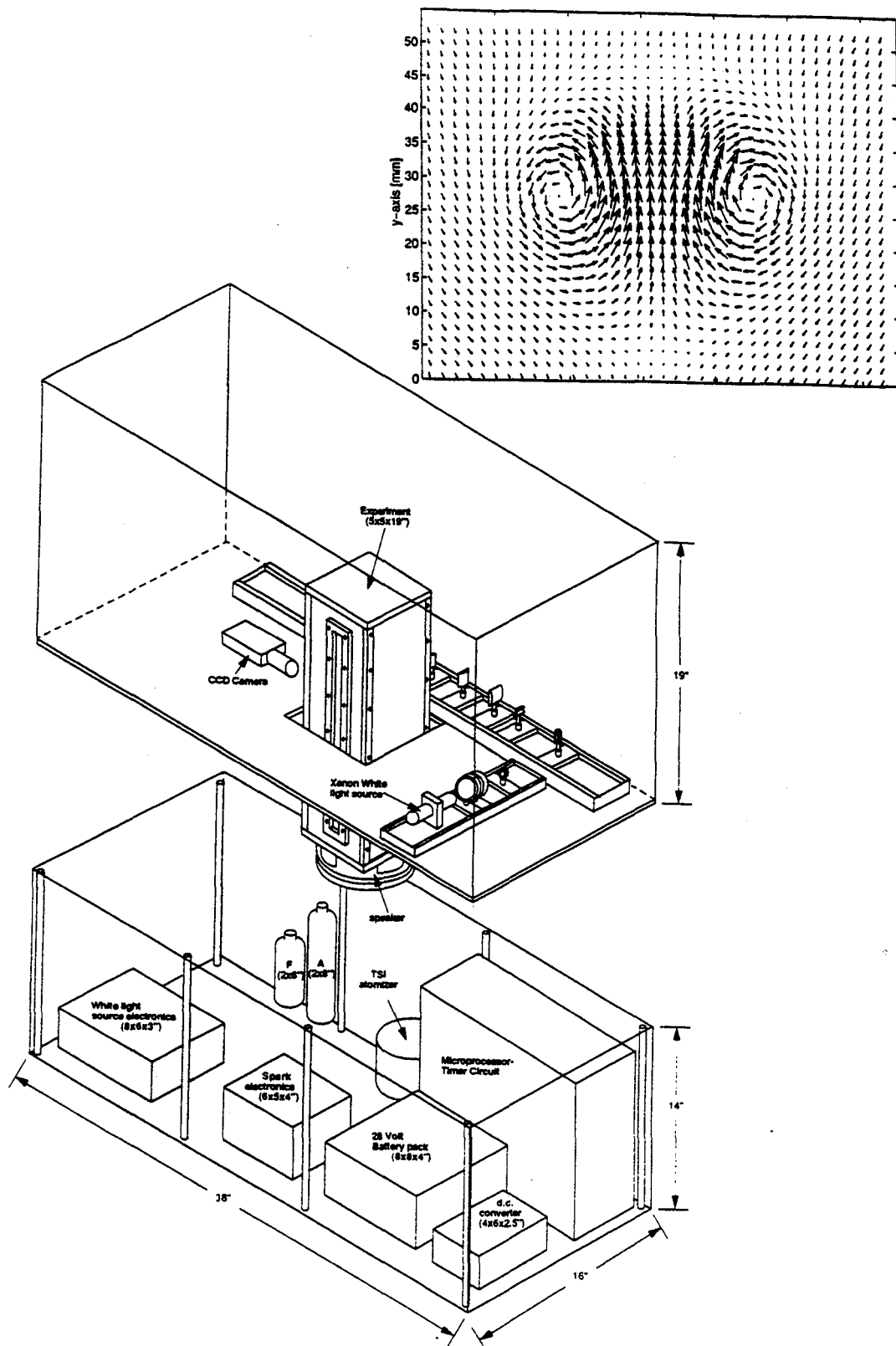


Figure 1. The Michigan Microgravity Flame-Vortex Experiment.

Shown above is a PIV velocity field image obtained at one-g; only one-third of the velocity vectors are plotted. The velocity resolution of 0.5 mm is sufficient to obtain consistent, repeatable images of the vorticity field and strain rates on the flame.

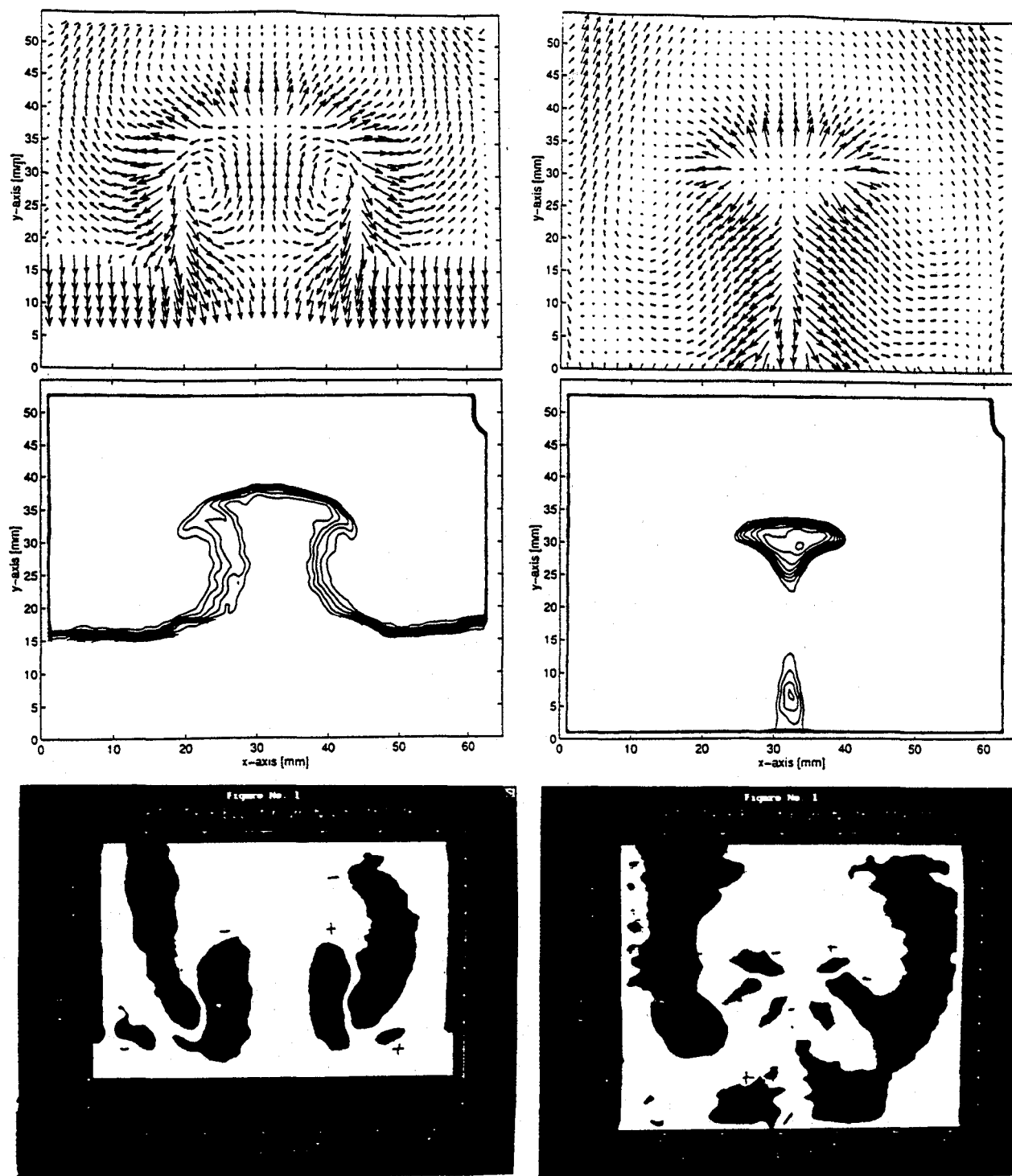


Figure 2. PIV Images of the Flame-Vortex Interaction Obtained During the One-G Baseline Tests.

Top image: velocity field (one-third of vectors plotted); middle images: premixed flame position from digitized Mie images; bottom images: vorticity field showing that the initial vortex has disappeared but flame-generated vorticity remains.

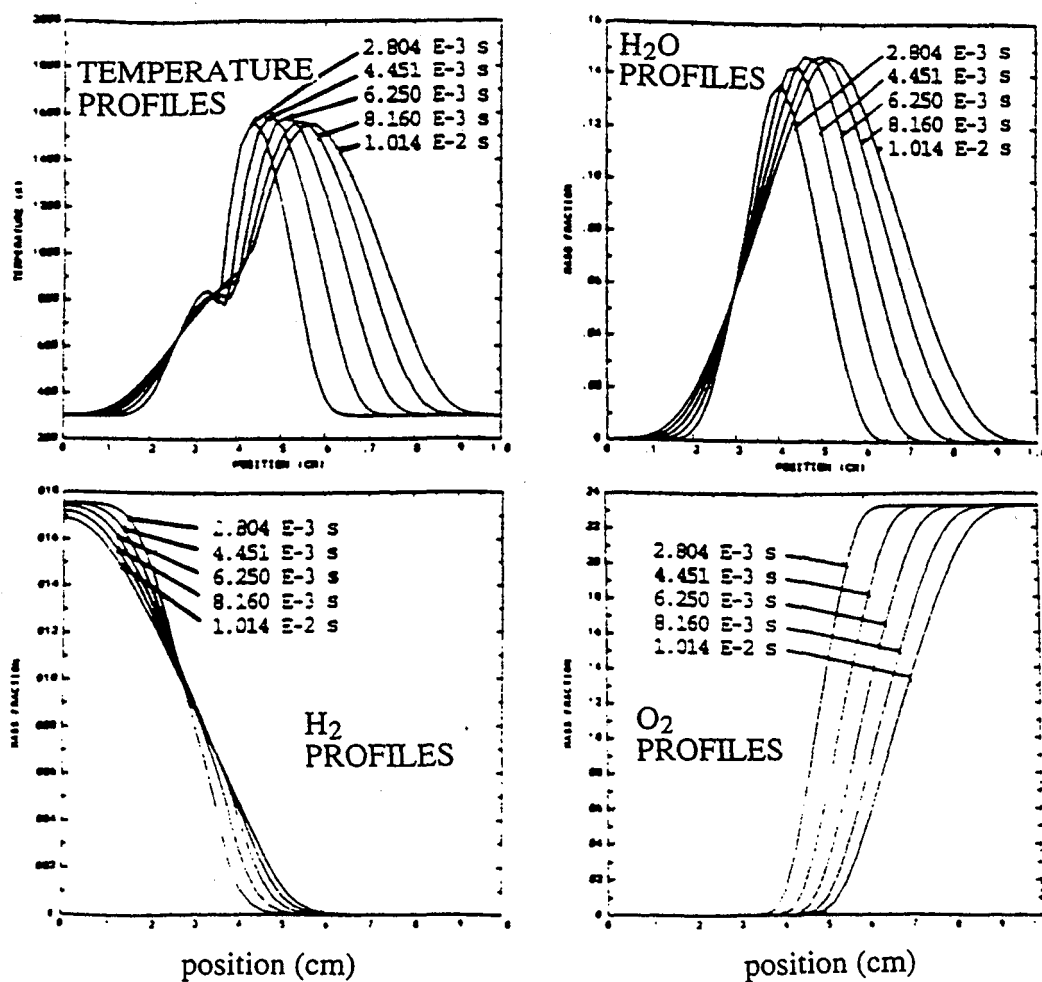


Figure 3. Calculated Temperature and Species Profiles at Different Times for An Unsteady Diffusion Flame With Full Chemistry and Differential Diffusion - to be included in future flame-vortex simulations. Collaborative effort involving F.S. Costa, K. Kailasanath (NRL), and M. Sichel.

EFFECTS OF GRAVITY ON SHEARED AND NONSHEARED TURBULENT NONPREMIXED FLAMES

Said Elghobashi, Yong-Yao Lee and Rongbin Zhong

Mechanical and Aerospace Engineering Department
University of California, Irvine, California 92717
Starting Date of Project : July 1994

1 The Problem Considered

The present numerical study is concerned with the fundamental physics of the multi-way interaction between turbulence, chemical reaction and buoyancy in a nonpremixed flame. The method of direct numerical simulation (DNS) is used to solve the instantaneous three-dimensional governing equations. Because of the present supercomputer limitations, we consider two *simple* flow geometries, namely an initially uniform flow without shear (equivalent to grid-generated turbulence) and an initially uniform shear flow. In each flow, the fuel and oxidant initially exist as two separate streams. As the reactants mix, chemical reaction takes place and exothermic energy is released causing variations in density. In the presence of a gravity field, the spatial and temporal distributions of the induced buoyancy forces depend on the local density gradients and the direction of the gravitational acceleration. The effects of buoyancy include the generation of local shear, baroclinic production or destruction of vorticity, and countergradient heat and mass transport. Increased vorticity and small-scale turbulence promote further mixing and reaction. However, if the strain-rates become too high, local flame extinction can occur.

Our objective is to gain an understanding of the complex interactions between the physical phenomena involved, with particular attention to the effects of buoyancy on the turbulence structure, flame behavior and factors influencing flame extinction.

2 Mathematical Description

2.1 Approach

We focus our attention to a location in the vicinity of the interface between two initially homogeneous gaseous reactant streams in an unbounded domain. The three-dimensional flow field is initially homogeneous isotropic or sheared turbulence with subsequent development due to density variation arising from chemical energy release and gravitational effects. A schematic of the flow configurations considered is shown in Figure 1. A simple one-step irreversible chemical reaction is considered:



in which two nonpremixed reactants (fuel F and oxidant O) react to form product P . Both finite and infinite reaction rates are considered. In the former, the reaction zone has finite thickness (flamelet), whereas the latter corresponds to the flame sheet approximation. The finite reaction rate is a function of both concentration and temperature. In the case of an infinite reaction rate, a conserved scalar formulation is employed. Transport properties of the fluid such as the mixture dynamic viscosity μ , thermal conductivity K , and mass diffusion coefficient ρD are assumed constant for the initial stages of the work. The dependence of these properties on temperature and concentration will be considered later in the study.

2.2 Governing Equations

We consider a low Mach-number turbulent flow with density variations arising from chemical energy release. Thus, the kinetic energy is small in comparison to the thermal energy. Since the time scales of the high frequency acoustic waves are several orders of magnitude smaller than those associated with the convection processes, the former do not interact effectively with the flow dynamics, and thus their effects can be filtered out from the fully compressible equations [6]. The resulting governing equations in nondimensional form are:

$$\frac{\partial \rho}{\partial t} + \nabla \cdot (\rho \mathbf{u}) = 0, \quad (2)$$

$$\nabla p^{(0)} = 0, \quad (3)$$

$$\frac{\partial (\rho \mathbf{u})}{\partial t} + \nabla \cdot (\rho \mathbf{u} \mathbf{u}) = -\nabla p^{(1)} - (1/Re) \nabla \cdot \boldsymbol{\tau} + (\rho \mathbf{e}_k)/Fr, \quad (4)$$

$$\rho \frac{\partial T}{\partial t} + \rho (\mathbf{u} \cdot \nabla) T = (1/Pr Re) \nabla \cdot (\nabla T) + Da Ce \dot{r}_T, \quad (5)$$

$$\frac{\partial (\rho Y_F)}{\partial t} + \nabla \cdot (\rho \mathbf{u} Y_F) = (1/Sc Re) \nabla \cdot (\nabla Y_F) + Da \dot{r}_F, \quad (6)$$

$$\frac{\partial (\rho Y_O)}{\partial t} + \nabla \cdot (\rho \mathbf{u} Y_O) = (1/Sc Re) \nabla \cdot (\nabla Y_O) + Da \dot{r}_O, \quad (7)$$

$$\rho = p^{(0)}/T, \quad (8)$$

where standard nomenclature is used and \mathbf{e}_k is a unit vector in the gravity direction. The pressures $p^{(0)}$ and $p^{(1)}$ are the (zeroth order) hydrostatic (or thermodynamic) pressure and the (first order) hydrodynamic pressure associated with fluid motion, respectively. In an open domain as considered here $p^{(0)}$ is constant. We also split $p^{(1)}$ into two parts, one is independent of gravity effects and the other equals $(\rho_o g z)$, thus we have in dimensionless form: $\nabla p^{(1)} = \nabla P + \mathbf{e}_k/Fr$. Equation (4) then becomes:

$$\frac{\partial}{\partial t} (\rho \mathbf{u}) + \nabla \cdot (\rho \mathbf{u} \mathbf{u}) = -\nabla P - (1/Re) \nabla \cdot \boldsymbol{\tau} + [(\rho - 1)\mathbf{e}_k]/Fr. \quad (9)$$

The non-dimensional reaction rates are

$$\dot{r}_T = (\rho Y_F)^{\nu_F} (\rho Y_O)^{\nu_O} e^{-Z_e/T}, \quad (10)$$

$$\dot{r}_i = \frac{W_i(\nu_i'' - \nu_i')}{W_F \nu_F} \dot{r}_T. \quad (11)$$

where W_i is the molecular weight of species i and ν_i' , ν_i'' are the stoichiometric coefficients for species i existing as reactant and product, respectively. The Reynolds number, Froude number, Prandtl, and Schmidt numbers are defined as

$$\begin{aligned} Re &\equiv \rho_o U_o L_o / \mu_o, \quad Fr \equiv U_o^2 / (L_o g), \\ Pr &\equiv \mu_o C_{p_o} / K_o, \quad Sc \equiv \mu_o / (\rho_o D_o), \end{aligned} \quad (12)$$

The subscript 'o' denotes the reference value for the particular quantity. The Damköhler number, defined as the ratio of the convective time to a characteristic chemical reaction time, is given by:

$$Da \equiv (L_o / U_o) / \left[\frac{W_F \nu_F}{W_F^{\nu_F} W_O^{\nu_O}} B \rho_o^{(\nu_F + \nu_O - 1)} \right]^{-1}, \quad (13)$$

where B is the pre-exponential coefficient in the dimensional expression for \dot{r}_T :

$$\dot{r}_T = (\rho Y_F / W_F)^{\nu_F} (\rho Y_O / W_O)^{\nu_O} B e^{-E_o / RT}. \quad (14)$$

The non-dimensional energy release parameter and activation energy (Zeldovich number) are:

$$\begin{aligned} Ce &\equiv [h_F^\circ W_F \nu_F + h_O^\circ W_O \nu_O - h_P^\circ W_P \nu_P] / [W_F \nu_F C_{p_o} T_o], \\ Ze &\equiv E_o / RT_o. \end{aligned} \quad (15)$$

In the limit of an infinite reaction rate, the reacting mixture is effectively at chemical equilibrium and the temperature and composition can be determined from a single conserved scalar. In this case, the above energy and species concentration equations are replaced with a single equation for the mixture fraction [8].

2.3 Numerical Procedure

The computational domain considered in the simulations is a finite cube of side length =1. The governing equations are discretized in space using finite differencing except those terms corresponding to the mean advection where a pseudospectral (Fourier) interpolation is used. In general, a finite-difference method requires a larger number of grid points for a given resolution as compared with a fully spectral method. However, the former allows more flexibility in prescribing the boundary conditions. Spatial homogeneity in the horizontal plane allows periodic boundary conditions to be imposed in the x - and y - directions. In the vertical direction, z , a convective outflow boundary condition is employed in order to allow expansion of the flow due to heat release. The simulations are initialized with divergence free velocity fields having random (Gaussian) fluctuations of prescribed correlation spectra. The initial scalar distribution represents two separate streams of (nonpremixed) reactants.

The basic numerical integration scheme follows that of [4]. Integration in time is performed via the Adams-Bashforth scheme. Pressure is treated implicitly and obtained using a Poisson solver. The basic procedure has been used to simulate both decaying isotropic and homogeneous sheared incompressible turbulence ([1] [2] [4] [3] [7]), and an exothermic turbulent nonpremixed reacting flow with zero gravity and infinite rate chemistry [8]. In the present work, further modifications have been made to include *finite rate* chemistry and *nonzero gravity*.

3 Results

Due to the imposed 6-page limit, we present only the results for $Da = \infty$ but with different values of Fr to examine the effects of gravity. As discussed earlier, for the case of $Da = \infty$ we replace equations (5), (6) and (7) with a single equation for the conserved mixture fraction. Distributions of the temperature and mass fractions of all the species are then obtained algebraically from that of the mixture fraction [8]. The results are obtained from a 96^3 mesh and initially homogeneous isotropic turbulence with $Re_{\lambda,0} = 25$, and the nondimensional energy release parameter, Ce , is prescribed such that the ratio $T_{flame}/T_o = 6$. These conditions insure the resolution of the Kolmogorov scale motion throughout the simulation. No mean shear is imposed on the flow. First we discuss the main features of the flow in **zero gravity** ($Fr = \infty$), *the base case*, using the vorticity transport equation :

$$\frac{D\omega}{Dt} = (\omega \cdot \nabla)u + \nu \nabla^2 \omega - \omega(\nabla \cdot u) + (1/\rho^2)(\nabla \rho \times \nabla p^{(1)}) . \quad (16)$$

The four terms on the rhs of Eq. (16) describe, respectively, the rate of change of ω due to stretching and tilting of the vortex lines, viscous diffusion, velocity divergence due to density variation, and baroclinic torque. In variable density flows, this last term is nonzero only if the density gradient is not aligned with the pressure gradient.

Since no mean shear is imposed on the present flow, both the vorticity and turbulence energy decay due to viscous action. In zero gravity, chemical reaction enhances the rate of vorticity decay in our flow for two reasons. First, the volumetric expansion, $(\nabla \cdot u)$, due to the exothermic energy release is positive and thus acts as a sink in Eq. (16). Second, the magnitude of the baroclinic torque near the reaction zone is small since ∇p and $\nabla \rho$ are nearly aligned parallel to the vertical direction in our flow in which the constant-density surfaces and constant-pressure surfaces are nearly horizontal. The reduction of vorticity in a mixing layer due to non-premixed chemical reaction has been also reported by McMurtry et al. [6] and by Mahalingam et al.[5] in their study of forced, low speed, axisymmetric jet diffusion flame.

The variance of the vorticity is the enstrophy which is completely determined from the turbulence energy spectrum, e.g. for incompressible flow the enstrophy is given by :

$$\omega^2(t)/2 = D(t)/(2\nu) = \int_0^\infty k^2 E(k,t) dk, \quad (17)$$

where D is the dissipation rate of the turbulence energy E , and k is the wave number. The transport equation for the enstrophy is

$$\frac{D(\omega^2/2)}{Dt} = (\omega \cdot S \cdot \omega) + \nu \nabla^2(\omega^2/2) - \nu \nabla \omega : (\nabla \omega)^T - \omega^2(\nabla \cdot u) + (1/\rho^2) \omega \cdot (\nabla \rho \times \nabla p^{(1)}), \quad (18)$$

where S is the rate of strain tensor. The terms on the rhs of Eq. (18) describe the rate of change of $(\omega^2/2)$ due to, respectively, vortex stretching or tilting, viscous diffusion, viscous dissipation, velocity divergence and baroclinic torque. It is seen that the velocity divergence and baroclinic torque have the same effect on the enstrophy as on the vorticity. Reducing the enstrophy means reducing the turbulence energy, E , and its dissipation rate, D . Reduction of D results in *increasing* the Kolmogorov scale, η , and hence a reduction of scalar gradients, scalar mixing and thus the reaction rate [8].

Simulations for **nonzero gravity** with two values of Fr (17.6 and 7.04) were performed.

Our results indicate that the baroclinic torque near the reaction zone increases with increasing the gravitational acceleration (i.e. reducing Fr). The evidence is clear both in the physical space results (contours of temperature, velocity and vorticity) and in the wave-number space (spectra of $E(k)$ and $D(k)$).

In the reaction zone, the buoyancy force causes hot products to rise in the z -direction and lower-temperature-fuel to move downwards toward the reaction zone. This is observed via the instantaneous contours of the w -velocity and temperature in any vertical (xz) plane. Thus alternating 'hot' and 'cold' fluid parcels cross the horizontal planes in the neighborhood of the reaction zone. A strong density gradient is thus established in the horizontal (x, y) directions in addition to that in the vertical direction. Accordingly $\nabla \rho$ and ∇p become misaligned thus increasing the magnitude of the baroclinic torque, the vorticity and the enstrophy. The instantaneous contours of ω_y show that it attains its maximum magnitude near the flame but it changes its sign across the reaction zone. The presence of the reaction zone between opposite-sign vorticities has been also observed by Mahalingam et al.[5] in their study of forced, low speed, buoyant axisymmetric jet diffusion flame.

Now we discuss the effect of buoyancy on the spectra of turbulence energy. Since the reacting flow is inhomogeneous in the z -direction, we can examine the spectra in horizontal planes. Figure 2 shows the spectra of the z -component of energy, $E_3(k)$, at times $t=2$ and $t=5$ and x - component of energy, $E_1(k)$, at $t=5$, for $Fr = \infty, 17.6, 7.04$ on the plane $z = 0.5$ which is the initial interface between fuel and oxidant streams. It is seen that $E_3(k)$ decreases with time for the zero-gravity case, $Fr = \infty$, as explained earlier. In contrast, the energy and dissipation (not shown) increase with lowering Fr , thus reducing the Kolmogorov length scale and increasing the integral length scale, i.e. increasing the turbulence Reynolds number. The result is a reduction of the thickness of the reaction zone and an increase of its surface area due to wrinkling, hence an increase of the total consumption rate of the reactants. The increase of energy occurs first in $E_3(k)$ at high wave numbers (Fig. 2) where chemical reaction takes place, then due to thermal diffusion all scales become affected as time increases. The transfer of turbulence energy from $E_3(k)$ to both $E_1(k)$ and $E_2(k)$ occurs via the pressure-strain interactions. The anisotropy of turbulence is seen in Fig.2 by comparing $E_3(k)$ and $E_1(k)$ at $t=5$. We also examined the balance of energy in the Fourier space:

$$dE(k)/dt = T(k) + G(k) + P(k) - D(k), \quad (19)$$

where the four terms on the rhs describe respectively the nonlinear transfer of energy in a given coordinate direction between the different scales, the transfer from potential to kinetic energy, the transfer of energy due to pressure gradients and the viscous dissipation. The time behavior of $G(k)$ shows that initially high wave numbers (small scales) are the first to be affected by gravity, and in time the peak of $G(k)$ shifts gradually to lower wavenumbers (larger scales). Also $G(k)$ is larger by at least an order of magnitude than the other terms on the rhs of Eq. (19) and increases monotonically as expected.

4 Future Work

The following phenomena will be studied in a stepwise manner during the next 3 years : 1) chemical kinetics for finite values of Da and examination of flame extinction in a range of values of Fr, Re_λ ; 2) uniform mean shear ; 3) varying the direction of the gravity vector relative to the F/O interface plane (normal or parallel) ; 4) dependence of fluid properties on temperature.

References

- [1] S.E. Elghobashi, T. Gerz, and U. Schumann. Direct simulation of turbulent homogeneous shear flow with buoyancy. *Fifth International Symposium on Turbulent Shear Flows, Cornell Univ.*, pages 227–233, 1985.
- [2] S.E. Elghobashi, T. Gerz, and U. Schumann. Direct simulation of the initial development and the homogeneous limit of the thermal mixing layer. *Sixth International Symposium on Turbulent Shear Flows, Toulouse, France*, pages 511–516, 1987.
- [3] S.E. Elghobashi and K.K. Nomura. Direct simulation of a passive diffusion flame in sheared and unsheared homogeneous turbulence. *Turbulent Shear Flows, Springer-Verlag, W.C. Reynolds, ed.*, 7:313–329, 1990.
- [4] T. Gerz, U. Schumann, and S. Elghobashi. Direct simulation of stably stratified homogeneous turbulent shear flows. *J. Fluid Mech.*, 200:563–594, 1989.
- [5] S. Mahalingam, B.J. Cantwell, and J. H. Ferziger. Full numerical simulation of coflowing axisymmetric jet diffusion flames. *Phys. Fluids*, A2:720–728, 1990.
- [6] P. A. McMurtry, J. J. Riley, and R. W. Metcalfe. Effects of heat release on the large-scale structure in turbulent mixing layers. *J. Fluid Mech.*, 199:297–332, 1989.
- [7] K.K. Nomura and S.E. Elghobashi. Mixing characteristics of an inhomogeneous scalar in isotropic and homogeneous sheared turbulence. *Phys. Fluids*, 4:606–625, 1992.
- [8] K.K. Nomura and S.E. Elghobashi. The structure of inhomogeneous turbulence in variable density nonpremixed flames. *Theoretical and Computational Fluid Dynamics*, 5:153–175, 1993.

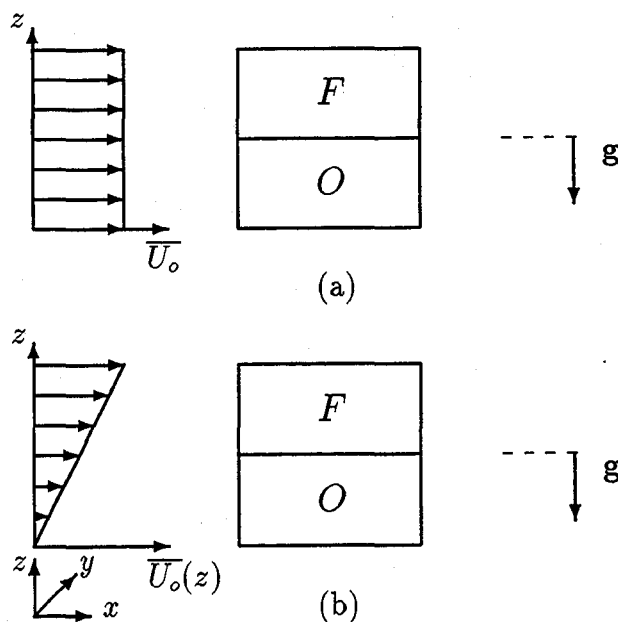


Figure 1: Schematic of flow configurations: (a) uniform mean velocity; (b) uniform mean velocity gradient in z -direction. The direction of the gravity vector may be either parallel or perpendicular to the initial interface between the fuel (F) and the oxidant (O), thus simulating a horizontal or vertical flame.

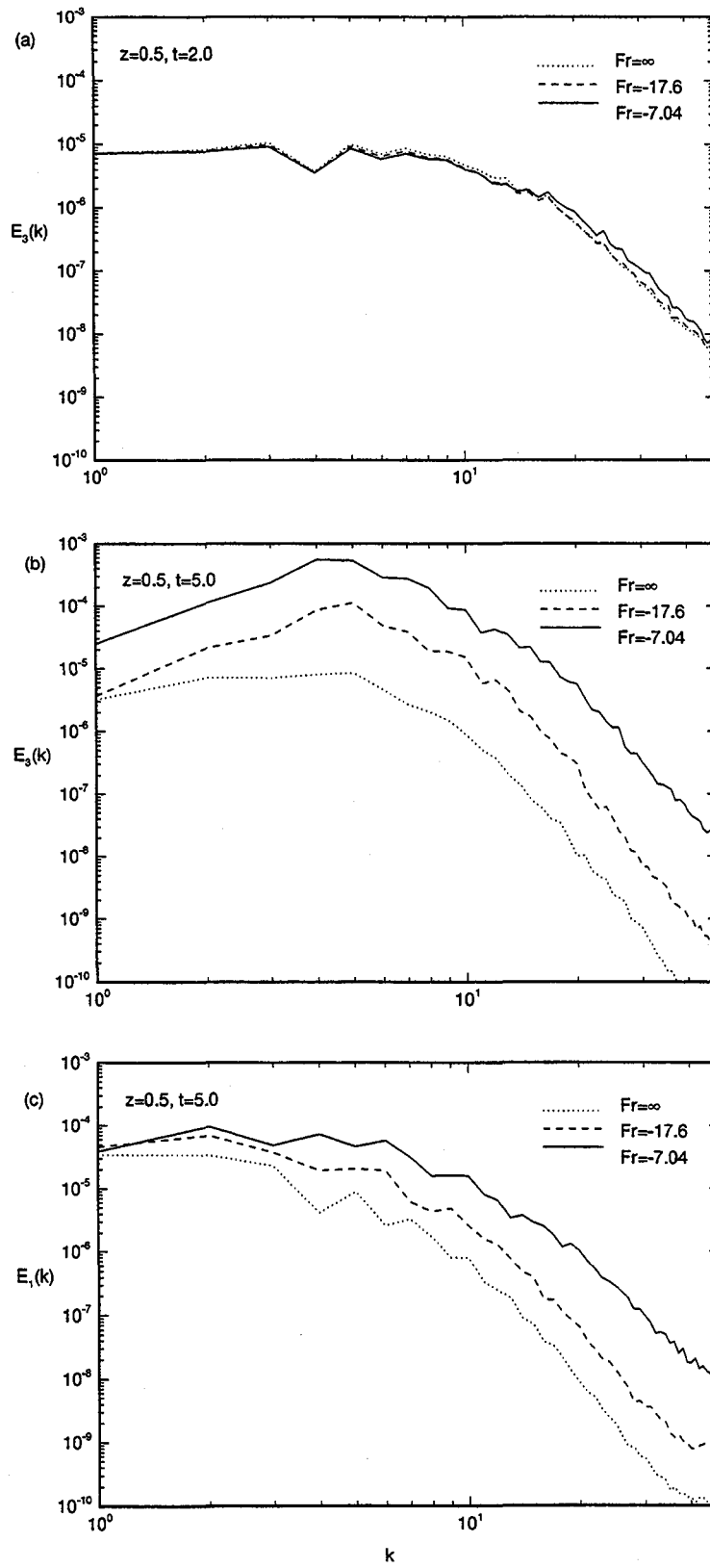


Figure 2: Spectra of turbulence energy components $E_3(k)$ and $E_1(k)$ on a horizontal plane ($z=0.5$) for different Fr .

LAMINAR SOOT PROCESSES

P.B. Sunderland, K.-C. Lin, and G.M. Faeth
The University of Michigan
Ann Arbor, Michigan

Introduction

Soot processes within hydrocarbon fueled flames are important because they affect the durability and performance of propulsion systems, the hazards of unwanted fires, the pollutant and particulate emissions from combustion processes, and the potential for developing computational combustion. Motivated by these observations, the present investigation is studying soot processes in laminar diffusion and premixed flames in order to better understand the soot and thermal radiation emissions of luminous flames. Laminar flames are being studied due to their experimental and computational tractability, noting the relevance of such results to practical turbulent flames through the laminar flamelet concept [1,2]. Weakly-buoyant and nonbuoyant laminar diffusion flames are being considered because buoyancy affects soot processes in flames while most practical flames involve negligible effects of buoyancy [1,2]. Thus, low-pressure weakly-buoyant flames are being observed during ground-based experiments while near-atmospheric pressure nonbuoyant flames will be observed during space flight experiments at microgravity. Finally, premixed laminar flames also are being considered in order to observe some aspects of soot formation for simpler flame conditions than diffusion flames. The present discussion of the investigation is brief, see Refs. 2-20 for more details.

An understanding of soot structure and optical properties is prerequisite to reliable measurements of soot processes in flames; therefore, the initial phases of the investigation emphasized this technology [3-8]. The structure of soot can be seen from the transmission electron microscope (TEM) photograph appearing in Fig. 1. Typical of past observations [21-23], the present soot consists of roughly spherical primary particles having nearly constant diameters at a particular location, collected into aggregates having widely varying numbers of primary particles per aggregate. Aggregates are open structured and can have maximum dimensions up to several μm ; therefore, the approximation of Mie scattering for an equivalent sphere is never justified while use of the Rayleigh scattering approximation is questionable [4]. Fortunately, use of the Rayleigh-Debye-Gans scattering approximation for polydisperse populations of fractal aggregates is effective for soot aggregates [4-7], see the comparison between measured and predicted scattering patterns illustrated in Fig. 2. Based on this technology, methods of finding soot volume fraction and soot temperature distributions from laser extinction and multiline emission imaging measurements, needed for both the ground based and the space flight experiments, have been developed [10-13].

Present ground-based experiments involve an extensive suite of measurements to find both soot and flame properties; in contrast, the space flight experiments have limited instrumentation (flame photographs, soot volume fractions and temperatures, soot structure (from TEM) and plume temperatures). As a result, computations of flame structure must be used for properties that are not measured in order to interpret soot processes (velocities and major species concentrations). These predictions are based on the conserved-scalar formalism in conjunction with the laminar-flamelet concept for soot-containing flames [2-4] which circumvents current limitations about fuel decomposition and soot chemistry. This approach involves full numerical simulation of flame structure for axisymmetric steady flow conditions [15-18]. A typical evaluation, involving results along the axis of a weakly-buoyant acetylene/air laminar jet diffusion flame, is illustrated in Fig. 3; the good agreement between predicted and measured velocities, mixture fractions and major species concentrations is evident.

In view of this status, the main emphasis of current work has been on measurements of soot nucleation and growth in laminar diffusion and premixed flames.

Laminar Diffusion Flames

Introduction. Present ground-based studies of laminar diffusion flames are considering laminar jet diffusion flames similar to the flight experiment. The objectives were to measure both soot and flame properties in hydrocarbon/air laminar jet diffusion flames and to exploit this information to study soot growth and nucleation in diffusion flames.

Experimental Methods. The experiments involved weakly-buoyant round laminar jet-diffusion flames at low pressures, as well as buoyant jet diffusion flames at atmospheric pressure. The following measurements were made: soot volume fractions using laser extinction, gas temperatures using thermocouples where soot is absent and multiline emission where soot is present, soot structure using thermophoretic sampling and analyses by TEM, gas compositions by sampling and analysis with gas chromatography and gas velocities by laser velocimetry.

Results and Discussion. Soot and flame properties along the axis of an acetylene/air flame at 0.25 atm. are illustrated in Fig. 4. Species concentrations for all the flames were in good agreement with generalized state relationships for major gas species [24], adding confidence to the laminar flamelet technique to be used to analyze the flight experiments. Significant levels of soot formation only are observed when temperatures exceed 1250K. The end of soot formation occurs when the concentrations of hydrocarbons become small, at a fuel-equivalence ratio of roughly 1.4. These properties were similar for all the flames [9-12]. The behavior of d_p was more complex, increasing during the early stages of soot formation but reaching a maximum well before the maximum f_s is reached; this behavior is caused by the greater temperature sensitivity of soot nucleation than soot growth so that large nucleation rates toward the end of soot formation yield numerous short residence time primary soot particles, tending to reduce the mean value of d_p .

The measurements were used to study soot growth and nucleation in laminar diffusion flames, inferring growth from the variation of f_s and nucleation from the variation of n_p . It was found that soot growth was reasonably correlated as functions of light hydrocarbon (C_2H_2 , C_2H_4 , CH_4) concentrations with a low activation energy, and thus best represented as collision efficiencies [9-12]. In addition, acetylene was the dominant light hydrocarbon present in the soot growth region, similar to premixed flames, see Refs. 25-27. It was also important to account for effects of simultaneous soot growth and oxidation due to the presence of soot oxidizing species (H_2O , CO_2 and O_2) within the soot growth region.

The present net soot growth rates, corrected for soot oxidation, are plotted as a function of acetylene concentrations in Fig. 5. The net growth rate has been plotted to anticipate a simple collision efficiency expression. Results shown on the plot involve acetylene/air diffusion flames (where acetylene is the main hydrocarbon present), other hydrocarbon/air diffusion flames (where C_2H_4 and CH_4 concentrations are comparable to C_2H_2 concentrations) and results from premixed flames from Refs. 25-27. When plotted in this manner, the growth rates for premixed flames exhibit a large vertical span, which is attributed to reduced surface reactivity with age, and growth rates generally lower than the diffusion flames, which may be caused by the uncertain estimates of soot surface areas and residence times for the results of Refs. 25-27. The results for acetylene/air diffusion flames over several studies and a wide range of conditions exhibit first-order behavior with respect to acetylene concentrations which is consistent with a rather reasonable acetylene collision efficiency of 0.39%. In contrast, measurements for other hydrocarbon/air diffusion flames exhibit a consistently higher apparent acetylene collision efficiency of 1.56%; this behavior suggests either parallel soot growth channels through ethylene

collisions (which is present in significant concentrations in these flames), or enhanced surface activation due to the presence of higher hydrogen concentrations in the soot growth region typified by the hydrogen abstraction carbon addition (HACA) mechanism of Mauss et al. [25] and references cited therein.

The rate of formation of primary particles could be associated with the concentration of acetylene in a relatively simple manner. Preliminary examination of the measurements indicated first-order behavior, in agreement with earlier assessments of soot nucleation for various soot formation processes [21, 28]. The resulting soot nucleation rate constant, k_n , is plotted as a function of temperature in Fig. 6, along with an earlier correlation of Leung et al. [28]. The results for all the present hydrocarbon/air flames are in reasonably good agreement with each other (although the scatter is large due to the sensitivity of measured nucleation rates to d_p). The results yield a modest activation energy of 35 kcal/gmol, which is reasonable for a recombination-like process like soot nucleation [21, 28]. Nevertheless, present nucleation rates are significantly lower than the correlation of Leung et al. [28]; this is not surprising because the data used in Ref. 28 involved optical determinations of d_p which are questionable and would tend to overestimate nucleation rates as indicated in Fig. 6 [4].

Laminar Premixed Flames

Introduction. Soot processes in laminar premixed hydrocarbon/air flames have received attention because the flame environment is simpler and more computationally tractable than laminar diffusion flames. Thus, the objective of the present investigation was to apply the techniques developed to study laminar diffusion flames to study soot processes in laminar premixed flames.

Experimental Methods. The measurements were completed using a 60 mm diameter water-cooled porous plug premixed flat flame burner surrounded by a nitrogen shroud flow. The measurements were the same as for the diffusion flames.

Results and Discussion. Measurements of u , d_p , T and f_s are illustrated as a function of height above the burner in Fig. 7. Increased distance from the burner causes increased u due to buoyancy, increased d_p due to growth, decreased T due to radiative heat losses and increased f_s due to soot nucleation and growth. Predictably, larger C/O ratios yield larger soot concentrations and lower temperatures. The measurements of flame and soot structure yield the variations of S , n_p , w_n and w_g illustrated in Fig. 8. Both S and n_p increase with height which implies continued soot nucleation and growth with increasing residence time although both rates decrease similar to past observations [25-27]. This behavior is consistent with the reduced temperatures with increasing distance from the burner exit because both the nucleation rates and the HACA mechanism exhibit temperature dependencies. Quantifying these effects, however, will require information about concentrations of light and heavy hydrocarbons in the flow; current work is carrying out measurements along these lines.

Nomenclature

[i] = molar concentration of species i , d = burner exit diameter, d_p = primary soot particle diameter, C/O = atomic carbon/oxygen ratio, f_s = soot volume fraction, $\overline{C_{ij}^A}$ = aggregate scattering cross section (i = incident, j = scattered polarization directions), k_n = soot nucleation rate constant, n_p = number of primary particles per unit volume, \overline{N} = mean number of primary particles per aggregate, Re = burner exit Reynolds number, S = soot surface area per unit volume, T = temperature, u = streamwise velocity, \overline{v}_i = mean molecular velocity of species i , w_g = soot growth rate, w_n = soot nucleation rate, X_i = mole fraction of species i , θ = angle of scattering from forward direction.

Acknowledgments

Research sponsored by NASA Grant No. NAG3-1245 under the technical management of D.L. Urban of the Lewis Research Center.

References

1. Law, C.K. and Faeth, G.M., Prog. Energy Combust. Sci., Vol. 20, 1994, pp. 65-116.
2. Faeth, G. M., *Proceedings of the AIAA/IKI Microgravity Science Symposium*, AIAA, Washington, 1991, pp. 281-293.
3. Köylü, Ü.Ö. and Faeth, G.M., Combust. Flame, Vol. 89, 1992, pp. 140-156.
4. Köylü, Ü.Ö. and Faeth, G.M., J. Heat Trans., Vol. 115, 1993, pp. 409-417.
5. Köylü, Ü.Ö. and Faeth, G.M., J. Heat Trans., Vol. 116, 1994, pp. 152-159.
6. Köylü, Ü.Ö. and Faeth, G.M., J. Heat Trans., Vol. 116, 1994, pp. 971-979.
7. Farias, T.L., Carvalho, M.G., Köylü, Ü.Ö. and Faeth, G.M., J. Heat Trans., Vol. 117, 1995, pp. 152-159.
8. Köylü, Ü.Ö., Faeth, G.M., Farias, T.L. and Carvalho, M.G., Combust. Flame, in press.
9. Sunderland, P.B., Mortazavi, S., Faeth, G.M. and Urban, D.L., Combust. Flame, Vol. 96, 1994, pp. 97-103.
10. Sunderland, P.B., Köylü, Ü.Ö. and Faeth, G.M., Combust. Flame, Vol. 100, 1995, pp. 310-322.
11. Lin, K.-C., Sunderland, P.B. and Faeth, G.M., Combust. Flame, in press.
12. Sunderland, P.B. and Faeth, G.M., Combust. Flame, in press.
13. Faeth, G. M. and Köylü, Ü.Ö., Combust. Sci. Tech., submitted.
14. Lin, K.-C. and Faeth, G.M., J. Prop. Power, submitted.
15. Mortazavi, S., Sunderland, P.B., Jurng, J., Köylü, Ü.Ö. and Faeth, G.M., AIAA Paper No. 93-0708, 1993.
16. Faeth, G.M., Sunderland, P.B., Köylü, Ü.Ö. and Urban, D.L., *Proceedings of International Symposium on Aerospace and Fluid Sciences*, Tohoku University, Sendai, Japan, 1993, pp. 185-198.
17. Köylü, Ü.Ö., Sunderland, P.B., Mortazavi, S. and Faeth, G.M., AIAA Paper No. 94-0428, 1994.
18. Sunderland, P.B. and Faeth, G.M., AIAA Paper No. 95-0149, 1995.
19. Lin, K.-C. and Faeth, G.M., AIAA Paper No. 95-0375, 1995.
20. Xu, F., Sunderland, P.B. and Faeth, G.M., *Proceedings of Spring Technical Meeting*, Canadian Section, The Combustion Institute, Victoria, B.C., in press.
21. Haynes, B. S. and Wagner, H. G., Prog. Energy Combust. Sci., Vol. 7, 1981, pp. 229-273.
22. Glassman, I., *Twenty-Second Symposium (International) on Combustion*, The Combustion Institute, Pittsburgh, 1988, pp. 295-311.
23. Howard, J.B., *Twenty-Third Symposium (International) on Combustion*, The Combustion Institute, Pittsburgh, 1990, pp. 1107-1127.
24. Sivathanu, Y.R. and Faeth, G.M., Combust. Flame, Vol. 82, 1990, pp. 211-230.
25. Mauss, F., Schäfer, T. and Bockhorn, H., Combust. Flame, Vol. 99, 1995, pp. 697-705.
26. Harris, S.J. and Weiner, A.M., Combust. Sci. Tech., Vol. 38, 1984, pp. 75-87.
27. Ramer, E.R., Merklin, J.F., Sorensen, C.M. and Taylor, T.W., Combust. Sci. Tech., Vol. 48, 1986, pp. 241-255.
28. Leung, K.M., Lindstedt, R.P. and Jones, W.P., Combust. Flame, Vol. 87, 1991, pp. 289-305.

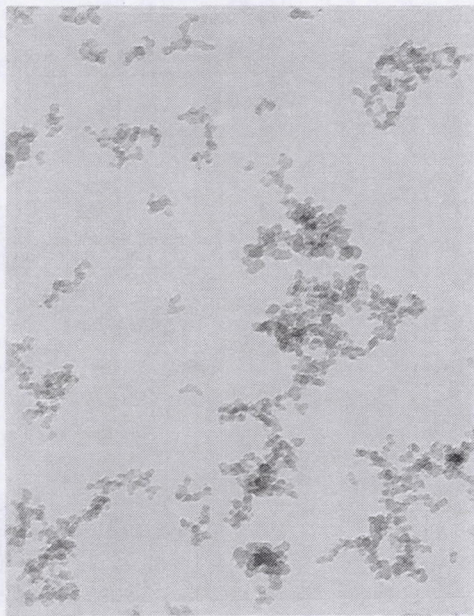


Fig. 1. TEM photograph of soot within a weakly-buoyant acetylene/air laminar jet diffusion flame. Figure dimensions roughly $1000 \times 1400 \mu\text{m}$.

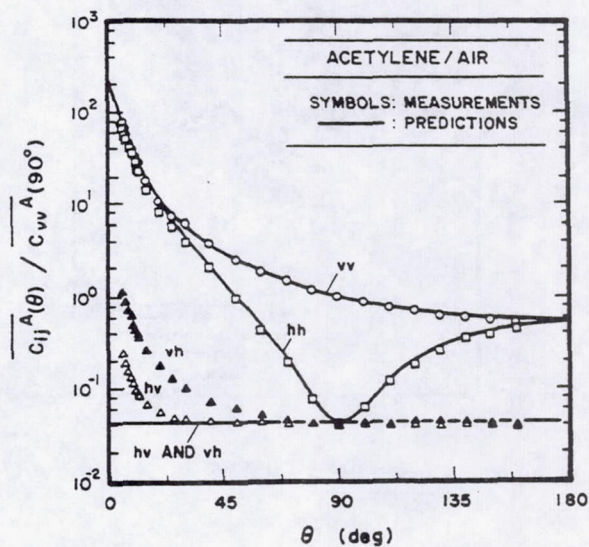


Fig. 2. Scattering pattern for soot emitted from acetylene/air buoyant turbulent diffusion flames. From Köylü and Faeth [5].

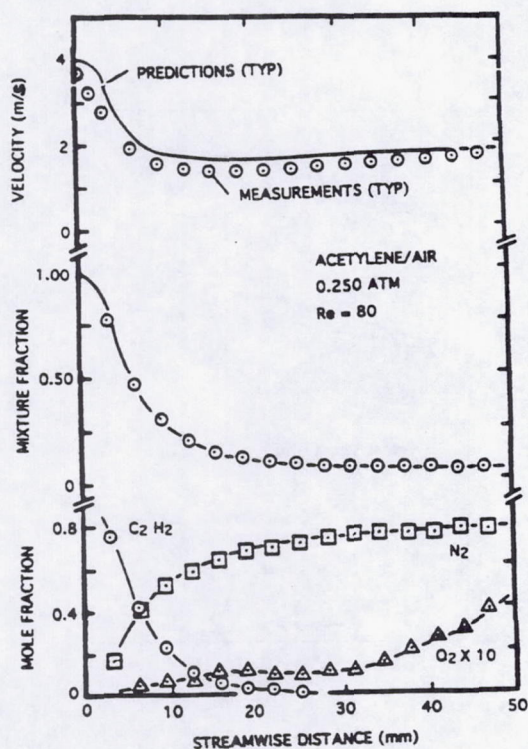


Fig. 3. Measured and predicted properties along the axis of a weakly-buoyant acetylene/air laminar jet diffusion flame. From Köylü et al. [17].

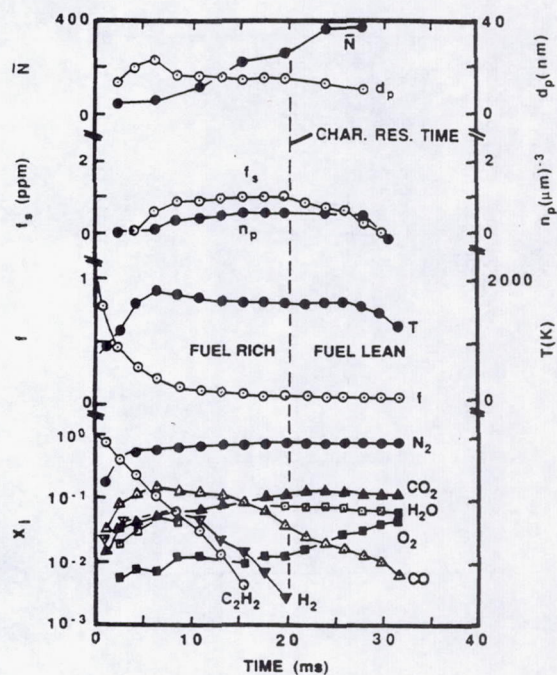


Fig. 4. Soot and flame properties along the axis of a weakly-buoyant acetylene/air laminar jet diffusion flame at 0.25 atm. From Sunderland et al. [10].

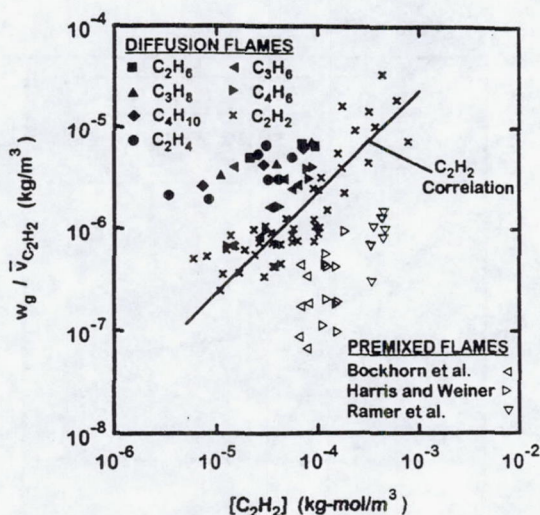


Fig. 5. Net soot growth rates after connection for oxidation within laminar hydrocarbon/air jet diffusion flames. From Sunderland and Faeth [12].

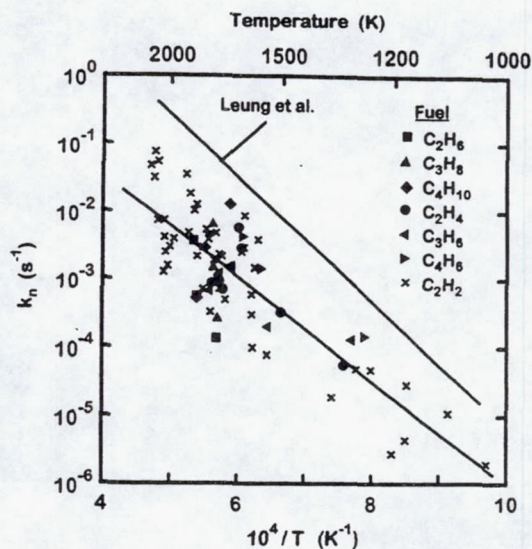


Fig. 6. Soot nucleation rates within laminar hydrocarbon/air jet diffusion flames. From Sunderland and Faeth [12].

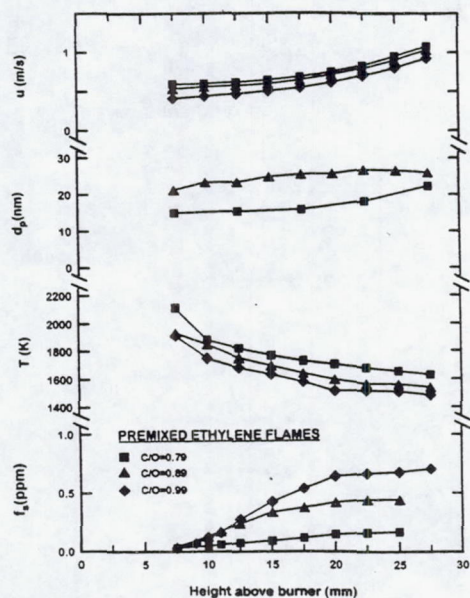


Fig. 7. Measured flame and soot properties along the axis of premixed laminar ethylene/air flames at atmospheric pressure. From Xu et al. [20].

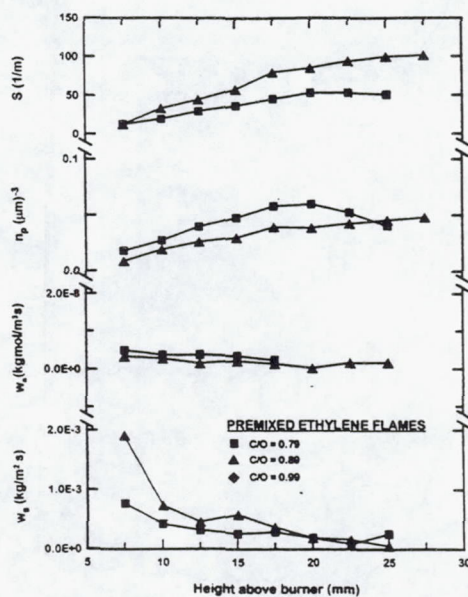


Fig. 8. Derived soot properties along the axis of premixed ethylene/air flames at atmospheric pressure. From Xu et al. [20].

UNSTEADY PLANAR DIFFUSION FLAMES: IGNITION, TRAVEL, BURNOUT

F. Fendell and F. Wu
TRW Space & Electronics Group
One Space Park
Redondo Beach, CA 90278

Introduction

Consider an impervious noncatalytic isothermal squat rectangular-solid container, with height significantly smaller than the length of a side of the square cross section [Fig.1(a)]. The container is taken to be filled initially with purely gaseous reactants, with the oxidizer separated from the fuel by a thin impervious planar diaphragm. Such a diaphragm might be formed by a stretched thin film of a hydrocarbon polymer such as parylene. For specificity, we take the upper half volume to be filled uniformly with oxygen diluted with helium, and the lower half volume to be filled uniformly with hydrogen diluted with argon, such that the two half volumes have equal pressure, temperature, density, and (hence) "average molecular weight". At time zero, with minimal disturbance, small perforations of the diaphragm are made at a multitude of sites, so that the contents of the upper and lower half volumes begin to interdiffuse. After a short interval of time, a layer, of thin but finite thickness and containing combustible mixture, is formed; the layer extends to each side of the midplane [Fig.1(b)]. Ignition of the combustible mixture results in a rapid laminar flame propagation through that portion of the container contents with mixture within the fuel-rich and fuel-lean flammability limits. For hydrogen and oxygen at roughly atmospheric pressure and ambient temperature, and not too far from stoichiometric proportion, such a flame propagation takes but a small fraction of a second to consume the combustible mixture, for a cross-section dimension of 10 cm or so. For a fuel-lean mixture, excess oxygen is available to convert the remnants of the diaphragm to purely gaseous products, so no soot forms. The result of the flame propagation is the formation of a vigorous planar diffusion flame at the interface between the hydrogen and oxygen [Fig.1(c)].

The narrow layer of hot combustion products will remain planar, and not rapidly disintegrate under buoyant instability (refs. 1, 2) into a convoluted pattern of adjacent "fingers" of relatively hot and cold gas, if the dimensionless Rayleigh number $Ra < O(2000)$, where by definition, $Ra \equiv [(\Delta T)/T_{ref}] g a^3 / (\nu \kappa)$. Here, T_{ref} denotes a typical temperature and (ΔT) , a characteristic temperature difference; g is the magnitude of the gravitational acceleration; a is a characteristic physical dimension along the direction of gravity; ν characterizes the kinematic viscosity of the gaseous medium and κ , the thermal diffusivity. For $(\Delta T)/T_{ref} \approx 8$, $(\nu \kappa) \approx 0.16 \text{ cm}^4/\text{s}^2$, $g = g_0 \approx 10^3 \text{ cm/s}^2$, the typical dimension of an experimental apparatus is restricted to significantly less than one-quarter of a centimeter. (We do not want even to approach the critical Rayleigh number, because the idealizations adopted in applying the criterion are many.) This minute scale is entirely impractical, not only for diagnostic instrumentation, but also because heat losses to encompassing cold walls in such close proximity would quench the burning. However, in a microgravity environment (ref. 3) such that $g = 10^{-5} g_0$, the critical dimension $a \approx 10 \text{ cm}$. Thus, in an apparatus of 5 cm in height, the fact that hot combustion products in the narrow burned layer lie below a colder, more dense oxygen/helium mixture should set off no symmetry-disrupting gravitational instability in a microgravity environment.

The upshot is that, in microgravity, a thin *planar* diffusion flame is created and thenceforth travels so that the flame is situated at all times at an interface at which the hydrogen and oxygen meet in stoichiometric proportion. If the initial amount of hydrogen is deficient relative to the initial amount of oxygen, then the planar flame will travel further and further into the half volume initially containing hydrogen [Fig.1(d)], until the hydrogen is (virtually) fully depleted. Of course, when the amount of residual hydrogen becomes small, the diffusion flame is neither

vigorous nor thin; in practice, the flame is extinguished before the hydrogen is fully depleted, owing to the finite rate of the actual chemical-kinetic mechanism. The rate of travel of the hydrogen-air diffusion flame is much slower than the rate of laminar flame propagation through a hydrogen-air mixture. This slow travel facilitates diagnostic detection of the flame position as a function of time, but *the slow travel also means that the time to burnout (extinction) probably far exceeds the testing time (typically, a few seconds) available in earth-sited facilities for microgravity-environment experiments.*

We undertake an analysis to predict: (1) the position and temperature of the diffusion flame as a function of time; (2) the time at which extinction of the diffusion flame occurs; and (3) the thickness of quench layers formed on side walls (i.e., on lateral boundaries, with normal vectors parallel to the diffusion-flame plane), and whether, prior to extinction, water vapor formed by burning will condense on these cold walls.

Issues Under Investigation

The simplest reasonable theoretical model not only adopts the standard Shvab-Zeldovich simplifications (refs. 4, 5) (direct one-step irreversible chemical reaction, binary diffusion, uniformity in space and time of the average molecular weight of the gaseous mixture, simple variation of the molecular-transport coefficients with thermodynamic state, constancy of the ratio of any two molecular-transport coefficients, etc.); the model goes further, in the manner of Burke and Schumann (refs. 4, 5) to idealize the rate of chemical reaction as effectively infinitely rapid, relative to the rate of transport. (The ratio of the reaction rate to the flow rate is defined to be the first Damköhler number, and is denoted D_1 .) The Burke-Schumann treatment is a *limiting* case in that only the rate of mixing, not the rate of reaction as well, impedes the rate of formation of product species. The limit is mathematically singular in that the flame is a Dirac-delta-function-type sink for reactant concentrations, and a source for product concentrations and heat: each of these thermodynamic state variables is continuous at the fuel-oxidizer interface, but each has first (and all higher) derivatives that are discontinuous at the interface. In the Burke-Schumann limit, the flame is an (in general, moving) boundary between fuel and oxidizer (refs. 6, 7), and the mathematical techniques usefully associated with the solution of Stefan problems (refs. 8, 9) may be applied in this aerothermochemical context. The Stefan-problem nature of diffusion-flame analyses is often obscured because attention is typically confined to steady scenarios, or at least to quasisteady scenarios in which the temporal dependence is approximated as parametric (and no explicit temporal derivatives are retained). The Stefan-problem nature of diffusion-flame analyses is obscured further because attention is usually confined to the special case of equal diffusion coefficients for all species and heat (and perhaps momentum as well). In this special case, the identity of convective-diffusive differential operators permits reformulation of the boundary/initial-value problem in terms of linear combinations of the dependent variables; the upshot is that the flame locus need be identified only *after* the formal solution is completed. In practice, the molecular diffusivities virtually always differ, and differ significantly for cases (such as the one cited here, involving hydrogen) in which the molecular weights of the major species differ significantly. In these cases, the time-varying position of the thin flame must be identified explicitly *during* the course of solution of the boundary/initial-value problem.

A hydrogen/oxygen diffusion flame, especially in the geometric simplicity afforded by microgravity, permits us, without the usual complicating need to account for the black-body radiation associated with soot, to test whether the Shvab-Zeldovich/Burke-Schumann formulation predicts experimentally observed behavior. In such a formulation, the ratio of the Fickian-diffusion coefficient for the fuel vapor, D_F , to the thermal diffusivity, κ --denoted as one Lewis-Semenov number, Le_F , and the ratio of the Fickian-diffusion coefficient for oxidizer, D_O , to the thermal diffusivity, κ --denoted as another Lewis-Semenov number, Le_O , are taken to be constant in space and time. (These convenient definitions are the inverse of the conventional definitions for Lewis-Semenov numbers.) In practice, the ratios vary in space and time within the flow, despite the fact that, in the *initial* configuration, we have diluted hydrogen with argon, and oxygen with helium, so that the average molecular weight is everywhere the same. We hope that the empirical assignment of optimal values for the Lewis-Semenov numbers, Le_F , and Le_O , will permit us to fit some of the microgravity data (explicitly, the position and temperature at the thin flame in some of the experiments). We further hope that the guidance from that experience will permit us to assign values to the Lewis-Semenov numbers to predict the corresponding observations in the remainder of the experiments. If so, the viability of the simple Shvab-Zeldovich/Burke-Schumann model to quantify, to a practically useful accuracy, key properties in a difficult-to-analyze diffusion flame will have been demonstrated.

The scenario in Fig.1 affords many simplifications beyond a modest role for radiative heat transfer. There is no "nitrogen chemistry", and no gasification of an initially condensed-phase fuel, to add complication. We expect no cellular behavior, which is associated with flame-scale instabilities in premixed flames, and which is typically not observed for modest-scale, vigorous diffusion flames. Aside from quenching near the cold lateral surface of the container, we are examining unsteady, planar phenomena, for which analysis can be carried out entirely in terms of a

convenient Lagrangian coordinate; such is not the case for spherical symmetry. Away from the quench layers, the only significant velocity component is perpendicular to the plane of the flame; hence, the problem is distinct from the counterflow, in which velocity components perpendicular and parallel to the plane of the diffusion flame arise.

Diffusion-Flame Extinction

By singular-perturbational analysis, it is possible to perturb about the Burke-Schumann limit (rate of reactant conversion limited by diffusive transport only), and to calculate when the conditions in a burn are sufficient for extinction, according to a direct one-step irreversible second-order large-Arrhenius-activation-temperature model of the finite-rate chemical kinetics. This sufficiency criterion is the consequence of the nonuniqueness of the solution to the formulation of steady burning in systems with separated "feeds" of fuel and oxidizer, for kinetics of the genre just described. Because, at extinction, kinetic effects are limited to a narrow quasisteady zone of reactant interpenetration (roughly) centered about the thin-flame site, we are able to apply, to our unsteady one-dimensional diffusion flame, the sufficient condition for extinction originally derived for a steady two-dimensional counterflow-type diffusion flame (refs. 10, 11). The sufficient condition for extinction amounts to identifying an explicit limiting value for the first Damkohler number, $(D_1)_\ell$, for a fixed set of other flow parameters. The checking for satisfaction of this explicit criterion for extinction may be facilely and rapidly carried out at each time step, as a peripheral calculation to the Shvab-Zeldovich/Burke-Schumann analysis. Indeed, paradoxically, owing to the singular-perturbation basis by which the sufficiency condition for extinction is derived, it is convenient to apply the criterion only if we have available the results for a Shvab-Zeldovich/Burke-Schumann analysis of the scenario of Fig. 1(d). If we simply adopt any reasonable finite-rate chemical-kinetic model and compute the predicted aerothermochemical evolution from the initial configuration, then, while we may try to infer when extinction occurs according to some intuitive criterion, no explicit sufficiency criterion for extinction is available. Thus, the availability of a solution in the Burke-Schumann limit not only affords a lowest-order estimate of the time to extinction based on total exhaustion of the deficient reactant; the solution is also a first step in obtaining a finite-reaction-rate-based upgrade of the lowest-order estimate of the time to extinction.

What Related Experiment Is Feasible in Earth Gravity?

Suppose the contents of the container in Figure 1(a) are altered to be stably stratified, so that relatively light gas lies over relatively heavy gas; explicitly, suppose the upper half-volume initially contains hydrogen diluted with helium, and the lower half-volume initially contains oxygen diluted with argon. (The motivation for the dilution is to avoid so hot a flame that complications arise, from dissociation of product species, from enhanced hot-gas radiation, and/or from thermal threat to the integrity of the container.) After ignition for fuel-deficient test conditions, the hot product species would be dominantly water vapor. The molecular weight of this species is much greater than that of hydrogen or helium, and much less than that of oxygen or argon. Thus, at least until diffusion permits argon significantly to enter the hydrogen-containing subdomain, and helium significantly to enter the oxygen-containing subdomain, there seems the possibility that the stabilizing stratification based on species-concentration profiles might override the destabilizing stratification based on thermal (hot-under-cold) considerations. Of course, the relative contributions to the density stratification along the (vertical) direction of the earth-gravity acceleration would determine whether the flame is stable. However, the alternative initial stratification described in this paragraph is not consistent with conditions amenable to Shvab-Zeldovich/Burke-Schumann modeling. Simplistic Shvab-Zeldovich modeling is expected to pertain only to those conditions in which the average molecular weight is at least roughly uniform at all sites in the container for all times of interest, and such is clearly not the case for the alternative initial stratification. A more meticulous theoretical treatment (e.g., of the equation of state) would be suitable for the alternatively stratified scenario--so the scenario lies outside the scope of our first objectives.

Accordingly, in this project, we confine attention to the scenarios depicted in Figure 1. Testing in the NASA Lewis Research Center drop tower with a two-seconds-duration microgravity environment is to be carried out during the summer of 1994. The objective is to demonstrate that we can achieve a planar diffusion flame, upon breaking the thin-film separator and igniting, probably by use of a hot wire. However, the available two-second testing time is exhausted before the flame has undergone virtually any translation. As we noted earlier, data collection must be deferred until testing is carried out in the prolonged microgravity environment available in space flight. In that prolonged microgravity environment, we anticipating measuring, as functions of time since ignition: the flame temperature and position (including the time of flame extinction); the sidewall-quench-layer thickness; the chamber pressure; and the heat transfer at each end wall and at multiple sites along one side wall. We also plan to measure the total hydrogen, oxygen, and water substance in the chamber at the time of extinction. For a given set of parameter assignments, the previously described model can be used to try to predict the observations. Whether accurate predictions are accessible via such a simplistic model, or whether the model is limited to diagnostic use (in

that empirical assignment of the Lewis-Semenov numbers remains requisite to recovering the observations) awaits the availability of data.

Examples of Model Prediction

For the fuel-lean or stoichiometric systems of hydrogen/argon initially segregated from oxygen/helium (Figure 1), the one-step irreversible reaction $2 \text{H}_2 + \text{O}_2 \rightarrow 2 \text{H}_2\text{O} - Q$ (heat) implies that the stoichiometrically adjusted mass fraction for fuel $F \equiv 9 \bar{Y}_{\text{H}_2}$, and that for oxidizer $\phi \equiv (9/8) \bar{Y}_{\text{O}_2}$, where \bar{Y}_j is the mass fraction of species j . If t denotes time since ignition; c_p and c_v , heat capacity at constant pressure and volume, respectively; p , pressure; ρ , density; T , temperature; u , speed in the z direction; and subscript i , initial value, then we nondimensionalize as follows:

$$\bar{z} \equiv z/a, \text{ where } -a \leq z \leq a, \quad -1 \leq \bar{z} \leq 1; \quad \tau \equiv \kappa_i t/a^2, \text{ where } t > 0;$$

$$\bar{T} \equiv T/T_i, \quad \bar{p} \equiv p/p_i, \quad \bar{\rho} \equiv \rho/\rho_i, \quad \bar{u} \equiv u/(\kappa_i/a^2), \quad \gamma \equiv c_p/c_v, \quad D_2 \equiv Q/(36c_p T_i).$$

The dimensionless flame position is denoted $Z_f(\tau)$; a stagnation plane, $Z_s(\tau)$. The following set of values for the six dimensionless parameters arising in a Shvab-Zeldovich/Burke-Schumann formulation for the "core" flow (i.e., ignoring side-wall quench layer) is termed nominal:

$$\text{Le}_F = 1.78, \quad \text{Le}_\phi = 0.432, \quad F_i = 0.914, \quad \phi_i = 0.914, \quad D_2 = 17.9, \quad \gamma = 1.4.$$

Sample results in the dimensionless physical coordinate \bar{z} (obtained by Crank-Nicholson integration, after transformation to "boundary-fixing" Lagrangian coordinates) are presented in Figures 2-6. With the anticipated availability of data from experiments in microgravity, we may ascertain what (if any) assignment of the Lewis-Semenov numbers permits this simplistic, convenient model to recover key combustion behavior, such as flame translation and flame temperature as functions of time.

Acknowledgments

This work was supported under NASA Lewis Research Center Contract NAS3-27264. The authors wish to thank the NASA project scientist Suleyman Gokoglu for informative guidance on microgravity testing, and for assisting us by independently carrying out some of the calculations reported here, for corroboration. The authors are also grateful to George Carrier for many helpful discussions, to Bruce Lake for indispensable cooperation, and to Peter Lee, Harry Rungaldier, Kenneth Beach, and NASA experiment manager Donald Schultz for insightfully designing the related experiment.

References

- ¹Landau, L. D. and Lifshitz, E. M., *Fluid Mechanics*, 1st ed., Pergamon, New York, 1959, pp. 212-1218.
- ²Tritton, D. J., *Physical Fluid Dynamics*, 2nd ed., Clarendon, Oxford, England, 1988, pp. 35-46, 359-365.
- ³Microgravity Combustion Group, "Microgravity Combustion Science: Progress, Plans, and Opportunities," NASA Technical Memorandum 105410, NASA Lewis Research Center, Cleveland, 1992.
- ⁴Fendell, F., "Ignition and Extinction in Combustion of Initially Unmixed Reactants," *Journal of Fluid Mechanics*, Vol. 21, February 1965, pp. 281-303.

⁵Zeldovich, Y. B., Barenblatt, G. I., Librovich, V. B., and Makhviladze, G. M., *The Mathematical Theory of Combustion and Explosions*, 1st ed., Consultants Bureau, New York, 1985, pp. 555-580.

⁶Carrier, G. F., Fendell, F. E., and Marble, F. E., "The Effect of Strain Rate on Diffusion Flames," *SIAM Journal on Applied Mathematics*, Vol. 28, March 1975, pp. 463-500.

⁷Fendell, F. E., Bush, W. B., Mitchell, J. A., and Fink IV, S. F., "Diffusion-Flame Burning of Fuel-Vapor Pockets in Air," *Combustion and Flame*, Vol. 98, August 1994, pp. 180-196.

⁸Hill, J. M., *One-dimensional Stefan Problems: an Introduction*, 1st ed., John Wiley, New York, 1987, pp. 1-29, 134-137.

⁹Carslaw, H. S. and Jaeger, J. C., *Conduction of Heat in Solids*, 2nd ed., Clarendon, Oxford, England, 1959, pp. 62-64, 282-296.

¹⁰Liñán, A., "The Asymptotic Structure of Counterflow Diffusion Flames for Large Activation Energies," *Acta Astronautica*, Vol. 1, July/August 1974, pp. 1007-1039.

¹¹Fendell, F. and Wu, F., "Unsteady Planar Diffusion Flames: Ignition, Travel, Burnout," AIAA 95-0147, American Institute of Aeronautics and Astronautics, Washington, DC, January 1995 (presented at the 33rd Aerospace Sciences Meeting and Exhibit, Reno, NV).

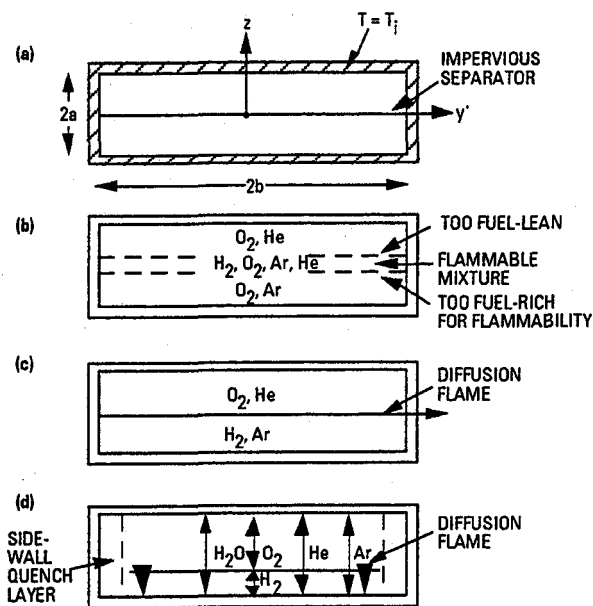


Figure 1. Geometry for a planar translating diffusion flame: (a) argon-diluted hydrogen, initially separated from helium-diluted oxygen, by a thin film, the contents of each half-volume V being at at, pressure p_i , density ρ_i , and temperature T_i ; (b) incipient interdiffusion of reactants after perforation of the separator; (c) diffusion flame, after ignition and deflagration of the narrow combustible layer; and (d) subsequent travel of the diffusion flame for a hydrogen-deficient scenario, with extinction near the lateral walls of the isothermal container.

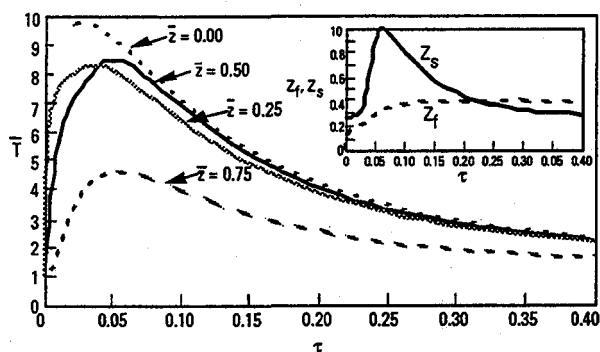


Figure 2. For nominal parametric values, the dimensionless temperature \bar{T} vs. the dimensionless time τ , for four values of the dimensionless spatial coordinate \bar{z} . The inset presents the diffusion-flame position, $Z_f(\tau)$, and the stagnation-plane position, $Z_s(\tau)$, for the velocity \bar{u} .

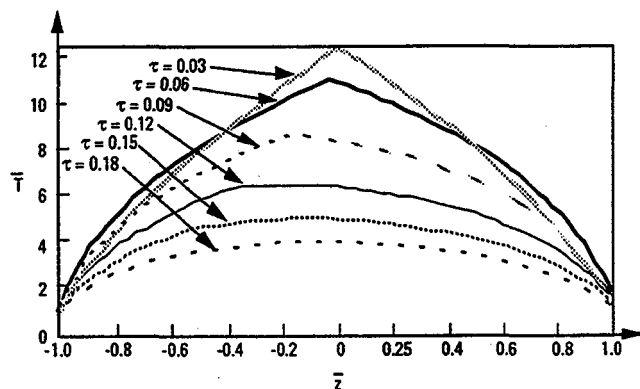


Figure 3. For the nominal case except $F_i/\phi_i = 0.5$, $\phi_i = 0.914$, $Le_F = 1.6$, and $Le_\phi = 0.4$, the dimensionless temperature \bar{T} vs. the dimensionless coordinate \bar{z} , at several dimensionless times (since ignition) τ .

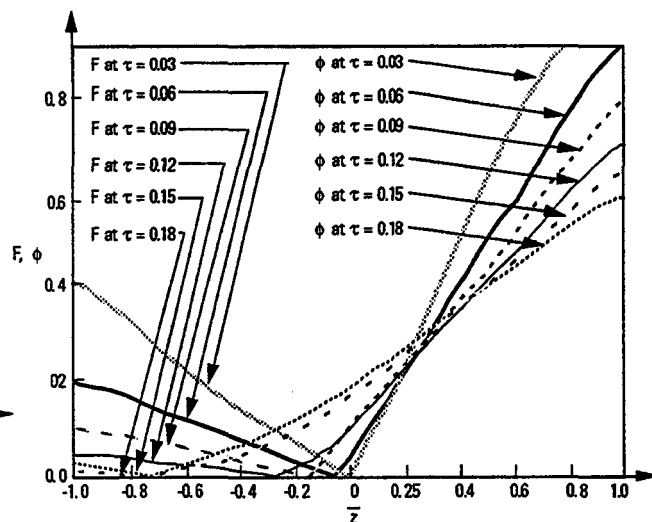


Figure 4. For the case of Figure 3, the stoichiometrically adjusted mass fraction for fuel F , and for oxidizer ϕ , vs. the dimensionless spatial coordinate \bar{z} , at several dimensionless times τ .

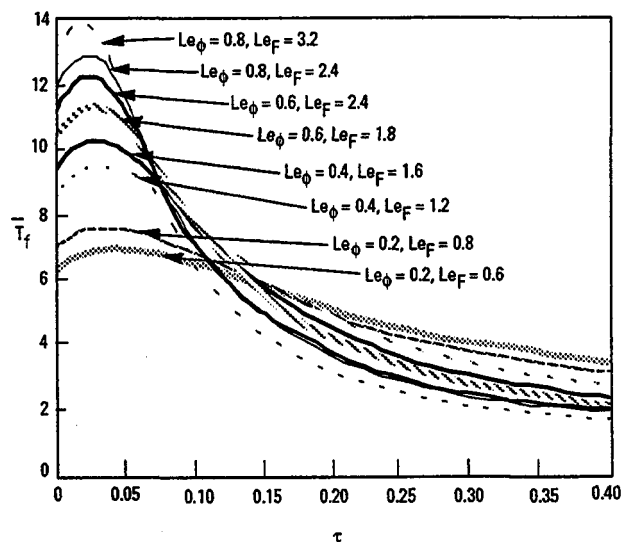


Figure 5. For the nominal case except for the values ascribed to the Lewis-Semenov numbers, Le_F and Le_ϕ , the dimensionless flame temperature \bar{T}_f vs. the dimensionless time τ .

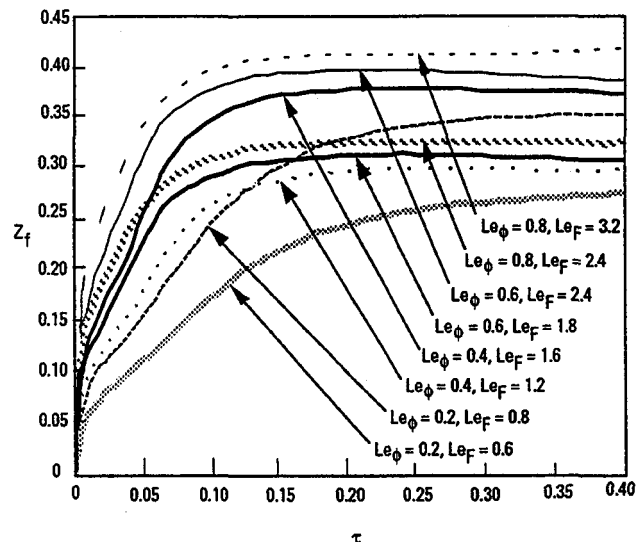


Figure 6. For the cases presented in Figure 5, the dimensionless flame position Z_f vs. the dimensionless time τ .

THREE-DIMENSIONAL FLOW IN A MICROGRAVITY DIFFUSION FLAME

Jean Hertzberg
Center for Combustion Research
Department of Mechanical Engineering
University of Colorado at Boulder

Mark Linne
Division of Engineering
Colorado School of Mines

Science Objectives

The objective of this work is to understand the fluid dynamics in the interaction of large scale, three-dimensional vortex structures and transitional diffusion flames in a microgravity environment. The vortex structures are used to provide a known perturbation of the type used in passive and active shear layer control techniques.

'Passive techniques' refers to manipulation of the system geometry to influence the three dimensional dynamics of vortex structures, and 'active' refers to any technique which adds energy (acoustic or kinetic) to the flow to influence the shear layer vortex dynamics. In this work the passive forcing is provided by an elliptic jet cross-section, and the active forcing is incorporated by perturbing the jet velocity.

Relevance and Applications

The study of transitional diffusion flames in a microgravity environment is important for several applications: fire safety in spacecraft environments, practical applications of flames in low earth orbit (such as welding and cutting torches for space construction and heating for industrial processes), but most importantly for better understanding and control of all turbulent diffusion flames.

Recent fundamental investigations of transitional, forced axisymmetric diffusion flames have led to increased understanding of the role of shear layer dynamics in the transition to turbulence of these flames. (refs. 1, 2) Experimental studies of the stabilization process of fully turbulent lifted jet flames (ref. 3) have illustrated the importance of large scale shear layer structures and their three-dimensional evolution in time. These results have important consequences for the control of efficiency and pollutant formation in turbulent jet flames via passive and active shear layer control techniques.

Passive shear layer control can be achieved through the use of asymmetric jets, i.e. not plane- or axis-symmetric jets. For instance, nonreacting small aspect ratio elliptic jets have been found to have entrainment ratios several times larger than either plane symmetric or axisymmetric jets (ref. 4). This high entrainment has been attributed to the dynamics of the noncircular vortex rings which form as coherent structures in the jet shear layers. These dynamics are governed by self induction, the effect of one portion of the vortex ring on another. The regions of an

elliptic vortex ring with higher curvature convect ahead of the rest of the ring, which in turn increases the curvature of the lagging portions. These portions then overtake and decrease the curvature of the initial high curvature sections (ref. 5). As a result, the elliptical shape is restored, but the axis which was initially the minor axis has become the major axis, and the motion then begins again. This behavior is also seen in the vortex rings formed in the shear layers of elliptic and rectangular jets, and is responsible for the increased entrainment and axis switching observed.

On a fundamental level, the application of passive techniques involves some form of three-dimensional perturbation to a shear layer, which may be separating burned and unburned reactants, or fuel and air. For instance, Grinstein and Kailasanath (ref. 6) demonstrate the effect of 3-d perturbations numerically in a square non-premixed flame, while Lasheras et al. (ref. 7) are studying high-order azimuthal perturbations to free jet diffusion flames. Lower order perturbations to premixed and annular diffusion flames (with an air core), corresponding to triangular, or elliptic configurations have been studied in some detail by Gutmark et al. (ref. 8). Increased mixing and higher centerline temperatures were found, confirming the utility of these configurations.

Active forcing in the form of periodic flow perturbations has been found to be effective in controlling many types of free shear layers by encouraging (or discouraging) pairing of the large scale structures which are responsible for much of the entrainment. Active forcing is also useful for the analysis of periodic flows since it organizes the flow by reducing the phase jitter of the large structures, and thus allows ensemble averaging based on the phase angle. In combustion, active forcing can be used to either suppress large scale flame/vortex interactions and enhance small scale mixing, as is useful in the control of combustion instabilities in ramjets, or it can be used to enhance the large scale vortex structures, as has been used to such advantage in pulse combustor technology.

The ultimate applications of these shear layer control techniques are at fully turbulent Reynolds numbers, however, study of a transitional flow allows clearer determination of the effect of the shear layer controls at a Reynolds number where mechanisms of the transition to turbulence can be traced. The major drawback to this approach is that buoyancy effects dominate the flow field under these conditions. In fully turbulent flames, buoyancy plays a much smaller role. In order to examine the transitional flow in the absence of buoyancy effects, the flame must be studied in a microgravity environment.

Research Approach

Experimental studies of the acoustically forced, elliptic jet diffusion flame will be made under normal gravity, inverted, and microgravity conditions. The flow field and the flame-flow interactions will be examined using a variety of flow visualization techniques. Particle Image Velocimetry (PIV) will be used in the stationary experiments, and a particle tracking technique will be developed for the 2.2 second drop tower experiments. A schematic of the system is shown in Figure 1. Ideally, full velocity field information would be determined for the microgravity case as well, however, appropriate diagnostics are not yet available. Knowledge of the velocity field under normal and inverted gravity conditions should provide insight into the microgravity flow field when coupled with the flow visualization and particle tracking measurements from the drop tower tests. The flow is expected to retain bilateral symmetry, so laser sheet techniques (including PIV) will provide useful information in the planes of symmetry.

The combustor consists of a 2:1 aspect ratio elliptic cross-sectioned nozzle (0.5 X 1.0 mm). The nozzle is connected to a plenum chamber which contains a 6.5 inch diameter loudspeaker. The fuel flow (methane) enters the plenum via a flow controller and a seeder device. The flame orientation will be horizontal, to provide the greatest possible length within the drop rig. The flow will be impulsively started and the flame ignited after drop to avoid buoyancy induced currents. The flow will be sinusoidally perturbed using the loudspeaker at the jet preferred mode and/or the plenum's resonant frequency, since high excitation levels will be required to affect the outer shear layer flow where the flame exists. All diagnostics will be phase-locked to the acoustic forcing signal.

Flow visualization techniques will focus on seeded flows, using both refractory particles which will survive the flame (for particle tracking) and oil droplet aerosols which can be used to mark the flame's thermal boundaries. Preliminary results have indicated that the flow rates to be used (10 to 80 ml/s) are insufficient to drive either

conventional aspirated aerosol seeders or cyclone particle seeders. In addition, both types of seeders require gravity to operate properly. To avoid these problems, the plenum is of a sufficient size to be charged with seeded flow at a high rate prior to the experiment. An ultrasonic aerosol generator is also being developed which can provide densely seeded flows independent of flow rate.

The flows will be imaged using conventional video and photographic techniques, including macro stereo photography. Time resolution and phase-locking will be provided by strobing the light source. Both conventional strobe lights and modulated visible laser diodes are being investigated.

Results

This project has been underway since July 1994, although some preliminary experiments were performed prior to that date, using an early prototype combustor. Results from the early combustor are presented here. The early combustor consists of a cylindrical plenum chamber containing a 6.5 inch diameter bass-reflex speaker enclosure. The axisymmetric nozzle is an 8.3 cm length of 4.5 mm inner diameter stainless steel tubing. The burr from using a wheel-type tube cutter is retained.

An unusual flame phenomenon has been observed. At specific excitation frequencies the flame can be driven to bifurcate into a central jet and one or two side jets as shown in Figure 2. A perpendicular mirror view is also shown. The bifurcation is accompanied by a partial detachment of the flame from the nozzle exit, a shortening of the flame by a factor of two, and a change from the common yellow color of soot radiation to a clear blue flame. Under some conditions, a yellow region is observed on one or both flame tips. This phenomenon is of practical interest because the ability to control soot production or product species in a diffusion flame using an open loop forcing technique is potentially quite useful. In addition, this phenomenon illustrates the effectiveness of active forcing on this type of flame.

The bifurcation behavior was observed at all flow rates ranging from the lowest measurable flow rate, 10 ml/s, to a flow rate just above that of lift-off, 95 ml/s. These conditions correspond to bulk velocities ranging from 0.5 m/s to 6 m/s and Reynolds numbers ranging from 240 to 1000. The behavior occurred at 246 +/- 20 Hz. This critical frequency range was found to be insensitive to the flow rate which indicates that the bifurcation is not strictly a shear layer or jet mode effect. The critical frequency was found to be independent of nozzle length, which suggests that it is not an effect of nozzle vibration. A plenum resonance is likely responsible for determining the critical frequency, and the bifurcation should appear whenever the forcing level is sufficient. In fact, the frequency is not sensitive to input forcing amplitude in that bifurcation would occur at low forcing amplitudes at the critical frequency, and not at higher amplitudes at other frequencies. The frequency response of the system must be measured to determine the actual velocity perturbation level at the nozzle. These measurements are in progress. Two possibilities for the resonance mechanism are the Helmholtz and a longitudinal standing wave pipe modes. The Helmholtz resonance mode for the nozzle and plenum combination was 4 Hz, well below any examined frequency. Like many such systems, there are many possible longitudinal modes. One is close to 240 Hz, a standing wave mode of the plenum calculated by using the speed of sound in pure methane and assuming 1.5 wavelengths in the plenum, that is, one closed and one open end. However, the plenum inlet tubing diameter is the same as the outlet, casting doubt on these end condition assumptions.

Outside of the critical frequency range the flame appeared to be an unremarkable transitional diffusion flame, although the flame height showed some sensitivity to the excitation frequency, particularly at low flow rates. The amplitude of forcing at 246 Hz required to cause bifurcation varied with flow rate, with the lower flow rates being more sensitive to forcing. Details of the bifurcation shape also varied with flow rate and forcing amplitude. For example, a splitting into three jets was observed under some conditions. At the highest levels of forcing (35 Vpp at the speaker) some form of bifurcation was always present. At lower levels of forcing the phenomenon was intermittent in time. Additional perturbations such as air currents could be used to induce transitions between the bifurcated and non-bifurcated (ordinary diffusion flame) states. Thus this phenomenon is a bifurcation both physically in space, and in time.

The nozzle lip condition is critical for the bifurcating behavior. A cleanly machined lip will not spontaneously produce a bifurcated flame. This is perhaps why this phenomenon is so rarely seen. While the study of perturbed jet diffusion flames is an active topic (refs. 7,9,10,11,12) few reports of any similar phenomenon have been made. Pfizenmaier (ref. 13) has observed a hydrogen jet flame to split when exposed to high amplitude transverse acoustic waves, and suggests that a helical jet mode instability is responsible. To our knowledge, the only other mention in the literature is a famous report by Tyndall (ref. 14) who studied the response of "naked" (unconfined) gas jet flames to sound, and observed "short, forked and brilliant" flames.

Flow visualization using alumina particles and a strobe light has been performed on a non-reacting air jet under the same Reynolds number and forcing conditions. The air jet was observed to bifurcate in what we assume to be a similar manner to the flame, shown in Figure 3. The phase-locked flow visualization in the air jet shows that a single vortex structure is formed each cycle. The base of the side jet remains fixed at an axial position, rather than convecting downstream with the primary vortex structure. This is consistent with a study of jets subject to high level axial velocity perturbations by Monkewitz and Pfizenmaier (ref. 15). They relate the formation of the side jets to a coupled effect of an azimuthal instability of the primary vortex ring structure with a strong braid structure. Other non-reacting jet bifurcations have been observed, but are due to specific transverse excitations.

Flow visualization experiments are underway to determine if an azimuthal instability mechanism can explain the bifurcated flame phenomenon. Presumably, the intense vortex structure premixes the fuel and air to some extent, resulting in the blue flame. The side jet may consist of more pure fuel, which would explain the yellow flame tip sometimes observed. The cause of the intermittent flame behavior has not been determined. However, the air jet responded to a much wider range of forcing conditions than the flame, was much less intermittent in time, and was insensitive to the nozzle lip condition. The air jet responded to frequencies from 60 to 260 Hz, at minimum amplitudes of approximately half of those required for the flame to bifurcate. These differences suggest that the flame is not passively following the fuel jet, but can intermittently 'overcome' a bifurcated fuel jet to burn in a normal (not bifurcated) manner. This point may be important for the successful application of active and passive forcing techniques to non-premixed flames.

Research Plans

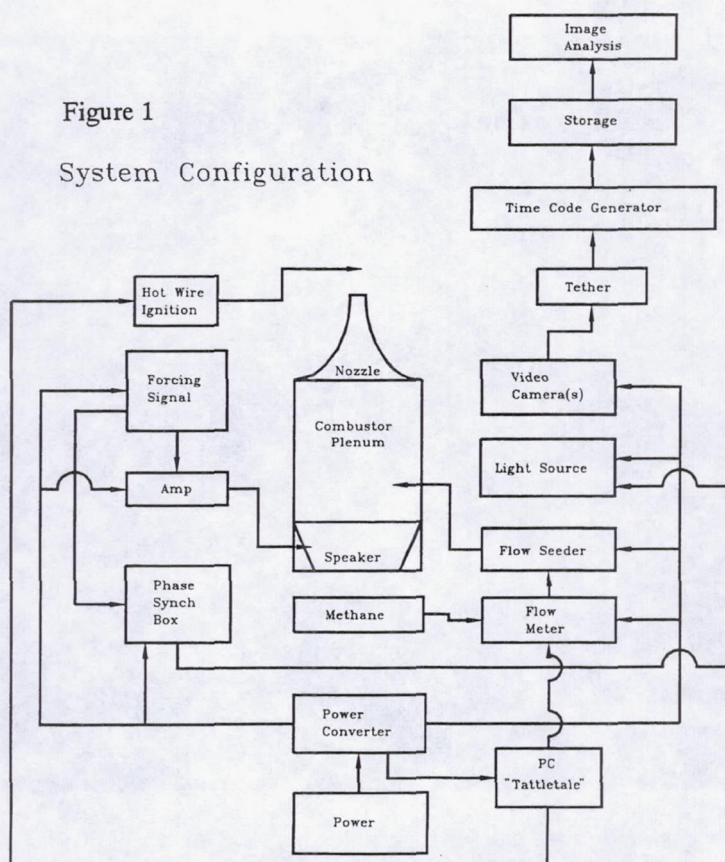
Since this is a new project, the first year is being spent building the combustor at CU Boulder, and conducting vertical and inverted experiments in 1-G. A variety of flow and forcing conditions will be examined, and flow visualization techniques will be refined. The second year will begin with quantitative velocity measurements in a limited number of flow/forcing conditions, using the PIV system at the Colorado School of Mines. The combustor system will also be integrated into the drop package, and a trip to NASA Lewis is planned for preliminary drop tests. One week will be devoted to checkout of the drop package, and 20 drops are projected for this stage. The third year will involve final tests in the drop tower. Approximately 20 drops should be required. Supporting flow visualization and PIV tests will be made at CU Boulder and CSM.

References

- ¹ Mahalingam, S., Cantwell, B.J., Ferziger, J.H., 'Full numerical simulation of coflowing, axisymmetric jet diffusion flames', *Physics of Fluids A* 2(5) 1990, pp. 720-728.
- ² Katta, V.R., and Roquemore, W.M., 'Role of inner and outer structures in transitional jet diffusion flame,' *Combustion and Flame* 92,1993, pp.274-282.
- ³ Schefer, R. W., Namazian, M., Filtopoulos, E.E.J., Kelly, J., 'Temporal evolution of turbulence/chemistry interactions in lifted turbulent jet flames,' *25th Symp. (Int'l) on Combustion*, In press, Combustion Institute, 1994.
- ⁴ Ho, C.M. and Gutmark, E., 'Vortex induction and mass entrainment in a small-aspect-ratio elliptic jet,' *Journal of Fluid Mechanics*, (1987) Vol. 179, pp. 383-405.
- ⁵ Kambe, T. and Takao, T., 'Motion of Distorted Vortex Rings', *Journal of the Physical Society of Japan*, 31, no.2,1971, pp. 591-599.

- ⁶ Grinstein, F.F., and Kailasanath, K., 'Three-dimensional numerical simulations of unsteady reactive square jets', *25th Symp. (Int'l) on Combustion*, In press, Combustion Institute, 1994
- ⁷ Lasheras, J.C., Lecuona, A. and Rodriguez, P., 'Vorticity dynamics in three-dimensional pulsating coflowing jet diffusion flames' *24th Symp. (Int'l) on Combustion*, In press, Combustion Institute, 1992, pp. 325-332.
- ⁸ Gutmark, E., Schadow, K.C., Parr, T.P., Hanson-Parr, D.M., and Wilson, K.J., 'Noncircular jets in combustion systems,' *Experiments in Fluids* 7, 1989, pp. 248-258.
- ⁹ Hsu, K.Y., Chen, L.D., Katta, V.R., Goss, L.P., Roquemore, W.M., 'Experimental and numerical investigations of the vortex-flame interactions in a driven jet diffusion flame,' AIAA 93-0455, 31st Aerospace Sciences Meeting, 1993.
- ¹⁰ Wilson, K.J., Gutmark, E., Schadow, K.C., and Smith, R.A. 'Active control of a dump combustor with fuel modulation,' AIAA-91-0368, 29th Aerospace Sciences Meeting, 1991.
- ¹¹ Chao, Y-C, Jeng, M-S, 'Behavior of the lifted jet flame under acoustic excitation,' *24th Symposium (Int'l) on Combustion*, Combustion Institute, 1992, pp. 333-340.
- ¹² Shaddix, C.R., Harrington, J.E., Smyth, K.C., 'Quantitative measurements of enhanced soot production in a flickering methane/air diffusion flame,' *25th Symposium (Int'l) on Combustion*, Combustion Institute, 1994, in press.
- ¹³ Pfizenmaier, E., Simon, J., Monkewitz, P., 'Bouquet with bifurcating jet diffusion flame,' *Gallery of Fluid Motion Supplement, Phys. Fluids A*, 5(9), 1993, pp. S9.
- ¹⁴ Tyndall, J., *Sound*, Third Edition, A.L. Fowle, pub. 1875, pp. 257-266.
- ¹⁵ Monkewitz, P.A., and Pfizenmaier, E., 'Mixing by "side jets" in strongly forced and self-excited jets,' *Physics of Fluids A*, 3(5), 1991, pp. 1356-1361.

Figure 1
System Configuration



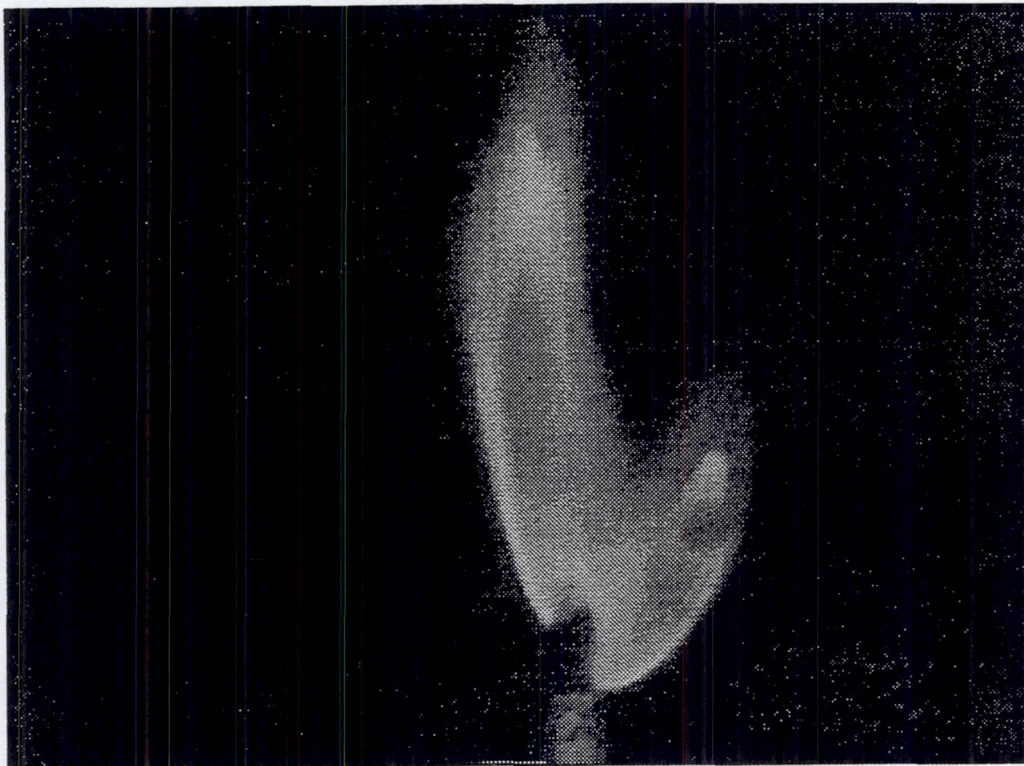


Figure 2: Bifurcated methane jet diffusion flame.

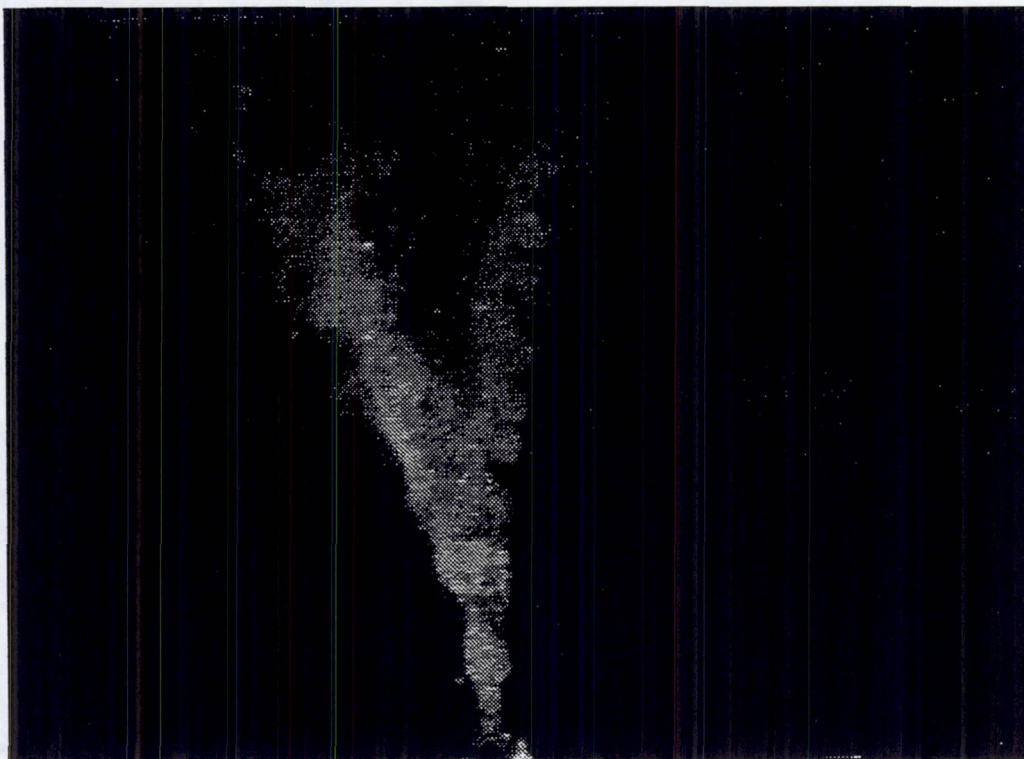


Figure 3: Strongly forced nonreacting jet.

EFFECT OF CF₃H AND CF₃Br ON LAMINAR DIFFUSION FLAMES IN NORMAL AND MICROGRAVITY

B. A. VanDerWege, Michael T. Bush and Simone Hochgreb
Massachusetts Institute of Technology
Cambridge, MA

and

Gregory T. Linteris
National Institute of Standards and Technology
Gaithersburg, MD

Introduction

Chemical inhibition of diffusion flames through addition of halogenated inhibitors is a problem of significant practical and scientific interest. Extensive studies on diffusion flames in microgravity have shown that these flames have significantly different characteristics than those under normal gravity [1,2]. However, the mechanisms through which inhibitors reach the reaction zone to suppress combustion in diffusion flames and the effectiveness of these compounds under reduced gravity have yet to be investigated.

This study reports preliminary results of investigations on the behavior of laminar jet diffusion flames upon the addition of bromotrifluoromethane (CF₃Br) and trifluoromethane (CF₃H) to the surroundings under normal and microgravity conditions. The results show that the flame structure in microgravity is significantly different from that under normal gravity conditions, and more importantly, that conditions for flame stability are less stringent under microgravity. Experiments show that flames that cannot be stabilized under normal gravity are quite stable under microgravity conditions. In addition, normal gravity experiments at reduced pressure (low buoyancy) did not reproduce the structure or stability limits of inhibited flames in microgravity.

Experiment

Experiments were conducted in the 2.2-second drop tower at the NASA-Lewis Research Center, utilizing an existing test rig, consisting of a 27 liter closed cylindrical vessel (254 mm diameter by 533 mm height) provided with four sideview windows. A CCD camera (Panasonic WV-CL352) provided images of the evolution of the flame during the drop. A single jet (1.7 mm diameter) was used in the presently reported experiments. Flow rates of methane were controlled by a pressure regulator and choked flow orifice, and peak flows measured using a 0-500 sccm Omega (FMA-5606-ST) mass flow meter. The flow rate of all experiments reported in this paper was 154 sccm, corresponding to a Reynolds number based on nozzle diameter of approximately 100. The tests were performed in a quiescent chamber environment containing 0-2 percent volume concentrations of CF₃Br and 0-12 percent CF₃H. A 2 percent methane environment was also tested for comparison with the inhibitor-laden oxidizing environment. Mixtures in the chamber were prepared by the partial pressure method, with initial evacuation and purging, followed by the addition of inhibitor, oxygen and nitrogen to the desired final pressure. Both atmospheric pressure and 0.25 atm tests were performed at normal and microgravity. The flames were ignited (after drop package release in microgravity experiments) by a retractable glow plug after about 20 ms of flow through the nozzle, and the images were then recorded.

Results

Atmospheric pressure experiments

The characteristics of the flames in normal and microgravity tests performed are listed in Table 1. The structures of the normal gravity, ambient pressure flames with and without inhibitor were essentially indistinguishable. The inhibited flames, however, exhibited a more intense flicker, and it was not possible to stabilize flames at concentrations beyond 1.5% CF₃Br in air at the present fuel flow rate. The structure of the diffusion flames under microgravity conditions, however, was extremely sensitive to the surrounding environment.

A typical methane laminar diffusion flame structure in microgravity is shown in Fig. 1, an oval, white, closed-tipped flame with $h/d \sim Re/2$ [2], with the base extending around the nozzle. At atmospheric pressure, addition of any amount of inhibitor or fuel to the oxidizing environment led to the appearance of an outer flame surrounding the core fuel jet flame. The addition of 4% CF₃H (by volume) to the oxidizing environment led to a somewhat more pronounced outer flame, and the opening of the flame tip (Fig. 2). At higher concentrations, the main observable effect of the addition of CF₃H was to completely suppress the sooty region, creating a flame with a blue base and no visible tip. This behavior (suppression of soot related luminosity) is consistent with the decrease of oxygen concentrations resulting from replacement by a diluent (in this case, the inhibitor itself) [3]. However, the flame which was observed was the size and shape of outer flames recorded in other experiments with fuel or inhibitor addition, which leads us to believe that there might be an inner flame which was however too dim to be registered by the camera.

In order to determine whether the outer flame could be attributed to the consumption of the inhibitor on the air side, 2 percent of methane was added to the surrounding air under microgravity conditions. The flame had approximately the same height as the flame without addition of methane, but the tip was open and a faint light halo surrounded the main reaction zone (Fig. 4).

The addition of CF₃Br to the oxidizing environment under microgravity at ambient pressure produced a marked change in structure (Fig. 5). There is an obvious 'tulip' double flame structure, with a visible region significantly shorter than the uninhibited flame. An open-tipped inner flame is surrounded by a wider outer flame whose visible region ends shortly before the outer flame. Instead of the rounded base, a flat circular base slightly upstream of the nozzle tip is visible. The visible outer flame is most likely a result of CF₃Br reaction, supported thermally by the main inner flame. Such behavior has been observed experimentally in coflowing two dimensional diffusion flames [4], opposed jet diffusion flames [5], and surmised from numerical simulations [6]. The study in coflowing flames identified the outer visible flame spectroscopically as greenish Br₂ emission. A Br₂ peak would be expected also from opposed stretched flame calculations [6]. The observed color of the outer flame was closer to yellow than green. It remains to be determined whether the yellow luminosity is a result of soot in the outer flame, or of the camera response at the given settings. The opening of the flame tip could be explained by the reduction in the maximum stretch supported by the diffusion flame at the tip with the addition of inhibitor [7]. However, that would not explain the flame tip opening in the case of addition of plain methane to the surroundings.

Low Pressure Experiments (0.25 atm)

The effects of reduction in pressure on normal and microgravity flames with the addition of CF₃Br. were explored to understand how normal gravity, weakly buoyant low pressure diffusion flames relate to microgravity flames. Experiments were performed both at normal and microgravity in a 0.25 atm quiescent environment (corresponding to a reduction in buoyancy by a factor of 16) with and without the addition of CF₃Br.

Reduction of pressure at normal gravity leads to elimination of flicker at 0.25 atm, and the presence of a stable oval white flame surrounded by a dim halo of glowing gases (Fig. 6). Addition of 1% CF₃Br causes the flame to lift off the nozzle and stabilize at about 25 mm from the nozzle as a flat blue-white flame with a circular base and an oval tip (Fig. 7). The stabilization mechanism is probably the same as in other lifted flames, where premixing at the base aids in the establishment of a stoichiometric region. With the addition of 2 percent CF₃Br, the flame lit but was promptly blown off.

Under microgravity conditions, however, apparently stable anchored flames (for the duration of the test) were observed for both 1 and 2 percent CF₃Br addition (Figs. 8-9). The flames were oval, with closed tip, a wide blue base and a broad gas halo. The ability to stabilize these flames shows once again that both under normal and lower pressures, conditions for the extinguishment of diffusion flames at these low pressures appear to be *more stringent* under microgravity than at normal gravity. Therefore, experiments under weakly buoyant conditions may not capture the stability limits of flames under inhibiting environments in microgravity.

Conclusions

The present experiments with laminar jet diffusion flames burning under normal and microgravity conditions in a quiescent environment with addition of halogenated hydrocarbons have yielded the following conclusions:

1. Stability limits of flames with the addition of CF₃Br and CF₃H to the oxidizer environment under microgravity are wider than those under normal gravity.
2. The addition of inhibitors to the oxidizer under microgravity conditions creates a double flame structure. The outer flame is probably a region where the inhibitor reacts, supported by the heat release of the inner fuel flame. This behavior is particularly clear in the case of CF₃Br.
3. Addition of halogenated inhibitors to μ g flames leads to shorter, open tipped flames. Addition of large amounts (>4%) of CF₃H suppresses the appearance of luminous soot.
4. At low pressures (0.25 atm), normal gravity diffusion flames resemble their microgravity counterparts more closely. However, flames at these pressures that cannot be stabilized under normal gravity appear to be stable under microgravity.

Future Work

The goal of the project is to understand the effectiveness and action of halogenated inhibitors on the extinction of diffusion flames at reduced gravity. Additional experimental work in microgravity and ground based normal gravity experiments are planned. Numerical and analytical work to interpret and explain the experimental findings is being prepared for the near future.

The effects of diluents, oxygen and inhibitor mole fractions, different halogenated inhibitors, fuel types and jet Reynolds numbers will continue to be investigated in the 2.2-second drop tower. In addition, the study of inhibited CO/H₂ flames is also being considered, given the obvious simplification of the fuel chemistry and the absence of soot. A normal gravity, low-pressure diffusion flame burner for normal and microgravity experiments is currently under construction at MIT. Additional diagnostics, including IR imaging, radiation measurement, and thermocouples, are being considered. Complementary experiments on the behavior of counterflow diffusion flames will be conducted at NIST this Spring to aid in the interpretation of the laminar jet flame observations.

Plans for numerical modeling of the system are: a) interpret the structure and validate chemical model for halogenated inhibitor addition using a 1D counterflow diffusion flame code; b) identify

potential paths for reduction of the chemical mechanism and c) incorporate the reduced mechanism into a 2D jet diffusion flame.

Acknowledgements

The invaluable expertise and generosity of Dr. David L. Urban in permitting and assisting us with the use of an existing rig for our initial drop tower experiments is gratefully acknowledged. This work is funded under NASA Microgravity Research Grant NAG3-160. Additional support was also provided by NSF through Graduate Research Fellowships for B. A. VanDerWege and M. T. Bush.

References

1. Law, C. K. and Faeth, G. M. , "Opportunities and Challenges of Combustion in Microgravity", *Prog. Combust. Sci.* **20**, pp. 65-113 (1994).
2. Bahadori, M. Y. and Edelman, R. B., "Effects of Buoyancy of Gas Jet Diffusion Flames", NASA Contractor Report 191109 (1993).
3. Bahadori, M. Y. and Edelman, R. B., "Effects of Oxygen Concentration on Radiative Loss from Normal Gravity and Microgravity Methane Diffusion Flames", AIAA paper 92-0243 (1992).
4. Simmons, R. F. and Wolfhard, H. G. "The Influence of Methyl Bromide on Flames, Part 2 - Diffusion Flames", *Trans. Far. Soc.* **52**, p. 53 (1956).
5. Trees, D., Ilincic, N., Weissweiler, T., Zamfirescu, N., Grudno, A. and Seshadri, K., "Experimental and Numerical Studies on Chemical Inhibition of Methane-Air Diffusion Flames by CF₃Br and CF₃H", to appear, Central States/Western States/Mexican National Sections of the Combustion Institute, April 23-26, 1995.
6. Masri, A. R. "Chemical Inhibition of Nonpremixed Flames of Hydrocarbon Fuels with CF₃Br", *Combust. Sci. and Tech.* **96**, pp 189-212 (1994).
7. Hamins, A., Trees, D., Seshadri, K. and Chelliah, H. K. "Extinction of Nonpremixed Flames with Halogenated Fire Supressants", *Combust. Flame*, **99**, 2, pp. 221 (1994).

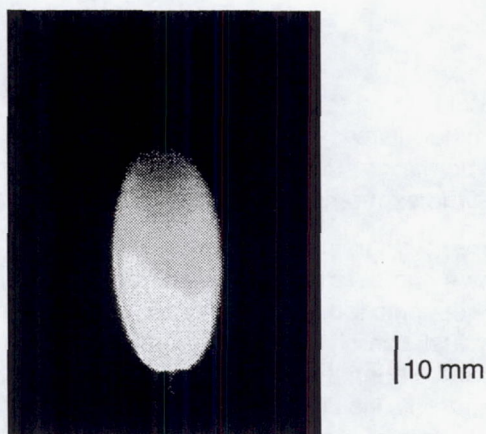


Figure 1. Uninhibited CH₄ laminar jet flame in microgravity and 1 atm ($d = 1.7$ mm, $Q = 154$ sccm, $Re = 98$). All subsequent figures show same flow conditions.

Table 1. Summary of experimental results for inhibited CH₄ laminar diffusion flames

(d = 1.7 mm, Re = 98, Q = 154 sccm, fuel: methane)

Environment ^a	P (atm)	μg/ng	h (mm) ^b	Characteristics
Air	1.0	ng	40±10	Sooty with blue base. >15 Hz flicker.
Air	1.0	μg	55	Sooty, closed-tip, rounded base. Flame transitions from yellow to red at the very tip.
1% CH ₄	1.0	ng	40±10	Indistinguishable from flame without CH ₄ added.
2%CH ₄	1.0	μg	45	Thin, dim outer flame, core flame sooty with open tip.
1% CF ₃ Br	1.0	ng	57±25	Blue base shrinks and flickers. Flamelets break off from the long tip.
1.5% CF ₃ Br	1.0	ng	75±15	Flame blows off and stabilizes unsteadily at about 25 mm above the nozzle with a circular rim of about 10 mm in diameter.
2% CF ₃ Br	1.0	ng		Flame ignites but is blown off almost immediately.
1% CF ₃ Br	1.0	μg	38 (inner) 27(outer)	Obvious double (inner-outer) flame structure. Inner flame is open tipped and about 20 mm in width. The outer flame is about 30 mm wide and sorter, with apparent flat blue base of about 10 mm diameter.
1.5% CF ₃ Br	1.0	μg	38 (inner) 25 (outer)	Very similar to 1% CF ₃ Br flame.
4 and 8% CF ₃ H	1.0	ng	45±12 / 50±15	Similar to uninhibited flame, with larger blue base and intense flickering.
4% CF ₃ H	1.0	μg	45	Dim but visible double flame structure. Inner flame is about 25 mm wide, orange and more diffuse than base flames, with a wide open tip. Outer flame is visible only near the base.
8 and 12%	1.0	μg	25 (outer?)	Visible flame region is 30 mm wide, with a conical blue base and apparently no soot, possibly due to the reduced oxygen concentrations under the high inhibitor mole fractions.
Air	0.25	ng	30	Oval white/blue flame surrounded by a thin halo of dimly glowing gasses.
1% CF ₃ Br	0.25	ng	25	Flame has a wide circular base lifted about 30 mm off nozzle, blue-white with oval tip. At 2%, flame lights and immediately blows off.
1 and 2% CF ₃ Br	0.25	μg	57 / 65	Closed tip oval blue-white flame with bottom half blue and upper half sooty, with a fairly broad halo of glowing gasses. At 2%, the halo is brighter, and a larger fraction of the flame white.

a) Balance air: 0.21% O₂, 0.79% N₂

b) For flickering flames, average height. For lifted flames, height is measured from flame base, not nozzle.

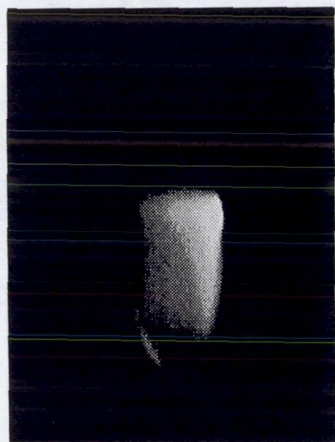


Fig. 2. 1atm/ μ g/4% CF₃H

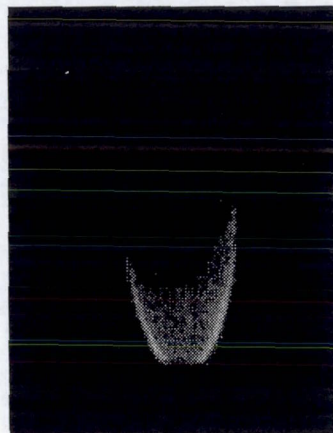


Fig. 3. 1atm/ μ g/8% CF₃H

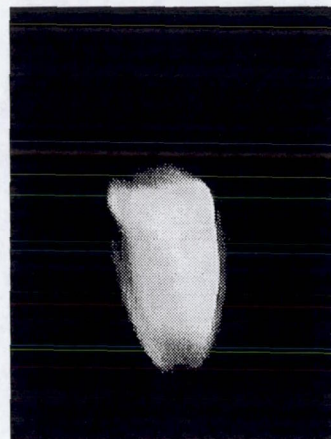


Fig. 4. 1atm/ μ g/2% CH₄

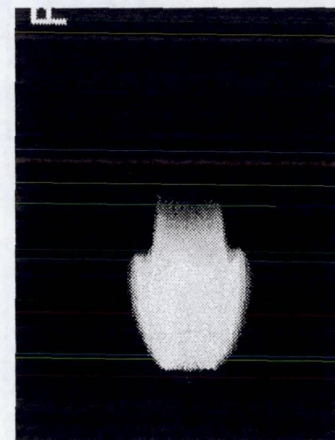


Figure 5. 1atm/ μ g/1% CF₃Br

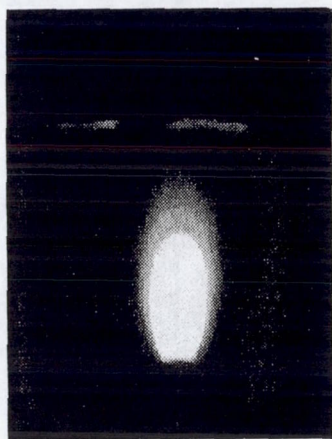


Fig. 6. 0.25 atm/ng/ air only

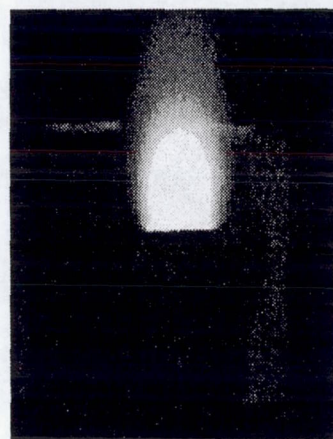


Fig. 7. 0.25 atm/ng/ 1% CF₃Br

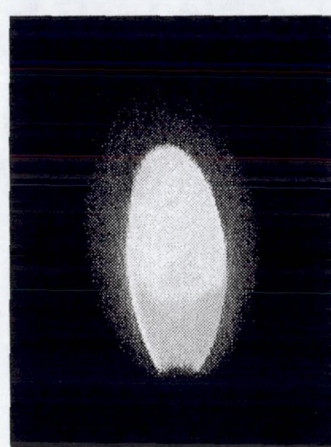


Fig. 8. 0.25 atm/ μ g/ 1% CF₃Br

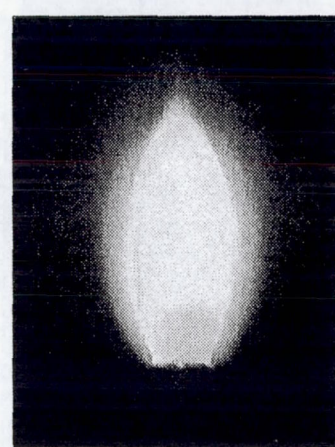


Fig. 9. 0.25 atm/ μ g/ 2% CF₃Br

DETAILED MODELING ANALYSIS FOR SOOT FORMATION AND RADIATION IN MICROGRAVITY GAS JET DIFFUSION FLAMES

Jerry C. Ku and Li Tong, Department of Mechanical Engineering, Wayne State University, Detroit, Michigan 48202
and
Paul S. Greenberg, Microgravity Combustion Branch, NASA/Lewis, Cleveland, Ohio 44135

Introduction

Radiation heat transfer in combustion systems has been receiving increasing interest (ref. 1). In the case of hydrocarbon fuels, a significant portion of the radiation comes from soot particles, justifying the need for detailed soot formation model and radiation transfer calculations. For laminar gas jet diffusion flames, results from this project (4/1/91-8/22/95) and another NASA study (ref. 2) show that flame shape, soot concentration, and radiation heat fluxes are substantially different under microgravity conditions.

Our emphasis is on including detailed soot transport models and a detailed solution for radiation heat transfer, and on coupling them with the flame structure calculations. In this paper, we will discuss the following three specific areas:

1. Comparing two existing soot formation models, and identifying possible improvements.
2. A simple yet reasonably accurate approach to calculating total radiative properties and/or fluxes over the spectral range.
3. Investigating the convergence of iterations between the flame structure solver and the radiation heat transfer solver.

Modeling of Jet Diffusion Flame Structure

The structure of turbulent jet diffusion flames is modeled using the Favre-averaged equations for conservation of mass, momentum, and mixture fraction. A conserved scalar approach (refs. 3, 4 and 5) with an assumed probability density function (pdf) and a k - ϵ - g turbulence model (ref. 6) are used. All governing equations can be written in a general form as (ref. 7)

$$\frac{\partial}{\partial x}(\bar{\rho}\bar{u}\phi) + \frac{1}{r}\frac{\partial}{\partial r}(r\bar{\rho}\bar{v}\phi) = \frac{1}{r}\frac{\partial}{\partial r}\left(r\mu_{eff}\frac{\partial\phi}{\partial r}\right) + S_\phi, \quad (1)$$

where $\phi = 1, \bar{u}$ (velocity), \bar{f} (mixture fraction), k (kinetic energy), ϵ (dissipation), or g (variance on f). Details for μ_{eff} (effective viscosity), S_ϕ (source term) and assumptions can be found in references. Buoyancy effects are considered in mean flow only, neglecting buoyancy-turbulence interactions. For laminar flames, Eq. (1) is simplified accordingly.

The system represented by Eq. (1) is solved using the block-tridiagonal code of Chen et al. (ref. 8). State relationships are constructed from equilibrium calculations using STANJAN (ref. 9) to allow chemical reactions to be decoupled from flow calculations. More accurate laminar flamelet approaches (refs. 10 and 11) may be considered in the future.

Modeling of Soot Formation and Oxidation

We have considered two sets of soot formation and oxidation models. Both describe the transport of soot particles based on Eq. (1). The two-equation model developed by Moss, Syed and Stewart (refs. 12 and 13) is based on number density (N) and volume fraction (f_v), and the two respective source terms are

$$S_{\hat{N}} = \bar{\alpha} - \bar{\beta}\bar{\rho}^2\hat{N}^2 - n_0^{1/3}\bar{\chi}\bar{\rho}\hat{f}_v^{-1/3}\hat{N}^{4/3}, \quad \phi = \hat{N} \equiv \frac{N}{\rho n_0}; \quad (2)$$

$$S_{\hat{f}_v} = n_0^{1/3}(\bar{\gamma} - \bar{\chi})\bar{\rho}\hat{f}_v^{2/3}\hat{N}^{1/3} + C_{\delta}\bar{\alpha}, \quad \phi = \hat{f}_v \equiv \frac{\rho_s f_v}{\rho}; \quad (3)$$

where $n_0 = 6 \times 10^{26}$ is Avogadro's number and ρ_s is the mass density of soot (typically 1.8-2.0 g/cm³). Rate-equations of Arrhenius type are used to model nucleation (α), growth (β), coagulation (γ) and oxidation (χ), in terms of flame temperature T , mixture density $\bar{\rho}$, fuel and gas mole fractions, and activation temperatures. Existing soot oxidation

models (refs. 14 and 15) are modified to include oxidation by both O_2 and OH . Details on model coefficients and the oxidation model can be found in ref. 16. For laminar flames, both Eq. (1) and rate-equation models are simplified, with the addition of a radial thermophoretic velocity $v_r = -0.54(v/T)(\partial T/\partial r)$.

Another model is a one-equation model, based on volume fraction only, developed by Khan et al. (refs. 17 and 18). This model characterizes soot formation by an Arrhenius-type equation, and the corresponding source term is

$$S_{\hat{f}_s} = C_k P_{fu} \phi^3 \left(\frac{\rho}{\rho_s} \right) \exp \left(-\frac{E_s}{RT} \right), \quad \phi = \hat{f}_v \equiv \frac{\rho_s \hat{f}_v}{\rho}; \quad (4)$$

where $C_k = 16.8 \text{ kg/Nms}$, P_{fu} denotes the partial pressure of unburned fuel, ϕ is the local fuel/air equivalence ratio, and $E_s = 40000 \text{ cal/mole}$ is the activation energy. The soot oxidation model of Lee et al. (ref. 19) is adopted, which is similar to Eq. (4), except with $\phi^3(\rho/\rho_s)$ replaced by \hat{f}_v/\sqrt{T} .

The model by Khan et al. is simpler, but it may not be as physically sound as that by Moss et al., since it does not include such mechanisms as coagulation which causes decreasing number density under constant volume fraction.

Solution for Flame Radiation Heat Transfer

Although it plays an important role, radiation heat transfer is usually not treated in detail in combustion analyses due to such difficulties as the accuracy and computational efficiency of various solutions for the radiative transfer equation (ref. 20), the coupling of radiation and combustion solvers, the accuracy of spectral radiative properties, and efficient methods for integrating fluxes and other results over the spectral range.

We chose the recently developed YIX method (refs. 21 and 22) for calculating the radiative heat flux \bar{q}_{rad} and its divergence. The YIX method is a numerical approach for solving the integral formulation of the radiative transfer equation by reducing the order of the multiple distance-angular integrals. The name YIX comes from the shape of the pattern of integration points for three, two, and four angular directions. One important attribute of this method is that these integration points can be pre-calculated and stored, significantly reducing computational time. For multi-dimensional geometries, discrete ordinate sets are used for angular quadratures. Although computationally quite intensive, the YIX method has proven to be very accurate and suitable for nonhomogeneous media (refs. 23 and 24). Simplified models such as a fixed percentage of local heat loss from equilibrium everywhere, a temperature modified from that under equilibrium as $T = T_{eq}[1 - \beta(T_{eq}/T_{eq,max})^4]$ (ref. 14), and a heat "sink" as $S_\phi = -\epsilon\sigma(T^4 - T_\infty^4)/\ell$ (ref. 25) have each been tested and found inaccurate. We derived the spherical harmonics (P_N) approximate solution for non-homogeneous media following ref. 26, but found it numerically unstable in optically-thin regions.

The radiation solver is coupled to the flame structure solver through the energy equation. For diffusion flames, the energy equation takes the same form as Eq. (1), with $\phi = H$ (total enthalpy) and $S_\phi = -\nabla \cdot \bar{q}_{rad}$, and the latter can be calculated from a solution for the radiative transfer equation. These two solvers, both depending on the temperature, are computationally incompatible. The solver for flame structure, soot transport, and the energy equation solves parabolic differential equations of Eq. (1) type. The solver for radiative transfer, YIX or otherwise, is inherently not parabolic, since radiation is an "integral" phenomenon over all distances and solid angles. We chose an iterative approach and used temperature as the convergence criterion. The iteration starts with the flame structure solver and an initial guess of $S_\phi = -\epsilon\sigma(T^4 - T_\infty^4)/\ell$ to calculate velocities, gas and soot concentrations, density, and flame temperature. The resulting temperature is used for calculating $\nabla \cdot \bar{q}_{rad}$ from the YIX solver. The resulting $\nabla \cdot \bar{q}_{rad}$ is substituted back into the structure solver to update (by averaging the two latest runs) velocities, concentrations, density, and temperature. This process is then repeated until a convergence on the temperature is accomplished between two subsequent iterations ($\Delta T/T < 0.002$). The turbulence-radiation interactions, which have been shown to be significant by Gore et al. (ref. 27), will be included in the future.

To evaluate spectral radiative properties, the absorption coefficient for soot aggregate is calculated from the Rayleigh solution (ref. 28) using the complex refractive index calculated from the Drude-Lorentz dispersion model and the parameter set of Habib and Vervisch (ref. 29). Scattering from soot particles is neglected at present to reduce computational time, but will be included in the future. The exponential-wide-band model of Edwards (ref. 30) is used to calculate the absorption coefficient for CO_2 and H_2O gases. The most accurate way to evaluate the total (i.e., across the spectral range) fluxes and divergence of flux is first to calculate them for each subdivided spectral range and then calculate the quadratures, but this is inefficient due to the large number of spectral subdivisions necessary to account for the steep variation of gas absorption coefficients and the number of iterations between the flame structure and the radiation solver. To focus on the convergence of iterations, we will test the Planck (a_p) and the Rossland (a_R) mean absorption coefficients given as (ref. 31)

$$a_p(T,P) = \frac{1}{\sigma T^4} \int_0^\infty a_\lambda(\lambda,T,P) e_{\lambda b}(\lambda,T) d\lambda, \text{ and } a_R(T,P) = \left[\int_0^\infty \frac{1}{a_\lambda(\lambda,T,P)} \frac{\partial e_{\lambda b}(\lambda,T)}{\partial e_b(T)} d\lambda \right]^{-1}. \quad (5)$$

In the future, we will examine other more sophisticated approaches.

Results and Discussions

We first compare the radiation heat transfer results from the YIX method based on true spectral integration (1 to 20 μm) and on both mean coefficients for a simulated turbulent ethylene diffusion flame. Fig. 1 shows a comparison of mixture spectral absorption coefficient against both means, and suggests that the Rossland mean should be reasonably accurate. Fig. 2 shows that the flux divergence based on the Rossland mean agrees quite well with that from integration. We thus base all subsequent "coupled" calculations on the Rossland mean coefficient.

We next compare the soot formation models by Moss et al. and by Khan et al. in Fig. 3(a) for flame temperature and in Fig. 3(b) for soot volume fraction, against experimental data for a laminar flame (ref. 32). From these figures, it is unclear which model is superior. However, calculations based on the experimental temperature, which is higher than predicted values around the centerline, reveal that Khan's model overpredicts the centerline volume fraction by a factor of 2, whereas Moss's changes only slightly. We therefore favor Moss's model at present. When we applied Moss's model with the same set of coefficients for the same fuel at different flow rates and compared with data, we found that the model is relatively insensitive to variations in fuel flow rate, and we will improve this in the future. Fig. 3(a) shows that the inclusion of radiative heat transfer provides a more accurate and correct trend in temperature profiles, when compared to those under adiabatic. Fig. 3(c) shows that the temperature converges smoothly in less than 10 iterations.

We then tested the model on normal gravity (1-g) and microgravity (0-g) laminar acetylene flames, for which we have measured soot volume fraction data for comparison. Fig. 4 shows comparisons between 1-g and 0-g for (a) measured soot volume fraction, (b) predicted soot volume fraction, and (c) predicted temperature. The dotted curves in temperature map are predicted flow streaklines, which also indicate the paths traversed by soot particles. Results in (b) and (c) were calculated using soot formation modeling coefficients slightly different from those for ethylene in Fig. (3). It is encouraging that the soot formation model is capable of accurately predicting the overall level and shape of the volume fraction distribution, especially since this is a smoking flame. It is also encouraging that the same 1-g soot modeling coefficients can be used to predict 0-g volume fraction with reasonable accuracy. Although the model predicts a wider soot shell than that measured for both 1-g and 0-g, it is expected that further adjustments in soot modeling coefficients will yield even better predictions.

Finally, we tested the model on turbulent ethylene flames, for which we should have measured data for comparison within a month or two. Fig. 5 shows a comparison of two predictions, one using the YIX solver and the other using the simple sink term model, against measured data for (a) volume fraction, and (b) temperature. Here, although it appears that the volume fraction results from the YIX solver are more accurate, the temperature results are roughly the same. Fig. 6 shows a comparison of 1-g and 0-g predictions for (a) volume fraction, and (b) temperature, using the same set of soot modeling coefficients and the YIX solver. Since this turbulent flame is momentum-dominant, the difference in flame shapes between 1-g and 0-g is not as substantial as that for the laminar flame in Fig. 4, which is more buoyancy-dominant.

In our future work, we will develop more accurate means of evaluating total radiative quantities, such as the wide-band model used by Song and Viskanta (ref. 33). Their derivation of the "mean" radiative transfer equation to include turbulence-radiation effects is also worth noting. To investigate turbulence-radiation effects, we must also study the implementation of joint pdf (refs. 27 and 34) for correlating enthalpy, temperature, and mixture fraction. We will look for developments in turbulence-buoyancy interactions (ref. 15), which should be influential on 0-g flames.

Acknowledgments The authors are indebted to J.-Y. Chen of UC/Berkeley for providing the turbulent flame code.

References

1. M. G. Carvalho, F. Lockwood, and J. Taine (Eds.), *Heat Transfer in Radiating and Combusting Systems*, Springer-Verlag, Berlin-Heidelberg, 1991.
2. M. Y. Bahadori and R. B. Edelman, NASA CR-191109, 1993.
3. R. W. Bilger, Prog. Energy Comb. Sci., Vol. 1, 87-109, 1976.
4. S.-M. Jeng and G. M. Faeth, Vol. 106, 721-727, 1984.
5. J. P. Gore and G. M. Faeth, 21st Symp. (Int'l) Comb., 1521-1531, 1986.
6. F. C. Lockwood and A. S. Naguib, Comb. Flame, Vol. 24, 109-124, 1975.
7. G. M. Faeth, S.-M. Jeng, and J. Gore, ASME HTD-Vol. 45 Heat Transfer in Fire and Comb. Systems, 137-151, 1985.

8. J.-Y. Chen, W. Kollmann, and R. W. Dibble, 18th Annual Pittsburgh Conf. Modeling and Simulation, 1987.
9. W. C. Reynolds, Department of Mechanical Engineering, Stanford University, 1986.
10. R. W. Bilger, Comb. Flame, Vol. 30, 277-284, 1977.
11. C. N. Peters and B. Rogg (Eds.), Reduced Kinetic Mechanisms for Applications in Combustion Systems, Springer-Verlag, Berlin-Heidelberg, 1993.
12. K. J. Syed, C. D. Stewart, and J. B. Moss, 23rd Symp. (Int'l) Comb., 1533-1541, 1990.
13. J. B. Moss, C. D. Stewart, and K. J. Syed, 22nd Symp. (Int'l) Comb., 413-423, 1988.
14. K. M. Leung, R. P. Lindstedt, and W. P. Jones, Comb. Flame, Vol. 87, 289-305, 1991.
15. M. Fairweather, W. P. Jones, and R. P. Lindstedt, Comb. Flame, Vol. 89, 45-63, 1992.
16. L. Tong, Ph. D. Dissertation, Wayne State University, expected May 1995.
17. I. M. Khan, G. Greeves, and D. M. Probert, Institution of Mechanical Engineers, p. 205, 1971.
18. I. M. Khan and G. Greeves, Chapter 25 in Heat Transfer in Flames, Afgan and Beer, Eds., Scripta Book Co, 1974.
19. K. B. Lee, M. W. Thring, and J. M. Beer, Comb. Flame, Vol. 6, 137-145, 1962.
20. T. W. Tong and R. D. Skocypec, Developments in Radiative Heat Transfer, S. T. Thynell et al., Eds., ASME HTD-Vol. 203, 235-264, 1992.
21. Z. Tan and J. R. Howell, J. Thermophys. Heat Transfer, Vol. 4, 419-424, 1990.
22. P.-F. Hsu, Z. Tan, and J. R. Howell, J. Thermophys. Heat Transfer, Vol. 7, 487-495, 1993.
23. P.-F. Hsu and J. C. Ku, J. Thermophys. Heat Transfer, Vol. 8, 434-440, 1994.
24. P.-F. Hsu and J. C. Ku, submitted to ICHMT Int'l. Symp. Radiative Transfer, 1995.
25. J. H. Kent and D. Honnery, Comb. Sci. Tech., Vol. 54, 383-397, 1987.
26. M. P. Menguc and R. Viskanta, J. Heat Transfer, Vol. 108, 271-276, 1986.
27. J. P. Gore, U.-S. Ip, and Y. R. Sivathanu, J. Heat Transfer, Vol. 114, 487-493, 1992.
28. J. C. Ku and K.-H. Shim, J. Heat Transfer, Vol. 113, 953-958, 1991.
29. Z. G. Habib and P. Vervisch, Comb. Sci. Tech., Vol. 59, 261-274, 1988.
30. D. K. Edwards, Advances in Heat Transfer, Vol. 12, T. F. Irvine, Jr. and J. P. Harnett, Eds., Academic Press, New York, 115-193, 1976.
31. R. Siegel and J. R. Howell, Thermal Radiation Heat Transfer, 3rd ed., Hemisphere, Washington, DC, 1992.
32. R. J. Santoro, T. T. Yeh, J. J. Horvath, and H. C. Semerjian, Comb. Sci. Tech., Vol. 53, 89-115, 1987.
33. T. H. Song and R. Viskanta, J. Thermophys. Heat Transfer, Vol. 1, 56-62, 1987.
34. J. Janicka and W. Kollmann, 17th Symp. (Int'l) Comb, 421-430, 1978.

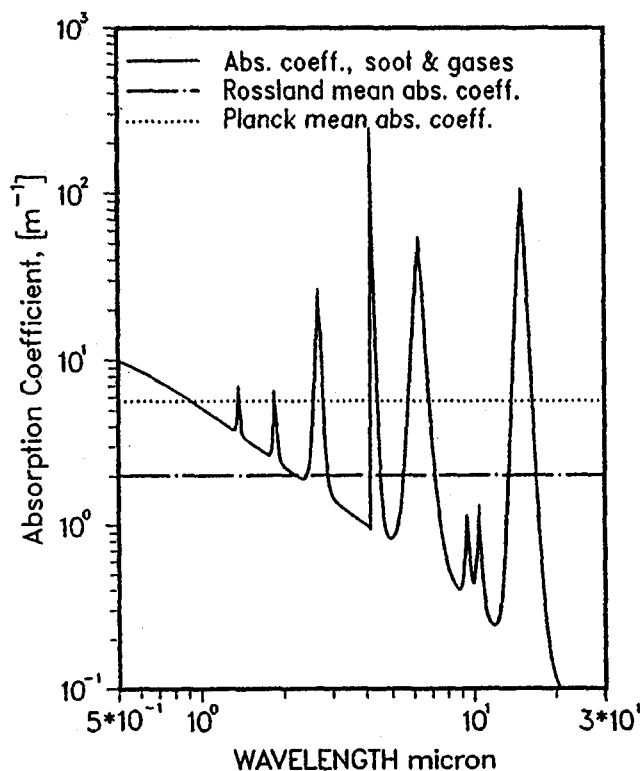


Fig. 1 Absorption coefficients for a soot and gases mixture at 1400K, with 0.1 mole fraction for CO_2 and H_2O , and a soot volume fraction of 10^{-6} .

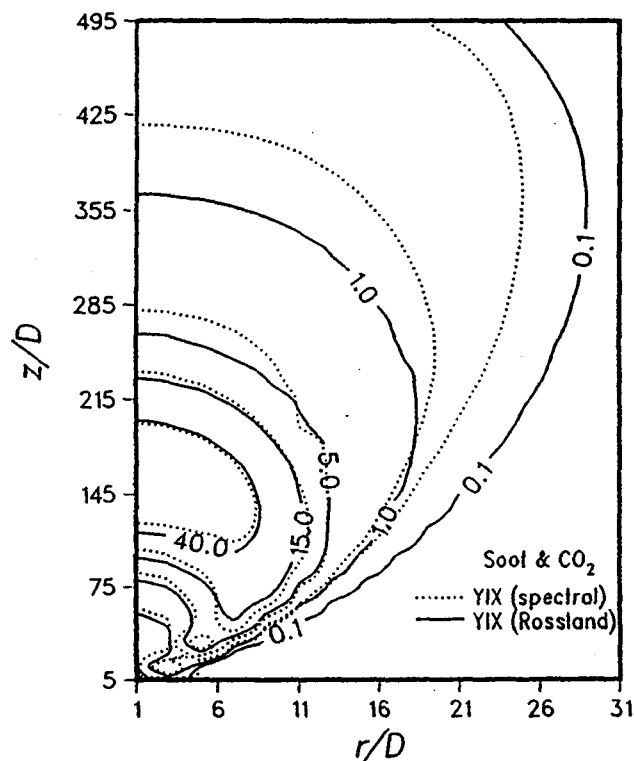


Fig. 2 The divergence of flux contours for a simulated ethylene diffusion flame ($D = 0.58$ mm, $\dot{Q} = 3.96$ cm³/sec, and $Re = 536$).

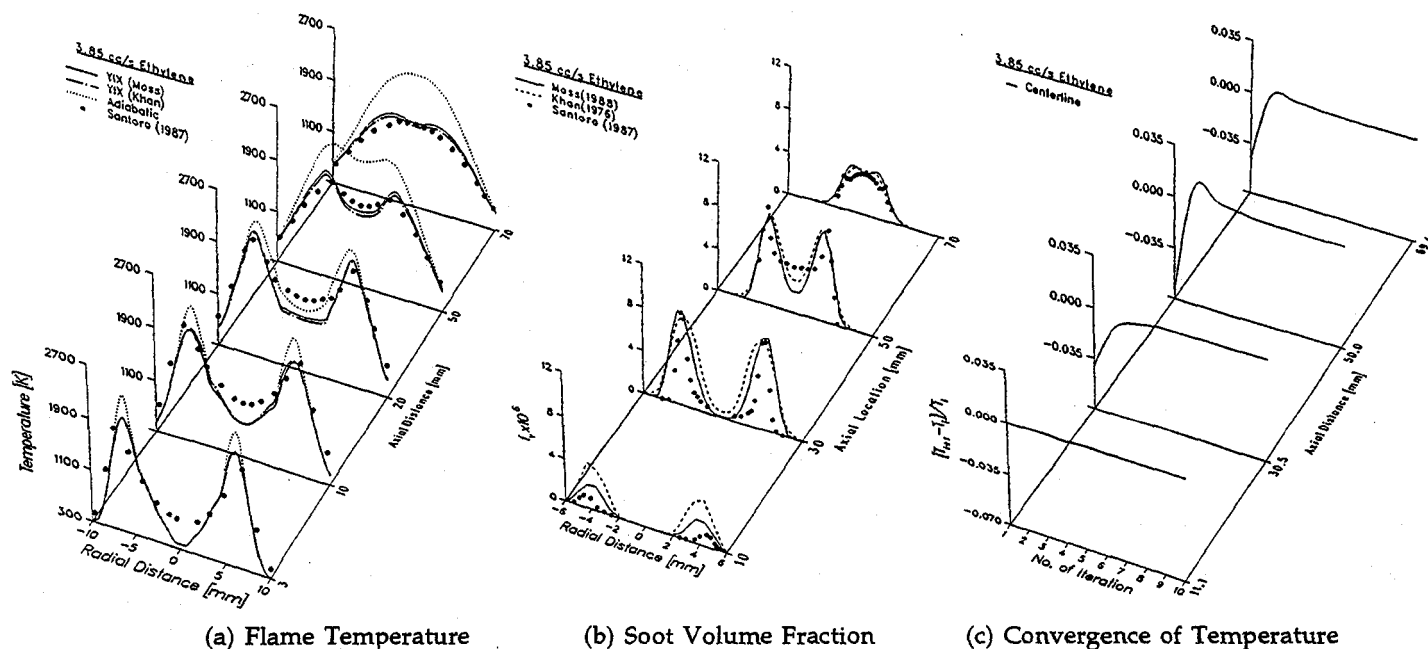


Fig. 3 Comparisons of model predictions to experimental data, and the trend of convergence of temperature during iterations between the structure and the radiation solver, for a laminar ethylene co-flow diffusion flame (ref. 32).

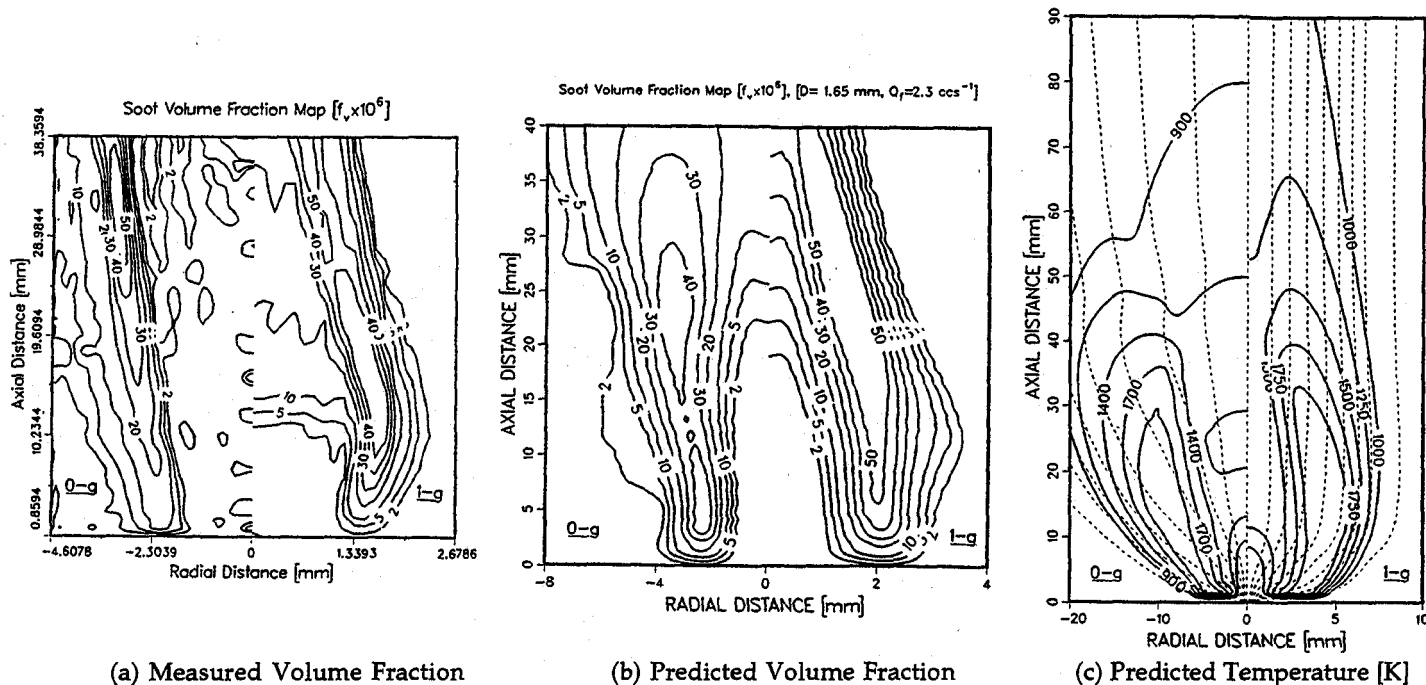


Fig. 4 Comparisons of model predictions to experimental data for a laminar acetylene jet diffusion flame.

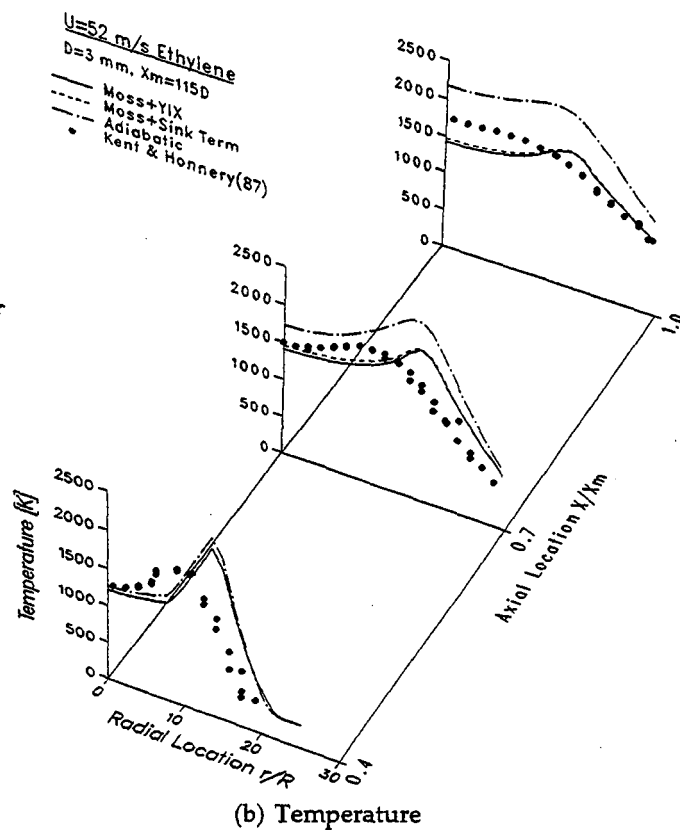
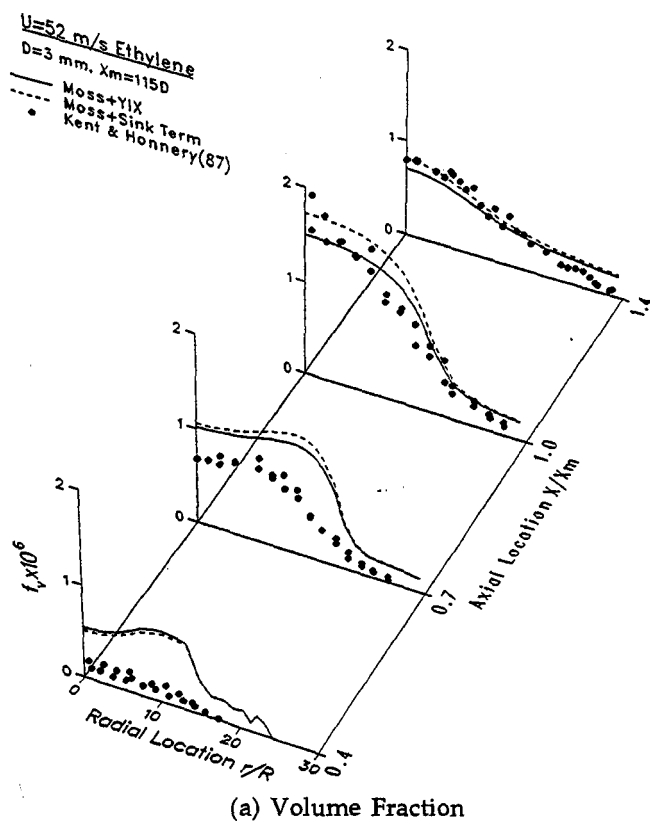


Fig. 5 Comparisons of model predictions to experimental data for a 1-g turbulent ethylene jet diffusion flame.

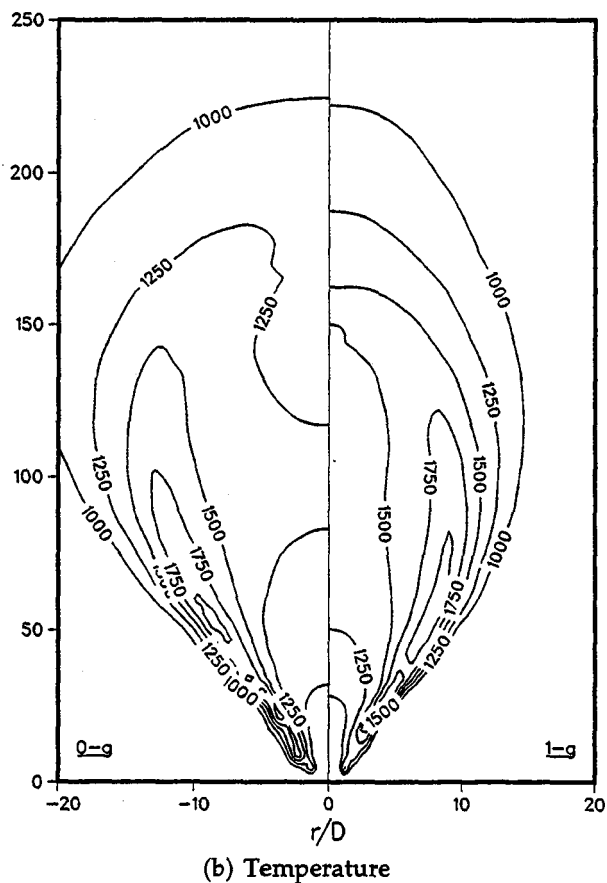
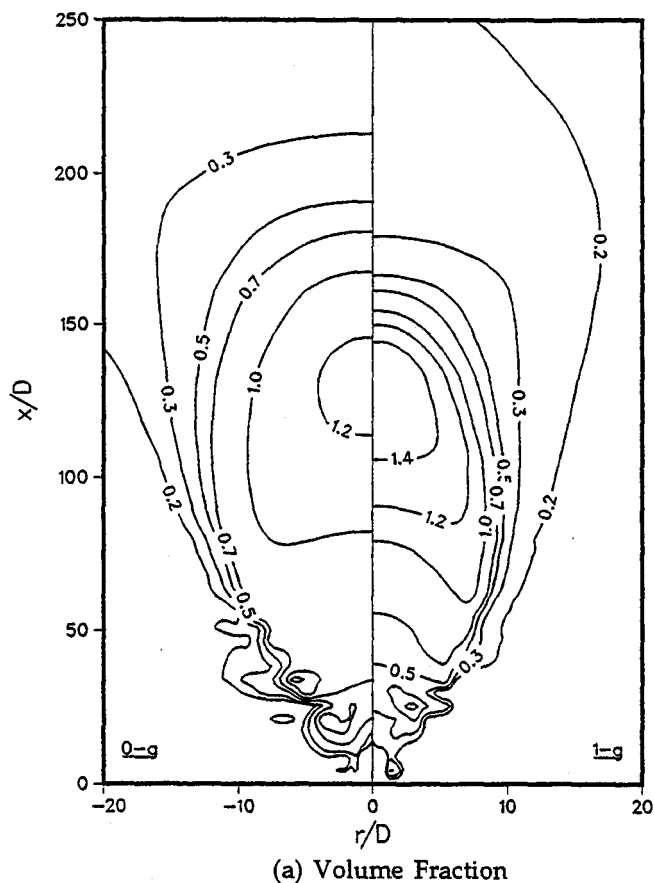


Fig. 6 Predictions for 1-g and 0-g turbulent ethylene jet diffusion flames ($D = 3$ mm, $V = 52$ m/s, and $Re = 9.62 \times 10^3$).

STRUCTURE AND DYNAMICS OF DIFFUSION FLAMES IN MICROGRAVITY

Moshe Matalon

McCormick School of Engineering and Applied Science
Northwestern University

Introduction

The objectives of this project are to gain insight into diffusion flames by modeling various configurations related to ongoing experimental investigations in the microgravity combustion science program. The emphasis of the work is to understand the structure and dynamics of diffusion flames. Improving our fundamental understanding of diffusion flames is most relevant to issues related to fire safety and fire prevention because most fires consist of diffusion flames.

Work on this project started in May 1994.

Near-limit Oscillations

From recent experiments of candle flames conducted in a reduced gravity environment [1], [2], the following observations were made:

- the flame shape is nearly a hemisphere as opposed to the elongated tear drop shape observed under normal gravity conditions
- the flame standoff distance is quite large; at the base of the flame that distance is about 5mm compared to 1mm in normal gravity conditions
- the flame is steady during most of the process, however, as the oxygen in the chamber is consumed, spontaneous oscillations develop prior to extinction
- the burning rate and the flame temperature are considerably reduced when compared with their values in normal gravity.

The goal of our current efforts is to shed light on these observations and in particular on the oscillations that occur during the last stages of the burning.

In microgravity the candle flame bears some similarity to the diffusion flame that surrounds a burning liquid droplet. Both have a spherical shape and both depend on the heat conducted back to the condensed phase. Hence their structure and dynamical properties are likely to be similar. In our first attempt to model the above observations we have therefore analyzed the droplet problem. To simulate the experimental conditions we consider the burning to occur in a reduced oxidant environment, i.e. the ambient mass fraction of the oxidant, X_∞ , is assumed small. Under these conditions the flame standoff distance is relatively large and the burning rate is reduced. The combustion field is now divided into a near-field, where fuel vapor in the absence of oxidant is transported outward by convection and diffusion, and a broad chemically reactive far-field where convection is effectively negligible. For steady burning the mass burning rate \dot{m} is expressed in the form

$$\dot{m} = \frac{4\pi a\lambda}{c_p} \left\{ \ln(1+B) + \frac{1}{L} \left(\frac{QX_\infty}{\nu_X W_X} \right) \frac{\mu}{1+B} \right\} \quad (1)$$

where a is the droplet radius, λ and c_p are the thermal conductivity and specific heat (at constant pressure) of the mixture, $B = c_p(T_\infty - T_s)/L$ is the transfer number for pure vaporization with T_s, T_∞ the surface and ambient temperatures respectively, L is the latent heat of vaporization and $Q/\nu_X W_X$ is the heat of reaction per unit mass of oxidant consumed (the subscript X identifies the oxidant). The parameter μ , obtained by numerically solving the reactive-diffusive far-field equations, depends on the physico-chemical parameters and in particular on the Damköhler number δ representing the ratio of diffusion time to chemical reaction time. We note that in the absence of heat loss $\mu \rightarrow 1$ as $\delta \rightarrow \infty$; eq. (1) then reduces to the classical expression for the burning rate (e.g. [3]) when expanded for small X_∞ . The dependence of the mass burning rate μ on the Damköhler number δ is shown in Fig. 1. The response curve exhibits different characteristics depending on the ambient oxidant concentration X_∞ and on the heat loss parameter h . For moderate values of X_∞ the familiar S-shaped response curve is obtained. However, by reducing the oxidant concentration the response curve becomes monotonic connecting the weakly burning state where $\mu \sim \delta^{1/2}$ (for small δ), to the equilibrium limit where μ tends to a constant ≤ 1 as $\delta \rightarrow \infty$. The asymptotic value reached for large δ depends of course on the heat loss parameter h . The steady problem in the absence of heat loss and with a unity Lewis number has been previously discussed in [4], as part of a complete discussion of a droplet combustion analysis.

The change in shape of the response curve has significant implications regarding the dynamics of the flame. For example, the concept of abrupt extinction is associated with the S-shaped response curve. If the Damköhler number δ is slowly decreased, say in an experiment, the upper branch corresponding to an intense burning is followed down to the turning point δ_E where the response jumps to the lower branch corresponding to a weak burning or an extinguished state. The point $\delta = \delta_E$ (which, in general, does not have to be the turning point) is associated with extinction. In contrast, a monotonic response curve indicates that the transition from an intense to a weak burning takes place in a gradual way. Behind this description is the assumption that the middle branch of the S-curve is unstable and therefore cannot be realized in practice. The monotonic curve on the other hand is often assumed to be stable for all δ . This hypothesis appears to be true when there is no heat loss.

In the presence of heat loss, however, it is found that part of the monotonic curve may become unstable (see Fig. 2). When perturbations proportional to $\exp(i\omega t)$ are sought, one finds that growing modes are possible for δ below some critical number. Furthermore, at the onset of instability $\text{Re}(\omega) \neq 0$ implying that a growing oscillatory mode develops. The frequency of oscillations is given by

$$\text{Re}(\omega) = \alpha \frac{\lambda \beta^{-2}}{\rho_\infty c_p a^2}$$

where $\beta = E/RT_\infty$ is the activation energy parameter, assumed large, and α is an $O(1)$ number. By slowly decreasing δ below its critical value, only a small change in the frequency (i.e. in α) is detected but the amplitude grows continuously. It is therefore anticipated that as the amplitude becomes sufficiently large the flame extinguishes. Hence near limit oscillations, similar to the one observed in the microgravity candle flame experiment [2], may result in the presence of heat loss.

Future plans include examining other source of perturbations which may also yield flame

oscillations. For example, near-limit oscillations have been observed in candle flames under normal gravity conditions at relatively low pressures [5]. It has been suggested that the presence of convective flows may be responsible for these oscillations. Although this does not appear to be the mechanism responsible for the oscillations in the microgravity experiments [2], it would be of interest to incorporate weak buoyant flows as a source of perturbations in the analysis in order to better understand the difference between these two environments. Attempt will also be made to model the candle flame itself, which more closely resembles a spherical cap rather than a complete sphere.

Flame Front Instabilities

Studies of intrinsic instabilities in flames have been predominantly concerned with premixed systems. A manifestation of an intrinsic instability is the spontaneous development of cellular structures, which is commonly observed in premixed flames. The competing effects of thermal and mass diffusivities play a central role in the development of cellular flames. One might therefore expect that they play a similar role in diffusion flames as well. However, very little has been done on the subject. The lack of experimental work in this area may be attributed to the fact that it is difficult to generate in the laboratory a one-dimensional diffusion flame free of the stabilizing influence of stretch. The most comprehensive experimental study [6] has been carried out only recently using a slot-jet flame. Using a spherical burner in microgravity a one dimensional spherical flame of sufficiently large size can be produced. This configuration may well be suited for studying the development of flame front instabilities in diffusion flames, both theoretically and experimentally. The goal of our current efforts is to pursue a theoretical study of thermal-diffusive instabilities in diffusion flames.

An important parameter in this study is the Damköhler number δ . In the limit $\delta \rightarrow \infty$, known as the Burke Schumann limit, the chemical reaction is concentrated in a thin sheet separating a region where there is fuel but no oxidant from a region where there is oxidant but no fuel. The requirement that fuel and oxidant do not co-exist and the requirement that fuel and oxidant must flow into the flame sheet from opposite sides in stoichiometric proportions, are sufficient conditions for complete determination of the combustion field including the instantaneous shape and location of the flame sheet. Stability analyses of simple flame configurations show that under such conditions the flame sheet is absolutely stable.

The situation is different when there is a leakage of fuel and/or oxidant. The mathematical formulation in this case is based on the assumption that δ is large but such that $\hat{\delta} = \delta\beta^{-3} \exp(-\beta/T_f)$, where $\beta \gg 1$ is the activation energy parameter and T_f is the flame temperature for complete combustion, is $O(1)$. The reduced Damköhler number $\hat{\delta}$ plays an important role in this description. The inner structure for a steady one-dimensional flame has been discussed by Linan [7]; it depends on two parameters $\hat{\delta}$ and γ . (Of practical interest is $|\gamma| < 1$; depending on its sign γ stands for the fractional excess of heat that is conducted to the fuel or oxidant side of the reaction zone). Numerical integration of the structure equation reveals the dependence of the combustion field on these parameters. The Burke Shumann limit is recovered when $\hat{\delta} \rightarrow \infty$. By reducing $\hat{\delta}$ a small leakage of fuel and/or oxidant develops and the flame temperature decreases. This behavior persists with the reactants leakage and the flame temperature reduction increasing continuously, until extinction occurs at $\hat{\delta} = \hat{\delta}_{ex}$.

For a steady one-dimensional flame the parameter $\hat{\delta}$ is a constant determined by the underlying flow field. For example, in a counterflow $\hat{\delta}$ is proportional to the imposed strain

rate. For a general three-dimensional corrugated flame $\hat{\delta}$ is only determined locally, for example in terms of the local orientation of the reaction sheet and the local fuel and oxidant concentrations, or in terms of the local gradients of the mixture fraction [3]. We have thus extended Linan's analysis to allow for temporal and spatial variations. To complete the mathematical formulation expressions for the reactant leakages and their dependence on $\hat{\delta}$ must be identified. Fig. 3 shows the results of the numerical integration of the structure equation for $\gamma > 0$. For $\gamma < 0$ the role of the fuel and oxidant are interchanged. Expressions for the leakages that best interpolate the numerical data of Fig. 3 take the form

$$Y_* \sim (\beta\hat{\delta})^{-1} \exp \left[-C_F(\hat{\delta} - \hat{\delta}_{ex})^a \right] \quad (2)$$

$$X_* \sim \beta^{-1} \exp \left[-C_X(\hat{\delta} - \hat{\delta}_{ex})^b \right] \quad (3)$$

where C_F, C_X, a, b depend only on γ . Clearly Y_* and X_* vanish as $\hat{\delta} \rightarrow \infty$. When $\gamma = 0$, equal amounts of fuel and oxidant leak through the reaction zone. As $\gamma \rightarrow 1$, however, the fuel leakage at extinction becomes excessively large, i.e. $Y_* = O(1)$, and the oxidant leakage becomes negligibly small, i.e. $X_* = 0$. The reverse is true when $\gamma \rightarrow -1$. This general formulation is suitable for investigating the stability of simple flame configurations. Preliminary results indicate that depending on the fuel and oxidant Lewis numbers instabilities leading to cellular structures may arise. This appears to be consistent with the experimental results of [6]. A systematic study is being carried out to identify the stability boundaries in terms of the relevant parameters.

Acknowledgments

This work was supported by the microgravity combustion program under NASA sponsorship. Thanks are also due to D. Dietrich from NASA for helpful discussions and to S. Cheatham from Northwestern for her technical assistance.

References

- [1] Ross H.D., Sotos R.G. and Tien J.S. "Observations of candle flames under various atmospheres in microgravity" *Combustion Science and Technology*, **75**, 1991, 151-160.
- [2] Dietrich D., Ross H.D. and Tien J.S. 1994, "Candle Flames in Non-Buoyant and Weakly Buoyant Atmospheres" AIAA paper #94-0429, presented at the 32nd Aerospace Sciences Meeting, Reno, NV, January 1994.
- [3] Williams F.A. "Combustion Theory" Benjamin/Cummings, 1985.
- [4] Normandia M.J. and Buckmaster J.D. "Near-Asphyxiated liquid fuel drop burning" *Combustion and Flame*, **29**, 1977, 277-282.
- [5] Chan W. and Tien J. "An experiment on spontaneous flame oscillation prior to extinction" *Combustion Science and Technology*, **18**, 1978, 139-143.

- [6] Chen R.H., Mitchell G.B. and Ronney P. "*Diffusive-thermal instability and flame extinction in nonpremixed combustion*" Twenty-Fourth Symposium (Int.) on Combustion, 1992, 213.
- [7] Linan A. "*The asymptotic structure of counterflow diffusion flames for large activation energies*" *Acta Astronautica*, 2, 1009.

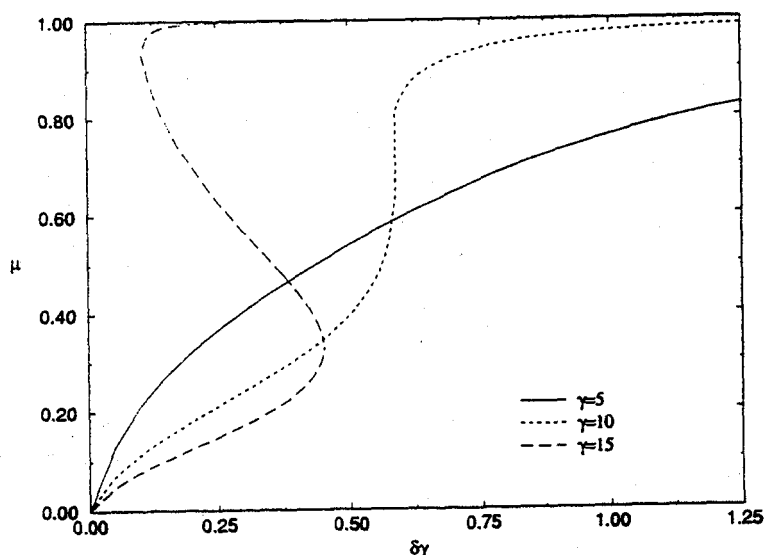


Fig.1 - The dependence of burning rate on the Damkohler number for selected values of $\gamma \sim X_{\infty}$; calculated for $h = 0$.

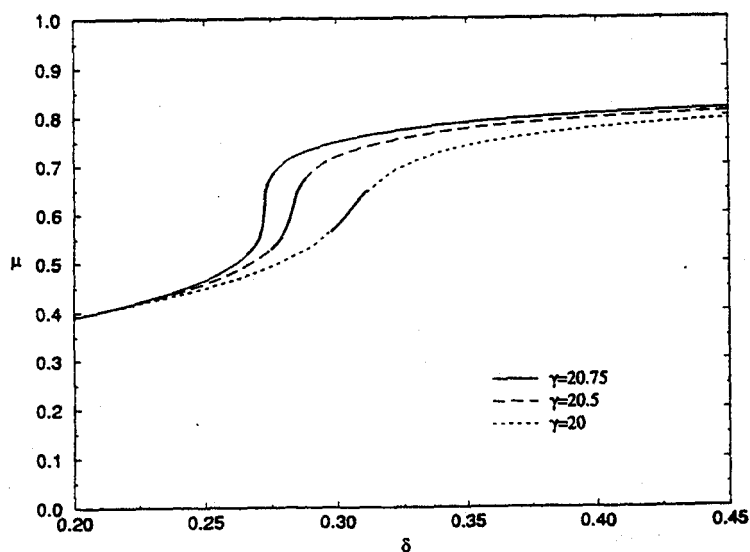


Fig.2 - Response curves for selected values of $\gamma \sim X_{\infty}$ with $h = 1$. The dark segments correspond to the unstable states where the oscillations occur.

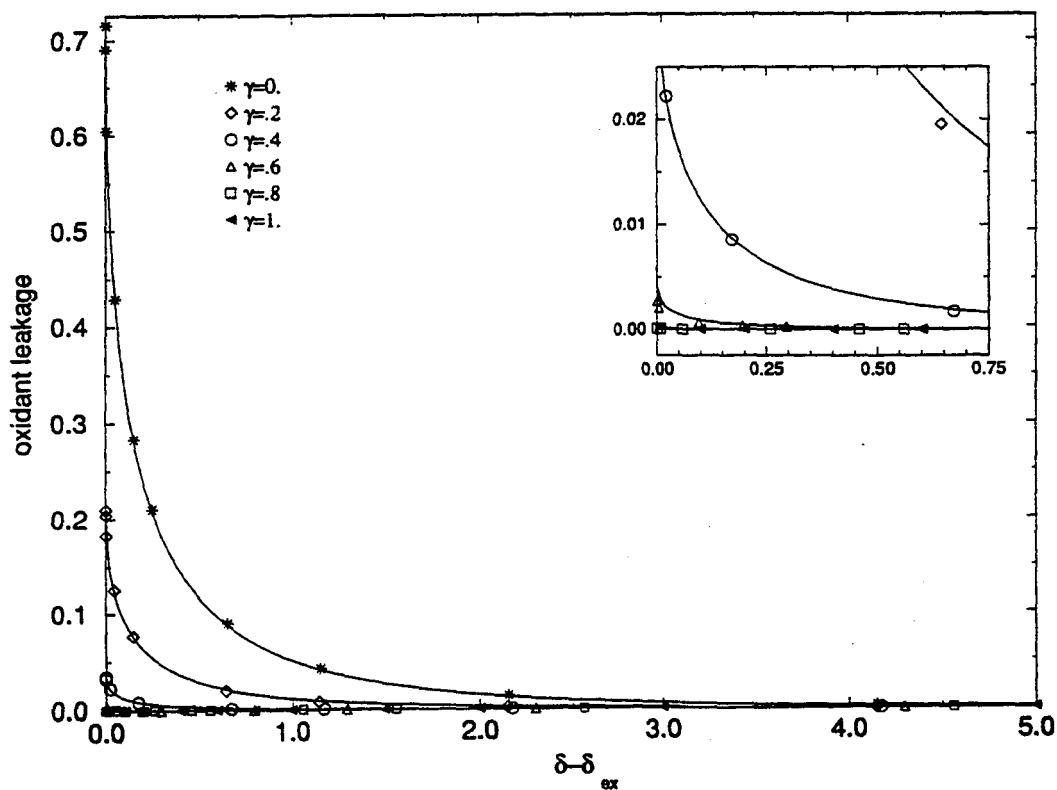
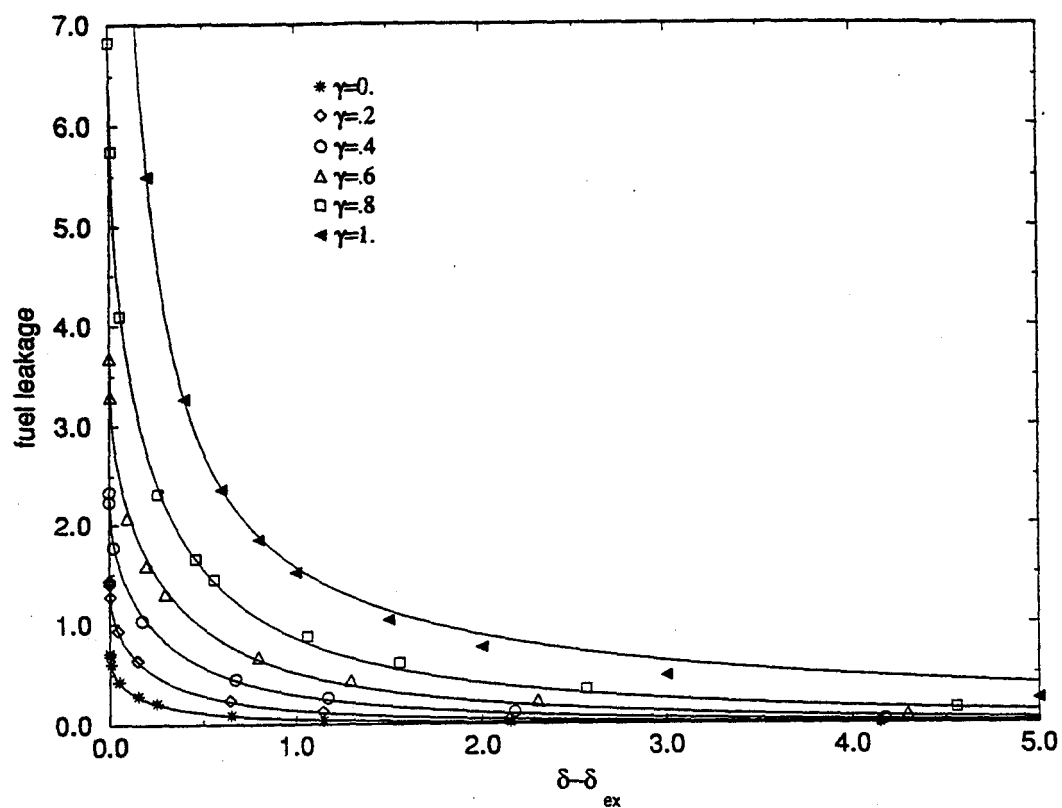


Fig.3 - Fuel and oxidant leakages through the reaction zone for selected values of γ .
For $\gamma < 1$ the role of fuel and oxidant are interchanged.

Premixed Gases

MODELING OF MICROGRAVITY COMBUSTION EXPERIMENTS

John Buckmaster
University of Illinois
Urbana, Illinois 61801

Introduction

This program started in February 1991, and is designed to improve our understanding of basic combustion phenomena by the modeling of various configurations undergoing experimental study by others. Results through 1992 were reported in the second workshop [1] and incomplete citations therein are listed, in complete form, below, [2] - [7]. Work since that time has examined the following topics: Flame-balls; Intrinsic and acoustic instabilities in multiphase mixtures; Radiation effects in premixed combustion; Smouldering, both forward and reverse, as well as two-dimensional smoulder.

Flame-balls

Flame-balls are stationary, premixed spherical flames observed in certain near-limit mixtures, [1] page 157 and page 165, [8]. Their analytic study is now a mature subject, and future work should probably emphasize a numerical strategy [9]. Variations of flame-radius with equivalence ratio for hydrogen/air mixtures have been calculated in [4] and are indicated schematically in Fig. 1, curve A. A small portion of the upper branch near the lean limit corresponds to stable solutions. This result, like all results obtained previously, neglects absorption of radiation from the flame-ball in the surrounding gas, a matter addressed in [10]. The motivation for [10] is two-fold: In Ronney's experimental program, SF_6 , a strong absorber of its own emission, has been used as a diluent [11]; and, if one accepts the proposition that an ideal one-dimensional unbounded flame for which all radiation losses are ultimately absorbed by the gas mixture will not display a flammability limit, this raises the question of the significance that can be attached to the lean limit of Fig. 1, curve A, when all radiation from the flame-ball is absorbed.

The effects of absorption upon the response are shown in Fig. 1, curves B and C. The lean flammability limit survives in the sense that no *local* stable solutions exist to the left of the turning point P. But, even to the left of P, a sufficiently large ignition source could push the system above the top-most (unstable) branch, and lead to a thick, loss-less propagating flame.

Instabilities in multi-phase mixtures

A preliminary investigation of acoustic instabilities in particle-cloud flames was reported in [5], and is believed to be relevant to instabilities that were observed in [12]. The essential mechanism is slip between the carrying gas and the particles. A more comprehensive treatment is presented in [13].

Preceding Page Blank

In this work, acoustic eigenvalue loci are calculated for a flame that moves down a tube from the open end to the closed end. Mode transition can occur. Thus, for example, a mode can start as the second harmonic but finish as the fundamental, (Fig. 2). An intrinsic (non-acoustic) instability that arises because of nonsimilarity between the temperature and fuel-concentration fields is also discussed, and it is shown that transitions can occur between the intrinsic mode and the acoustic modes. All of these instabilities tend to be suppressed in spherical flames generated by point ignition in a confinement vessel, (Fig. 3). The triggering of acoustic instabilities in gas turbines by slip between fuel drops and air is discussed, and we show that the role of slip is quite different when the condensed phase is injected at a finite point rather than being dispersed throughout the gas phase.

A more elaborate discussion of the gas-turbine spray problem (a 'spin-off' problem not directly related to the current microgravity program) is presented in [14] and [15].

Radiation effects in premixed combustion

The role that radiation can play in defining flammability limits is an important one, and the addition of fine inert particles to flammable mixtures can introduce a measure of control of emission and absorption that is otherwise not possible. The current experimental program includes studies of this nature, and our theoretical program is designed to provide useful physical insights. Reference [16] examines the effects of radiation on the classical thermal-diffusive stability boundaries of premixed flames. The calculations are numerical in nature, and cover a wide range of Planck lengths and Boltzmann numbers. It is shown that radiation tends to suppress the cellular instability, in agreement with experiment [17]. And the pulsating/traveling-wave instability associated with Lewis numbers greater than 1 can be enhanced.

Reference [17] is a report of preliminary experimental studies of unsteady flames generated by point ignition in dusty gases, and [18] describes a preliminary theoretical treatment of this problem. A hydrodynamic description is adopted, with stretch effects accounted for using an empirical formula, and we examine the competition between the Zeldovich-Spalding effect in which radiative losses on the diffusive scale tend to quench the flame, and the Joulin effect in which radiative preheating on the scale of the Planck length tends to strengthen the flame. It is shown that, in due course, the Joulin effect should dominate and lead to super-adiabatic flame speeds. Superadiabatic flame-speeds have not been observed in the experiments, but too much should not be made of this in view of the preliminary nature of the work. In the experimental studies, actual particle loadings are not known. And although the strategy adopted in the theoretical study is both plausible and natural, it may be that it is oversimplified. More elaborate treatments will certainly be justified when the experimental record is clarified.

Smouldering combustion

A microgravity experimental program has been underway for some time, [1] page 251, and the problem has long been studied at 1g. There is interest in one-dimensional reverse (co-flow) smoulder in which the solid fuel and air enter the reaction zone from the same side, as in a premixed flame; in one-dimensional forward (counter-flow) smoulder in which the fuel and air enter the reaction zone from opposite sides, as in a diffusion flame; and in two-dimensional smoulder.

It is not difficult to construct a simple model of reverse smoulder which, with plausible choices for the several parameters, yields a structure, propagation speed, and maximum temperature which are consistent with experiment. Elaborations of the simple model are difficult to justify in the absence of some distinct qualitative behavior that remains unexplained, since detailed quantitative comparisons are meaningless in the context of simple models. Observations reported in [19] reveal an unexplained phenomenon, namely quenching at high blowing rates. As the blowing rate is

increased from small values the burning rate first increases, reaches a maximum, decreases, and then quenching occurs at a non-zero burning rate. A simple analysis predicts the maximum, but not the subsequent quenching, and the addition of classical heat loss terms is no remedy. However, in [20] it is shown that endothermic pyrolysis in the oxygen-free region behind the exothermic reaction zone can lead to quenching. Responses are shown in Fig. 4 with and without pyrolysis.

The analysis of [20] assumes equilibrium between the two-phases. This assumption will first break down within the reaction zone, if this is thin, modifying the structure, an issue briefly discussed in [21].

Counter-flow smoulder is necessarily unsteady, with thermal energy accumulating within the combustion field. The first decent analysis appears to be that described in [22], and the nature of the combustion field is sketched in Fig. 5. In [23] we enlarge on the discussion of the pyrolysis wave, and examine reactant leakage through the oxidation zone. Leakage has been observed experimentally, [24].

Reference [25] describes an analysis of two-dimensional smoulder, modeled as an oxygen-limited free-boundary problem. The configuration is sketched in Fig. 6. Solutions are obtained for different air velocities under the assumption that the wave is shallow, a consequence of the large bulk solid density relative to the gas density. Results are consistent with recent simulations carried out by DiBlasi [26].

Other work

Reference [27] contains a numerical treatment of plane vapor-diffusion flames and their stability, an attempt to obtain insights into phenomena observed in annular pool fires. During the extinction phase of total pool burning, when the flame is fragmented, it is noted that the edge of a fragment can advance or retreat. The model provides an explanation of how this can come about.

References

- [1] Proceedings of the *Second International Microgravity Combustion Workshop*, NASA Conference Publication 10113, 1992.
- [2] Buckmaster, J. and Joulin, G., *Combustion Science and Technology*, **89**, 57-69, 1993.
- [3] Buckmaster, J. Gessman, R., and Ronney, P., *Proceedings of the 24th Symposium (International) on Combustion*, pp. 53-59, 1992.
- [4] Buckmaster, J., Smooke, M., and Giovangigli, V., *Combustion and Flame*, **94**, 113-124, 1993.
- [5] Buckmaster, J. and Clavin, P., *Proceedings of the 24th Symposium (International) on Combustion*, pp. 29-36, 1992.
- [6] Buckmaster, J. and Lee, C.J., *Proceedings of the 24th Symposium (International) on Combustion*, pp. 45-51, 1992.
- [7] Buckmaster, J., article in *Annual Review of Fluid Mechanics*, pp. 21-53, 1993.
- [8] Ronney, P., *Combustion and Flame*, **82**, 1-14, 1990.
- [9] Smooke, M., This proceedings.
- [10] Lozinski, D. and Buckmaster, J., *Combustion and Flame*, **97**, 301-316, 1994.
- [11] Ronney, P.D., Whaling, K.W., Abbud-Madrid, A., Galto, J.L., and Pisowicz, V.L., *AIAA Journal*, **32**, 569-577, 1994.
- [12] Berlad, A.L., Ross, H., Facca, L., and Tangirala, V., *Combustion and Flame*, **82**, 448, 1990.
- [13] Lee, C.J., Buckmaster, J., and DiCicco, M., *Combustion Science and Technology*, **98**, 161-184, 1994.
- [14] DiCicco, M., Buckmaster, J., AIAA reprint, AIAA 94-0103, 1994.

- [15] DiCicco, M., Buckmaster, J., "The role of slip in the generation of acoustic instabilities in gas turbines," *J. of Propulsion and Power*, to appear, 1995.
- [16] Buckmaster, J. and Jackson, T., "The effects of radiation on the thermal-diffusive stability boundaries of premixed flames," *Combustion Science and Technology*, to appear.
- [17] Abbud-Madrid, A. and Ronney, P., *AIAA Journal*, **31**, No. 11, 2179-2181, 1993.
- [18] Buckmaster, J. and Agarwal, A., "Unsteady spherical flames in dusty gases," *Combustion Science and Technology*, to appear.
- [19] Torero, J.L., Fernandez-Pello, A.C., and Kitano, M., *Combustion Science and Technology*, **91**, 95-117, 1993.
- [20] Lozinski, D. and Buckmaster, J., "Quenching of reverse smoulder," *Combustion Science and Technology*, to appear.
- [21] Buckmaster, J. and Lozinski, D., "Some topics in reverse smoulder," Proceedings of the Hawaii workshop, *Modeling in Combustion*, eds. J. Buckmaster and T. Takeno, 1995, to appear.
- [22] Dosanjh, S.S. and Pagni, P.J., *Proceedings of the 1987 ASME/JSME Thermal Engineering Joint Conference*, eds. P.J. Mareto and I. Tanasawa, pp. 165-173, 1987.
- [23] Buckmaster, J. and Lozinski, D., "An elementary discussion of forward smoldering," unpublished paper, 1994.
- [24] Fernandez-Pello, C., private communication.
- [25] Buckmaster, J., "A theory of shallow smoulder waves," unpublished paper, 1994.
- [26] DiBlasi, C., "Mechanisms of two-dimensional smoldering propagation through packed fuel beds," unpublished paper, 1994.
- [27] Fischer, J., Buckmaster, J., Lozinski, D., and Matalon, M., "Vapor diffusion flames, their stability, and annular pool fires," Proceedings of the Hawaii workshop, *Modeling in Combustion*, eds. J. Buckmaster and T. Takeno, 1995, to appear.

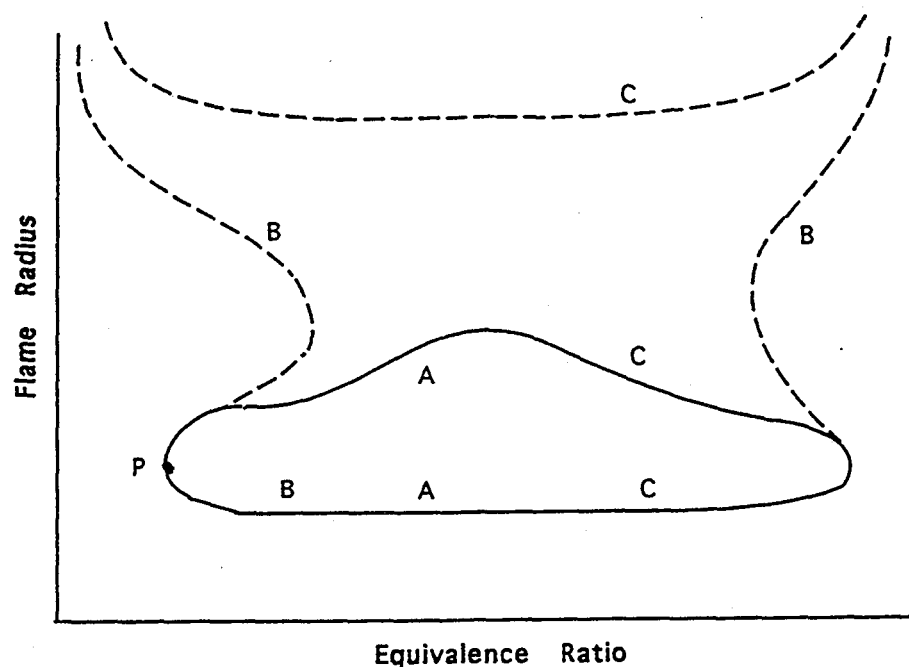


Fig. 1. Flame-ball response. A (closed curve): No absorption. B: Moderate absorption. C: Weak absorption.

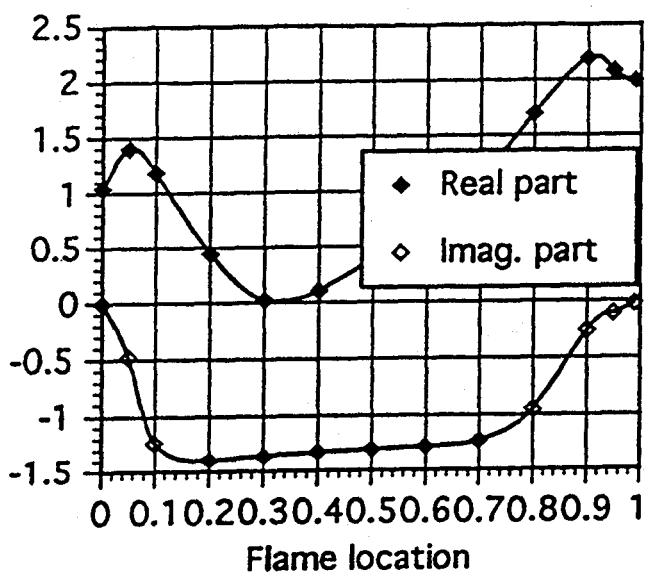


Fig. 2. Frequency of an acoustic mode that is the second harmonic at 1, the fundamental at 0. The mode is unstable when the Imag. part is negative.

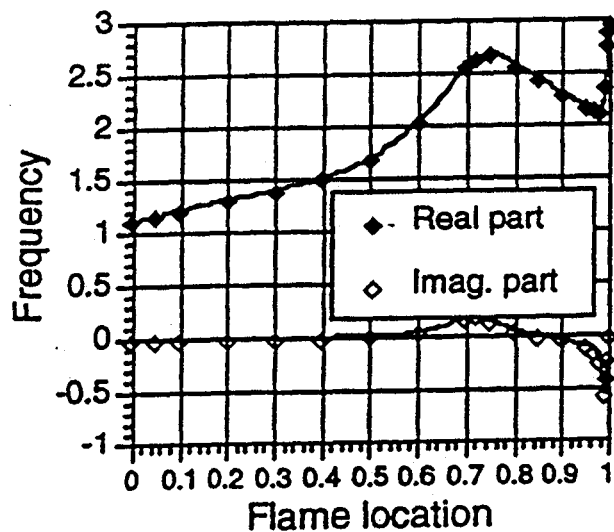


Fig. 3. An acoustic mode in a spherical vessel. Instability is only predicted for a flame radius greater than 0.83.

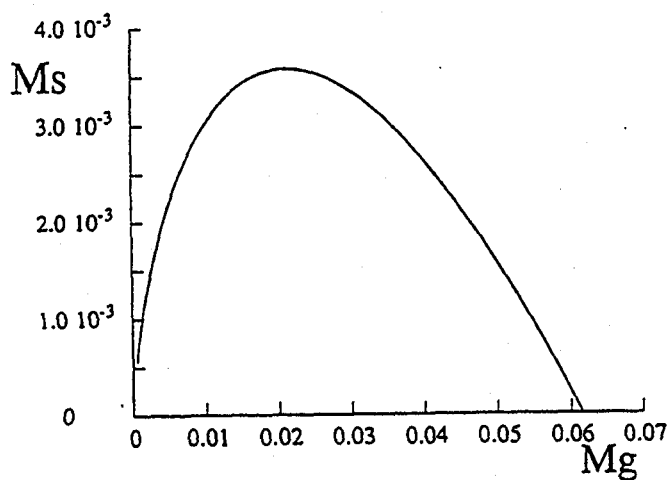


Fig. 4a. Mass flux of solid vs. blowing rate in co-flow smoulder, no pyrolysis.

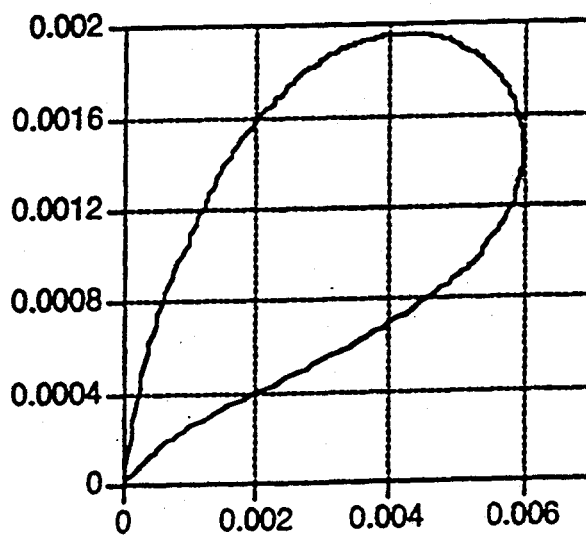


Fig. 4b. Mass flux of solid vs. blowing rate with pyrolysis.

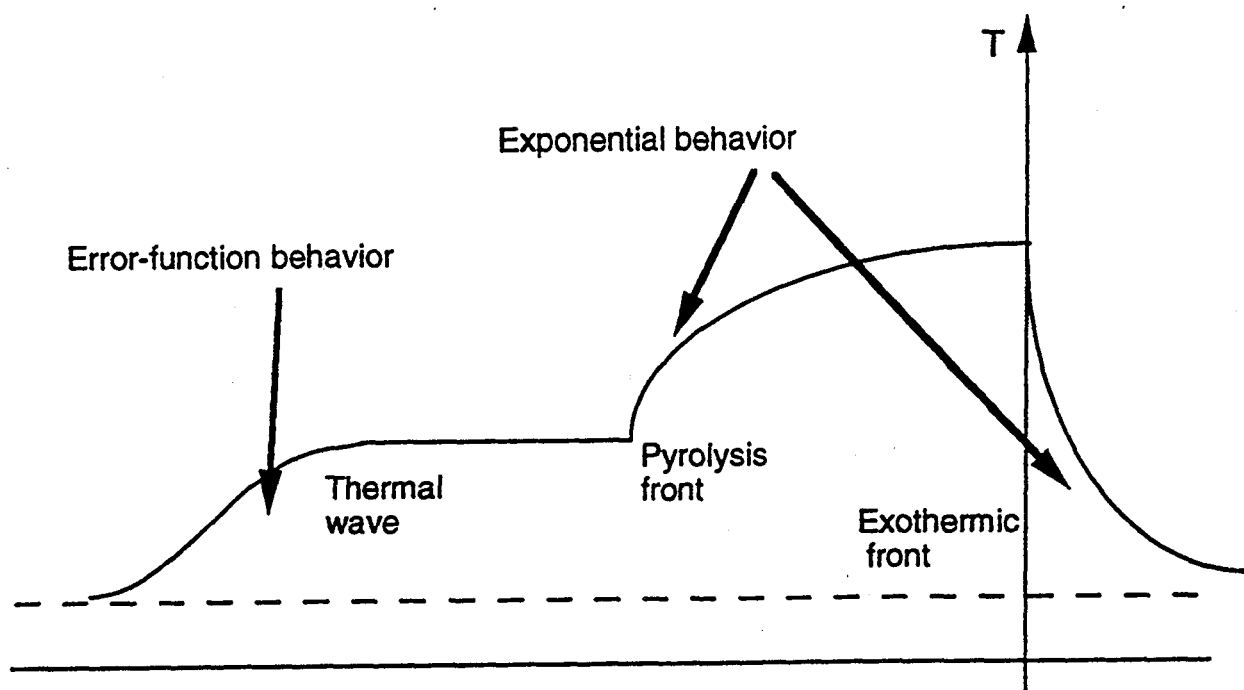


Fig. 5. Temperature profile in counter-flow smoulder. In a frame attached to the exothermic front there is an endothermic pyrolysis front moving to the left at fixed speed, and to the left of that, a convective-diffusive thermal wave.

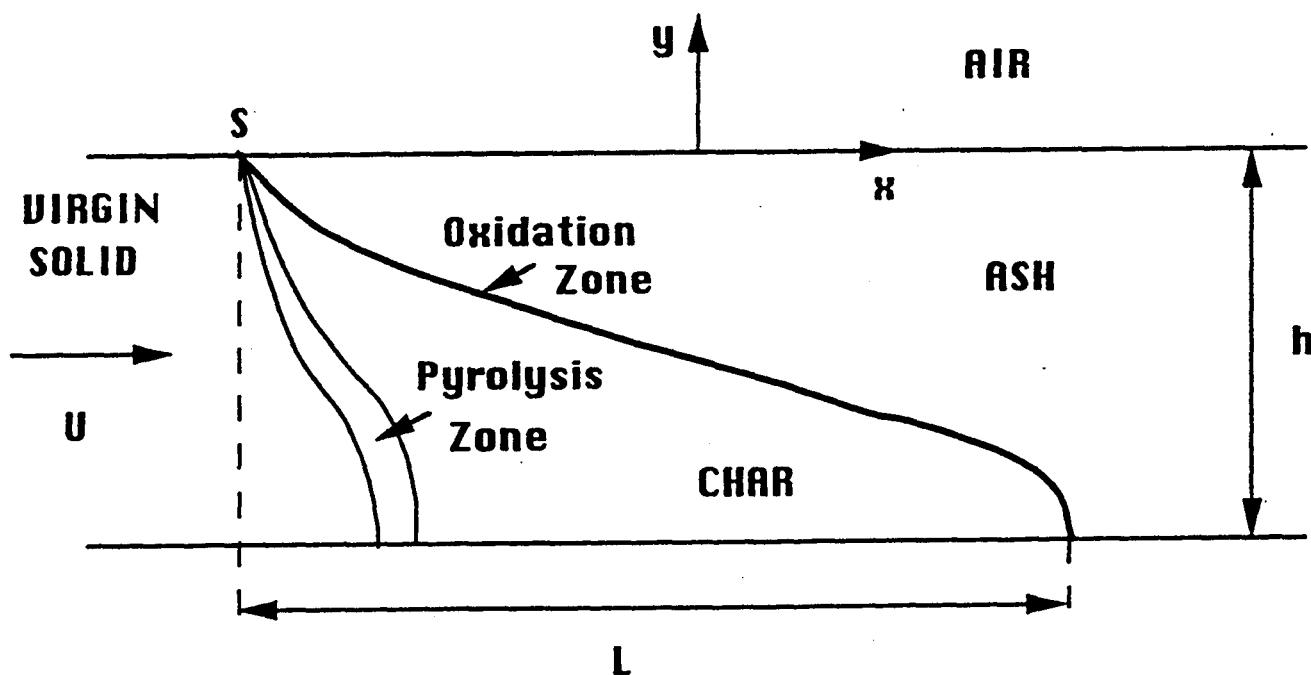


Fig. 6. The structure of a two-dimensional smoulder wave. The oxidation front is modeled as a steady two-dimensional free-boundary problem.

COUPLING OF WRINKLED LAMINAR FLAMES WITH GRAVITY

Benoit Bédard, Larry W. Kostik* and Robert K. Cheng

Combustion Group
Energy & Environment Division
Lawrence Berkeley Laboratory
Berkeley, CA 94720

Project start date : June 1991.

Introduction

Turbulent combustion involves complex coupling of chemical and fluid mechanical processes and is considered as one of the most challenging fundamental combustion research problems today. Though the effects of gravity are not very significant in power generating systems (e.g., IC engines and turbines), laboratory burners with open flames, and small to medium furnaces and boilers are affected by buoyancy. Because the physical processes through which gravity affects combustion are poorly understood, it is difficult to access if flame orientation has any impact on extinction, burning rate, and formation of pollutants. Theoretically, buoyancy is often neglected in turbulent combustion models [1] for the sake of simplicity. Yet the modeling results are routinely compared with experiments of open laboratory flames that are obviously affected by buoyancy. This inconsistency is an obstacle to merging experiments and theories. Consequently, a fundamental understanding of the coupling between turbulent flames and gravity is significant to both turbulent combustion science and applications.

The overall effect of gravity relates to the dynamic interaction between the flame and its surrounding, i.e., the so-called elliptical problem. For laminar and mildly turbulent flames, the coupling of gravity, flame geometry, flow momentum and heat release determines the flowfield, flame shape, flame instability and perhaps burning rate. Although few aspects of the coupling of steady flames with gravity have been explored, fundamental studies of unsteady flame propagation have shown that gravity can affect flame speed and ignition limits [2,3]. Intuitively, the role of gravity should become much less important with increasing flow momentum. This is the justification for not including gravity in high Reynolds number turbulent combustion models. However, there has yet to be a systematically experimental investigation to determine the criteria or limits for the conditions under which gravitational forces would become insignificant.

The overall objective of our research is to understand flame-gravity coupling processes in laminar and low turbulent Reynolds number, Re_1 , premixed flames (i.e. wrinkled laminar flames). The approach we have developed is to compare the flowfields and mean flame properties under different gravitational orientations. Key to our study is the investigation of microgravity (μg) flames. These μg experiments provide vital information to reconcile the differences between flames in normal gravity (+g, flame pointing upward) and reverse gravity (-g, flame pointing downwards). Traditionally, gravity effects are assumed to be insignificant or circumvented in the laboratory, therefore, not much is available in the literature on the behavior of -g flames. As for μg premixed flames, Durox and co-workers investigated slightly to very rich laminar Bunsen flames and reported that these conical flames tend to grow slightly taller in μg [4] and the number of cells form in polyhedral flames are also affected. Their use of directly photography, however, did not enable them to extract quantitative information that are amenable for analysis.

* current address Department of Mechanical Engineering, University of Alberta, Edmonton, Alberta, Canada

Diagnostics and apparatus

Laser schlieren is used in our μg experiments [5,6]. This technique requires relatively low power light source and the optics are relatively easy to align. We use a CCD cameras with high shutter speeds (up to 1/10000 sec) to capture the changes in mean flame properties. One innovation of our work is to exploit the interlace feature of standard video recording to double the recording rate from 30 to 60 Hz. The schlieren system is housed in a standard drop-package for the NASA LeRC 2.2 second drop tower. It employs a 0.5 mW He-Ne laser light source and has a field of view of 75 mm. An opaque spot etched on a glass window is used as the schlieren stop that produces a reverse field image (i.e., dark background), and regions of high density gradients appear bright. The burner has a 25 mm diameter outlet supplied by a converging nozzle mounted on a cylindrical settling chamber. The converging nozzle is designed to produced laminar flows with uniform velocity distribution. Turbulence is generated by placing a perforated plate 20 mm upstream of the exit. Two different flame configurations have been investigated. To generate v-flame, a rod of 2mm diameter is place across the center of the burner exit. To generate conical flames, a ring is fitted to the exit. This ring stabilizes very lean flames and has potential for use in practical application. A patent application has been filed for this stabilizer ring.

Experimental Conditions

We have completed thus far three μg experimental campaigns. Two were performed in the 2.2 second tower and the latest one in the Learjet. The experimental conditions cover flow rates from 0.2 to 0.9 liter/sec (mean velocity, U , of 0.5 to 2.0 m/s), and methane/air equivalence ratio, ϕ , from 0.65 to 1.0. The turbulent intensity is less than 1% for the laminar flame and is 8% when the perforated plate is used. These conditions produce flame that are classified as wrinkle laminar flames. The laboratory studies cover a wider range of experimental conditions to investigate if the +g and -g flames are indistinguishable at high flow rates. In addition to using laser schlieren, laser Doppler anemometry (LDA) was used to determined the mean and turbulent flowfields of +g and -g flames. These velocity data provide the necessary background of the flowfield to interpret changes observed in the μg flames.

Results

Conical Flames

Laser schlieren images of laminar and turbulent conical flames in +g, -g and μg are compared in Figure 1. Starting with the +g laminar case (top-left), the smooth conical flame is seen at the center. It is surrounded by a buoyancy driven unstable interface formed between the hot products and the ambient air. As shown on the videos, it pulsates at a regular characteristic frequency, ν , and causes the flame to flicker. The schlieren image of the turbulent flame (bottom-left) is characterized by the wrinkled flame cone. The turbulent flame has no noticeable effect on the product/air interface. It remains wrinkle free and pulsates the same way as those of laminar flames. The effects of reversing the gravitational orientation are shown by the images of -g laminar flame (top-center) and -g turbulent flame (bottom-center). The most obvious change is that buoyancy causes the products to stagnate and reverse the flow direction. The product/air interface appears just below the tip of the flame and it curves up to cover the flame cone. These interfaces do not pulsate in the vicinity of the flame and so the flame ceases to flicker (top and bottom right). In the absence of buoyant forces, μg flames do not flicker. This is the same observation reported by Durox et. al [4]. Our schlieren videos show that product/air interface is no longer unstable and becomes invisible. This implies a decrease in the density gradients associated with broadening of the product/air interface thickness. Without buoyancy to transport the hot products away from the flame zone, the products form a pocket around the flame that expands into the ambient air. The

flow in this pocket loose its momentum quickly because of divergence. As the volume of this pocket can increase indefinitely, an interesting implication is whether or not μg flames ever attain steady states.

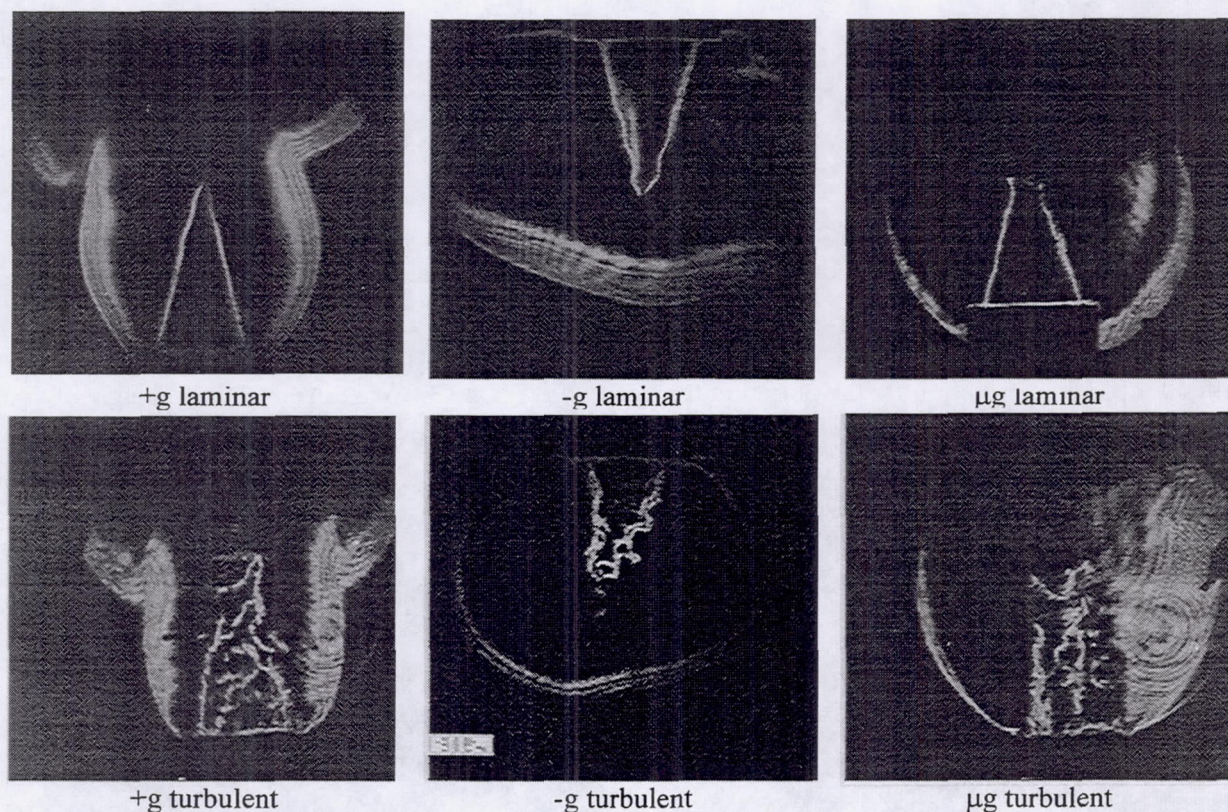


Figure 1 Schlieren images of laminar ($\phi = 0.9$, $Q = 0.42$ l/sec.) and turbulent ($\phi = 0.75$, $Q = 0.45$ l/s) conical flames

As the pulsating product/air interface of +g flame has far-reaching effects throughout the flame flowfield, analysis of the characteristic pulsating frequency, ν , (i.e., the flame flickering frequency), would be useful to identify the relevant processes that control flame/gravity coupling. We begin the analysis by considering the relevant forces acting on the plume of hot gases. These forces are the momentum of the jet, viscous drag on the surroundings, buoyancy of the products, and a dynamic force that causes the flow to fluctuate. Ratios of these forces are the Strouhal number, St , the Richardson number, Ri , the Reynolds number Re and the Grashoff numbers. We adopted a reduced Strouhal number, $St^* = (St/(\tau+1))$ to account for the effects of heat release (τ is the heat release ratio of the combustion process). This analysis produces an empirical relationship that expresses the ratio between the fluctuation and buoyancy forces (expressed in terms of a reduced Strouhal number, St^* and the Richardson number, Ri) to Reynolds number, Re . As demonstrated in Figure 2, the expression $St^{*2}/Ri = 0.0018 Re^{2/3}$ correlated all of our data and most of the data of Durox. This correlation will be useful for theoretical prediction of buoyancy induced flame instabilities.

A comparison of the flame heights, h_f , obtained for $\phi = 0.9$ in +g, -g and μg are compared in Figure 3. At lower flowrates the μg flames are taller than both +g and -g flames implying an opening of the flame cones. Durox et. al. also [4] observed flame grew taller in μg but did not quantify this change. The rate of h_f increase for -g flames, however, are higher than the rate of +g h_f . Their divergent trends show that the effects of gravity on mean flame properties may persists even with increase flow momentum.

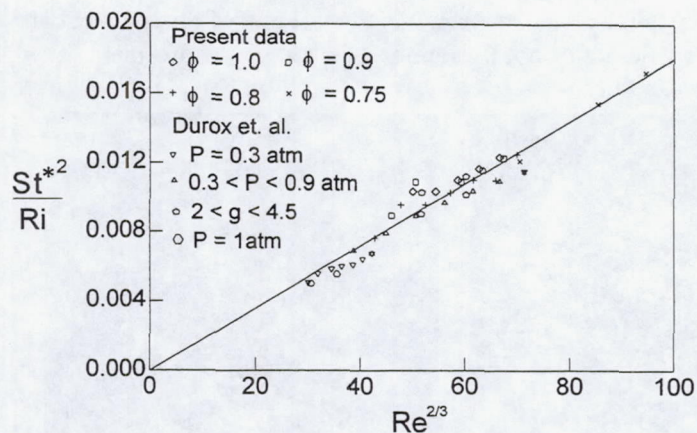


Figure 2 Empirical correlation for the pulsating frequency generated by conical flames

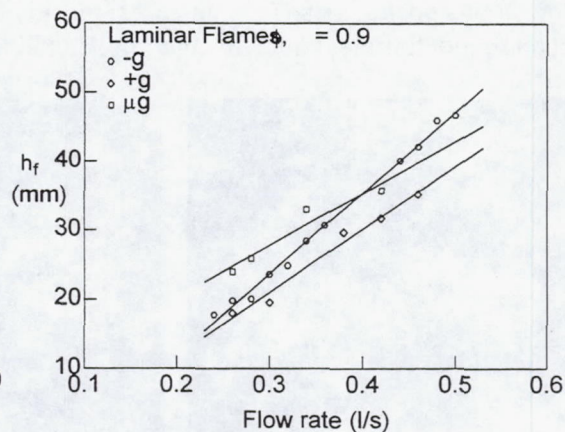


Figure 3 Comparison of flame height of +g, -g and μg flames.

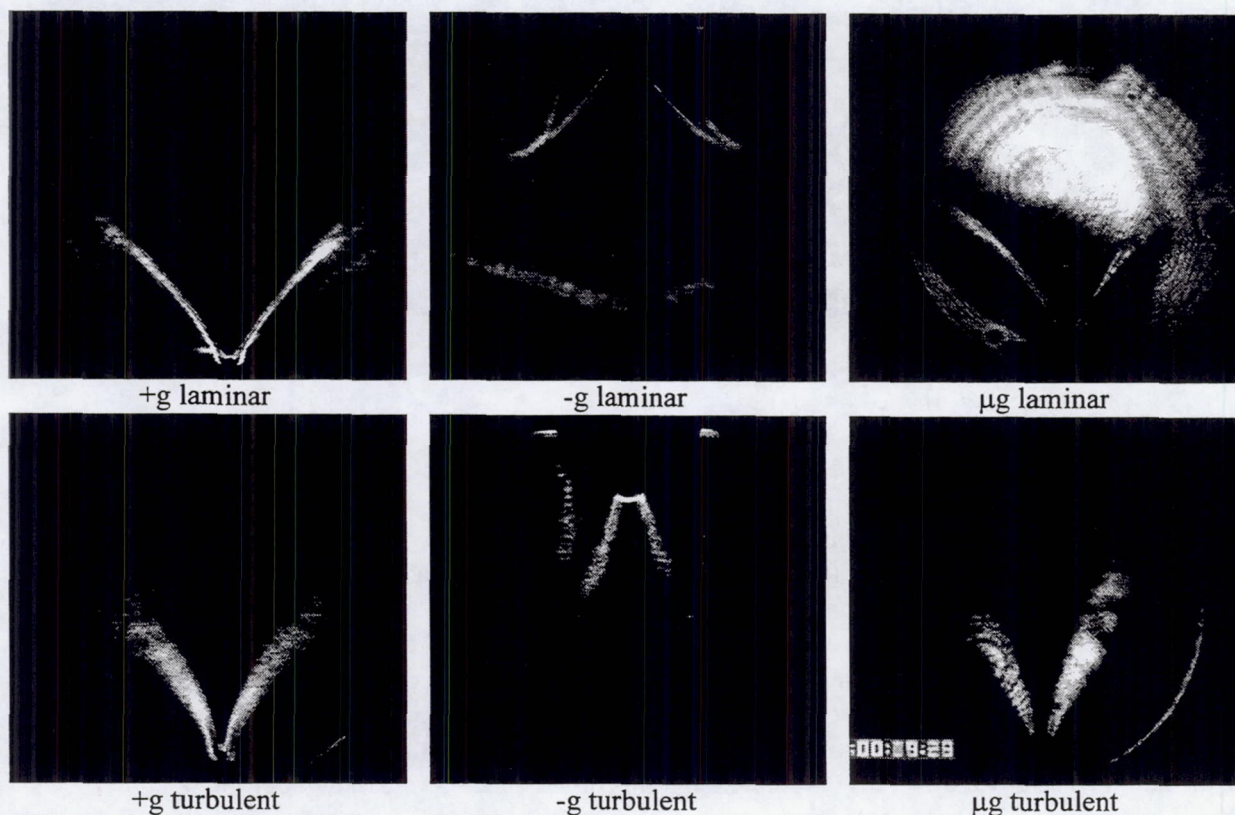


Figure 4 Composite schlieren images of laminar ($\phi = 0.8$, $Q = 0.6$ l/sec.) and turbulent ($\phi = 0.7$, $Q = 0.8$ l/s) v-flames flames

V-Flame Studies

Schlieren images of laminar and turbulent v-flames in +g, -g and μg are compared in Figure 4. These images are not individual frames. They are composite images obtained by summing 200 frames for use in determining the mean flame angle. The +g laminar flame image (top-left) shows two relatively smooth flame fronts evolving into a broader flame zone far away from the stabilizer. The video shows that the broadening is caused by buoyancy induced pulsation. An estimate of this pulsating frequency

shows that it is comparable to those observed in the conical flames. Broadening of the flame zone is not found in -g (top-center). For the case shown here with relatively low flow velocity, attachment of the flame to the burner exit rim is shown. Flame attachment is also shown on the image of the μg flame (top right). Note that only the right side is attached. The schlieren sequence shows that the flame is not attached in normal gravity. Attachment only occurs about 0.5 second after the start of the drop. The schlieren image of the +g turbulent flames show two broadened flame brushes. Because the v-flame brushes are parallel to the laser beam direction, details of the flame wrinkles are difficult to discern. Compared to the +g flame, it is clear that the flame brush thickness is increased due to turbulence. The -g turbulent flame (bottom center) appears much shorter than the +g flame. This is because the inherent unstable -g situation generated larger flame wrinkles structures and the composite schlieren appears to be diffused. The μg turbulent flame image (bottom right) does not look very different than the +g turbulent flame except that the μg flame brushes are not as curved as the +g flame brushes.

The mean flame angles for the laminar v-flames in +g, -g and μg are compared in Figure 5. These angles are obtained by linear fit of the centroid of the schlieren silhouettes. Only the linear flame portion close to the stabilize are used. This avoids the need to correct for the flame curvature. The results are normalized by $\alpha_t^*(\tau-1)$ where α_t is the theoretical flame angle $\sin^{-1}(S_L/U)$. The comparison show that the +g and -g flame angles are only different when the flow velocity is below 1.0 m/s. The +g and -g results seem to merge at higher velocities. All the μg v-flames we have investigated have velocities larger than 1.0 m/s. Their flame angles are also consistent with those of +g and -g flames. This results together with our analysis of the conical flame height clearly illustrate the effects flame-gravity coupling are strongly dependent on the flame configuration.

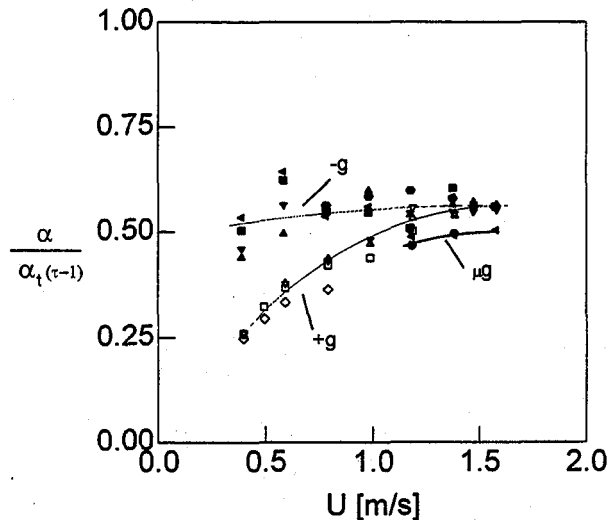


Figure 5 Normalized mean v-flame angles under +g -g and μg conditions with $0.62 < \phi < 0.85$.

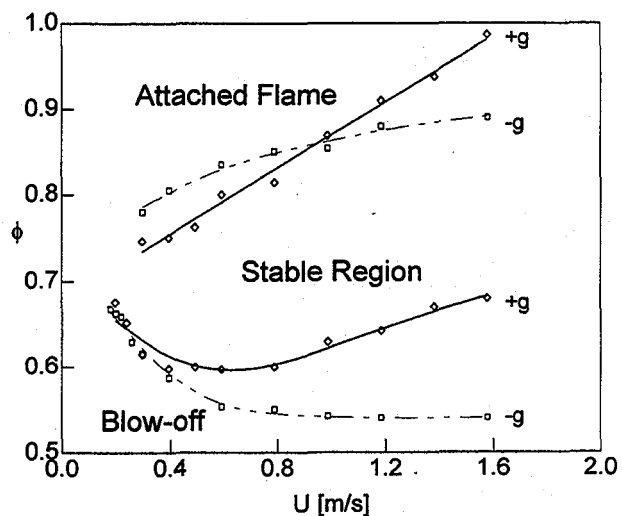


Figure 6 Effect of gravity on blow-off and attached limits of laminar v-flames

During the course of our μg experiments, we observed that the lean flame blow-off limit is also affected by gravity. Laboratory investigation of the lean blowoff limits in +g and -g would be useful. The results obtained for laminar v-flames is shown in Figure 5. These results show that reversing the gravity extends the blow-off limit to much leaner conditions. We also discovered that reversed gravity can stabilize freely propagating adiabatic laminar flames. Under the appropriate conditions, flow divergence induced by the buoyant products generate the flowfield for the flame to be stabilized away from the burner rim. These flames are very stable and flat. Heat loss is minimal because the flame is not in contact with any physical surfaces. We are continuing with the characterization of the conditions under which these flame

can be stabilized. We also plan to make detailed velocity and density measurements. We believe that this adiabatic flame would be of interest to fundamental studies of combustion chemistry for it does not have the upstream heat transfer problem as in the flat flame burner which is the current standard.

Planned activities and diagnostic development

We plan to continue with the analysis of the v-flame data to compare the turbulent flame angles. Measurement of the pulsating frequencies of laminar and turbulent v-flames will test the generality of the correlation we have found for the conical flames. Investigation of the buoyancy stabilized laminar that we have discovered will continue with detailed measurement of the velocity flowfield by LDA and density measurements by Rayleigh scattering. Our schlieren studies of μg flames point to the need of more sophisticated quantitative laser diagnostics to characterize the changes in flame properties. One of the techniques we shall consider is a single beam schlieren technique which will be exploited for measuring the flame crossing frequencies at a point. The deflection of a He-Ne laser beam traversing the flame zone can be quantified by the use of a diode. Fast Fourier transform of the diode output will produce a spectrum of the flame crossing frequency that is directly related to the flame wrinkle sizes. Another option is to use tomography to determine in two dimensions the flame wrinkle scales. The use of laser tomography represents a major effort in development of diagnostics for μg research. We are evaluating the possibility of developing this technique in collaboration with other participants of the NASA Microgravity Combustion Program.

Acknowledgment

This work is supported by NASA Microgravity Sciences and Applications Division. Technical support is provided by NASA Lewis Research Center under contract No. C-32000-R. Project Scientists are Dr. Karen J. Weiland and Dr. Renalto Colantonio.

References

1. Bray, K. N. C., Libby, P. A., and Moss, J. B., *Combustion and Flame* 61:87-102 (1985).
2. Ronney, P. D., and Wachman, H. Y., *Combustion and Flame* 62:107-120 (1985).
3. Ronney, P. D., *Combustion and Flame* 62:121-134 (1985).
4. Durox, D., Baillot, B., Scoufflaire, P. and Prud'homme, R. *Combustion and Flame* 82:66-74 (1990).
5. Kostiuk, L. W., and Cheng, R. K., *Experiments in Fluids* 18, 59-68 (1994).
6. Kostiuk, L. W., and Cheng, R. K., "The Coupling of Concise Wrinkled Laminar Flames with Gravity," to appear *Combustion and Flame* (1995).

AERODYNAMIC, UNSTEADY, KINETIC AND HEAT LOSS EFFECTS ON THE DYNAMICS AND STRUCTURE OF WEAKLY-BURNING FLAMES

Fokion N. Egolfopoulos
Department of Mechanical Engineering
University of Southern California
Los Angeles, California 90089-1453

Introduction

Under realistic combustion conditions, flames can be unsteady and strained, exchange heat and mass through interactions with flames, combustion products and walls, and lose heat through radiation. Previous studies [1,2] have shown that the sensitivity of the flame response to strain, heat (radiative) loss, and chemical kinetics is particularly heightened for weakly-burning flames which are characterized by reduced flame temperatures and burning rates. For these flames, low activation energy termination reactions start competing strongly for the important H radicals with the high activation energy main branching reaction $\text{H} + \text{O}_2 \rightarrow \text{OH} + \text{O}$ and a critical balance between them is required for the establishment of vigorous burning. This balance can be easily lost by perturbations of the imposed strain and/or heat loss, and for premixed flames this sensitivity appears to increase as certain concentration limits are approached beyond which burning is not possible; these limits are typically referred as the lean and rich "flammability limits" [3]. The dynamic response of weakly-burning flames is of interest to turbulent combustion in which the highly non-uniform flowfields will preferentially affect and extinct the weaker flamelets first.

Premixed flames burning close to their flammable limits are characterized by slow flame speeds (of the order of 1-5 cm/s) and their experimental investigation under the influence of the earth gravity is complicated by the buoyancy-induced convection and instabilities. This has been the motivation for near-limit studies in microgravity, which have included the use of the standard flammability tube and spherical bomb. In both cases, however, the systematic accounting for the effects of the wall heat and radical losses (tube) or transient strain (spherical bomb) can not be easily obtained and the only accountable parameters are the inherently present radiative heat losses and the Lewis (Le) number effect [4,5].

The experimental configuration which provides near-adiabatic flames and the effect of strain can be systematically determined is the opposed jet counterflow [6,7]. This technique has been extensively used for experimental as well as theoretical studies on strained premixed and diffusion flames and its use has resulted to significant insight into the effects of strain on flame ignition, propagation, structure, and extinction [6-8]; experiments have only been conducted at earth gravity. Extinction studies for near limit concentrations have also resulted to an alternative method of determining flammability limits by extrapolating to zero strain the extinction strain rates at various near-limit concentrations [9]. The technique, however, has limitations when the concentrations are such that the flame speed drops below 5 cm/s and the forced convective transport is reduced. First, the whole flame ensemble is pushed upward because of the buoyant forces so that the flowfield symmetry is not preserved and the imposed strain and molecular transport are being altered. Second and more important, the upper jet becomes unstable since the less-dense fluid around the flame zone is beneath the more-dense fluid of the unreacted mixture and that causes a wavy motion which makes the whole counterflow system unstable; these effects become more severe at elevated pressures. Previous work on the pressure limits [9] by using the counterflow technique was limited to a maximum pressure of 3 atm and minimum flame speeds of the order of 5 cm/s.

The coupling of strain, radiation, and chain mechanisms can be also assessed by studying diffusion flames in a counterflow configuration in which the impinging streams are characterized by low convective velocities and, therefore, large flame thicknesses. Similarly to the premixed near-limit flames, buoyancy induces instabilities because of the existence of the more-dense jet above the less-dense flame regime.

The majority of the present knowledge on the effects of strain and heat loss and their coupling with the chemical kinetics has been obtained by studying steady flames. Unsteadiness, however is inherently present in any realistic situation and it is important that its effect is independently quantified and understood. The strain and heat loss introduce characteristic time scales which have to be simultaneously considered and compared to the characteristic transport and chemical times. Flow field unsteadiness introduces an additional time scale which further complicates the analysis. The unsteadiness can lead to permanent extinction or temporal extinction followed by reignition, depending on the magnitude of the imposed strain, flame thickness, and the frequency of oscillations [10]. Such behavior can be especially profound for weakly-burning, easy-to-extinct flames which typically have increased thicknesses.

Objectives

In view on the above considerations, the first objective of the program (initiated in June of 1994) is to introduce the meritorious counterflow methodology in microgravity in order to quantify the steady and unsteady characteristics of weakly-burning premixed and diffusion flames for a wide variety of conditions including elevated pressures. Subsequently, through detailed modeling and comparisons with the experimental data, to provide physical insight into the elementary mechanisms controlling the flame response. The configuration offers good control over the parameters of interest and can be modelled closely.

The knowledge which will be gained from the counterflow flames will be subsequently used to analyze near-limit phenomena related to other configurations by conducting detailed numerical simulations including multidimensional ones. Among the problems to be analyzed are the downward and upward propagation of near-limit flames in tubes and phenomena observed in spherical and cylindrical geometries.

Experimental Methodology

The counterflow configuration includes the use of two opposed, aerodynamically shaped nozzles from which the reactant streams emerge and impinge onto each other. The nozzles are of variable diameter ranging from 20 to 40 mm and the burner assembly is housed into a variable pressure chamber which operates between 0.1 and 10 atm. Based on the dimensions and time scales of the experiments, the 2.2 sec drop tower and the KC-135 plane will be used.

One of the innovations of the proposed experiment is the study of unsteady strained flames by oscillating the nozzle exit velocities. The flow oscillator operates through the rotation of a cylinder cut at an angle. As the cylinder turns, it smoothly opens and closes the flow passageway. The partial closure of the passage decreases the flow rate to the burners until the passage begins to open again.

The measurements include the determination of the flame location and flow velocities. The flame location is monitored by recording the flame luminous zone and a visible ruler by using high-speed cine-photography in real time. The velocity measurements constitute the most challenging part of the program, since they require laser diagnostics systems with dimensions and power requirements appropriate for the microgravity facilities. Experiments are being currently performed in the 2.2 sec drop tower, and the flame response is quantified by using the mass continuity equation and estimating global strain rates by dividing the nozzle exit velocities by the nozzle separation distance. The results of detailed numerical simulations are also being used to provide an accurate correlation between the global and local preflame strain rates. Subsequently, the Laser Doppler Velocimetry (LDV) and Digital Particle Image Velocimetry (DPIV) techniques will be implemented for the more accurate description of the velocity field.

Numerical Methodology

Numerical simulation of the counterflow is being conducted by solving the unsteady conservation equations of mass, momentum, energy, and species for the stagnation streamline in a finite domain with the addition of radiative transfer from CH_4 , H_2O , CO_2 , and CO [2,10]. The numerical simulation of spherical and cylindrical geometries is being conducted by solving the one-dimensional, unsteady, conservation equations of mass, momentum, energy, and species in the appropriate coordinates. The numerical simulation of the laminar flow in tubes is being conducted by solving the

axisymmetric unsteady conservation equations of mass, momentum, energy, and species. All codes are integrated to CHEMKIN [11] and transport [12] codes and detailed kinetics are being used.

Propagation and Extinction of Near-Limit Premixed Flames

Understanding of the behavior of near-limit premixed flames is of particular interest to lean-burn combustors and safety. The behavior of lean flames appears to have significant differences compared to near-stoichiometric flames for a number of reasons. As the fuel concentration decreases and the flammability limit is approached, substantial chemical kinetics and Le number effects become important. The lower flame temperature starts favoring low activation energy reactions which typically have retarding effects on burning [1]. At the same time, the fuel becomes the deficient species and the magnitude of its mass diffusivity becomes a critical factor on the flame response to fluid mechanics [4,5]. Furthermore, the effect of thermal radiation starts becoming important since the magnitude of the radiative losses becomes comparable to the heat release rate. Thus, the burning rate is reduced [1] and extinction is facilitated [2] significantly compared to their adiabatic counterparts as it also shown in Figs. 1 and 2 respectively. Lean flames are also particularly sensitive to pressure variations due to the kinetic imbalance between two-body and three-body reactions which significantly affect the overall burning intensity.

Dynamics of Weakly-Burning Diffusion Flames

The application of aerodynamic straining on a diffusion flame, results to reactant leakage and flame temperature reduction which eventually can lead to flame extinction. Furthermore, as the straining increases, the mass burning rate increases and the thickness of the flame transport zone decreases. Contrary to premixed flames, whose burning rate is controlled by the flame speed, the burning rate of diffusion flames can be arbitrarily augmented by increasing the convective fluxes. By reducing the value of the convective transport of the reactant streams towards zero, the thickness of the diffusion flame increases and the radiation heat transfer is enhanced.

The effect of radiation on the extinction of strained counterflow diffusion flames due to the reduction of the methane mass fraction, Y_{CH_4} , in the fuel stream can be seen in Fig. 3 for various nozzle exit velocities, u_{exit} [2]. In Fig. 3a, $u_{exit}=180$ cm/s which results to large K (200 to 250 s^{-1}) and, therefore, small flame thickness. It can be seen that as Y_{CH_4} is reduced, the maximum flame temperature, T_{max} , is reduced and extinction is obtained at sufficiently low Y_{CH_4} values as indicated by the rapid reduction of the T_{max} . However, the overall response of the flame to Y_{CH_4} variations minimally depends on radiation. This indicates that for flames with small thickness, the magnitude of the radiative loss is reduced and its effect on the flame characteristics and extinction is not crucial.

In Fig. 3b, the results correspond to $u_{exit}=5$ cm/s which results to substantially reduced K (about 1 s^{-1}), and, therefore, increased flame thickness. The results demonstrate that the inclusion of the radiative loss mechanism indeed affects the flame response as indicated by the substantial reduction of the T_{max} , and the different Y_{CH_4} values at extinction. Such effect is due to the increased magnitude of the radiative loss as induced by the increased flame thickness and, therefore, increased volume of the radiating species. In Fig. 3b, results are also shown for 5 atm flames and it is seen that as the pressure increases, the T_{max} increases and that the temperature reduction due to radiation increases. This is reasonable since the gas emissivity increases directly proportional with pressure. Furthermore, it is seen that the limit Y_{CH_4} values at extinction are higher for the 5 atm case. This happens because as extinction is approached, the three-body main termination reaction ($H+O_2+M \rightarrow HO_2+M$) is favored over the two-body main branching reaction ($H+O_2 \rightarrow OH+O$) and extinction is facilitated at larger Y_{CH_4} values.

The results presented herein demonstrate that there can be a significant coupling between the processes of straining and radiation as the strain rate is reduced significantly. Such conditions can be encountered in situations of flame spread since no substantial strain is applied on the flame surface while it spreads.

3. Unsteady and Radiation Effects on Weakly-Burning Strained Flames

The effect of radiative loss under the presence of unsteady strain rate has also been examined for both premixed and diffusion flames [2]. For the premixed flames, cases close to the lean flammability

limit were studied. For the diffusion flames, conditions allowing for elevated and near zero strain rates during a cycle were examined.

In Fig. 4, the effects of unsteady strain and radiation on the dynamic response of a $\phi=0.5$ CH₄/air atmospheric flame are shown in terms of the variation of the value of the maximum heat release, Q_{\max} , versus a non-dimensional time, t' , resulting from the scaling of the real time with the period. It can be seen that by conducting adiabatic calculations, the flame responds in a sinusoidal manner to the imposed sinusoidal u_{exit} variations and permanent extinction does not occur. More specifically, Q_{\max} , which is directly proportional to the mass flux under vigorous burning conditions, assumes its peak (trough) value when u_{exit} is at its peak (trough) value. The inclusion of radiation, however, leads to reduced flame strength and permanent extinction is obtained at low frequencies. At higher frequencies, extinction is either delayed or suppressed and that depends on the relative magnitudes of the time required for extinction and the time during which the flame remains into the "unfavorable" strain regime [10]. For the 1 Hz adiabatic and the 40 Hz radiative cases, it can be seen that although permanent extinction does not occur, partial extinction and subsequent reignition occur as indicated by the reduction and subsequent increase of Q_{\max} at the high strain part of the cycle.

In Fig. 5, the effect of unsteady strain and radiation on the response of a diffusion flame is shown. The results have been obtained for a mean $u_{\text{exit},0}=30$ cm/s and an amplitude $u_{\text{exit},A}=25$ cm/s which results to peak and trough values of u_{exit} equal to 55 and 5 cm/s respectively, and, therefore, to large variations of the flame thickness throughout the cycle. For this reason, it was conjectured that when $u_{\text{exit}}=5$ cm/s the radiation will be enhanced compared to the $u_{\text{exit}}=55$ cm/s condition. This is indeed shown in Fig. 5a in which the variation of the maximum flame temperature, T_{\max} , is shown as function of t' . It can be seen that, at low frequencies, as the u_{exit} is reduced from its mean value, T_{\max} initially increases because of the reduced O₂ leakage through the main reaction zone. This increase, however, is subsequently arrested and a reduction of T_{\max} is observed although u_{exit} keeps decreasing, and this is due to the radiation effect which results from the increased flame thickness as u_{exit} is reduced. Subsequently, T_{\max} reaches a local minimum and then starts increasing again at the regime at which u_{exit} starts increasing, leading, therefore, to reduced flame thickness and radiative loss. This T_{\max} increase is subsequently arrested at the point at which u_{exit} becomes large enough to cause substantial O₂ leakage and T_{\max} reduction. When u_{exit} is at the upper part of its cycle, the asymmetry observed in the lower part of the cycle is not seen anymore, and the flame responds to the u_{exit} variations according to mechanism of O₂ leakage; the T_{\max} values are in all cases lower compared to the ones resulting from adiabatic calculations. As the frequency increases, it can be seen that there is a tendency for "smoothing" of the T_{\max} asymmetry in the low part of the u_{exit} cycle, and for frequencies higher than about 5 Hz the T_{\max} variation with t' is controlled by the mechanism of O₂ leakage. This indicates that the characteristic time of oscillations becomes comparable to the characteristic time for the flame cooling as caused by the thermal radiation loss. Calculations were conducted for the determination of the characteristic cooling time, t_{cool} , of the flame, by dividing the local energy density throughout the flame by the rate of the radiative loss, q'' . Results are shown in Fig. 5b, and it can be seen that at the vicinity of the maximum flame temperature, t_{cool} assumes values at the vicinity of 0.25 to 0.75 sec. This explains the fact that the mechanism of flame cooling due to the radiative loss couples with the imposed oscillations at frequencies of the order of 2 to 4 Hz.

Summary

Weakly-burning flames are particularly sensitive to the complex interactions between aerodynamic straining, unsteadiness, chemical kinetics and radiative losses. The use of the counterflow technique for the independent probing of such effects can provide a whole new dimension in our understanding of these complex phenomena.

Acknowledgements

This research is supported by NASA under the technical supervision of Dr. Fletcher Miller of the Lewis Research Center.

References

1. Law, C.K. and Egolfopoulos, F.N. (1992). A Unified Chain-Thermal Theory of Fundamental Flammability Limits. *Twenty-Fourth Symposium (International) on Combustion*, Combustion Institute, p. 137.
2. Egolfopoulos, F. N. (1994) Geometric and Radiation Effects on Steady and Unsteady Strained Laminar Flames. To appear in the Proceedings of the *Twenty-Fifth Symposium (International) on Combustion*, Combustion Institute.
3. Williams, F.A. (1985). *Combustion Theory*, 2nd ed. Benjamin-Cummings, Menlo Park, California.
4. Ronney, P.D. (1988). On the Mechanisms of Flame Propagation Limits and Extinction Processes at Microgravity. *Twenty-Second Symposium (International) on Combustion*, Combustion Institute, p. 1615.
5. Ronney, P.D. (1988). Effect of Chemistry and Transport Properties on Near-Limit Flames at Microgravity. *Combust. Sci. Tech.* 59, 123.
6. Law, C.K. (1989). Dynamics of Stretched Flames. *Twenty-Second Symposium (International) on Combustion*, The Combustion Institute, 1381-1402.
7. Egolfopoulos, F.N., Cho, P., and Law, C.K. (1989). Laminar Flame Speeds of Methane-Air Mixtures Under Reduced and Elevated Pressures. *Combust. Flame* 76, 375-391.
8. Kreutz, T.G., Nishioka, N. and Law, C.K. (1994). The Role of Kinetic Versus Thermal Feedback in Nonpremixed Ignition of Hydrogen Versus Heated Air. To appear in the Proceedings of the *Twenty-Fifth Symposium (International) on Combustion*, Combustion Institute.
9. Law, C.K. and Egolfopoulos, F.N. (1990). A Kinetic Criterion of Flammability Limits: The C-H-O-Inert System. *Twenty-Third Symposium (International) on Combustion*, Combustion Institute, p. 413.
10. Egolfopoulos, F.N. (1994). Dynamics and Structure of Unsteady, Strained, Laminar Premixed Flames. To appear in the Proceedings of the *Twenty-Fifth Symposium (International) on Combustion*, Combustion Institute.
11. Kee, R.J., Rupley, F.M. and Miller J.A. (1989). Chemkin-II: A Fortran Chemical Kinetics Package for the Analysis of Gas-Phase Chemical Kinetics. *Sandia Report SAND89-8009*.
12. Kee, R.J., Warnatz, J., and Miller J.A. (1983). A FORTRAN Computer Code Package for the Evaluation of Gas-Phase Viscosities, Conductivities, and Diffusion Coefficients. *Sandia Report SAND83-8209*.

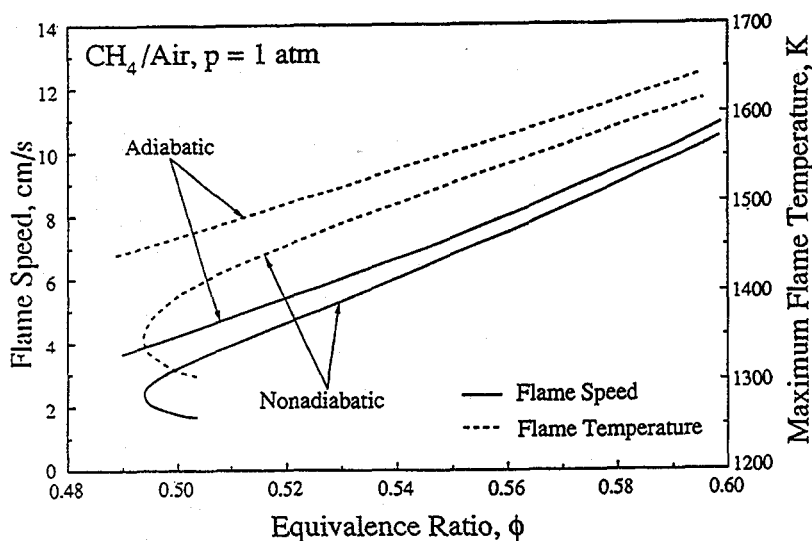


Figure 1. Effects of equivalence ratio and radiation on one-dimensional, steady, planar, lean premixed flames

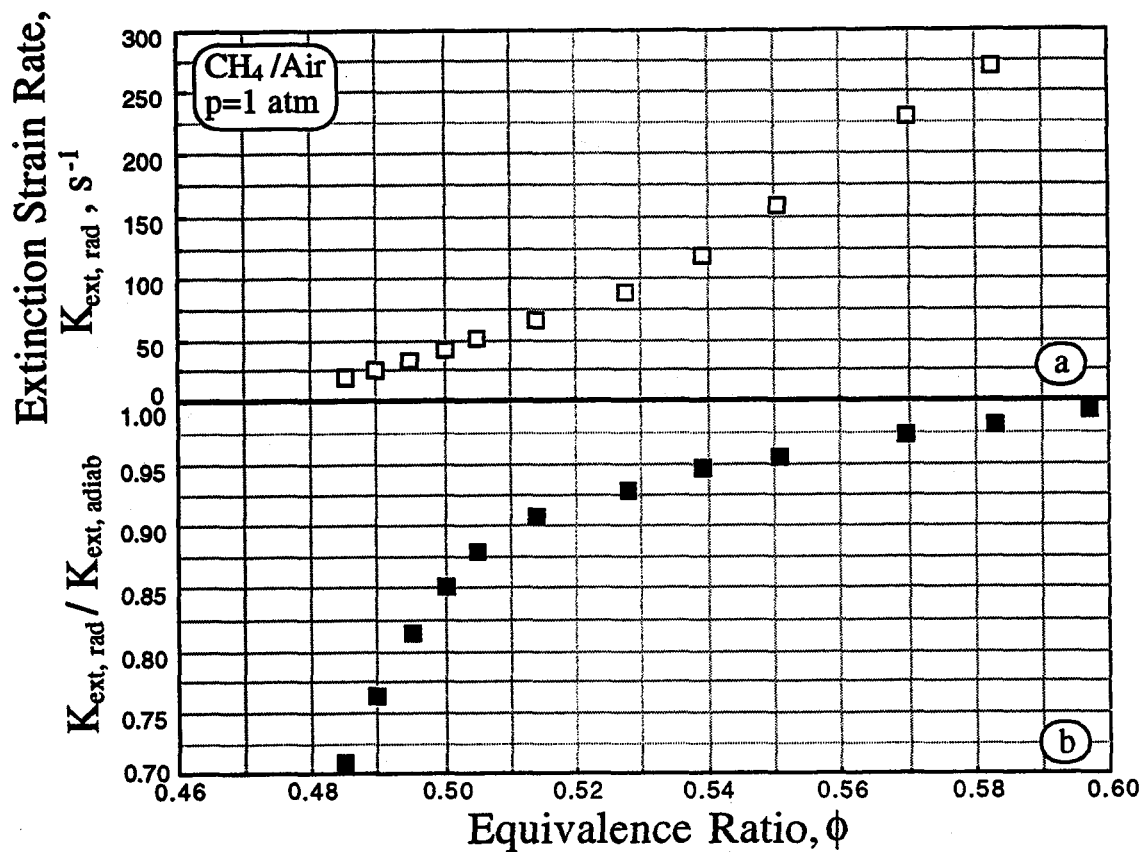


Figure 2. Effects of equivalence ratio and radiation on the extinction of steady, strained, lean premixed flames

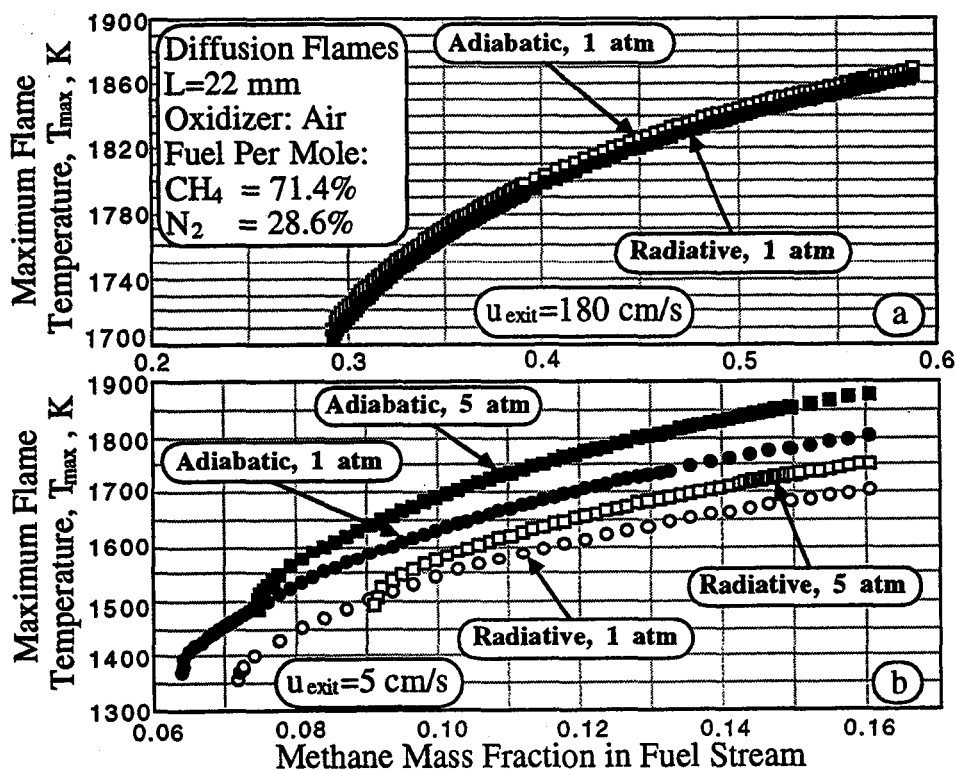


Figure 3. Effects of radiation and pressure on weakly and substantially strained diffusion flames

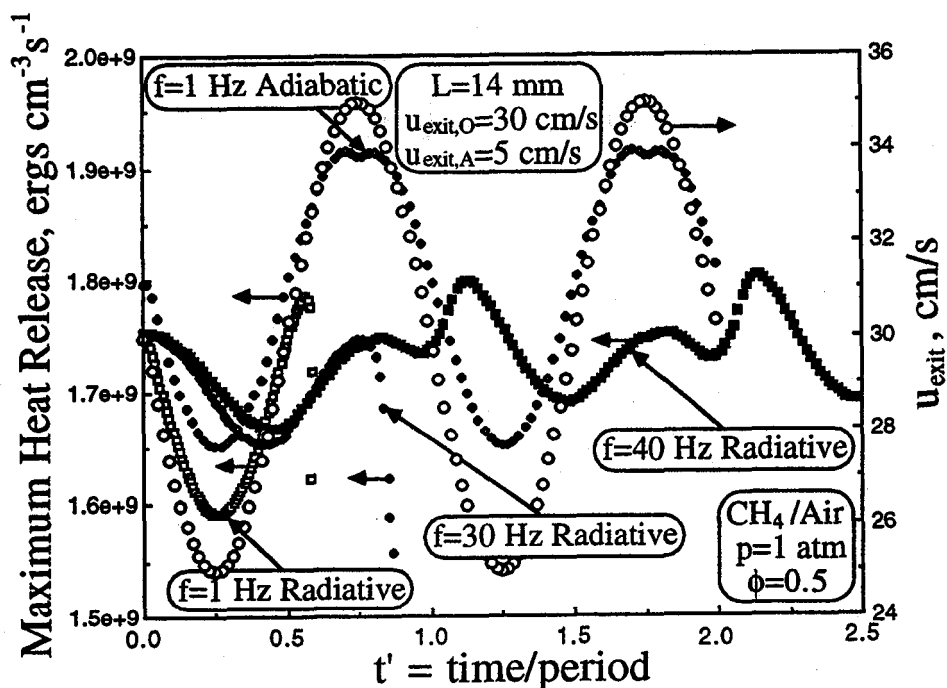


Figure 4. Effects of radiation and frequency on unsteady, strained, lean premixed flames

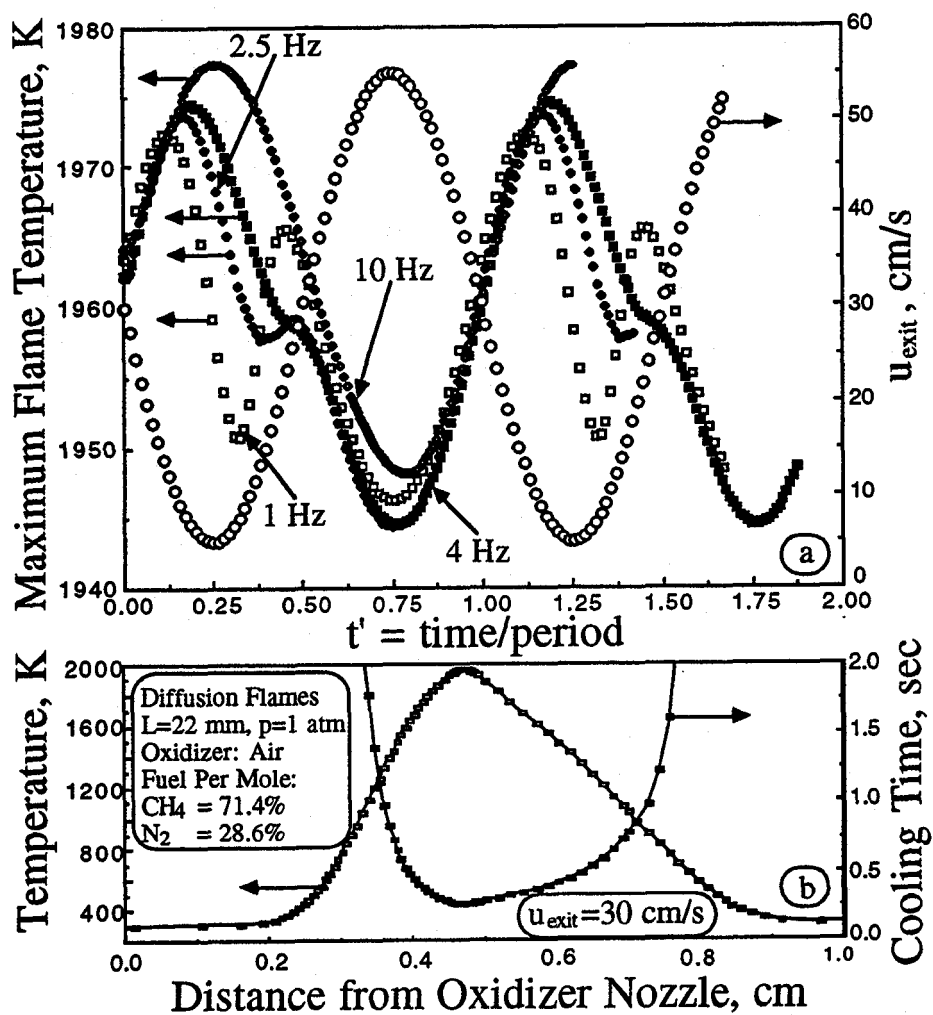


Figure 5. Effects of radiation and frequency on unsteady, strained, diffusion flames

UNSTEADY NUMERICAL SIMULATIONS OF THE STABILITY AND DYNAMICS OF FLAMES

K. Kailasanath, G. Patnaik* and E.S. Oran
Laboratory for Computational Physics & Fluid Dynamics
Naval Research Laboratory
Washington, DC

Introduction

In this report we describe the research performed at the Naval Research Laboratory in support of the NASA Microgravity Science and Applications Program over the past three years (from Feb. 1992) with emphasis on the work performed since the last microgravity combustion workshop. The primary objective of our research is to develop an understanding of the differences in the structure, stability, dynamics and extinction of flames in earth gravity and in microgravity environments. Numerical simulations, in which the various physical and chemical processes can be independently controlled, can significantly advance our understanding of these differences. Therefore, our approach is to use detailed time-dependent, multi-dimensional, multispecies numerical models to perform carefully designed computational experiments. The basic issues we have addressed, a general description of the numerical approach, and a summary of the results are described in this report. More detailed discussions are available in the papers published which are referenced herein.

Some of the basic issues we have addressed recently are 1) the relative importance of wall losses and gravity on the extinguishment of downward-propagating flames, 2) the role of hydrodynamic instabilities in the formation of cellular flames, 3) effects of gravity on burner-stabilized flames, and 4) effects of radiative losses and chemical-kinetics on flames near flammability limits. We have also expanded our efforts to include hydrocarbon flames in addition to hydrogen flames and to perform simulations in support of other on-going efforts in the microgravity combustion sciences program. Modeling hydrocarbon flames typically involves a larger number of species and a much larger number of reactions when compared to hydrogen. In addition, more complex radiation models may also be needed. In order to efficiently compute such complex flames recent developments in parallel computing have been utilized to develop a state-of-the-art parallel flame code. This is discussed below in some detail after a brief discussion of the numerical models.

Numerical Models

Most of the computations discussed in this report have been performed using the two-dimensional time accurate flame code, FLIC2D [1]. Some issues that do not require a multidimensional solution are addressed using FLAME1D [2]. Both of these codes developed at NRL solve the multispecies coupled partial differential reactive-flow equations. These models include a detailed chemical kinetics mechanism coupled to algorithms for convection, thermal conduction, radiation, viscosity, molecular diffusion, thermal diffusion, and external forces. The

* Berkeley Research Associates, Springfield, VA 22150.

external force, gravity, can be in any direction relative to flame propagation and can have a range of values. All of the chemical and physical processes are solved sequentially and then coupled asymptotically by time step splitting [3]. Space restriction does not allow the elaboration of the models here but details can be found in previous reports [1,2].

Summary of Research

Our recent research can be broadly divided into the following topics: (a) the extinguishment of downward-propagating flames [4], (b) role of hydrodynamic instabilities [5], (c) burner-stabilized flames [6,7], (d) effects of radiative losses of flames near flammability limits, (e) development of a parallel flame code [8], and (f) cellular structure of methane flames [9]. Each of these topics is discussed briefly below.

The Extinguishment of Downward-Propagating Flames

In the continuation of our research on the similarities and differences between zero-gravity and earth gravity flames, we have studied the detailed dynamics and mechanism of extinguishment of downward-propagating flames in two-dimensional channels [4]. The details of the extinguishment process in this mixture has been analyzed and found to be in excellent agreement with experimental observations. In experiments, the flame is first observed to halt its downward propagation and then actually move back up into the burnt products [10]. From the simulations we can understand the reason for this observed behavior. The simulations indicate that the flame is quenched at the walls and tongues of colder gases, comprised mainly of burnt products, flow down the sides. This sets up a recirculatory flow which causes an upward motion of the gases at the center of the channel, causing the flame to rise up into the burnt products. Further analysis of the simulations also indicate that the dilution of the unburnt mixture with the products of combustion is an essential step in the extinguishment process. This mechanism may explain the extinguishment of flames in other fuel-air mixtures also (during downward propagation). Currently, this is being tested for flames in lean methane-air mixtures.

The actual limit obtained from the computations for a downward propagating flame in an isothermal channel is around 9.75% and is in good agreement with experimental observations. Our earlier simulations have shown that a flame can propagate downward even in a 9% mixture in a channel with adiabatic walls indicating that heat losses to the walls are essential to the observed limit. Cellular flames are also observed to occur in this mixture, both in simulations and experiments, in a zero-gravity environment. These observations, taken in conjunction with our current simulations, indicate that both heat losses and gravity are simultaneously required to cause the observed limit.

Role of Hydrodynamic Instabilities

Recently, we have been able to clarify the relative role of hydrodynamic and thermo-diffusive effects for hydrogen flames [5]. In earlier simulations, rich hydrogen-oxygen-nitrogen (3:1:16) flames were flat in 2 cm and 5.1 cm wide systems even in zero-gravity, while theory would predict them to be non-planar due to the hydrodynamic instability. Recently, when the system size was increased to 9 cm, the flame indeed developed a curved structure due to hydrodynamic effects. These results imply that except for very large systems (system size/flame thickness greater than about 20), the diffusive transport effects dominate the hydrodynamic effects in hydrogen systems. Whether this is true for hydrocarbon systems is a matter that needs to be investigated.

Furthermore, even this flame curvature due to the hydrodynamic instability is suppressed if gravity effects (downward) are turned on, indicating that the hydrodynamic instability is indeed a weak effect. The structure of these flames are also quite different from the classical cellular flame structure.

Burner-Stabilized Flames

We have systematically explored the effects of different burner boundary conditions (Hirschfelder, isothermal, etc.) on the structure and dynamics of both one- and two-dimensional flames stabilized on burners. The different boundary conditions are different ways of characterizing the heat losses to the burner. In addition to reproducing well known features of burner-stabilized flames, these simulations have been used to isolate the role of heat losses, gravity and burner boundary conditions.

Our one-dimensional simulations [6] have shown that, for high inlet velocities, the structure of burner-stabilized flames is similar to that of unconstrained flames. However, for low inlet velocities, the inflection point is absent in the temperature profiles. The characteristic "C-shaped" curve, suggesting two flame temperatures for each flame stand-off distance, is observed as predicted by theory. However, this does not mean that there are two solutions, as suggested by some investigators. A unique solution is seen if the stand-off distance is plotted as a function of the inlet velocity. We conclude that the inlet velocity should be considered as the independent variable, rather than the stand-off distance, as is sometimes done in theoretical analyses. For a Hirschfelder burner, blow-off occurs at a much lower velocity than for the isothermal burner cases studied. In all cases, the blow-off velocity is higher than the burning velocity of an unconstrained flame at the room/coolant temperature. In general, the blow-off velocity corresponds to the burning velocity of an unburnt mixture initially at the burner temperature.

Our two-dimensional flame simulations show that a flame can be stabilized at inlet velocities much higher than the 1-D blow-off velocities because of the curvature of the flame. Cell formation occurs for high inlet velocities but new cells are not formed by cell splitting, as observed in the unconstrained case. At low inlet velocities, cellular structure is suppressed due to increased heat losses and a flat flame is established on the burner. Similar behavior is observed for the isothermal and Hirschfelder burners but at different inlet velocities. The observed differences with the two different burner boundary conditions imply that a characterization of the burner used in experiments is required to make meaningful comparisons with experiments.

The suppression of cellular structures for low inlet velocities occurs in both zero-gravity and downward-propagation burner-stabilized flames. This, in conjunction with our earlier observations on unconstrained flames in these mixtures in zero-gravity indicates that heat losses to the burner are more dominant than gravity in determining the structure and dynamics of these flames [7]. This observation is also in agreement with the conclusions of Dunskey and Fernandez-Pello [11].

Flammability Limits

As discussed earlier, we have a detailed description of the behavior of flames at the downward-propagation limit and both conductive heat losses and gravity are found to be required simultaneously to explain the observations. Similar studies of zero-gravity and upward-propagating flames must await the development of a three-dimensional flame model. Meanwhile, we have also been studying the issue of fundamental flammability limits in a zero-gravity environment using one-dimensional simulations of flames in mixtures that are not expected to show multidimensional structures.

Results from the numerical simulations indicate that a steady burning velocity is not obtained for very rich hydrogen-air mixtures [12]. As the amount of hydrogen is increased, at first a damped oscillation is observed in the flame and burning velocities, and then with further increase in the amount of hydrogen, an undamped oscillation with a complex set of frequencies is observed. Further analysis shows that the oscillations are due to a competition for H atoms

between chain branching and chain-terminating reactions. However, the limiting mixture predicted by these simulations is beyond the experimentally observed limit. We speculated earlier that these differences may be because of the neglect of phenomena such as stretch and radiative heat losses.

Simulations of spherically expanding flames indicate that stretch effects (due to curvature) will cause the oscillations to occur in less rich mixtures than that observed for planar flames. Further calculations including radiative heat losses indicate that radiation can indeed shift the apparent flammability limit to less rich mixtures. However, the oscillations observed in the burning velocities are still present even when the effects of radiative heat losses are included. Uncertainty in the chemical-kinetic parameters and multidimensional effects may also play a role in the absolute value of the limiting mixture. Further calculations are currently being carried out to more fully understand the effects of these parameters on the rich flammability limit.

Calculations of flames in lean methane-air mixtures using the one-dimensional flame code show that with radiative losses, a zero-gravity flammability limit of about 5.15% is obtained which is in agreement with experimental data from drop-tower tests. Without radiative losses, flame propagation can be observed in much leaner mixtures.

Development of a Parallel Flame Code

Detailed three-dimensional flame simulations, or even two-dimensional simulations of complex hydrocarbon flames, need a tremendous amount of computer resources. It appears that more cost-effective and efficient computations can be carried out taking advantage of the developments in parallel computing. Therefore, a major research effort was undertaken in the past year to develop and test a parallel version of the multidimensional flame code. The parallel version includes the same physics and employs the same numerical methods used in the vectorized code described above.

The parallel version of the flame code has now been implemented on the Intel Paragon and the IBM SP2 computers. A good test of the parallelism is the scaling of the computation time with the number of processors. Figure 1 shows the timings of the important processes for the computation of a downward-propagating methane-air flame. For this methane computation on a 256 X 256 grid, it requires 50 nodes of the Intel Paragon to equal one CRAY C-90 processor. All processes except the fluid convection scale well. The fluid convection does not scale due to the large amount of communication and scalar code required by the multigrid solution procedure. The chemistry takes 60 - 70% of the total time; thus it is very important that a good load balance is achieved. As shown in the figure, the chemistry module scales extremely well with the number of processors. If a large number of processors are utilized, these computers have the capability to solve a two-dimensional problem with detailed chemistry or even three-dimensional problems with some simplifications.

Cellular Structure of Methane Flames

Cellular structures in methane flames have been studied using a moderately detailed reaction mechanism, popularly called the "skeletal mechanism" involving 16 species and 35 reactions. This mechanism has been used as the starting point for deriving systematically reduced mechanisms. It is unlikely that the reduced mechanisms will provide satisfactory results if the skeletal mechanism itself is unsatisfactory. Simulations of flames in lean methane-air mixtures using this mechanism did not show prominent cellular structures as observed in lean hydrogen-air mixtures. The cellular structures may not have been prominent because the Lewis number of the mixture, though less than one is close to unity (0.9). Theoretical analysis [13] indicates that the deviation from unity is an important parameter determining the cellular structure of flames. The Lewis number can be decreased by adding carbon dioxide as a diluent. Therefore, further simulations were carried out with carbon dioxide dilution.

A 56.5% carbon dioxide diluted methane mixture with an equivalence ratio of 0.5 is particularly interesting since it has a burning velocity of about 7.5 cm/s which is close to the burning velocity of near-limit CO₂ diluted mixtures studied experimentally. Figure 2 shows the time evolution of the OH mole fraction at 15 ms intervals. The vertical scale in this figure has been expanded two times for clarity. The variations in the OH concentration along the flame are not as large as in hydrogen-air flames making the cellular structures appear more like ripples on the flame. Though the Lewis number of this mixture is small (0.7), it is still large than those of lean hydrogen-air flames (~0.3) and probably accounts for the differences in the flame structure. The cellular structures are however much more prominent than in lean methane-air flames indicating that the deviation of the Lewis number from unity is important in determining the size and strength of the cellular structures, in accordance with the theory [13].

The size of the cells observed in the simulations, 5 cells in a 5.1 cm channel, is in good agreement with experimental observations (elsewhere in this volume) of Ronney, 10-11 cells in a 10 cm diameter tube. However, the limiting mixture though having a comparable burning velocity to those in experiments, is quantitatively different. The dilution limit observed in the computations is about 56.5% CO₂ while the experimental limit is between 57.4-58.3% dilution. While there are details in the configuration used in the experiments and simulations, the uncertainties in the chemical parameters could also account for such differences. Further studies with the one-dimensional flame code indicates small changes in the third-body efficiencies used in the chemical reaction scheme could significantly alter the limit mixtures and burning velocities. The skeletal mechanism used may also be inadequate for mixtures diluted with large amounts of CO₂. Further studies with more comprehensive reaction mechanisms will be useful to resolve this issue.

Work in Progress and Future Plans

Currently, the detailed mechanism of the extinguishment of downward-propagating methane-air flames is being studied using the newly developed parallel version of the flame code. This study will help confirm if the mechanisms observed earlier in the extinguishment of lean hydrogen-air flames is also true for methane. A similar study for a higher hydrocarbon such as propane may also be needed to generalize the observation.

The studies of flames with CO₂ dilution suggest that some simulations with more detailed methane mechanisms is needed before moving on to more reduced reaction mechanisms. Even with the development of the parallel version of the flame code, simplified mechanisms will be needed to simulate transient three-dimensional phenomena such as the breakdown of flame strings to flame balls. Three-dimensional simulations are also needed to predict extinguishment of upward-propagating and zero-gravity flames. So a major effort in the next year will be to develop and test a three-dimensional version of the flame code.

Recently, collaborations have also been established with the group at the University of Michigan to perform simulations that are complementary to the experiments being planned such as the interaction between a vortex and a flame in a premixed gas in a tube. The collaboration has already produced some interesting results on unsteady diffusion flames that can be found elsewhere in this volume.

Acknowledgments

This work was also partially supported by the Office of Naval Research through the Naval Research Laboratory. The development of the parallel version of the flame code was made possible by a collaboration with the Computer Sciences Department at the University of Maryland and with

contributions from Dr. David Fyfe at NRL. The authors wish to thank Prof. Paul Ronney for many helpful discussions and sharing his unpublished data on flames in CO₂ diluted methane mixtures. Computer time for this study has been provided by the DOD High Performance Computing program and the NASA Numerical Aerodynamic Simulation Facility.

References

1. Patnaik, G., Laskey, K.J., Kailasanath, K., Oran, E.S. and Brun, T.A., NRL Memorandum Report 6555, Naval Research Laboratory, Washington, D.C., 1989.
2. Kailasanath, K., Oran, E.S., and Boris, J.P., NRL Memo. Report No. 4910, Washington, D.C., 1982.
3. Oran, E.S., and Boris, J.P., Numerical Simulation of Reactive Flow, Elsevier, New York, 1987.
4. Patnaik, G. and Kailasanath, K., Proceedings of the 24th Symposium (International) on Combustion, pp. 189-195, The Combustion Institute, Pittsburg, PA., 1992.
5. Kailasanath, K., and Patnaik, G., Presented at the 14th International Colloquium on the Dynamics of Explosions and Reactive Systems, Coimbra, Portugal, Aug. 1-6, 1993.
6. Patnaik, G. and Kailasanath, K., AIAA Paper 93-0241, AIAA, Washington, DC, 1993.
7. Patnaik, G. and Kailasanath, K., Combust. Flame 99: 247-253, 1994.
8. Patnaik, G., Fyfe, D., Kailasanath, K., Moon, B., Bennett, R., Sussman, A., and Saltz, J., Proceedings of the Fall Technical Meeting of the Eastern States Section of the Combustion Institute, pp. 341-344, 1994.
9. Patnaik, G. and Kailasanath, K., AIAA Paper 95-0130, AIAA, Washington, DC, 1995.
10. Jarosinski, J., Prog. Energy Combust. Sci., 12: 81-116, 1986.
11. Dunskey, C.M., and Fernandez-Pello, A.C., Proceedings of the 23rd Symposium (International) on Combustion, p. 1657, The Combustion Institute, Pittsburg, PA., 1991.
12. Kailasanath, K., Patnaik, G. and Ganguly, K., Prog. Astro. Aero. 151: 247-262, 1993.
13. Pelce, P. and Clavin, P., J. Fluid Mech., 124:219-237, 1982.

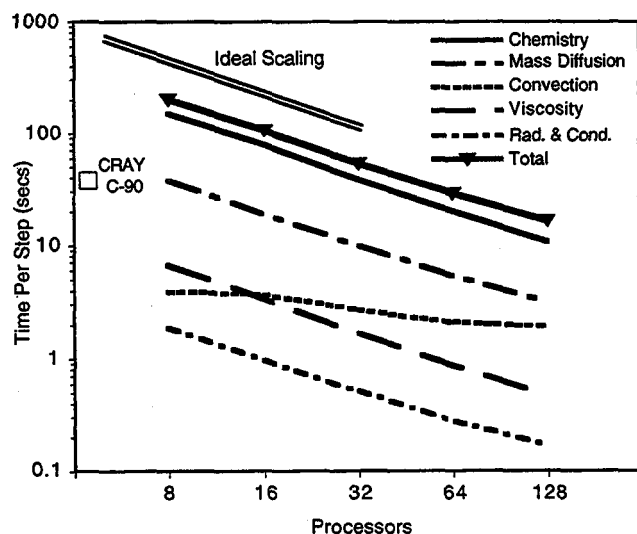


Fig. 1. Computation times on Intel Paragon.

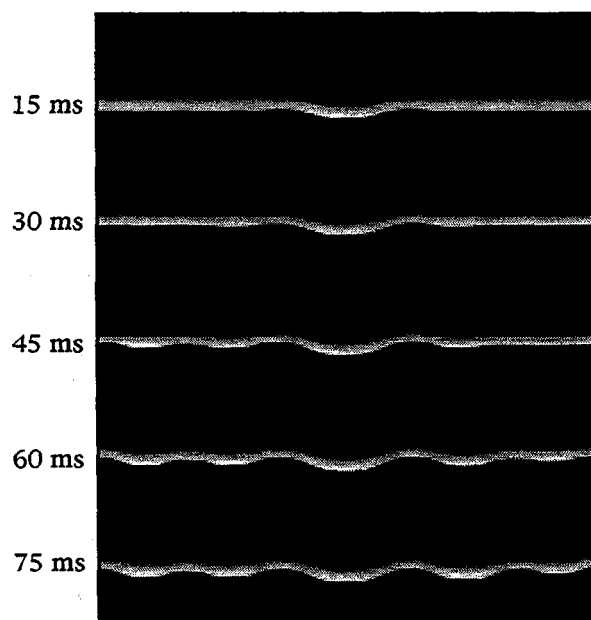


Fig. 2. Cellular structures in a 56.5% Methane - CO₂ Flame

ON BURNER-STABILIZED CYLINDRICAL PREMIXED FLAMES IN MICROGRAVITY

James A. Eng, Delin Zhu and Chung K. Law
Department of Mechanical and Aerospace Engineering
Princeton University, Princeton, NJ 08544

Introduction

A class of one-dimensional premixed flames that has the potential of eliminating heat loss and stretch effects is the burner-generated cylindrical and spherical flames, where a premixed gas flows through a porous cylindrical or spherical burner and the resulting flame is formed at some distance from the burner, as shown in Figs. 1a and 1b. To demonstrate that such flames are curved but not stretched, we consider the general expression for the stretch rate experienced by a flame surface [1,2],

$$\kappa = \frac{1}{A} \frac{dA}{dt} = -\mathbf{n} \cdot \nabla \times (\mathbf{u}_f \times \mathbf{n}) + (\mathbf{s}_f \cdot \mathbf{n})(\nabla \cdot \mathbf{n}) \quad (1)$$

where A is the area of an infinitesimal element of the flame surface, \mathbf{u}_f the flow velocity evaluated at the flame, \mathbf{s}_f the velocity of the flame, and \mathbf{n} the unit normal vector of the surface. Equation (1) shows that, since the flame is stationary ($\mathbf{s}_f = 0$), and the flow is normal to the flame surface ($\mathbf{u}_f \times \mathbf{n} = 0$), the stretch rate vanishes identically. Furthermore, while such a flame can be stabilized by heat loss to the burner, the divergent nature of the flow provides an additional stabilization mechanism. That is, as the flow rate is continuously increased, the flame recedes from the burner and heat loss can be eventually reduced to become negligible as compared to the heat generated at the flame. At this point the flame temperature is expected to be close to the adiabatic flame temperature. Further increase in the flow rate is then accommodated by an increase in the flame standoff distance to a position where the flame speed again balances the flow velocity. Thus, the cylindrical/spherical geometry offers a unique advantage for the study of adiabatic, one-dimensional, stretch-free flames that is not present in other commonly used experimental systems. Such flames, however, can only be established, and studied, in a microgravity (μg) environment because of the distorting nature of the buoyant flow under normal gravity conditions.

In view of the above considerations, an experimental and theoretical program on cylindrical and spherical premixed flames in microgravity has been initiated. We are especially interested in: (1) assessing heat loss versus flow divergence as the dominant stabilization mechanism; (2) understanding the effects of flame curvature on the burning intensity; and (3) determining the laminar burning velocity by using this configuration. In the present study we have performed analytical, computational, and μg -experimental investigations of the cylindrical flame. The results are presented in the following sections.

Asymptotic Analysis and Qualitative Behavior

The problem analyzed is shown in Fig. 1a. Here a premixture of temperature T_u , mass flow rate m , and consisting of a deficient, rate-limiting reactant F (fuel) with mass fraction $Y_{F,u}$ issues from a unit-length, internally-cooled porous cylinder which has a radius r_s and surface temperature T_s , where the subscript s designates the burner surface. From continuity, the mass flow rate $m = 2\pi r u$ is a conserved quantity along the radial distance r , where u is the r -velocity. Upon ignition, a cylindrical flame is established concentric with the burner, with the thin reaction zone located at r_f and the preheat zone extending from the burner surface to r_f , where the subscript f designates the reaction zone. From the experimental point of view, the parameter which can be independently and conveniently controlled is m . Thus for a given m , the cooling rate of the burner and hence the heat loss rate from the flame, Q_s , can be adjusted to achieve a constant T_s . The flame temperature T_f and flame standoff location r_f will also adjust accordingly for the given m and T_s .

A straightforward application of activation energy asymptotics yields the following flame responses,

$$\left(\frac{\tilde{m}}{\tilde{r}_f}\right)^2 = Le \Delta \quad (2)$$

$$\tilde{T}_f = (\tilde{T}_f^o + \tilde{T}_s - \tilde{T}_u) - \tilde{q}_s \quad (3)$$

$$\tilde{q}_s = \tilde{r}_f^{-\tilde{m}} \quad (4)$$

where $\Delta(\tilde{T}_f) = 2Da (\tilde{T}_f^2/\tilde{T}_a)^2 \exp(-\tilde{T}_a/\tilde{T}_f)$ is a reduced Damköhler number,

$$Da = \left(\frac{BY_{O,u}}{W_O}\right) \left(\frac{\rho_b^2 r_s^2}{\lambda/c_p}\right) \quad (5)$$

is the Damköhler number, Le the Lewis number, $\tilde{m} = m/(2\pi\lambda/c_p)$, $\tilde{T} = c_p T/Y_{F,u} q_c$, $\tilde{Y}_F = Y_F/Y_{F,u}$, $\tilde{\rho} = \rho/\rho_b$, $\tilde{r} = r/r_s$, $\tilde{q}_s = [r_s/(Y_{F,u} q_c)] q_s$, T_a is the activation temperature, ρ the density, Y_O the mass fraction of the abundant species, λ the thermal conductivity, c_p the specific heat, q_c the chemical heat release per unit mass of fuel, q_s the specific heat loss per unit length of burner, and B the frequency factor. The subscripts u and b respectively designate the unburnt and burnt states of the flame, and the superscript "o" designates the adiabatic, one-dimensional planar flame. We shall also assume that there is no downstream heat loss such that $T_f = T_b$.

For large values of \tilde{r}_f the above solution approaches the adiabatic limit, with $\tilde{q}_s \rightarrow 0$, $\tilde{T}_f \rightarrow \tilde{T}_f^o$ and $\Delta(\tilde{T}_f) \rightarrow \Delta(\tilde{T}_f^o)$ which is a constant. The last relation, when interpreted in the context of Eq. (2), implies that (\tilde{m}/\tilde{r}_f) becomes a property of the mixture in this limit, being independent of the burning rate \tilde{m} and the flame curvature which is proportional to \tilde{r}_f^{-1} . This result has the following implications.

First, since $\tilde{r}_f \sim \tilde{m}$, the flame accommodates an increase in the mass flow rate from the burner by moving to a larger radial distance and hence attaining a larger flame surface area. The flame is therefore stabilized through flow divergence. This stabilization mechanism and hence flexibility do not exist for the flat-burner flame, which loses its planar nature when the burner discharge rate exceeds that of the adiabatic value.

Second, if we evaluate \tilde{m} at the reaction zone, then $(\tilde{m}/\tilde{r}_f) = (\rho_b u_r r_s)/(\lambda/c_p)$ is simply a nondimensional mass flux at \tilde{r}_f , say \tilde{f}_f , where $\tilde{f} = \tilde{r}_f/(\lambda/c_p)$ is the nondimensional f . Furthermore, since this quantity is independent of \tilde{r}_f and hence the flame curvature in the adiabatic limit, it must be equal to the (constant) mass flux of the adiabatic planar flame, $\tilde{f}^o = \tilde{f}_u^o = \tilde{f}_f^o$, for which r_s can be considered as an arbitrary length for nondimensionalization. We therefore have the following sequence of identities in the adiabatic limit:

$$\left(\frac{\tilde{m}}{\tilde{r}_f}\right)^2 = (\tilde{f}_f)^2 = (\tilde{f}^o)^2 = Le \Delta. \quad (6)$$

The invariance of \tilde{f}_f to flame radius variations provides a simple relation for an experimental determination of the laminar burning velocity of the one-dimensional planar flame. That is, since $m (=2\pi r_f \rho_b u_r)$ is given while the flame radius can also be easily measured photographically, the laminar burning flux is simply

$$f^o = \frac{m}{2\pi r_f}. \quad (7)$$

Furthermore, since $f^o = f_u^o = \rho_b u_u^o$, the laminar burning velocity is then given by $s_u^o = u_u^o = f^o/\rho_u$. Our experimental result agrees well with Eq. (7), as will be shown later.

Third, since $f_f = f_u^o$ while $f_f < f_u$ because of flow divergence, we must have $f_u^o < f_u$. Thus if f_u is identified as the flame propagation rate relative to the freestream, then the concave nature of the present cylindrical flame renders it to have a higher flux and hence propagation rate than the planar flame. This is the same curvature effect which causes the tip of a unity Lewis number Bunsen flame to have a higher burning velocity than its shoulder.

The characteristics of the cylindrical flame can be better demonstrated with the following quantities,

$$\hat{m}_s^2 = \left(\frac{\tilde{m}}{\tilde{m}_s^o}\right)^2 = (\tilde{r}_f)^2 \left(\frac{\tilde{T}_f}{\tilde{T}_f^o}\right)^4 \exp\left[\tilde{T}_a \left(\frac{1}{\tilde{T}_f^o} - \frac{1}{\tilde{T}_f}\right)\right] \quad (8)$$

$$\hat{Q}_s = \left(\frac{\hat{m}}{\hat{m}_s^o} \right) \tilde{q}_s = \hat{m}_s \tilde{r}_f^{-\hat{m}} \quad (9)$$

where \hat{m}_s is the ratio of the mass burning rate of the cylindrical flame to that of the adiabatic planar flame with the same cylinder surface area, or $\hat{m}_s^o = 2\pi r_s \rho_s s_u^o$. We also define a flame standoff distance $\hat{d}_f = r_f - r_s$, with $r_s = 0$ for the planar case, and nondimensionalize it by the laminar flame thickness $\delta^o = (\lambda/c_p)/f^o$ such that $\hat{d}_f = d_f/\delta^o$.

For comparison, we note that for the nonadiabatic planar flame stabilized over a flat burner [3, 4, 5], $\hat{m}_s = \hat{f} = f/f^o$ such that

$$\hat{m}_s^2 = \left(\frac{\tilde{T}_f}{\tilde{T}_f^o} \right)^4 \exp \left[\tilde{T}_a \left(\frac{1}{\tilde{T}_f^o} - \frac{1}{\tilde{T}_f} \right) \right] \quad (10)$$

$$\hat{Q}_s = \hat{m}_s \exp(-\hat{m}_s \hat{d}_f) \quad (11)$$

while Eq. (3) still holds for the relation between \tilde{T}_f and \tilde{q}_s .

Calculated results using representative values show that both the planar and cylindrical cases yield a dual solution behavior in that there are two values of the mass burning rate \hat{m}_s for either a given heat loss rate \hat{Q}_s or a given flame standoff distance \hat{d}_f . The behavior for the planar case is a well known observation [6, 7, 8] which has also been recently explained [4, 5] by noting that by taking \hat{m} as the independent parameter with \tilde{T}_s fixed, the flame responses in terms of \hat{Q}_s and \hat{d}_f are actually unique. By similar reasoning we then expect that the responses of the cylindrical flame are also unique when \hat{m}_s is the independent parameter.

For the cylindrical flame, it is further found that when the cylinder radius is large, the flame behavior follows closely that of the planar flame up to $\hat{m}_s \approx 1$, as expected. In this regime heat loss is the dominant flame stabilization mechanism. For $\hat{m}_s > 1$, the planar flame does not exist while the cylindrical flame can still be maintained due to flow divergence. In this regime the flame is practically adiabatic, with $\hat{Q}_s \approx 0$ and $\tilde{T}_f \approx \tilde{T}_f^o$. For smaller cylinder radius, the response of the cylindrical flame deviates significantly from that of the planar flame. The flame is almost adiabatic and is stabilized by flow divergence at higher values of \hat{m}_s .

To identify the influence of curvature on the burning flux at the upstream boundary of the flame, we have also computed $\hat{f}_u = f_u/f_u^o$, with the unburnt state evaluated at the location of the 1% temperature rise from the freestream temperature according to the suggestion of Tien and Matalon [9]. The results are quite insensitive to the actual state selected as long as it is close to the ambient state. It is found that with increasing \hat{m}_s , \hat{f}_u initially increases to values of $\hat{f}_u > 1$. It then decreases and eventually approaches the adiabatic, planar case of $\hat{f}_u = 1$ as $\hat{r}_f \rightarrow \infty$. The important point to note is that f_u can exceed f_u^o , in agreement with the previous discussion of curvature-enhanced burning flux and hence burning velocity.

Microgravity Experimentation

The experimental apparatus for the cylindrical flame is shown in Fig. 2. The cylindrical burner was made of a porous bronze tube with 5 μm pore size, 1.25 cm diameter, and 3.76 cm active length. The thickness of the porous wall is 4.7 mm. Since uniformity of the flow through the porous wall depends on the pressure differential across it, the reactant mixture was supplied from both ends of the burner tube so as to minimize the internal pressure gradient in the axial direction of the cylinder. Furthermore, stainless steel tubes with small holes at various locations were positioned inside the burner to further even the axial pressure distribution. A cross sectional view of the burner with the internal tubes is shown in the inset of Fig. 2. The axial pressure distribution was measured (under normal gravity conditions) by drilling small holes in the porous wall and connecting water manometers to the pressure taps. For the best achieved design of the number and placement of the holes in internal tubes at a typical flow rate, the inlet gage pressure to the burner was 60 cm water and the axial pressure variation was ± 2 cm water, a 10% variation.

Due to the small burner size and the limited duration of the microgravity experiments, no cooling was used for the burner. A thermocouple was inserted inside the burner wall to record the burner temperature. A hot wire mounted on a rotary solenoid was used to ignite the mixture. Experiments were performed under microgravity conditions at the NASA-Lewis 2.2 second drop tower. Mass flow rates were measured by using sonic flow nozzles whose upstream pressures were recorded by using pressure transducers. A video camera was used to record the flame shape and standoff distance.

Computational Simulation

The experimental situation was numerically simulated by using the Sandia premixed flame code [10], with modifications to ensure strict mass conservation in the divergent flow field. The program solves the governing equations of mass, energy and species using finite difference approximation, allowing for detailed chemical kinetics, multicomponent diffusion and variable thermal properties. The chemical mechanism used was that developed by Egolfopoulos et al. [11], which has 30 species and 153 reaction steps.

The independent variable for the burner stabilized flame is the mass flow rate \dot{m} . The necessary boundary conditions are the burner surface temperature, T_s , and the reactant mixture mass flux fractions. The boundary conditions imposed on the product side are vanishing gradients for species and temperature, dY_i/dr and dT/dr . The program solves the governing equations to determine the temperature profile through the flame, from which the flame location and heat loss to the burner can be found.

Experimental and Computational Results

A mixture of $\text{CH}_4 + 2\text{O}_2 + 7.52\text{N}_2 + 5.665\text{He}$, with an effective Lewis number of 1.88, was used for the cylindrical flame experiments. Helium was added to enhance flamefront stability. There are two causes for the enhanced flame stability with helium addition. First, the effective Lewis number of the mixture increases, which reduces the thermal-diffusional instability. Second, the adiabatic flame temperature is reduced, which reduces the density jump across the flame and the propensity to develop the hydrodynamic (Landau) instability. For this mixture the adiabatic flame temperature for the unburned mixture temperature of 300 K is 1885 K, and the calculated laminar flame speed is 20.8 cm/s, which corresponds to a mass burning flux of 0.016 gm/cm²-s.

Figure 3 compares the calculated and measured flame standoff distance as a function of the normalized mass flow \dot{m}_g . The inset shows a typical recorded flame configuration, which exhibits some large-scale, weak wrinkling. This wrinkling is believed to be caused by the pressure variation in the burner and leads to a variable standoff distance of $\pm 15\%$ in the axial direction. The spread in the experimental data therefore represents the extent of flame nonuniformity as measured by the minimum and maximum standoff distances. The flame location for the numerical results is taken as that of the maximum CH radical concentration, since this species is chiefly responsible for the luminosity of the flame and assumes its maximum concentration in the active reaction zone of the flame. The heat loss to the burner is also presented for the calculated results, and shows that around a normalized flow rate of $\dot{m}_g \sim 1.4$, the heat loss is essentially zero. At this point the stabilization mechanism has changed from heat loss to flow divergence. The figure also shows that all the microgravity data are in the regime where the flame is stabilized by flow divergence. This is further substantiated by the experimental result that the thermocouple temperature basically remained at the ambient value during the experiment. The comparison shows that the flame is situated further away than calculated, with about 1 to 2 mm differences. Overall, the experimental and computational results agree quite well, at least qualitatively, considering the difficulties usually associated with microgravity experimentation.

Figure 4 compares the calculated and observed mass flux through the reaction zone. As discussed, the calculated result in the adiabatic limit should be close to the independently calculated laminar burning flux for the adiabatic planar flame. Exact agreement is not expected because while the calculated result is a constant for the planar flame, it depends on the present choice of the maximum CH radical location as that of the reaction zone for the cylindrical flame. The uncertainty, however, is not expected to be large because the flame thickness is much smaller than its standoff distance. It is seen that the calculated laminar mass flux attains a value of about $\dot{f}_f = 0.0156$ gm/cm²-s in the divergence-stabilized regime, which compares very favorably with the independently calculated value of $\dot{f}^\circ = 0.016$ gm/cm²-s for the adiabatic planar flame. Figure 4 further shows that the experimentally measured values also agree well with the computed results, being slightly smaller. This demonstrates the feasibility of determining the laminar burning flux, and hence the laminar burning velocity, by using the cylindrical/spherical flame as proposed herein.

The difference between the calculated and measured values for the flame location and burning flux can be attributed to the small influence of gas-phase heat loss in the experiment, which is not included in the calculations. Perhaps most importantly, while the calculation assumes an adiabatic downstream, in the experiments the downstream temperature is that of the ambience. This downstream heat loss reduces the flame burning rate, which in turn causes the slightly weakened flame to move to a larger radial location so that stabilization is achieved with the reduced radial velocity.

Concluding Remarks

In the present investigation we have demonstrated the usefulness of the stationary cylindrical flame for fundamental flame studies, especially when the flame is stabilized by flow divergence and hence is basically adiabatic. Since these curved flames are stretchless, the influence of curvature on the flame structure and response can be unambiguously studied. Specifically, we have shown that the downstream burning flux of such flames are unaffected by the flame curvature and hence is equal to the constant burning flux of the adiabatic freely-propagating planar flame, while the upstream burning flux exceeds it due to flow divergence. This understanding is useful to the study of the general nature of stretched flames subjected to the influence of flame curvature, especially within the context of laminar flamelets in the modeling of turbulent flames.

We have also successfully produced a nearly-cylindrical and adiabatic flame in the microgravity environment of the drop tower. While the quality of the flame still needs to be improved, the viability of the concept is nevertheless established, especially in light of the favorable agreement between the microgravity results and detailed numerical computation.

A further contribution of the present study is the possibility of determining the laminar burning velocities of combustible mixtures by using the cylindrical flame in the nearly-adiabatic regime. While microgravity experiments are fairly complex and possibly also costly in terms of their operation, the simplicity of the experimental configuration and concept renders this methodology a useful substantiating alternative to other approaches for such a determination, at least for reasonably smooth flames.

Finally, we do wish to emphasize again the difficulty in obtaining perfectly cylindrical flames without wrinkles, even with the addition of helium. If such wrinkles are inherent to the flame, as manifestations of some hydrodynamic instabilities [12], then there would exist a limitation on the quantitative accuracy in determining the flame responses such as the burning rate of practical combustion mixtures. Studies are currently underway to assess the nature of such wrinkles. Experiments will also be conducted with spherical flames; it is anticipated that the additional curvature could partially "absorb" the extent of wrinkling.

References

1. Law, C. K., *Twenty-Second Symposium (International) on Combustion*, The Combustion Institute, Pittsburgh, 1988, pp. 1381-1402.
2. Matalon, M., *Combust. Sci. Tech.* 31: 169-181 (1983).
3. Margolis, S. B., *Combust. Sci. Tech.* 22: 143-169 (1980).
4. Chao, B. H. and Law, C. K., *Combust. Sci. Tech.* 62: 211-237 (1988).
5. Eng, J. A., Zhu, D. L. and Law, C. K., "On the Structure, Stabilization, and Dual Response of Flat-Burner Flames," *Combust. Flame*, in press.
6. Spalding, D. B. and Yumlu, V. S., *Combust. Flame* 3: 553-556 (1959).
7. Ferguson, C. R. and Keck, J. C., *Combust. Flame* 34: 85-98 (1979).
8. Yamazaki, S. and Ikai, S., *Trans. Japan Soc. Mech. Engrs.* 37. 293: 121-130 (1971).
9. Tien, J. H. and Matalon, M., *Combust. Flame* 84: 238-248 (1991).
10. Kee, R. J., Grear, J. F., Smooke, M. D. and Miller, J. A., *A Fortran Program for Modeling Steady Laminar One-Dimensional Premixed Flames*, Sandia National Laboratories Report No. SAND85-8240, 1985.
11. Egolfopoulos, F. N., Du, D. X. and Law, C. K., *Combust. Sci. Tech.* 83: 33-75 (1992).
12. McIntosh, A. C., *J. Fluid Mech.* 161: 43-75 (1985).

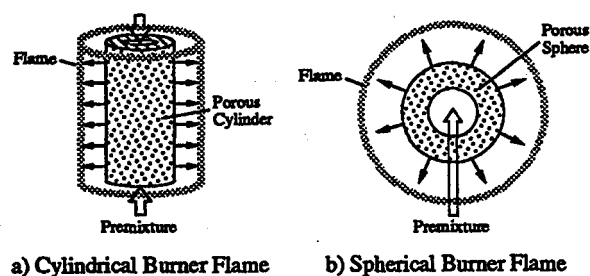


Figure 1. Configurations of (a) cylindrical, and (b) spherical flames which are curved but unstretched.

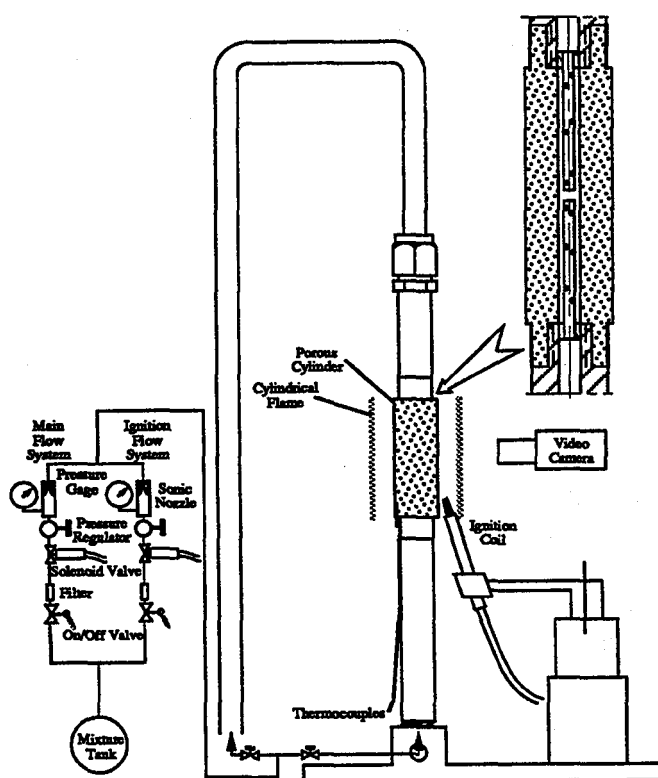


Figure 2. Schematic of the experimental apparatus. Inset is the cross-section of the cylindrical burner.

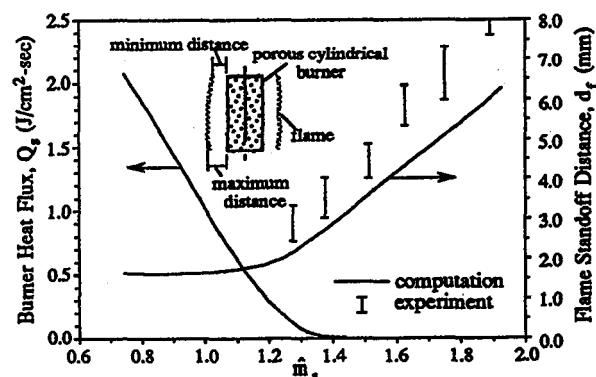


Figure 3. Computed heat loss flux and flame standoff distance, and experimental flame standoff distance, as functions of the discharge rate. Inset is a representative experimental flame configuration.

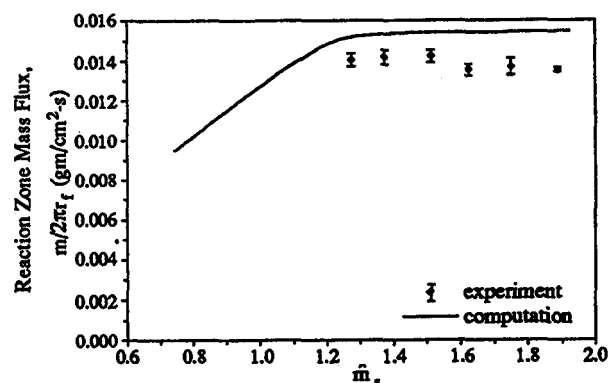


Figure 4. Computed and reaction zone mass flux as function of the discharge rate.

PREMIXED TURBULENT FLAME PROPAGATION IN MICROGRAVITY

S. Menon*, J. Jagoda** and R. Sujith***
Georgia Institute of Technology
Atlanta, Georgia

Objective and Relevance of the Study

To reduce pollutant formation there is, at present, an increased interest in employing premixed fuel/air mixture in combustion devices. It is well known that greater control over local temperature can be achieved with premixed flames and with lean premixed mixtures, significant reduction of pollutant such as NO_x can be achieved. However, an issue that is still unresolved is the predictability of the flame propagation speed in turbulent premixed mixtures, especially in lean mixtures. Although substantial progress has been made in recent years, there is still no direct verification that flame speeds in turbulent premixed flows are highly predictable in complex flow fields found in realistic combustors.

One of the problems associated with experimental verification is the difficulty in obtaining access to all scales of motion in typical high Reynolds number flows, since, such flows contain scales of motion that range from the size of the device to the smallest Kolmogorov scale. If L denotes the integral length scale, η the Kolmogorov scale, then the range of scales increase with Reynolds number ($Re_L = u' L / \nu$) by the relation $L / \eta = (Re_L)^{3/4}$. Here,

u' is the turbulence intensity and ν is the kinematic viscosity. In addition, high Reynolds number flows typically involve high velocities, large scales, high pressure or low temperature (in gases) or a combination of all four. High pressure in reacting systems is undesirable in the laboratory, especially in premixed systems while low temperature is excluded in flames by their very nature. Since, in laboratory devices, the large scales are fixed by the size of the device, a possible approach to access the micro scales in a turbulent flow field is to reduce the flow velocity. This would increase the microscale (e.g., the Kolmogorov scale) to observable size while still retaining Reynolds numbers of realistic turbulence. However, in this case, the large scale turbulent stresses responsible for momentum transport become overwhelmed by buoyancy stresses (at 1g). Since this phenomena is not present in real devices, experiments in a microgravity environment is required to allow the reduction of gravitational effects while still maintaining reasonable operating pressure, combustion temperature and observable scales at all sizes.

The overall objectives of this study is to characterize the behavior of turbulent premixed flames at reasonable high Reynolds number, Re_L . Of particular interest here is the thin flame limit where the laminar flame thickness,

$\delta_F = \alpha / S_L$ is much smaller than the Kolmogorov scale, L_K . Here, S_L is the laminar flame speed and α is the thermal diffusivity. Thin flames occur in many practical combustion devices and will be numerically studied using a recently developed new formulation (that is described briefly below).

* Associate Professor, School of Aerospace Engineering,

** Professor, School of Aerospace Engineering

***Post Doctoral Fellow, School of Aerospace Engineering

Research sponsored by NASA Lewis Research Center, Grant No. NAG 3-1610, Start Date: June 1994.

To achieve the requirements noted above, a Couette Flow configuration will be used. A Couette flow is a flow between two parallel plates moving in opposite directions at a fixed velocity U and is a classical textbook flow. This flow presents some interesting tests for computation, while being fundamentally simple. Past studies (e.g., Reichardt, 1956) have shown that in cold flows, for a Reynolds number ($Re = UH/\nu$, where H is the distance between the two plates) larger than 1800 the flow becomes turbulent. Thus, the Reynolds number needed to attain sustained turbulent flow is not too large, the mean flow speed is quite low, and therefore, only a limited range of scales needs to be resolved.

Research Approach

The present study is a combined experimental and numerical approach. The experimental effort will be ground based and the use of the NASA Lewis 2.2 sec drop tower is envisioned in the third or fourth year of this research. In the following, the experimental and numerical approaches are briefly discussed.

Experimental Approach

The experimental device currently under construction is designed to be consistent with the dimensions of the frame used in drop tower experiments. Thus, compared to some of the earlier experimental devices (e.g., Reichardt, 1956; Aydin and Leutheusser, 1987; Tillmark and Alfredsson, 1992), the current configuration is relatively smaller. To resolve all the measurement issues in this new facility, the first phase of the experiments focuses on cold flow, to be followed later by reacting flows. Therefore, the device under construction is designed only for cold flow. Figure 1 shows a schematic of the experimental setup. The Couette flow channel is made of infinite-belt type, where both walls move at the same speed, but in opposite directions. The belt is made of Mylar, which is a transparent plastic, so as to allow optical access to the channel for diagnostics. The belt is 0.1 mm thick and 305 mm wide and is supported and driven by two solid Aluminum cylinders, 76 mm in diameter. A DC motor is used to drive one of the cylinder while the other cylinder has adjustments available to adjust the tension of the belt. In order to minimize the flutter of the belt, it is supported by 10 mm thick glass plates on either side. The belt speed is determined using a proximity switch that measures the rpm of the driving shaft. To study a range of Reynolds numbers, both the belt speed and the belt spacing can be varied. A maximum belt speed of 2 m/s is possible with the current configuration and the belt spacing H which is controlled by two steel guide rollers on each side and 25 mm in diameter, can be varied from 10 mm to a maximum of 76 mm. Thus, a range of Reynolds number upto a maximum of around 10,000 can be achieved in the present facility which has a test section 381 mm long where measurements can be made.

The entire Couette flow set-up is enclosed in a glass box whose dimensions are 889 mm x 737 mm x 356 mm, and 10 mm thick. Thus, optical access is possible from the side and top directions and the dimensions of the box are designed to be larger than that of the belt assembly, in order to provide a stagnation chamber at both ends (and, in which the rotating cylinders reside) larger than the size of the test section. A similar arrangement was used in an earlier study (Tillmark and Alfredsson, 1992) where it was shown that this approach reduces reflection from the rotating cylinders and thus, a sustained Couette flow can be achieved for a relatively long time.

For reacting flows (to be studied later) we are primarily interested in fuel-air gas mixtures such as hydrogen-air/oxygen and methane-air. Therefore, to mimic such mixtures in the present cold flow facility, non-reactive gas mixtures such as air and Helium-air/oxygen will be studied.

The mean and fluctuating velocities and the Reynolds stresses will be measured in this facility. In addition, two-point spatial correlations will be obtained for a variety of Reynolds number. The Reynolds number will be varied by changing both the belt speed and the belt spacing to characterize the turbulence in this facility. The velocity measurements in the Couette channel will be made using laser Doppler Velocimeter (LDV). A 5 watt two-component Argon-ion TSI LDV system operating at 488 nm and 514.5 nm wavelengths will be used. At the beam crossing, there is an elliptical probe volume of diameter 0.07 mm and length 0.5 mm with the fringe spaced at 1.8 microns. Therefore, it is estimated that a spatial resolution of the order of 1 mm can be attained. The entire Couette flow assembly will be mounted on a three axis translation table to enable measurements over a three dimensional grid of points.

For the reacting case (to be studied later), an issue of significant interest is the structure and propagation speed of the flame front. However, this issue cannot be addressed in the cold flow facility. Another interesting phenomena of considerable interest is the turbulent diffusion of a passive specie in the present configuration since there is no data available. Therefore, we plan to take advantage of the cold flow facility to address this phenomenon by using planar laser-induced fluorescence (PLIF). Acetone has been found to be a suitable tracer for concentration measurements using PLIF in gaseous flows (Lozano et al., 1992). Acetone absorbs over a broad band of wavelengths (225-320 nm) with a maximum between 270 and 280 nm. The fluorescence emission is broadband in the blue (350-550 nm) with peaks at 445 nm and 480 nm. Acetone is nontoxic and is economical and therefore, is an ideal choice for seeding in this case. A tunable Lambda Physik excimer laser will be used as the light source for this study. Planar images of the diffusion front will be acquired using a Kodak Ektapro 1012 intensified, digital, high speed video system. The camera has a resolution of 239 x 192 pixels, and a framing rate of 1000 Hz while acquiring full images; however, a framing rate as high as 12,000 Hz can be obtained by reducing the frame size proportionately.

The images obtained in this study will be used to provide qualitative information about turbulent diffusion of a passive scalar in the Couette flow environment.

Computational Approach

Computational modeling of the experimental facility will be carried out in parallel to the experimental study. In fact, computational results for the reacting flow case will be obtained prior to the construction of the hot flow facility to address issues regarding the measurement requirements. Since the flow of interest is unsteady, time-accurate simulations are required. Some preliminary direct numerical simulations (DNS) of cold flows are underway; however, for reacting flows DNS is impractical and therefore, methodology based on large-eddy simulations (LES) is being developed. In LES, all scales larger than the grid resolution are resolved in a space- and time-accurate manner while the small scales are modeled by subgrid models. For the momentum transport, it is well known that the small scales typically provide a dissipative mechanism for the energy transferred from the large scale motion and thus, subgrid models based on eddy-viscosity concepts have been successfully used in the past. With recent development of dynamic subgrid models (models whose coefficients adjust to the flow as a part of the solution) for the subgrid kinetic energy (Kim and Menon, 1995), the LES approach is capable of handling the momentum and large-scale energy transport reasonably well. However, for reacting flows, this approach is not possible because (i) combustion occurs at the small scales (that are not resolved), (ii) the nonlinear production/destruction terms due to finite-rate kinetics are difficult, if not impossible to model, and, (iii) inclusion of full kinetics prohibitively increases the computational cost of the simulations.

To circumvent these problems, a LES modeling approach has been developed that removes all these limitations. For premixed combustion, in the thin flame limit (appropriate for the present study), a model equation for the propagating flame front can be used in which the local flame speed u_F explicitly appears. If the local flame speed is known, a progress variable G can be defined that is governed by the equation (Kerstein et al., 1988; Menon and Jou, 1991): $\partial G / \partial t + \vec{u} \cdot \nabla G = -u_F |\nabla G|$, where \vec{u} is the fluid velocity. This equation describes the convection of the flame by the local fluid velocity and the flame propagation into the unburnt mixture through a Huygens type mechanism, $u_F |\nabla G|$. Here, by definition, $G = 1$ corresponds to the premixed fuel, $G = 0$ corresponds to the fully burnt state, and the flame is located at prescribed $G = G_o$ level surface, where $0 < G_o < 1$. For laminar flows, the local speed u_F is the laminar flame speed S_L which contains all the information on the chemical kinetics and molecular dissipative mechanism. Thus, this approach avoids the cost of simulating multiple species conservation equations since all the kinetics information is implicit in the specification of the laminar flame speed. However, for turbulent flows, the flame speed u_F is the local turbulent flame speed u_T which is known to be a function of the local turbulence intensity u' and S_L . Various models (e.g., Yakhot, 1989) have been proposed; however, the exact relation is a matter of considerable uncertainty. In conventional LES, implementation of the turbulent flame speed

model such as the one proposed by Yakhot (1989) requires explicit knowledge of the subgrid turbulence kinetic energy. This approach has been successfully employed in past studies by using a one-equation model for the subgrid kinetic energy to close both the subgrid stresses in the momentum equation and to obtain a local estimate of the turbulent flame speed.

However, the conventional approach is subject to the same limitations as subgrid closures for other molecular properties and furthermore, the determination of a general functional relationship between the turbulent and laminar flame speed which is valid for all types of fuels and flow conditions appears to be difficult. Therefore, in this study, a new formulation (described in more details in Menon et al., 1993, 1994) will be employed that no longer requires a specification of the turbulent flame speed and in fact, allows a direct estimation of the local turbulent flame speed. Thus, this approach can be used to examine models developed in the past. The basic approach is to carry out the combustion process within the subgrid scales while the large-scale features (as resolved by the LES equations) are computed as in conventional LES. The key feature of the new approach is the separate treatment of the three primary physical processes within the small scales: (i) local laminar flame propagation of the thin flamelets, (ii) turbulent wrinkling of the flame front due to the local small-scale turbulence, and, (iii) thermal expansion due to heat release. To maintain and resolve the distinction between all relevant small scales, the evolution of the scalar field is simulated in one (linear) spatial dimension which represents a characteristic statistical state of the scalar field within each LES cell. This linear dimension can be considered as a time varying space curve aligned with the local subgrid scalar gradient (e.g., Kerstein, 1990; Menon et al., 1994).

The large-scale LES computed processes are coupled to the subgrid combustion processes by two mechanisms. The first mechanism which involves the transport of the subgrid scalar field across the LES cell boundaries as prescribed by the large-scale resolved velocity field is implemented by convective transport mechanism. The second mechanism which involves the transfer of the effect of subgrid processes (heat release and thermal expansion) onto the large-scale momentum and energy transport is implemented by obtaining the cell-averaged properties (from the subgrid scalar field) and then utilizing this information to update the LES resolved density and temperature fields. Detailed description of this methodology is given elsewhere and omitted here for brevity (Menon et al., 1994).

The key feature of this approach is that since the flamelets are allowed to propagate using the local laminar flame speed while simultaneously undergoing wrinkling due to local turbulence, no closure of the production/destruction term is required and furthermore, locally within each LES cell, the local flame speed is S_L (which is well known given the fuel-air mixture) is used. In addition, the local subgrid processes within each LES cell can be used to estimate the effective local (turbulent) flame speed. Thus, given the turbulence intensity (from the experimental data) and the laminar flame speed (known for a given fuel-air mixture), it will be possible to determine the turbulent flame speed from the simulation. Furthermore, new information on the local geometrical structure of the flame front (e.g., the local flame curvature) can be determined from the simulation data.

Progress to Date

This project started in June 1994 and since then, the design of the cold flow test facility has been completed and the construction of the facility is well underway. The schematic of this facility is shown in Figure 1. The facility is expected to be completed by the end of April 1995. The data acquisition and the LDV systems have been set up and it is expected that preliminary results will become available by July 1995.

The numerical methodology is currently under validation studies. For this purpose, both DNS and LES are being carried out for a configuration for which data is available from other studies (e.g., Kristoffen et al., 1993; Aydin and Leutheusser, 1987). Preliminary cold flow results for the mean velocity profile, obtained using a constant-coefficient and a dynamic subgrid model for the subgrid kinetic energy is shown in Figure 2, along with earlier experimental and numerical data. The results show that the present scheme (which is based on a second-order time-accurate and fourth-order spatially accurate finite volume MacCormack scheme) is capable of resolving mean motion. Further validation of the LES methodology will be carried out before studying the flow field similar to the current experimental setup. The subgrid combustion model is currently being validated (under a ONR sponsored project) and is expected to be available soon.

Future Work Plan

The current work plan envisions detailed validation of the cold flow facility within the next few months by obtaining detailed turbulence data for a range of Reynolds numbers. Subsequently, the study of diffusion of a passive scalar will be investigated using acetone seeding. The turbulence data will be used to initialize the LES code and numerical simulations will be carried out for cold flows. Once the baseline LES code is validated for the present test configuration, the LES model will be extended to study thin flame combustion using both the conventional approach (using the turbulence flame speed model) and the new subgrid combustion approach. Preliminary numerical simulations should provide information on the behavior of the propagating flame front. Note that, for the reacting flow experiments it is going to be quite difficult to characterize the flame front shape. Therefore, given the turbulence intensity data from the experiments, it is hoped that the LES data will be able to characterize the turbulent flame front shape.

References

- Aydin, E. M., and Leutheusser, H. J. (1987), "Experimental Investigation of Turbulent Plane-Couette Flow," ASME Forum on Turbulent Flows, FED Vol. 51, pp. 51-54.
- Kerstein, A. R., Ashurst, W. T., and Williams, F. A. (1988) "Field Equation for Interface Propagation in an Unsteady Homogeneous Flow Field," Phys. Rev. A, Vol. 37, pp. 2728-2731.
- Kerstein, A. R. (1990) "Linear-Eddy Modeling of Turbulent Transport. III: Mixing and Differential Molecular Diffusion in Round Jets," J. Fluid Mech., Vol. 216, pp. 411-425.
- Kim, W. W., and Menon, S. (1995) "A New Dynamic One-Equation Subgrid Model for Large-Eddy Simulations," AIAA Paper 95-0356, 31st Aerospace Sciences Meeting.
- Kristoffen, R., Bech, K. H., and Andersson, H. I., (1993), "Numerical Study of Turbulent Couette Flow at Low Reynolds Number," Appl. Sci. Res., Vol. 51, pp. 337-343.
- Loxano, A., Yip, B., and Hanson, R. K. (1992), "Acetone: A Tracer for Concentration Measurements in Gaseous Flows by Planar Laser-Induced Fluorescence," Experiments in Fluids, Vol. 13, pp. 369-376.
- Menon, S., and Jou, W.-H. (1991) "Large-Eddy Simulations of Combustion Instability in an Axisymmetric Ramjet Combustor," Comb. Sci. and Tech., Vol., 75, pp. 53-72.
- Menon, S., McMurtry, P. A., and Kerstein, A. R. (1993) "A Linear Eddy Subgrid Model for Turbulent Combustion: Application to Premixed Combustion," AIAA Paper 93-0107.
- Menon, S., McMurtry, P. A., and Kerstein, A. R. (1994) "A Linear-Eddy Mixing Model for LES of Turbulent Combustion," in Large-Eddy Simulations of Complex Engineering and Geophysical Flows, eds. S. A. Orszag and B. Galperin, Cambridge University Press.
- Reichardt, H. (1956), "Ueber die Geschwindigkeitsverteilung in einer geradilinen Turbulenten Couettestroemeung," ZAMM, Sonderneft, pp. 526-529.
- Robertson, J. M., and Johnson, H. F. (1970), "Turbulence Structure in Plane Couette Flow," J. Eng. Mech., Proc. of Am. Soc. of Civil Engg., Vol. 6, pp. 1171-1182.
- Tillmark, N., and Alfredsson, P. H. (1993), "Turbulence in Plane Couette Flow," Appl. Sci. Res., Vol. 51, pp. 237-241.
- Yakhot, V. (1989) "Propagation Velocity of Premixed Turbulent Flame," Comb. Sci. and Tech., Vol. 60, pp. 191-214.

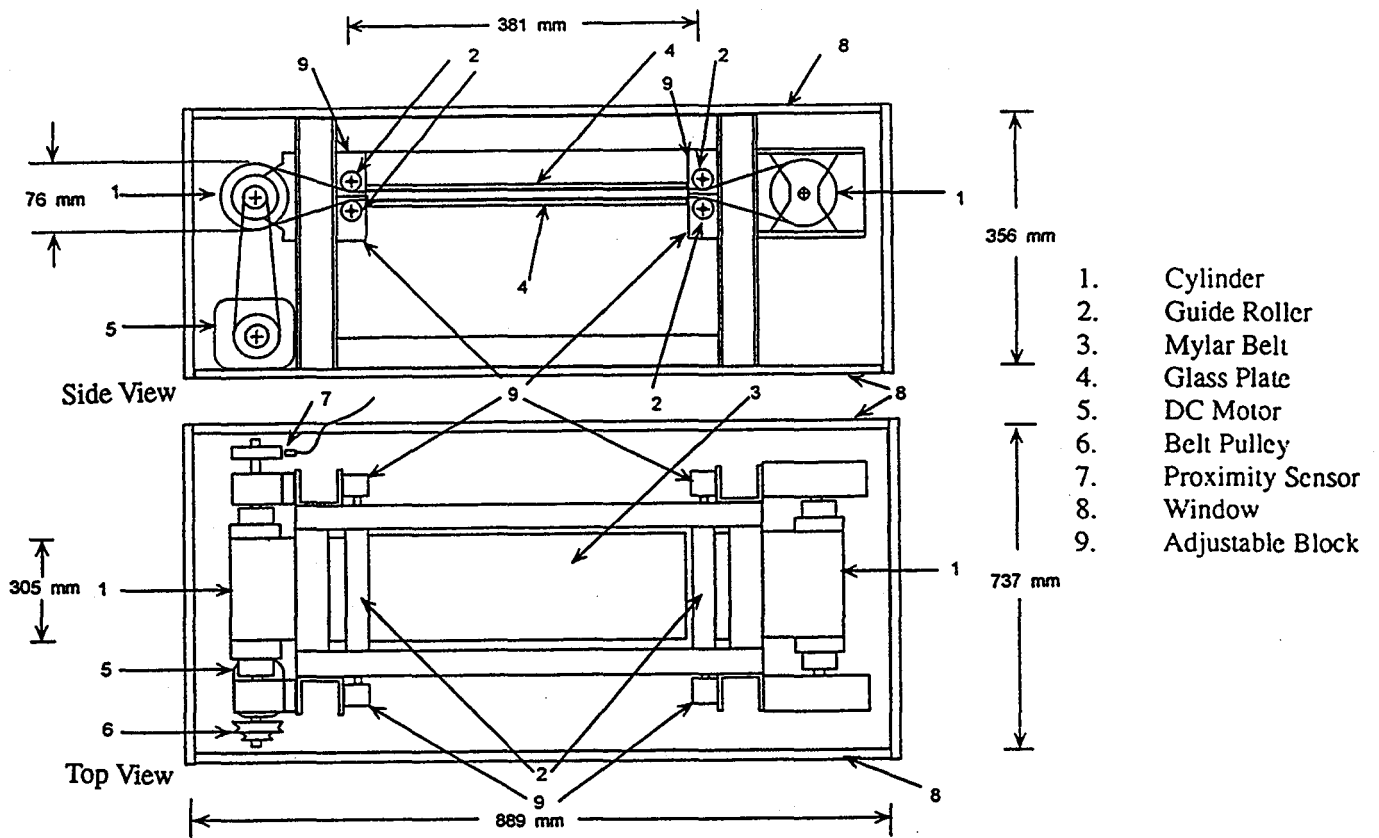


Figure 1. Schematic of the Couette Flow Experimental Set-up.

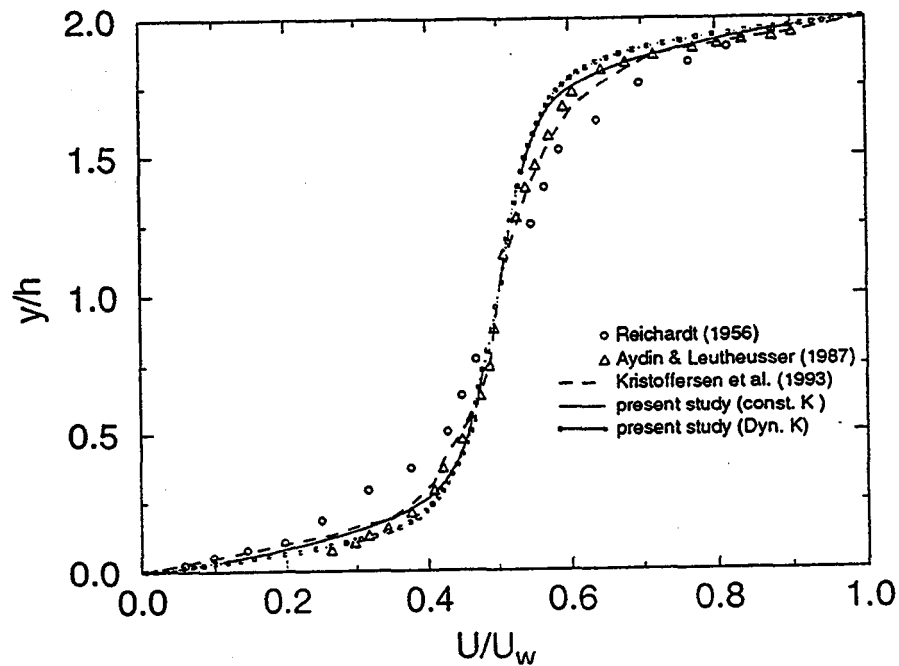


Figure 2. Turbulent mean velocity profile predicted by the present LES code using constant coefficient (Const. K) and dynamic model (Dyn. K) for the subgrid turbulent kinetic energy. Experimental data (Aydin and Leutheusser, 1987; Reichardt, 1956) and numerical study (Kristoffen et al., 1993) are also show for comparison. Test case for $H = 0.026m$ and $Re_H = 5200$ simulated using a grid resolution $48 \times 64 \times 32$.

JAPAN'S RESEARCH ON GASEOUS FLAMES

Takashi Niioka

Institute of Fluid Science, Tohoku University
2-1-1 Katahira, Aoba-ku, Sendai 980-77, JAPAN

Introduction

Although research studies on gaseous flames in microgravity in Japan have not been one-sided, they have been limited, for the most part, to comparatively fundamental studies. At present it is only possible to achieve a microgravity field by the use of drop towers, as far as gaseous flames are concerned.

Compared with experiments on droplets, including droplet arrays, which have been vigorously performed in Japan, studies on gaseous flames have just begun. Experiments on ignition of gaseous fuel, flammability limits, flame stability, effect of magnetic field on flames, and carbon formation from gaseous flames are currently being carried out in microgravity. Seven subjects related to these topics are introduced and discussed herein.

Ignition of Gaseous Fuel (PI : M. Kono)

A methane- or hydrogen-air mixture in a cylindrical vessel with a diameter of 60 mm and a length of 16 mm was ignited by a heated metal wire, 100 μm in diameter, the temperature of which was measured by an optical pyrometer[1]. Since yields of the upward flow are due to the buoyancy before ignition in normal gravity, ignition times should increase in comparison with ignition times in microgravity. A numerical approach was also conducted for microgravity conditions.

Ignition delays due to the use of a tungsten wire for the stoichiometric methane-oxygen mixture are plotted in Fig.1, showing that ignition delays in normal gravity are quite scattered and longer than those in microgravity. For the methane-air mixture, however, there are no differences between normal gravity and microgravity. Numerical calculation showed that the ignition point in methane-oxygen is some distance from the hot wire, while ignition in methane-air occurs near the wire. This means that the buoyancy effect is stronger in the case of methane-oxygen.

Figure 2 shows the temperature histories of platinum wire for the hydrogen-air mixture. In the case of the equivalence ratio $\phi = 0.3$, there are abundant oxygen molecules around the wire, and so ignition times are shorter than those for $\phi = 1$ and the discrepancy between normal gravity and microgravity is not recognized. In the case of $\phi = 1$, however, the effect of the natural convection which supplies oxygen to the wire surface and promotes the surface reaction is quite large. Therefore, ignition takes place faster in this case.

Burning Velocity (PI : S. Okajima)

To measure the flammability limits and the burning velocities near the limits, a

closed cylindrical vessel with a diameter of 116 mm and a length of 120 mm was installed in a freely falling chamber [2,3]. The burning velocities were obtained from schlieren streak photographs.

Figure 3 shows the burning velocities plotted against the equivalence ratio for methane and propane. The burning velocities were compared with those obtained by other methods, and it was concluded that the burning velocities in this experiment agreed well with those obtained by the counterflow twin-flame method [4], which will be explained in the next section.

By use of the same apparatus, cellular flames were also observed for methane and propane [5]. The authors concluded that there was an equivalence ratio which indicated the maximum probability of the appearance of a cellular flame, and that the cell structure of both fuels became fine as the initial pressure in the vessel increased.

Flammability Limit (PI: T. Niioka)

The objective of this experiment was to obtain the flammability limit and to observe the flame behavior near the limit by use of the technique of counterflow twin premixed flames, because flames in extremely low velocity fields can be stabilized in microgravity, as shown in Fig.4.

Usually, keeping the concentration constant, the counterflow velocity is increased and extinction is observed. Here, fuel concentration was decreased according to a computer-programmed control, keeping the low flow velocity constant. The most difficult point in the study of this very low speed flow is whether the flame is followed by slight flow control. Figure 5 shows that there was little difference between the equivalence ratio controlled arbitrarily and the flame interval.

Figure 6 is a plot of the equivalence ratio and the distance between twin flames versus time. In the case of methane, the twin flames approached monotonously and were extinguished after they becoming united. This proved to be true as expected. In the case of propane, however, twin flames were united and extinguished as well, although it was expected that extinction would occur when the flames were still separate, owing to the Lewis number effect.

Since sudden changes of the flame interval were always recognized in the case of propane, the location of the symbol (*) in Fig.6(b) was defined as the point of flammability limit. This is because, after this point, flames cannot maintain their self-propagation characteristics and only unstable flames can exist. The variation of the nominal stretch rate with the equivalence ratio at extinction showed that the flammability limit of the propane/air mixture was 0.50.

Blowoff Limit (PI: J. Sato)

The flow velocity gradient at the burner rim has a great effect on the blowoff condition of premixed flames. When the flow velocity of the mixture is small, however, the effect of buoyancy may also be significant, and so it is expected that there is a discrepancy between the case for that in normal gravity and for that in microgravity for a very lean or a very rich mixture. This experiment is now being conducted using methane as a fuel.

Diffusion Flame (PI : J. Sato)

Methane is issued from a tube with an inner diameter of 5 mm, and an airflow nozzle with a diameter of 54 mm is constructed in a concentric configuration. The thickness of the fuel burner rim is 0.1 mm to avoid the effect of turbulence at the rim. In normal gravity, flickering of the diffusion flame with a frequency of about 10 Hz was observed at a fuel velocity of 25.5 cm/s when the outer airflow is stopped.

Switching from this condition in normal gravity (Fig.7(a)) to the same condition in microgravity, the flame shape changed as shown in Fig.7(b), (c) and (d), in that order, within one second. Since air is not supplied by natural airflow convection and is transferred only by diffusion, the flame becomes weak and only blue flame exists around the burner port, as shown in Fig.7(d). It can be seen in Fig.7(d) that the diffusion flame developed below the burner port owing to the downward diffusion of methane.

In the present study, only the diffusion flame was observed, but in the next step, the turbulent flame will be observed to determine the contribution of natural convection to the turbulent diffusion flame. In addition, we plan to study the effect of air temperature on the diffusion flame.

The Effect of Magnetic Field (PI : K. Ito)

Oxygen molecules are paramagnetic, and therefore the transport of oxygen should be influenced by a magnetic field. The objectives are not only to investigate the combustion mechanism in a magnetic field but also to promote combustion, for example, by utilizing the change of the flame shape.

A butane diffusion flame was established on a circular tube with an inner diameter of 0.6 cm. The tube was made of copper so as to be independent of magnetic field. Figure 8 shows the arrangement of the burner, the flame(R) and the magnet (A), the magnetic force (H) of which had a certain distribution. Butane was chosen as the fuel.

A comparison of the flame shapes is shown in Fig. 9. Standardizing flame (A) in normal gravity and without magnetic field, totally, flames (B, C) without magnetic field changed more drastically, while flames (A', B', C') with magnetic field did not change much. Actually, it was not possible to establish a flame in microgravity (C), although it was possible to sustain a flame if the field was magnetized (C'). This means that the effect of the magnetic field on oxygen transport is very strong and that the flame shape is not greatly affected by natural convection.

Carbon Formation (PI : K. Ito)

From a circular tube with a diameter of 0.6 cm, butane was flowed out and ignited in a stagnant oxidant atmosphere. The fuel flow rate was 0.3 through 1.2 cm³/s. Figure 10 is a schematic representation of what the flame looked like from above.

Large particles of soot with a diameter of over 100 μm were formed in 50% oxygen air, which was 200 to 500 times greater than the case in normal gravity. The carbon zone is located in a ring-shaped region on the top of a spherical diffusion flame, as seen in Fig.10(b).

REFERENCES

1. Nagata, H., Kim, H.M., Sato, J. and Kono, M.: Twenty-fifth Symp. (Int.) on Combustion, (to be printed).
2. Okajima, S., Inuma, K., Kawaguchi, S. and Kumagai, S.: Twentieth Symp. (Int.) on Combustion, The Combustion Institute, pp.1951-1956(1984).
3. Okajima, S.: archivum combustionis, vol.13, pp.7-14(1993).
4. Yamaoka, I. and Tsuji, H.: Twentieth Symp. (Int.) on Combustion, The Combustion Institute, pp.1883-1892(1994).
5. Kawakami, T. and Okajima, S.: archivum combustionis, vol.13, pp.15-20(1993).
6. Wakayama, N.I.: Combustion and Flame, Vol.93, pp.207-213(1993).
7. Ito, H., Fujita, O. and Ito, K.: Combustion and Flame, Vol.99, pp.363-370 (1994).

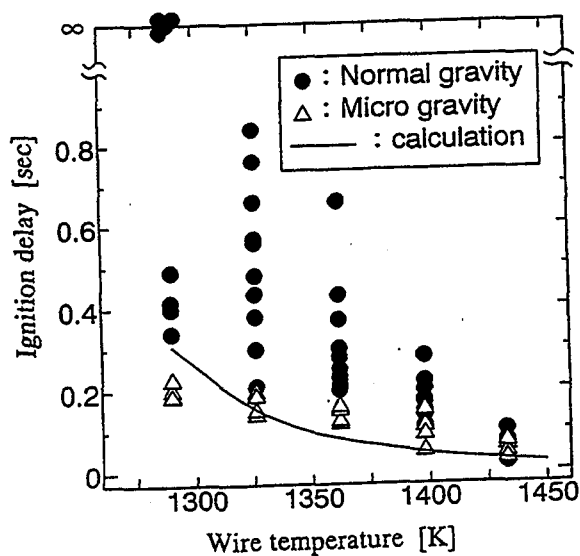


Figure 1. Comparison of ignition delay times of a stoichiometric methane-oxygen mixture in normal gravity with such times in microgravity.

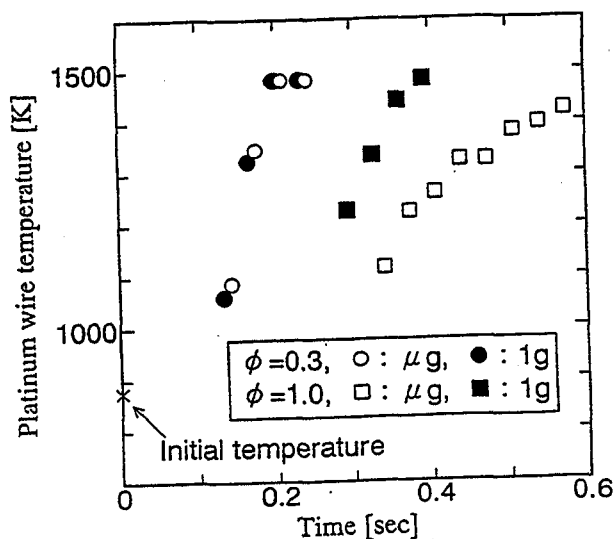


Figure 2. Histories of platinum wire temperature for a hydrogen-air mixture.

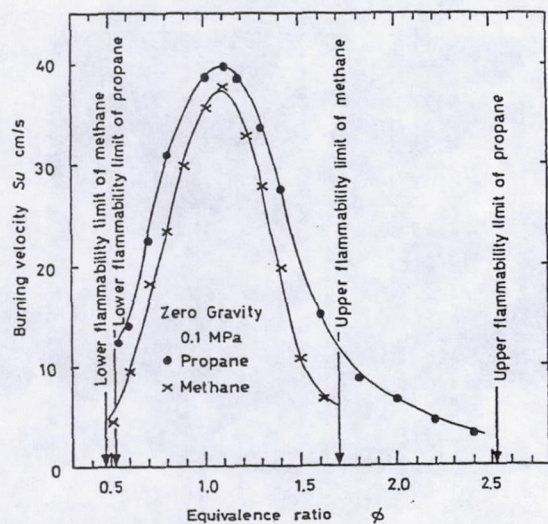


Figure 3. Burning velocities versus equivalence ratio for propane- and methane-air.

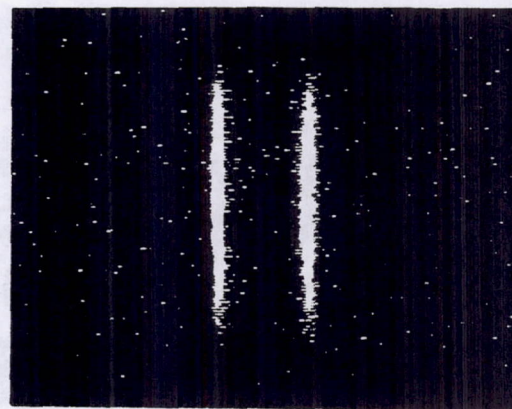


Figure 4. Direct photo of twin flames in a low velocity counterflow field in microgravity.

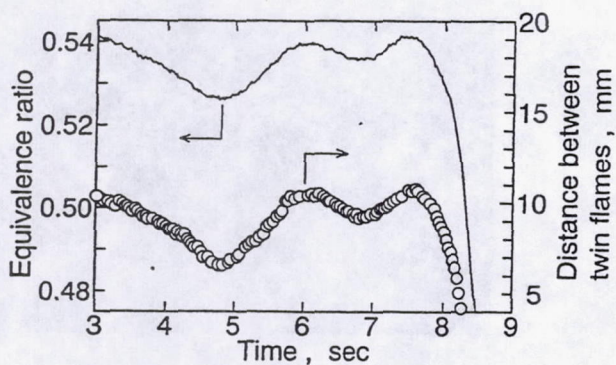


Figure 5. Variation of twin flame distance with time when the equivalence ratio was changed arbitrarily.

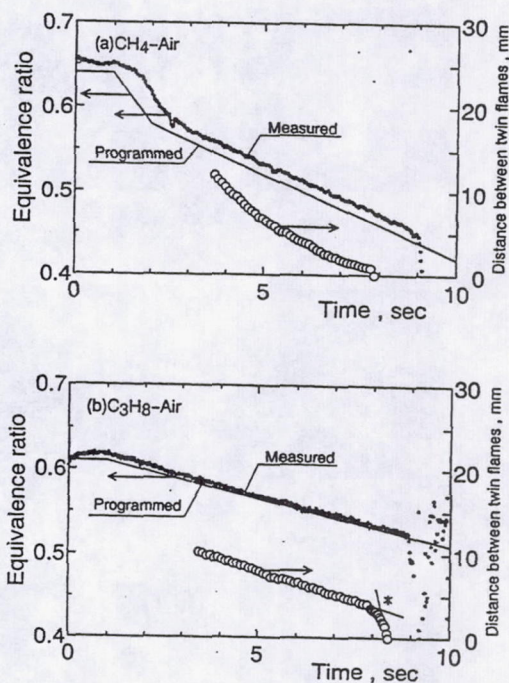


Figure 6. The variation of twin flame distance with time for methane (a) and propane (b).

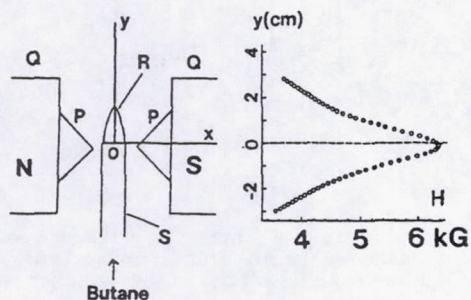


Figure 8. Arrangement of experimental apparatus for a flame in a magnetic field.

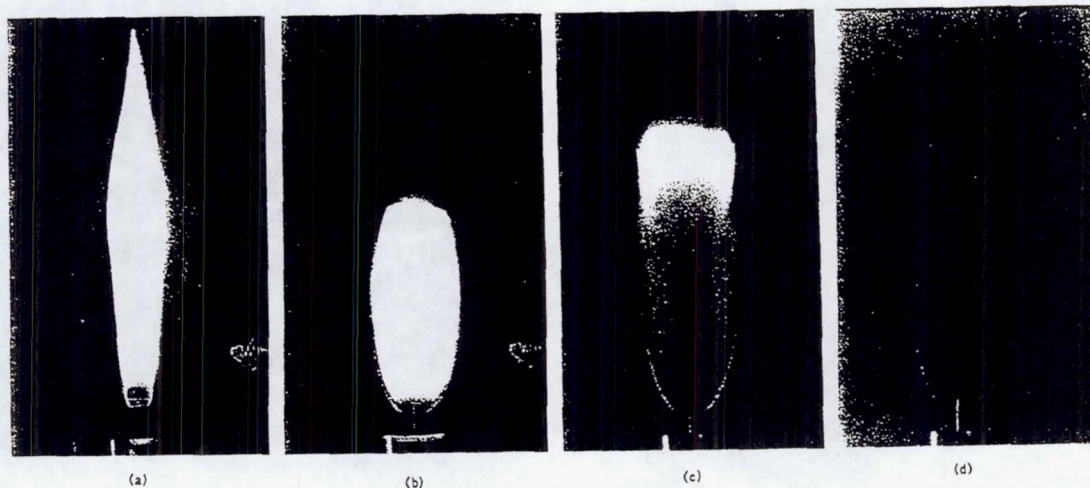


Figure 7. Diffusion flame of methane without forced convection of air. (a) in normal gravity, (b) about 0.3 sec after drop, (c) about 0.6 sec after drop, (d) about 1 sec after drop.

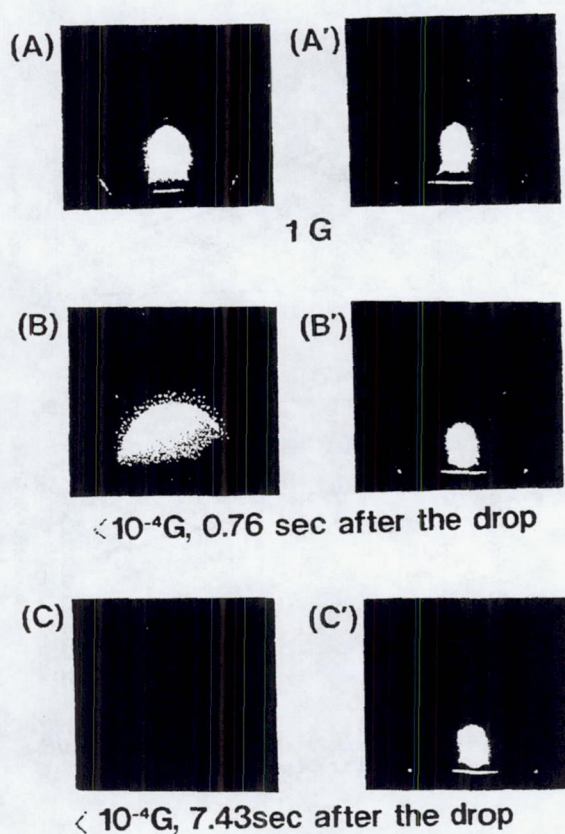


Figure 9. Flame shape changes in a magnetic field.

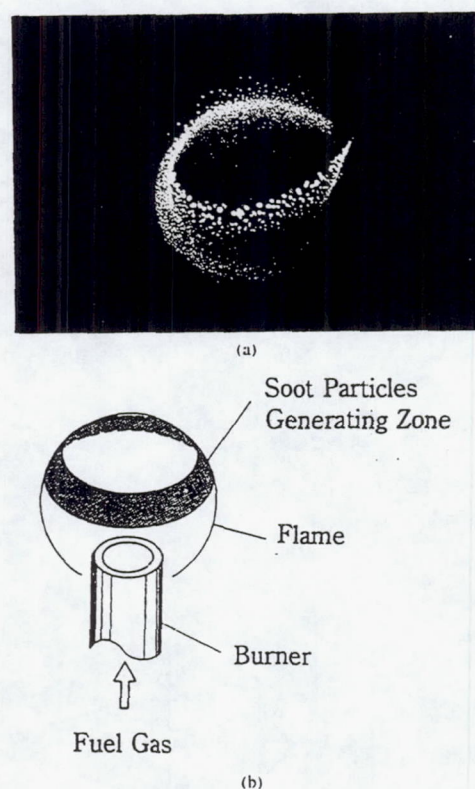


Figure 10. Picture of a flame with luminous spots taken from above the flame under microgravity (a) and schematic representation of the formation region.

Excitable Dynamics in High-Lewis Number Premixed Gas Combustion at Normal and Microgravity

Howard Pearlman
NRC Research Associate
NASA Lewis Research Center
Cleveland, Ohio

Abstract

Freely-propagating, premixed, gas flames in high-Lewis (Le) number, quiescent mixtures are studied experimentally in tubes of various diameter at normal ($1g$) and microgravity (μg). A premixture of lean butane and oxygen diluted with helium, argon, neon, nitrogen or a mixture of multiple diluents is examined such that the thermal diffusivity of the mixture (and to a lesser extent, the mass diffusivity of the rate-limiting component) is systematically varied. In effect, different diluents allow variation of the Le without changing the chemistry. The flames are recorded with high speed cinematography and their stability is visually assessed.

Different modes of propagation were observed depending on the diameter of the tubes (different conductive heat loss), the composition of the mixture and the g -level. At $1g$, four modes of propagation were observed in small and intermediate diameter tubes (large conductive heat loss): (1) steadily propagating flames, (2) radial and longitudinal pulsating flames, (3) "wavering" flames and (4) rotating spiral flames. As the diameter of the tube increases, the radial modes become more pronounced while the longitudinal modes systematically disappear. Also, multiple, simultaneous, spatially-separated "pacemaker" sites are observed in intermediate and large diameter tubes. Each site starts as a small region of high luminosity and develops into a flamelet which assumes the form of one of the forementioned modes. These flamelets eventually interact, annihilate each other in their regions of intersection and merge at their newly created free-ends. For very large tubes, radially-propagating wave-trains (believed to be "trigger waves") are observed. These are analogous to the radial pulsations observed in the smaller diameter tubes. At μg , three modes of propagation have been observed: (1) steadily propagating flames, (2) radial and longitudinal pulsating flames and (3) multi-armed, rotating flames.

Since the pulsating mode exists at μg and $1g$, buoyant flicker is not the mechanism which drives the pulsations. Moreover, all of the instabilities at $1g$ and μg have characteristic frequencies on the $O(100Hz)$. This value is lower than the fundamental, longitudinal acoustic frequencies of the tubes which suggests that the instabilities are not acoustically driven.

The patterns formed by this reaction bear remarkable similarities with the patterns formed in most excitable media when the behavior of the system is driven by couplings between chemical reaction and diffusion (e.g., Belousov-Zhabotinsky reaction, patterns in slime molds, spiral waves in the retina of a birds eye). While it is recognized that the chemical mechanism associated with this premixed gas reaction is exponentially sensitive to temperature and undoubtedly different from those which govern previously observed excitable media (most are isothermal, or weakly exothermic, liquid phase reactions), similar spatial and temporal patterns should not come as a complete surprise considering heat and mass diffusion are self-similar.

It is concluded that this premixed gas system is a definitive example of a diffusive-thermal, gas-phase oscillator based on these experimental results and their favorable comparison with theory.

1. Introduction

To verify the existence of the high- Le number diffusive-thermal instability in premixed gas combustion, μg tests were initially performed using a mixture of butane and oxygen diluted with helium ($Le=3$) in a flame tube opened at the ignition-end and closed at the other end. Based on a scale analysis, the frequency of the oscillation (ω) is expected to scale with the square of the laminar burning velocity divided by the thermal diffusivity of the mixture and the amplitude of the oscillation (δ) is expected to scale with the thermal diffusivity divided by the burning velocity. At μg , the laminar burning velocity in near-limit mixtures is not affected by buoyant convection and thus may be lower than the burning velocity at $1g$. Hence, by reducing the flame speed, ω should decrease and δ should increase, making it easier to see. This idea, originally proposed by Ronney [1], seemed plausible considering the only experimental evidence to support the existence of the high- Le number, diffusive-thermal instability [2] was complicated by complexities of heat loss to the burner and sensitivity to the local hydrodynamic field. By considering freely-propagating flames in quiescent mixtures, rather than burner-stabilized flames, the heat loss and hydrodynamic problems are eliminated. Also, at μg , buoyant convection is eliminated as a potential source of any observed instability. This was the starting point approximately two years ago.

During the past two years, we learned several new things about the high- Le number diffusive-thermal instability:

1. The instability exists at $1g$ and μg .

2. The instability manifests itself in several different forms depending on the composition of the mixture (hence, Le), the conductive heat loss to the walls, and the g-level.
3. A critical $Le_c (>1)$ exists. Below Le_c (but still >1), the flames propagate in a stable, uniform manner. Above Le_c , the flames are unstable.

These findings are described in this paper. The μg experimental apparatus and results is presented in Section 2 followed by the 1g tests on downwardly propagating flames in Section 3. A brief summary and description of work-in-progress is presented in Section 4.

2. Microgravity Apparatus and Results

Freely-propagating flames are studied experimentally at μg in the 2.2 sec drop tower at the NASA Lewis Research Center [3]. The tests are performed in a 14.3cm i.d., polycarbonate flame tube, 40.0cm in length. The tube is permanently closed at one end and initially sealed with a mylar membrane at the opposite end. A hot-wire/ nitrocellulose igniter is situated on the nonreactive side of the membrane. The resistively heated wire ignites the nitrocellulose releasing approximately 40.0J. This is sufficient to completely consume the membrane, thereby open the ignition-end to ambient conditions, and ignite the mixture. The flame shape and its evolution are recorded at 200frames/sec with a high-speed Millikan 16mm movie camera. Although higher framing rates are desirable, the visible light from the flame is insufficient to leave a trace on the film at rates greater than 250 frames/sec, even with the most sensitive film. A schematic of the drop rig is shown in Fig. 1.

The tube is filled by the partial pressure method to local atmospheric pressure, 740-750 Torr, with a mixture of C_4H_{10} - O_2 -He. A fan is installed on the closed end of the tube to mix the reactants prior to ignition. The fan is turned on during the fill procedure and it is turned off approximately five minutes prior to the drop. This is about five times longer than a characteristic viscous dissipation time (53 sec) based on the ratio of the square of the radius of the tube to the kinematic viscosity of helium at room temperature.

Careful scrutiny of the film suggests that a multi-armed, rotating wave and a radial and longitudinally pulsating flame exist as the flammability limit is approached. The characteristic temporal frequencies of both the pulsating and traveling waves are on the order of 70-100 cycles/s.

Despite the limited camera resolution, three distinct modes of propagation can be identified according to the volumetric fuel concentration in the mixture,

- (1) *Stable* propagating flames occur in mixtures containing 1.30% (or more) C_4H_{10} ,
- (2) *Rotating waves* occur in mixtures containing 1.21-1.22% C_4H_{10} , and
- (3) *Combined radial and longitudinal pulsations* occur in mixtures containing 1.21-1.25% C_4H_{10} .

Figure 2 shows an axial view of a radial and longitudinally pulsating flame. Each pulsation cycle starts with a bright, centrally-located, "pacemaker" region. This bright region radially expands and decreases in luminosity as the flame propagates axially into the reactants. As the flame nears its minimum intensity and maximum surface area (when it approaches the wall), another bright region appears at (or near) the center and the cycle repeats. Although it is not clear whether these bright zones are the flame or are traveling on the surface of a much less visible flame, the latter is presently speculated to be the case since it would otherwise be difficult to justify why the radial propagation speed (as high as 2.0m/s) is roughly ten times the axial flame propagation speed. One possible argument, proposed by Art Winfree, suggests that the phase of the oscillation may vary from one part of the flame to another where the "observed" speed is proportional to the inverse of the phase gradient. This would allow for infinitely large radial speeds.

The rotating wave (Fig. 3) observed at μg consists of six periodic, azimuthally-distributed bright and dark zones which rigidly rotate around the axis of the tube, tracing out a helical trajectory as the flame axially propagates into the reactants. While this mode appears to be unique to μg , additional tests are planned to determine whether a correlation exists between this multi-armed structure and a multi-armed, rotating spiral wave observed at 1g (discussed in Section 3).

3. Normal-Gravity Apparatus and Results

Three different internal diameter (i.d.) Plexiglas tubes (5.1, 10.2 or 14.3cm), approximately 1.2m in length, are used to study downwardly propagating flames at 1g. The bottom of the tubes is permanently closed with a Plexiglas window while the other end is initially closed with a plate connected to a solenoid. When the solenoid is activated, the plate is lifted vertically off of an o-ring seal. Similar to the μg tests, a hot wire/ trinitrocellulose igniter is situated at the open-end (top).[†]

The tube is filled by the partial pressure method or mass flow rate with a mixture of C_4H_{10} , O_2 and an inert (or inert mixture). A fan is attached to the removable end plate and used to ensure homogeneous mixing of the reactants. It is turned off approximately five minutes after the last constituent is added at which time the mixture is allowed ten minutes to quiesce prior to ignition; this waiting period is at least ten times the viscous dissipation time (53 sec).

[†] Additional tests were performed using the same tubes with a membrane and igniter at the open-end (similar to the μg tests) to eliminate the possibility of any convective flow induced by the movable end plate.

High-speed video is obtained using two Kodak EktaPro intensified video cameras each recording the flame at 1000 frames/sec. One camera is axially positioned in the middle of the tube (field of view is 20cm) while a second camera obtains a radial view from a mirror positioned at a 45° angle with respect to the base (closed-end) of the tube. The video outputs are recorded using a high-speed tape drive and then downloaded at 30 frames/sec to VHS video.

A summary of the "instabilities" is given for each tube diameter. The word "instabilities" is in quotes because it can be a misnomer; these modes of propagation are quasi-stable for most experimental conditions, except for exceptionally near-limit flames which spontaneously transition between modes.

Also, note that all of the observed "instabilities" exist within approximately 0.2 molar percent (or less) C_4H_{10} from the lean flammability limit (LFL) where the LFL's are determined experimentally to be 1.52, 1.44 and 1.29 percent C_4H_{10} in a 21% O_2 -He environment for the 5.1, 10.2 or 14.3cm i.d. tubes, respectively. Conductive heat loss apparently governs the limit in the small tubes whereas buoyant convection and radiative losses govern the limit in the larger diameter tubes.

5.1cm i.d. tube: In the smallest tube tested, four modes of propagation (Fig. 5) are observed:

- (a) stable, uniformly-propagating, axisymmetric flames in mixtures containing 1.68% C_4H_{10} (or more),
- (b) longitudinal, axisymmetric pulsations ($\omega \sim 170$ -200Hz) in mixtures containing 1.60-1.67% C_4H_{10} , and
- (c) tristable modes of propagation in mixtures containing 1.52-1.59% C_4H_{10} . The flame alternates between three modes: (1) a longitudinal pulsation (Fig. 5b), (2) a "wavering" mode, characterized by a bright spot on the flame swaying from one side of the flame to the other, tracing out a nonaxisymmetric, zig-zag path (Fig. 5c), or (3) a rotating spiral wave (Fig. 5d). While the longitudinal oscillations are easy to visualize, the "wavering" mode and spiral wave deserve some attention. By propagating in a zig-zag or spiral path, the flame can gain a foothold in the reactants without having to propagate in discrete, longitudinal steps. In this way, the flame can propagate in a spatially continuous fashion. Interestingly, many crystals grow in an analogous way [4]. The molecules escape from the solid into the surrounding vapor at a rate dependent on the surface temperature and the molecules condense on the surface at a rate proportional to the vapor concentration. At very slight supersaturations (as low as 1%), crystals grow in a spiral ramp or a series of interlaced, zig-zagging concentric rings, due to pure diffusion. Rather than counterdiffusion of a single species, counterdiffusion of heat and mass apparently induce similar spatial patterns in our premixed gas flame.

10.3cm i.d. tube Four modes are also observed in a tube with twice the i.d. (Fig. 6):

- (a) stable, uniformly propagating, axisymmetric flames in mixtures containing 1.56% C_4H_{10} (or more),
- (b) combined radial and longitudinal pulsations in mixtures containing 1.48 ± 0.01 to 1.54% C_4H_{10} (while the amplitude of the longitudinal pulsation is measurably smaller than in the 5.1cm i.d. tube),
- (c) trinary mode of propagation in mixtures containing 1.45 to 1.48 ± 0.01 % C_4H_{10} . Similar to the flames in the 5.1cm i.d. tube, the flame alternates between three modes: (1) a combined radial and longitudinal pulsation, (2) a "wavering" mode, or (3) a rotating spiral wave.

14.3cm i.d. tube Similar modes are observed in a larger diameter tube (Fig. 7a,b,c). Once again,

- (a) stable, uniformly propagating, axisymmetric flames occur in mixtures containing greater than 1.50% C_4H_{10} (or more),
- (b) radial pulsations occur in mixtures containing 1.35-1.50% C_4H_{10} , and
- (c) bistable modes of propagation occur in mixtures containing 1.29-1.35% C_4H_{10} . The flame alternates between a rotating spiral wave and a radial pulsation.

In addition, multiple, simultaneous pacemaker sites are observed at the same cross-section of the tube for these very near-limit mixtures. Each "site" develops into a radial pulsation or a rotating spiral wave (CW or CCW). Since the flames compete for the same reactants, they inevitably coalesce, annihilate one another in their regions of intersection and either merge at their free-ends or separate into flamelets which ultimately meet again. In Fig. 7d, the initiation and development of two counter-propagating radial pulsations are shown. In Fig. 7e, two co-rotating spiral waves have developed separately and then joined at their pivoting endpoints to form a two-armed rotating spiral wave.

30.5cm x 30.5cm x 153cm square duct: A few preliminary tests have been performed in a large square duct, open at the top and closed at the bottom. Mixtures containing 1.32 to 1.47% C_4H_{10} were tested, where the LFL has been determined to be 1.32% C_4H_{10} in a 21% O_2 -He environment (compare with the value of 1.29% in the 14.3 cm i.d. tube). For this range of experimental parameters, multiple, radial propagating wave-trains appear and propagate outward in a very systematic fashion. In the smaller tubes, these "wave-trains" appear as radial pulsations since the characteristic spacing between waves is on the order of the tube diameters. In other words, the radial propagating flames previously observed quench at the tube walls before another radial (concentric ring) wave develops.

These wave-trains are believed to be "trigger waves"--waves of chemical activity whose existence depends on the interaction of reaction and diffusion. They are characterized by the fact that they can be

blocked by impermeable barriers. Analogous waves have been observed in the Belousov-Zhabotinsky [5] reaction and should not be confused with kinematic waves (phase or frequency gradient waves) which are independent of diffusion [6]. Experimental evidence which supports this contention will be presented under separate cover.

4. Discussion and Work-in-Progress

To summarize the results so far, freely-propagating flames in C_4H_{10} - O_2 mixtures diluted with pure helium exhibit several different modes of propagation near the LFL. These modes have been classified according to the volumetric percent fuel in the mixture (i.e., equivalence ratio) from which the Le can be determined. Also, above a critical equivalence ratio, the flames propagate in a steady manner and do not visually display any evidence of "instability."

Preliminary tests have also been performed using four component mixtures where the fourth component is a second "inert" gas (Ne, Ar, N_2) such that the Le of the bulk mixture is systematically varied without varying the equivalence ratio. Experimentally, the percent He in the earlier mixtures is reduced and replaced with an equivalent percent of an additional inert. These results indicate that flames which are "unstable" (do not propagate in a steady manner) in a pure He-diluted mixture stabilize above a critical [He]/[diluent] ratio. This suggests that the Le of the bulk mixture must be sufficiently greater than one for onset of "instability." Stability diagrams (Le vs. conductive heat loss) are currently being constructed where the values of the mixture Le's are evaluated using CHEMKIN thermodynamic transport data as input into the Sandia multicomponent transport code.

As mentioned before, the spatio-temporal patterns formed by this premixed gas flame rival those observed in other excitable media. Both systems display rotating spiral waves and concentric ring waves. Initially, these ring waves in our premixed system appeared to be pulsations since the wavelength (spacing between rings) is on the order of the tube diameter. In addition, this premixed gas reaction displays simultaneous, multiple "pacemaker" sites which initially propagate as though they were independent entities. They eventually collide and quench in their regions of intersection, due to local depletion of the rate-limiting component (C_4H_{10}), and then continue to develop in the form of a combined entity or break-up into distorted shapes. This is representative of chemical turbulence.

Perhaps, it is also worth noting that analogous modes of propagation have been observed in solid flames [7] which also have very large Le's due to their very small mass diffusivities. Those who have studied these phenomena have seen steady flames, auto-oscillations, spinning spiral waves, and "chaotic" modes. Interestingly, the "chaotic" modes appear when points in the combustion wave move around independently of one another. These phenomena may be similar to the thermally-driven instabilities that are observed in our premixed gas flames, where the "chaotic" mode seen in the solid flames may correspond to the existence of multiple, simultaneous pacemaker sites which subsequently perform their own dynamics. Unfortunately, one cannot easily see the face of the moving front in the solid phase.

Acknowledgments

I wish to express my thanks to Dr. Howard Ross for giving me the freedom to experiment. I extend my gratitude to Dr. Paul Ronney for exciting conversations about these flames, not to mention the fact that he initially suggested looking at high-Le flames at μg . My thanks also go to Dr. David Urban who invested a great deal of time setting up and linking the CHEMKIN thermodynamic transport data and the Sandia multi-component computer code. These will be invaluable resources in future work with four or more component mixtures.

References

1. Personal communication.
2. (a) el-Hamdi, M., M. Gorman, and Robbins, K. "Deterministic chaos in laminar premixed flames: experimental classification of chaotic dynamics," *Combust. Sci. and Tech.*, **94**, 87 (1993).
(b) el-Hamdi, M., Gorman, M., and Robbins, K. "A picture book of dynamical modes of flat, laminar premixed flames," 2nd ed., personal communication (1990).
3. (a) Pearlman, H. and Ronney, P. "Near-limit behavior of high lewis number premixed flames in tubes at normal and low gravity," *Physics of Fluids*, **6** (12) 4009 (1994).
(b) Pearlman, H. and Ronney, P. "Self-organized spiral and circular waves in premixed gas flames," *J. Chem. Phys.* **101** (3), 2632 (1994).
4. Fullman, R.L. "The growth of crystals," *Scientific American*, March, 74 (1955).
5. Zaikin, A.N. and Zhabotinskii, A.M. "Concentration wave propagation in two-dimensional liquid-phase self-oscillating system," *Nature* **225**, 535 (1970).
6. Tyson, J.J. *The Belousov-Zhabotinskii Reaction*, Springer-Verlag, Berlin, Germany, 70-120 (1976).
7. (a) Merzhanov, A.G., Filonenko, A.K. and Borovinskaya, I.P. "New phenomena in combustion of condensed systems," *Proc. Acad. Sci. U.S.S.R., Phys. Chem. Sec.*, **208**, 122 (1973).
(b) Merzhanov, A.G. "Solid Flames: Discoveries, Concepts and Horizons of Cognition," *Combust. Sci. and Tech.*, **98**, 326-330 (1994).

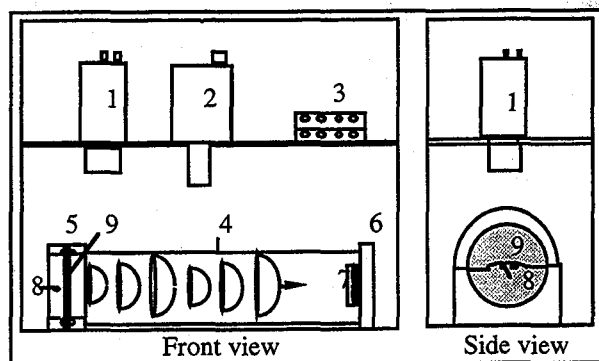


Fig. 1.- Microgravity drop apparatus (1) Standard (30 frame/sec) Video Camcorder, (2) Millikan High Speed 16mm Camera, (3) Electronics, (4) Flame Tube, (5) Ignition-End, (6) Closed End, (7) DC Fan, (8) Igniter, (9) Membrane

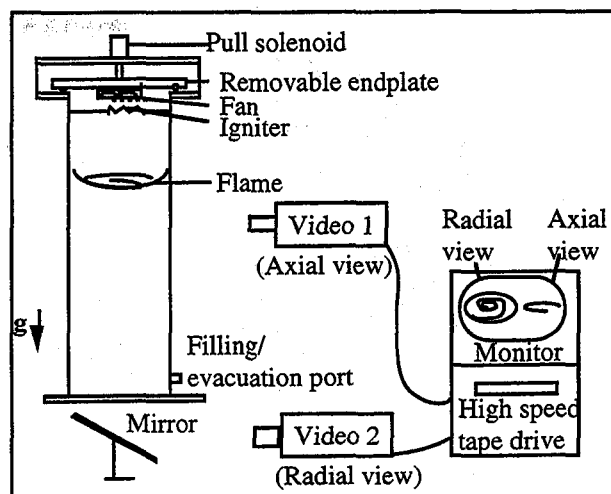


Fig.4. - Normal-Gravity Experimental Apparatus



Fig. 2: Pulsating flame at μg in 1.21% C_4H_{10} -21.0% O_2 -He. The time between sequential frames is 1/200 sec.

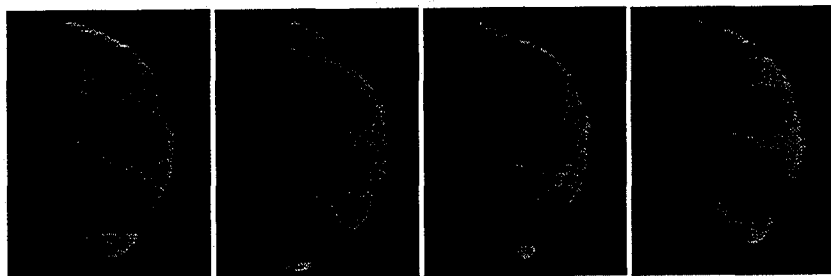


Fig. 3: Spinning propagation at μg in 1.21% C_4H_{10} -21.0% O_2 -He. The time between sequential frames is 1/200 sec.

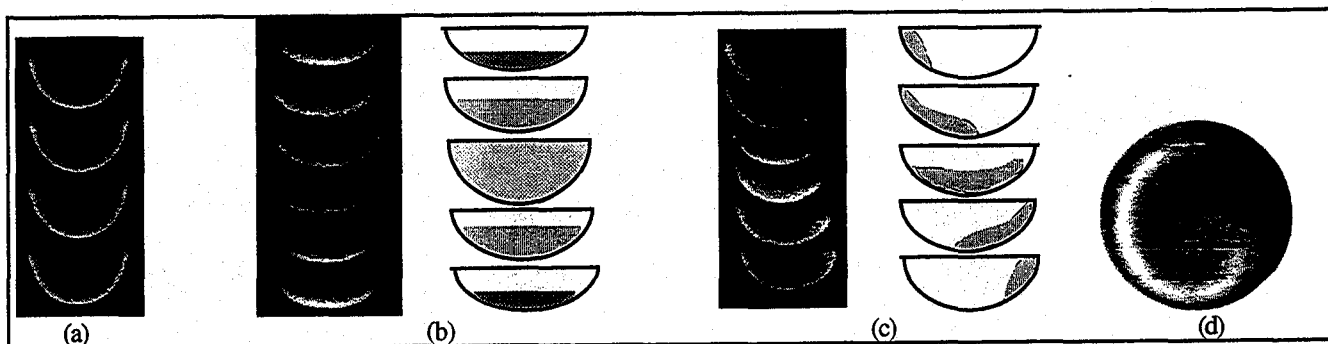


Fig. 5.- (a) stable flame in 1.69% C_4H_{10} -21% O_2 -He, (b) longitudinal oscillations in a mixture containing 1.63% C_4H_{10} -21% O_2 -He, (c) "wavering" flame in a mixture containing 1.53% C_4H_{10} -21% O_2 -He (axial view), (d) radial view of a rotating spiral wave in a mixture containing 1.53% C_4H_{10} -21% O_2 -He; the horizontal bands are due to a tracking problem with the high speed video. The time between sequential images is 1/1000s.

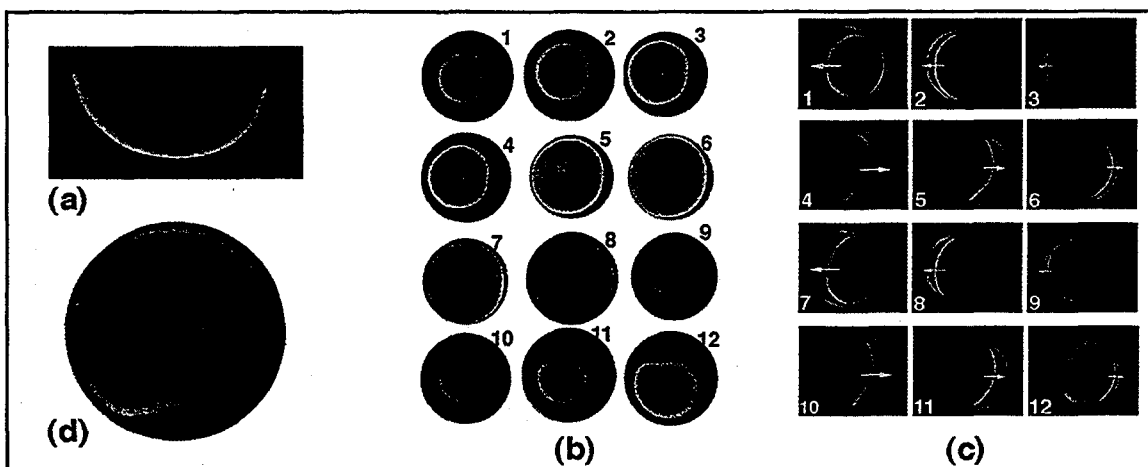


Fig. 6.- (a) stable flame in 1.56% C_4H_{10} -21% O_2 -He, (b) radial oscillations in 1.45% C_4H_{10} -21% O_2 -He (radial view), (c) "wavering" flames in 1.45% C_4H_{10} -21% O_2 -He (radial view); arrows indicate direction of propagation; axial view is similar to Fig. 5c, (d) radial view of spiral flame in 1.45% C_4H_{10} -21% O_2 -He. The time between sequential images is 1/1000s in (b) and 1/200s in (c).

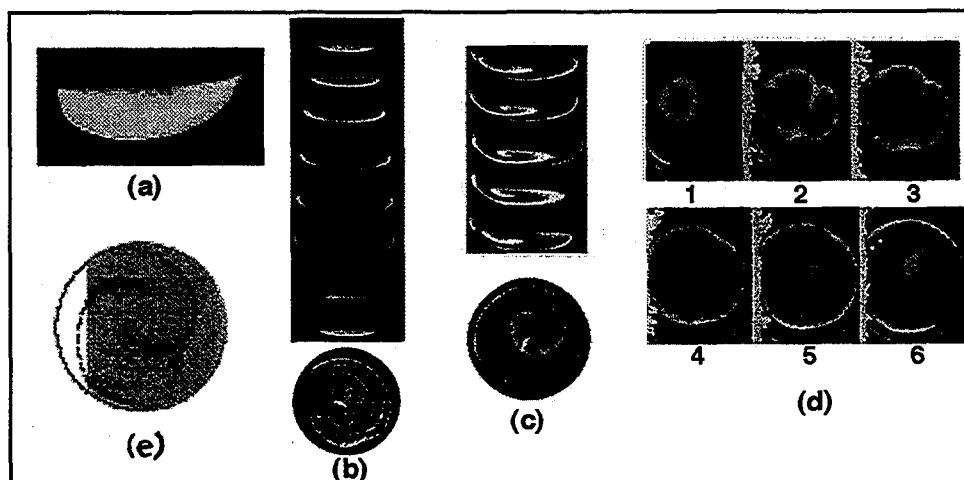


Fig. 7.- (a) stable flame in 1.50% C_4H_{10} -21% O_2 -He (axial view), (b) radial pulsations in mixture containing 1.35% C_4H_{10} -21% O_2 -He (axial and radial views), (c) spiral wave in a mixture containing 1.30% C_4H_{10} -21% O_2 -He (axial and radial views), (d) the intersection and evolution of two simultaneous, radial pulsations (radial view), (e) negative image a multi-armed rotating spiral wave (radial view). Time between sequential images is 1/1000s in (b and c) and 1/500s in (d).

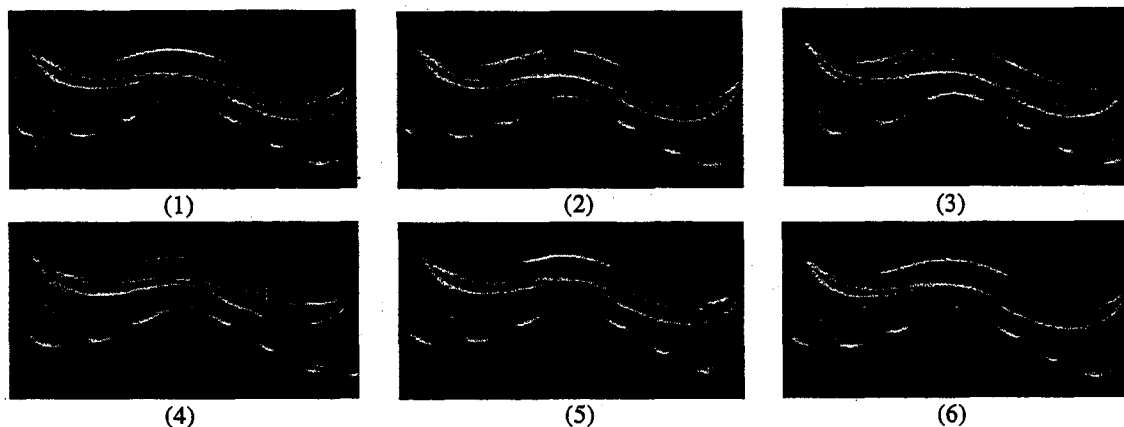


Fig.8.-Wave-trains (believed to be "trigger-waves") emanating from the center are observed in large diameter vessels. The mixture is 1.34% C_4H_{10} -21% O_2 -He. The time between sequential images is 1/1000s.

Structure of Flame Balls at Low Lewis-number (SOFBALL)

Paul D. Ronney
Department of Mechanical Engineering,
University of Southern California, Los Angeles, CA 90089-1453

Objective

The work of the PI supported by NASA Grant No. NAG3-1523, starting date 9/9/93, has encompassed several topics related to the experimental and theoretical study of combustion limits in premixed flames at microgravity. These topics include: (1) flame structure and stability at low Lewis number (which is the basis for the SOFBALL space flight experiment), (2) flame propagation and extinction in cylindrical tubes, and (3) experimental simulation of combustion processes using autocatalytic chemical reactions. Progress on each of these topics is outlined below.

Progress

1. Flame structure and stability at low Lewis number

In support of several unresolved engineering issues concerning the CM-1/SOFBALL space flight experiment, scheduled for an April 1997 launch, five weeks of low-gravity flight tests were performed on NASA's KC-135 research aircraft. A brief overview is given here.

The KC-135 flights have led to a better understanding of many aspects of flight-like hardware and operational procedures. The most important lessons learned include:

- The possibility of the etching of chamber windows during flight experiments due to corrosive combustion by-products, probably from the SF₆-diluted mixtures.
- It has not been possible to obtain agreement between calculated (based on partial pressures) and measured (by gas chromatography) gas compositions
- The radiometers work as expected, but for H₂-air mixtures their signal is too weak to resolve without some pre-amplification
- Operational confidence in the flight hardware can be significantly enhanced by checking operation of diagnostics during pump-down and filling of the chamber, along with judicious use of chamber lighting

- The Xybion cameras work well, but can be damaged by intense chamber lighting

The most significant problem found with the KC135 hardware was that the transparency of the chamber windows may deteriorate significantly, apparently due to chemical etching by the combustion products of SF₆-diluted mixtures. However, many of the mixtures tested burned more strongly than those contemplated for space flight, because problems with the KC135 gas mixing and ignition systems prevented us from burning more dilute, weaker burning mixtures. Furthermore, the accuracy of the gas mixing process makes it uncertain what the actual burned compositions were.

Concerning the gas mixing issues, the following actions were recommended: test partial pressure accuracy for lower total pressure filling, evaluate automated gas mixing system, maintain constant-temperature environment during filling and evaluate a mass-based (gravimetric) gas mixing system

A radiometer preamplifier circuit has been designed, built, and evaluated on real gaseous flames. It has been agreed to use this system on the next set of KC-135 flights in conjunction with software enabling auto-ranging of the radiometer signals. These tests are particularly important for the H₂-air flames which emit only weak (but fundamentally important) thermal radiation that is difficult to detect without preamplification of the radiometer signal.

The PI has implemented a computerized IBM-PC based image processing system for use in his laboratory. One finding to date is that many of the tests run in CM-1 KC135 tests have resulted in saturated (i.e. overexposed) images. This may indicate a need for a new criterion for determining the optimal gain setting based on visual interpretation of video images.

A Hewlett-Packard workstation for conducting flame ball modeling calculations has been delivered and configured. A one-dimensional, unsteady flame code employing detailed chemical and transport sub-models, developed by B. Rogg at Cambridge University, has been obtained and is being installed on the HP workstation. This system forms the basis of ongoing flame ball modeling calculations to be used for comparison with the SOFBALL experimental results.

Several flight PI's have considered the use of some alternative to electric sparks for flame ignition because of the potential difficulties with high voltages and electromagnetic interference. The PI had evaluated the use of heated wire sources and found them to be inadequate for some cases, particularly very lean or dilute mixtures, because of limitations on the amount of energy that could be deposition in the gas in a short period of time without melting the wire. Recently, the PI has initiated a small effort to study flame ignition by laser sources and evaluate their viability for future ground-based and space-flight based μ g experiments. The USC portion of this effort consists of one undergraduate student and is performed in collaboration with The Aerospace Corporation (El Segundo, CA), who provides the equipment and facilities along with pulsed laser expertise. To date, we have tested the minimum ignition energies of methane-air mixtures at one atmosphere initial pressure as a function of fuel-air ratio and compared these results to prior spark ignition experiments and numerical modeling (Fig. 1). The results suggest a critical

role of the size of the energy deposition region, and the potential for significantly reduced minimum ignition energies compared to classical experiments if the size of the deposition region is made small enough.

2. Flame propagation and extinction in cylindrical tubes

The emphasis of the SOFBALL project is, as the title indicates on combustible mixtures with low Lewis number. As a complement to this study, the PI has participated in a study of flame propagation at high Lewis number. The PI suggested this study to Dr. Howard Pearlman, an NRC postdoctoral research associate at NASA-Lewis. Dr. Pearlman has conducted all of the experiments, both at low gravity and at earth gravity; the PI has provided guidance and contributed to the writing of the manuscripts based on this work. Theory predicts at high Lewis number, pulsating and traveling-wave instabilities should occur. The experiments have shown, in addition to these modes, spiral-wave flame fronts (Fig. 2). None of these modes had been conclusively observed experimentally in previous works, probably because Dr. Pearlman's experiments employed more advanced diagnostics and mixtures with higher Lewis numbers than any previous work of its type.

3. Experimental simulation of combustion processes using autocatalytic chemical reactions

In prior work, in order to study the behavior of propagating flames at high turbulence levels, without the complications of density changes or heat losses, the PI introduced the use of an aqueous autocatalytic reaction, which produces propagating fronts, as a paradigm for turbulent premixed combustion. These experiments suggested that heat losses or initiation conditions are probably responsible for the observed quenching in gaseous combustion experiments. Comparison of these results to theory suggested that Yakhot's Renormalization Group (RNG) theory provides the best description of turbulent flame propagation (Fig. 3) for large Damköhler number (Da) (ratio of mean chemical reaction rate to mean turbulent strain rate). At lower Da , Damköhler's original (1940) hypothesis (not shown) fits these data well. The fractal dimensions of these fronts compare favorably with Kerstein's heuristic model. The PI and his collaborators have also developed an extension of Yakhot's model to consider the effect of turbulence scales which are smaller than the flame thickness, and find that this model provides very good predictions of the propagation rates under these conditions.

A limitation on the utility of aqueous fronts is that even the small fractional density change across the aqueous front leads to significant buoyancy influences at one-g (g_0) because of their very low S_L . Only when $u' \gg S_L$ is this limitation unimportant. Gaseous flames with $u' \gg S_L$ cannot be observed because of quenching which results from the hydrodynamic strain at high $U \equiv u'/S_L$; this makes it impossible to compare the results of aqueous and gaseous front experiments at the same U , and thereby assess the role of density changes. Quenching is not a problem in the aqueous fronts because of their high Schmidt

number (Sc) (ratio of kinematic viscosity (ν) to mass diffusivity (D)) which reduces the effect of hydrodynamic strain. High U is also inaccessible to computational studies because of numerical difficulties, especially when density changes are included. This discussion indicates the need for studying aqueous fronts at μg to eliminate buoyancy influences, enabling the study of front propagation at low U and thereby allowing comparison of front propagation in aqueous and gaseous fronts at the same u'/S_L .

An ideal flow for studying the interaction of propagating fronts with flow disturbances, and one which suffers from these buoyancy influences, is the Taylor-Couette flow in the annulus between two rotating concentric cylinders. When only the inner cylinder is rotated, pairs of counter-rotating toroidal vortex pairs (Taylor vortices) fill the annulus. To obtain these vortices, the Reynolds number $Re \equiv \omega d r_i / \nu$, where ω is the angular rotation rate of the inner cylinder, d the cylinder gap and r_i is the inner cylinder radius, must be larger than about 75. Using known properties of the Taylor vortex flow and the effect of buoyancy on the autocatalytic fronts, along with representative values for the relevant parameters, we find that to avoid buoyant convection, we require $d < 0.1$ cm at $g = g_0$ and $d < 2.0$ cm at $g = 10^{-4}g_0$. (The latter g is a typical figure in space flight experiments.)

Our scaling analysis has shown that in a space experiment, it is possible to study aqueous fronts with $U \approx 7$ at $g = 10^{-4}g_0$ without buoyant convection, whereas $U \approx 140$ is the lowest possible U at $g = g_0$ without buoyant convection. It is possible to study $U = 7$ in gas combustion without quenching, whereas $U = 140$ is not possible. Thus, space experiments would enable us to study the aqueous fronts at values of U accessible to gas combustion experiments and numerical simulations, enabling us to create a "bridge" between studies of fronts with and without substantial density changes. Consequently, the PI has proposed the Front Interaction with Vortex Experiment (FIVE) as a space shuttle glovebox experiment.

One open issue concerning the aqueous autocatalytic chemically reacting fronts is the response of these fronts to hydrodynamic strain. This response is well established for gaseous flames, and while there is no obvious reason why the same physical mechanisms would not apply to the aqueous system as well, there is no experimental proof of this suggestion. Conventional apparatuses for studying strained flames, e.g. the opposed-jet configuration, are not suitable for such experiments because of the much slower flows required in the aqueous case. Consequently, a Taylor four-roll mill, where the strain rate is determined by the rate of rotation of the rollers, has been constructed and will be employed. To avoid buoyancy-induced flow, the upper flow region will be heated electrically to a temperature a few $^{\circ}C$ above ambient. Again, laser-induced fluorescence will be used to image the fronts and determine their propagation rate.

Refereed Journal Publications

Ronney, P. D., Haslam, B. D., Rhys, N. O., "Front Propagation Rates in Randomly Stirred Media," to appear in *Physical Review Letters* (1995).

Lim, E. H., McIlroy, A., Ronney, P. D., Syage, J. A., "Detailed Characterization of Minimum Ignition Energies of Combustible Gases Using Laser Ignition Sources," to appear in: *Proceedings of the 8th International Symposium on Transport Phenomena in Combustion*, Taylor and Francis, 1995.

Haslam, B. D., Ronney, P. D., "Fractal Properties of Propagating Fronts in a Strongly Stirred Fluid," to appear in *Physics of Fluids* (1995).

Ronney, P. D., "Some Open Issues in Premixed Turbulent Combustion," to appear in *Modeling in Combustion Science* (J. D. Buckmaster and T. Takeno, Eds.), Lecture Notes In Physics Series, Springer-Verlag (1995).

Zhu, J. Y., Ronney, P. D., "Simulation of Front Propagation at Large Non-dimensional Flow Disturbance Intensities," *Combustion Science and Technology*, Vol. 100, pp. 183-201 (1994).

Pearlman, H. G., Ronney, P. D., "Near-Limit Behavior of High Lewis-Number Premixed Flames in Tubes at Normal and Low Gravity," *Physics of Fluids*, Vol. 6, pp. 4009-4018 (1994).

Pearlman, H. G., Ronney, P. D., "Self-Organized Spiral and Circular Waves in Premixed Gas Flames," *Journal of Chemical Physics*, Vol. 101, pp. 2632-2633 (1994).

Lozinski, D., Buckmaster, J. D., Ronney, P. D., "Absolute Flammability Limits and Flame Balls in Optically Thick Mixtures," *Combustion and Flame*, Vol. 97, pp. 301-316 (1994).

Ronney, P. D., Whaling, K. N., Abbud-Madrid, A., Gatto, J. L., Pisowicz, V. L., "Stationary Premixed Flames in Spherical and Cylindrical Geometries," *AIAA Journal*, Vol. 32, pp. 569-577 (1994).

Ronney, P. D., "Laser versus Conventional Ignition of Flames," *Optical Engineering* Vol. 33, pp. 510-521 (1994).

Abbud-Madrid, A., Ronney, P. D., "Premixed Flame Propagation in an Optically-Thick Gas," *AIAA Journal* Vol. 31, pp. 2179-2181 (1993).

Sloane, T. M., Ronney, P. D., "A Comparison of Ignition Phenomena Modeled with Detailed and Simplified Kinetics," *Combustion Science and Technology*, Vol. 88, pp. 1-13 (1993).

Work presented but not yet published

Wu, M.-S., Ronney, P. D., "Numerical Simulation of Flame Ball Structure and Stability," Joint Technical Meeting, Combustion Institute, Central States/Western States/Mexican Sections, April 23-26, 1995, San Antonio, TX (to be presented).

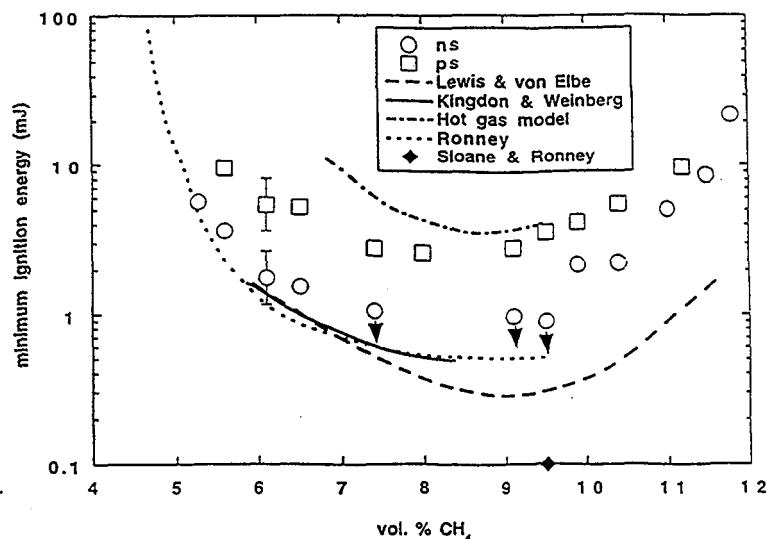


Figure 1. Measured and calculated minimum ignition energies of CH_4 -air mixtures at 1 atm. Downward pointing arrows at near-stoichiometric conditions indicate conditions for which it was not possible to form sufficiently small spark energies to observe non-ignitions. For comparison, also shown are results from electric spark ignition experiments by Lewis and von Elbe and Ronney, laser spark ignition experiments by Kingdon and Weinberg, a detailed numerical computation by Sloane and Ronney and a simple hot gas model by Syage *et al.*

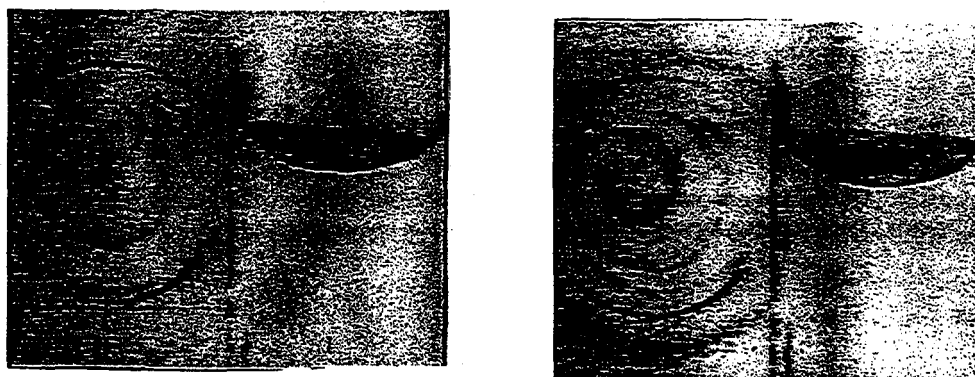


Figure 2. Images of spiral-shaped flames in a lean, near-limit C_3H_8 - O_2 -He mixture propagating down a 15 cm diameter tube. In each image pair, the left image is the axial view and the right image is the radial view. The second group of images was taken 0.004 sec after the first.

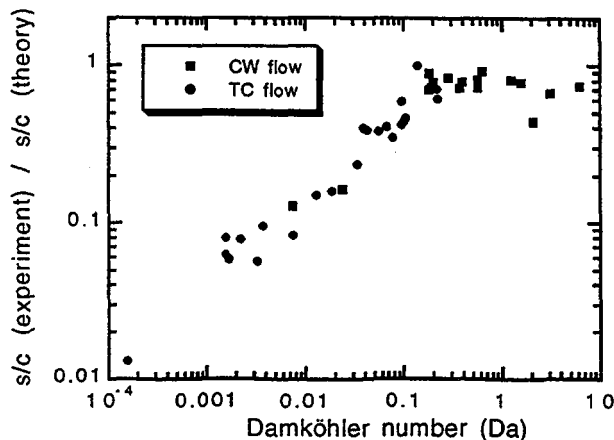


Figure 3. Comparison of measured values of turbulent front propagation rate (s) normalized by the laminar, undisturbed propagation rate (s) to the values of s/c predicted by Yakhot's renormalization group model, for fronts in a Taylor-Couette (TC) and capillary wave (CW) flow. The Damköhler number (Da) indicates the ratio of mean chemical reaction rate to mean turbulent strain rate.

NUMERICAL MODELING OF FLAME-BALLS IN FUEL-AIR MIXTURES

Mitchell D. Smooke and Alexandre Ern¹
Department of Mechanical Engineering
Yale University
New Haven, CT 06520
Start Date July 1, 1994

Introduction

For over forty years it has been known that, as a result of buoyancy, the ignition of near limit hydrogen-air mixtures can lead to the formation of flame-caps-discrete curved flames which are small on the scale of the confinement vessel [1]. More recently it has been shown that at low gravity, when buoyancy effects are small, flame-balls can be generated [2]. These are stationary spherical structures whose existence appears to require a near-limit mixture, a small Lewis number and heat losses from radiation. It is our goal to combine computational modeling with existing experimental and theoretical studies (NASA) of these structures so that an improved understanding of flammability limits and near-limit phenomena will occur. The question of flammability limits is of fundamental importance and has long been examined. It is of great practical importance to predict, from first principles, a limit mixture strength that agrees with experimental values for the configuration at hand. Flame-balls provide an excellent configuration in which convective losses can be eliminated and the resulting stable solutions are produced from a diffusive, reactive and radiative balance.

Problem Formulation

Although analytical modeling provides convincing evidence that the key physical ingredients of flame-balls have been identified, quantitative confirmation can only come from detailed numerical simulations. Our goal is to predict theoretically the mass fractions of the species and the temperature as functions of the independent coordinate r . Upon neglecting viscous effects, body forces, and the diffusion of heat due to concentration gradients, the equations governing the structure of a steady, spherically symmetric, isobaric flame-ball are

$$-\frac{1}{r^2} \frac{d}{dr} (r^2 \rho Y_k V_k) + \dot{\omega}_k W_k = 0, \quad k = 1, 2, \dots, K, \quad (1)$$

$$\frac{1}{r^2} \frac{d}{dr} \left(r^2 \lambda \frac{dT}{dr} \right) - \sum_{k=1}^K \rho Y_k V_k c_{p_k} \frac{dT}{dr} - \sum_{k=1}^K \dot{\omega}_k h_k W_k - \frac{1}{r^2} \frac{d}{dr} (r^2 q_R) = 0, \quad (2)$$

$$\rho = \frac{p \bar{W}}{RT}. \quad (3)$$

¹ Permanent address: CERMICS, ENPC, La Courtille F-93167, Noisy-le-Grand Cedex, FRANCE

In these equations r denotes the independent spatial coordinate; T , the temperature; Y_k , the mass fraction of the k^{th} species; p , the pressure; ρ , the mass density; W_k , the molecular weight of the k^{th} species; \bar{W} , the mean molecular weight of the mixture; R , the universal gas constant; λ , the thermal conductivity of the mixture; c_p , the constant pressure heat capacity of the mixture; c_{pk} , the constant pressure heat capacity of the k^{th} species; $\dot{\omega}_k$, the molar rate of production of the k^{th} species per unit volume; h_k , the specific enthalpy of the k^{th} species; q_R the radiative heat flux and V_k , the diffusion velocity of the k^{th} species.

Utilizing the kinetic theory of dilute gas mixtures, we can write the following expression for the species diffusion velocities

$$V_k = - \sum_{l=1}^K D_{kl} \nabla X_l - \theta_k \nabla \log(T), \quad (4)$$

where D_{kl} , $1 \leq k, l \leq K$, are the species diffusion coefficients and θ_k , $1 \leq k \leq K$, are the thermal diffusion coefficients. The species diffusion coefficients are symmetric and satisfy the important relations

$$\sum_{k=1}^K Y_k D_{kl} = 0, \quad 1 \leq l \leq K, \quad \sum_{k=1}^K Y_k \theta_k = 0, \quad (5)$$

which guarantee the mass conservation constraint

$$\sum_{k=1}^K Y_k V_k = 0. \quad (6)$$

Using the recent theory of iterative transport algorithms [3], rigorous kinetic theory expressions can be derived for all of the transport coefficients. In particular, the thermal conductivity, the diffusion coefficients and the thermal diffusion coefficients are obtained by solving constrained singular linear systems. These approximate expressions are accurate and computationally much more cost-effective than a direct numerical inversion of the associated linear systems. Moreover, the approximate species diffusion coefficients and thermal diffusion coefficients automatically satisfy the mass conservation constraint (6).

Since radiation plays a key role in defining the structure and stability of flame-balls, it is necessary to construct a careful estimate of the radiation term q_R . We assume that for hydrogen-air mixtures the only significant radiating species is H_2O (For methane-air systems additional terms from CO and CO_2 will be included). By utilizing an optically thin limit in which self absorption of radiation is neglected, the divergence of the net radiative flux is given by

$$\frac{1}{r^2} \frac{d}{dr} (r^2 q_R) = 4\pi \sum_i \alpha_i B_i(T) \quad (7)$$

where $B_i(T)$ is the Planck function evaluated at the band centers of the contributing vibration-rotation or pure rotational bands whose integrated intensities are given by α_i [4,5].

To complete the specification of the problem, boundary conditions are needed at both ends of the computational domain. The boundary conditions in the fresh mixture are given by

$$T(\infty) = T_f, \quad Y_k(\infty) = Y_{k,f}, \quad k = 1, 2, \dots, K. \quad (8)$$

Symmetry conditions at the origin are given by

$$\frac{dT}{dr}(0) = 0, \quad \frac{dY_k}{dr}(0) = 0, \quad k = 1, 2, \dots, K. \quad (9)$$

Finally, we point out that the chemical production rates and transport coefficients are evaluated with optimized and highly efficient libraries [3,6].

Method of Solution

The equations in (1-4,7-9) form a nonlinear two-point boundary value problem. The solution method for a single solution has been discussed in detail elsewhere and we outline only the essential features here [7,8]. Our goal is to obtain a discrete solution of the governing equations on the finite difference mesh \mathcal{M} . By replacing the continuous differential operators by finite difference expressions, the problem of finding an analytic solution of the governing equations is converted into one of finding an approximation to this solution at each point of the mesh \mathcal{M} . We seek the solution U^* of the nonlinear system of difference equations

$$F(U) = 0. \quad (10)$$

Assuming we can obtain an initial solution estimate U^0 that is sufficiently "close" to U^* , the system of equations in (10) can be solved by Newton's method. We write

$$J(U^k)(U^{k+1} - U^k) = -\lambda_k F(U^k), \quad k = 0, 1, \dots, \quad (11)$$

where U^k denotes the k^{th} solution iterate, λ_k the k^{th} damping parameter ($0 < \lambda \leq 1$) and $J(U^k) = \partial F(U^k)/\partial U$ the Jacobian matrix. A system of linear block tridiagonal equations must be solved at each iteration for corrections to the previous solution vector. As we found in the solution of burner-stabilized and freely propagating premixed laminar flames, the cost of forming (we use a numerical Jacobian) and factoring the Jacobian matrix can be a significant part of the cost of the total calculation. In such problems we apply a modified Newton method in which the Jacobian is re-evaluated periodically.

The solution of combustion problems, such as the flame-ball system, requires that the computational mesh be determined adaptively. We equidistribute the mesh \mathcal{M} on the interval $[0, \infty]$ with respect to the non-negative function W and the constant C . Specifically, we form the mesh by employing a weight function that equidistributes the difference in the components of the discrete solution and its gradient between adjacent mesh points.

In addition to the generation of a single solution for these systems, we have studied the dependence of these flames (the flammability limits) on the equivalence ratio ϕ . While the solution method discussed above can be utilized to generate a single solution, it is not effective for the computation of solutions as one approaches turning points of the system. To be able to study flames in the neighborhood of extinction, we must apply a phase-space, pseudo-arclength continuation method with Newton-like iterations and global

adaptive gridding [9-11]. The set of governing equations for the flame-ball configuration reduces to a system of the form

$$\mathcal{F}(\mathcal{X}, \phi) = 0, \quad (12)$$

where $\mathcal{X} = (T, Y_1, \dots, Y_K)$ is the solution vector. The solutions (\mathcal{X}, ϕ) in (12) form a one-dimensional manifold which, as a result of the presence of turning points, cannot be parameterized in the form $(\mathcal{X}(\phi), \phi)$. The upper part of the manifold denotes the stable solutions and the lower part the unstable ones assuming there are no Hopf bifurcations.

To generate this solution set, (\mathcal{X}, ϕ) is reparameterized into $(\mathcal{X}(s), \phi(s))$ where s is a new independent parameter and ϕ becomes an eigenvalue. The system in (12) can now be written

$$\mathcal{F}(\mathcal{X}(s), \phi(s)) = 0, \quad (13)$$

and the dependence of s on the augmented solution vector (\mathcal{X}, ϕ) is specified by an extra scalar equation

$$\mathcal{N}(\mathcal{X}(s), \phi(s), s) = 0, \quad (14)$$

which is chosen such that s approximates the arclength of the solution branch in a given phase space. Rather than solving the coupled system in (13) and (14), we replace ϕ by a function ϕ of z and we let the unknown $\mathcal{Z} = (\mathcal{X}^T, \phi)^T$ be the solution of a three-point limit value problem

$$\mathcal{H}(\mathcal{Z}, s) = \begin{bmatrix} \mathcal{F}(\mathcal{X}, \phi) \\ \frac{d\phi}{dz} \\ \mathcal{N}(\mathcal{X}(\hat{z}), \phi(\hat{z}), s) \end{bmatrix} = 0, \quad (15)$$

where \hat{z} is a given point in $[0, \infty]$. The system in (15) is solved by combining a first-order Euler predictor and a corrector step involving Newton-like iterations and adaptive gridding.

Numerical Results

During the first eight months of the project our goals have included verifying the sensitivity of the flame ball radius and the value of the lean and rich flammability limits to 1) the hydrogen-air chemistry, 2) the transport model and 3) the radiation approximation. Our previous hydrogen-air flame ball computations [12] employed a Curtiss-Hirschfelder transport approximation with a radiation model in which interpolated emissivity data was used to construct an approximation for the divergence of the radiative heat flux.

Utilizing a modified hydrogen-air reaction mechanism [13] with the transport model employed in [12], we computed flame balls as a function of the equivalence ratio ϕ . Temperature and radii results are compared with our original computations in Figures 1a and 1c. While the temperature and the size of the flame ball at the rich limit show only minor changes, there is a modest increase of the rich flammability limit with the new mechanism. Only very small changes occur on the lean side but they move in the direction of increased agreement with the experiments [12]. In Figures 1b and 1d we compare the temperature and radii as a function of the equivalence ratio for the new mechanism/old transport calculations with calculations made with the new mechanism and the transport and radiation models discussed above. Essentially no major differences were found. Nevertheless, due to its more accurate formulation, the detailed transport and band radiation models will be utilized in all future flame ball calculations.

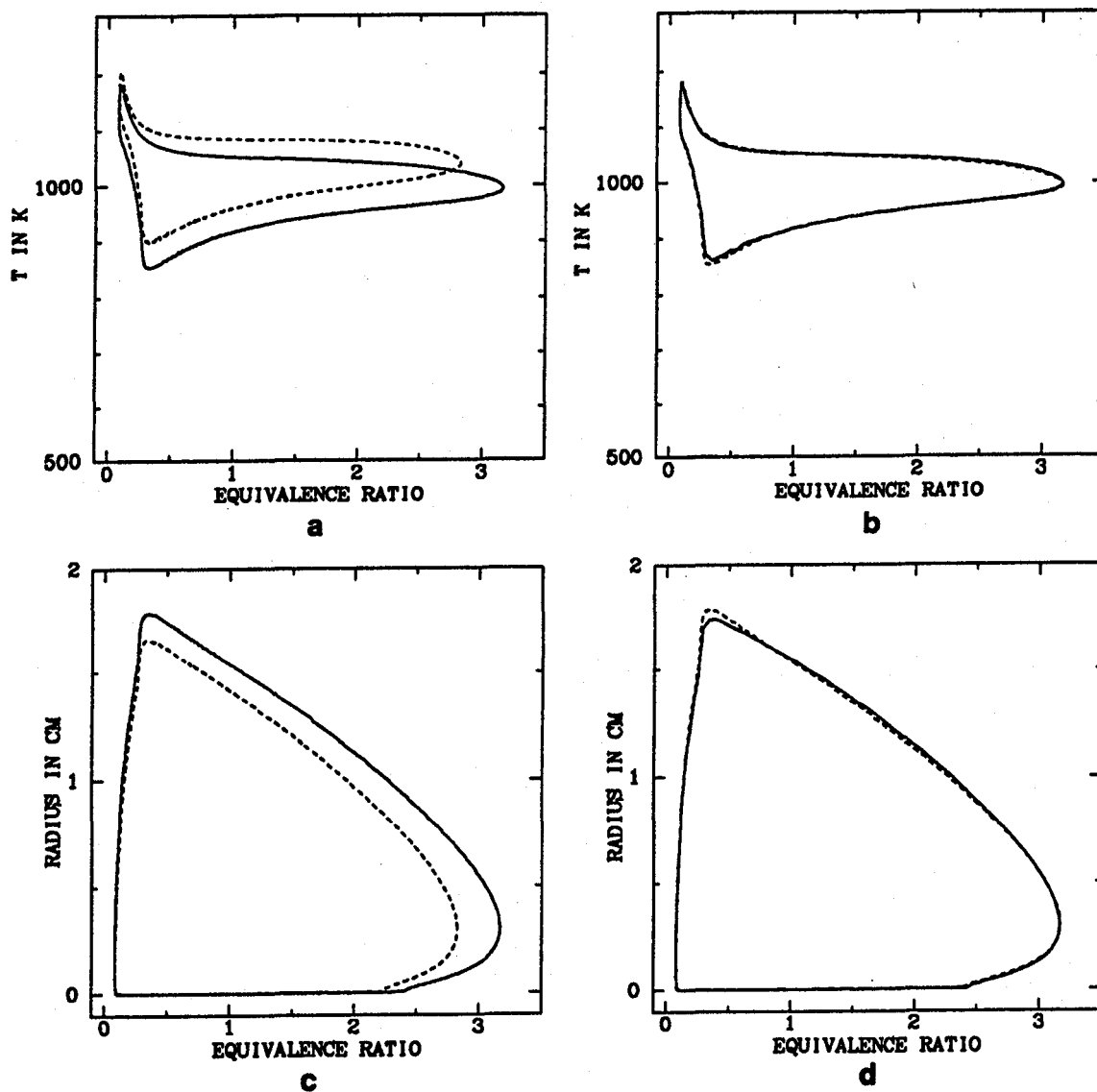


Figure 1 (a) A comparison of the temperature versus the equivalence ratio for hydrogen-air flame balls utilizing the old mechanism and old transport (dash) with computations utilizing the new mechanism and old transport (solid); (b) a comparison of the temperature versus the equivalence ratio for the new mechanism and old transport (dash) with computations utilizing the new mechanism, transport and radiation models (solid); (c) a comparison of the flame ball radius versus the equivalence ratio for the old mechanism and old transport (dash) with computations utilizing the new mechanism and old transport (solid); (d) a comparison of the flame ball radius versus the equivalence ratio for the new mechanism and old transport (dash) with computations utilizing the new mechanism transport and radiation models (solid).

References

1. Lewis, B. and von Elbe, G., *Combustion, Flames and Explosions of Gases*, Academic, New York, (1961).
2. Ronney, P., *Comb. and Flame*, **82**, (1990).
3. Ern, A. and Giovangigli, V., *Multicomponent Transport Algorithms*. New Series Monographs, Volume m 24 of Lecture Notes in Physics, Springer-Verlag, Heidelberg, (1994).
4. Hall, R. J., *J. Quant. Spec. Rad. Tran.*, **49**, (1993).
5. Hall, R. J., *J. Quant. Spec. Rad. Tran.*, **51**, (1994).
6. Giovangigli, V., and Darabiha, N.: Vector Computers and Complex Chemistry Combustion, in *Proceedings of the Conference on Mathematical Modeling in Combustion*, Lyon, France, NATO ASI Series, (1987).
7. Smooke, M. D., *J. Comp. Phys.*, **48**, (1982).
8. Smooke, M. D., Miller, J. A. and Kee, R. J., "Solution of Premixed and Counter-flow Diffusion Flame Problems by Adaptive Boundary Value Methods," in *Numerical Boundary Value ODEs*, U. M. Ascher and R. D. Russell, Eds., Birkhauser, Basel, (1985).
9. Keller, H. B.: *Numerical Solution of Bifurcation and Nonlinear Eigenvalue Problems*, in *Applications of Bifurcation Theory*, P. Rabinowitz, Ed., Academic Press, New York, (1977).
10. Giovangigli, V. and Smooke, M. D.: *Comb. Sci. and Tech.*, **53**, (1987).
11. Giovangigli, V. and Smooke, M. D.: *Applied Numerical Mathematics*, **5**, (1989).
12. Buckmaster, J., Smooke, M. D. and Giovangigli, V., *Comb. and Flame*, **94**, (1993).
13. Trees, D., Brown, T. M., Seshadri, K., Smooke, M. D., Balakrishnan, G., Pitz, R. W., Giovangigli, V. and Nandula, S. P., "The Structure of Nonpremixed Hydrogen-Air Flames," to be published *Comb. Sci. and Tech.*, (1995).

Report on German Five-Year Space Plan

Germany's Five Year Space Plan

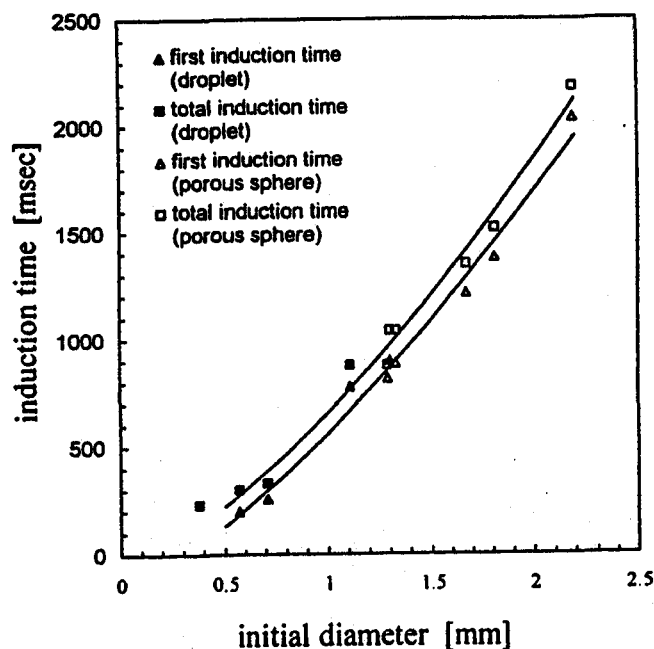
Christian Eigenbrod

Center of Applied Space Technology and Microgravity ZARM,
University of Bremen, Germany

Introduction

Up to now microgravity combustion research has mainly been a powerful tool to apply on basic research items. The absence of thermal convection and thus the ability to experimentally verify simulations supposing buoyancy-free boundary conditions were ideally suited to improve knowledge about fundamental combustion processes. Beyond reasonable doubt the necessity to perform basic experiments will still be given in future in many disciplines. But the more scientists from more and more countries enter the field of microgravity combustion research and the more facilities are built for ground-based as well as suborbital and orbital research, the more application-relevant items are requested to be investigated on. Thus, the German microgravity combustion research program tries to enhance both, fundamental as well technological aspects. The four projects described in the following are utilizing or technologically advancing ground based facilities like drop tower, drop shaft and parabolic aircrafts. Which items will be the German part of the European participation on the 'International Space-Station Alpha ISSA' has not yet been decided.

Development and Research Program On Pollutant-Reduced Combustion Systems **DROP-COS**



n-Dodecane, $P_a = 0.5$ MPa, $T_a = 700$ K, Droptower experiments

Fig. 1: Influence of initial diameter on induction times, spontaneous ignition of isolated droplets and porous spheres

In the joint national **DROP-COS** project models describing the interactions during mixture formation and ignition in two-phase combustion systems shall be developed. These models will extend existing process simulations into the area near the injection nozzles and the pre-mixing. For this purpose, institutes of terrestrial combustion research, as well as μ g-research laboratories will work together on specific questions regarding technical installations. Droplet group experiments and direct simulations will be compared with mechanisms taking place within simple plug-flow burners. Advanced laser diagnostic techniques will be applied on both, terrestrial as well as microgravity experiments.

The microgravity relevant objectives are: multidroplet- and droplet-gas phase interactions during autoignition

in high temperature/ high pressure environment based on the recent single droplet two-stage ignition investigations. To match similarities to gas-turbine and prevaporized-premixed PPM combustion experiments will be made on large droplet diameter arrangements. Figure 1 shows recent results of drop tower experiments on the comparability of fuel droplet autoignition to porous sphere autoignition. Porous spheres are indispensable for large droplet autoignition experiments. The microgravity related part of the program is in co-operation with the Japanese NEDO and Japanese research institutes. Beside the Bremen drop tower, the utilization of the Kamisunagawa drop shaft as well as parabolic aircrafts is planned.

PI: Hans J.Rath, Christian Eigenbrod, ZARM, Bremen

Co-operative partners: Norbert Peters, ITM, Aachen
Hans Kremer, LEAT, Bochum
Heiner Pfof, LDuG, Bochum
Wolfgang Triebel, IPHT, Jena

Support: German Space Agency, DARA, April 95 - March 98
Federal Ministry of Education and Science, Research and Technology,
BMBF, March 94 - Dec. 95, to be cont.

References:

1. Eigenbrod, Dinkelacker, König, Rath, "Development and Research Program on Pollutant-Reduced Combustion Systems", *Proceedings of the Drop Tower Days '94*, Bremen
2. Tanabe, Kono, Sato, König, Eigenbrod, Rath, "Effects of Natural Convection on Two Stage Ignition of an n-Dodecane Droplet", *25th. (Int.) Symp. on Comb., 1994*, Irvine

Development of a Laser-Diagnostic-System (LDS) for Drop Tower Use

The application of modern laser diagnostical measurement techniques for combustion research in earth-based laboratories has brought essential experimental progress. This project is to develop a UV-Laser-Diagnostic-System, which for the first time allows the application of two dimensional laser spectroscopic measurement techniques to microgravity research.

Two UV-excimer laser are used in an oscillator-amplifier configuration (Lambda Physik LPX 100i, LPX 200i) equipped with an external narrowband unit using a tunable Littrow grating. With this equipment high pulse repetition rates of 250 Hz can be combined with high energies up to 400 mJ per pulse and tunable narrowband properties to obtain high temporal and spectral resolution.

The laser system is mounted at the top of the tower attached to the inner evacuated drop tube. The laser beam follows the falling drop capsule and enters it from above through a quartz window. Details of the optical arrangement are shown schematically in Fig. 2. In order to fix the position of the laser beam within the experimental apparatus (e.g. the combustion chamber) with an accuracy in the sub-mm range, the drift between capsule and laser beam has to be compensated. Experiments in the drop tower have shown that this drift, in the range of 20 mm, is induced by oscillations in the concrete drop tower, from momentum of the release mechanism and from improperly compensated coriolis force.

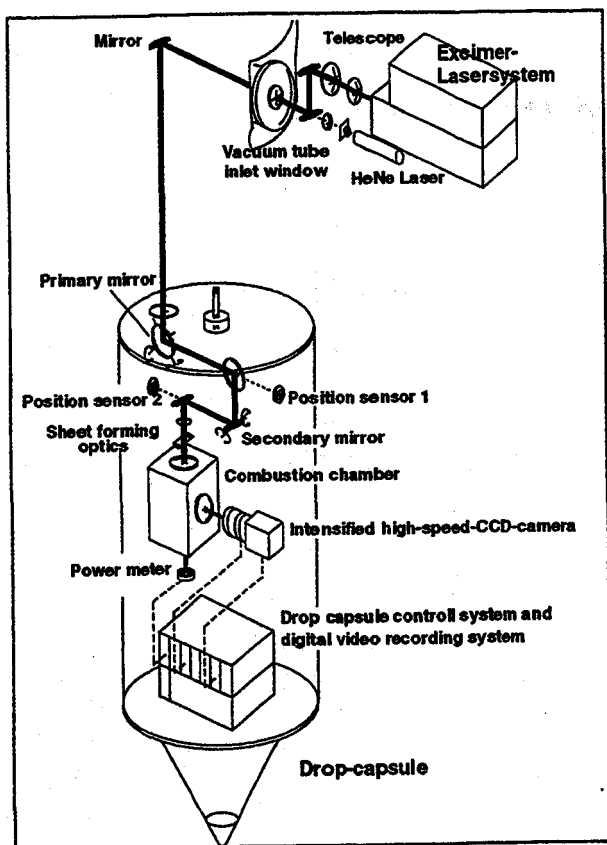


Fig. 2: Schematics of the optical arrangement at the top of the drop tower and within the drop bus

The positioning system is based on a guiding HeNe-laser beam which is coupled coaxially into the optical path of the excimer laser, and on a positioning unit at the top of the capsule. With two beam-splitter plates the HeNe-laser beam is directed on two planar position sensing detectors (PSD). A control unit drives two motorized mirrors with two axes of rotation each. Thus the lateral and the angular drift between the drop capsule and the laser beam can be compensated. With a cylindrical telescope the laser beam is focused to a suitable two dimensional light-sheet of about 30 mm height and a width of about 800 μm (FWHM).

In order to enable the investigation of rapid instationary processes like auto-ignition phenomena within the drop time of 4.74 seconds the frame rate of the laser diagnostic system is maximized to 250 frames per second. The image intensified CCD-camera with 256 x 256 squared pixels has also the capability to take 250 frames per second. By means of a compact industrial system based on a Motorola chip (MC68030) with an 8 bit

A/D converter with 18 MHz sampling rate and a high speed video-interface, up to 96 Mbytes data (5s) can be stored during the drop time directly on the video-RAM. Image acquisition and data storage equipment are integrated within the capsule.

Immediately after finishing the drop experiment the image data can be transferred via radio transmission link to a large data storage outside the drop tube. From here a first evaluation of the obtained raw image data is possible, and extensive automatic digital image processing can be done.

For triggering the image acquisition system by the laser pulse a fast UV-photo-diode is used within the drop capsule. With temporal pulse to pulse fluctuations (jitter) of the laser below 3 ns, a pulse length below 20 ns, a temporal drift due to the moving capsule below 1 ns per pulse and a gate time of the image intensifier of 100 ns it is possible to trigger the acquisition of an image with the previous laser pulse.

FIRST EXPERIMENTAL RESULTS

The images on the following page show first 1g and μg experiments applying the laser system to a configuration which is comparable to the 'Emmons Problem'. The burner is a methanol drenched glass wool bed 50mm long and 20mm wide.

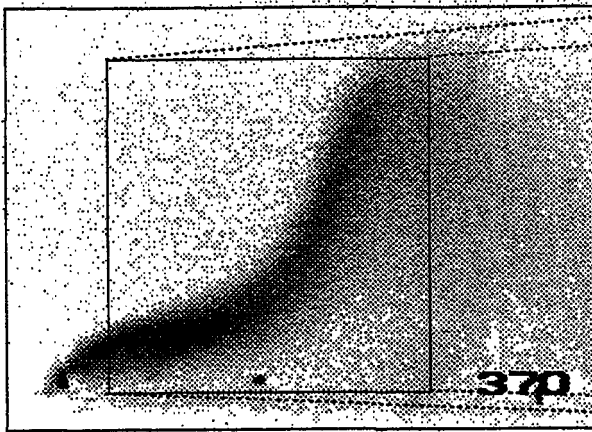


Fig. 3: Video image of a 1g methanol diffusion flame, forced air flow from left hand side

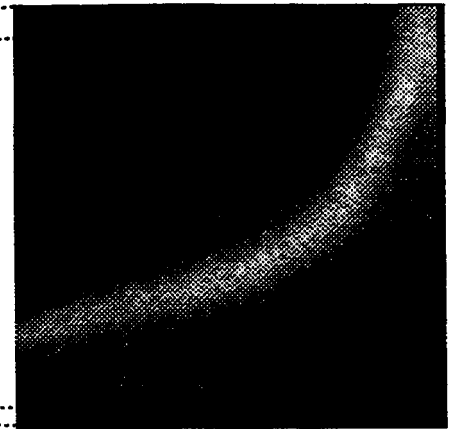


Fig. 4: OH-LIPF single shot image achieved at 120m distance from the laser, frame rate 250Hz, 248nm, excitation via $P_2(8)$ transition

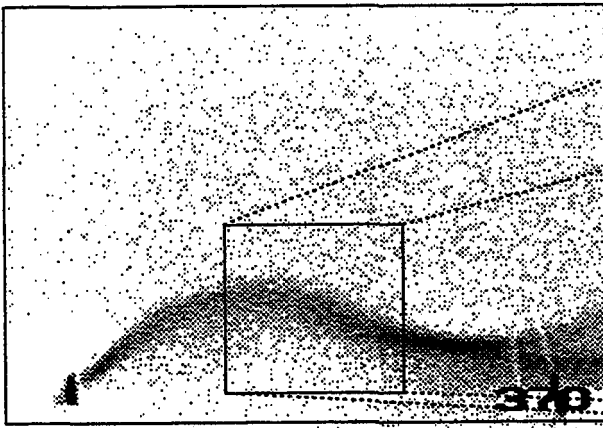


Fig. 5: Video image of the 0g flame, 0.3s after release of the capsule

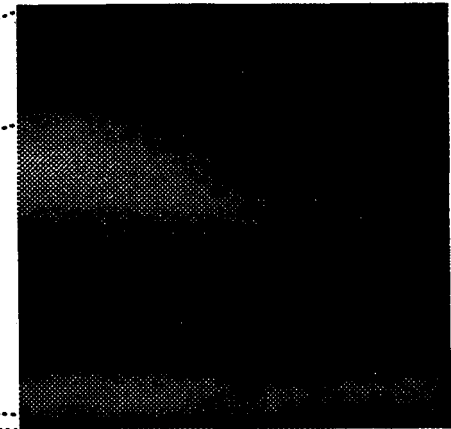


Fig. 6: OH-LIPF 250Hz single shot image of the marked area, $P_2(8)$ transition

Further applications might be:

- 2D - Measurements of the interaction of two and more droplets during ignition, flame spread and burning, which is an important step in understanding the processes of spray combustion.
- Measurement of the flame structure of premixed or diffusion flames in buoyant-free surrounding.
- 1D - Raman / Rayleigh Spectroscopy for simultaneous measurement of different major species and temperature focusing the laser sheet to a focal line and using an OMA system, where the emission wavelength is measured against the spatial coordinate with high temporal resolution.
- 2D - flow field measurements like particle tracking velocimetry or laser speckle velocimetry for various applications in fluid mechanics under microgravity conditions, where small seeding particles can be illuminated stroboscopically with the planar laser light sheet, so that the two velocity components in this plane can be measured simultaneously.
- Use of the UV laser beam for photochemical processes (e.g. photo-polymerization) under microgravity condition)

PI: Hans J.Rath, Christian Eigenbrod, ZARM, Bremen

Co-operative partner: Wolfgang Triebel, IPHT, Jena

Support: German Space Agency, DARA, (50 WP 9251), Sept. 92 - Aug. 95

References:

1. Ch. Eigenbrod, J. König, T. Bolik, T. Behrens, F. Dinkelacker, H. J. Rath, H. Albrecht, D. Müller, Th. Schröder and W. Triebel, Development of an UV-laser-diagnostic system for Combustion Research under Zero-Gravity at Drop Tower „Bremen“, *7th Int. Symp. on Application of Laser Techniques to Fluid Mechanics*, Lisbon, 6.3 (1994).
2. J.König, F.Dinkelacker, Ch.Eigenbrod, H.J.Rath, Th.Schröder, H.Albrecht, D.Müller, W.Triebel, "Application of UV-Laser Diagnostics to Combustion Research under Zero-Gravity", *Adv. Space Res. Vol.16, No.7, pp. (7)145-(7)148, 1995.*

Theoretical and Experimental Investigations on Lean Flammability Limits and Laminar Flame Speeds under High Pressure and Microgravity Conditions

For reasons of safety, the knowledge of flammability limits is essential for space and nuclear reactor technology. Investigations of the lean flammability limits for fuels such as hydrogen and methane under normal gravity conditions have shown a clear dependence on the direction of flame propagation. Therefore the lean flammability limit is lower for an upward traveling flame than for a downward traveling flame. This gives the clear evidence for buoyancy effects superimposed to the flammability limits caused by reaction kinetics. These kinetically based flammability limits also have been subject to detailed numerical analysis in order to investigate reduced reaction mechanisms. These numerical results are difficult to compare with the experimental data, because the extinction process strongly depends on the configuration of the flame and the definition of flammability. To have a better insight into the kinetic aspects of flammability limits, experiments under zero gravity conditions are necessary. Figure 7 on the next page depicts the spherical high pressure combustion chamber. The inner diameter is 100mm. The chamber's pressure resistance of up to 700 bar has been tested. The premixture is loaded by means of partial pressures. Ignition is initiated concentrically, Schlieren method is applied to observe flame propagation because the lean flame is not expected to be luminous enough for direct observation.

The time being, the equipment is ground tested and 1g experiments are ongoing. First microgravity experiments are scheduled for autumn this year.

PI: Norbert Peters, ITM, Aachen

Support: German Space Agency, DARA, (50 WM 9439), May 94 - April 97

References:

1. N.Peters, "Reduced Mechanisms, Reduced Kinetic Mechanisms and Asymptotik Approximations for Methane-Air Flames", *Lecture Notes in Physics*, (M.D. Smooke, Ed.), Springer, 29-47, (1991)

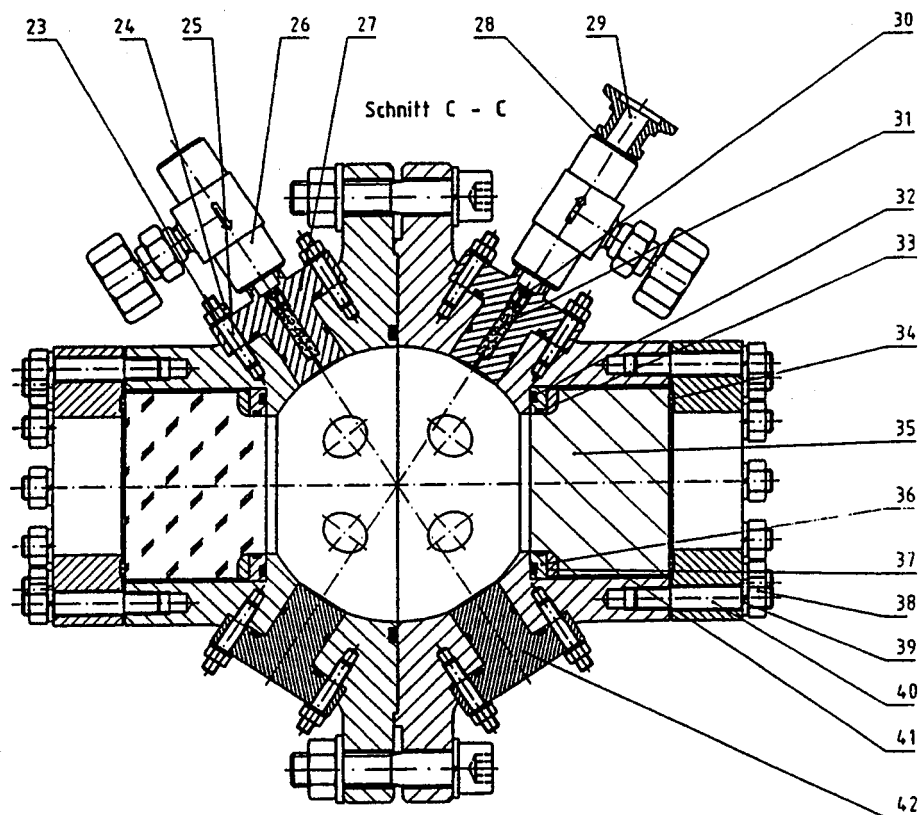


Fig. 7: Spherical High Pressure Combustion Chamber

Investigation on Laminar H_2 Diffusion Flames by Means of Solid-State-Electrolyte Sensors (Gaspotentiometric Method)

Objective of this project is to investigate flame structure of laminar H_2 - diffusion flames without the presence of buoyant effects. The experiments shall validate the numerical models describing the flame structures of different fuels without convection. The refined model will then be applied on flames influenced by gravity. Beside video observation, specially developed solid-state-electrolyte sensors will be used to detect species concentration and temperature distribution quantitatively. These measurements yield spatially and timely resolved information on flame structures and thus might help to analyse chaotic dynamics in real systems. The miniaturization of the sensors will be a side-effect of this project.

PI: H.Rau, Otto-von-Guericke-Universität, Magdeburg
R.Grabski, Institute of Fire-Department of Saxony-Anhalt

Support: German Space Agency, DARA, Jan. 95 - June 96

References:

1. K.Tittmann, H.Rau, L.Sitzki, R.Grabski, "Investigation of a Laminar Hydrogen Diffusion Flame under Microgravity by Means of Solid-State-Electrolyte Sensors", *Proc. Drop Tower Days 94*, Bremen

Session Summaries

Report on Session I: Droplets and Aerosols

(Prepared by C. K. Law)

Microgravity droplet combustion, initiated in the mid-seventies, has grown in its scope and size. The interests have extended from the traditional measurements of the burning rates to include effects of multicomponent fuels, soot formation, flame chemistry, supercritical environments, multiple droplet interaction, solid spheres, and aerosols and dusts. The session consisted of twelve papers; the highlights of which are topically reviewed in the following. The principal investigators involved in each topical program are also listed.

1. Soot Formation and Characterization (Avedisian, Choi)

Perhaps one of the most outstanding contributions of microgravity droplet combustion is the observation of Williams and Dryer, that in the absence of asymmetrical forced and natural convection, a soot shell is formed between the droplet surface and the flame, exerting an influence on the droplet combustion response far greater than previously recognized. Avedisian has shown in his presentation that the amount of soot formed increases with the droplet diameter. While an obvious cause for this increase is the larger amount of fuel burnt, what is not clear is the influence of the residence time on soot formation. Estimates have also been made on the thermophoretic force acting on the soot particles through modeling of the heptane combustion process with complex chemistry. An experimental program aiming to measure the soot volume fraction and temperature using light extinction and two-color pyrometry respectively has also been initiated.

2. Supercritical Droplet Combustion (Williams, Gokalp)

Supercritical droplet combustion is ideally suited for microgravity investigation because of the inherently strong buoyancy effect present under high pressure situations. An interesting issue here is the earlier observation that in microgravity the droplet lifetime attains a minimum around the critical state. Recent studies by Williams further confirm this results while those by Gokalp do not seem to show such a minimum.

3. Flame Chemistry (Dryer, Williams)

The interest in studying flame chemistry via microgravity droplet combustion is the aerodynamically clean environment offered by its well-controlled, spherically-symmetric one-dimensional configuration. Both methanol and heptane are being studied, with methanol being a fuel whose chemistry is reasonably well understood while heptane is probably the smallest liquid alkane which can be experimentally studied without too much complication due to volatility. Furthermore, its volatility also resembles that of gasoline. The droplet combustion processes have

been theoretically studied using computational simulation with detailed chemistry and transport, and asymptotic analysis with reduced mechanisms and constant properties. The detailed modeling emphasizes that quasi-steadiness does not exist for some of the slow gas-phase reactions.

4. Bicomponent Droplet Combustion (Avedisian, Dryer, Kadota, Kono, Sato, Shaw, Williams)

Several issues are addressed here. First, microgravity experiments have shown that the combustion characteristics of a bicomponent droplet with vastly different volatilities (e.g. heptane/hexadecane) exhibit the three-staged behavior originally observed by Wang *et al.* in the mid-eighties on normal-gravity, freely-falling droplets. Specifically, the burning consists of two fairly steady stages separated by a short period of droplet re-heating, slow burning rate, and flame shrinkage. The efficiency of liquid-phase mass diffusional resistance is also addressed. There is evidence that it is not as strong as previously thought in that some phenomena appear to be describable by assuming either a well-mixed droplet interior or a moderately large gasification Peclet number. A maximum in the droplet lifetime was also observed for bicomponent droplets under elevated pressures. The interest in water/oil emulsions has re-emerged, and the stability and micro-explosion of the emulsions studied. Since the experiment was conducted with suspended droplets, the influence of the suspension fiber on micro-explosion is not clear.

5. Droplet Arrays (Dietrich, Kono, Niioka)

Two and three droplet arrays have been studied, showing the phenomena of flame merging and oxygen competition leading to a reduction in the burning rate, as originally observed by Miyasaka *et al.* for normal-gravity, reduced-pressure environments. Ignition of droplet arrays has also been studied.

6. Spray and Dust Flames (Gomez, Hiroyasu, Niioka, Sato)

Several interesting observations were reported. First, the counterflow versus co-flow spray flame structure were studied. The flame characteristics were found to be similar to those of the gaseous flame, including flickering of the co-flow flame. Spray flames dominated by homogeneous and heterogeneous burning were observed. Dust flames were studied for PMMA particles with and without methane addition, and for coal particle flames. Strong heterogeneous burning was observed.

7. PMMA Sphere Burning (Yang)

An experiment on PMMA sphere burning was initiated. Preliminary results show extensive amount of bubbling occurring during burning.

Session Chair Report

Parallel Session I

Wednesday 12 April, 8:00 am-12:30 pm

Robert A. Altenkirch

Metals, Combustion Synthesis, and Fire Safety

The session was comprised of eleven contributions in the areas detailed in the session title.

In the area of metals combustion, development of an experiment to investigate the ignition of bulk metal samples in reduced gravity on board the DC-9 aircraft was described. Metals under investigation in pure oxygen are Fe, Ti, Zr, Mg, Zn, and Cu. These particular metals were chosen in order to study the two different combustion modes of metals, i.e., heterogeneous surface oxidation or gas-phase combustion of the metal vapor, and because these metals are important structural elements, so there is a direct application to safety. Experiments were conducted at normal and elevated gravity to complement the planned reduced-gravity experiments.

Elevated gravity results show that the time to ignition increases from 1 to 5 g, but beyond 5 g, the trend is reversed, and the ignition time decreases with increasing g. Presumably the increased ignition time at the lower g is due to convective heat losses due to buoyancy, and the reduced ignition time at the higher g is due to enhanced oxygen transport to the sample and an increased heat release rate that compensates for the heat losses. The shape of the molten metal pool that forms during ignition will depend on the gravitational level as gravitational and surface tension forces balance.

Droplet combustion of Al and Zr, formed in an apparatus that provides repeatable formation of uniform metal droplets with controllable velocity and initial temperature was investigated at normal gravity. Results indicate that oxygen may dissolve in the burning Al and Zr particles. Proposed transition of the metal-oxygen solution to the oxide provides an explanation of the observed brightness, jumps in temperature, and explosions. Early in the combustion process, burning is symmetrical, but eventually the symmetry is lost at normal gravity. Development of a microgravity experiment is underway that will elucidate the processes resulting in the loss of symmetry of the combustion zone following the symmetrical regime just following ignition.

Quenching distances for Al dusts have been measured in normal gravity. The dusts were

prepared in a novel experimental apparatus consisting of a syringe-type feeder in which the dust supply rate is controlled by the "piston" speed and a dispersal chamber in which high velocity jets pick up the dust and transport it through a diffuser to the combustion chamber. Ground-based results show that the flame speed and quenching distance depend weakly on the dust concentration for rich mixtures. Parabolic aircraft flights have revealed that beyond those dust concentrations the "minimum" quenching distance of 5 mm from ground-based experiments continues to decrease, with an increase of concentration beyond that which can be established on the Earth, and would appear to be below 4 mm for 5.4 micron dust.

Some areas of potential collaboration between NASA and the Russian Academy of Sciences in the area of SHS, i.e., self-propagating high-temperature synthesis, were reviewed. Intensification of SHS processes at elevated gravity was considered, and microgravity experiments on the production of foams that do not suffer gravity-induced damage are two areas of such collaboration. Several different systems for study were identified, e.g., those producing foam carbides, borides, silicides, nitrides, intermetallics, and composites were considered. Applications of such SHS processes include synthesis of foam materials in situ for use on spacecraft as opposed to transportation of the high volume foam.

SHS of cylindrical samples of titanium, carbon black, and an additive that gasifies in quartz tubes heated at one end and allowed to expand along the axis of the cylinder were studied aboard parabolic aircraft. The diameter of the samples remains fairly constant as the product is formed, while the length is several times the original. The processes contributing to the increase in sample length as the product is formed are the melting of one component and subsequent capillary flow coupled with decomposition of the additive to form a gas that gives rise to an increased gas pressure in the pores of the sample.

The formation of ceramic-metal composites via SHS from a few model reaction systems was reviewed. Reaction systems were chosen that generate a liquid, e.g., Al, and/or a gas, e.g., B_2O_3 , near the reaction zone. Gravity influences the micro and macrostructure of the product because of its influence on the liquid and gaseous species. In reduced gravity, segregation of the liquid phase is minimized, which results in more uniform distribution of the resultant product. Reduced heat losses at low g results in higher combustion temperatures such that gravity may provide a control of the product grain size. The synthesis of metal composites, e.g., Ni-Al, from elemental Ni and Al powders, with and without the addition of the presence of TiB_2 , also form a more uniform microstructure in microgravity than in normal gravity.

Smoldering and SHS are both examples of combustion in porous media, and, as a result

have aspects of commonality, but they are different in that in SHS the objective is to maintain the combustion wave propagation to maximize product formation while smoldering is generally an unwanted phenomenon. Modelling allows for the description of several different possible structures for forward and opposed flow smolder, and SHS modelling allows for description of the relative motion of individual components of the mixture as the SHS process proceeds resulting in the separation of products. Gravity affects smoldering and SHS through the way in which it affects the transport of oxygen to the smolder zone and the densification of SHS products.

Safety topics addressed included the effects of gravity on the toxicity of particulate and gaseous products formed when fluorocarbon polymers are heated and decompose (fluorocarbons having such applications as wire insulation); the impact of venting, i.e., pressure reduction, on fire suppression; and development of smoke detection devices for low-g fires. Thermal degradation studies of polytetrafluoroethylene (PTFE) in N_2 and wet and dry air show the major gas product to be C_2F_4 with the N_2 environment yielding the highest concentrations. In the air environments, less C_2F_4 is produced, but smoke production is much greater than in N_2 .

Venting has been proposed as a method for extinguishing fires in spacecraft, although it is possible that transient effects in venting that induce flows could result in an intensification of the fire. Normal gravity experiments on PMMA cylinders were used to develop a pressure-temperature flammability boundary. The low pressure limit decreases with an increase in the solid center temperature. Low-g experiments conducted on NASA's Learjet did not reveal a flammability boundary, but g-jitter was observed to extinguish flames under conditions that are known to be flammable without the g-jitter.

As spacecraft missions increase in length, the need for effective, crew independent fire detection systems increases. Previously, UV detectors and ionization detectors have been used, while smoke detectors are planned for use on ISSA. Limited data indicate that particulate formed at microgravity are larger than those formed at normal gravity, and a glovebox experiment is under development that will generate particulates in the Shuttle from combustion of samples in the glovebox facility. These particulates will be transported to an ionization detector and the ISSA smoke detector, which uses laser obscuration, for performance tests in order to make a meaningful assessment of detector performance on low-g particulate.

Session Chair Report

Parallel Session II
Wednesday 12 April, 2:00-5:00 P.M.

Raymond Friedman

Ignition and Flame Spread

Nine papers were presented, eight of which dealt specifically with ignition and/or spread on solids (paper, PMMA, insulated wire, polystyrene foam, cotton). The ninth paper (CNRS) used ethane gas and a porous metal plate to simulate a pool fire.

Five of the papers included substantial theoretical or computational material, but all the papers except one (Wichman, Michigan State) contained experimental results or work in progress.

The various theoretical descriptions of flame spread over a solid surface did not duplicate one another but differed in a number of ways: steady state versus transient, two-dimensional versus three-dimensional, degree of consideration of gas radiation and radiation to or from the surface, wind presence or absence and direction thereof, detailed consideration of the flame tip, treatment of the flame chemistry, etc. None of the theories was presented as being finished products; in each case, further development is planned. Some of the courses are much more computationally intensive than others.

Microgravity experiments were performed by six of the investigators, using drop towers, airplanes flying parabolic trajectories, and orbital vehicles. Steady-state spread rates were obtained for thin fuels but only transient behavior for thick fuels, because of experimental constraints. In many cases, the instrumentation was not entirely adequate to reveal all important features. Much more work is needed on flame spread with an imposed air flow.

It is clear that flame spread can occur under microgravity conditions and in a substantially different way than at normal gravity. Much more work is needed, both experimentally and theoretically, to provide a good base for understanding these phenomena.

The international flavor of the flame spread studies (Russia, Japan, France, United States) should be noted.

Session Chair Report
Parallel Session II
Wednesday 12 April, 2:00-5:00 P.M.

Jack B. Howard

Combustion Diagnostics

The ten papers presented in this session reported impressive progress toward the development of equipment and techniques for flame observations and measurements under μg conditions. The combustion being studied is often near the limits of flammability, ignition or stability, where the flames are dim and measurements challenging. The equipment has to be rugged, compact, low in power consumption, and rapid in operation.

In general, there is extensive use of solid state lasers in μg combustion research. The need is to obtain from the flame a signal carrying with spatial and temporal resolution and to record it for subsequent detailed processing. Only a few examples were presented of material samples being taken from the flame for subsequent analysis.

The task of making laser doppler velocimetry compatible with μg combustion conditions has benefited from progress in solid state lasers, photo-detectors, and signal processors. Paul Greenberg of NASA Lewis reported that the difficulty of making point by point volume fraction measurements within a sooting flame during the short times available under μg conditions has been addressed using a full-field or image based technique, which allows measurements at 250,000 simultaneous spatial locations at a rate of 30 Hz. Apparatus to perform soot volume fraction imaging has been implemented in a 2 sec drop package and used to study the soot around drops.

Laser normally used for particle imaging velocimetry at 1g are incompatible with μg facilities because of power requirement, size and lack of ruggedness. DeVon Griffin of NASA Lewis described the use of measuring pulsed light using a special laser built to satisfy the μg requirements and capable of measuring particle velocities of 3 to ~ 1700 cm/s. The laser has been used to study gas jet diffusion flames seeded with SiO_2 particles.

A range of diagnostics being studied in Japan was presented by Dr. Toshie Kadota of Osaka Prefectural University. The methods include Raman, Raleigh and Mie scattering, laser induced fluorescence, interferometry, Schlieren, emission spectroscopy and velocimetry. Applications include measurement of soot concentration profile away from the surface of a burning drop, fluorescence measurements of hexadecene droplets evaporating in inert gas and burning in air, and a new planar induced fluorescence method for detection of flame radicals.

Prabhakar Misra of Howard University described the development of a portable, compact, low-power consuming LIF-based analytical unit suitable for in-space flame characterization. A solid state laser which meets these requirements has been built and demonstrated for detection of hydroxyl and methoxy radicals.

A diagnostic system being developed for measurement of instantaneous fuel droplet diameter, regression rate, and internal temperature profiles at high data rates in μg combustion experiments was presented by Subra Sankar of Aerometrics. The method is based on rainbow thermometry and point-diffraction interferometry. Issues already handled or being addressed are how to deal with deviations from perfect sphericity or with radial inhomogeneity of the droplets.

The quantitative measurement of oxygen in μg conditions was discussed by Joel Silver of Southwestern Sciences. A new type of diode laser, called a vertical cavity surface-emitting laser, is being used to measure oxygen mole fraction without accurately knowing temperature or to measure temperature. These lasers are now available at selected wavelengths below $1\mu\text{m}$, and their usefulness for compact intrinsically safe monitoring sensor aboard spacecraft is to be demonstrated.

A laser induced incandescence method for soot volume fraction measurement with spatial resolution in real time, being developed and applied at NASA Lewis and University of Illinois, was presented by Randy Vander Wal of NYMA, Inc. A pulsed high-energy laser is used to heat soot within the laser beam to $\sim 4300\text{K}$. Thermal emission from the heated particles is in the blue, and is nearly proportional to soot volume fraction. The method that uses this emission from different positions along the beam is used for the volume fraction measurement without problems from absorption by polycyclic aromatic hydrocarbons or scattering.

In visible and ultraviolet imaging, Karen Weiland of NASA Lewis described the use of intensified array cameras to overcome the problem of flames being too dim to detect by film or standard video cameras. High-speed operation has been achieved, and the cameras have been used in 2 sec drop tests. Also, infrared imaging for temperature measurement, fluorescence imaging for OH and CH radical concentration measurement, and Schlieren imaging are being used. In support of the NASA Lewis work, Wallace Wong of SSG, Inc., is developing for μg use an imaging spectrometer. This spectrometer is designed for spatially scanning images of flames to provide detailed spectra from selected regions in an image. A flame image is recorded as ~ 5 Mbytes of information in ~ 1.2 sec.

Michael Winter of United Technologies Research Center is using LIF spectroscopy for study flame around burning droplets. An electrodynamic balance for droplet levitation has been built and packaged for μg work.

Session Chair Report
Parallel Session III
Thursday 13 April, 8:00 A.M.-12:30 P.M.

Gerard Faeth

Gaseous Diffusion Flames

Introduction. There were twelve reports/presentations in the area of gaseous diffusion flames. These results were limited to short duration or imperfect (disturbed) low-gravity conditions using ground-based facilities. Thus, all the results are compromised to some extent by transient and buoyancy effects that can only be completely resolved by long term tests at microgravity in space-based facilities.

The research on gaseous diffusion flames can be grouped into four main areas, as follows: (1) turbulent-like interactions, (2) stability and extinction, (3) simulation and analysis, and (4) soot processes. Each of these areas will be discussed, in turn, in the following. The present discussion will identify specific investigations by title and Principal Investigator and will be brief; individual presentations in the proceedings should be consulted for summaries listing all participants and more details for each investigation.

Turbulent-Like Interactions. Work in this area seeks a better understanding of turbulent diffusion flames by studying effects of vorticity on flame properties in microgravity where rates of flame distortion can be slowed down to allow measurements of flame properties. Studies in this area include: "Flame-vortex interactions imaged in microgravity," by J. F. Driscoll where a toroidal laminar vortex ring is observed while interacting with both diffusion and premixed flames that are laminar; "Dynamic response of a pulsed Burke-Schumann diffusion flame," by L.-D. Chen where the fuel flow is pulsed in a coflowing laminar jet diffusion flame; "Three-dimensional flow in a microgravity diffusion flame," by J. Hertzberg where both elliptic jet cross sections and forced flow rates create interactions; "Characteristics of transitional and turbulent jet diffusion flames in microgravity," by M. Y. Bahadori where the behavior of laminar, transitional and turbulent gas jet diffusion flames in normal- and micro-gravity are contrasted; and "Effects of energy release in near field flow structure of gas jets," by A. K. Agrawal where effects of buoyancy on the structure of the shear layer and the development of fluid dynamic instabilities are being studied in the near jet exit region of jet diffusion flames.

Stability and Extinction. Work in this area seeks a better understanding of effects of buoyancy on the stability and extinction properties of gaseous diffusion flames, exploiting both measurements and analysis (numerical simulation). Studies in this area include: "Effect of CF₃H and CF₃Br on laminar diffusion flames in normal and microgravity," by S. Hochgreb which is studying effects of halogen gases added to the air on the properties of laminar jet diffusion flames; and "Radiant extinction of gaseous diffusion flames," by A. Atreya which is considering effects of radiation on extinction for a variety of laminar diffusion flame geometries.

Analysis and Simulation. Virtually all the studies of gaseous diffusion flames involve some degree of either analysis or numerical simulation of flame properties. A few studies, however, are

mainly focused on the use of either analysis or numerical simulation to formally study effects of buoyancy on diffusion flame properties. These studies include: "Effects of gravity on sheared and nonsheared turbulent nonpremixed flames," by S. E. Elghobashi which involves three-dimensional time-dependent numerical simulations of low Reynolds number turbulent-like flames; "Structure and dynamics of diffusion flames in microgravity," by M. Matalon which is considering various laminar diffusion flame configurations being studied in the microgravity combustion science program using asymptotic methods; and "Unsteady planar diffusion flames," by F. E. Fendell which involves numerical simulation of the transient development of laminar diffusion flames having a variety of classical geometries.

Soot Processes. Studies in this area are motivated by the fact that soot in flames convects with mean flow velocities which implies vastly different soot paths, and thus soot processes, in buoyant laminar diffusion flames when compared to nonbuoyant laminar diffusion flames. Thus, existing information about soot processes in practical nonbuoyant flames is very limited because laboratory flames that are tractable for detailed measurements of soot properties are invariably buoyant. Studies in this area include: "A detailed modeling analysis for soot formation and radiation in microgravity gas jet diffusion flames," by J. C. Ku which involves developing numerical models for soot formation and radiation properties in turbulent diffusion flames; and "Laminar soot processes," by G. M. Faeth which involves experimental and computational studies of soot formation, oxidation and optical properties in both diffusion and premixed flames that are laminar.

Session Chair Report
Parallel Session III
Thursday 13 April, 8:00 A.M.-12:30 P.M.

Mitchell Smooke

Premixed Gases

The Thursday morning session on premixed flames consisted of ten presentations. The talks covered experimental, computational and theoretical aspects of premixed microgravity combustion. The presentations ranged from computational studies of flame balls to multidimensional measurements of premixed turbulent combustion. Each of the talks is discussed in some detail below.

J. Buckmaster's (University of Illinois) research is primarily theoretical in nature. He is focusing on the analytical modeling of configurations undergoing experimental study in NASA's microgravity combustion program. The major areas of study include flame balls, intrinsic and acoustic instabilities in multiphase mixtures and smoldering.

R. Cheng (LBL) and coworkers are using moderate to low turbulence Reynolds number flames to characterize and quantify turbulent flame structure under microgravity. Experiments have been carried out using both qualitative and quantitative flow visualization techniques. These are being coupled with video recording and computer controlled image analysis.

F. Egolfopoulos (USC) has begun a program that considers the steady and unsteady characteristics of weakly burning premixed and diffusion flames in microgravity. The flames are primarily counterflow in configuration. The project includes both an experimental and a computational component.

The presentation of K. Kailasanath (NRL) described a computational study in which the propagation and extinction of gas-phase flames in both microgravity and Earth environments was investigated. Downward propagating time-dependent multidimensional flames were studied. The NRL group has also investigated the role of hydrodynamic instabilities on the formation of cellular flames.

The work of E. Law (Princeton University) combines experimental and theoretical analyses of cylindrical and spherical premixed and nonpremixed flames in microgravity. In particular, the effects of flame curvature on the burning intensity is being studied.

The talk by S. Menon (Georgia Tech) outlined the goals of a new project that will combine experimental and computational techniques in the study of premixed turbulent flames in microgravity.

T. Niioka (Tohoku University) presented an overview of microgravity research in Japan on gaseous flames.

H. Pearlman (NRC/NASA) investigated instabilities in downward propagating premixed flames with large Lewis numbers. Pulsating, spiraling and traveling wave flames were observed.

P. Ronney (USC) considered combustion limits in premixed flames in microgravity. He examined the effects of radiation in these systems as well as the structure and stability of these flames at low Lewis numbers. His work also considered flame propagation in cylindrical tubes and the simulation of autocatalytic chemical reactions.

The work by M. Smooke (Yale University) focused on a computational study of flame balls in premixed fuel-air mixtures. He has computed flame ball structure as a function of the equivalence ratio using a model that includes radiative losses.

Third International Microgravity Combustion Workshop

Attendance List
April 11-13, 1995
Cleveland, Ohio

Angel Abbud-Madrid
University of Colorado/Boulder
Mechanical Engineering Dept.
Campus Box 427
Boulder, CO 80309-0427
Phone: 303 492-8920
Fax: 303 492-3498
E-mail: abbudmad@colorado.edu

Mohamed Abid
University of Southern California
Aerospace/Mechanical Engineering
VHE 213
Los Angeles, CA 90089
Phone: 213 747-9523
E-mail: abid@chap.usc.edu

Alex Abri
ADF
2001 Aerospace Pkwy.
Brook Park, OH 44142
Phone: 216 977-1096
Fax: 216 977-1467

Thomas H. Acquaviva
NASA LeRC
Space Experiments
M.S. 500-115; 21000 Brookpark Rd.
Cleveland, OH 44135
Phone: 216 433-8020
Fax: 216 433-8660

Ajay K. Agrawal
University of Oklahoma
School of Aerospace & Mechanical Engineering
Room 212; 865 Asp Ave.
Norman, OK 73019
Phone: 405 325-1754
Fax: 405 325-1088
E-mail: agrawal@mailhost.ecn.uoknor.edu

Sanjay Agrawal
University of Michigan
Mechanical Engineering Dept.
Ann Arbor, MI 48109
Phone: 313 763-7471
Fax: 313 747-3170

Ralph C. Aldredge
University of California/Davis
Mechanical & Aeronautical Engineering
Davis, CA 95616-5294
Phone: 916 752-5016
Fax: 916 752-4158
E-mail: rcaldredge@ucdavis.edu

Anatoly P. Aldushin
Northwestern University
Engineering Sciences & Applied Math. Dept.
2145 Sheridan Road
Evanston, IL 60208
Phone: 708 491-5396
Fax: 708 491-2178
E-mail: tolia@zeldovich.eecs.nwu.edu

Robert A. Altenkirch
Mississippi State University
College of Engineering
P.O. Drawer DE
Mississippi State, MS 39762
Phone: 601 325-2270
Fax: 601 325-8573
E-mail: raa@de.msstate.edu

Scott Anderson
University of Michigan
Aerospace Engineering Dept.
1320 Beal St.
Ann Arbor, MI 48109
Phone: 313 763-9304
Fax: 313 763-0578
E-mail: andersd@engin.umich.edu

Preceding Page Blank

Ralph A. Anthenien, Jr.
University of California/Berkeley
Mechanical Engineering Dept.
44 Hesse Hall
Berkeley, CA 94720
Phone: 510 643-5282
Fax: 510 642-1850
E-mail: anthenien@euler.berkeley.edu

Arvind Atreya
University of Michigan
Mechanical Engineering & Applied Math. Dept.
2158 G.G. Brown
Ann Arbor, MI 48109-2125
Phone: 313 747-4790
Fax: 313 747-3170
E-mail: aatreya@engin.umich.edu

Philip J. Austin
NIST
Fire Science Division
NIST Bldg. 224 Rm. B258
Gaithersburg, MD 20899
Phone: 301 975-4508
E-mail: pjaustin@enh.nist.gov

Tom Avedisian
Cornell University
MAE Dept.
550 Del Rey Avenue
Ithaca, NY 14853
Phone: 607 255-5105
Fax: 607 255-1222

William Bachalo
Aerometrics, Inc.
Sunnyvale, CA 94086
Phone: 408 738-6688
Fax: 408 738-6871

M. Yousef Bahadori
SAIC
Thermal Sciences Division
21151 Western Ave.
Torrance, CA 90501
Phone: 310 781-8723
Fax: 310 781-8730

Tiejun Bai
Clark Atlanta University
Dept. of Engineering
223 James P. Brawley Drive
Atlanta, GA 30314
Phone: 404 880-6938
Fax: 404 880-6853
E-mail: tbai@cau.aud.edu

H. Balwada
Notre Dame University
Chemical Engineering Dept.
182 Fitzpatrick Hall
Notre Dame, IN 46601
Phone: 219 631-5692
Fax: 219 631-8366

Hasan Bedir
Case Western Reserve University
Mechanical & Aerospace Eng. Dept.
10900 Euclid Avenue
Cleveland, OH 44106
Phone: 216 368-4588
Fax: 216 368-6445

Subrata Bhattacharjee
San Diego State University
Mechanical Engineering Dept.
5300 Camponile Drive
San Diego, CA 92182-0416
Phone: 619 594-6080
Fax: 619 594-6005
E-mail: subrata@voyager5.sdcu.edu

David Blachly
ADF
2001 Aerospace Pkwy.
Brook Park, OH 44142
Phone: 216 977-1298
Fax: 216 977-1269

Nora G. Bozzolo
Analex Corporation
AOS; 3001 Aerospace Pkwy.
Brook Park, OH 44142
Phone: 216 977-0086
Fax: 216 977-0200

Melvyn C. Branch
University of Colorado
Mechanical Engineering Dept.
Boulder, CO 80309-0427
Phone: 303 492-7427
Fax: 303 492-2863
E-mail: branch@spot.colorado.edu

Kenneth Brezinsky
Princeton University
Mechanical & Aerospace Engineering Dept.
Eng. Quad D329
Princeton, NJ 08544
Phone: 609 258-5225
Fax: 609 258-5963

John Brooker
NASA Lewis Research Center
M.S. 500-115; 21000 Brookpark Rd.
Cleveland, OH 44135
Phone: 216 433-6543
Fax: 216 433-8660
E-mail: jbrooker@lerc.nasa.gov

John Buckmaster
University of Illinois/Urbana-Champaign
Aeronautical & Astronautical Eng. Dept.
104 S. Wright St.
Urbana, IL 61401
Phone: 217 333-1803
Fax: 217 244-0720

Michael T. Bush
Massachusetts Institute of Technology
Mechanical Engineering Dept.
31-061; 77 Massachusetts Ave.
Cambridge, MA 02139
Phone: 617 253-3310
Fax: 617 253-9453
E-mail: mtbush@mit.edu

John M. Card
Sandia National Laboratories
Combustion Research Facility
Livermore, CA 94551-0969
Phone: 510 294-1354
Fax: 510 294-1004
E-mail: jmc card@mars.ca.sandia.gov

Brad Carpenter
NASA Headquarters
Code UG
Washington, DC 20546
Phone: 202 358-0826
Fax: 202 358-3091

S.H. Chan
University of Wisconsin/Milwaukee
Mechanical Engineering Dept.
P.O. Box 784
Milwaukee, WI 53201
Phone: 414 229-5001
Fax: 414 229-6958
E-mail: shc@csd.uwm.edu

Christian Chauveau
Centre National de la Recherche Scientifique
SPI/Laboratoire de Combustion et Systemes Reactifs
IC av. de la Recherche Scientifique
Orleans Cedex 02, France 45071
Phone: 33 38515486
Fax: 33 38517875
E-mail: chauveau@cnsr-orleans.fr

Harsha K. Chelliah
University of Virginia
Mechanical Aerospace & Nuclear Eng. Dept.
Thornton Hall
Charlottesville, VA 22903
Phone: 804 924-6037
Fax: 804 982-2037
E-mail: harsha@virginia.edu

Gung Chen
Yale University
Mechanical Engineering Dept.
P.O. Box 208286
New Haven, CT 06520
Phone: 203 432-4390
Fax: 203 432-7654

Lea-Der Chen
University of Iowa
Dept. of Mechanical Engineering
Iowa City, IA 52242
Phone: 319 335-5674
Fax: 319 335-5669
E-mail: ldchen@icaen.uiowa.edu

Robert K. Cheng
Lawrence Berkeley Laboratory
Energy & Environment Div.
B29C-102; 1 Cyclotron Rd.
Berkeley, CA 94720
Phone: 510 486-5438
Fax: 510 486-7303
E-mail: rkc@csa.lbl.gov

Sergey Cheskis
Tel Aviv University
School of Chemistry
Ramat Aviv
Tel Aviv, 69978 Israel
Phone: 97236408324
Fax: 97236409293
E-mail: cheskis@ccsg.tau.ac.il

Mun Young Choi
University of Illinois/Chicago
Dept. of Mechanical Engineering; MC 251
2019 Engineering Res. Fac.; 842 W. Taylor St.
Chicago, IL 60607-7022
Phone: 312 996-7389
Fax: 312 413-0447

Jacob N. Chung
Washington State University
Mechanical & Materials Engineering Dept.
Pullman, WA 99164-2920
Phone: 509 335-3222
Fax: 509 335-4662
E-mail: chung@wsuvm1.csc.wsu.edu

Ron Colantonio
NASA Lewis Research Center
M.S. 500-115; 21000 Brookpark Rd.
Cleveland, OH 44135
Phone: 216 433-6370
Fax: 216 433-8660

Leon S. Collins
NASA Lewis Research Center
M.S. 333-1; 21000 Brookpark Rd.
Cleveland, OH 44135
Phone: 216 433-2360

Robert Corban
NASA Lewis Research Center
M.S. 500-217; 21000 Brookpark Rd.
Cleveland, OH 44135
Phone: 216 433-6642
Fax: 216 433-8660
E-mail: rcorban@lerc.nasa.gov

Thomas O. Cressman
NASA Lewis Research Center
M.S. 86-10; 21000 Brookpark Rd.
Cleveland, OH 44135
Phone: 216 433-3788
Fax: 216 433-2215

Roger K. Crouch
NASA Headquarters
Code UGS
Washington, DC 20546-0001
Phone: 202 358-0818
Fax: 202 358-3091
E-mail: rkrcrouch@gm.hq.nasa.gov

Werner Dahm
University of Michigan
Aerospace Engineering Dept.
Ann Arbor, MI 48109-2118
Phone: 313 764-4318
Fax: 313 763-0578

Larry DeLucas
University of Alabama/Birmingham
Center for Macromolecular Crystallography
Birmingham, AL 35242
Phone: 205 934-5329
Fax: 205 934-0480
E-mail: delucas@orion.cmc.edu

Michael A. Delichatsios
Factory Mutual Research
Noorwood, MA 02062
Phone: 617 255-4981
Fax: 617 255-4024

Kim Destro-Sidik
Tal-Cut Company
M.S. 500-216; 21000 Brookpark Rd.
Cleveland, OH 44135
Phone: 216 433-8449
Fax: 216 433-8545
E-mail: destro@lerc.nasa.gov

Dan L. Dietrich
NASA Lewis Research Center
M.S. 110-3; 21000 Brookpark Rd.
Cleveland, OH 44135
Phone: 216 433-8759
Fax: 216 433-3793
E-mail: daniel@lms01.lerc.nasa.gov

Edward L Dreizin
AeroChem Research Labs, Inc.
Princeton, NJ 08542
Phone: 609 921-7070
Fax: 609 329-8292

James F. Driscoll
University of Michigan
Aerospace Engineering Dept.
3004 FXB Bldg.
Ann Arbor, MI 48109-2118
Phone: 313 936-0101
Fax: 313 763-0578
E-mail: jamesfd@engin.umich.edu

Frederick L. Dryer
Princeton University
Mechanical & Aerospace Engineering Dept.
P.O. Box CN5263
Princeton, NJ 08544-5263
Phone: 609 258-1914
Fax: 609 258-1939
E-mail: fldryer@pucc.princeton.edu

Fokion Egolfopoulos
University of Southern California
Mechanical Engineering Dept.
3650 McClintock Avenue
Los Angeles, CA 90089-1453
Phone: 213 740-0480
Fax: 213 740-8071
E-mail: egolfopo@alnitak.usc.edu

Sergei Egorov
Russian Space Agency
Keldysh Scientific Research Inst. of Thermal Processes
8, Onezhskaya, Moscow, Russia 125438
Phone: 7 095-456-4656
Fax: 7 095-456-8228

Christian Eigenbrod
ZARM
Drop Tower, Bremen
Center of Applied Space Tech. & Mic
28359 Bremen, Germany 49
Phone: 49-421-218-4078
Fax: 49-421-218-4946
E-mail: eigen@zarm9.zarm.uni-bremen.de

Said E. Elghobashi
University of California, Irvine
Mechanical & Aerospace Engineering Dept.
Irvine, CA 92717
Phone: 714 824-6131
Fax: 714 824-8585
E-mail: selghoba@uci.edu

Jamie S. Ervin
University of Dayton
Mechanical Engineering Dept.
300 College Park
Dayton, OH 45469-0210
Phone: 513 229-2998
Fax: 513 229-3433
E-mail: jamie@snake.appl.wpafb.af.mil

David A. Everest
NIST
Building and Fire Research Laboratory
Bldg. 224; Rm 3360 NIST
Gaithersburg, MD 20899
Phone: 301 975-6870
Fax: 301 975-4052
E-mail: dave@cfr50.cfr.nist.gov

Gerard M. Faeth
University of Michigan
Aerospace Engineering Dept.
3000 FXB Bldg.
Ann Arbor, MI 48109-2118
Phone: 313 764-7202
Fax: 313 763-0578
E-mail: gmfaeth@um.cc.umich.edu

Francis E. Fendell
TRW Space & Electronics Group
Ocean Technology Dept.
One Space Park (RI/1062)
Redondo Beach, CA 90278
Phone: 310 812-0327
Fax: 310 812-7589
E-mail: frank@astrodog.sp.trw.com

Paul V. Ferkul
Analex Corporation
M.S. 500-115; 21000 Brookpark Rd.
Cleveland, OH 44135
Phone: 216 433-8107
Fax: 216 433-8660
E-mail: paul.ferkul@lerc.nasa.gov

Carlos Fernandez-Pello
University of California/Berkeley
Mechanical Engineering Dept.
6105 Etcheverry Hall
Berkeley, CA 94611
Phone: 510 642-6554
Fax: 510 642-6163
E-mail: ferpello@euler.me.berkeley.edu

Colleen Fitzpatrick
Rice Systems
1820 E. Garry St.
Tustin, CA 92705
Phone: 714 964-0324
Fax: 714 964-9338
E-mail: rxgk36a@prodigy.com

Rainer Forke
DARA GmbH
Koenigswinterer Strasse 522-524
Bonn, Germany 53227
Phone: 02-28-144-7327
Fax: 02-28-144-7327

Raymond Friedman
17 Cambridge Drive
Boynton Beach, FL 33436
Phone: 407 738-6073

Robert Friedman
NASA Lewis Research Center
M.S. 500-115; 21000 Brookpark Rd.
Cleveland, OH 44135
Phone: 216 433-5697
Fax: 216 433-8660
E-mail: rfriedm@lims01.lerc.nasa.gov

Robert J. Frye
NASA Lewis Research Center
M.S. 500-115; 21000 Brookpark Rd.
Cleveland, OH 44135
Phone: 216 433-5296
Fax: 216 433-8660

David Gerding
Cleveland State University
AMC Dept.
1751 E. 23 St.
Cleveland, OH 44114
Phone: 216 687-4603
Fax: 216 687-9260

Iskender Gokalp
Centre National de la Recherche Scientifique
SPI/Laboratoire de Combustion et Systemes Reactifs
I C av. de la Recherche Scientifique
Orleans Cedex 02, France 45071
Phone: 33-13-851-5463
Fax: 33-13-851-7875
E-mail: gokalp@cnsr-orleans.fr

Suleyman Gokoglu
NASA Lewis Research Center
M.S. 500-115; 21000 Brookpark Rd.
Cleveland, OH 44135
Phone: 216 433-5499
Fax: 216 433-8660
E-mail: msgokog@mars.lerc.nasa.gov

Jeffrey S. Goldmeer
NASA Lewis Research Center
M.S. 500-115; 21000 Brookpark Rd.
Cleveland, OH 44135
Phone: 216 433-3686
Fax: 216 433-8660
E-mail: goldmeer@proxima.lerc.nasa.gov

Subramanyam Gollahalli
University of Oklahoma
School of Aerospace & Mechanical Engineering
Room 212; 865 Asp Avenue
Norman, OK 73019
Phone: 405 325-5011
Fax: 405 325-1088
E-mail: gollahal@mailhost.ecn.uoknor.edu

Alessandro Gomez
Yale University
Mechanical Engineering Dept.
New Haven, CT 06977
Phone: 203 432-4384

Sam Goroshin
McGill University
Dept. of Mechanical Engineering
Montreal, PQ H3A 2K6 Canada
Phone: 514 398-6309
Fax: 514 398-7365
E-mail: goroshin@mecheng.lan.mcgill.edu

Paul S. Greenberg
NASA Lewis Research Center
M.S. 110-3; 21000 Brookpark Rd.
Cleveland, OH 44135
Phone: 216 433-3621
Fax: 216 433-3793
E-mail: paulg@straugguess.lerc.nasa.gov

DeVon Griffin
NASA Lewis Research Center
M.S. 110-3; 21000 Brookpark Rd.
Cleveland, OH 44135
Phone: 216 433-8109
Fax: 216 433-3793
E-mail: devon@baggms.lerc.nasa.gov

Jacques Yves Guigne
Guigne International Ltd.
82 St. Thomas Line
Paradise, NF A1L 1C1 Canada
Phone: 709 895-3819
Fax: 709 895-3822
E-mail: guigne@nl.net.nf.ca

Jaime Guzman
Colorado School of Mines
Metallurgical & Materials Engineering Dept.
Golden, CO 80401
Phone: 303 273-3559

Uday Hegde
NYMA, Inc.
2001 Aerospace Pkwy.
Brook Park, OH 44142
Phone: 216 433-8744
Fax: 216 433-8660

Jurgen R. Held
Daimler-Benz Aerospace/Dornier
RIX 321
Friedrichshafen, Germany D-88039
Phone: 49-75-458-5607
Fax: 49-75-458-4429

Roger D. Helmick
Analex Corporation
3001 Aerospace Parkway
Brook Park, OH 44142
Phone: 216 977-0458
Fax: 216 977-0200

Jean Hertzberg
University of Colorado/Boulder
Mechanical Engineering Dept.
Campus Box 427
Boulder, CO 80309-0427
Phone: 303 492-5092
Fax: 303 492-2863
E-mail: hertzberg@colorado.edu

David Hirsch
Allied Signal Aerospace
P.O. Drawer MM
Las Cruces, NM 88005
Phone: 505 524-5532

Simone Hochgreb
Massachusetts Institute of Technology
Mechanical Engineering Dept.
31-169; 77 Massachusetts Ave.
Cambridge, MA 02139
Phone: 617 253-0927
Fax: 617 253-9453
E-mail: simone@mit.edu

Linton Kaneki Honda
University of Southern California
Mechanical Engineering Dept.
OHE 430 H
Los Angeles, CA 90089-1453
Phone: 213 740-0496
Fax: 213 740-8071
E-mail: honda@scf.usc.edu

Jack B. Howard
Massachusetts Institute of Technology
Chemical Engineering Dept.
MIT 66-454; 77 Massachusetts Ave.
Cambridge, MA 02139-4307
Phone: 617 253-4574
Fax: 617 258-5042
E-mail: jbhoward@athena.mit.edu

Steve Hwang
Notre Dame University
Chemical Engineering Dept.
182 Fitzpatrick Hall
Notre Dame, IN 46601
Phone: 219 631-5160
Fax: 219 631-8366

Mounir Ibrahim
Cleveland State University
Mechanical Engineering Dept.
Cleveland, OH 44115
Phone: 216 687-2580
Fax: 216 687-9280

Kenichi Ito
Hokkaido University
Mechanical Engineering Dept.
Kita-13, Nishi-8, Kita-ku
Sapporo, Japan 060
Phone: 81 11-706-6385
Fax: 81 11-706-7889

Dwight Janoff
Lockheed/Martin
Materials Technologies, Manufacturing & Testing Dept.
2400 NASA Rd.
Houston, TX 77058
Phone: 713 333-6072
Fax: 713 333-7727
E-mail: janoff@lock.jsc.nasa.gov

Jozef Jarosinski
Aviation Institute
Dept. of Piston Engines
Aloja Krakowska 110/114
Warszawa, Poland 02-256
Phone: 48-22-464495
Fax: 48-22-464432

Subash Jayawardena
NASA Lewis Research Center
M.S. 500-102; 21000 Brookpark Rd.
Cleveland, OH 44135
Phone: 216 433-2842
Fax: 216 433-8050
E-mail: ssj4200@lims01.lerc.nasa.gov

Ching-Biau Jiang
2500 Derbyshire Rd. #10
Cleveland Hts., OH 44106
Phone: 216 397-9169
E-mail: cxj13@po.cwru.edu

Sang W. Joo
Wayne State University
Dept. of Mechanical Engineering
Detroit, MI 48202
Phone: 313 577-3782
Fax: 313 577-8789
E-mail: joo@fluid.eng.wayne.edu

Pierre Joulain
Laboratoire de Combustion et Detonique
ENSMA Universite de Poitiers UPR 9028 au CNRS
BP 109 Site du Futuroscope
8690 Futuroscope Cedex, France
Phone: 33 49-49-8290
Fax: 33 49-49-8291

Toshikazu Kadota
University of Osaka Prefecture
Dept. of Mechanical Engineering
Gakuen-cho
Sakai, Osaka, Japan 593
Phone: 81-0722-50-2328
Fax: 81-0722-50-2328

Kazhikathra Kailasanath
Naval Research Laboratory
Laboratory for Computational Physics & Fluid Dynamic
Code 6410; Naval Research Laboratory
Washington, DC 20375
Phone: 202 767-2402
Fax: 202 767-4798
E-mail: kailas.@lcp.nrl.navy.mil

Takashi Kashiwagi
NIST
Building & Fire Research Laboratory
B224/Room B258
Gaithersburg, MD 20899
Phone: 301 975-6699
Fax: 301 975-4052
E-mail: tkfire@enh.nist.gov

Viswanath R. Katta
Systems Research Labs
2800 Indian Ripple Rd.
Dayton, OH 45440-3696
Phone: 513 255-8781
Fax: 513 255-1125

Kazunori Kawasaki
Nissan Motor Co. Ltd.
Aerospace Division
3-5-1 Momoi Sugunami-ku
Tokyo, Japan 167
Phone: 81-3-3301-6670
Fax: 81-3-3301-6711

Merrill K. King
NASA Headquarters
Code UGS; 300 E Street SW
Washington, DC 20546-0001
Phone: 202 358-0817
Fax: 202 358-3091
E-mail: mking@gm.olmsa.hq.nasa.gov

Fred J. Kohl
NASA Lewis Research Center
M.S. 500-115; 21000 Brookpark Rd.
Cleveland, OH 44135
Phone: 216 433-2866
Fax: 216 433-8660

Darin R. Kohles
Orbital Technologies Corporation
402 Gammon Place Suite 200
Madison, WI 53719
Phone: 608 833-1992
Fax: 608 833-5050

Joseph F. Konecny
Case Western Reserve University
Mechanical & Aerospace Engineering Dept.
10900 Euclid Ave.
Cleveland, OH 44106
Phone: 216 368-4584
Fax: 216 368-6445

Michikata Kono
University of Tokyo
Dept. of Aeronautics & Space
7-3-1 Hongo, Bunkyo-ku
Tokyo 113, Japan
Phone: 81-3-3812-2111
Fax: 81-3-3818-7493
E-mail: mkono@tansei.cc.u-tokyo.ac.jp

Jerry C. Ku
Wayne State University
Mechanical Engineering Dept.
5050 Anthony Wayne Drive
Detroit, MI 48202
Phone: 313 577-3814
Fax: 313 577-8787
E-mail: jku@eng.wayne.edu

Keiichi Kuwahara
IHI
Research Institute
1, Shin-Nakahara-cho, Isogu-ku
Yokohama, Japan 235
Phone: 81-45-759-2175
Fax: 81-45-759-2185

Ming-Chia Lai
Wayne State University
Mechanical Engineering Dept.
5050 Anthony Wayne Drive
Detroit, MI 48202
Phone: 313 577-3893
Fax: 313 577-8789
E-mail: lai@moon1.eng.wayne.edu

Nandu Lakkaraju
Michigan State University
Dept. of Mechanical Engineering
East Lansing, MI 48824
Phone: 517 353-9180
Fax: 517 353-1750

Richard W. Lauver
NASA Lewis Research Center
M.S. 500-115; 21000 Brookpark Rd.
Cleveland, OH 44135
Phone: 216 433-2860
Fax: 216 433-8660
E-mail: rwlxx1.lims01.nasa.lerc.gov

Chung K. Law
Princeton University
Mechanical & Aerospace Engineering Dept.
P.O. Box CN 5263
Princeton, NJ 08544
Phone: 609 258-5271
Fax: 609 258-6233

Stephen Lawn
Analex Corporation
AOS; 3001 Aerospace Pkwy.
Brook Park, OH 44142
Phone: 216 977-0255
Fax: 216 977-0200
E-mail: sclawn@lims01.lerc.nasa.gov

Anthony S. Lee
University of Virginia
Mechanical Engineering Dept.
570 Edgemont Rd.
Charlottesville, VA 22903
Phone: 804 982-5354
Fax: 804 982-5357
E-mail: asl9c@virginia.edu

Jack Lekan
NASA Lewis Research Center
M.S. 500-216; 21000 Brookpark Rd.
Cleveland, OH 44135
Phone: 216 433-3459
Fax: 216 433-8660
E-mail: lekan@lims01.lerc.nasa.gov

Mark Linne
University of Colorado/Boulder
Mechanical Engineering Dept.
C.B. 427
Boulder, CO 80309-0427
Phone: 303 492-2351
Fax: 303 492-2863

Gregory T. Linteris
NIST
Fire Science Division
Gaithersburg, MD 20899
Phone: 301 975-2283
Fax: 301 975-4052
E-mail: linteris@cfr16.cfr.nist.gov

Jianbang Liu
University of Southern California
Mechanical Engineering Dept.
OHE 430 H
Los Angeles, CA 90089-1453
Phone: 213 740-0496
Fax: 213 740-8071

Marshall Long
Yale University
Mechanical Engineering Dept.
P.O. Box 208284
New Haven, CT 06520
Phone: 203 432-4229
E-mail: mblong@cld3.eng.yale.edu

David Lozinski
McMaster University
Mathematics Dept.
Hamilton Ontario, L8S 4K1 Canada
Phone: 905 525-9140 X27361
Fax: 905 522-0935
E-mail: lozinsk@icarus.math.mcmaster.ca

Stephen B. Margolis
Sandia National Lab.
Combustion Research Facility
M.S. 9051
Livermore, CA 94551-0969
Phone: 510 294-3073
Fax: 510 294-1004
E-mail: margoli@california.sandia.gov

Moshe Matalon
Northwestern University
Engineering Sciences & Applied Math. Dept.
2145 Sheridan Road
Evanston, IL 60208
Phone: 708 491-5397
Fax: 708 491-2178
E-mail: matalon@nwu.edu

Bernard J. Matkowsky
Northwestern University
Engineering Sciences & Applied Math. Dept.
2145 Sheridan Road
Evanston, IL 60208
Phone: 708 491-5396
Fax: 708 491-2178
E-mail: mat@mat.esam.nwu.edu

Tania Mattor
301 Malley Dr. #309
Northglen, CO 80233
Phone: 303 450-6728
Fax: 303 450-6728
E-mail: tmattor@colorado.mines.edu

Paul J. McGinn
Notre Dame University
Chemical Engineering Dept.
182 Fitzpatrick Hall
Notre Dame, IN 46601
Phone: 219 631-6151
Fax: 219 631-8366

Kevin McGrattan
NIST
Building & Fire Research Laboratory
Room A-345; Polymers Bldg.
Gaithersburg, MD 20899
Phone: 301 975-2712
Fax: 301 869-3531
E-mail: mcgratta@cam.nist.gov

J. Thomas McKinnon
Colorado School of Mines
Chemical Engineering Dept.
1500 Illinois St.
Golden, CO 80401
Phone: 303 273-3098
Fax: 303 273-3730
E-mail: jmckinno@mines.colorado.edu

Constantine Megaridis
University of Illinois Chicago
Mechanical Engineering Dept.
M/C 251; 842 W. Taylor Street
Chicago, IL 60607
Phone: 312 996-3436
Fax: 312 413-0447
E-mail: cmm@dino.me.uic.edu

Simon Melikian
Analex Corporation
AOS; 3001 Aerospace Pkwy.
Brook Park, OH 44142
Phone: 216 977-0262
Fax: 216 977-0200
E-mail: scmeli@lims01.lerc.nasa.gov

Suresh Menon
Georgia Institute of Technology
School of Aerospace Engineering
Atlanta, GA 30332
Phone: 404 853-9160
Fax: 404 894-2760
E-mail: menon@falcon.ae.gatech.edu

Alexander G. Merzhanov
Russian Academy of Sciences
Institute of Structural Macrokinetics
Chernogolovka, Moscow, Russia 142432
Phone: 7-096-517-1157
Fax: 7-095-201-7357

Fletcher Miller
NASA Lewis Research Center
M.S. 110-3; 21000 Brookpark Rd.
Cleveland, OH 44135
Phone: 216 433-8845
Fax: 216 433-3793
E-mail: fletcher@rosebud

Prabhakar Misra
Howard University
Physics & Astronomy Dept.
Laser Spect. Lab.; 2355 Sixth St., N.W.
Washington D.C., 20059
Phone: 202 806-4913
Fax: 202 806-4429
E-mail: misra@cldc.howard.edu

John J. Moore
Colorado School of Mines
Metallurgical & Materials Engineering Dept.
Golden, CO 80401
Phone: 303 273-3770
Fax: 303 273-3795
E-mail: jjmoore@flint.mines.colorado.edu

Emily Nelson
NASA Lewis Research Center
M.S. 105-1; 21000 Brookpark Rd.
Cleveland, OH 44135
Phone: 216 433-3268
Fax: 216 433-5033
E-mail: emily@sarah.lerc.nasa.gov

Takashi Niioka
Tohoku University
Institute of Fluid Science
Sendai, Japan

David A. Nordling
NASA Lewis Research Center
M.S. 110-3; 21000 Brookpark Rd.
Cleveland, OH 44135
Phone: 216 433-9417
Fax: 216 433-3793
E-mail: nordlin@lims01.lerc.nasa.gov

Sandra Olson
NASA Lewis Research Center
M.S. 500-115; 21000 Brookpark Rd.
Cleveland, OH 44135
Phone: 216 433-2859
Fax: 216 433-8660
E-mail: sandra.olson@lerc.nasa.gov

M. Volkan Otugen
Polytechnic University
Aerospace Engineering Dept.
Six Metrotech Center
Brooklyn, NY 11201
Phone: 516 755-4385
Fax: 516 755-4404
E-mail: votugen@rama.poly.edu

Howard B. Palmer
Penn State University
Fuel Science Dept.
224 Academic Projects Bldg.
University Park, PA 16802
Phone: 814 863-8039
Fax: 814 856-3075

Gopal Patnaik
Berkeley Research Associates
P.O. Box 852
Springfield, VA 22150
Phone: 202 767-3531
Fax: 202 767-4798
E-mail: patnaik@lcp.nrl.navy.mil

Howard Pearlman
1305 Bobby Lane #104
Westlake, OH 44145
Phone: 216 433-3710
Fax: 216 433-8660

Rick Pettegrew
NASA Lewis Research Center
M.S. 500-115; 21000 Brookpark Rd.
Cleveland, OH 44135
Phone: 216 433-8321
Fax: 216 433-8660
E-mail: rdp4@po.cwru.edu

Nancy Piltch
NASA Lewis Research Center
M.S. 110-3; 21000 Brookpark Rd.
Cleveland, OH 44135
Phone: 216 433-3637
Fax: 216 433-3793
E-mail: piltch@ariel.lerc.nasa.gov

Mark D. Poljak
NASA Lewis Research Center
M.S. 500-115; 21000 Brookpark Rd.
Cleveland, OH 44135
Phone: 216 433-3571
Fax: 216 433-8660

Ishwar K. Puri
University of Illinois Chicago
Mechanical Engineering Dept.
M.C. 251; 842 W. Taylor St. Rm 2039 ERF
Chicago, IL 60607-7022
Phone: 312 413-7560
Fax: 312 413-0447
E-mail: ilpuri@uic.edu

Jun Qian
403B Deveraux Ave.
Princeton, NJ 08540
Phone: 609 258-5178
E-mail: qiun@blaze.princeton.edu

Bassem Ramadan
Michigan State University
Dept. of Mechanical Engineering
East Lansing, MI 48824
Phone: 517 353-9180
Fax: 517 353-1750

Christopher Raymond
Northwestern University
Engineering Sciences & Applied Math. Dept.
2145 Sheridan Road
Evanston, IL 60208
Phone: 708 491-5396
Fax: 708 491-2178
E-mail: craymond@courant.eecs.nwu.edu

Mark Reeder
NASA Lewis Research Center
M.S. 77-1; 21000 Brookpark Rd.
Cleveland, OH 44135
Phone: 216 433-3646
E-mail: mreeder@lms02.lerc.nasa.gov

Robert C. Rhome
NASA Headquarters
Microgravity Sciences & Applications Division
Code UG
Washington, DC 20546-0001
Phone: 202 358-1490
Fax: 202 358-3091
E-mail: rrhome@hq.nasa.gov

Eric E. Rice
Orbital Technologies Corporation
402 Gammon Place; Suite 200
Madison, WI 53719
Phone: 608 833-1992
Fax: 608 833-5050

Judith Robey
NASA Headquarters
Code UG; 300 E Street, S.W.
Washington, DC 20546
Phone: 202 358-0823
Fax: 202 358-3091

Alex Rogachev
Notre Dame University
Chemical Engineering Dept.
182 Fitzpatrick Hall
Notre Dame, IN 46601
Phone: 219 631-5699
Fax: 219 631-8366

Dennis W. Rohn
NASA Lewis Research Center
M.S. 86-15; 21000 Brookpark Rd.
Cleveland, OH 44135
Phone: 216 433-2044
E-mail: lvrohn@lms.lerc.nasa.gov

James Roncace
ADF, Inc.
M.S. ADF; 3003 Aerospace Parkway
Brook Park, OH 44142
Phone: 216 977-0348
Fax: 216 977-0350

Paul Ronney
University of Southern California
Dept. of Mechanical Engineering
OHE 430 L
Los Angeles, CA 90089-1453
Phone: 213 740-0490
Fax: 213 740-8071
E-mail: ronney@rcf.usc.edu

Howard Ross
NASA Lewis Research Center
M.S. 500-115; 21000 Brookpark Rd.
Cleveland, OH 44135
Phone: 216 433-2562
Fax: 216 433-8660
E-mail: hross@lerc.nasa.gov

Gary Ruff
Drexel University
Mechanical Engineering & Mechanics Dept.
32nd & Chestnut Sts.
Philadelphia, PA 19104
Phone: 215 895-1373
Fax: 215 895-1478
E-mail: gruff@coe.drexel.edu

Kurt Sacksteder
NASA Lewis Research Center
M.S. 500-115; 21000 Brookpark Rd.
Cleveland, OH 44135
Phone: 216 433-2857
Fax: 216 433-8660
E-mail: kurt.sacksteder@lerc.nasa.gov

Takashi Sakuraya
Japan Space Utilization Promotion Center
Drop Facilities Utilization Dept.
3-30-16 Nishiwaseda Shinjuku
Tokyo, Japan
Phone: 81-3-5273-2745
Fax: 81-3-5273-0705

Jack Salzman
NASA Lewis Research Center
M.S. 500-201; 21000 Brookpark Rd.
Cleveland, OH 44135
Phone: 216 433-2868
Fax: 216 433-8660

Subra Sankar
Aerometrics, Inc.
550 Del Rey Avenue
Sunnyvale, CA 94086
Phone: 408 738-6688
Fax: 408 738-6871

Jun'ichi Sato
IHI Research Institute
Fluid Dynamics & Combustion Dept.
3-1-15 Toyosu Koto-Ku
Tokyo 135, Japan
Fax: 81-3-3534-3322

David N. Schiller
Univ. of California/Irvine
Mechanical & Aerospace Engineering Dept.
3101 Engineering Gateway
Irvine, CA 92717
Phone: 714 824-7160
Fax: 714 824-8585
E-mail: dschille@uci.edu

Kathy Schubert
NASA Lewis Research Center
M.S. 500-217; 21000 Brookpark Rd.
Cleveland, OH 44135
Phone: 216 433-5331
Fax: 216 433-8660

Daniel Schult
Northwestern University
Engineering Sciences & Applied Math. Dept.
2145 Sheridan Road
Evanston, IL 60208
Phone: 708 491-5396
Fax: 708 491-2178
E-mail: dan@zeldovich.eecs.nwu.edu

Donald Schultz
NASA Lewis Research Center
M.S. 500-115; 21000 Brookpark Rd.
Cleveland, OH 44135
Phone: 216 433-5352
Fax: 216 433-8660

Richard Seasholtz
NASA Lewis Research Center
M.S. 77-1; 21000 Brookpark Rd.
Cleveland, OH 44135
Phone: 216 433-3754
Fax: 216 433-8643
E-mail: seasholtz@lerc.nasa.gov

Tariq Shamim
University of Michigan
Mechanical Eng. & Applied Mechanics Dept.
2042 G.G. Brown Labs
Ann Arbor, MI 48109-2125
Phone: 313 763-7471
Fax: 313 747-3170
E-mail: shamim@umich.edu

Benjamin D. Shaw
University of California
Mechanical & Aeronautical Engineering Dept.
Davis, CA 95616
Phone: 916 752-4130
Fax: 916 752-4158
E-mail: bdshaw@ucdavis.edu

Hsin-Yi Shih
Case Western Reserve University
Mechanical & Aerospace Engineering Dept.
10900 Euclid Avenue
Cleveland, OH 44106
Phone: 216 368-5041
Fax: 216 368-6445

Konstantin Shkadinsky
Northwestern University
Engineering Sciences & Applied Math. Dept.
2145 Sheridan Road
Evanston, IL 60208
Phone: 708 491-5396
Fax: 708 491-2178
E-mail: kostia@zeldovich.eecs.nwu.edu

Alexander Shteinberg
Russian Academy of Sciences
Institute of Structural Macrokinetics
Chernogolovka, Moscow, Russia 142432
Phone: 7-096-517-1157
Fax: 7-095-201-7357

Martin Sichel
University of Michigan
Dept. of Aerospace Engineering
Ann Arbor, MI 48109-2118
Phone: 313 764-3388
Fax: 313 763-0578

Joel A. Silver
Southwest Sciences, Inc.
Santa Fe, NM 87505
Phone: 505 984-1322
Fax: 505 988-9230

Bhim S. Singh
NASA Lewis Research Center
M.S. 500-102; 21000 Brookpark Rd.
Cleveland, OH 44135
Phone: 216 433-5396
Fax: 216 433-8660

William A. Sirignano
University of California/Irvine
Mechanical & Aero. Engineering Dept.
Irvine, CA 92717
Phone: 714 824-3700
Fax: 714 824-3773
E-mail: sirignan@uci.edu

Lars Sitzki
Otto Von Guericke Universitat-Magdeburg
Chemisches Institute
Fakultat fur Naturwissenschaften; Universitatsplatz 2
D-39106 Magdeburg, Germany
Phone: 49-391-559-2223
Fax: 49-391-559-2131
E-mail: mkoch@physik.uni.magdeburg.de

Edward A. Sloat
Canadian Space Agency
Microgravity Sciences Program
6767 route de l'Aéroport
St. Hubert, Quebec, J3Y 8Y9 Canada
Phone: 514 926-4771
Fax: 514 926-4766

Alexander A. Smirnov
ANSER
Suite 800; 1215 Jefferson Davis Highway
Arlington, VA 22202
Phone: 703 416-3464
Fax: 703 416-8440

Mitchell Smooke
Yale University
Dept. of Mechanical Engineering
P.O. Box 208284; 15 Prospect St.
New Haven, CT 06520
Phone: 203 432-4344
Fax: 203 432-6775

Andrzej Sobiesiak
Queen's University
Mechanical Engineering Dept.
McLaughlin Hall
Kingston, Ontario, K7L 3N6 Canada
Phone: 613 545-6579
Fax: 613 545-6489
E-mail: andrzej@mech01.queen's.ca

Siavash Sohrab
Northwestern University
Dept. of Mechanical Engineering
2145 Sheridan Road
Evanston, IL 60208
Phone: 708 491-3572
Fax: 708 491-3915
E-mail: s-sohrab@nwu.edu

Thomas H. St. Onge
NASA Lewis Research Center
M.S. 500-217; 21000 Brookpark Rd.
Cleveland, OH 44135
Phone: 216 433-3557
Fax: 216 433-8660

Philip Stehno
NASA Lewis Research Center
M.S. 500-115; 21000 Brookpark Rd.
Cleveland, OH 44135
Phone: 216 433-8456
Fax: 216 433-8660
E-mail: pas4427@lims01.lerc.nasa.gov

Dennis Stocker
NASA Lewis Research Center
M.S. 500-115; 21000 Brookpark Rd.
Cleveland, OH 44135
Phone: 216 433-2166
Fax: 216 433-8660
E-mail: darkwod@lerc.nasa.gov

Peter M. Struk
NASA Lewis Research Center
M.S. 500-115; 21000 Brookpark Rd.
Cleveland, OH 44135
Phone: 216 433-2643
Fax: 216 433-8660
E-mail: pms@po.cwru.edu

Peter Sunderland
408 E. Kingsley St.; Apt. 12
Ann Arbor, MI 48104
Phone: 313 668-0475
Fax: 313 763-0578
E-mail: sunderla@engin.umich.edu

Thomas Sutliff
NASA Lewis Research Center
M.S. 500-216; 21000 Brookpark Rd.
Cleveland, OH 44135
Phone: 216 433-3887
E-mail: tsutliff@lerc.nasa.gov

James S. T'ien
Case Western Reserve University
Dept. of Mechanical & Aerospace Eng.
10900 Euclid Avenue
Cleveland, OH 44106
Phone: 216 368-4581
Fax: 216 368-6445

Fumiaki Takahashi
University of Dayton
Research Institute
300 College Park
Dayton, OH 45469-0140
Phone: 513 252-8138
Fax: 513 252-9917
E-mail: fumi@snake.appl.wpafb.af.mil

Ghassan Tashtoush
University of Kentucky
Mechanical Engineering Dept.
521 CRMS Bldg.
Lexington, KY 40506
Phone: 606 257-6262
Fax: 606 257-3304
E-mail: gmtashoo@ukcc.uky.edu

Karsten Tittmann
Otto Von Guericke Universitat-Magdeburg
Chemisches Institute
Fakultat fur Naturwissenschaften; Universitatsplatz 2
D-39106 Magdeburg, Germany
Phone: 49-391-559-2223
Fax: 49-391-559-2131

Jose L. Torero
Laboratoire de Combustion et Detonique
ENSMA Univ. de Poitiers UPR 9028 au CNRS
BP 109 Site du Futuroscope
86960 Futuroscope Cedex, France
Phone: 33-49-49-8290
Fax: 33-49-49-8291

James D. Trolinger
MetroLaser
18006 Skypark Circle; Suite 108
Irvine, CA 92714-6428
Phone: 714 553-0688
Fax: 714 553-0495

Gretar Tryggvason
University of Michigan
Mechanical Engineering Dept.
315 Automotive Lab
Ann Arbor, MI 48109-2121
Phone: 313 763-1049
Fax: 313 764-4256
E-mail: gretar@engin.umich.edu

Stephen D. Tse
University of California/Berkeley
Mechanical Engineering Dept.
44 Hesse Hall
Berkeley, CA 94720
Phone: 510 643-5282
Fax: 510 642-1850
E-mail: sdytse@euler.berkeley.edu

Li-Keng Tseng
Purdue University
Mechanical Engineering Dept.
Rm. 128 Chaffee Hall, TSPC
West Lafayette, IN 47906-1003
Phone: 317 494-1513
Fax: 317 494-0530
E-mail: likeng@ecn.purdue.edu

Alan Tulkki
University of Michigan
Aerospace Engineering Dept.
3004 FXB Bldg.
Ann Arbor, MI 48109
Phone: 313 936-0111
Fax: 313 763-0578

David Urban
NASA Lewis Research Center
M.S. 500-115; 21000 Brookpark Rd.
Cleveland, OH 44135
Phone: 216 433-2835
Fax: 216 433-8660
E-mail: dlurban@proxima.lerc.nasa.gov

Brad VanDerWege
Massachusetts Institute of Technology
Mechanical Engineering Dept.
31-061; 77 Massachusetts Ave.
Cambridge, MA 02139
Phone: 617 253-3310
Fax: 617 253-9453
E-mail: bvdw@mit.edu

Randall Vander Wal
NYMA, Inc.
2001 Aerospace Pkwy.
Brook Park, OH 44142
Phone: 216 433-9065

Arvind Varma
Notre Dame University
Chemical Engineering Dept.
182 Fitzpatrick Hall
Notre Dame, IN 46601
Phone: 219 631-6491
Fax: 219 631-8366

M. Vedha-Nayagam
NASA Lewis Research Center
M.S. 500-115; 21000 Brookpark Rd.
Cleveland, OH 44135
Phone: 216 433-8702
Fax: 216 433-8660
E-mail: scvedha@mars.lerc.nasa.gov

Belimar Velazquez
Analex Corporation
3001 Aerospace Pkwy.
Brook Park, OH 44142
Phone: 216 977-0012
Fax: 216 977-0200

Vladimir A. Volpert
Northwestern University
Engineering Sciences & Applied Math. Dept.
2145 Sheridan Road
Evanston, IL 60208
Phone: 708 491-5396
Fax: 708 491-2178
E-mail: volodia@wave.esam.nwu.edu

Hannes Walter
ESA
Physics, Fluid & Material Sciences
Microgravity Dept.; 8-10, rue Mario-Nikis
75738 Paris, Cedex 15, France
Phone: 33-1-42-73-7319
Fax: 33-1-42-73-7560

David Walther
University of California/Berkeley
Mechanical Engineering Dept.
UC Berkeley Campus; 44 Hesse Hall
Berkeley, CA 94720
Phone: 510 643-5282
Fax: 510 642-1850
E-mail: walther@firebug.berkeley.edu

Joseph Wehrmeyer
University of Missouri/Columbia
Mechanical & Aerospace Engineering Dept.
Engineering Bldg. East
Columbia, MO 65211
Phone: 314 882-0878
Fax: 314 884-5090
E-mail: wehrmeyer@ecvax2.ecn.missouri.edu

Karen Weiland
NASA Lewis Research Center
M.S. 110-3; 21000 Brookpark Rd.
Cleveland, OH 44135
Phone: 216 433-3623
Fax: 216 433-3793
E-mail: karen@daisy.ler.nasa.gov

Bret N. Whiteside
Analex Corporation
3001 Aerospace Pkwy.
Brook Park, OH 44142
Phone: 216 977-0030
Fax: 216 977-0200

Indrek Wichman
Michigan State University
Dept. of Mechanical Engineering
East Lansing, MI 48824
Phone: 517 353-9180
Fax: 517 353-1750

Forman A. Williams
University of California/San Diego
Applied Mechanics & Eng. Sciences Dept.
Center for Energy & Combustion Res.; 9500 Gilman Dr.
La Jolla, CA 92093-0411
Phone: 619 534-5492
Fax: 619 534-5354
E-mail: faw@ames.ucsd.edu

Michael Winter
United Technologies Research Center
Advanced Optical Diagnostics
411 Silver Lane
East Hartford, CT 06108
Phone: 203 727-7805
Fax: 203 727-7911
E-mail: mw@utrc.utc.com

Wallace K. Wong
SSG, Inc.
150 Bear Hill Rd.
Waltham, MA 02154
Phone: 617 890-0204
Fax: 617 890-1267

Travis Woodger
Colorado School of Mines
Metallurgical & Materials Engineering Dept.
Golden, CO 80401
Phone: 303 273-3559

Jong-shinn Wu
University of Michigan
Aerospace Engineering Dept.
1839 Shirley Lane #785
Ann Arbor, MI 48105
Phone: 313 662-1446
Fax: 313 763-0578
E-mail: wwjjss@engin.umich.edu

Ming-Shin Wu
University of Southern California
Mechanical Engineering Dept.
OHE 430 H
Los Angeles, CA 90089-1453
Phone: 213 740-0496
Fax: 213 740-8071

Jiann C. Yang
NIST
Building. & Fire Research Laboratory
Building 224; Rm. B356
Gaithersburg, MD 20899
Phone: 301 975-6662
Fax: 301 975-4052
E-mail: jcy@enh.nist.gov

William Yanis
NASA Lewis Research Center
M.S. 110-3; 21000 Brookpark Rd.
Cleveland, OH 44135
Phone: 216 433-9410
Fax: 216 433-3793
E-mail: wyanis@redneck.lerc.nasa.gov

Yaw D. Yeboah
Clark Atlanta University
Dept. of Engineering
P.O. Box 141; 223 James P. Brawley Drive
Atlanta, GA 30314
Phone: 404 880-6619
Fax: 404 880-6880
E-mail: yyeboah@cau.auc.edu

Hu Chun Yi
Notre Dame University
Chemical Engineering Dept.
182 Fitzpatrick Hall
Notre Dame, IN 46601
Phone: 219 631-5699
Fax: 216 631-8366

Shinichi Yoda
NASDA
Space Experiment Dept.
2-1-1 Sengen Tsukuba-shi
Ibaraki-ken, Japan 315
Phone: 81-298-52-2775
Fax: 81-298-50-2233

Zeng-guang Yuan
NASA Lewis Research Center
M.S. 500-115; 21000 Brookpark Rd.
Cleveland, OH 44135
Phone: 216 433-2838
Fax: 216 433-8660
E-mail: zgyuan@convx1.lerc.nasa.gov

Bernard Zappoli
CNES
CT/ED/MV/FM
31055 Toulouse Cedex, France 31055
Phone: 33-61-27-4468
Fax: 33-61-27-4013
E-mail: zappoli@cst.cnes.fr

Liming Zhou
NASA Lewis Research Center
M.S. 500-115; 21000 Brookpark Rd.
Cleveland, OH 44135
Phone: 216 433-8087
Fax: 216 433-8660
E-mail: lzhou@lzhou.lerc.nasa.gov

Jingyi Zhu
University of Utah
Dept. of Mathematics
Salt Lake City, UT 84112
Phone: 801 581-3236
Fax: 801 581-4148
E-mail: zhu@math.utah.edu

Author Index

- Abbud-Madrid, Angel, 123
 Agrawal, Ajay K., 311
 Agrawal, Sanjay, 319
 Aharon, Israel, 95
 Altenkirch, Robert A., 11, 189, 463
 Andreeva, T. V., 195
 Atreya, Arvind, 319
 Avedisian, C. Thomas, 47
 Bachalo, William D., 269
 Bahadori, M. Yousef, 327
 Balashov, E. V., 195
 Baum, Howard R., 207, 319
 Bédât, Benoit, 395
 Belayev, A. Yu, 195
 Bhattacharjee, Subrata, 11, 189
 Branch, Melvyn C., 123
 Buckmaster, John, 389
 Buermann, Dale H., 269
 Bundy, Matthew, 11
 Bush, Michael T., 369
 Chao, Ruian, 189
 Chauveau, Christian, 71
 Chen, Gung, 77
 Chen, Lea-Der, 333
 Cheng, Robert K., 395
 Choi, Mun Young, 53, 285
 Dahm, Werner J. A., 339
 Daily, John W., 123
 Dietrich, Daniel L., 31, 59, 103, 285
 Dreizin Edward L., 129
 Driscoll, James F., 339
 Dryer, F. L., 65
 Duan, H. M., 147
 Dubinskiy, Mark A., 263
 Egolfopoulos, Fokion N., 401
 Egorov, S. D., 195
 Eigenbrod, Christian, 453
 Elghobashi S., 345
 Eng, James A., 415
 Ern, Alexandre, 445
 Faeth, G. M., 351, 469
 Fendell, F., 357
 Ferkul, Paul, 219
 Fernandez-Pello, A. Carlos, 19
 Friedman, Raymond, 466
 Frost, D., 141
 Fujita, Osamu, 201
 Gage, James W., 95
 Gard, Melissa Y., 175
 Gökalp, Iskender, 71
 Goldmeer, Jeffrey S., 135
 Gollahalli, Subramanyam R., 311
 Gomez, Alessandro, 77
 Goroshin, S., 141
 Greenberg, Paul, 25, 219, 247, 375
 Griffin, DeVon W., 175, 253, 311
 Hamins, Anthony, 115
 Hegde, Uday G., 327
 Held, T. J., 65
 Hertzberg, Jean, 363
 Hochgreb, Simone, 369
 Howard, Jack B., 467
 Hoy, Michael, 175
 Ito, Kenichi, 201
 Ivanov, A. V., 195
 Jagoda, J., 421
 Jenkins, Andrew J., 95
 Jensen, Kirk, 53
 Jiang, Ching-Biau, 219
 Joulain, P., 227
 Kadota, Toshikazu, 257
 Kahoe, Thomas J., 95
 Kailasanath, K., 409
 Kamal, Mohammed M., 263
 Kashiwagi, Takashi, 25, 207
 King, Merrill K., 3
 Kleine, H., 141
 Klimin, L. P., 195
 Kono, Michikata, 83, 103
 Kostiuik, Larry W., 395
 Ku, Jerry C., 375
 Law, Chung, 129, 415, 461
 Lee, J. H. S., 143
 Lee, J. C., 65
 Lee, Kyeong-Ook, 53
 Lee, Y. Y., 345
 Lin, K.-C., 351
 Linne, Mark, 363
 Linteris, Gregory T., 369
 Marchese, A. J., 65
 Matalon, Moshe, 381
 Matkowsky, Bernard J., 153
 McGinn, Paul J., 181
 McGrattan, Kevin, 207
 McKinnon, J. Thomas, 147
 Menon, S., 421
 Merzhanov, A. G., 159
 Mikami, Masato, 103
 Miller, Fletcher, 37
 Misra, Prabhakar, 263
 Molodetsky, Irinia E., 129
 Moore, John, 165
 Most, J. M., 227
 Niioka, Takashi, 427
 Olson, Sandra L., 19, 189
 Oran, E. S., 409
 Patnaik, G., 409
 Pearlman, Howard, 433
 Pettegrew, Richard D., 219
 Pickett, Kent, 319
 Ronney, Paul D., 213, 439
 Ross, Howard D., 31, 37
 Sacksteder, Kurt, 11, 25, 219, 309
 Sankar, Subramanian V., 269
 Sato, Jun'ichi, 89, 103
 Scherbakov, Vladimir A., 171
 Schiller, David, 37
 Semenov, A. V., 195
 Shamim, Tariq, 309
 Shaw, Benjamin D., 95
 Sheu, Jyh-Cherng, 333
 Shteinberg, Alexander S., 171
 Sichel, Martin, 339
 Silver, Joel A., 279
 Sirignano, William, 37
 Small, James F., Jr., 327
 Smooke, Mitchell D., 445, 471
 Stocker, Dennis P., 19, 327, 333
 Sujith, R., 421
 Sunderland, P. B., 351
 T'ien, J. S., 31, 135, 219
 Tang, Lin, 11, 189
 Thomas, Peter C., 11, 183
 Tong, Li, 375
 Torero, Jose L., 19, 227
 Urban, David, 135, 175, 233
 Vander Wal, Randy L., 285
 VanDerWege, B. A., 369
 Varma, Arvind, 181
 Voiteshonok, V. S., 195
 Weiland, Karen J., 291
 West, Jeff, 11, 189
 Wichman, Indrek S., 239
 Williams, Forman A., 103, 109
 Winter, Michael, 297
 Wong, Wallace K., 295
 Wu, F., 357
 Yang, Jiann C., 115
 Yanis, William, 253
 Yi, Hu Chun, 181
 Zaitsev, E. N., 195
 Zhong, R., 345
 Zhou, Liming, 327
 Zhou, Zhiquang, 285
 Zhu, Delin, 415

Preceding Page Blank

REPORT DOCUMENTATION PAGEForm Approved
OMB No. 0704-0188

Public reporting burden for this collection of information is estimated to average 1 hour per response, including the time for reviewing instructions, searching existing data sources, gathering and maintaining the data needed, and completing and reviewing the collection of information. Send comments regarding this burden estimate or any other aspect of this collection of information, including suggestions for reducing this burden, to Washington Headquarters Services, Directorate for Information Operations and Reports, 1215 Jefferson Davis Highway, Suite 1204, Arlington, VA 22202-4302, and to the Office of Management and Budget, Paperwork Reduction Project (0704-0188), Washington, DC 20503.

1. AGENCY USE ONLY (Leave blank)		2. REPORT DATE August 1995	3. REPORT TYPE AND DATES COVERED Conference Publication	
4. TITLE AND SUBTITLE Third International Microgravity Combustion Workshop			5. FUNDING NUMBERS WU-963-80-0J	
6. AUTHOR(S) Howard D. Ross, compiler				
7. PERFORMING ORGANIZATION NAME(S) AND ADDRESS(ES) National Aeronautics and Space Administration Lewis Research Center Cleveland, Ohio 44135-3191			8. PERFORMING ORGANIZATION REPORT NUMBER E-9727	
9. SPONSORING/MONITORING AGENCY NAME(S) AND ADDRESS(ES) National Aeronautics and Space Administration Washington, D.C. 20546-0001			10. SPONSORING/MONITORING AGENCY REPORT NUMBER NASA CP-10174	
11. SUPPLEMENTARY NOTES Responsible person, Howard D. Ross, organization code 6711, (216) 433-2562.				
12a. DISTRIBUTION/AVAILABILITY STATEMENT Unclassified - Unlimited Subject Category 29 This publication is available from the NASA Center for Aerospace Information, (301) 621-0390.			12b. DISTRIBUTION CODE	
13. ABSTRACT (Maximum 200 words) This Conference Publication contains 71 papers presented at the Third International Microgravity Combustion Workshop held in Cleveland, Ohio, from April 11 to 13, 1995. The purpose of the workshop was twofold: to exchange information about the progress and promise of combustion science in microgravity and to provide a forum to discuss which areas in microgravity combustion science need to be expanded profitably and which should be included in upcoming NASA Research Announcements (NRA).				
14. SUBJECT TERMS Microgravity; Combustion; Fires; Flammability			15. NUMBER OF PAGES 504	
			16. PRICE CODE A22	
17. SECURITY CLASSIFICATION OF REPORT Unclassified	18. SECURITY CLASSIFICATION OF THIS PAGE Unclassified	19. SECURITY CLASSIFICATION OF ABSTRACT Unclassified	20. LIMITATION OF ABSTRACT	